ULTRALOW THERMAL CONDUCTIVITY AND NOVEL THERMOELECTRIC MATERIALS

by

Jan-Hendrik Pöhls

Submitted in partial fulfillment of the
requirements for the degree of
Doctor of Philosophy

at

Dalhousie University
Halifax, Nova Scotia
August 2017

Contents

List of Tables

List of Figures

Abstract

More than half of the energy produced worldwide is lost as heat and even recovering a fraction of that would be beneficial for global climate change. Thermoelectric materials can recover waste heat and convert it to useful energy. However, thermoelectric materials are not commercially applied in many areas due to low efficiency. The search for high-performance thermoelectric materials is challenging because thermoelectrics require enhanced electronic properties and low thermal conductivity. A potential route to discover novel high-performance thermoelectric materials can be provided by first-principles calculations.

While the electrical properties can be calculated with a high accuracy, an accurate prediction of the heat transport is currently not feasible. However, insight into the heat transport can be given by computing the lowest limit of heat transport. In the present study, a new model for minimum thermal conductivity was developed in which the thermal energy is transported between entities of phonons oscillating in a range of frequencies and limited by the phonon mean speed.

This model was motivated by understanding the lowest experimental thermal conductivity reported to date for a fully dense solid, measured here for PCBM (κ = 0.07 W m^{-1} K^{-1} at 300 K) which agrees with the present model. Slightly higher thermal conductivities were determined herein for porous ZnO tetrapod composites. The latter experimental results were confirmed with finite element calculations.

In a high-throughput screening within The Materials Project the electronic properties of ∼48,000 inorganic compounds were calculated and two novel high-performance thermoelectric classes, XYZ_2 (X, Y: rare earth or transition metals; Z: Group VI elements) and metal phosphides, show promise. A variable relaxation time was developed using a semi-empirical approach to accurately calculate the temperature-dependent electronic properties.

Three compounds of the XYZ_2 class were synthesized and their thermoelectric properties were analyzed in both computational and experimental studies. All compounds exhibit extremely low thermal conductivity and a maximum figure of merit of ∼0.73 was found. As an example of metal phosphides, NiP_2 was synthesized and the experimental thermoelectric properties agree well with computation. The low thermal conductivity of the thermoelectrics was confirmed with the present model.

List of Abbreviations and Symbols Used

a	Unit cell length
a, b, c	Constants
a, b, c	Lattice constants
A	Absorption
A, B, C	Taylor expansion coefficients of Helmholtz energy
A_0, s, t	Fitting parameters for electron mobility
A_1, A_2, x, y, z	Fitting parameters for thermal conductivity
A_{cross}	Cross-sectional area
a_{dist}	Interatomic distance
$A_{surface}$	Surface area
A_α	Correction of absorption
B	Bulk modulus
$\vec{B}$	Magnetic field vector
B	Magnetic field
b_{drift}	Drift voltage
B_L	Peak broadening due to crystallite size
B_{VRH}	Voigt-Reuss-Hill averaged bulk modulus
B_ε	Peak broadening due to inhomogeneous strain
c, c_p	Specific heat (at constant pressure)
C	Heat capacity
C	Curie constant
c_{11}	Longitudinal elastic constant
C_D	Debye heat capacity
C_{el}	Electronic contribution of the heat capacity
$C_{element}$	Mass concentration of the element
c_{ij}	$6\times$ 6 elastic tensor
C_{k-g}	Expansion coefficient in reciprocal space
C_{mol}	Molar heat capacity
c_{offset}	Offset voltage
C_p	Heat capacity at constant pressure
$C_{p,pl}$	Heat capacity of platform and grease
$C_{p,pls}$	Heat capacity of platform, grease, and sample

$C_{p,sa}$	Heat capacity of the sample
$C_{p,sapphire}$	Heat capacity of sapphire
C_r	Heat capacity of the reference
$C_s(\omega)$	Heat capacity per unit volume
C_{sp}	Heat capacity of the sample
$C_{standard}$	Mass concentration of the standard
C_V	Heat capacity at constant volume
$C_{V,E}$	Einstein heat capacity
c_ε	Constant
d	Spacing between two lattice planes
d_{grain}	Grain size
$D_i(\omega)$	Phonon density of states
d_s	Diameter of the sample
E	Energy
$\vec{E}$	Electric field vector
$\vec{E}_0$	Electric (field) wave of incident light
$E_{acceleration}$	Acceleration potential energy
E_b	Energy of ideal supercell
E_{bin}	Binding energy
$E_{bin,secondaryedge}$	Binding energy of the secondary edge
E_c	Energy of the conduction band
E_{CBM}	Energy of the conduction band minimum
E_{decomp}	Energy difference between compound and competing phase
$E_{d,q}$	Energy of defect containing supercell
E_{edge}	Energy of the band edge
$E_{electrons}$	Energy of electrons
E_F^0	Fermi energy
E_g	Band gap energy
$E_{g,GS}$	Goldsmid-Sharp band gap energy
E_{IC}	Image-charge correction energy
E_k	Possible energy states of ‘free’ electrons
E_{kin}	Kinetic energy
E_{las}	Energy of the laser
$E_{unoccupied}$	Energy of unoccupied states

E_{VBM}	Energy of valence band maximum
E_α	Correction of extinction
f	Probability density function
F	Fluorescence
$\vec{F}$	Generalized force
$f(E,T)$	Fermi-Dirac distribution
F_e	External force
$f_{element}$	Matrix factor of the element
f_i	Fraction of atoms
$F_j(\eta)$	Fermi integral
$F_n(\vec{r})$	Quasi-Fermi level
$f_{standard}$	Matrix factor of the standard
f_α	Atomic scattering factor
$F(\Delta\dot{Q},t)$	Area of heat flow with respect to time
$F(\eta)$	Helmholtz energy
G	Shear modulus
G	Electrical conductance
$\vec{G}$	Reciprocal wave vector
G^*	Absorbing radiation
G^*_{amb}	Ambient irradiation
G^*_{ext}	External irradiation
G^*_m	Mutual irradiation from other boundaries
G_{VRH}	Voigt-Reuss-Hill averaged shear modulus
$h = 6.62607 \cdot 10^{-34}$ J·s	Planck constant
h,k,l	Miller indices
$\hbar = \frac{h}{2\pi} = 1.05457 \cdot 10^{-34}$ J·s	reduced Planck constant or Dirac constant
H	Enthalpy
H	Magnetic field strength
I	Electrical current
I_D	Intensity of the defect-induced peak
$I_{element}$	Intensity of the element
I_h	Heater current
I_G	Intensity of the 'graphite' peak
I_{max}	Maximum electrical current
$I_{standard}$	Intensity of the standard
$j_{n,x}$	Current density
$k = \frac{2\pi}{\lambda}$	Wave vector

K	Scherrer constant
$k_B = 1.3806485 \cdot 10^{-23}$ J K^{-1}	Boltzmann constant
k_f	Magnitude of outgoing wave vector
k_i	Magnitude of incoming wave vector
L	Thickness
L_0	Initial thickness
L_{box}	Length of a three-dimensional box
L_c	Crystallite size
L_{eff}	Effective Lorenz number
$L_{eff,0} = 2.44 \cdot 10^{-8}$ W Ω K^{-2}	Lorenz number for metals
L_α	Lorentzian-polarization factor
m	Ratio of the resistance of the load with respect to the resistance of the thermoelectric material
M	Magnetic moment
$barm$	Average atomic mass on crystallographic site
$\bar{M}$	Average atomic mass
M_1, M_2	Atomic masses
$m^*_\parallel$	Longitudinal component of the band effective mass
$m^*_\perp$	Transverse component of the band effective mass
m^*_b	Band effective mass
$m_{background}$	Mass of the empty pan (background)
m^*_{DOS}	Density of states effective mass
m_{dry}	Mass of dry sample
$m_e = 9.109 \cdot 10^{-31}$ kg	Mass of an electron
m_i	Mass of atom
$m_{pan,sapphire}$	Mass of aluminimum pan and sapphire sample
$m_{pan,sample}$	Mass of aluminimum pan and sample
$M_{red} = (M_1^{-1} + M_2^{-1})^{-1}$	Reduced mass
$m_{submerged}$	Mass of submerged sample
M_α	Multiplicity
n	Carrier concentration
n	Integer
N	Number of atoms in the unit cell
$\vec{n}$	Surface vector
n_0	Number of charge carriers
N_{Na}	Number of Na atoms

n_D	Number of atoms in the unit cell for the Debye model
n_E	Number of atoms in the unit cell for the Einstein model
N_e	Number of electrons
n_H	Hall carrier concentration
n_p	Principal quantum number
N_v	Electronic band degeneracy or valley degeneracy
n_α	Change in number of atoms (± 1)
p	Pressure
p	Momentum
$\vec{P}$	Polarization
P_0	Constant heater power
PF	Power factor
PF_{const}	Computed power factor with constant relaxation time
$PF_{variable}$	Computed power factor with variable relaxation time
P_α	Preferred orientation factor
$q = 1.602 \cdot 10^{-19}$ C	Elementary charge
Q	Heat flux
$\vec{Q}$	Heat flux vector
Q_c	Total heat flux
Q_{ext}	External energy source
Q_+	Released heat
Q_-	Absorbed heat
$\dot{Q}_r$	Heat flux of the reference
Q_{rad}	Energy per unit area and per unit time
$\dot{Q}_{sp}$	Heat flux of the sample
$R = 8.31446$ J mol^{-1} K^{-1}	Universal gas constant
R	Total electrical resistance
$\bar{r}$	Average atomic radius on crystallographic site
R_h	Heater resistance
r_H	Hall factor
R_H	Hall coefficient
R_{Hall}	Hall resistance
r_i	Radius of atom
R_L	Load resistance
R_{phr}	Thermal resistance between pan and heating stage for the reference

R_{phs}	Thermal resistance between pan and heating stage for the sample
R_{sp}	Thermal resistance between pan and sample
R_{wp}	Weighted Bragg factor
$R_{\Delta T}$	Residual of the temperature difference
$R_{\Delta V}$	Residual of the potential difference
$R_{\rho_{el}}$	Residual of the electrical resistivity
S	Seebeck coefficient
S_f	Scaling factor
S_{hkl}	Structure factor
s_{ij}	Compliance
S_n	n-type Seebeck coefficient
S_p	p-type Seebeck coefficient
T	Absolute temperature
$\bar{T} = \frac{T_h - T_c}{2}$	Average temperature
∇T	Temperature gradient
T_0	Cryostatic temperature
$t_{1/2}$	Time of temperature rise is half of the maximum temperature
T_{amb}	Ambient temperature
T_c	Cold-side temperature
T_C	Curie temperature
T_g	Glass transition temperature
T_h	Hot-side temperature
T_N	Néel temperature
T_{onset}	Onset temperature
T_{peak}	Peak temperature
T_r	Temperature of the reference
T_{sp}	Temperature of the sample
T_{trans}	Phase transition temperature
U	Internal energy
u, v	Thermoelectric functions
$U_k(\vec{r})$	Bloch function
$\langle U \rangle$	Average internal energy
u_α, v_α, w_α	Fractional coordinates in real space
V	Volume

$\bar{v}$	Average phonon mean speed
$v_g = \frac{\partial\omega}{\partial k}$	Group velocity
$\langle v_g \rangle$	Average group velocity
V_g	Voltage of the electron gun
v_i	Phonon mean speed
V_m	Molar volume
$v_p = \frac{\omega}{k}$	Phase velocity
$\langle v_p \rangle$	Average phase velocity
V_{PA}	Correction of the alignment of the electrostatic potential
V_{pp}	Peak-to-peak voltage *vs.* time signal of the AC measurement
v_s	Speed of sound
$v_{s,L}$	Longitudinal speed of sound
$v_{s,T}$	Transverse speed of sound
V_{UC}	Unit cell volume
W_{in}	Net work input
W_{out}	Net work output
x	Position
$X[\omega(\vec{k}), \vec{k}]$	Collective excitations
$x_D = \frac{\hbar\omega}{k_B T}$	Debye coefficient
Y	Young's modulus
z	Temperature-dependent thermoelectric figure of merit
Z	Atomic number
zT	Thermoelectric figure of merit

α	Coefficient of linear thermal expansion
α	Thermal diffusivity
α_V	Coefficient of volumetric thermal expansion
β	Interatomic force constant
β	Thermoelectric beta function
$\beta_{300\mathrm{K}}$	Thermoelectric beta function at 300 K
β_T	Isothermal compressibility
γ	Grüneisen parameter
Γ	Brillouin zone center
γ_0, CN_0, a	Fitting parameters for Grüneisen parameter
γ_{el}	Sommerfeld constant

ΔG	Change in Gibss energy
ΔH	Change in enthalpy
$\Delta H_{d,q}$	Defect formation energy
ΔH_{trs}	Change in enthalpy at the phase transition
Δl	Change in angular momentum
ΔL	Change in thickness
Δm_l	Change in magnetic quantum number
$\Delta \dot{Q}$	Change in heat flux
$\Delta \dot{Q}_{background}$	Heat flow of the background
$\Delta \dot{Q}_{sapphire+pan}$	Heat flow of the sapphire sample
$\Delta \dot{Q}_{sample+pan}$	Heat flow of the sample
ΔS	Change in entropy
Δt	Time difference between transmitted and received pulse
$\Delta T = T_h - T_c$	Temperature difference
ΔT_∞	Steady-state temperature difference between hot and cold side
ΔT_{max}	Maximum temperature difference
$\Delta T_{model}(t)$	Fitting temperature equation for thermal conductivity in continuous mode
ΔV	Potential difference
ΔV_{Hall}	Hall voltage drop
ΔV_∞	Steady-state potential difference
$\Delta V_{model}(t)$	Fitting potential difference equation for Seebeck coefficient
$\Delta \mu_\alpha$	Change in chemical potential with reference to its standard state
ε_T	Emissivity
$\varepsilon = E k_B^{-1} T^{-1}$	Reduced energy
ε	Inhomogeneous Strain
$\varepsilon_0 = 8.854 \cdot 10^{-12}$ F·m^{-1}	Electric permittivity of free space
ζ	Reduced carrier energy
$\eta = \frac{\zeta}{k_B T}$	Reduced chemical potential
η	Thermoelectric efficiency
η_c	Carnot efficiency
η_F	Order parameter

η_{max}	Maximum thermoelectric efficiency
θ	Angle between incoming X-rays and Miller planes
2θ	Bragg angle
θ_D	Debye temperature
θ_E	Einstein temperature
κ	Thermal conductivity
K	Total thermal conductance
κ_0	Star of wave vectors
κ_{bulk}	Bulk thermal conductivity
κ_{cell}	Sample thermal conductivity (blackbody radiation was excluded for the calculation)
κ_{el}	Electrical contribution to thermal conductivity
K_{empty}	Thermal conductance of the empty powder cell with blackbody radiation
$K_{empty,cell}$	Thermal conductance of the empty powder cell without blackbody radiation
K_{filled}	Thermal conductance of the filled powder cell with blackbody radiation
$K_{filled,cell}$	Thermal conductance of the filled powder cell without blackbody radiation
K_g	Thermal conductance between platform and sample
κ_{min}	Minimum thermal conductivity or amorphous limit
$\kappa_{min,Cahill}$	Minimum thermal conductivity based on the Cahill, Watson, and Pohl model
$\kappa_{min,Cahill,HT}$	Minimum thermal conductivity based on the Cahill, Watson, and Pohl model at high temperature
$\kappa_{min,CP,E}$	Minimum thermal conductivity based on the Cahill, Watson, and Pohl model from elastic constants
$\kappa_{min,CP,s}$	Minimum thermal conductivity based on the Cahill, Watson, and Pohl model from speeds of sound measurements
$\kappa_{min,dyn}$	Minimum thermal conducitivity based on the present model limited by dynamic disordering
$\kappa_{min,Einstein}$	Minimum thermal conductivity based on the Einstein model
$\kappa_{min,pho}$	Minimum experimental lattice thermal conductivity
$\kappa_{min,present}$	Minimum thermal conductivity based on the present model

$\kappa_{min,static}$	Minimum thermal conducitivity based on the present model limited by static disordering
κ_{pho}	Phononic contribution to thermal conductivity
$\kappa_{pho,aco}$	Acoustic term of the lattice thermal conductivity
$\kappa_{pho,aco,min}$	Lowest limit of the acoustic term of the lattice thermal conductivity
κ_{porous}	Measured (porous) thermal conductivity
K_{sample}	Thermal conductance of the sample
κ_{SE}	Thermal conductivity using the semi-empirical approach
K_{shoes}	Thermal conductance of the shoes
κ_{total}	Sample thermal conductivity (blackbody radiation was included for the calculation)
K_w	Thermal conductance between sample platform and heat sink
λ	wavelength
λ_{pho}	Phonon mean free path
λ_S	Scattering parameter
μ	Chemical potential of the electrons
$\mu_0 = 4\pi \cdot 10^{-7}$ H·m^{-1}	Permeability of vacuum
μ_{el}	Electron mobility
$\mu_{el,n}$	Electron mobility of electrons
$\mu_{el,p}$	Electron mobility of holes
μ_H	Hall mobility
μ_r	Relative permeability
μ_α^0	Chemical potential of element in standard state
ν	Frequency of X-rays
ν	Poisson's ratio
Ξ	Deformation potential
Π	Peltier coefficient
ρ	Mass density
ρ_{el}	Electrical resistivity
$\rho_{el,defect}$	Electrical resistivity due to defects
$\rho_{el,phonons}$	Electrical resistivity due to electron-phonon interactions
ρ_{liquid}	Mass density of the liquid
ρ_{sample}	Mass density of the sample
$\sigma_T = 5.67 \cdot 10^{-8}$ W m^{-2} K^{-4}	Stefan-Boltzmann constant

σ	Screening constant
σ_{const}	Computed electrical conductivity with constant relaxation time
σ_{el}	Electrical conductivity
$\sigma_{el,n}$	Electrical conductivity due to electrons
$\sigma_{el,p}$	Electrical conductivity due to holes
$\sigma_{variable}$	Computed electrical conductivity with variable relaxation time
τ	Torque
τ_1	Long time constant for heat capacity measurement
τ_2	Short time constant for heat capacity measurement
τ_2'	Time constant
τ_{el}	Relaxation time of conducting electrons
$\tau_{el,variable}$	Variable relaxation time
$\tau_{rel}(\omega) = \frac{\lambda_{pho}}{v_g}$	Relaxation time
$\tau_{rel,B}$	Relaxation time due to grain boundary scattering
$\tau_{rel,PD}$	Relaxation time due to point defect scattering
$\tau_{rel,U}$	Relaxation time due to Umklapp scattering
Φ	Porosity
$\Phi_{analyzer}$	Work function of the analyzer
Φ_B	Magnetic flux
Φ_g	Work function of the electron gun
Φ_{sample}	Work function of the sample
χ	Magnetic susceptibility
χ^2	Goodness of the PXRD refinement
$\overline{\overline{\chi}}_e$	Electric susceptibility tensor
Ψ	Thermoelectric function
ψ_+	Wavefunction of incoming wave
ψ_-	Wavefunction of reflected wave
$\psi_k(\vec{r})$	Position-dependent wavefunction
$\omega = 2\pi\nu$	Angular frequency
Ω	Volume of the k-space
ω_0	Initial angular frequency
ω_D	Debye frequency
ω_E	Einstein frequency
ω_{max}	Maximum angular frequency

ACMS	AC/DC Measurement System
AE	Auger electrons
ATAT	Alloy Theoretic Automated Toolkit
BHJ	Bulk hetero-junction
BSE	Backscattered electrons
C	Cooling
CBM	Conduction band minimum
CFEG	Cold field emission gun
CFESEM	Cold field emission scanning electron microscope
CN	Coordination number
c-NiP_2	NiP_2 in the cubic phase
CNT(s)	Carbon nanotube(s)
CNTT(s)	Carbon nanotube tube(s)
D peak	Defect-induced Raman peak
DFPT	Density functional perturbation theory
DFT	Density functional theory
DSC	Differential scanning calorimetry
DOS	Density of states
DTAC	Dodecyltrimethylammonium chloride
e^-	Electrons
EDS	Energy-dispersive X-ray spectroscopy
FACS	Finned air cooling system
fcc	Face-centered-cubic
FEM	Finite element method
FL	Infiltration
FT	Fourier transform
FWHM	Full-width half-maximum
G peak	'Graphite' peak
GGA	Generalized gradient approximation
H	Heating
h^+	Holes
HHI	Herfindahl-Hirschmann index
HT	High-temperature
IL	Ionic liquid
IPES	Inverse photoemission spectroscopy
LFA	Laser flash analysis
LNCS	Liquid nitrogen cooling system

LT	Low-temperature
LVDT	Linear variable differential transformer
MD	Molecular dynamics
m-NiP_2	NiP_2 in the monoclinic phase
MWCNT(s)	Multi-walled carbon nanotube(s)
'N' process	Normal process
NSOC	no spin orbit coupling
oh	Octahedral
PAW	Projector augmented wave
P3HT	Poly(3-hexylthiophene-2,5-diyl)
PBE	Perdew-Burke-Ernzerhof
PCBM	[6,6]-phenyl-C_{61}-butyric acid methyl ester
PFTE	Polytetrafluoroethylene
PGEC	Phonon glass-electron crystal
PMMA	Polymethyl methacrylate
PPMS	Physical Properties Measurement System
PVB	Polyvinyl butyral
PXRD	Powder X-ray diffraction
SE	Secondary electrons
SEM	Scanning electron microscope
SOC	Spin orbit coupling
SPB	Single parabolic band
TDTR	Time-domain thermoreflectance
TGA	Thermogravimetric analysis
th	Tetrahedral
TLS	Two-level system
TTO	Thermal transport option
'U' process	Umklapp process
UPS	Ultraviolet photoelectron spectroscopy
VASP	Vienna Ab initio Simulation
VBM	Valence Band Maximum
WDS	Wavelength-dispersive X-ray spectroscopy
XPS	X-ray photoelectron spectroscopy

Acknowledgements

First of all, I would like to thank my supervisor, Dr. Mary Anne White, for her guidance and support during the course of my PhD. Her door was always open when I wanted to discuss a project and her enthusiasm in research and education has shaped my abilities as a researcher and teacher. Furthermore, I appreciate the financial support from NSERC CREATE Dalhousie Research in Energy, Advanced Materials and Sustainability (DREAMS) and the Nova Scotia Scholarship.

I would like to acknowledge the members of my committee, Dr. Mark Obrovac and Dr. Ian Hill, who provided not only guidance in the research but also helped to perform the experiments. I would like to thank my external examiner, Professor Brent Fultz, California Institute of Technology, for the fantastic PhD defense and the great comments. I acknowledge the help from the group of Dr. Mark Obrovac, in particular, Dr. Tim Hatchard, Ryan Fielden, and Lituo Zheng who trained me on various instruments and/or gave helpful guidance. Furthermore, I am thankful for the XPS/UPS/IEPS measurements by Jon Paul Sun.

Additionally, I would like to thank the Mary Anne White group, past and present, Dr. Andrew Ritchie, Dr. Samer Kahwaji, Dr. Kimberly Miller, Dr. Alex Bourque, Dr. Carl Romao, Dr. Louis Desgrosseilliers, Dr. Julan Zeng, Paul Allred, John Niven, John Noël, Sarah Ellis, Stefan Juckes, Catherine O'Neill, and Jacy Conrad. In particular, I thank Mike Johnson who helped me with the measurements and to make sure that everything in the laboratory is running smoothly.

For this work many instruments were used and I am thankful for instruction concerning and use of those instruments. I would like to thank Dr. Jeff Dahn, Dr. Robie Sanderson, Dr. Kevin Plucknett, Patricia Scallion, Dr. Kevin Hewitt, Christopher Lee, Dr. Ted Monchesky, Dan MacDonald, Alex Paterson, Dr. Julian O'Flynn, Addison Rayner, and Dr. Stephen Corbin for various measurements. Furthermore, several pieces of equipment were required for the research and I would like to acknowledge Andy George, Mike Boutilier, Todd Carter, and Kevin Borgel for the technical support. Without your help this study would not be possible.

In addition to the experimental work, I would like to acknowledge the people from Dalhousie University who helped with the understanding of the theory. For the understanding of DFT, I would like to thank Dr. Erin Johnson, Dr. Josef Zwanziger, Matthew Christian, Luc LeBlanc, and Stephen Dale. For helping me with the finite element analysis, I am thankful for the help from Dr. Dominic Groulx.

In my PhD program, I have had the fortune to carry out research under the supervision of Dr. G. Jeff Snyder. Thank you for hosting me and helping me to understand the underlying physics of thermoelectrics. Furthermore, I would like to thank his group, in particular, Stephen Dongmin Kang, Saneyuki Ohno, Sevan Shanakian, Rochelle Weber, Dr. Zachary Gibbs, Dr. Guodong Li, Dr. Saurabh Bajaj, and Dr. Umut Aydemir. Umut was not only my direct supervisor at Caltech, but he is also a good friend. Thanks for everything.

For the computational study in this thesis, I would like to acknowledge 'The Materials Project', in particular, Dr. Gerd Ceder, Dr. Kristin Perrson, Anubhav Jain, Dr. Geoffroy Hautier, Dr. Mark Asta, Dr. Hong Zhu, Dr. Wei Chen, Dr. Gian-Marco Rignanese, Dr. Francesco Ricci, Dr. Guodong Yu, Dr. Alireza Faghaninia, and Dr. Guido Petretto. Furthermore, I like to thank Luo Zhe for various computations and discussions. Thank you!

For the synthesis of ZnO tetrapods, I would like to acknowledge Fabian Schütt, Jorit Gröttrup, Dr. Yogendra Kumar Mishra, and Dr. Adelung. Thank you also for discussions about the physical properties of ZnO tetrapods.

I would like to thank the staff at Dalhousie University, in particular, the Chemistry, Physics, and German Departments. Thanks for the help, the food, and the various conversations. Furthermore, I would like to thank all my friends around the world. I appreciate your support and I am very thankful to have you all in my life. Thanks for coloring my life. Furthermore, I would like to thank my girlfriend Madison for the support, many helpful discussions, and her love.

Finally, I would like to thank my parents and my sister. Thank you for all the support (although from far away) and being the first teachers in my life. You provided me with everything and I am very grateful for your support.

Chapter 1

Introduction

In recent decades the need for renewable energy has increased due to a dramatic rise in world-wide energy usage. The world's energy cannot be generated by a single source of renewable energy and, therefore, energy has to come from a variety of sources, such as solar, wind, water, and biomass [1]. As more than half of the United States' energy is lost in the form of heat [2], recovering a fraction of the lost energy can provide a significant contribution to global energy. For instance, only ∼25% of the fuel combustion energy is used for the motion of a car with a combustion engine whereas about 40% is lost as waste heat in the exhaust gas [3]. Thermoelectric materials are considered as a potential way to recover the 'lost' energy and convert it to useful electrical energy [4, 5].

Since the discovery of thermoelectric materials, they have been applied in diverse areas such as space exploration [6] and the automotive industry [7]. Thermoelectric devices were used in the Voyager 1 mission, the furthest human-made object from earth, powering the probe since 1977 [8]. Furthermore, thermoelectric materials are used as solid-state refrigeration devices [9] which have the advantages of no moving parts and precise temperature control. Moreover, thermoelectrics can convert solar energy into electricity [10]. Due to their wide range of applications, the interest in thermoelectric materials has dramatically increased in the last few decades. However, due to their low efficiency and high cost, thermoelectric materials are not yet used widely. Therefore, exploration for new thermoelectric materials is key.

1.1 Thermoelectric Effects

The fundamental principle of thermoelectricity is based on three related effects: the Seebeck effect, the Peltier effect, and the Thomson effect (see Figure 1.1) [11]. The Seebeck effect was first reported by Thomas Johann Seebeck in 1826 [12]. He observed that a circuit consisting of two dissimilar metals with different

temperatures at the two junctions produced a force which deflected the needle of a compass. The temperature gradient across a solid generates a potential difference which is proportional to the Seebeck coefficient, S, also known as thermopower (see Figure 1.1 (a) [13]. Depending on the type of charge carrier the Seebeck coefficient can be positive (p-type) or negative (n-type).

A second related effect, the Peltier effect, was discovered by Jean Charles Athanase Peltier shortly after the report of the Seebeck effect. The Peltier effect is observed when an applied electrical current causes a temperature change at a junction of dissimilar materials [5]. While at one junction heat is released ($+Q$), heat is absorbed at the other junction ($-Q$) as shown in Figure 1.1. The Peltier effect is separate from the contribution of Joule heating [11]. (The Seebeck and Peltier coefficients are further discussed in Section 2.3.)

While the Seebeck and Peltier effects require two dissimilar conducting materials, the Thomson effect is defined by the absorption and emission of heat along a single conductor, with a temperature gradient, as a current is applied (see Figure 1.1 (c)) [11]. All three thermoelectric effects are interdependent by the Kelvin relations (see Section 2.3) indicating the high potential of thermoelectric materials for various applications of heat generation and energy recovering.

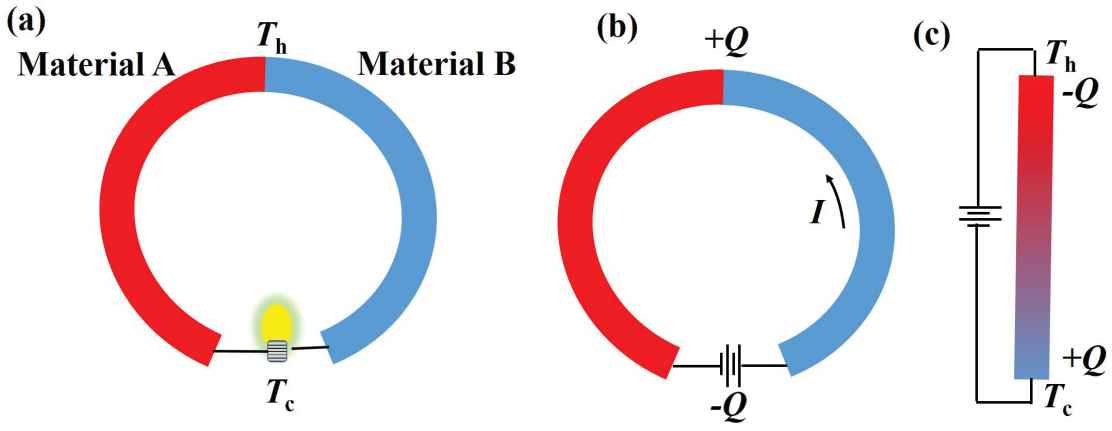

Figure 1.1: Schematic view of the (a) Seebeck effect, (b) Peltier effect, and (c) Thomson effect. While the Seebeck effect requires a temperature gradient where T_h is the hot-side temperature and T_c is the cold-side temperature, heat is absorbed/released (Q_-/Q_+) at the Peltier effect. Adapted from reference [14].

1.2 Thermoelectric Materials

To enhance the performance of thermoelectric devices, p-type and n-type thermoelectric materials are set electrically in series and thermally parallel (see Figure 1.2). In Figure 1.2 (a), a temperature gradient causes both holes and electrons to travel from the hot side to the cold side, generating an electrical current [15]. Similar behavior is observed for Peltier cooling where a current is applied and heat is released or absorbed at each end (Figure 1.2 (b)). To obtain a large net thermoelectric power thermoelectric devices contain many p- and n-type thermoelectric materials.

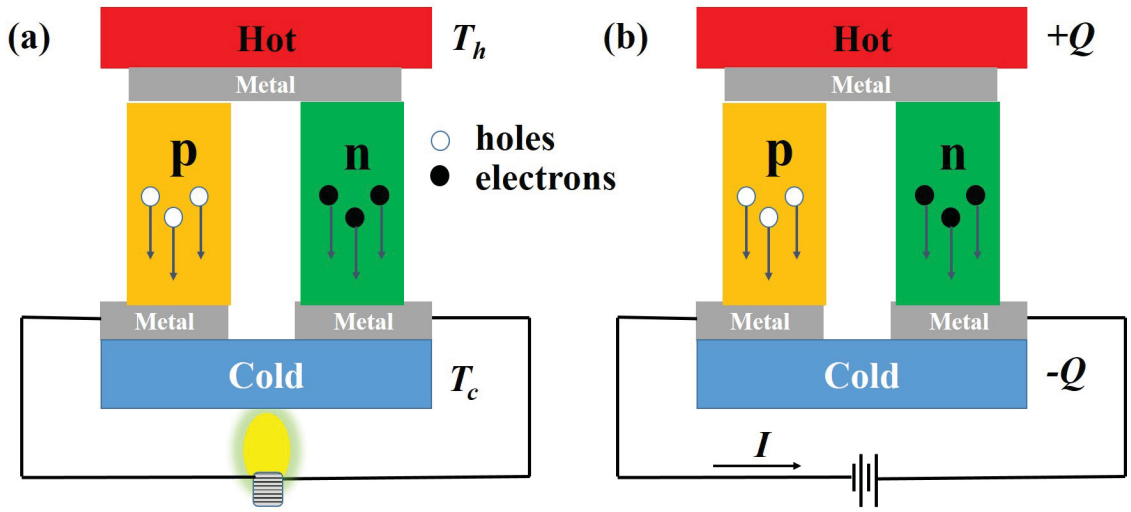

Figure 1.2: (a) Thermoelectric power generation and (b) Peltier cooling. The p-type and n-type are set electrically in series and thermally parallel. (a) While a temperature gradient ($T_h - T_c$) produced a potential difference, (b) an electrical current absorbs ($-Q$) and release ($+Q$) heat. Adapted from reference [13].

1.2.1 Thermoelectric Figure of Merit [1]

The thermoelectric potential of a material can be described by its thermoelectric figure of merit, zT. To derive zT for a thermoelectric device (*e.g.*, Figure 1.2 (a)), several assumptions are made. Although the thermoelectric materials are connected to the hot and cold side by a metal, electrical or thermal contact resistances are assumed

[1] In the present study, zT (which is dimensionless) is defined as thermoelectric figure of merit whereas z is defined as temperature-dependent thermoelectric figure of merit.

to be zero at the connections [16]. Furthermore, heat is assumed to be transported only by thermal conduction (*i.e.*, convection and blackbody radiation are neglected in the derivation), and no heat is released or absorbed from the branches (*i.e.*, the Thomson coefficient is zero).

The heat flux, Q, is the difference between the Peltier heat flux due to the current, I, and the thermal conduction produced from the resulting temperature difference in x-direction, $\frac{\mathrm{d}T}{\mathrm{d}x}$. Therefore, the heat flux for a p-type thermoelectric material is given by

$$Q_p = S_p I T - \kappa_p A_{cross,p} \frac{\mathrm{d}T}{\mathrm{d}x} \tag{1.1}$$

and for n-type by

$$Q_n = -S_n I T - \kappa_n A_{cross,n} \frac{\mathrm{d}T}{\mathrm{d}x} \tag{1.2}$$

where S is the Seebeck coefficient, T is the absolute temperature, κ is the thermal conductivity, and A_{cross} is the cross-sectional area [16]. Note that the Seebeck coefficient of the n-type branch is negative leading to a positive Peltier heat flow.

The heat flux from Joule heating opposes the thermal flow and results in a non-uniform temperature gradient along the branch, given for the p-type by

$$-\kappa_p A_{cross,p} \frac{\mathrm{d}^2 T}{\mathrm{d}x^2} = \frac{I^2 \rho_{el,p}}{A_{cross,p}} \tag{1.3}$$

and for the n-type,

$$-\kappa_n A_{cross,n} \frac{\mathrm{d}^2 T}{\mathrm{d}x^2} = \frac{I^2 \rho_{el,n}}{A_{cross,n}} \tag{1.4}$$

where ρ_{el} is the electrical resistivity [16]. This equation can be linked to the heat equation (Equation 2.9) where the external heat source is due to Joule heating per unit length. Furthermore, it is assumed that the Thompson coefficient is zero, therefore, no heat is supplied or extracted by the thermoelectric current within the branches [16]. To solve the partial differential equations, $T_{x=0} = T_c$ and $T_{x=L_{p,n}} = T_h$ with L as thickness are chosen as boundary conditions, leading to

$$\kappa_p A_{cross,p} \frac{\mathrm{d}T}{\mathrm{d}x} = -\frac{I \rho_{el,p} \left(x - \frac{L_p}{2} \right)}{A_{cross,p}} + \frac{\kappa_p A_{cross,p} \left(\Delta T \right)}{L_p} \tag{1.5}$$

and

$$\kappa_n A_{cross,n} \frac{\mathrm{d}T}{\mathrm{d}x} = -\frac{I\rho_{el,n}\left(x - \frac{L_n}{2}\right)}{A_{cross,n}} + \frac{\kappa_n A_{cross,n}\left(\Delta T\right)}{L_n} \tag{1.6}$$

where $\Delta T = T_h - T_c$ [16]. Equations 1.5 and 1.6 can be combined with Equation 1.1 and 1.2 giving the total heat flux at $x = 0$ of:

$$Q_c(x=0) = Q_p + Q_n = \left(S_p - S_n\right) I T_c - K\Delta T - \frac{1}{2} I^2 R \tag{1.7}$$

where

$$K = \kappa_p \frac{A_{cross,p}}{L_p} + \kappa_n \frac{A_{cross,n}}{L_n} \tag{1.8}$$

is the total thermal conductance and

$$R = \rho_{el,p} \frac{L_p}{A_{cross,p}} + \rho_{el,n} \frac{L_n}{A_{cross,n}} \tag{1.9}$$

is the total electrical resistance of the system [16]. To find the maximum current for Peltier cooling, the first derivative of the total heat flux with respect to the current is set to zero and the maximum current, I_{max}, is

$$I_{max} = \frac{\left(S_p - S_n\right) T_c}{R}. \tag{1.10}$$

From the maximum current, the maximum temperature difference, ΔT_{max}, can be calculated if $Q_c(x=0) = 0$:

$$\Delta T_{max} = \frac{(S_p - S_n)^2 T_c^2}{2KR} \tag{1.11}$$

and the temperature-dependent thermoelectric figure of merit, z, is defined by [16]

$$z = \frac{(S_p - S_n)^2}{KR}. \tag{1.12}$$

The temperature-dependent thermoelectric figure of merit is therefore twice the maximum temperature difference with respect to the cold-side temperature square and depends only on sample-dependent properties (*i.e.*, S, K, and R). However, the thermal conductance and the resistance are both dependent on the dimensions of the branch. The figure of merit is optimized when

$$\frac{L_n A_{cross,p}}{L_p A_{cross,n}} = \left(\frac{\rho_{el,p}\kappa_p}{\rho_{el,n}\kappa_n}\right)^{1/2} \tag{1.13}$$

where ρ_{el} is the electrical resistivity, leading to [16]

$$z = \frac{(S_p - S_n)^2}{\left(\left[\rho_{el,p}\kappa_p\right]^{1/2} + \left[\rho_{el,n}\kappa_n\right]^{1/2} \right)^2}. \tag{1.14}$$

Equation 1.14 is based on a system of a p-type and n-type branch (see Figure 1.2 (a)) and thus, the thermoelectric figure of merit for a single p-type or n-type is defined as [5, 13, 16]

$$zT = \frac{S^2 T}{\rho_{el}\kappa}. \tag{1.15}$$

The thermal conductivity can be further divided into the phononic contribution, κ_{pho}, and an electrical contribution, κ_{el}, where [5]

$$\kappa = \kappa_{pho} + \kappa_{el}. \tag{1.16}$$

To some extent, all properties are inter-related by the charge carrier concentration as shown in Figure 1.3 [5]. The electrical conductivity, $\sigma_{el} = \rho_{el}^{-1}$, increases with increasing carrier concentration whereas a reduction in the Seebeck coefficient is observed with increased carrier concentration. The product of the square of the Seebeck coefficient and the electrical conductivity is defined as the power factor, PF:

$$PF = S^2 \cdot \sigma_{el}. \tag{1.17}$$

Because the electrical contribution to the thermal conductivity is proportional to the electrical conductivity, increasing carrier concentration causes an increase in the electronic contribution of the thermal conductivity, similar to the trend of the electrical conductivity; see Figure 1.3. The resulting zT peaks generally in a carrier concentration range between 10^{19} and 10^{21} cm^{-3}, as shown in Figure 1.3 [5].

In addition to charge carrier optimization, the phononic contribution of the thermal conductivity has to be reduced to achieve useful thermoelectric materials. A potential way to decrease the thermal conductivity is by reducing the phonon mean free path. Several strategies have been applied to drop the phonon mean free path, such as point defect scattering, alloy scattering, grain-boundary scattering or interface scattering [17]. For instance, the thermal conductivity in Bi_2Te_3 systems

was decreased from 2.4 to 1.5 W m^{-1} K^{-1} by impurity scattering enhancing the figure of merit from 0.6 to 1.0 [1]. Furthermore, nanostructuring can result in very short phonon mean free paths, reducing the thermal conductivity and hence, enhancing the thermoelectric figure of merit. Biswas *et al.* reduced the thermal conductivity by scattering of short, intermediate, and long phonons, improving the figure of merit in PbTe from 1.7 to 2.2 [18].

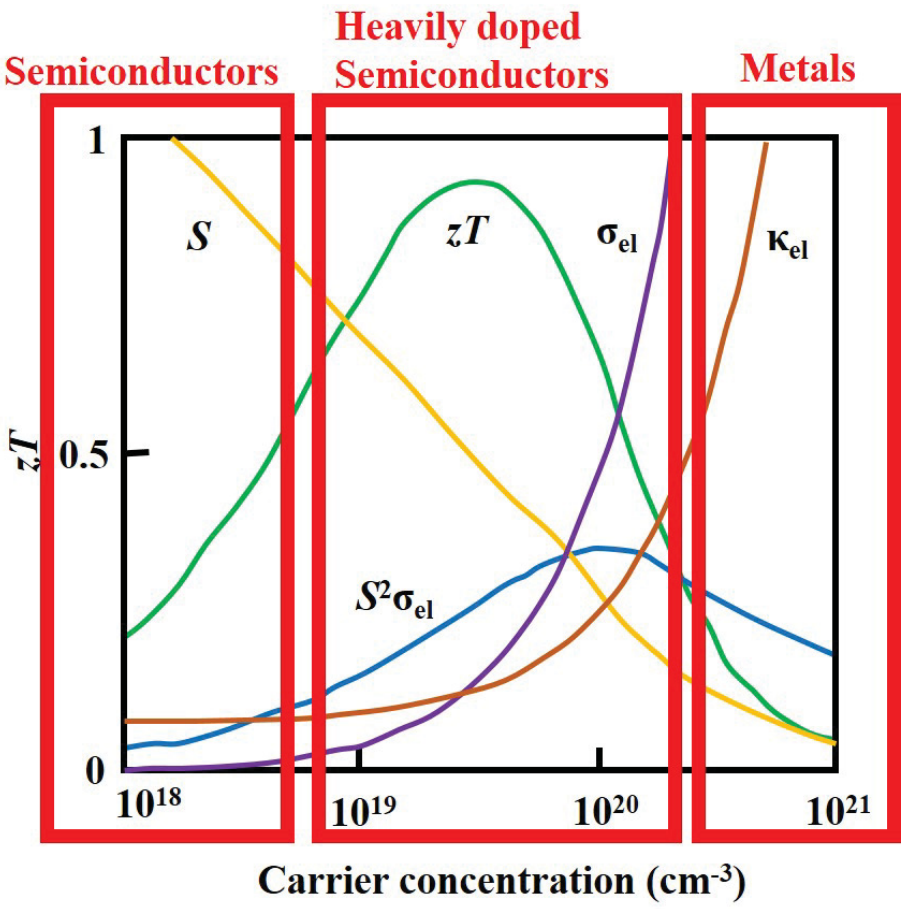

Figure 1.3: Thermoelectric transport properties as a function of carrier concentration. While the electrical conductivity and electronic contribution of the thermal conductivity increase with carrier concentration, the Seebeck coefficient decreases with carrier concentration leading to an optimum zT in the range from 10^{19} to 10^{21} cm^{-3} using an arbitrary temperature. Figure adapted from reference [5] with permission.

In addition to the reduction of the phonon mean free path, several materials have intrinsically low lattice thermal conductivity as observed in clathrates [19], or

Zintl pinictides [20]. The low lattice thermal conductivity in Zintl pinictides can be related to the complex structure of tens of atoms in the unit cell, whereas the thermal conductivity in clathrates is reduced by the vibrations of the guest atoms in the cage-like structure [21].

1.2.2 Thermoelectric Efficiency

The thermoelectric figure of merit is related to the thermoelectric efficiency, η, which can be calculated from

$$\eta = \frac{W_{out}}{W_{in}} = \frac{W_{out}}{Q_c} \tag{1.18}$$

where Q_c is taken from Equation 1.7, W_{in} and W_{out} are the network input and output, respectively [22]. The maximum Carnot efficiency for a system, where no heat is dissipated, is given by [23, 24]

$$\eta_C = \frac{\Delta T}{T_h}. \tag{1.19}$$

If a load is connected to the thermoelectric device, *e.g.*, the lightbulb in Figure 1.2 (a), the net work output is given by the Joule heating of the load resistance, R_L, and hence,

$$W_{out} = I^2 R_L. \tag{1.20}$$

Equations 1.7 and 1.20 can be substituted in Equation 1.19 leading to

$$\eta = \frac{I^2 R_L}{SIT_h + \kappa A_{cross}\left(T_h - T_c\right) - \frac{1}{2} I^2 R}. \tag{1.21}$$

The electrical current of the system can be described as $I = \frac{S\Delta T}{R+R_L}$ and the ratio of the resistance of the load to the resistance of the thermoelectric material, $m = \frac{R_L}{R}$, are resulting in [25]

$$\eta = \frac{\Delta T}{T_h} \cdot \frac{\left(\frac{m}{m+1}\right)}{1 + \frac{KR(m+1)}{S^2 T_h} - \frac{\Delta T}{2(m+1)T_h}} \tag{1.22}$$

and the maximum efficiency of a thermoelectric device, η_{max}, in terms of the load is calculated from the first derivative of the efficiency with respect to m $\left(\frac{\mathrm{d}\eta}{\mathrm{d}m} = 0\right)$:

$$\eta_{max} = \frac{\Delta T}{T_h} \cdot \frac{\sqrt{1 + z\bar{T}} - 1}{\sqrt{1 + z\bar{T}} + \frac{T_c}{T_h}} \tag{1.23}$$

where $\bar{T} = \frac{T_h - T_c}{2}$ is the average temperature [22]. As $zT \to \infty$, the thermoelectric efficiency approaches the Carnot efficiency.

1.2.3 Thermoelectric Performance

The maximum reported thermoelectric figure of merit has been dramatically enhanced in the last decade and the current best thermoelectric material is SnSe with a zT of 2.62 at 923 K [26, 27]. In comparison with the state of art of thermoelectric materials in 2011 shown in Figure 1.4 [28] where $PbTe_{1-x}Se_x$ had the highest zT ($\sim$ 1.8 at $\sim$850 K) [29], the best thermoelectric performance has increased by more than 45% in the last six years. In addition to SnSe, Bi_2Te_3 and PbTe are common thermoelectric materials for low-temperature and high-temperature applications, respectively. Although the thermoelectric materials Bi_2Te_3 and PbTe have been known for more than a century [30], the thermoelectric figures of merit of both compounds have been dramatically increased in the last years. PbTe has currently a maximum p-type zT of 2.2 at 825 K [31] and Bi_2Te_3 has a maximum zT of 1.23 at 480 K [32].

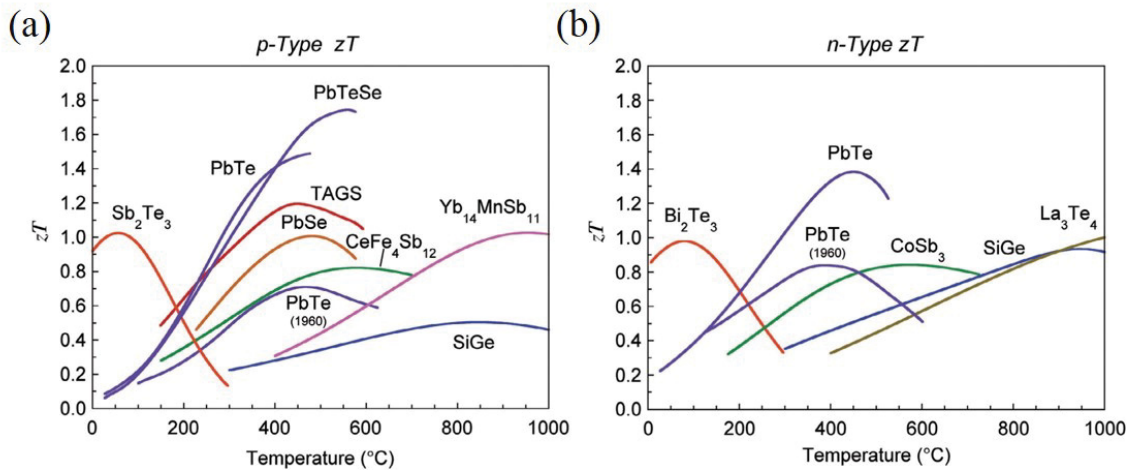

Figure 1.4: State of the art (a) p-type and (b) n-type thermoelectric materials as of 2011. Figure from reference [28] with permission.

The thermoelectric efficiency also has been increased over time and the maximum thermoelectric efficiency is currently at $\eta = 16.7\%$ for SnSe between $T_c = 300$ K and $T_h = 773$ K [27]. This is the efficiency from the material itself; in a device with p-type and n-type branches the highest reported efficiency of 12% was reported for Bi_2Te_3-based alloys and $CoSb_3$-based skutterudites leading to a power density of 1.4 W cm^{-2} [33]. To get comparable results to home refrigerators ($\eta \sim 30\%$), the thermoelectric

figure of merit has to be increased to ∼4 [34].

However, due to the complex interdependency of the thermoelectric properties, it is time-consuming to discover new high-performance thermoelectric materials. Furthermore, low thermoelectric performance can be a result of non-optimized carrier concentration and therefore, it is not always clear if the low thermoelectric figure of merit is intrinsic or due to the carrier concentration. A potential way to accelerate the search for new high-performance thermoelectric materials is using first-principles calculations. Especially due to the exponential growth in computational power, the thermoelectric properties of thousands of inorganic compounds can be analyzed in a short amount of time.

1.3 High-Throughput Screening[2]

First-principles calculations already have been successfully employed to discover new materials in several areas, such as batteries [36, 37] and photocatalysts [38]. However, only a few computational studies focused on the discovery and optimization of potential high-performance thermoelectric materials [39, 40, 41, 42, 43, 44]. Recently, the thermoelectric properties of a wide variety of thermoelectric families were analyzed in high-throughput studies which were based on first-principles calculations (TE Design lab [45, 46]) or machine learning (Citrine [47]). Whereas the machine learning approach considers only the chemical formula of the compounds resulting in qualitative studies, first-principles calculations also consider the crystal structure and the electronic band structure. Therefore, first-principles calculations can provide a more quantitative analysis of the thermoelectric performance and enhance the prediction of thermoelectric compounds.

In this way, the thermoelectric properties of more than 48,000 inorganic

[2]Parts of this section were adapted from: W. Chen, J.-H. Pöhls, G. Hautier, D. Broberg, S. Bajaj, U. Aydemir, Z. M. Gibbs, H. Zhu, M. Asta, G. J. Snyder, B. Meredig, M. A. White, K. Persson and Anubhav Jain, 'Understanding thermoelectric properties from high-throughput calculations: trends, insights,and comparisons with experiment', *Journal of Materials Chemistry C*, 2015, **4**, 4414–4426, DOI: 10.1039/C5TC04339E - Reproduced by permission of the Royal Society of Chemistry. (Figures are taken with permission and labeled with reference [35]). The author's contribution was the comparison of computation and experiments and writing the corresponding sections in the manuscript.

compounds have been computed within 'The Materials Project' (https://materialsproject.org) [48]. The electronic properties were calculated from the electronic band structures and Boltzmann transport equations using the software BoltzTrap [49] and a constant relaxation time set to 10^{-14} s.

The datamining results of 48,700 inorganic compounds are summarized in a flow diagram shown in Figure 1.5. The electronic properties were calculated for a carrier concentration of 10^{20} cm^{-3} at a temperature of 600 K. The term 'doping' on the left side of the diagram refers to the majority carriers (*i.e.*, holes for *p*-type and electrons for *n*-type) producing the highest power factors, PF (see Equation 1.17). Most of the compounds have higher *n*-type power factors than *p*-type, most likely due to the fact that ∼70% of the inorganic compounds contain oxygen. In the study, oxygen-containing compounds generally possess higher *n*-type PFs (∼61%) than *p*-type PFs (∼39%). A possible reason for the lower *p*-type PFs might be the larger contribution of the oxygen *p*-orbitals to the valence band structure.

The second column indicates that most compounds studied had anisotropic properties (*i.e.*, the uncertainty between the eigenvalues of the PF tensor was larger than 10%). Although anisotropy can lead to higher PFs [50], the samples would have to be single crystals or aligned polycrystals. The third column in Figure 1.5 shows the electronic band gap energies in eV, computed with the Perdew-Burke-Ernzerhof (PBE) generalized gradient approximation (GGA) [51] and projector augmented wave (PAW) [52] method to model core electrons. The PBE-GGA functional normally underestimates the band gap energy by ∼0.7 eV compared to experiments [53, 54]. Nevertheless, most compounds have a high computed band gap energy (>2 eV) using the PBE-GGA functional. In additional to the large-band gap semiconductors, a large number are metallic (*i.e.*, zero band gap). Only a small fraction are low band gap energy (0.01-0.5 eV) materials which are typically preferable for thermoelectrics.

The largest fraction of the investigated inorganic compounds have estimated maximum PFs (in any crystallographic direction) in the medium range (1-3 mW K^{-2} m^{-1}) whereas the smallest fraction of compounds had a high PF (>3 mW K^{-2} m^{-1}). Although only a small portion of the studied thermoelectrics have high calculated PFs, even several of these materials had not been considered previously

as thermoelectric materials. Note that the thermal conductivity can dramatically influence the thermoelectric performance and therefore has to be included in the study, *e.g.*, skutterudites have high experimental power factors ($\sim$4 mW K^{-2} m^{-1}) but also relative high thermal conductivities (>2.6 W m^{-1} K^{-1}) [55].

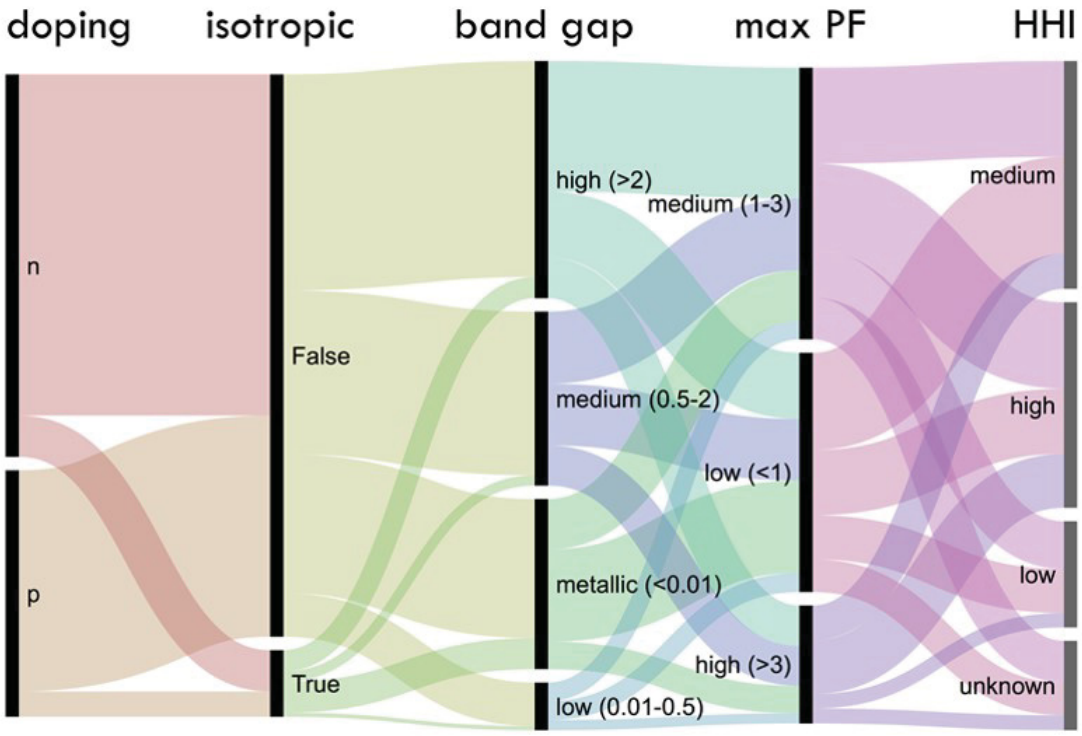

Figure 1.5: Flow diagram to demonstrate several calculated thermoelectric-related properties of 48,700 inorganic compounds. Doping indicates the type (p- or n-type) which provides the highest power factor, PF, in mW K^{-2} m^{-1}. Materials which have PFs within 10% in all directions are considered as isotropic. The Herfindahl-Hirschmann index (HHI) of the elements indicates if the elements in the compounds are geographically confined ('high', undesirable) or geographically dispersed ('low', desirable) [56]. Figure from reference [35].

In the last column of Figure 1.5, the Herfindahl-Hirschmann Index (HHI) values of the elements were used as an indicator of the sustainability of the potential thermoelectric materials [56]. A high HHI refers to known reserves of the elements in the thermoelectric compounds being geographically confined, while a low HHI means that the reserves of the elements are geographically dispersed, which is desirable from a economical point of view because the thermoelectric material would

be less dependent on the global economy [56]. Furthermore, it is shown here that only a tiny fraction of the studied inorganic compounds have the combined favourable properties of high PF and low HHI (see Figure 1.5) as would be preferable for mass production of thermoelectric materials.

High-performance thermoelectric materials typically include heavy anions, *e.g.*, Te^{2-} in PbTe and Bi_2Te_3 or Se^{2-} in SnSe. One interesting group of anions is group VI: oxides, sulfides, selenides, and tellurides. The distribution of the maximum computed power factors indicates that tellurides have the highest average power factors, followed by selenides and sulphides (see Figure 1.6). The lowest average maximum power factors were estimated for oxides. In addition to the lower median, oxides have also a small variance, resulting in fewer materials with high power factors. The high power factors in tellurides can be correlated to the greater hybridization leading to more valley degeneracy which is desirable in thermoelectrics [50].

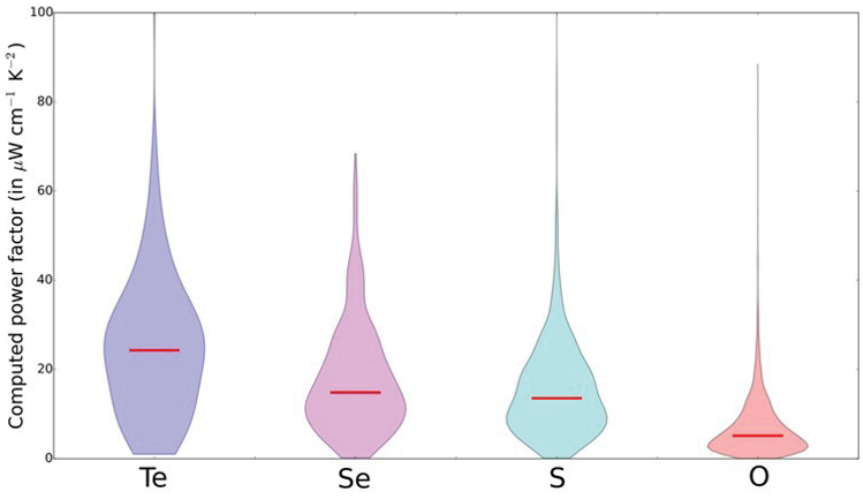

Figure 1.6: Violin plots indicating the distribution of computed maximum power factors for various group VI anions. The red line shows the median computed maximum power factor. Maximum power factors were calculated from the average over the three crystallographic directions for a carrier concentration of 10^{20} cm^{-3} at 600 K with a constant relaxation time of 10^{-14} s. Figure taken from reference [35].

Tellurides are preferable to oxides for thermoelectric materials due to the higher atomic mass and the smaller band gaps. The thermal conductivity is in general higher for lighter anion elements leading to a decrease in the thermoelectric

performance [57]. Furthermore, smaller band gap semiconductors are easier to dope to high carrier concentrations than are large band gap semiconductors [58]. Because the band gap decreases from oxides to tellurides, it is challenging to produce high-performance thermoelectric oxides and the focus of the search for new thermoelectric materials should be on group VI elements with high atomic number, *e.g.*, selenides and tellurides.

The computed thermoelectric properties were compared to experimental data, where available. For the comparison, both the Seebeck coefficient and power factor were computed at the same temperature and carrier concentration shown experimentally to give the maximum values for these quantities. Furthermore, the three eigenvalues of the properties in the three crystallographic directions were averaged. A strong correlation between computation and experiments was observed for the Seebeck coefficient for most materials (see Figure 1.7 (a)) as described by the Pearson correlation coefficient ($\sim$0.79), but the calculated Seebeck coefficient tends to be underestimated. In addition, the computed Seebeck coefficient in small band gap semiconductors can deviate from experiments due to an underestimation of the band gap energy. The estimation of the Seebeck coefficient was improved by a 'scissor operation' (Pearson correlation coefficient of 0.9) where the conduction bands and valence were translated to match the computed band gaps with the experimental values. The computed power factors, otherwise, have a weak correlation with experiments which cannot be improved with a 'scissor operation' (see Figure 1.7 (b)). One major reason for the large discrepancy between the computed and experimental power factor is the use of the constant relaxation time approximation. The relaxation time can vary, *e.g.* due to selection of the material, temperature, and level of impurities.

1.4 Estimation of Thermal Conductivity

Whereas electronic properties can be computed with a relatively high accuracy, it is not currently feasible to estimate thermal conductivity from first-principles calculations in a high-throughput screening (except for simple crystal structures [59, 60]). In 1960 Ziman proposed that the thermal conductivity can be calculated using a Boltzmann transport approach and the variational principle [61]. However,

the trial functions were too complex to solve at that time. Due to increase in computing power, several first-principle approaches based on density functional theory (DFT) [62, 63] and molecular dynamics [64] have been reported since then but they are limitated to small systems and are computational expensive or have not been tested on a large data set. For example, Broido *et al.* proposed a Boltzmann formalism combined with DFT to calculate the harmonic and anharmonic interatomic force constants [62]. They computed the lattice thermal conductivity of various semiconductors (*e.g.*, silicon and germanium), but the technique is limited to high-symmetry systems. For more complex systems, Tang and Dong reported a technique which numerically combines the Peierls-Boltzmann transport equation with electronic band structure theory [63]. In their approach they assumed that the phononic scattering rate is only limited by isotope mass disorder (which has a significant contribution at low temperature) and third-order anharmonicity (which limits the thermal conductivity especially at high temperature). This technique has the advantage of computing the lattice thermal conductivity in terms of temperature and pressure [63], however, it is expensive to run the calculations in high-throughput and mostly limited to small unit cells with high symmetry. Furthermore, at elevated temperature or strong anharmonicity the approaches based on Boltzmann transport can introduce large uncertainties. A recent study by Carbogno *et al.* proposed a first-principle formulation of the Green-Kubo theory to calculate the thermal conductivity of low- and high-thermal conductivity materials [64]. In this approach, the stress tensor is calculated using DFT and the thermal conductivity is computed with the Green-Kubo formula. However, for the prediction of the thermal conductivity a large number of atoms and long time scale are required, which are severe limitations. Although the prediction of the thermal conductivity has dramatically enhanced in the last decade, the methods have to be further improved to apply to more complex systems in high-throughput approaches.

A potential way to get insight concerning the thermal transport in materials can be provided by the calculated minimum theoretical thermal conductivity. The first attempt to describe the lowest limit of thermal conductivity was made by Einstein, who assumed that heat is transported between individual atoms all vibrating

incoherently with the same frequency, with the phonon mean free path limited by the interatomic distance [65]. This model did not agree with many materials and was modified by Cahill, Watson, and Pohl by a Debye-like approach in 1988 [66, 67]. They proposed that thermal energy is transported between entities of atoms (*i.e.*, phonons) and that all atoms oscillate coherently with a range of frequencies. A similar approach was proposed earlier by Ziman who described the thermal conductivity in glasses with a Debye-like approach [61]. Furthermore, Ziman predicted that short wavelengths are scattered by grain boundaries and the phonon mean free path is temperature-independent while long wavelengths are not scattered efficiently and the phonon mean free path is proportional to T^{-2} [61]. The Cahill, Watson, and Pohl model for minimum thermal conductivity agrees well for many materials, but in recent years several materials have been found to have lower experimental thermal conductivities than the predicted lowest limit. The thermal conductivity in these materials is referred as to 'ultralow'. The origins of the ultralow thermal conductivity in these materials had not been delineated.

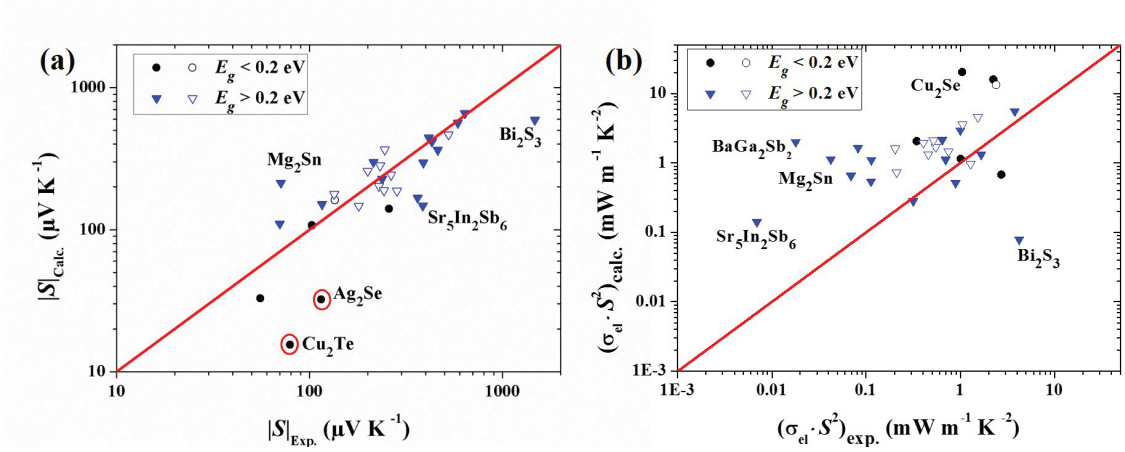

Figure 1.7: Comparison of the calculated and experimental (a) Seebeck coefficients and (b) power factors for different undoped (filled symbols) and extrinsic doped (hollow symbols) thermoelectric materials. The band gap energies were scissored to experimental band gaps if the difference was larger than 50%. Thermoelectric properties were calculated with a constant relaxation time of 10^{-14} s. The red circles indicate cases for which the sign of the Seebeck coefficient was incorrect and the line indicates optimum correlation between computation and experiment. Figure taken from reference [35].

In addition to the prediction of the minimum thermal conductivity, a semi-empirical approach for thermal conductivity was recently developed by Miller *et al.* [68]. While the minimum thermal conductivity describes the lower bound of the thermal conductivity, the semi-empirical approach provides an average thermal conductivity. However, the accuracy of the semi-empirical approach has not be proven yet. For instance, the coordinated-dependent Grüneisen parameter which is used to calculate the thermal conductivity is not based on a fundamental theory and might work only for certain compounds. Further investigations of the semi-empirical model are required to make a conclusion.

1.5 Present Research and Motivation

In the present study, the origins of the ultralow thermal conductivity were delineated and new classes of thermoelectric materials, showing potential for high-performance thermoelectric materials, were investigated. Furthermore, a new experimental technique was developed to determine the thermal conductivity of powders.

In Section 4.1 the origins of ultralow thermal conductivity were investigated for [6,6]-phenyl-C_{61}-butyric acid methyl ester (PCBM) due to its record low thermal conductivity. The ultralow thermal conductivity reported for PCBM thin films by Duda *et al.* ($\kappa = 0.03$ W m^{-1} K^{-1} at room temperature) [69] was more than ten times lower than its estimated lowest limit of thermal conductivity. To exclude that the low thermal conductivity was an effect of the low-dimensions in thin films, the thermal properties of consolidated PCBM pellets was determined. A new model for minimum thermal conductivity is presented to describe the ultralow thermal conductivity in PCBM and C_{60}/C_{70} fullerite.

Powders can have low thermal conductivities, even below the thermal conductivity of 'true' vacuum [70, 71]. The measurement of the thermal conductivity in powders is challenging due to their low thermal conductivity and poor mechanical stability. In Section 4.2, the determination of the thermal conductivity of pristine and metal oxide-coated ZnO tetrapods using a custom-developed powder cell is described. The powder cell has the potential to measure the thermal conductivity of various powders. The measurements were confirmed by a finite element study. Furthermore, ZnO tetrapods

have extremely low thermal conductivity. With the inclusion of carbon nanotubes (CNT) on the ZnO tetrapods, the measured electrical and thermal conductivities are presented.

In the following sections (Section 5.1 and Section 5.2), computational and experimental studies of two novel classes of thermoelectric materials, XYZ_2 (X, Y: rare earth or transition metals and Z: group VI) and metal phosphides are presented. Because tellurides typically have a lower thermal conductivity, higher power factors, and enhanced dopability, various tellurides XYZ_2 were tested experimentally. The computational thermoelectric properties using a constant relaxation time of 10^{-14} s overestimates the electrical conductivity, and thus a novel variable relaxation time depending on the crystal structure and temperature is introduced. Variable relaxation times can enhance the prediction of thermoelectric materials using first-principles calculations.

In Section 5.3, the thermal properties of germanium type II clathrates with partially Na-filling were analyzed. Clathrates have complex structures and thus the electrical and thermal properties can be described by the 'phonon glass-electron crystal approach', first introduced by Slack [72]. The framework of the clathrate provides a continuous conductive pathway for electricity (electron crystal), and the encaged guest atoms, often referred to as 'rattlers', provide dynamic disorder ('phonon glass') that hinders phonon propagation and hence, gives low thermal conductivity.

The overall goal of the present study is the enhancement of the prediction of thermal and electrical properties in thermoelectric materials. Thus, novel high-performance thermoelectric materials can be revealed, contributing to the global energy solution.

Chapter 2

Theory

Thermoelectric materials are described by their dimensionless thermoelectric figure of merit, zT, which increases with increasing power factor (see Equation 1.17) and decreases with rise in thermal conductivity (see Equation 1.15).

These physical properties can be described by considering the behavior of electrons and the dynamics of atoms [14]. The latter can describe the heat capacity, C, and the phononic contribution of the thermal conductivity, whereas the electronic contribution of the thermal conductivity, the electrical conductivity, and the Seebeck coefficient are strongly related to the electronic band structure and the carrier concentration.

In addition to the relevant physical properties, the Boltzmann transport approach to predict the electronic properties from the electron band structures and the single parabolic band (SPB) model are described herein.

2.1 Heat Capacity

Heat capacity, C, is defined as the amount of energy required to increase the temperature of a material by one Kelvin. Heat capacity can be described under two conditions: the heat capacity under constant volume, C_V, which is the more fundamental property and provides information concerning the phonon density of states (DOS), and the heat capacity under constant pressure, C_p, which is generally what is determined experimentally. The heat capacity at constant volume is described in terms of the internal energy, U:

$$C_V = \left(\frac{\partial U}{\partial T}\right)_V \tag{2.1}$$

whereas the heat capacity at constant pressure is described in terms of the enthalpy, H, [73]:

$$C_V = \left(\frac{\partial H}{\partial T}\right)_p . \tag{2.2}$$

The heat capacity at constant pressure is larger than the heat capacity at constant volume because work due to thermal expansion is required, and the difference, on a molar basis for an isotropic material, is given by

$$C_p - C_V = V_m T \frac{\alpha_V^2}{\beta_T} \tag{2.3}$$

where V_m is the molar volume, $\alpha_V = \frac{1}{V}\left(\frac{\partial V}{\partial T}\right)_p$ is the coefficient of volumetric thermal expansion, and $\beta_T = -\frac{1}{V}\left(\frac{\partial V}{\partial p}\right)_T$ is the isothermal compressibility [73]. The isothermal compressibility is equal to the inverse of the bulk modulus, $B = -V\left(\frac{\partial p}{\partial V}\right)_T$. The coefficient of the volumetric thermal expansion is in general determined from the linear coefficient of thermal expansion, α, in dilatometry measurements ($\alpha_V = 3\alpha$ for a cubic material). The linear coefficient of thermal expansion is defined as

$$\alpha = \frac{1}{L_0}\frac{\Delta L}{\Delta T} \tag{2.4}$$

where L_0 and ΔL are the initial thickness and the change in thickness, respectively [73]. The $(C_p - C_V)$ term can significantly contribute to the total C_p at high temperature.

In addition to the heat capacity contribution from thermal expansion, electrons can contribute to the experimental heat capacity, and the contribution can be significant especially at low temperature (< 1 K) and high temperatures. The electronic contribution of the heat capacity is given by

$$C_{el} = \gamma_{el} \cdot T \tag{2.5}$$

where γ_{el} is the Sommerfeld constant. Furthermore, the heat capacity can be divided in two special cases: the specific heat, c, which is the heat capacity for unit mass, and the molar heat capacity, C_{mol}, which is the heat capacity per mole.

In the harmonic case, the temperature dependence of the heat capacity is in general described by the phonon DOS, $D_i(\omega)$, and the average energy and the average internal energy, $\langle U(\omega)\rangle$, with respect to the temperature

$$C_V(T) = \sum_{i=0}^{3} \int_0^{\omega_{max}} D_i(\omega) \frac{\mathrm{d}\langle U(\omega)\rangle}{\mathrm{d}T} \mathrm{d}\omega \tag{2.6}$$

where ω and ω_{max} is the angular frequency and the maximum angular frequency. The average internal energy is given by the Bose-Einstein distribution ($\langle U(\omega)\rangle =$

$\frac{\hbar\omega}{e^{\hbar\omega/k_BT}-1}$) [74]. The temperature-dependent heat capacity can be calculated by two different models. Einstein considered each atom as an independent quantum harmonic oscillator and assumed that all atoms vibrate incoherently with the same frequency ω_E, known as the Einstein frequency. Therefore, the phonon DOS can be described by a *delta*-function ($D_i(\omega) = N\delta(\omega - \omega_E)$ with N as the number of atoms) [74] and the Einstein heat capacity is given by

$$C_{V,E} = 3Nk_B \left(\frac{\hbar\omega}{k_BT}\right)^2 \frac{e^{\hbar\omega/k_BT}}{\left(e^{\hbar\omega/k_BT}-1\right)^2} \tag{2.7}$$

where $k_B = 1.3806485 \cdot 10^{-23}$ J K^{-1} is the Boltzmann constant, $\hbar = 1.05457 \cdot 10^{-34}$ J·s is the reduced Planck constant or Dirac constant ($h/2\pi$), and $\frac{\hbar\omega}{k_B}$ is the Einstein temperature, θ_E [73]. The Einstein model is a good approximation for optical modes, which are nearly dispersionless. The optical modes for a polyatomic solid dominate at elevated temperature and the heat capacity approaches the Dulong-Petit law ($\lim_{T\to\infty} C_V = 3R$ for monoatomic systems where R is the universal gas constant) at high temperature [73] (see Figure 2.1). However, the Einstein model underestimates the heat capacity at low temperature [23]. A better approximation of the heat capacity of a compound at intermediate temperatures can be obtained from the Neumann-Kopp "law" which states that the molar heat capacity of a compound is almost equal to the sum of molar heat capacities of its constituent molar heat capacities [23]. Although use of the Neumann-Kopp "law" gives better the predicted high-temperature heat capacity compared to the Dulong-Petit value, it has to be treated with due caution. For example, the individual atomic molar heat capacities most likely have different ($C_p - C_V$) contributions than the corresponding compound, introducing uncertainties.

In contrast to the Einstein model, Debye assumed that all atoms oscillate in a range of frequency from zero to a maximum frequency, also known as the Debye frequency, ω_D [73]. The Debye model describes the acoustic phonons in a harmonic approach and the phonon DOS can be approximated by the volumetric DOS ($D_i(\omega) = V\frac{\omega^2}{2\pi^2 v_p^2 v_g}$) [75]. The velocities $v_p = \frac{\omega}{k}$ and $v_g = \frac{\partial\omega}{\partial k}$ are the phase and group velocity, respectively. The wave vector $k = \frac{2\pi}{\lambda}$ is inversely proportional to the wavelength, λ.

The Debye heat capacity is described by

$$C_D = 9Nk_B \frac{\hbar\omega}{k_B T} \int_0^{x_D} \frac{x^4 \mathrm{e}^x}{(\mathrm{e}^x - 1)^2} \mathrm{d}x \tag{2.8}$$

where $x_D = \frac{\hbar\omega_D}{k_B T}$ [73]. An important parameter for the Debye model is the characteristic Debye temperature, $\theta_D = \frac{\hbar\omega_D}{k_B}$ which is strongly related to the stiffness of the solid. A stiffer compound has a higher Debye temperature and its heat capacity increases more slowly with temperature [73].

The Debye model also enhances the prediction of the experimental heat capacity at constant volume. At high temperature, the Debye model approaches the Dulong-Petit value as for the Einstein model, however, at low temperature the heat capacity goes to zero with T^3 behavior in the Debye model (see Figure 2.1), as observed experimentally. It is important to note that a compound with N atoms per unit cell has three acoustic phonons and $3N - 3$ optical phonons [73] and therefore, a combination of the Debye model (for the acoustic phonons) and the Einstein model (for the optical phonons) is needed to describe the temperature dependence of the heat capacity of a compound.

2.2 Thermal Conductivity

Heat transport in solids can be divided in three fundamental mechanisms: thermal conduction, convection, and blackbody radiation. In most applications, multiple mechanisms can contribute to heat transfer. For instance, heat is mostly transported by thermal conduction and convection in thermal barrier coatings [76]. For thermal conductivity measurements of solids, convection can be normally neglected because the experiments are generally performed under vacuum.

With the exclusion of convection, the heat transfer in solids can be described by

$$\rho C_p \frac{\partial T}{\partial t} - \nabla \cdot (\kappa \nabla T) = Q_{ext} \tag{2.9}$$

where ρ is the mass density, the first and second term are the heat storage and the thermal conduction, respectively, and Q_{ext} is an external energy source (*e.g.*, blackbody radiation). In contrast to convection, blackbody radiation has to be considered for the thermal conduction measurements because it does not require a medium to conduct heat [77]. Although the contribution of blackbody radiation can

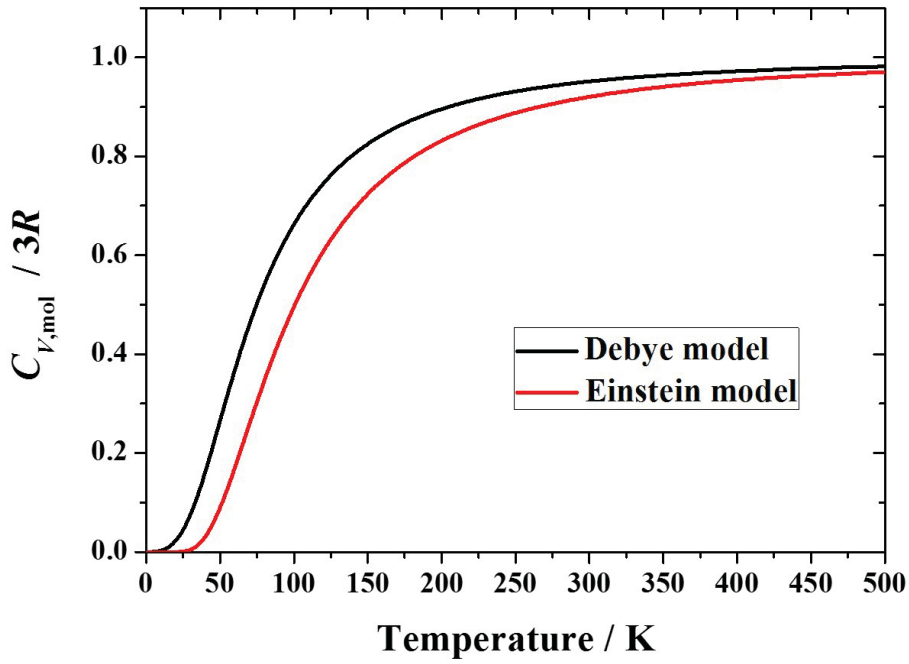

Figure 2.1: Comparison of the Einstein model and Debye model of monatomic species using the same Debye and Einstein temperature ($\theta_D = \theta_E = 100$ K). Whereas both models approach the Dulong-Petit value ($3R$) at high temperature, the low-temperature heat capacity is better predicted using the Debye model.

be neglected at low temperature, it can contribute significantly at high temperature due to the T^4-dependence. According to the Stefan-Boltzmann law the energy per unit area and per unit time, Q_{rad}, is given by

$$Q_{rad} = \varepsilon_T \sigma_T (T_{amb}^4 - T^4) \tag{2.10}$$

where ε_T is the emissivity, $\sigma_T = 5.67 \cdot 10^{-8}$ W m^{-2} K^{-4} is the Stefan-Boltzmann constant, and T_{amb} is the ambient temperature [77].

Thermal conduction is generally the most dominant term for heat transport in condensed matter. The thermal conduction term in Equation 2.9 is defined by Fourier's law:

$$\vec{Q} = -\kappa \vec{\nabla} T \tag{2.11}$$

where $\vec{Q}$ is the heat flux vector, which is the energy transmitted through a unit area per unit time [78]. The negative sign indicates that the heat flows in the opposite

direction to the temperature gradient (*i.e.*, from hot to cold) [73]. Thermal conduction is a non-equilibrium phenomenon because a temperature gradient ∇T is required for a thermal current [14]. Although Equation 2.11 is described for classical, isotropic materials, it can be expanded for anisotropic materials in which the thermal conductivity is described by a second-order tensor, κ_{ij},

$$\vec{Q}_i = -\sum_j \kappa_{ij} \vec{\nabla} T. \tag{2.12}$$

The thermal conductivity for bulk solids can range over about five orders of magnitude at room-temperature. While high thermal conductivity was found for very pure diamond ($\kappa = 3320$ W m^{-1} K^{-1}) [79], extremely low thermal conductivity was measured for [6,6]-phenyl-C_{61}-butyric acid methyl ester (PCBM) in the present study ($\kappa = 0.07 \pm 0.01$ W m^{-1} K^{-1}).

The thermal conductivity can be separated into a phononic contribution, κ_{pho}, which is related to the lattice dynamics in the compound, and an electronic contribution, κ_{el}, which is the dominant mechanism in metals.

2.2.1 Phononic Contribution to Thermal Conductivity

The phononic contribution is dominant in intrinsic semiconductors and insulators, where heat is predominantly transported by phonons. A phonon is defined as a quantized lattice wave which travels with a characteristic phonon mean speed through a crystal. For an enhanced understanding of lattice vibrations reference [80] is highly recommended.

2.2.1.a Dispersion Relations

In a simple crystalline model, all atoms can be treated as spheres which are connected by springs to each other in a three-dimensional space as shown in Figure 2.2. In this model, motion of atoms can be considered as harmonic around the equilibrium position. Due to the coupling of the atoms with each other, the motion of one atom affects the motion of the neighboring atoms resulting in propagation of the motion through the crystal and hence the creation of a phonon. With increasing temperature, the thermal energy of the atoms and the number of activated phonons increase.

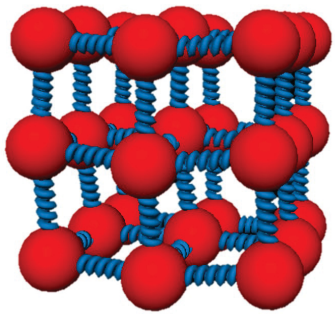

Figure 2.2: Simple model of a crystal where the atoms are considered connected to each other as if by elastic springs.

Phonons can be divided into acoustic and optical modes, as described above for the Debye and Einstein model. (The term 'optical' was chosen because the modes can be excited by electromagnetic waves in ionic crystals [14]). To illustrate the dispersion of both types of modes a diatomic linear chain is considered with two different masses, M_1 and M_2, a unit cell length of a, and an interatomic force constant, β; see Figure 2.3 [14]. From the displacements of the atoms the dispersion relation, $\omega(\vec{k})$, can be calculated with [14]

$$\omega(\vec{k})^2 = \beta\left(\frac{1}{M_1}+\frac{1}{M_2}\right) \pm \beta\sqrt{\left(\frac{1}{M_1}+\frac{1}{M_2}\right)^2 - \frac{4}{M_1 M_2}\sin^2\left(\frac{\vec{k}a}{2}\right)}. \tag{2.13}$$

As an example of the dispersion relation of a linear diatomic chain, a mass ratio of $M_1/M_2 = 3$ was chosen (see Figure 2.4). The two branches (acoustic and optical) have different behavior at the Brillouin zone center, Γ. The frequency of the acoustic branch goes to zero at small wave vectors. At low wave vectors the angular frequency has a linear relationship with the wave vector describing the dispersion-free propagation of sound waves [14].

Note that the atoms vibrate coherently in the acoustic modes, whereas the oscillation of the atoms is out of phase in the optical branch. Thus, the optical branch has two limits. At the Brillouin zone center, the displacements of each sublattice (M_1 and M_2) are identical and therefore, the sublattices vibrate against each other and the angular frequency is proportional to the reduced mass ($M_{red} = \left(M_1^{-1} + M_2^{-1}\right)^{-1}$) [75]. At the Brillouin zone edge, k/a, one sublattice is at rest and the angular frequency is equal to $\left(2\beta M_2^{-1}\right)^{1/2}$ [14]. The difference between

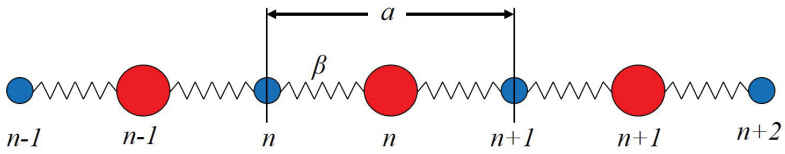

Figure 2.3: Linear diatomic chain with a unit cell length of a and an interatomic force constant, β. Adapted from reference [14].

the acoustic band maximum and the optical band minimum is defined as the phononic band gap and it increases with increasing mass ratio, M_1/M_2.

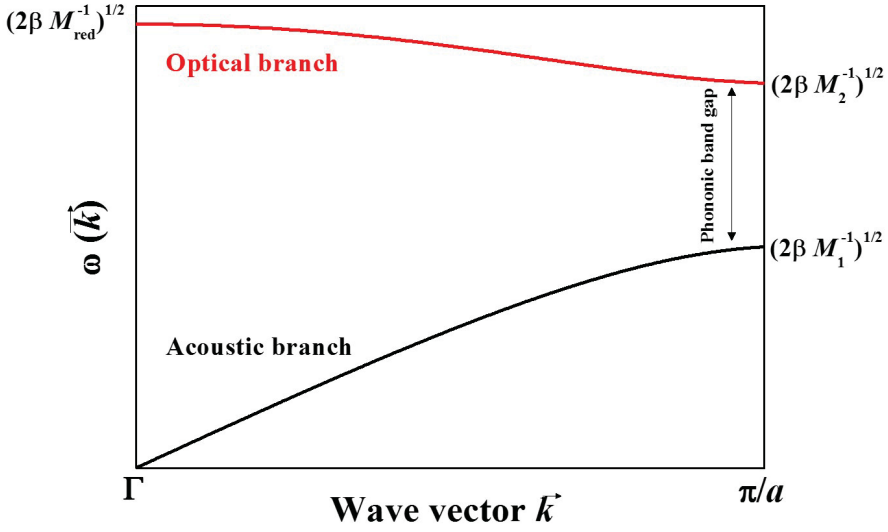

Figure 2.4: Dispersion of acoustic and optical branches of a linear diatomic chain in the first Brillouin zone. The phononic band gap increases with increasing mass ratio. Adapted from reference [75].

2.2.1.b Scattering Mechanisms

The phononic contribution of the thermal conductivity, also known as lattice thermal conductivity, is normally described by the Callaway model defined as

$$\kappa_{pho}(\omega) = \int_0^{\omega_{max}} \frac{1}{3} C_s(\omega) v_g(\omega)^2 \tau_{rel}(\omega) \mathrm{d}\omega \tag{2.14}$$

where $C_s(\omega)$ is the heat capacity per unit volume, $\tau_{rel}(\omega) = \frac{\lambda_{pho}}{v_g}$ is the relaxation time, and λ_{pho} is the phonon mean free path [81]. While the group velocity has only a slight temperature dependence the heat capacity and relaxation time are strongly temperature dependent. On the one hand, the heat capacity dramatically increases at low temperature (Debye T^3-law) and is nearly constant at high temperature according to the Dulong-Petit law (*vide supra*). On the other hand, the relaxation time decreases with increasing temperature [82] which cannot be explained with the assumption of harmonic oscillators. If the lattice vibrations were solely harmonic, the phonons could be scattered only by boundaries or lattice defects, which would be temperature-independent (*vide infra*). Therefore, the relaxation time can be decreased by phonon-phonon interactions due to anharmonic behavior.

There are two types of phonon-phonon interactions, as shown in Figure 2.5. At low temperature two phonons with wave vectors $\vec{k}_1$ and $\vec{k}_2$ interact to give a single phonon with wave vector $\vec{k}_3$. This process is called Normal or 'N' process, given by $\vec{k}_1 + \vec{k}_2 = \vec{k}_3$ [14]. In the Normal process, the resultant phonons are in the same direction as the corresponding original phonons and increase the length of the wave vectors (see Figure 2.5 (a)).

With increasing temperature the wave vectors are getting longer and two phonons can interact to give a single phonon with a wave vector which would be larger than the first Brillouin zone, the boundary for phonons [75]. The out-of-boundary phonon with wave vector, $\vec{k}_3'$, is brought back in the first Brillouin zone by the reciprocal wave vector, $\vec{G}$, and therefore, the resultant phonon with wave vector, $\vec{k}_3''$, is in the opposite direction to the original phonons with wave vectors, $\vec{k}_1'$ and $\vec{k}_2'$, as shown in Figure 2.5 (b) ($\vec{k}_1' + \vec{k}_2' - \vec{G} = \vec{k}_3''$) [75]. This process is called Umklapp (German for 'flip-over') or 'U' process, which is counter to the general direction of thermal conductivity. Because the phonon population is temperature-dependent, the relaxation time due to Umklapp scattering, $\tau_{ref,U}$, decreases with temperature and is given by

$$\tau_{rel,U} = \frac{(6\pi^2)^{1/3}}{2} \frac{\bar{M} v_g v_p^2 N^{1/3}}{k_B V_{UC}^{1/3} \gamma^2 \omega^2 T} \tag{2.15}$$

where V_{UC} is the unit cell volume, $\bar{M}$ is the average atomic mass and γ is the Grüneisen parameter [82]. Due to the γ^2 behavior, prediction of the Grüneisen parameter is required to accurately estimate the thermal conductivity. The Grüneisen parameter

describes the anharmonicity in the system and is in general defined by

$$\gamma = V\left(\frac{\partial p}{\partial U}\right)_V \tag{2.16}$$

where p is the pressure [83]. Using the definition for the bulk modulus ($B = -V\left(\frac{\partial P}{\partial V}\right)_T$), the coefficient of volumetric thermal expansion ($\alpha_V = \frac{1}{V}\left(\frac{\partial V}{\partial T}\right)_p$), and the molar heat capacity at constant volume (see Equation 2.1) the Grüneisen parameter can be estimated from [83]

$$\gamma = V_m \frac{\alpha_V \cdot B}{C_{V,\mathrm{mol}}}. \tag{2.17}$$

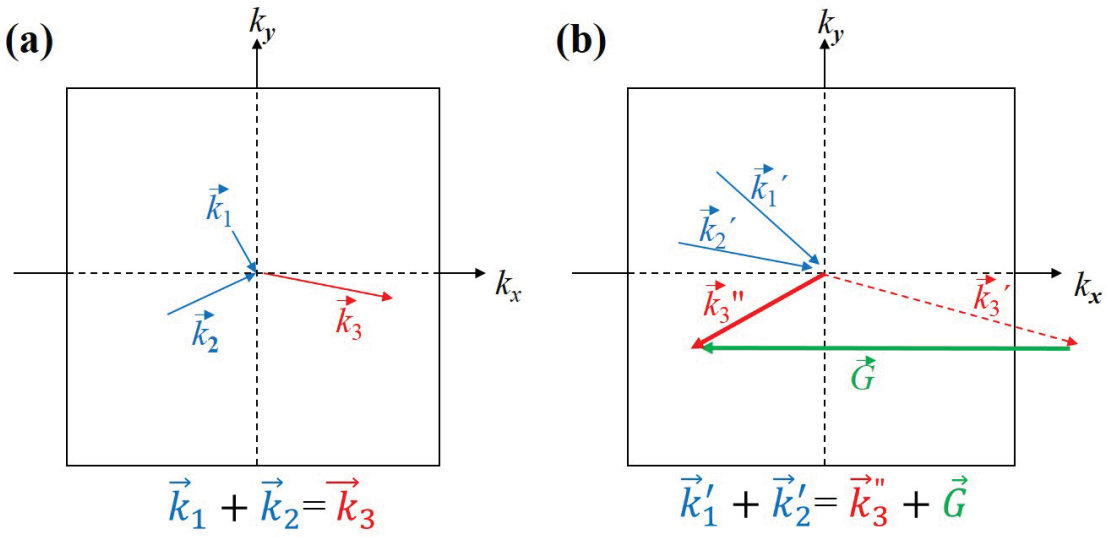

Figure 2.5: (a) Normal and (b) Umklapp processes in the first Brillouin zone. Whereas the original phonons (blue) travel in the same directions as the resultant phonon (red) in the Normal process, the resultant phonon, $\vec{k}_3'$ is longer than the first Brillouin zone in the Umklapp process and was brought back by the reciprocal vector, $\vec{G}$ (green). Adapted from reference [75].

In addition to the Umklapp process, other scattering mechanisms, such as grain boundary and point defects, can reduce the phononic relaxation time and the total relaxation time is defined by [82]

$$\tau_{rel}^{-1} = \sum_i \tau_{rel,i}. \tag{2.18}$$

Therefore, the relaxation time is limited by the shortest relaxation time of the various scattering mechanisms. Scattering by point defects is especially important in extrinsically doped compounds because it arises from mass and strain contrast within the lattice [82]. In the case in which a crystallographic site is occupied with another element (with mass m_i, radius r_i, and fraction of atoms, f_i), point defect scattering is given by

$$\tau_{rel,PD}(\omega)^{-1} = \frac{V\omega^4}{4\pi v_p^2 v_g} \sum_i f_i \left(\left[1 - \frac{m_i}{\bar{m}}\right]^2 + \left[1 - \frac{r_i}{\bar{r}}\right]^2 \right) \tag{2.19}$$

where $\bar{m}$ and $\bar{r}$ are the average mass and radius on the site, respectively [82].

While the phonon-phonon scattering and point defect scattering are frequency-dependent, the relaxation time due to grain boundary scattering, $\tau_{rel,B}$, is independent of the frequency and only limited by the grain size, d_{grain}, as given by [82]

$$\tau_{rel,B} = \frac{d_{grain}}{v_g}. \tag{2.20}$$

Grain boundary scattering is dominant at low frequencies, whereas phonon-phonon scattering and point defect scattering are dominant at high frequencies.

In (heavily doped) semiconductors, the heat transport through free electrons can also contribute significantly to the thermal conductivity and therefore, the electronic contribution to thermal conductivity is discussed.

2.2.2 Electronic Contribution to Thermal Conductivity

The contribution of the electrons to the thermal conductivity is dominant in metals resulting in relatively high thermal conductivities, *e.g.* the thermal conductivity of copper is 398 W m^{-1} K^{-1} [73]. The electronic thermal conductivity is given by

$$\kappa_{el} = \frac{\pi^2 n k_B^2 \tau_{el}}{3 m_b^*} T \tag{2.21}$$

where n is the carrier concentration, τ_{el} is the relaxation time of conducting electrons, and m_b^* is the band effective mass [75]. The band effective mass is given by the second derivative of the energy, E, with respect to the wave vector and can be described by

$$m_b^* = \frac{1}{\hbar^2} \frac{\partial^2 E(\vec{k})}{\partial \vec{k}^2}. \tag{2.22}$$

The electronic contribution of thermal conductivity of a metal can be calculated from the Wiedemann-Franz law. According to the Wiedemann-Franz law, in metals the ratio of the electronic contribution of the thermal conductivity to the electrical conductivity (σ_{el} [further discussed below]) is linearly proportional to the temperature

$$\frac{\kappa_{el}}{\sigma_{el}} = \frac{\pi^2 k_B^2}{3q^2} T = L_{eff} T \tag{2.23}$$

where $q = 1.602 \cdot 10^{-19}$ C is the elementary charge [14]. The proportional factor is known as the effective Lorenz factor, L_{eff}, which is nearly constant for metals ($L_{eff} = L_{eff,0} = 2.44 \cdot 10^{-8}$ W Ω K^{-2}) [73]. However, the effective Lorenz number decreases for semiconductors and can be approximated by different models, such as the SPB model (see Section 2.5). Recently, the effective Lorenz number [in W Ω K^{-2}] in semiconductors was estimated by

$$L_{eff} = \left(1.5 + \exp\left[-\frac{|S|}{116}\right]\right) \cdot 10^{-8} \tag{2.24}$$

with S as the Seebeck coefficient [84]. For this estimation of the Lorenz number, only the experimental Seebeck coefficient is needed, and it can be predicted with a maximum error of 26% [84]. The Seebeck coefficient is discussed in the following section.

2.3 Peltier and Seebeck Coefficients

The Seebeck coefficient, S, also known as thermopower, is an important parameter for thermoelectric materials due to the S^2 dependence of the thermoelectric figure of merit (see Equation 1.15). For simplicity, the related Peltier coefficient, Π, is first discussed.

If two materials (A and B) are connected and a current, I, is applied, a temperature gradient is generated at the connecting points [22]. In the case of electrons as dominant charge carrier, the electrons flow via the conduction bands. If material A's conduction band has lower energy than that of material B, the electrons require energy to be excited into the conduction band of material B. The electrons take thermal energy from the environment and therefore, the temperature at this connection decreases. On the other side, when the electrons flow from the higher conduction band of material B to that of material A, energy is released and

the temperature on this side increases. The heat flow, Q, is proportional to the current and the Peltier coefficient, Π, as given by

$$Q = \Pi I. \tag{2.25}$$

The definition of the Seebeck coefficient is similar. If materials A and B are placed in a temperature gradient, charge carriers are promoted by thermal energy from the valence band into the conduction band. These charge carriers diffuse to a region of lower temperature where charge builds up and a voltage is generated. However, through opposite charge carriers at the hot and cold side, an electric field is also built up, forcing the charge carriers from the cold side to hot side. If the temperature gradient remains constant, the charge carrier migrations equalize resulting in a larger number of charge carriers on the cold side. The Seebeck coefficient is proportional to the potential difference, ΔV, and defined as [16]

$$S = -\frac{\Delta V}{\Delta T}. \tag{2.26}$$

The Seebeck and Peltier coefficients are related by the Kelvin equation ($\Pi = TS$) [16]. Two different charge carriers can be dominant in the Seebeck coefficient. If holes are the majority charge carrier, the Seebeck coefficient, S_p, is positive and the semiconductor is defined as p-type. *Vice versa*, if electrons are the dominant charge carriers, the Seebeck coefficient, S_n, is negative and the semiconductor is defined as n-type.

The temperature-dependence of the Seebeck coefficient can be described by the Mott relation for nearly free electrons

$$S(T) = \frac{2k_B^2}{3q\hbar^2}\left(\frac{\pi}{n}\right)^{2/3}(1+\lambda_S)m^*_{DOS}T \tag{2.27}$$

where m^*_{DOS} is the density of states (DOS) effective mass and λ_S is the scattering parameter (*e.g.*, $\lambda_S = 0$ for acoustic phonon scattering which is typical in thermoelectric materials) [85]. Equation 2.27 depicts the inverse relationship between the Seebeck coefficient and the carrier concentration, *i.e.*, the Seebeck coefficient decreases with increasing carrier concentration. Furthermore, the Seebeck coefficient is proportional to the DOS effective mass at the band edges which includes the band effective mass, m^*_b, and the electronic band degeneracy, N_v [50]:

$$m^*_{DOS} = N_v^{2/3} \cdot m^*_b. \tag{2.28}$$

A high Seebeck coefficient requires a high DOS effective mass and a low carrier concentration. (Further discussion of the effective mass is given in the next section.) Due to the high carrier concentration in metals, the Seebeck coefficient is lower in metals than in semiconductors ($|S_{\text{metal}}| \sim$ few µV K^{-1}; $|S_{\text{semiconductor}}| \sim$ few hundred µV K^{-1}) [13].

According to Equation 2.27 the Seebeck coefficient increases with temperature. However, the total Seebeck coefficient is the sum of the contributions from the majority and minority charge carriers weighted by the electrical conductivities and can be calculated from

$$S_{total} = \frac{S_p \sigma_{el,p} + S_n \sigma_{el,n}}{\sigma_{el,p} + \sigma_{el,n}} \tag{2.29}$$

where $\sigma_{el,p}$ and $\sigma_{el,n}$ is the electrical conductivity due to holes and electrons, respectively [86]. Whereas at low temperature the contribution of the minority charge carriers is low, the minority charge carriers exponentially increase with temperature. The Seebeck coefficient of the minority charge carriers can be higher than the majority charge carriers according to Equation 2.27 leading to a peak in the total Seebeck coefficient. The origin of the Seebeck coefficient peak is normally referred to as the onset of the bipolar contribution [86].

2.4 Electrical Conductivity

As the thermal conductivity describes the ability to conduct thermal energy, the electrical conductivity, σ_{el}, is the ability to conduct electrical current. The electrical conductivity is in general determined from the electrical resistance, R, which is defined by Ohm's law

$$R = \frac{\Delta V}{I} \tag{2.30}$$

where an electrical current is applied and the potential difference across the sample is measured [73]. The electrical resistance is an extrinsic property (*i.e.*, the property depends on the dimensions of the sample). To compare it values, the electrical resistance is converted to the intrinsic properties of electrical conductivity and electrical resistivity, ρ_{el}, respectively, described by

$$\sigma_{el} = \frac{1}{\rho_{el}} = \frac{L}{R \cdot A_{cross}} \tag{2.31}$$

where L and A_{cross} is the thickness and the cross-sectional area, respectively, of the sample [73]. Equation 2.31 holds only for isotropic materials and the electrical conductivity and electrical resistivity are both second rank tensors for anisotropic materials.

Materials can be classified based on the electrical conductivity. Aside from superconductors, metals have the highest electrical conductivity ($\sigma_{el} < 10^{-3}$ S m^{-1})[1], followed by semiconductors (10^{-3} S m$^{-1} < \sigma_{el} < 10^{4}$ S m^{-1}) and insulators ($\sigma_{el} < 10^{-3}$ S m^{-1}) [73]. Note that the electrical conductivity of non-superconductors ranges over 26 orders of magnitude whereas thermal conductivity ranges just over five orders of magnitude [73]. The electrical properties of materials also can be classified by the band structure and the carrier concentration as further discussed below.

2.4.1 'Free-Electron Gas' Theory

The high electrical conductivity in metals can be described by the 'free-electron gas' theory which assumes that all conduction electrons are delocalized and can move freely in a metal while the surface acts as an infinite barrier [14]. The interactions of electrons with atomic cores are neglected. The possible energy states of the 'free' electrons, E_k, in a three-dimensional box with length, L_{box}, and fixed boundary conditions are given by the time-independent Schrödinger equation

$$-\frac{\hbar^2}{2m_e}\nabla^2\psi_k(\vec{r}) = E_k\psi_k(\vec{r}) \tag{2.32}$$

leading to the solution of the wavefunction $\psi_k(\vec{r})$

$$\psi_k(\vec{r}) = L_{box}^{-3/2}\mathrm{e}^{i\vec{k}\cdot\vec{r}} \tag{2.33}$$

and of the possible energy states for a particle

$$E_k = \frac{\hbar^2\vec{k}^2}{2m_e} = \frac{\hbar^2}{2m_e}\left(k_x^2 + k_y^2 + k_z^2\right). \tag{2.34}$$

where $m_e = 9.109 \cdot 10^{-31}$ kg is the mass of an electron [14]. The wave vector, $\vec{k}$, is quantized and given by

$$k_n = \frac{\pi}{L_{box}}n_n \tag{2.35}$$

[1] Siemens [S] = [Ω^{-1}]

where $n_p = 1, 2, 3...$ is the principal quantum number [75]. According to the Pauli exclusion principle, each energy state can be occupied by two electrons, one of each spin [75].

At absolute zero, the highest occupied energy level is defined as the Fermi energy, E_F^0, which is given by

$$E_F^0 = \frac{\hbar^2}{2m_e}\left(\frac{3\pi^2 N_e}{V}\right)^{2/3} \tag{2.36}$$

for a 3D system with N_e electrons and a volume, V [14]. Above the Fermi energy the energy states are unoccupied, but the electrons can be thermally excited to higher energy states with increasing temperature. The temperature and energy dependence of the probability that an energy state is occupied is defined by the Fermi-Dirac distribution function

$$f(E,T) = \frac{1}{\mathrm{e}^{(E-\mu)/k_B T} + 1} \tag{2.37}$$

where μ is the chemical potential of the electrons, also known as the Fermi level. Note that the Fermi level is the energy where the bands are half-filled and the Fermi level equals the Fermi level, *i.e.*, $\mu = E_F^0$, at $T = 0$ K.

Whereas the 'free-electron gas' theory can explain the heat capacity, thermal conductivity, and electrical conductivity of metals, the theory fails for semiconductors and insulators because the interaction of the conduction electron waves with ion cores of the crystal has to be considered. The electrical conductivity in nonmetals can be better described by the band theory.

2.4.2 Band Theory

In contrast to the 'free-electron gas' theory, band theory considers the interactions between the delocalized electron waves and the ion cores in the crystals, resulting in a separation between the electron bands [75]. The region where no wavelike electron orbital exists is defined as the band gap or energy gap [14].

The ion cores in the crystal can be modelled by a periodic potential leading to a plane wave solution of the time-independent Schrödinger equation [14]. The plane waves are modulated by a function which includes the periodicity of the lattice and

is given by

$$U_k(\vec{r}) = \sum_G C_{k-G} \mathrm{e}^{-i\vec{G}\cdot\vec{r}} \tag{2.38}$$

where C_{k-G} is an expansion coefficient in reciprocal space and $\vec{G}$ is a reciprocal lattice vector [75]. The modulated function is known as the Bloch function leading the to modulated plane wave, also known as Bloch wave [75],

$$\psi_k(\vec{r}) = U_k(\vec{r})\mathrm{e}^{i\vec{k}\cdot\vec{r}}. \tag{2.39}$$

According to Bloch's theorem, many parabolic bands exist which are shifted by reciprocal lattice vectors and therefore, the energies are periodic functions of $\vec{k}$ and $\vec{G}$,

$$E_k(\vec{k}) = E_k(\vec{k} + \vec{G}). \tag{2.40}$$

The electrons act as plane waves which travel in the first Brillouin zone and are reflected at their zone boundaries. A standing wave is produced from the superposition of the incoming and reflected wave with the two wavefunctions ψ_+ and ψ_- [14]. The maximum charge density of the electrons in state ψ_+ are at the ion cores whereas the electrons in state ψ_i have the maximum charge densities between the ion cores, resulting in a higher energy compared with free electrons. The energy difference between the electrons in states ψ_+ and ψ_- and free electrons leads to a divergence of the bands and hence, a band gap. According to the tight-binding approximation, larger overlap of atomic orbitals increases the band gap energy, E_g [75].

The electronic properties of materials can be classified by the band gap energy. The electronic band structure of a metal (Cu; space group: $Fm\bar{3}m$) and a semiconductor (Si; space group: $Fd\bar{3}m$) are shown in Figure 2.6. The bands with energy lower than the Fermi energy are called valence bands and the bands with higher energy are defined as conduction bands.

If there is no band gap, the solid has metallic behavior (see Figure 2.6 (a)). Semiconductors and insulators have a band gap between valence and conduction bands at absolute zero (Figure 2.6 (b)). There is no exact value where the behavior switches from semiconducting to insulating, but if the band gap is smaller than 2 eV

the solid is considered to be a semiconductor whereas above 2 eV the material has insulating behavior [87]. However, doping can change the behavior from insulating to semiconducting and therefore, the carrier concentration also has to be considered.

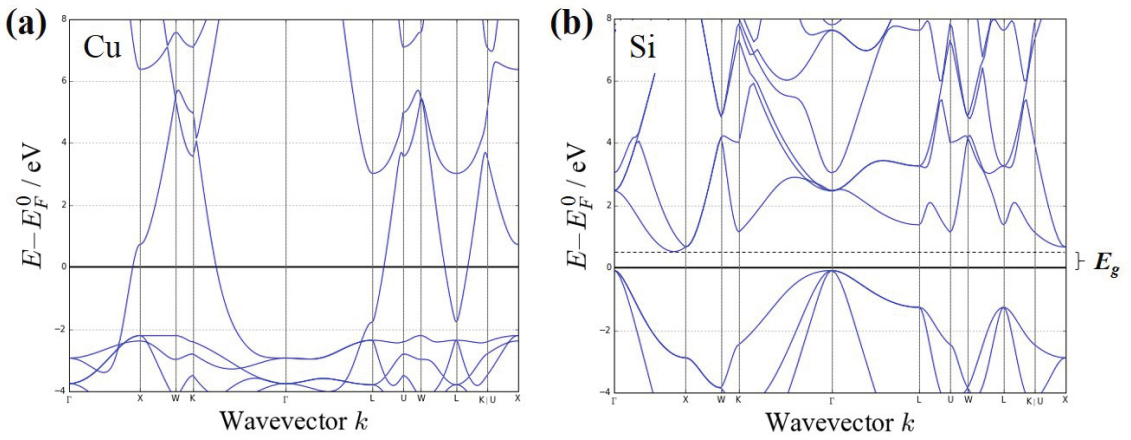

Figure 2.6: Computed electronic band structure of (a) metallic Cu (space group: $Fm\bar{3}m$) and (b) semiconducting Si (space group: $Fd\bar{3}m$). Si has a computed band gap energy of 0.6 eV. Electronic band structures were taken from 'The Materials Project' [48].

2.4.3 Temperature Dependence of Electrical Conductivity

The temperature dependence of the electrical conductivity is generally different for metals and semiconductors and can be explained by the Drude model. According to the Drude model, the electrical conductivity is given by

$$\sigma_{el}(T) = q\mu_{el}(T)n(T) \tag{2.41}$$

where $\mu_{el}(T)$ is the electron mobility and $n(T)$ is the carrier concentration [75]. While the carrier concentration is nearly temperature-independent in metals, the electron mobility can dramatically change with temperature, as described by

$$\mu_{el}(T) = q\frac{\tau_{el}(T)}{m_b^*(T)}. \tag{2.42}$$

The effective band mass is nearly temperature independent for metals and therefore, the temperature dependence of the electrical conductivity in metals is strongly

related to the relaxation time. The most common scattering mechanism is acoustic deformation potential scattering for which the relaxation time is given by

$$\tau_{el,ac}(T) = \frac{\pi\hbar^4 c_{11}}{2^{0.5}(m_b^*)^{1.5}(k_B T)^{1.5}\Xi^2}\varepsilon^{-0.5} \tag{2.43}$$

where c_{11} is the longitudinal elastic constant, Ξ is the deformation potential, and $\varepsilon = Ek_B^{-1}T^{-1}$ is the reduced energy [50]. The relaxation time for acoustic deformation potential scattering is inversely proportional to temperature and therefore the electrical conductivity should linearly decrease with temperature. This behavior is also described by Matthiessen's rule where the electrical resistivity has two components, a temperature-independent component due to defects, $\rho_{el,defect}$, and a temperature-dependent one due to electron-phonon interactions, $\rho_{el,phonons}$ [75]. The temperature-dependent electrical resistivity in metals is, therefore, given by

$$\rho_{el,\text{metal}}(T) = \rho_{el,defect} + \rho_{el,phonons}(T). \tag{2.44}$$

.

In nonmetals, in addition to the electron mobility, the carrier concentration is also temperature-dependent and increases rapidly with increasing temperature [14]. The carrier concentration in intrinsic semiconductor is given by

$$n(T) \propto T^{3/2}\mathrm{e}^{-\frac{E_g}{2k_B T}}, \tag{2.45}$$

and with increasing band gap energy, the carrier concentration decreases [88]. The electron mobility in semiconductors, similar to metals, decreases with temperature and is mostly limited by acoustic phonons $\mu_{el} \propto T^{-3/2}$ [88]. The electrical conductivity for semiconductors is calculated by combining the temperature behavior of the carrier concentration and of the electron mobility leading to

$$\sigma_{el,\text{semiconductor}} = qn_0\left(\mu_{el,n} + \mu_{el,p}\right)\mathrm{e}^{-\frac{E_g}{(2k_B T)}} \tag{2.46}$$

where n_0 is the number of charge carriers, and $\mu_{el,n}$ and $\mu_{el,p}$ are the electron mobilities of the electrons and holes, respectively [89].

Equation 2.42 is only valid for isotropic materials and the electron mobility can change by more than an order of magnitude in different directions in anisotropic materials due to changing band effective masses in different crystallographic directions.

2.4.4 Anisotropy of Electrical Conductivity

In the case of a single parabolic band, the Fermi surface is spherical and the band effective mass, given by the second derivative of the energy with respect to its wave vector, is a constant [50]. However, in real electronic band structures the bands are off-center and several degenerate bands contribute to the electron transport. Therefore, the valleys or carrier pockets cannot be described by spherical Fermi surfaces and are often approximated by ellipsoids using two different band effective masses [50]. The two band effective masses are defined as the longitudinal, $m_{\parallel}^{*}$, and transverse, $m_{\perp}^{*}$, component and the band effective mass is averaged by [50]

$$m_b^* = \left(\left[m_{\perp}^* \right]^2 m_{\parallel}^* \right)^{1/3}. \tag{2.47}$$

The DOS effective mass is not affected by anisotropy because it is proportional to the average band effective mass (see Equation 2.28) whereas the band effective mass can change in different directions due to distorted spherical Fermi surfaces. Therefore, anisotropy can lead to high power factors in certain crystal directions [50].

2.5 Single Parabolic Band Model

The single parabolic band (SPB) model is a useful model for thermoelectric materials to determine the optimum carrier concentration. The model has the advantage that only a single sample is required to determine the highest thermoelectric figure of merit. The model is based on the assumption of a single parabolic band, *i.e.*, the band effective mass is constant, and the contribution of the minority carrier to the electron transport is negligible [90]. Furthermore, it is assumed that acoustic scattering is the limiting factor for the electron mobility ($\mu_{el} \propto T^{-3/2}$) which is often the case in thermoelectric materials. For calculation with the SPB model, the experimental Hall mobility, μ_H, Hall carrier concentration, n_H, Seebeck coefficient, and thermal conductivity are required. The Hall carrier concentration

$$n_H = \frac{1}{R_H q} \tag{2.48}$$

and the Hall mobility

$$\mu_H = \frac{R_H}{\rho} \tag{2.49}$$

can be calculated from the Hall coefficient, R_H, and the electrical conductivity [90]. Although the Hall carrier concentration and Hall mobility are not the same as the carrier concentration and the electron mobility, the SPB model can provide a good estimation of the conversion factor (*vide infra*).

In the first step of the SPB calculation, the DOS effective mass is determined from the Seebeck coefficient and the Hall carrier concentration by numerically solving

$$S = \frac{k_B}{q}\left(\frac{2F_1}{F_0} - \eta\right) \tag{2.50}$$

and

$$n_H = 4\pi\left(\frac{2m^*_{DOS}k_BT}{h^2}\right)^{3/2}\frac{F_{1/2}}{r_H}. \tag{2.51}$$

The Fermi integral is given by

$$F_j(\eta) = \int_0^\infty \frac{\zeta^j}{1+\mathrm{e}^{\zeta-\eta}}\mathrm{d}\zeta \tag{2.52}$$

where $\zeta = \frac{varepsilon}{k_BT}$ is the reduced carrier energy, $\eta = \frac{\zeta}{k_BT}$ is the reduced chemical potential [90] and

$$r_H = \frac{3}{2}F_{1/2}\frac{F_{-1/2}}{2F_0^2} \tag{2.53}$$

is the Hall factor. The Hall factor is required to convert the Hall mobility and Hall carrier concentration to the electron mobility. For parabolic bands at high carrier concentrations and low temperature, the Hall carrier concentration and chemical carrier concentration are nearly the same, however, in the non-degenerate electron gas, the chemical carrier concentration can be 20% higher than the Hall carrier concentration when acoustic scattering is assumed to be limiting factor for the mobility [90]. The chemical carrier concentration

$$n = \frac{n_H}{r_H} \tag{2.54}$$

and the electron mobility

$$\mu_{el} = \mu_H\frac{2F_0}{F_{-1/2}} \tag{2.55}$$

can be calculated numerically with the Fermi integral determined from the experimental Seebeck coefficient (see Equation 2.50). The next step is to calculate the effective Lorenz number from

$$L_{eff} = \left(\frac{k_B}{q}\right)^2 \frac{3F_0F_2 - 4F_1^2}{F_0^2} \tag{2.56}$$

which can be used to determine the electronic contribution of the thermal conductivity (Equation 2.23). The electronic contribution is subtracted from the total thermal conductivity to obtain the lattice thermal conductivity. The thermoelectric figure of merit zT can be determined from the Seebeck coefficient, the effective Lorenz number, the electron mobility, the DOS effective band mass, and the lattice thermal conductivity by

$$zT = \frac{S^2}{L + (\Psi\beta)^{-1}} \tag{2.57}$$

where the thermoelectric functions Ψ and β are

$$\Psi = \frac{8\pi q}{3}\left(\frac{2m_e k_B}{h^2}\right)^{3/2}(1+\lambda_S)F_\lambda \tag{2.58}$$

and [90]

$$\beta = \frac{\mu_{el}\left(m^*_{DOS}/m_e\right)^{3/2}T^{5/2}}{\kappa_{pho}}, \tag{2.59}$$

respectively. With constant DOS effective mass, electron mobility, lattice thermal conductivity, and temperature, the thermoelectric figure of merit can be calculated for various carrier concentrations. However, the model fails for multi-bands effects and non-parabolic bands due to changes in DOS effective mass with carrier concentration [90]. Furthermore, to change the carrier concentration experimentally, the compounds is generally doped which can influence both the effective band mass and the phononic contribution of the thermal conductivity, *e.g.*, point defect scattering.

2.6 Boltzmann Transport

The Boltzmann transport calculation takes a semi-classical approach to describe the electrical and thermal transport properties of a material. In thermal equilibrium (*i.e.*, homogeneous temperature and no external force), the distribution can be

estimated by the Fermi-Dirac equations (see Equation 2.37). However, in non-equilibrium conditions, the distribution function changes over time and can be represented by

$$\frac{\partial f}{\partial t} + \vec{v} \cdot \nabla_r f + \vec{F}_e \cdot \nabla_p f = \left(\frac{\partial f}{\partial t}\right)_{coll} \tag{2.60}$$

where f is the probability density function, $\vec{F}_e = -q\vec{E} + q\vec{v} \times \vec{B}$ is the external force, p is the momentum of electrons and phonons, $\vec{E}$ is the electric field vector, and $\vec{B}$ is the magnetic field vector [14, 75]. This equation is known as the Boltzmann transport equation. The collision term $\left(\frac{\partial f}{\partial t}\right)_{coll}$ describes the in- and out-scattering and it can be approximated by the constant relaxation time approach [14]. In the constant relaxation time approach, it is assumed that the distribution does not vary significantly from the equilibrium distribution, f_0, in time τ_{el}. Therefore, the collision term can be written as

$$\left(\frac{\partial f}{\partial t}\right)_{coll} = -\frac{f - f_0}{\tau} = -\frac{\delta f}{\tau_{el}} \tag{2.61}$$

The negative sign in the constant relaxation time approach brings the distribution f back to equilibrium [14]. The steady-state Boltzmann transport equation (*i.e.*, $\frac{\partial f}{\partial t} = 0$) without external magnetic field is described by

$$\vec{v} \cdot \nabla_r f - \frac{q}{\hbar}\vec{E} \cdot \nabla_p f = -\frac{\delta_f}{\tau_{el}}. \tag{2.62}$$

Under the assumption that the solution is near-equilibrium ($f(\vec{p}) = f_0(\vec{p}) + \delta f(\vec{p}) \simeq f_0(\vec{p})$), Equation 2.62 is given by

$$\left(\vec{v} \cdot \nabla_r f_0 - \frac{q}{\hbar}\vec{E} \cdot \nabla_p f_0\right) \cdot \tau_{el} = \delta_f \tag{2.63}$$

using the Fermi function,

$$f_0(\vec{p}) = \frac{1}{1 + \exp}\left[E_c(\vec{r}) + E(\vec{p}) - F_n(\vec{r})\right] \tag{2.64}$$

where E_c is the energy of the conduction band and the Fermi level is replaced by the quasi-Fermi level, $F_n(\vec{r})$, because it is position-dependent [91]. Applying the chain rule, the steady-state, near-equilibrium solution of the Boltzmann transport equation is given by

$$\delta f = \tau_{el}\left(-\frac{\partial f_0}{\partial E}\right)\left[\vec{v} \cdot \vec{F}\right] \tag{2.65}$$

with the generalized force [91]

$$\vec{F} = -\nabla_r F_n(\vec{r}) + T\left[E_c(\vec{r}) + E(\vec{k}) - F_n(\vec{r})\right]\nabla_r\left(\frac{1}{T}\right). \tag{2.66}$$

The generalized force contain two driving forces ($\nabla_r F_n$ as the gradient in the quasi-Fermi level, and $\nabla_r\left(\frac{1}{T}\right)$ as the gradient in inverse temperature).

With the steady-state, near equilibrium Boltzmann transport equation, the electrical conductivity can be calculated from the current density, $j_{n,x}$, for an isothermal solid which has a potential different only in the x-direction

$$j_{n,x} = \frac{1}{\Omega}\sum_k q^2 v_x^2 \tau_{el}\left(-\frac{\partial f_0}{\partial E}\right)\left(\frac{\mathrm{d}F_n/q}{\mathrm{d}x}\right) = \sigma_{el}\left(\frac{\mathrm{d}F_n/q}{\mathrm{d}x}\right) \tag{2.67}$$

where Ω is the volume of the k-space [91]. The sum is converted to an integral and the electrical conductivity for parabolic bands (*i.e.*, $E - E_c = \frac{\hbar^2 k^2}{2m_b^*}$) with energy-independent relaxation time can be written as

$$\sigma_{el} = q\left(\frac{q\tau_{el}}{m_b^*}\right)N_v\frac{1}{3}\left(\frac{2m_b^*}{\pi\hbar^2}\right)^{3/2}\int_{E_C}^{\infty}(E - E_C)^{3/2}\left(-\frac{\partial f_0}{\partial E}\right)\mathrm{d}E \tag{2.68}$$

where N_v is the valley degeneracy [91]. For more information about the Boltzmann transport equation reference [91] is recommended.

In the present study, the Boltzmann transport properties were computed with the software BoltzTrap [49].

Chapter 3

Experimental Techniques

This chapter gives insight concerning the instruments and experimental techniques used in this study, both to characterize the materials and to determine the transport properties. In the first section the characterization techniques used to identify the chemical compositions, morphology, temperature-dependency as well as the crystal and molecular structure are described. In the following part, the instruments and measurement techniques to determine the relevant physical properties of the materials are presented. In addition to the theoretical understanding of these methods, the limitations and uncertainties of the thermoelectric properties are discussed. In the last section, a finite-element modelling technique which was used to determine the accuracy of heat transport in a lab-developed powder cell is described.

3.1 Characterization

3.1.1 Powder X-ray Diffraction

One of the most important characterization techniques in materials science is powder X-ray diffraction (PXRD). It is a fast and non-destructive technique to characterize the crystal structure as well as the crystallinity of materials. In addition to the crystal structure and crystallinity, the stoichiometric composition, *i.e.* the occupation of atoms on a lattice site, and the crystallite size can be obtained from PXRD measurements.

3.1.1.a Theory

In the PXRD method a monochromatic beam of X-rays is diffracted by electrons in the crystal lattice planes and the diffracted beams generate an interference pattern. Each constructive interference of the diffracted beams corresponds to a family of planes in real space, also known as Miller planes. The condition for constructive

interference is given by Bragg's law,

$$n\lambda = 2dsin(\theta) \tag{3.1}$$

where n is an integer, λ is the wavelength of the X-ray, d is the spacing between two lattice planes, and θ is the angle between the incoming X-rays and the Miller planes [14]. A geometric derivation is shown in Figure 3.1 (a) where two beams are diffracted by the electrons of two consecutive lattice planes separated by the distance d. The path difference of the two beams is given by $2d\sin(\theta)$ (shown by the red line). To fulfill the constructive interference condition the path difference has to be an integral multiple of λ [14].

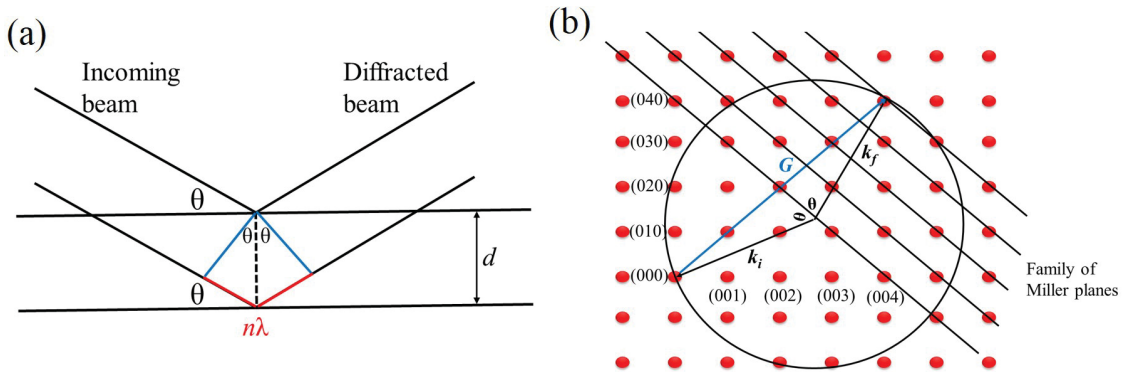

Figure 3.1: Derivation of Bragg's law. (a) The geometric derivation of Bragg's law shows that the path difference (red line) has to be an integral multiple of the wavelength for constructive interference. (b) The Ewald construction in reciprocal space requires that the Laue condition is fulfilled. Diffracted beams only appear when the reciprocal point intersects with the surface of the Ewald sphere. Adapted from reference [14].

A more physical derivation of Bragg's law uses the Ewald construction where an Ewald sphere is constructed in reciprocal space (Figure 3.1 (b)) [14]. Under the assumption that energy is conserved, meaning the scattering between X-rays and electrons is elastic ($k_i = k_f = \frac{2\pi}{\lambda}$ where k_i and k_f are the magnitudes of the incident and outgoing wave vectors, respectively), diffracted beams are only created whenever a reciprocal point coincides with the surface of the Ewald sphere. Thus, the Laue condition has to be fulfilled for diffraction, *i.e.* the difference between the incident and outgoing wave vector has to be equal to the reciprocal vector, $\vec{G}$ ($\vec{k_f} - \vec{k_i} = \vec{G}$)

[14]. As shown in Figure 3.1, diffraction is only observed if the diffraction vector, *i.e.* the vector normal to the surface, is parallel to the normal vector of the lattice plane.

While single crystals show only certain reflections, powder samples have thousands of random oriented grains and all reflections of the crystal are recorded. This means that PXRD can project a 3D crystal into a 1D diffractogram where each family of lattice planes corresponds to a certain Bragg angle, 2θ.

In addition to the position of the peaks in 2θ, the intensity of the peaks provides information about the relative positions, occupation, identity, and thermal distortion due to atomic vibrations [92]. The peak intensity is proportional to the structure factor which is given by

$$S_{hkl} = \sum_{\alpha} f_{\alpha} e^{-2\pi i(hu_{\alpha}+kv_{\alpha}+lw_{\alpha})} \tag{3.2}$$

where h, k, l are Miller indices, f_{α} is the atomic scattering factor and u_{α}, v_{α}, and w_{α} are the fractional coordinates in real space for the αth atom [14]. The atomic scattering factor is proportional to the number of electrons and also depends on the shape of the orbitals, *i.e.*, the more electrons, the more intense is the scattering. The exponential term relates the atomic position in real space to the reciprocal vector. A slight change in atomic position might have a large effect on the structure factor. In some cases, the structure factor also contains the Debye-Waller factor which includes the effects of thermal motion and distortion to the peak intensity [92].

Furthermore, the peak shape provides details about the morphology of the sample. If the sample and the diffractometer were perfect, the peaks would be very sharp lines. However, in real life, the peaks are broader due to small crystallite size, inhomogeneous strain, and/or instrumental effects. While the effect of the crystallite size, L_c, on the broadening, B, can be described by the Scherrer equation

$$B_L(2\theta) = \frac{K\lambda}{L_c \cos(\theta)} \tag{3.3}$$

with K as Scherrer constant [93], the broadening effect of the inhomogeneous strain, ε, is given by Stokes-Wilson equation

$$B_{\epsilon}(2\theta) = c_{\varepsilon}\varepsilon \tan(\theta) \tag{3.4}$$

where c_{ε} a constant depending on the nature of ε [94].

In many materials, both inhomogeneous strain and small crystallite size are responsible for broadening. Williamson-Hall plots are, in general, used to determine ε and L_c from plotting $(B_L(2\theta) + B_\epsilon(2\theta))\cos(\theta)$ vs. $\sin(\theta)$ [95]. The slope provides the strain component ($c_\varepsilon\varepsilon$) and the intercept gives the crystallite size ($\frac{K\lambda}{L_c}$). However, Williamson-Hall plots are based on many assumptions, *e.g.* the strain has to be isotropic and the peak shape has to be Lorentzian, and therefore, this method is more qualitative than quantitative. A more sophisticated method to determine L_c and ε was described by Warren and Averbach where the diffraction peaks are expressed as Fourier series and the two components, ε and L_c, are derived from the calculated coefficients [96]. The peak broadening can be determined with the open software package BREADTH [97, 98]. The software uses the double-Voigt method where the Gaussian and Lorentzian functions are deconvoluted. The crystallite size can be obtained from the Williamson-Hall plot of the Lorentzian function, while the inhomogeneous strain can be extracted from a combination of Lorentzian and Gaussian strain terms [98]. It is important to note that the instrumental broadening has to be removed using a standard sample.

For more details about X-ray diffraction techniques, refer to *X-Ray Diffraction Crystallography: Introduction, Examples and Solved Problems* [99] and *Full Profile Analysis of X-ray Diffraction Patterns for Investigations of Nanocrystalline Systems* [92].

3.1.1.b Instruments

For this study, three different powder X-ray diffractometers were used. PXRD diffractograms were primarily acquired in the laboratory of Dr. Mark Obrovac, Department of Chemistry, Dalhousie University, using a *Rigaku Ultima IV* diffractometer, equipped with a Cu Kα (λ = 1.541 Å) X-ray source, a graphite monochromator, and a scintillator. To prepare the measurement, the powder was ground with mortar and pestle (if necessary) and used to fill a stainless steel sample holder. For air-sensitive materials, a lab-built sample holder containing an arc-shape aluminized Mylar window was used and the sample was loaded under Ar atmosphere. If the sample quantity was low or the powder was consolidated to a pellet, a Si (510) zero background holder was applied.

For temperature-dependent measurements, a *Siemens D-500* powder diffractometer with a Cu Kα X-ray source, a monochromator, and a point detector was used in the laboratory of Andy George, Department of Physics and Atmospheric Science, Dalhousie University. The powder was consolidated to a pellet and the diffractograms were obtained in the temperature range from 123 K to 473 K.

The diffractograms of the thermoelectric materials with the nominal composition XYZ_2 were acquired with the assistance of Dr. Umut Aydemir in the laboratory of Dr. Sossina Haile, Department of Chemical Engineering, California Institute of Technology, using a a *PANalytical X'Pert Pro* diffractometer equipped with a Cu Kα X-ray source and an *XCelerator* line detector with no monochromator. High-temperature measurements were conducted using a lab-built high-temperature sealed stage under He atmosphere.

3.1.1.c Refinement Methods

To identify the phase(s) of the compound, the intensities and positions of the recorded Bragg peaks were compared to the PDF-2 database [100] using the commercial software package MATCH! [101]. If the phase agreed with literature, the diffractograms were refined using the Le Bail method followed by the Rietveld method, both implemented in the open-source software package Rietica [102]. The Le Bail method is a quick method to refine the lattice parameters as well as the space group and also can be employed for low quality diffractograms [103]. In this method, the lattice parameters, background, peak shapes, and instrumental parameters were refined without fitting the intensities, *i.e*, the atomic identities and positions were neglected in the refinement. In the second step, the parameters determined in the Le Bail method were implemented in the Rietveld refinement. The Rietveld refinement also included the intensity of the peaks which is given by

$$I_\alpha = S_f M_\alpha L_\alpha |S_{hkl_\alpha}|^2 P_\alpha A_\alpha E_\alpha \tag{3.5}$$

with S_f as a scaling factor, M_α as the multiplicity, L_α as the Lorentzian-polarization factor, P_α as the preferred orientation factor, and A_α as well as E_α as correction of the absorption and extinction, respectively, for the αth Bragg reflection [104]. For

both refinement methods, a Newton-Raphson algorithm [105] was applied where the peak shape was fitted with a pseudo-Voigt peak profile function, *i.e.* a convolution of Gaussian and Lorentzian functions. A tutorial on the Le Bail and Rietveld refinement can be found in reference [106].

3.1.2 Raman Spectroscopy

In addition to the crystal structure, the molecular structure can be examined using Raman spectroscopy. Raman spectroscopy measures the inelastic scattering of monochromatic light by elementary excitations, such as phonons, magnons, or plasmons [14]. It is a fast and non-destructive technique that provides information about the vibrational dynamics, in particular, the optical phonons that contribute to the heat capacity at elevated temperature.

3.1.2.a Theory

Light can interact with electrons of the material elastically, *e.g.* Rayleigh or Mie scattering, or inelastically, such as Raman scattering. For Raman scattering, the energy ($\hbar\omega$) and momentum ($\hbar k$) still have to be conserved and energy can be absorbed or emitted by a phonon [14]. Due to the long wavelength of visible or near-infrared light used in Raman spectroscopy, the wave vector of the incident and scattered light is small compared to the reciprocal lattice vector. This leads to the assumption that the monochromatic light interacts only with optical phonons at the center of the Brillouin zone.

The interaction of the light with atoms is a result of the polarizability of the valence electrons [14]. The electric wave of the incident light, $\vec{E}_0$, induces a polarization, $\vec{P}$,

$$\vec{P}(t) = \varepsilon_0 \overline{\overline{\chi}}_e \vec{E}_0(t) \tag{3.6}$$

where $\varepsilon_0 = 8.854 \cdot 10^{-12}$ F·m^{-1} is the electric permittivity of free space and $\overline{\overline{\chi}}_e$ is the electric susceptibility tensor [14]. The electric field of the incident light can be described by $\vec{E}_0(t) = \vec{E}_0(\omega_0)\cos(\omega_0 t)$ and therefore, $\vec{P}$ oscillates with the angular frequency, ω_0, if $\overline{\overline{\chi}}_e$ is constant. Due to the periodic modulation of $\vec{P}$ a scattering wave is emitted only at the frequency ω_0 [14]. This is the case for elastic scattering in linear optics.

However, in non-linear optics the polarizability of the valence electrons is highly dependent on the location of the atoms, *i.e.* $\overline{\overline{\chi}}_e$ is a function of the nuclear coordinates which is related to the collective excitations $X[\omega(\vec{k}), \vec{k}] = X_0 \cos(\omega(\vec{k})t)$ [14]. For small excitations $\overline{\overline{\chi}}_e$ can be expressed by the Taylor series

$$\overline{\overline{\chi}}_e(X) = \overline{\overline{\chi}}_e^0 + \frac{d\overline{\overline{\chi}}_e}{dX} X \tag{3.7}$$

where $\overline{\overline{\chi}}_e^0$ is the susceptibility in equilibrium position. If Equations 3.6 and 3.7 are combined with the expression for the electric field of the incident light, the polarization of a non-linear system can be written as [14]

$$\vec{P} = \varepsilon_0 \overline{\overline{\chi}}_e^0 \vec{E}_0(\omega_0)\cos(\omega_0 t) + \frac{1}{2}\varepsilon_0 \frac{d\overline{\overline{\chi}}_e^0}{dX} X_0 E_0(\omega_0)\{\cos[\omega_0 + \omega(\vec{k})]t + \cos[\omega_0 - \omega(\vec{k})]t\}. \tag{3.8}$$

The first term describes the elastic Rayleigh scattering which radiates at the frequency ω_0. However, the latter two terms are referred to as the Raman side bands. If the energy of the scattered wave is lost to a phonon $(\omega_0 - \omega(\vec{k}))$, the Raman side band is called a Stokes line. Alternately, with absorbing energy of the phonons the frequency of the scattered wave will increase $(\omega_0 + \omega(\vec{k}))$ and these Raman side bands are known as anti-Stokes lines. The intensities of the Raman side bands are much weaker than the elastic scattering and therefore, it is important to filter the elastic scattering.

For more information about Fourier transform Raman spectroscopy the book *Fourier Transform Raman Spectroscopy: From Concept to Experiment* [107] is recommended.

3.1.2.b Instruments

A Nicolet *NXR 9650* FT-Raman Spectrometer (Thermo Fisher Scientific), based on Fourier transform spectroscopy, was used in the laboratory of Dr. Mary Anne White, Department of Chemistry, Dalhousie University. Fourier transform (FT) spectroscopy is a faster technique than conventional Raman spectroscopy and also has the advantage that it reduces laser-induced fluorescence encountered with conventional Raman techniques [107]. This FT-Raman spectrometer is equipped with a Nd:YVO_4 laser ($\lambda_{Nd:YVO_4}$ = 1064 nm) and an InGaAs detector. Furthermore, it has a temperature stage to record the Raman spectra in the

temperature range from 123 K to 423 K. For the present measurements the sample was mounted on a holder (if the sample was a pellet) or filled in NMR tubes (if the sample was a powder) and the laser power and resolution were set to 0.04 W and 2 cm^{-1}, respectively. However, a FT-Raman spectrometer has the disadvantage that black samples are challenging to measure due to the light absorption resulting in heating of the sample and a large background emission.

For black powder samples, the Raman spectra were acquired in the laboratory of Dr. Kevin Hewitt with the assistance of Christopher Lee, Department of Physics and Atmospheric Science, Dalhousie University, using a *Jobin-Yvon T64000 Micro Raman Triple Grating spectrometer*. The micro Raman spectrometer is equipped with an argon laser ($\lambda_{Ar} = 632.8$ nm) and open electrode CCD detector. The micro Raman spectrometer has the advantage of high spatial (1 µm) and spectral resolution (0.2 cm^{-1}).

3.1.3 Energy-/Wavelength-dispersive X-ray Spectroscopy

As shown in Section 3.1.1, PXRD refinement can provide details about the composition and occupation of lattice sites in crystalline materials. However, PXRD is a semi-quantitative technique to analyze the chemical composition and cannot determine the chemical composition in semi-crystalline or amorphous phases. A more sensitive analysis of the chemical composition can be acquired using energy-dispersive X-ray spectroscopy (EDS) and/or wavelength-dispersive X-ray spectroscopy (WDS). EDS and WDS are non-destructive techniques which can also topographically map the composition.

3.1.3.a Theory

In EDS a primary high-energy electron beam interacts with the electrons in the material where a core electron is removed from the atom. An electron from a higher energy state fills the vacancy and the energy difference between the higher energy state and lower energy state is emitted as an X-ray [108]. Each element has characteristic energies for the X-rays corresponding to their allowed transitions. For an allowed transition, the total angular momentum (atom and photon) must be conserved, *i.e.*, $\Delta l = \pm 1$, and the angular momentum in the z direction has to

change by $\pm\hbar$ or less ($\Delta m_l = 0, \pm 1$ with Δm_l as the change in magnetic quantum number) [77].

In addition to the characteristic X-ray energies, a continuous X-ray spectrum is produced from zero to the incident electron energy. This spectrum is also known as Bremsstrahlung (German for 'deceleration radiation') due to the deceleration of the electron by an atomic nucleus resulting in an emission of an X-ray [108]. The intensity of the Bremsstrahlung is nearly proportional to the average atomic number where heavier elements produce more background noise.

The combination of characteristic X-ray energies from different transitions is unique for an element. However, peaks of different elements can overlap due to low energy resolution, *i.e.* the full width at half maximum of a peak is broad. For a qualitative or even quantitative analysis the number of transitions has to be maximized. To increase the number of transitions for an element the incident electron energy has to be increased. Based on Moseley's law, the energy to remove an electron from a shell is proportional to $(Z - \sigma)^2$ where Z is the atomic number and σ is the screening constant [109]. However, if the incident electron energy is too high, the intensity of the characteristic peak decreases and the background increases. Higher-energy electrons are going deeper in the material where they lose their energy and ability to emit characteristic X-rays. The number of continuous X-rays, however, increases as the electrons are more deflected and decelerated through the material. As a general rule, the minimum energy of the primary electrons has to be twice as high as the energy to remove an electron from the heaviest element in the material [108].

EDS can be used for qualitative, *i.e.* detection of all elements from $Z = 4$ to $Z = 92$ in an unknown material, and quantitative analysis, *i.e.*, to determine the concentration of each element. For the qualitative analysis, all characteristic lines are compared to a database and all identified excited peaks are removed from the spectrum to resolve hidden interference peaks.

In quantitative analysis, the concentration can be determined with Castaing's approximation which states that the mass concentration is proportional to the intensity of the peak [110]. Therefore the concentration of the element, $C_{element}$, can

be given by

$$C_{element} = \left(\frac{I_{element}}{I_{standard}}\right)\left(\frac{f_{element}}{f_{standard}}\right) C_{standard} \tag{3.9}$$

where $I_{element}$ and $I_{standard}$ are the intensities of the element and the standard, respectively, $f_{element}$ and $f_{standard}$ are the matrix factors of the element and the standard, respectively, and $C_{standard}$ is the mass concentration of the standard [110]. The matrix factors are corrections to obtain the 'true' concentration. The most important matrix correction factor is the ZAF correction. The ZAF correction incorporates the effects from the atomic number, Z, the absorption, A, and the fluorescence, F [108].

In contrast to EDS which measures all elements simultaneously and sorts the X-rays based on the energy, WDS examines each element separately and sorts the X-rays based on the wavelength. The operation principle of WDS is similar to EDS except that WDS uses a single crystal to diffract the X-rays before entering the detector [108]. The diffraction depends on the wavelength, the orientation and lattice spacing of the single crystal and only a specific wavelength is detected at a time according to Bragg's law (see Section 3.1.1). Even though this method is more time consuming, it is more quantitative than EDS because the effect of overlapping peaks and interference of different peaks are minimized.

For more information about EDS and WDS the chapter *Electron microprobe analysis* [108] can be consulted.

3.1.3.b Instruments

EDS and WDS were carried out by Dan MacDonald in the Robert M. MacKay Electron Microprobe Laboratory, Department of Earth Sciences, Dalhousie University, using a *JEOL 8200 Superprobe* equipped with five wavelength dispersive spectrometers, a Noran energy-dispersive spectrometer and a cathodoluminescence photomultiplier. The samples were mounted with carbon or copper tape on the sample holder to avoid static charging. The spatial resolution is approximately 1-2 µm and the EDS detector has an energy resolution of 128 eV.

The XYZ_2 compounds were analyzed by using a *JEOL JXA-8200* microprobe equipped with five wavelength dispersive spectrometers and one energy dispersive

X-ray spectrometer in the laboratory of Dr. Chi Ma, Analytical Facility, California Institute of Technology. A precision of better than 1 % and an accuracy of 1-2 % of the chemical composition can be acquired.

3.1.4 Scanning Electron Microscopy

A scanning electron microscope (SEM) is based on an operation principle similar to EDS and is, in general, used to show the morphology of the micro-/nanostructure of the material. Furthermore, it has the advantage that the contrast in the SEM images can provide information about mixed-phases, topology, and crystal orientation.

3.1.4.a Theory

The SEM is an electron microscope which scans the surface of the sample with a high-energy electron beam in a raster pattern. The electron beam is focussed on the surface and interacts with the atoms of the surface. Through the interaction, four different signals are generated: Auger electrons (AE), secondary electrons (SE), backscattered electrons (BSE), and X-rays [111].

AEs are produced when a core electron is removed and the vacancy is filled with an electron of a higher state. The release in energy leading emission of an AE. AEs contain chemical information from the surface (about 1 nm deep) but they have low energies and are difficult to detect. SEs are produced when the electrons of the primary beam ionize an atom and an electron is emitted. These SEs can carry information from deeper locations (about 5 nm for metals and 75 nm for insulators) [111]. If the electrons from the primary beam are reflected from the sample by elastic scattering, they have more energy to leave the sample and the emission depth can increase up to 0.1 µm, depending on the atomic number of the elements in the sample as well as the energy of the primary electrons. These electrons are known as BSEs. X-ray emission is similar to AE and the generation is described in Section 3.1.3. X-rays can provide information up to 5 µm in depth [111]. The energy of the X-rays is characteristic of the elements in the compounds and can be detected with a combined EDS and SEM system. With this technique, both a quantitative analysis of the elements of the material and also the distribution of the elements can be topographically mapped.

SE and BSE signals are usually used to create an image of the sample surface. While the spatial resolution of SEs is higher, BSEs can provide more details about the composition and topology [111]. The number of generated BSEs is proportional to the atomic number and therefore compounds with higher atomic numbers elements appear brighter. This method is normally use to determine the morphology, grain size, and distribution of different compositions in the material.

For more information about scanning electron microscopy, the book *Science of Microscopy* [111] is recommended.

3.1.4.b Instruments

SEM images were taken in the laboratory of Dr. Kevin Plucknett with the assistance of Patricia Scallion, Faculty of Engineering, Dalhousie University, using a *Hitachi S4700* cold field emission scanning electron microscope (CFESEM) with a *Oxford Inca Energy Dispersive X-ray analysis system*. CFESEMs have higher resolution than common SEMs and a cold field emission gun (CFEG) as electron source was used. A CFEG consists of a very sharp oriented tungsten single crystal held at ultrahigh vacuum (10^{-12} to 10^{-13} bar) and operating at room temperature. Therefore, the electron spread is lower than for other electron sources. All samples were mounted with double-sided carbon tape on a pin mount stub adapter. It is important to note that the samples were electrically conductive and did not require a conductive coating to dissipate static charges as is common with SEM.

The SEM images of the thermoelectric class XYZ_2 were acquired with the assistance of Dr. Umut Aydemir in the laboratory of Dr. Chi Ma, Analytical Facility, California Institute of Technology, using a *Zeiss 1550 VP Field Emission* SEM equipped with *Oxford X-Max SDD* EDS system.

SEM images of larger microstructures ($>$ 10 µm) were taken using a benchtop *nanoScience Instruments Phenom G2 Pro* desktop SEM with a back scattering detector in the laboratory of Dr. Jeff Dahn, Department of Physics and Atmospheric Science, Dalhousie University.

3.1.5 X-ray/Ultraviolet Photoelectron Spectroscopy

Other techniques to determine the chemical composition of the surface are X-ray photoelectron spectroscopy (XPS) and ultraviolet photoelectron spectroscopy (UPS). In addition to the chemical composition, XPS and UPS can give details about the binding energy, the oxidation state, the chemical environment, and the density of state below the Fermi energy [112]. Furthermore, the composition can be plotted as a function of depth and therefore, the interface between two materials can be analyzed.

3.1.5.a Theory

In XPS the sample is irradiated with (monochromatic or non-monochromatic) X-rays which will interact with the core electrons of the surface atoms. If the energy of the X-ray is sufficient high, a core electron is removed from the atom with a specific kinetic energy, E_{kin}, from the sample surface. E_{kin} is related to the binding energy, E_{bin},

$$E_{kin} = h\nu - E_{bin} - \Phi_{sample} \tag{3.10}$$

where $h = 6.626 \cdot 10^{-34}$ J·s is Planck's constant, ν is the frequency of the X-ray, and Φ_{sample} is the work function of the sample [112]. The work function of the sample is small and nearly constant. Each element has a set of characteristic binding energies and therefore the chemical composition of the surface (< 10 nm deep) can be determined. In addition to the ejected photoelectrons, AE also are created by auto-ionization (see Section 3.1.4) which can give information of the surface composition (< 1 nm deep) [112]. Both, photoelectron and AEs are recorded in the XPS spectrum. To distinguish AE and photoelectron peaks, XPS is recorded with two different X-ray sources. While the E_{kin} value of the photoelectron is proportional to the energy of the X-ray and changes with the X-ray source, AE depends only on the transition energies of the element and E_{kin} of the AEs is not affected by the X-ray source. The elements can be analyzed by comparing the XPS peaks to binding energies in a database.

However, the precise binding energy depends on the chemical environment and a change in oxidation state of the atom or the local chemical and physical environment results in small shifts of the peaks, also known as chemical shift [112]. The binding energy of the core electrons increases or decreases when the valence electrons are

drawn away or towards from the atom, respectively, due to change in electrostatic screening. This means that bonds with atoms of higher electronegativity have the peak shifted to higher binding energies. Also atoms with a higher oxidation state increase the binding energy due to the increase in Coulombic interaction between the core electron and the nucleus. Furthermore, the sample has to be conductive as static charges on the surface of non-conductive materials can shift the binding energy. If charging occurs, the XPS spectrum has to be corrected by the charging potential using the binding energy of carbon 1s (284.8 eV) [113]. In general, carbon contamination could be observed if the sample was exposed to air causing to form a thin layer of carbonaceous materials, also known as adventitious carbon, on the surface of the sample.

For higher-resolution measurements of the valence electrons, UPS is used. The operational principle of ejection of photoelectrons is similar to XPS. However, instead of an X-ray source, a gaseous discharge light source is used to generate photons in the ultraviolet range. These photons have lower energy than X-rays, resulting in the ejection of valence electrons rather than core electrons [112]. Due to its higher resolution and interaction of valence electrons UPS can be used to record the density of states below the Fermi energy.

Furthermore, the work function of the material can be determined using secondary electrons. Secondary electrons are inelastic scattered electrons in the sample and have a continuous range of kinetic energies from nearly the photon energy to zero. The zero kinetic energy electrons define the secondary edge which is used to determine the work function [114]. However, the analyzer also has a work function, $\Phi_{analyzer}$, and the contact potential between the sample and analyzer, $\Phi_{sample} - \Phi_{analyzer}$, adds to the kinetic energy

$$E_{kin} = h\nu - E_{bin} - \Phi_{sample} + \Phi_{sample} - \Phi_{analyzer} = h\nu - E_{bin} - \Phi_{analyzer}. \quad (3.11)$$

This means that the kinetic energy of all peaks and the secondary edge are increased by the contact potential. In addition to the contact potential, the analyzer also produces a secondary edge with zero kinetic energy which interferes with the secondary edge of the sample. The work function of the sample cannot be obtained because it is challenging to examine where the secondary edge of the sample begins. Therefore, an acceleration potential energy, $E_{acceleration}$, is applied to separate the

secondary edges of the analyzer and the sample. While the secondary edge of the sample increases by $E_{acceleration}$, the secondary electrons in the analyzer are not accelerated [114]. Due to the separation of the secondary edges the work function of the sample can be determined with

$$\Phi_{sample} = h\nu - E_{acceleration} - E_{bin,secondaryedge} \tag{3.12}$$

where $E_{bin,secondaryedge}$ is the binding energy of the secondary edge.

3.1.5.b Instruments

XPS spectra were acquired by Jon-Paul Sun in the laboratory of Dr. Ian Hill, Department of Physics and Atmospheric Science, Dalhousie University, using a combined XPS and UPS system with a *Specs Phoibos 150* hemispherical analyzer. Two different X-ray sources, Mg K_α (E_{Mg,K_α} = 1253.6 eV) and Al K_α (E_{Al,K_α} = 1486.6 eV), were used and a pass energy of 20 eV was applied. For the UPS measurements, a HeI ($h\nu$ = 21.21 eV) and HeII ($h\nu$ = 40.82 eV) gaseous discharge light source were used and the pass energy was 3 eV. The energy steps were 0.5 eV and 0.02 eV for XPS and UPS, respectively.

Prior the measurements the samples were polished and cleaned with acetone and isopropanol to remove any grease and other surface contaminations. In addition to the cleaning, the surface of the material was sputtered with Ar in the analysis chamber to decrease surface oxidation. All samples were electrically conductive and mounted on the XPS holder with Cu tape. It is important to note that the measurements were carried out under ultrahigh vacuum and therefore, samples studied could not contain elements with high vapor pressures, such as Zn, S, and P. The work function of the sample was determined using a HeI light source and an acceleration potential energy of $E_{acceleration}$ = 3 eV. The kinetic energy can be converted to the binding energy using the work function of the analyzer (see Equation 3.11). $\Phi_{analyzer}$ was calibrated with a sputtered polycrystalline Ag sample and the calibration is included in the XPS software.

3.1.6 Inverse Photoemission Spectroscopy

Additionally to the determination of the occupied states, inverse photoemission spectroscopy (IPES) was applied to examine the unoccupied density of states above the Fermi energy. Together with UPS (see Section 3.1.5) the density of states of the valence and conduction bands relative to the Fermi energy can be described which provides information about the electronic properties of the material.

3.1.6.a Theory

The operation principles of UPS and IPES are complementary. While a photon is used to eject an electron in UPS, an electron is injected into the sample to emit a photon in IPES. An IPES is equipped with an electron gun which fires a beam of mono-energetic electrons on the sample. The energy of the electrons, $E_{electrons}$, is proportional to the voltage of the electron gun, V_g, and given by

$$E_{electrons} = qV_g + \Phi_g \tag{3.13}$$

where $q = 1.602 \cdot 10^{-19}$ C is the elementary charge and Φ_g is the work function of the gun [115]. The electrons are not stable at the excited state and fall into the lowest unoccupied state to reduce the total energy of the system. The change in energy is emitted as a photon. Under the assumption that the Fermi energy of the gun is the same as the Fermi energy of the sample, the energy of the unoccupied states relative to the Fermi energy can be described by [115]

$$E_{unoccupied} = E_{electrons} - h\nu = |qV_g| + \Phi_g - h\nu. \tag{3.14}$$

The Fermi level of the gun is, in general, not the same as the Fermi energy of the sample. Furthermore, it is challenging to measure Φ_g. The system is, therefore, calibrated with a high-purity metal to determine the Fermi energy relative to the recorded $E_{unoccupied}$.

IPES can be used in two different modes. If the energy of the electron beam is held constant and the analyzer detects the full range of photons, the mode is called spectrograph [115]. Conversely, if the energy of the electron beam varies and the detector measures only a certain wavelength, the mode is known as isochromat.

3.1.6.b Instruments

IPES spectra were obtained by Jon-Paul Sun in the laboratory of Dr. Ian Hill, Department of Physics and Atmospheric Science, Dalhousie University. The IPES measurements were performed in the same analysis chamber as XPS and UPS. A lab-built spectrometer with a resolution of 0.5 eV was used in the isochromat mode. The photodetector consisted of a KCl+SrF_2 bandpass window with a peak transmission of about 9.5 eV. The samples were mounted with Cu tape on the sample holder and the measurements were carried out under high vacuum. The Fermi energy was calibrated with a polycrystalline Ag thin film and the value was manually subtracted from the recorded spectrum.

3.1.7 Thermogravimetric Analysis

In addition to the chemical composition and the morphology of the material, the crystal structure can change with temperature and at high temperature the material might decompose. In the next two sections, the methods to determine phase transformations and decomposition are described.

Thermogravimetric analysis (TGA) is a simple method to record the change of mass as a function of temperature or time in a controlled atmosphere. In most studies, the measurements take place under inert atmosphere, *e.g.* nitrogen or argon, to avoid oxidation and to determine the decomposition temperature. In some cases, however, the measurements are conducted in oxygen atmosphere to observe the effect of oxidation.

A TGA consists of a microbalance to measure subtle changes in mass and a furnace tube for controlled sample heating. Small aluminium pans at low temperature ($T <$ 600 °C), or alumina pans at higher temperature, are used as sample holders which are set on the balance. A thermocouple is incorporated inside the sample pan holder of the balance arm and the temperature of the sample is recorded.

For more details about TGA, refer to the *Handbook of Thermal Analysis* [116].

3.1.7.a Instruments

The TGA thermograms were acquired with the assistance of Dr. Robie Sanderson in the laboratory of Dr. Jeff Dahn, Department of Physics and Atmospheric Science, Dalhousie University, using a *TA Instruments SDT Q600* and with the assistance of Sarah Ellis in the laboratory of Dr. Mark Obrovac, Department of Chemistry, Dalhousie University, using a *Netzsch TG 209F3*. Both TGAs have a microbalance with a precision of 0.1 µg. For the measurements, the alumina pans were first heated to high temperature ($T > 400$ °C) to remove water and contaminations from the pan and sample chamber. TGA for the XYZ_2 thermoelectric class was recorded by Dr. Timothy Davenport in the laboratory of Dr. Sossina Haile, Department of Chemical Engineering, California Institute of Technology, using a *Netzsch STA 449 C Jupiter* thermal analyser. All measurements were recorded under argon atmosphere with a flowrate of 50 mL min^{-1}.

3.1.8 Differential Scanning Calorimetry

In addition to TGA, differential scanning calorimetry (DSC) is another technique where the temperature profile of a material can be examined. While TGA can only measure a change in mass, DSC can also provide information about phase transformations, and changes in enthalpy and entropy as well as the transition temperatures. Furthermore, it is a useful technique to determine the heat capacity at elevated temperatures.

3.1.8.a Theory

In a DSC apparatus, a sample and reference are placed on two separate heating stages with imbedded thermocouple junctions (Figure 3.2 (a)). While the sample and reference are scanned such that the temperature difference between sample and reference is kept constant at zero ($\Delta T = T_{sp} - T_r$=0), each heating stage separately reports its power (heat flux) to the sample, $\dot{Q}_{sp}$, and the reference, $\dot{Q}_r$. For an ideal system, the temperature of the heating stage is the same as the temperature of the sample ($T_{sp} = T_{phs} = T$). Therefore, the heat flux to the sample and reference can be written as the product of heat capacity of the sample, C_{sp}, and reference, C_r,

respectively, and the scanning rate, $\mathrm{d}T/\mathrm{d}t$ [117]:

$$\dot{Q}_{sp} = C_{sp}\frac{dT}{dt} \tag{3.15}$$

and

$$\dot{Q}_r = C_r\frac{dT}{dt}. \tag{3.16}$$

The change in difference in the heat flux of the sample compared to the reference, $\Delta\dot{Q} = \dot{Q}_{sp} - \dot{Q}_r = (C_{sp} - C_r)\frac{dT}{dt}$, is monitored with respect to temperature or time and can be used to determine if the event is endothermic or exothermic [117]. In the case of an endothermic process, $\Delta\dot{Q} > 0$ because the events require energy, *e.g.*, melting, evaporation, or thermal decomposition [118]. Conversely, for an exothermic event, $\Delta\dot{Q} < 0$ and heat is released. Exothermic processes include crystallization, polymerization, and combustion [118].

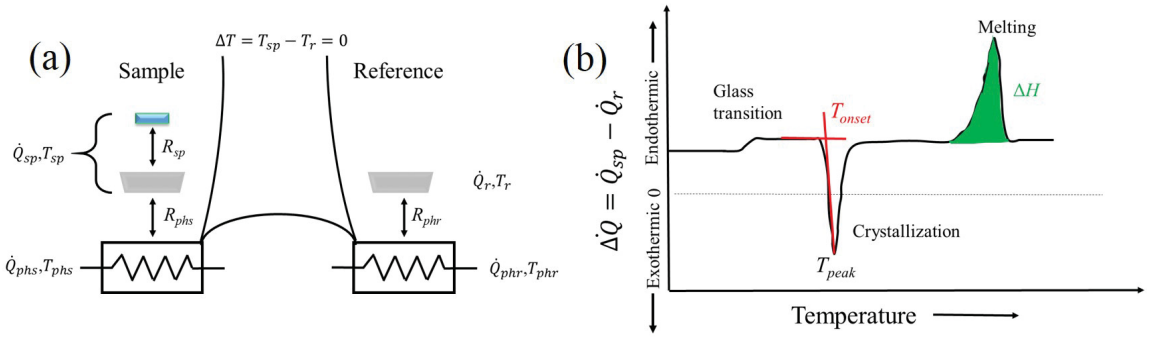

Figure 3.2: (a) Scheme of a differential scanning calorimeter (DSC). While the temperature of the reference and sample is kept identical, *i.e.*, $\Delta T = T_{sp} - T_r = 0$, the required heat to the sample and reference is recorded separately. The difference in heat flux between sample and reference, $\Delta\dot{Q} = Q_{sp} - Q_r$, is measured as a function of temperature or time. R_{sp} is the thermal resistance between the pan and sample, and R_{phs} and R_{phr} are the thermal resistances between the pan and the heating stage for the sample and reference, respectively. (b) DSC thermogram of a polymer on heating. The glass transition and melting are endothermic while crystallization is exothermic. Three important parameters of a transition are the onset temperature, T_{onset}, the peak temperature, T_{peak}, and the change in enthalpy, ΔH. Adapted from reference [117].

It is important to note that the sample is, in general, encapsulated in a pan to avoid contamination of the heating stage and sample chamber. The reference, on the other

hand, is generally an empty pan made of the same material as the sample pan. Due to its higher thermal mass, the heat capacity of the sample/pan assembly is higher than the reference pan and therefore, the baseline has a positive slope proportional to $C_{sp} - C_r$. However, these assumptions are only valid in a perfect system where no heat losses appear due to thermal resistance between the heating stage and pan, R_{phs} and R_{phr}, as well as the sample and the pan, R_{sp} (Figure 3.2 (a)). The difference between the temperature of the heating stage and the pan of the sample is given by

$$T_{phs} - T_{sp} = C_{sp} R_{phs} \frac{dT}{dt} \tag{3.17}$$

where the thermal lag between the heating stage and the sample scales with the heat capacity of the sample and the scanning rate. To reduce the uncertainty of the temperature lag, the instrument has to be calibrated with the same scanning rate prior the experiment.

A DSC thermogram of polyethylene terephthalate on heating is shown in Figure 3.2 (b) [117]. The polymer goes from a rigid glass phase to a supercooled liquid phase at the endothermic glass transition. At higher temperature the supercooled liquid crystallizes (exotherm) and finally melts (endotherm) [117]. Several important parameters can be obtained from the thermogram. The peak temperature, T_{peak}, is the temperature where the change in heat flux difference is the maximum. The onset temperature, T_{onset}, on the other hand, is the temperature where the tangent of the maximum slope intersects with an extrapolated baseline (as shown by the red lines in Figure 3.2 (b)). While T_{peak} changes with scanning rate, T_{onset} is nearly independent of the scanning rate or thermal conductivity of the sample and therefore, it is more representative of the transition temperature [118].

The area under a transition peak scales with the change in enthalpy, ΔH (indicated by the green area in Figure 3.2 (b)). The change in enthalpy is the product of the power supplied and the change in time. To get accurate results for ΔH, the instrument has to be calibrated with known standards and several runs with different masses have to be carried out. Furthermore, while a low scanning rate provides an accurate result for the transition temperature (see Equation 3.17), higher scanning rates are preferable for ΔH measurements [117]. With low scanning rates some of the enthalpy change can fade in the baseline and the change in enthalpy is underestimated [117]. In addition to ΔH, the change in entropy, ΔS,

can be determined in first-order transitions, such as melting and crystallization. Gibbs energy does not change at a first-order phase transition ($\Delta G = 0$) and therefore, $\Delta S = \frac{\Delta H}{T_{onset}}$ [117].

For more information about DSC the book *Differential Scanning Calorimetry* [118] and the chapter *Thermal Methods* [117] are recommended.

3.1.8.b Instruments

For the measurement of the DSC thermograms a *TA Instrument Q200* DSC equipped with *TZero*™ DSC cell was used in the laboratory of Dr. Mary Anne White, Department of Chemistry, Dalhousie University. The *TZero*™ DSC cell improves the baseline and the signal-to-noise ratio by incorporating the imbalance of thermal resistance, capacitance, and heating rate between the sample and reference stage [119, 120].

Two different cooling units, liquid nitrogen cooling system (LNCS) for low temperature (123 K to 473 K) and finned air cooling system (FACS) for high temperature (323 K to 773 K), were used. The sample chamber was purged with helium (25 mL min^{-1}) and nitrogen (50 mL min^{-1}) for LNCS and FACS, respectively. The samples, powder and pellets, were hermetically sealed in aluminum pans and the mass of the sample was determined using a Sartorius *CPA225D* semi-microbalance with an uncertainty of 10 µg. Prior to each experiment the instrument was calibrated with the solid-liquid phase transition of indium (99+%, TA Instruments, $m = 5.12 \pm 0.01$ mg). It is important to note that the calibration scanning rate has to be the same as used in the measurements. The instrument has a temperature accuracy of ±0.1 K and a baseline reproducibility of ±10 µW [121]. For the change in enthalpy at the phase transition, an uncertainty of 10% was estimated.

The specific heat was measured with the enthalpy method (Figure 3.3) [122]. In the enthalpy method, 10 K intervals were recorded with a scanning rate of 1 or 2 K min^{-1}. Before and after each interval the calorimeter was held isothermally for 5 min. Three experiments were required to determine the specific heat: a background measurement (empty hermetically sealed aluminium pan of known mass, $m_{background}$), a standard sample measurement (sapphire powder or sapphire pellet),

and the sample measurement. The standard sample and sample were hermetically sealed in an aluminium pan of known mass, $m_{pan,sapphire}$ and $m_{pan,sample}$, respectively.

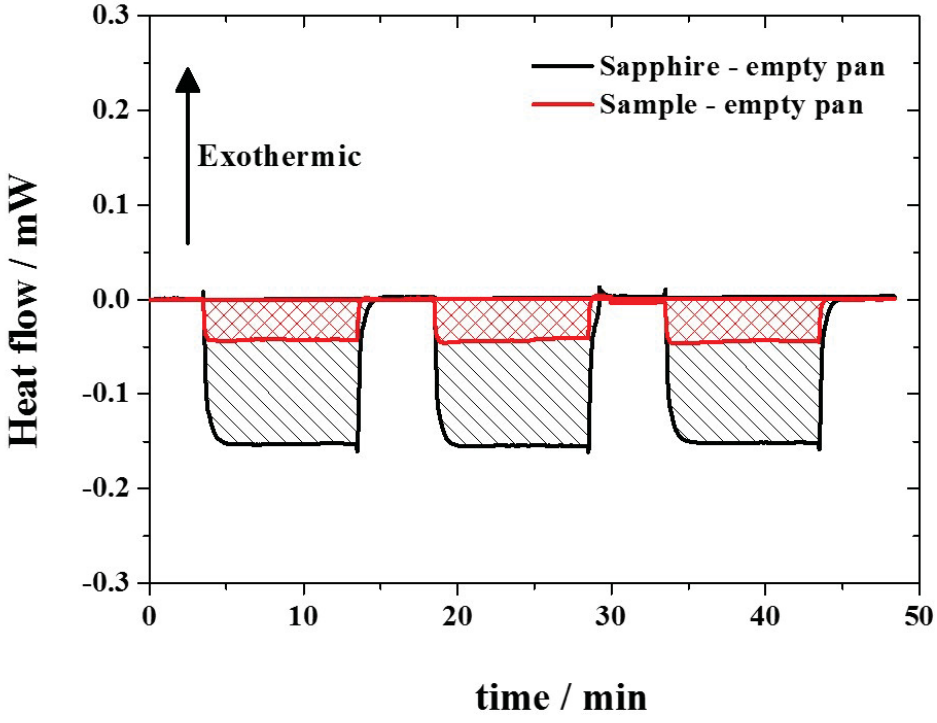

Figure 3.3: Enthalpy method to determine the specific heat using DSC. The empty pan was removed from the standard sample and the sample, respectively, and the heat flow for three intervals is plotted against time. From the areas under the curve the specific heat was calculated.

The heat flow of the background, $\Delta\dot{Q}_{background}$, was subtracted from the heat flows of the standard sample, $\Delta\dot{Q}_{sapphire+pan}$, and sample, $\Delta\dot{Q}_{sample+pan}$, using the mass ratio of the aluminium pans of the background and the standard sample/sample, respectively:

$$\Delta\dot{Q}_{sapphire/sample} = \Delta\dot{Q}_{sapphire+pan/sample+pan} - \frac{m_{pan,sapphire/sample}}{m_{background}}\Delta\dot{Q}_{background} \tag{3.18}$$

Each interval was integrated over time as shown by the shaded areas, $F(\Delta\dot{Q}, t)$, in

Figure 3.3. The sample specific heat was calculated from:

$$C_{p,sample} = \frac{F(\Delta\dot{Q},t)_{sample}}{F(\Delta\dot{Q},t)_{sapphire}} \frac{m_{sample}}{m_{sapphire}} C_{p,sapphire} \tag{3.19}$$

where the heat capacity of sapphire, $C_{p,sapphire}$, was taken from reference [123].

Specific heat measurements using the DSC are very sensitive and require good thermal contact between heating stage and pan as well as pan and sample. It was shown that the reproducibility is challenging because if the sample is even removed and placed back on the heating stage, an uncertainty up to 45% can be recorded [124]. High uncertainties were also recorded in a round-robin study where the specific heat from various DSC measurements scattered more than 15% between individual laboratories [125]. Therefore, prior the total run of the background, standard sample or sample, the sample pan was placed on the sample heating stage on slightly different positions and an interval was measured from 323 K to 333 K until $F(\Delta\dot{Q},t)$ reached its maximum value. Another challenge appears at high temperature ($T > 623$ K) as the vapor pressure in the pan can deform the bottom of the pan resulting in an increase of the thermal resistances. Therefore, for high temperature specific heat measurements a pinhole was made in the top of each pan to release the pressure. After each measurement, the mass of the sample/pan assembly was nearly the same ($\pm$0.6 mg).

3.2 Physical Properties

In this section, the instruments and techniques to obtain various physical properties of the materials are described. The physical properties include electrical properties (electrical conductivity, Hall coefficient, and Seebeck coefficient), thermal properties (thermal conductivity, heat capacity, and thermal expansion), magnetic properties, and speed of sound.

High-temperature heat capacity measurements were already described in the characterization section (see Section 3.1.8) because DSC was used as both a characterization method and a method to determine the heat capacity. Low-temperature heat capacity and other low-temperature properties were acquired in a single instrument, a *Quantum Design Physical Properties Measurement*

System™(PPMS). Before the techniques for the measurements of the low temperature properties are described, the PPMS is introduced.

3.2.1 Physical Properties Measurement System

The *Quantum Design Physical Properties Measurement System*™(PPMS) is a versatile instrument. It can measure electrical, thermal, and magnetic properties in the temperature range from 1.9 K (or even to 0.4 K for heat capacity and electro-transport measurements) to 400 K. The properties can be obtained separately or simultaneously, *e.g.* magnetoresistance which measures the effect of the magnetic field on the resistance. A scheme of the configuration of the PPMS probe is shown in Figure 3.4.

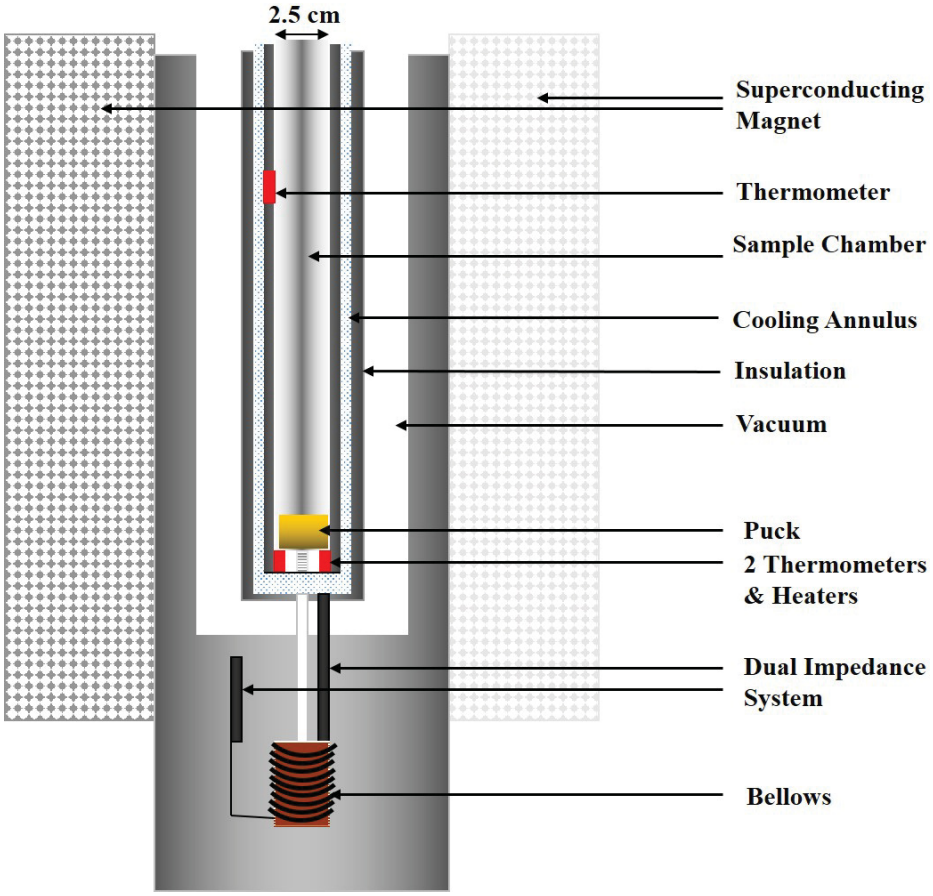

Figure 3.4: Cross-section of the PPMS probe with sample installed. Adapted from reference [126].

The outer wall of the PPMS is a longitudinal superconducting magnet capable of producing magnetic fields in the center of the chamber where the magnetic fields are vertically aligned. The superconducting magnets are cooled with liquid helium and reach magnetic fields up to 9 T. In the interior of the probe the sample chamber is cooled via liquid helium drawn through the impedance system. The cooling system is connected to the impedance system which controls the flow of liquid helium through the cooling annulus. Incorporated in the Dewar design in a coldhead refrigerator, called the Evercool™ system, which recondenses the recirculated He gas as well as the natural boil-off of liquid He in the Dewar. The sample chamber as well as the cooling annulus are surrounded by a vacuum jacket and thermal insulation to avoid thermal exchange with the environment and to keep a better control of the temperature in the sample chamber.

A 12-pin male connector is fixed at the base of the sample chamber where the sample platform can be installed. In the PPMS the sample platform is referred to as sample puck. The sample pucks are constructed from Au-plated Cu for high thermal conductivity. They have a diameter of 21 mm; a selection of sample pucks is shown in Figure 3.5. For thermal measurements the puck is covered with a heat shield, also made out of gold-platted Cu to reduce the effect of black body radiation. The sample connections are made on the top of the puck and the puck is already pre-wired to a 12-pin female connector at the underside. This technology has the advantage of fast sample exchange and reliable electrical contact in the probe.

Mounted below the sample puck are a heater and two thermometers to control and monitor the temperature of the base and sample. A thermometer is installed 15 cm above the base to determine the temperature gradient due to thermal fluctuations and provide a feedback loop for the heaters. Thermal fluctuations are avoided by two configurations. On the one hand, the bottom of the sample chamber is made out of Cu which has the advantage of providing a constant temperature as well as reduced black body radiation. On the other hand, the convection in the sample chamber is minimized by employing a high vacuum ($<10^{-7}$ bar). The bellows at the bottom of the probe compensate for the thermal expansion difference between the vacuum tube and the heat shield.

For these studies, the following properties were determined with the PPMS: heat

capacity at constant pressure, C_p, down to 0.4 K and under varying magnetic field; thermal conductivity, κ; electrical conductivity, σ_{el}; Seebeck coefficient, S; Hall coefficient, R_H (used to determine the Hall carrier concentration, n_H, and Hall mobility, μ_H); and DC magnetization. The techniques are described in the following sections.

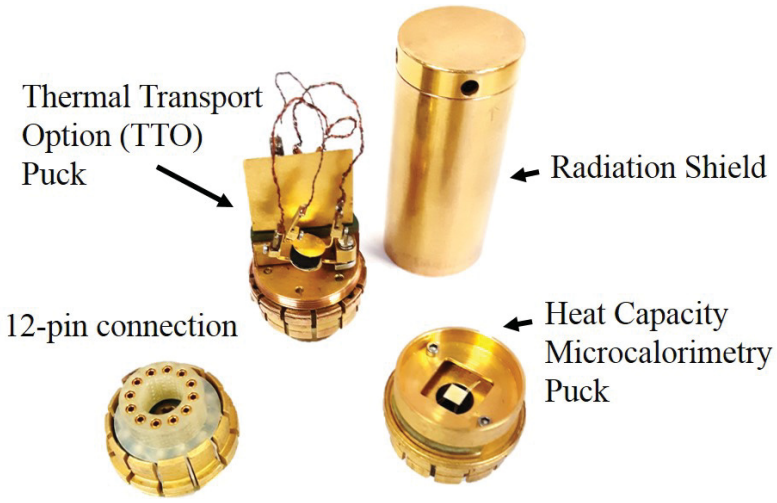

Figure 3.5: A selection of PPMS pucks. The heat capacity puck includes a small isolated platform where the sample is mounted while the thermal transport option (TTO) puck has three wires and a heat sink connected to the sample. The wires are connected to the 12-pin connector on the back.

3.2.2 Heat Capacity

Heat capacity is an intrinsic property and accurate measurements of the heat capacity can provide insights concerning the vibrational dynamics and the thermal conductivity of a material. More details about the theory of heat capacity are given in Section 2.1.

In these studies, the low-temperature heat capacity at constant pressure was obtained using relaxation micro-calorimetry in a PPMS. One of the many advantages is that small samples can be used. The lateral dimensions of the sample should not be larger than 3 mm $\times$ 3 mm and the mass can be as small as 1 mg to about 200 mg. Larger masses usually improve the accuracy of the measurements as long as the thermal conductivity is high. Large masses with low thermal

conductivity would increase the experimental time and the sample might have a temperature gradient through the sample resulting in an underestimation of the heat capacity [127].

To provide good thermal contact between the sample and the alumina sample platform, the sample is mounted on the platform with an *Apiezon*® grease (see Figure 3.6 (a)). The temperature of the sample is controlled and monitored by a *Cernox*™ thermometer and a RuO thin film heater under the sample platform. Furthermore, the sample platform is connected to the puck frame which acts as the heat sink after the heater power was turned off. A second thermometer is built into the puck to measure the cryostatic temperature, T_0. The top of the puck is closed with a heat shield made out of gold-coated Cu to minimize uncertainties from black-body radiation.

For the measurements of the heat capacity, the sample platform was heated from the cryostatic temperature, T_0, to $T_0+\Delta T$ where ΔT is normally 2% of T_0 (see Figure 3.6 (b)). The heater power was turned off and the the relaxation time towards T_0 was monitored over time. Two modes can be used to describe the heat capacity. In the simple single-tau model, the thermal resistance between the sample and platform is assumed to be negligible and the temperature of the platform on cooling is given by

$$T_{pl}(t) = T_0 + \Delta T \mathrm{e}^{-t/\tau_1} \tag{3.20}$$

where τ_1 is the time constant and given by $\tau_1 = C_{p,pls}/K_w$ (see Figure 3.6 (c)) [128]. The thermal conductance between the sample platform and the heat sink, K_w, is well known and the heat capacity of the platform, grease, and sample, $C_{p,pls}$, can be determined. However, this mode is mostly used for the background (addendum) measurement which records the heat capacity of a thin layer of grease on the sample platform.

When a sample is placed on the grease, the two-tau mode is usually used to include the imperfect thermal conductance between the platform and the sample, K_g, as shown in Figure 3.6 (d). The relaxation time is the sum of two exponential decay functions; one describes the heat transfer from platform to the heat sink, $\tau_1 = C_{p,pl}/K_w$, also known as the long time constant, and the other provides the heat transfer from the sample to the platform, $\tau_2 = C_{p,sa}/K_g$, which is called the short time constant. $C_{p,pl}$ and $C_{p,sa}$ are the heat capacities of the platform+grease as well

as the sample, respectively. The temperature of the platform is given by

$$T_{pl}(t) = T_0 + ae^{-t/\tau_1} + be^{-t/\tau_2} \tag{3.21}$$

where a and b are constants [128]. From the two-tau model, the total heat capacity (sample, grease, and platform) as well as the thermal coupling of the sample can be computed using the long and short time constants.

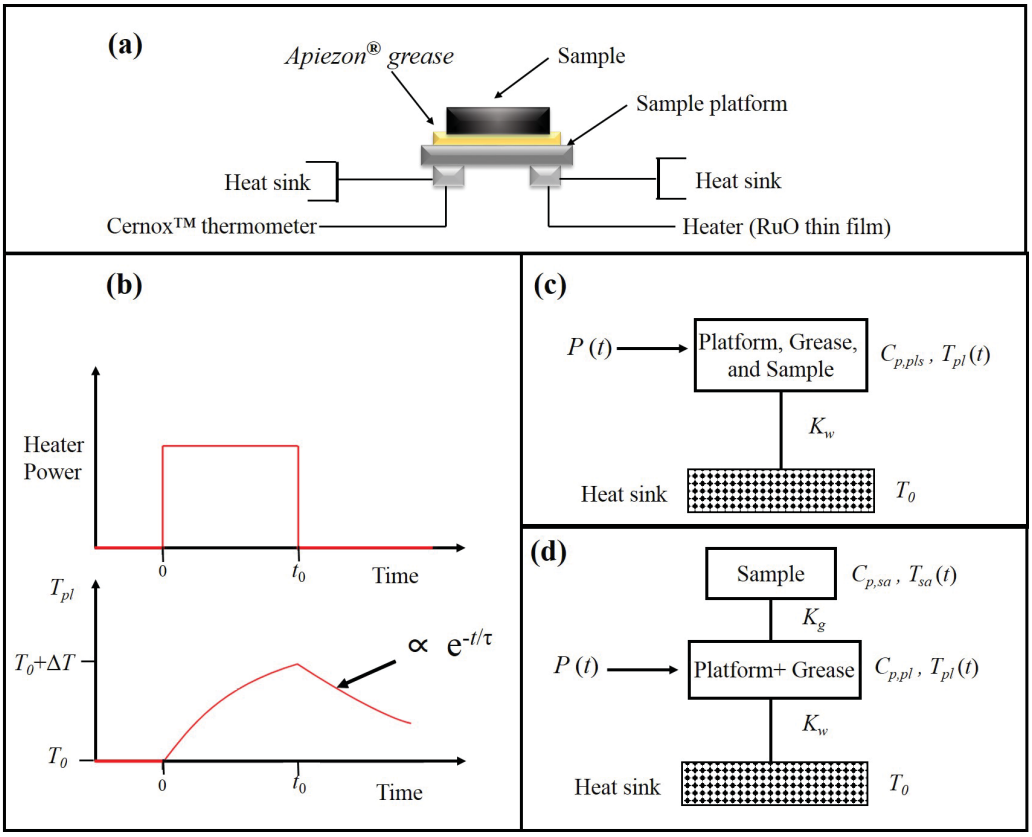

Figure 3.6: (a) Scheme of the relaxation micro-calorimeter puck with sample affixed with grease. (b) Measurement of the heat capacity using the single-tau mode. After the sample was heated, the relaxation time is recorded and analysed to determine the heat capacity. (c) Scheme of the simple single-tau mode. Only the thermal contact between the platform and the heat sink, K_w, is relevant for the determination of the heat capacity. (d) The two-tau model also includes the thermal conductance between the platform and the sample, K_g, which affects the heat capacity of the sample, $C_{p,sa}$. Adapted from reference [126].

To determine the heat capacity of a material, two measurements are carried out. In the first run, a thin layer of Apiezon® grease is measured to determine the addendum.

In the second run, the sample is placed on the grease and the addendum is subtracted from the total heat capacity (sample, grease, and platform). It is important to note that the sample has to be carefully pressed on the sample platform without removing any grease.

3.2.2.a Instruments

The low-temperature heat capacity was obtained in the laboratory of Dr. Mary Anne White, Department of Chemistry, Dalhousie University, using a Quantum Design PPMS system (see Section 3.2.1). Powder samples were consolidated to a pellet using a 2.7 mm diameter hardened steel die which can withstand pressures up to 1.1 GPa by cold-pressing. Hot-pressed samples synthesized in a 1.28 cm diameter graphite die and pressure up to 80 MPa were either cut with a diamond saw in Andy George's laboratory, Department of Physics and Atmospheric Science, Dalhousie University, or else a broken shard was used.

The sample was mounted with Apiezon® grease on the sample stage. Depending on the temperature range, one of two greases were applied. Apiezon®N grease retains its properties to liquid He temperatures but melts around 320 K and thus is the grease of choice for the temperature range from 4 K to 300 K. Furthermore, this grease has an anomaly at about 215 K and a first-order transition at 290 K [129]. Apiezon®H does not melt and is suitable for temperatures up to 390 K; it does crystallize at low temperature however and Apiezon®H was applied for high-temperature heat capacity measurements ($T = 210$ K to 390 K).

First, the heat capacity of the sample holder and Apiezon® grease (addendum) was determined. The heat capacity was generally measured from 300 K to 2 K with three repetitions at each temperature set-point. For lower temperatures (down to 0.4 K) a ^{3}He cooling probe was used. High-temperature heat capacity measurements were acquired from 270 K to 370 K to compare with the high-temperature heat capacity recorded with the DSC. If a phase change was observed at low temperatures ($T <$ 10 K), the heat capacity was measured under varying magnetic fields up to 9 T if magnetic transition was suspected, *i.e.*, due to the presence of unpaired electrons. The total heat capacity (platform, grease, and sample) was not necessarily measured at the same temperature as the addenda and the interpolated addendum heat capacity was

subtracted from the total heat capacity giving the sample heat capacity. Furthermore, the heat capacity was measured for different masses to test for the effect of the mass on the heat capacity [127].

3.2.2.b Accuracy and Limitations

For high-accuracy heat capacity measurements two conditions have to be fulfilled: The thermal coupling between the sample platform+grease and the sample has to be at least 90% and the sample heat capacity should contribute at least 35% to the total heat capacity [127]. The thermal coupling is given by $\frac{K_g}{K_g+K_w} \times 100$ [128]. A high thermal coupling means that the thermal contact between the platform+grease and the sample is good. Lower thermal couplings would lead to inaccurate temperatures in the sample resulting in an underestimation of the heat capacity. If these requirements are fulfilled, the accuracy of the heat capacity determination is about 1% in the temperature range from 5 K to 300 K and 5% in the range from 0.7 K to 5 K [127].

For low thermal conductivity materials, the material requires more time to reach an equilibrium temperature through the entire sample and therefore, before each set temperature no action was taken for a certain period of time. The heat capacity should be self-consistent with increasing waiting time.

Accurate heat capacities are challenging to obtain when the thermal conductivity and the mass density of the material are both low. The required conditions, good thermal coupling and large contribution of the sample heat capacity to the total heat capacity, cannot be fulfilled simultaneously, and therefore, different masses of the material have to be measured to get an accurate heat capacity.

3.2.3 Thermal Conductivity

To understand the origins of low thermal conductivity, it is essential to determine the thermal conductivity with high accuracy. In these studies, two different instruments were used to measure the thermal conductivity. While the low temperature thermal conductivity was measured directly using the thermal transport option (TTO) in the Quantum Design PPMS, the thermal conductivity at high temperature was determined with the laser flash method. The laser flash method measures the thermal diffusivity in the material, and the thermal

conductivity is calculated from the diffusivity, heat capacity, and mass density. The theory of thermal conductivity is described in Section 2.2.

3.2.3.a Thermal Transport Option in the PPMS - Thermal Conductivity

The thermal transport option (TTO) has the advantage that in addition to the thermal conductivity, the electrical conductivity and Seebeck coefficient also can be measured simultaneously. With these properties, the thermoelectric figure of merit, zT, can be measured in one setup and the change in properties through cycling can be neglected. Before the technique to determine the thermal conductivity is described, an overview of the sample preparation and the TTO puck is given. The techniques for the measurement of the Seebeck coefficient and electrical conductivity are presented in the Section 3.2.4 and Section 3.2.5, respectively.

For the TTO measurements, samples need to have a regular geometry, whether it is cut to shape or molded. For powders samples, the powder usually is consolidated to a pellet in cylinder form (with a diameter less than 6 mm) or to a bar. In addition, a new technique is introduced in these studies where the transport conductance of powders or liquids can be also measured with the TTO method. This method is described in the Section 4.2 and was tested for liquids in reference [130]. For the consolidated pellets, the sample was mounted between two gold-coated Cu plates (diameter of 6.2 mm) with silver epoxy (Loctite Ablestik 2902) as shown in Figure 3.7 (a). The gold-coated plates have the advantage that heat is supplied uniformly over the entire surface of the sample and the silver epoxy provides good electrical and thermal contact. In the case of a bar-shaped sample, four contacts were glued on the sample with silver epoxy.

Figure 3.7 (a) shows that each plate has two contacts. The sample is connected to three leads, also known as shoes, and to a heat sink, often referred to as coldfoot. On the hot side, a shoe with a resistive heater chip (2 kΩ) applies heat on the sample with a constant power up to 50 mW [131]. On the same shoe, a current source is installed for electrical measurements. The other two shoes contain each a *Cernox*™ 1050 thermometer and a voltage lead. All shoes are connected to the puck by long and thin wires (5.1 cm long, 76 µm in diameter) to reduce the heat transfer from the sample to the puck [131]. The wires except the wire to the current source are

manganin alloy which has a small Seebeck coefficient and low thermal conductivity. The wire to the current source *PD-135* is low-resistance copper alloy. The cold side is additionally connected directly to the coldfoot to maximize the heat transport from the sample. The coldfoot acts also as the ground for electrical measurements.

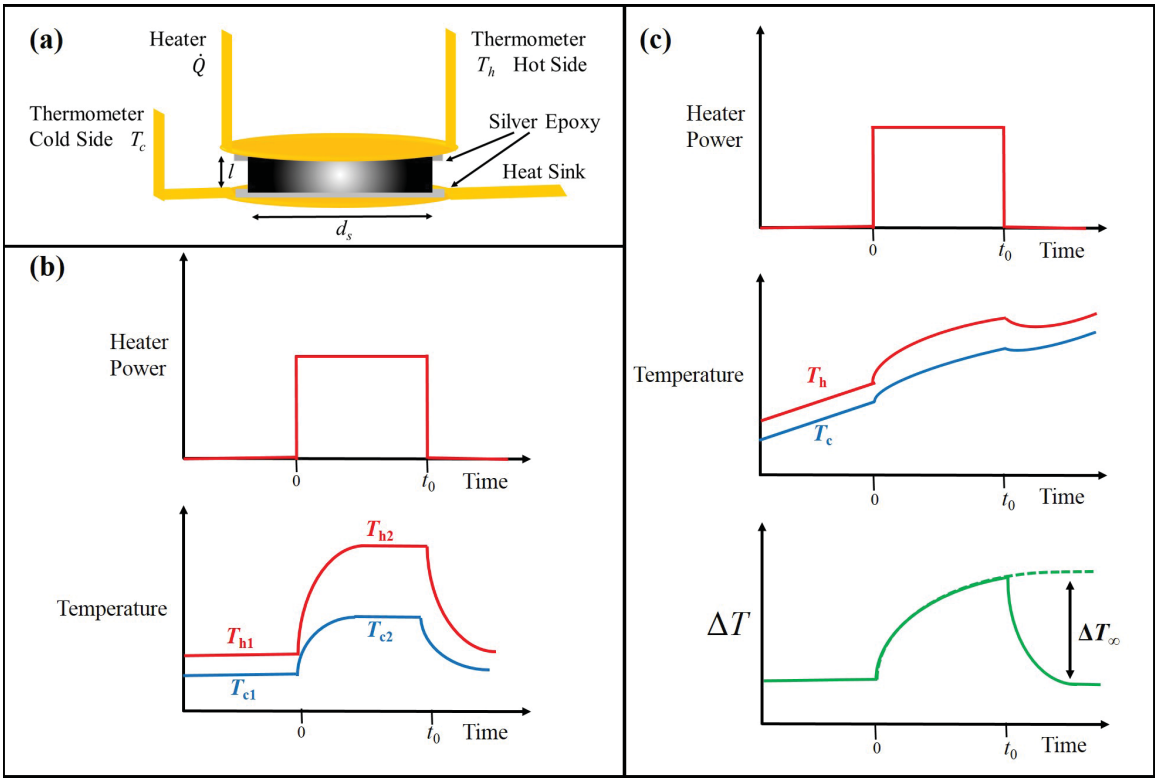

Figure 3.7: (a) Scheme of the thermal transport option (TTO) sample mounted between two gold-coated plates with silver epoxy. Idealized measurements of the thermal conductivity using the (b) steady-state method and (c) continuous method. In the steady-state method the cryostatic temperature is constant while the temperature slightly changes in the continuous mode. Adapted from reference [131].

To avoid thermal losses through radiation or convection, the puck is covered with a heat shield made out of gold-plated copper and the measurements carried out under high vacuum (10^{-7} bar). Furthermore, radiative losses from the sample are estimated (*vide infra*) and subtracted from the measurements.

The TTO thermal conductivity, κ, was measured using a power-pulse method. In the measurement, a constant heater power, P_0, is applied and the temperature of

both sides are monitored. The total thermal conductance, K, can be calculated from

$$K = \frac{P_0}{\Delta T_\infty} \tag{3.22}$$

with ΔT_∞ as the steady-state temperature difference between the hot and cold side. However, the total thermal conductance has to be corrected for the radiative loss due to black-body radiation, Q_{rad}, and the thermal conductance of the shoes, K_{shoes}. The radiative loss is proportional to the surface area ($A_{surface} = d_s\pi \cdot L$ with d_s and L as the diameter and thickness of the sample, respectively) and given by a modified Stefan-Boltzmann law (see Equation 2.10)

$$Q_{rad} = \sigma_T \frac{A_{surface}}{2} \varepsilon_T (T_h^4 - T_c^4) \tag{3.23}$$

where T_h and T_c are the temperature of the hot and cold side, respectively [131]. Due to the T^4 behavior the black-body radiation is significant at higher temperatures ($T > 300$ K) and a good estimation of the emissivity is desirable. If the radiative losses and the heat loss of the shoes are included, the thermal conductance of the sample can be written as

$$K_{sample} = \frac{P_0 - Q_{rad}}{\Delta T_\infty} - K_{shoes} \tag{3.24}$$

where $K_{shoes} = aT + bT^2 + cT^3$ with a, b, and c as constants [131]. The shoes were calibrated and the constants for K_{shoes} are included in the PPMS software. The sample thermal conductivity, κ, is determined from its cross-section area, $A_{cross} = \pi \left(\frac{d_s}{2}\right)^2$, the thickness, L, and the sample thermal conductance as,

$$\kappa = K_{sample} \frac{L}{A_{cross}}. \tag{3.25}$$

The thermal conductivity can be measured with two methods in the TTO: the single-measurement method or the continuous method. In the single-measurement method the cryostatic temperature is kept constant and no heat was applied until the thermometers are stable. After the temperature of both thermometers is constant, heater power is turned on until the temperature difference is stable (see Figure 3.7 (b)). The temperature difference is given by $\Delta T_\infty = (T_{h2} - T_{c2}) - (T_{h1} - T_{c1})$ and should be 2-3% of the cryostatic temperature. If ΔT_∞ is too low, the accuracy of the measurement decreases. However, if ΔT_∞ is too high, blackbody-radiation has a

large effect on the thermal conductivity and the uncertainty increases. To estimate ΔT_∞, knowledge of the thermal conductance of the sample is advantageous.

The single-measurement mode has different settings for measuring ΔT_∞. On the one hand, ΔT_∞ is recorded when the temperature difference changes less than a (relative or absolute) value. On the other hand, the heat pulse can be applied for a certain period of time without considering temperature stability and after the heating time runs out, ΔT_∞ is obtained. In most cases, it is a combination of both. ΔT_∞ is measured when the temperature difference is stable or the heating time runs out. This has the advantage that set points which do not fulfill the stability condition are not stuck in an infinite loop. In addition to the heating time, a waiting time is employed before each measurement to ensure a constant temperature in the sample. Although the single-measurement method requires more time, it provides more accurate thermal conductivity data and is highly recommended for low thermal conductivity materials.

For high thermal conductivity materials, the continuous mode is more practical because this mode has the advantage of generating a high density of data in a short experiment time. In this method, the cryostatic temperature changes slightly and steadily while a heat pulse of constant power is simultaneously applied (see Figure 3.7 (c)). In the continuous mode, only a short heat pulse is applied and ΔT_∞ is determined from an extrapolation of the difference in temperature of the hot and cold thermometer as shown in the bottom graph in Figure 3.7 (c). An adaptive algorithm is used to optimize the parameters, such as heater current and heating period. To determine ΔT_∞, the recorded temperature difference, ΔT, is fit with a least-squares routine to the equation

$$\Delta T_{model}(t) = \Delta T_\infty \left[1 - \frac{\tau_1 \cdot \exp\left(-\frac{t}{\tau_1}\right) - \tau_2 \cdot \exp\left(-\frac{t}{\tau_2}\right)}{\tau_1 - \tau_2} \right] \tag{3.26}$$

with τ_1 and τ_2 as the long and short empirical time constants, respectively [131]. The three fitting parameters, ΔT_∞, τ_1 and τ_2, are optimized until a global minimum in the residual of the curve fit is identified.

3.2.3.b Laser Flash

The laser flash method is the most common technique to determine the thermal conductivity at high temperature. In this method, a laser pulse is focussed on one

side of the sample and the thermal response on the other side is recorded as a function of time using an infrared detector. Under the assumption the heat pulse has the shape of a delta function, no heat losses occur, and the heat is transported in one direction, the thermal diffusivity, α, can be determined by

$$\alpha = \frac{\ln(4) l^2}{\pi^2 t_{1/2}} \tag{3.27}$$

where $t_{1/2}$ is the time when the recorded temperature rise on the top surface is half of the maximum [132]. However, the three simplifications described above have to be corrected to calculate the 'true' thermal diffusivity. The heat loss through radiation and convection was taken into account by Cowan [133]. In particular, for samples with large surface-to-volume ratio, radiation and convection have to be considered for accurate thermal diffusivity measurements. In addition to the heat losses, the laser pulse shape is also corrected to a rectangular energy pulse in the Cowan correction [133]. For thicker samples, the heat transfer is not solely in one direction, but also in radial directions towards the sides of the sample, and the thermal diffusivity has to be corrected for the corresponding heat loss. The non-one-dimensional effects are taken into account in the Cape-Lehman correction which also applies a finite square energy pulse [134].

In contrast to the thermal conductivity, the thermal diffusivity measures how quickly heat is transported through the sample. The thermal conductivity can be calculated from the thermal diffusivity using the heat capacity at constant pressure, C_p, and the mass density, ρ,

$$\kappa = \alpha C_p \rho. \tag{3.28}$$

3.2.3.c Instruments

The thermal conductivity at low temperature was measured in the laboratory of Dr. Mary Anne White, Department of Chemistry, Dalhousie University, using a Quantum Design PPMS (see Section 3.2.1) and the thermal transport option. Powder samples were consolidated in a 5.1 mm diameter, hardened steel die with a maximum pressure of 1.1 GPa. The hot-pressed samples were cut in dimensions 3 mm $\times$ 3 mm with a diamond saw in the laboratory of Andy George, Department of Physics and

Atmospheric, Dalhousie University. The pellets should have a flat surface to get an optimum contact and a homogeneous thickness.

The samples were mounted with silver epoxy on gold-coated Cu plates. Air-sensitive samples were polished before mounting and the samples were cured under vacuum while the other samples were cured in a box furnace (T = 80-100 ^{o}C). It was found to be important to mount the Cu plate on one side and let it cure (sample up) before mounting the second plate. In particular for porous samples, the viscous epoxy can incorporate in the sample due to gravity and affect the thermal conductivity of the investigated sample. Furthermore, the sample/epoxy/lead preparation is clamped during curing to ensure a homogeneous contact and to keep the epoxy layer thin.

In most cases, the thermal conductivity was determined with the steady-state method using an emissivity of one, unless stated otherwise. The heater power was adjusted such that the temperature difference was 2% and the temperature stability was $\Delta T/T < 0.1\%$. The cryostatic temperature between set points was changed with a small heating/cooling rate to avoid sample cracking through thermal expansion stress. The samples were cycled at least once to identify any hysteresis through cracking on heating/cooling.

The thermal diffusivity at high temperature was recorded with the assistance of Dr. Umut Aydemir in the laboratory of Dr. G. Jeffrey Snyder, California Institute of Technology, using a *Netzsch LFA 457* laser flash apparatus. Prior the measurements, the samples were coated with graphite to improve the light absorption and the infrared thermal response on the other side. The thermal diffusivity measurements were conducted under dynamic Ar flow of 50 mL min^{-1}. At each temperature point, three laser pulses were shot on the sample and the average thermal diffusivity was taken. The thermal diffusivity results were corrected with the Cowan approach. The thermal conductivity was calculated from the thermal diffusivity, heat capacity, and mass density using Equation 3.28.

The heat capacity was measured with DSC (see Section 3.1.8) and the mass density was determined using the Archimedes method. In the Archimedes method, a lab built device containing a stage hanging from an arm in a liquid with known density was placed on a microbalance. The beaker containing the liquid was on a separate platform. The mass of the dry sample, m_{dry}, and the mass of the submerged sample,

$m_{submerged}$, were measured in two different runs. The density of the sample was calculated from

$$\rho_{sample} = \frac{m_{dry} \cdot \rho_{liquid}}{m_{dry} - m_{submerged}} \tag{3.29}$$

where ρ_{liquid} is the known mass density of the liquid. This method has the advantage that even the density from non-uniform shapes can be determined.

3.2.3.d Accuracy and Limitations

Thermal conductivity measurement using TTO can have several possible sources of error. On the one hand, the dimensions cannot be measured exactly. The caliper has an absolute uncertainty of 0.01 mm. However, most samples are fragile or compressible leading to a larger estimated uncertainty of 0.04 mm. On the other hand, the thermal conductance can have a large uncertainty, in particular, for low thermal conductivity materials. The accuracy of the thermal conductance provided by Quantum Design is ±2 µW K^{-1} for $T < 15$ K, ±20 µW K^{-1} for 15 K $< T <$ 200 K, ±0.5 mW K^{-1} for 200 K $< T <$ 300 K, ±1 mW K^{-1} for $T >$ 300 K or ±5%, whichever is greater [131]. The standard deviation estimated by the software of the thermal conductivity is given by:

$$\sigma(\kappa) = \kappa \cdot \sqrt{\left(\frac{R_{\Delta T}}{\Delta T_\infty}\right)^2 + \left(\frac{2 I R_h \delta I_h}{P_0}\right)^2 + \left(\frac{0.2 \cdot P_{loss}}{P_0}\right)^2 + \left(\frac{0.1 \cdot T_\infty \cdot K_{shoes}}{P_0}\right)^2} \tag{3.30}$$

where $R_{\Delta T} = \sqrt{\frac{\sum_i (\Delta T_i - \Delta T_{i,model})^2}{64}}$ is the residual, I_h is the heater current, and R_h is the heater resistance [131]. The first term is the fit of the thermal curve (in the continuous mode), the second term is the error of the heater due to digital-analog converter, the third and fourth term is the error in the estimation of the radiative losses and the thermal conductance leak from the shoe assemblies, respectively [131]. The estimation of the radiative loss due to black-body radiation is challenging because the emissivity is in general unknown and a precise measurement of the surface area is difficult and therefore, a combined error of 20% is estimated by the Quantum Design software [131].

Another uncertainty is the thermal contact between the sample, silver epoxy, and the Cu plates. The thermal contact resistance is normally in the range from 10^{-3} to

10^{-5} m^2 K W^{-1} [78]. For accurate thermal conductivity measurements, the thermal contact resistance has to be much less than the ratio of the sample thickness to the thermal conductivity [78]. For low thermal conductivity materials, $\frac{l}{\kappa}$ is higher than the thermal contact resistance and therefore, the thermal contact resistance can be neglected. For the thermal conductivity in the present study an uncertainty of 5% was estimated, unless stated otherwise.

For the analysis of the thermal conductivity data, it is important to consider the morphology of the sample because powders, liquids, and monoliths of the same material can lead to different thermal conductivities. While monoliths have typically higher thermal conductivities at low temperatures due to longer phonon mean free path, powders can have low thermal conductivities as grain boundary scattering is the dominant scattering mechanism at low temperature. Grain boundary scattering can be also dominant in polycrystalline samples. On the other hand, the phonon mean free path in single crystals is not limited by the grain boundary and higher thermal conductivities are expected at low temperature. Low and high thermal conductivities are challenging to determine using the TTO method in a PPMS. While the temperature gradient is limited by the maximum applied power (50 mW in a PPMS) for high thermal conductivities, low thermal conductivities require a low applied power because the temperature difference should not be larger than 2% of the set point temperature to obtain accurate results. Furthermore, porosity can dramatically decrease the thermal conductivity as further discussed in the next chapter.

The laser flash method is considered as more accurate at higher temperature than the steady-state method because the laser flash method is not as sensitive to radiative losses as the steady-state method [135]. In a study performed by Wang *et al.*, the laser flash method was compared to a steady-state method from the Ioffe Institute [136]. The thermal conductivity of PbSe was measured with high precision from different groups using the laser flash method while the steady-state method indicated a ∼50% higher thermal conductivity [136]. However, the laser flash method also requires an accurate measurement of the thickness for exact thermal diffusivity measurements. Furthermore, the graphite coating can have a large influence of the thermal diffusivity due to an increase in heat capacity and thermal resistance. In

particular for thin samples, a thick graphite layer or a poor adhesion between sample and graphite can cause large errors [135, 137].

In addition to the geometry and the graphite layer, the uncertainty in heat capacity (see Section 3.2.2 and Section 3.1.8) and in mass density lead to a significant error in the thermal conductivity using the laser flash method. The mass density is measured with the Archimedes method which is more exact than the density determined from the geometry. However, porous samples can absorb the liquid resulting in an overestimation of the density. Furthermore, the mass density is only determined at room temperature and normally decreases with temperature due to thermal expansion. Therefore, an uncertainty of 5% for the mass density and a combined uncertainty of 15% of the thermal conductivity using the laser flash method were estimated for the present experiments. This is consistent with the value from a round-robin study where an uncertainty of ∼9.2% at room temperature and 17.9% at 475 K from laser flash method was reported [125].

3.2.4 Seebeck Coefficient

The Seebeck coefficient is an intrinsic parameter and is related to the electronic band structure and carrier concentration. Based on the nature of the carriers, the Seebeck coefficient can be positive (if holes are the major charge carriers) or negative (if electrons are the major charge carriers). More details about the theory can be found in Section 2.3. The Seebeck coefficient can be measured by applying a temperature difference, ΔT, while recording the resulting potential difference across two points, ΔV. Therefore, good thermal and electrical contacts are required to acquire accurate results. It is important to note that the Seebeck coefficient of the sample is measured relative to the Seebeck coefficient of the wires of the apparatus used to measure it.

In these studies, two different types of measurements were used to determine the Seebeck coefficient. The low-temperature Seebeck coefficient was measured with the TTO method in a Quantum Design PPMS [131] and the high-temperature Seebeck coefficient measurements were performed with a high-temperature Seebeck apparatus using a uniaxial 4-probe contact geometry as reported by Iwanaga *et al.* [138]. While the TTO option measures only one single point per set-point temperature, the high-temperature Seebeck apparatus measures several points at

different ΔT and the Seebeck coefficient is determined by the slope of ΔV and ΔT [135].

3.2.4.a Thermal Transport Option in a PPMS - Seebeck Coefficient

The thermal transport option is described in Section 3.2.3.a. Similar to the thermal conductivity measurements, the Seebeck coefficient can be measured in the single-measurement mode or in the continuous mode. The Seebeck coefficient is given by the potential difference, ΔV_∞, and the temperature difference, ΔT_∞, at steady state:

$$S = \frac{\Delta V_\infty}{\Delta T_\infty}. \tag{3.31}$$

In the single-measurement mode, ΔV_∞ is measured between the two gold-plated Cu plates when the temperature has reached steady-state conditions.

In contrast to the single-measurement mode, the determination of the Seebeck coefficient requires a complex fitting routine. Similar to the fit of $\Delta T_{model}(t)$, ΔV can be fit with a least-square routine to

$$\Delta V_{model}(t) = \Delta V_\infty \cdot \left[1 - \frac{\tau_1 \cdot \exp\left(-\frac{t}{\tau_1}\right) \pm \tau_2' \cdot \exp\left(-\frac{t}{\tau_2'}\right)}{\tau_1 - \tau_2'}\right] + b_{drift} \cdot t + c_{offset} \tag{3.32}$$

where τ_2' is a time constant, b_{drift} and c_{offset} are parameters for the drift and offset voltages, respectively [131]. The variation in thermal voltages in the wires and the slow microvolt-level drift in the preamp electronics are included in b_{drift}. While τ_1 can be taken from the fit of Equation 3.26 to the ΔT data, τ_2' is swept from zero to τ_1 and for each τ_2' a linear regression in ΔV_∞, b_{drift}, and c_{offset} is performed [131]. This has to be done for the plus and the minus sign between the exponential terms because the sign of the Seebeck coefficient for τ_2', *i.e.*, the leads, can be opposite to the sign of the Seebeck coefficient of τ_1, *i.e.*, the sample. The Seebeck coefficient is calculated from $\frac{\Delta V_\infty}{\Delta T_\infty}$.

3.2.4.b High-Temperature Seebeck Coefficient

The high-temperature Seebeck coefficient was measured with a uniaxial 4-probe contact geometry as described by Iwanaga *et al.* [138]. A scheme of the uniaxial

4-probe contact geometry is shown in Figure 3.8 (a). The heaters made of boron nitride are placed directly on the surface of the sample increasing the heat flux through the sample due to a large contact area. The thermocouples are inserted in the heater blocks measuring the temperature and voltage directly on the isothermal surface of the sample. This can reduce the cold finger effect where heat is drawn away from the sample through the thermocouple [135]. In contrast to the 2-probe contact geometry used in the TTO, the uniaxial 4-probe contact geometry has the advantage that the electrical and the effects due to thermal contact resistances are minimized, improving the accuracy of the measurement.

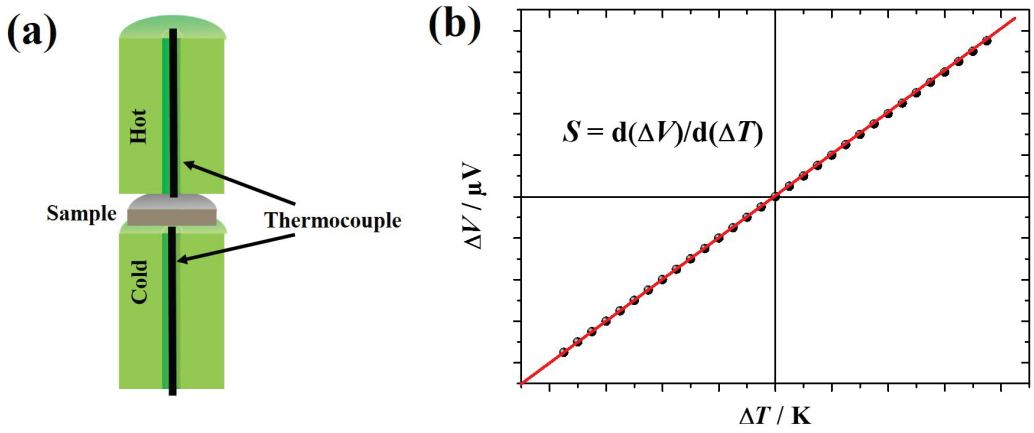

Figure 3.8: (a) Transverse section of the uniaxial 4-probe contact geometry used to determine the high-temperature Seebeck coefficient. The sample is placed between two heater blocks (green) with embedded thermocouples. A temperature gradient is applied across the sample and the temperature difference as well as the voltage difference are recorded from the isothermal surface. (b) An example of the determination of the Seebeck coefficient. The temperature difference oscillates from positive to negative and the corresponding potential difference for each temperature difference is recorded. The Seebeck coefficient is the slope of the potential difference over the temperature difference (red line). Adapted from references [135, 138].

The thermocouples consist of a 4-bore ceramic tube (mullite, 1.59 mm in diameter) and two wires (niobium and chromel) [138]. Niobium and chromel wires have the advantage in that they are mostly non-reactive with typical elements of thermoelectric materials (*e.g.*, heavy metals) at high temperature. Furthermore, the

voltage error from temperature difference between temperature and voltage measurements is reduced due to the near-zero Seebeck coefficient of niobium which is used for the voltage measurement. Chromel, on the other hand, has a high Seebeck coefficient to generate a good signal for the temperature measurement. A small cross-section area is used for the wires (diameter is about 125 µm) improving the accuracy of the measurements because the temperature difference between the voltage and temperature measurements is reduced [138]. However, the measurement has to be performed in oxygen-free environment and therefore, a high vacuum or inert gas must be applied.

Another benefit of the uniaxial 4-probe contact geometry is the application of larger forces on the sample causing a better thermal and electrical contact between thermocouple/heater and sample [138]. The spring system of the heater is independent of the spring system of the thermocouple and all springs exert compressive forces on the sample. With this setup, different sample shapes can be examined and even the Seebeck coefficient of fragile samples can be determined because no tensile or shear forces are exerted on the sample.

The lab-coded software using *National Instruments LabView*™ oscillates the temperature of the two heater blocks around a set-point temperature, so the average temperature of the two heater blocks is nearly the same at the set-point temperature. The temperature and voltage are measured with the *delta method, i.e.*, first the temperatures of the hot and cold side are measured, then the voltage difference, and finally the temperature of the hot and cold side is measured again with the same time interval [138]. The temperature difference is average from the hot and cold side before and after the voltage difference measurement. At each set-point temperature, several temperature differences and corresponding voltage differences are measured and the Seebeck coefficient is calculated from the slope of the voltage difference and the temperature difference (see Figure 3.8 (b)). The slope method has the advantage that the offset voltage can be corrected; it can be significant at elevated temperature due to differences in thermocouple wires and reactive samples [135].

For more information about the high-temperature Seebeck coefficient apparatus, refer to the publication by Iwanaga *et al.* [138].

3.2.4.c Instruments

The low-temperature Seebeck coefficient was measured with the TTO in the Quantum Design PPMS in the laboratory of Dr. Mary Anne White, Department of Chemistry, Dalhousie University. For details, see the measurement of thermal conductivity using TTO (Section 3.2.3.c).

The high-temperature Seebeck coefficient was measured in the continuous mode with the assistance of Dr. Umut Aydemir in the laboratory of Dr. G. Jeffrey Snyder, California Institute of Technology, with a lab-built Seebeck coefficient apparatus as described by Iwanaga *et al.* [138]. The samples were placed between the heaters and a polycrystalline graphite foil was included between the thermocouple and sample for further reduction of potential chemical reaction. The Seebeck coefficient was measured with a scanning rate of 100 K h^{-1} under high vacuum and the temperature gradient oscillated in the range of $\pm$7.5 K.

3.2.4.d Accuracy and Limitations

The accuracy of the Seebeck coefficient is highly related to the contact geometry. Three different contact geometries can be applied: 2-probe contact geometry (used in the TTO), uniaxial 4-probe contact geometry (used in the high-temperature Seebeck coefficient apparatus), and off-axis 4-probe contact geometry where voltage probes and thermocouples are individual attached to the sample [135]. The latter geometry can be also applied in the Quantum Design PPMS.

The accuracy of the 2-probe contact geometry is limited by the electrical and thermal contact resistance. A low contact resistance is required for accurate measurements. However, a higher thermal and electrical contact resistance can occur in the off-axis 4-probe contact geometry due to a smaller contact area. In a study performed by Martin, it was shown that the cold finger effect in an off-axis 4-probe contact geometry overestimates the magnitude of the Seebeck coefficient due to bad thermal contact while the 2-probe contact geometry slightly underestimates the absolute Seebeck coefficient [139]. In particular at high temperature, overestimation of the Seebeck coefficient can be high due parasitic heat fluxes between the sample and thermocouple perturbing the local temperature field [139].

It is assumed that the uniaxial 4-probe contact geometry can determine the Seebeck coefficients most accurately. Because the thermocouples are embedded in the heater the cold finger effect is reduced in the uniaxial 4-probe contact geometry. A further reduction of the cold finger effect was achieved by the usage of mullite for the 4-bore ceramic due to its low thermal conductivity. In addition to the reduction of the cold finger effect, high compressive forces can be exerted on the sample surface causing good thermal and electrical contact [138]. This has also the advantage that fragile and thin samples in different shapes can be examined. However, poor thermal contact, *e.g.*, oxide layer on the surface, can result in under- or overestimation of the absolute Seebeck coefficient but the error is assumed to be lower than the error using the other geometries [135].

Furthermore, the sample can react with the thermocouples although a graphite foil is placed between the sample and thermocouple. In particular, if the thermocouple is contaminated a large error in temperature can cause incorrect Seebeck coefficients. Due to the thin wire it is difficult to observe contamination and the wires should be replaced periodically or used to compare to a standard sample.

In addition to the errors due to the geometry, the errors of the measurement method can be significant. In particular, if only one point is measured the offset voltage might affect the Seebeck coefficient. The offset voltage can range from µV to mV at high temperature resulting in incorrect Seebeck coefficients [138]. Although the slope method can correct the offset voltage in most cases, the offset voltage can be dependent on the temperature difference resulting in a non-linear behavior between potential difference and temperature difference.

For the continuous mode in the TTO, the standard deviation of the Seebeck coefficient is given by

$$\sigma(S) = S \cdot \sqrt{\left(\frac{R_{\Delta V}}{\Delta V_\infty}\right)^2 + \left(\frac{R_{\Delta T}}{\Delta T_\infty}\right)^2} \tag{3.33}$$

where $R_{\Delta V} = \sqrt{\frac{\sum_i (\Delta V_i - \Delta V_{i,model})^2}{64}}$ is the residual of the voltage [131]. Although the offset voltage can be determined by Equation 3.32, contact resistance can increase the error. Furthermore, the manganin shoes have a Seebeck coefficient of ≤ 1 µV K^{-1} which is corrected by the instrument [131].

It is challenging to predict an accurate value for the uncertainty of the Seebeck

coefficient. In the thermoelectric community, an uncertainty of 5% is estimated and this value was used for the uncertainties of the present Seebeck coefficient measurements. This value is consistent with a round-robin study which reported a precision of 5.5% for the measurement of the Seebeck coefficient at high temperatures [140].

3.2.5 Electrical Conductivity and Hall Coefficient

The electrical conductivity and the Hall coefficient were measured with different methods. The Hall coefficient is important to determine the Hall carrier concentration and the Hall mobility and can be calculated using Equations 2.48 and 2.49, respectively. Although the Hall carrier concentration and Hall mobility are not the same as the carrier concentration and mobility used in the Drude model, they are good approximations and the Hall properties can be converted to the carrier concentration and mobility with the single parabolic band (SPB) model using Equations 2.54 and 2.55, respectively. For more details about the SPB model, refer to Section 2.5.

The electrical conductivity can be measured with a two-probe configuration, *i.e.*, the same probe is used for voltage and current lead, or four-probe technique, *i.e*, two probes for applying a current and two probes to measure the voltage. The latter has the advantage that the contact resistance does not affect the resistivity measurement. In this study, both techniques were used. For more information about the electrical conductivity and the Hall coefficient, see Section 2.4.

The low-temperature electrical conductivity and Hall coefficients were measured with a PPMS with a two-probe as well as four-probe configuration, while the high-temperature electrical properties were determined with the van der Pauw technique in a lab-built instrument described in reference [141].

3.2.5.a Thermal Transport Option in a PPMS - Electrical Conductivity

The electrical conductivity can be measured with the TTO in a Quantum Design PPMS, similar to the thermal conductivity and Seebeck coefficient. The TTO is described in more detail in Section 3.2.3.a. In the TTO technique, the electrical conductivity is measured using the two-probe configuration. This has the advantage

that the electrical conductivity can be measured simultaneously with the thermal conductivity and Seebeck coefficient, but the contact resistance can affect the results, in particular for materials with high electrical conductivity.

Each copper plate is connected to a precision DSP current source and a phase-sensitive voltage probe [131]. An AC current flows through the sample and the voltage drop is measured across the sample. From the current and the corresponding voltage drop, the resistance is calculated using Ohm's law (see Equation 2.30). However, the total resistance is the sum of the sample resistance and twice the contact resistance; if the latter is large it can result in a large uncertainty in the sample's electrical conductivity. The electrical conductivity is determined from the geometry of the sample using Equation 2.31. The electrical resistivity is measured before the thermal conductivity and Seebeck measurement because both sides of the sample should have a similar temperature for this measurement.

3.2.5.b Four-probe Electrical Conductivity & Hall Coefficient in a PPMS

The electrical conductivity also can be measured with a four-probe configuration in a Quantum Design PPMS using the resistance option. The resistance puck is shown in Figure 3.9 (a) with a sample attached to measure the electrical conductivity and the Hall coefficient simultaneously. The ends of the sample are attached to the current leads and the voltage drop is measured in the center of the sample. The sample generally has to be longer than wide to increase the distance between the voltage leads. In the resistance method, the resistance is measured from a linear fit of several DC currents and the corresponding voltage drops ($R = \frac{\mathrm{d}(\Delta V)}{\mathrm{d}I}$). In some cases, the $I - \Delta V$ curve is not linear due to, *e.g.*, Joule heating. With the four-probe method the non-linear behavior can be detected and the measurement can be repeated with lower currents to reduce Joule heating, whereas using a single-point measurement would show current-dependent resistances. Furthermore, in comparison to the two-probe, the four-probe configuration has the advantage that the contact resistance does not contribute to the total measured resistance and only the resistance of the sample is measured.

The Hall coefficient is measured at the same temperature set points and DC currents as the resistance measurement but additionally several magnetic fields with

varied magnetic strength, B, are applied in the horizontal direction. The Hall voltage drop, ΔV_{Hall}, is measured perpendicular to the DC current and the magnetic field. The Hall resistance, R_{Hall}, is first measured using the slope of the $I - \Delta V_{Hall}$ curve similar to the resistance measurement for each magnetic field. The Hall coefficient, R_H, is calculated from the slope of the calculated Hall resistance to the magnetic field using

$$R_H = \frac{R_{Hall} A_{cross}}{B \cdot L} \tag{3.34}$$

where A_{cross} and L are the cross-sectional area and thickness of the sample, respectively. For accurate measurements, the Hall voltage leads have to be exactly perpendicular to the current flow.

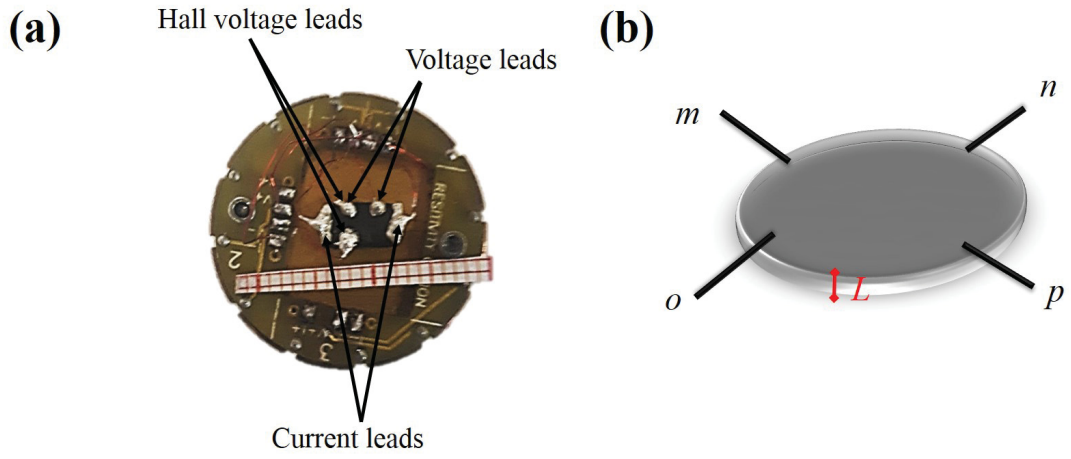

Figure 3.9: (a) PPMS resistance puck with $TmAgTe_2$ sample shown. The current leads are attached to the end of the samples and the voltage drop was measured parallel to the current for the resistance and perpendicular to the current for the Hall coefficient. A magnetic field was applied in horizontal direction. (b) In the van der Pauw technique four electrodes which can apply a current or measure the voltage drop were placed on the sample. The magnetic field was perpendicular to the sample and the Hall coefficient as well as the resistivity were measured with this configuration. Adapted from reference [141].

3.2.5.c High-Temperature Electrical Conductivity & Hall Coefficient

The high-temperature electrical conductivity was measured with the van der Pauw method in a lab-built instrument [141]. The van der Pauw method has the advantage

that the Hall coefficient can be determined using the same contacts as for the electrical conductivity measurement. The lab-built instrument contains of a sample holder with embedded heater and thermoelements, an electromagnet, and a chamber to control the atmosphere. The electromagnet has a distance of 2.5 cm between the pole caps generating a magnetic field of 2 T [141]. To provide nearly isothermal conditions for the measurement, the magnet is water-cooled and the sample holder, which is made out of boron nitride, is shielded by woven glass fibers to reduce radiation loss. Boron nitride has a high thermal conductivity and the heat can easily dissipate. The measurement is conducted under vacuum (10^{-8} bar) which reduces the convection between the chamber and the sample (holder). However, elements with high vapor pressure can evaporate out of the sample at high temperatures. Therefore, for high-temperature measurements the sample was coated with boron nitride to minimize evaporation.

For the electrical contacts, four molybdenum electrodes were pressed on the surface of the sample as shown in Figure 3.9 (b). Molybdenum has good mechanical and electrical properties over a wide range of temperature. The electrodes were pressed with stainless steel on the sample. For the Hall measurement, the electrodes have to be placed exactly opposite to each other. Small displacements can reduce the accuracy of the Hall measurement because the sample resistance is contributing to the Hall voltage [141].

In the van der Pauw method, two resistances are measured to determine the electrical conductivity. A DC current is applied between the contacts n, p and o, p, respectively (see Figure 3.9 (b)), and the voltage drop is measured between the corresponding other two contacts. With the resulting resistances, $R_{mo,np} = \frac{V_{mo}}{I_{np}}$ and $R_{mn,op} = \frac{V_{mn}}{I_{op}}$, the electrical conductivity is calculated from [141]

$$\exp\left(-\pi L R_{mo,np}\sigma_{el}\right) + \exp\left(-\pi L R_{mn,op}\sigma_{el}\right) = 1. \tag{3.35}$$

It is important to note that inhomogeneous contact can influence the measurement and therefore, the contact resistance of each electrode is measured before a test run, as follows. For the contact resistance measurement, one electrode is grounded and a positive voltage is applied on the other three electrodes.

In contrast to the low-temperature electrical measurements, the high-temperature electrical conductivity and Hall coefficient is measured with the continuous mode

using a constant heating rate. The resistances are averaged over several measurements with a constant current and Ohmic behavior is assumed.

For the Hall coefficient, the magnetic field was applied and the resistance ($R_{mp,no} = \frac{V_{mp}}{I_{no}}$) was measured. The Hall coefficient is given by

$$R_H = \frac{R_{mp,no}L}{B} \tag{3.36}$$

where $B = \pm 2$ T. The two different magnetic fields (plus zero field) are applied to detect deviations from a linear behavior. Furthermore, a second Hall coefficient was measured during which the current was applied between the contacts m and p and the voltage drop was measured between n and o. The Hall coefficient was averaged over both measured Hall coefficients. For more information about the measurement technique, the study by Borup *et al.* is recommended [141].

3.2.5.d Instruments

The low-temperature electrical conductivity and Hall coefficient were measured with the TTO and the resistance option in the Quantum Design PPMS with the assistance of Michel B. Johnson in the laboratory of Dr. Mary Anne White, Department of Chemistry, Dalhousie University. For details of the electrical conductivity measurement using TTO, see the measurement section of thermal conductivity (Section 3.2.3.c). The setup for the resistance option is shown in Figure 3.9 (a). For this measurement, the samples were polished to remove surface oxidation and copper wires were attached with silver epoxy to the polished surface. It is important that the current leads cover the entire end while the voltage leads should have only a small contact area. The copper wires were soldered with tin solder on the resistance puck and the sample was attached to the puck with double-sided adhesive tape. The measurements were conducted under soft vacuum ($\sim 4 \cdot 10^{-3}$ bar). The temperature was set to 400 K and cooled to 5 K with zero magnetic field. The voltage drop and the Hall voltage drop were measured for four different currents at each set point. The temperature increments between the set points decreased with decreasing temperature. At 5 K the magnetic field was set to 1 T and the same sequence as for cooling was used to measure the voltage drops. The same procedure was used with a magnetic field of 2 T on the cooling cycle and

-2 T on the heating cycle.

The high-temperature electrical conductivity and Hall coefficient were acquired with the assistance of Dr. Umut Aydemir in the laboratory of Dr. G. Jeffrey Snyder, California Institute of Technology, with a lab-built apparatus in the continuous mode as described by Borup *et al.* [141]. The samples were polished prior to measurement and then fixed with pressured-assisted molybdenum electrodes on the sample holder. The contact resistance of the electrodes was measured to assure good electrical contact. The sample was coated with boron nitride to avoid evaporation of elements with high vapor pressures under high vacuum. A small DC current (100 mA) was applied and the voltage drops were measured. The temperature was changed continuously with a constant scanning rate of 1.5 K min^{-1} and a constant magnetic field of $\pm$2 T was applied.

3.2.5.e Accuracy and Limitations

The accuracy of electrical conductivity measurements is similar to the thermal conductivity, limited by the sample geometry. Exact measurements of the dimensions are required to get the most accurate results. While dimensions of stiff materials can be measured with an uncertainty of $\pm$0.01 mm, fragile and compressible materials can increase the error to $\pm$0.04 mm leading to a large relative uncertainty in thin samples. For very thin and fragile samples here, the thickness was measured with a *Mitutoyo* linear gage in the laboratory of Dr. Jeff Dahn, Department of Physics and Atmospheric Science, Dalhousie University. The gauge has an uncertainty of 0.005 mm and a small force of <1.5 N is applied reducing the compression of the sample. Furthermore, the contact area of the voltage leads in the 4-probe configuration has to be narrow to enhance the accuracy of the resistivity measurements [135]. Although the distance between the voltage leads has to be large to decrease the uncertainty of the error in dimensions, the voltage leads should not be too close to the current leads, to ensure a uniform current. Therefore, the sample has to be long ($\sim$ 8 mm) in a 4-probe configuration for low-temperature electrical measurements. For cold-pressed samples, it was not feasible to prepare large samples and the lateral dimensions of these samples are limited by the diameter of the die ($\sim$ 5 mm).

The low-temperature electrical properties of cold-pressed samples were measured with the 2-probe configuration in the TTO. In addition to the uncertainty of the dimensions, the accuracy is also limited by the contact resistance between the sample and silver epoxy. In particular, the contact resistance can have a large contribution to the total resistance for materials with high electrical conductivity. Under the assumption that the contact resistance is temperature-independent, the electrical conductivity can be empirically adjusted to the high-temperature electrical conductivity. The instrument also has its own uncertainty for the TTO measurement which is given by the standard deviation

$$\sigma(\rho_{el}) = \rho_{el}\frac{R_{\rho_{el}}}{V_{pp}} \tag{3.37}$$

where $R_{\rho_{el}} = \sqrt{\frac{\sum_i(\Delta V_i - \Delta V_{i,model})^2}{128}}$ is the residual of the resistivity and V_{pp} is the peak-to-peak voltage *vs.* time signal of the AC measurement [131].

The van der Pauw method is not as sensitive to the lateral dimensions as the other methods because the electrical conductivity depends only on uniform thickness of the sample [135]. But high-temperature electrical conductivity measurements can have several other factors which limit the accuracy of the measurements. The thickness might increase with temperature due to thermal expansion and thus, the electrical conductivity is overestimated. The electrodes are flexible at high temperature and information about the thermal expansion is required to receive accurate measurements (for thermal expansion measurements, see Dilatometry; Section 3.2.7). Another source of error is the hot- or cold-finger effect of the thermoelements as already described in Section 3.2.4. At high temperatures, the temperature can be non-uniform in the sample and the thermoelements can produce different Seebeck voltages which influence the conductivity measurement.

Thermoelectric materials can have an additional source of error, in particular if the Seebeck coefficient is high and electrical conductivity is low. Based on the Peltier effect, electrical current transports heat from one end to the other and therefore, a temperature gradient generated in the sample can cause an additional Seebeck voltage [135]. This Seebeck voltage results in an underestimation of the electrical conductivity. Similar to Joule heating, the Peltier effect leads to a non-linear behavior

between current and voltage which can be detected by applying several currents. Considering all the potential sources of uncertainties, it is challenging to get a value for the accuracy of the measurement. In the thermoelectric community an accuracy of 5% is chosen which is also taken in this study as the accuracy of the electrical conductivity measurement. However, in a round-robin study a precision of 5% near room temperature and 9% at elevated temperature (∼470 K) was reported for the electrical conductivity [140].

The Hall coefficient has sources of errors similar to the electrical conductivity measurements. However, the measured voltage drop is in general much lower than the voltage drop of the electrical conductivity measurements and therefore, it is important to place the electrodes of the current and the Hall voltage in a perfect cross. Slight deviations can create a voltage offset which can be corrected for using different magnetic fields, *e.g.*, 0 and 2 T. As shown in Equation 2.48, the Hall coefficient as well as the Hall voltage are inversely related to the carrier concentration, *i.e.*, the higher the carrier concentration, the lower the Hall voltage drop. The Hall coefficient of materials with high carrier concentration can be noisy as the Hall voltage approaches the limit of detection in the voltmeter and other effects, such as Joule heating, can influence the Hall coefficient. In addition to the Joule heating, magnetoresistance can also affect the Hall measurement for materials with high mobility and the Hall voltage drop has to be measured with different magnetic fields, in positive as well as in negative directions [135]. The Hall voltage versus magnetic field curves are parabolic for magnetoresistance and linear for Hall coefficient so they can be easily separated. Although the accuracy decreases with increasing carrier concentration due to an increase in noise, the uncertainty of the Hall coefficient is likely less than 5% for the lab-built instrument [141]. For this study, an accuracy of 5% was chosen for the Hall coefficient.

3.2.6 DC Magnetization Measurement

With the DC magnetization measurement, the magnetic moment, M, of the sample can be determined as a function of temperature and magnetic field. The magnetic momentum is related to the magnetization by the volume. This measurement is important to indicate the magnetic class of the material.

3.2.6.a Theory

The magnetic moment is defined as the factor of the torque, τ, to an external magnetic field ($\tau = M \cdot B$). Although the magnetic moment can be measured in the PPMS, the more common magnetic parameter is the magnetic susceptibility, given by

$$\chi = \frac{M}{H} \tag{3.38}$$

where H is the magnetic field strength [73]. The magnetic field strength can be determined from the magnetic field ($B = \mu_0 \mu_r H$ with μ_0 and μ_r are the permeability of vacuum and relative permeability, respectively). From the sign and strength of the magnetic susceptibility, the magnetic properties can be divided in different magnetic classes, such as diamagnetic, paramagnetic, ferromagnetic, and antiferromagnetic [73]. A negative susceptibility indicates that the material is diamagnetic and the magnetic field is expelled from the material resulting in a reduction of the external magnetic field inside the material. The electrons in diamagnetic materials are all paired and the material has no net magnetic moment. Although diamagnetism can be found in all matter, due to its weak effect diamagnetic behavior can be only observed in some materials, *e.g.*, noble gases.

If the material has a permanent magnetic moment due to unpaired electrons, the magnetic behavior is paramagnetic (or Pauli paramagnetic) for small magnetic susceptibilities and ferromagnetic for large susceptibilities [73]. In both cases, the magnetic flux density in the material increases by applying an external magnetic field. However, in ferromagnets the susceptibility is larger because the magnet moments behave cooperatively due to a strong exchange energy interaction [73]. The magnetic moments of paramagnets, on the other hand, are slightly disordered, even in the presence of an external magnetic field. If the magnetic field is removed, the magnetic moments go to zero for dia- and paramagnets while ferromagnets have a residual magnetic moment due to the permanent dipole moment.

In addition to the strength and sign of the magnetic susceptibility, the magnetic behavior of the material can be classified from the magnetic moment versus temperature curve under magnetic field. While the magnetic moment is independent of temperature in diamagnetic materials, the magnetic moment decreases with increasing temperature ($\propto \frac{1}{T}$) in paramagnetic materials.

Ferromagnetic materials switch to paramagnetic behavior as the temperature is increased due to thermal motion. The magnetic phase transition temperature is known as Currie temperature. Another magnetic phase transition temperature is the Néel temperature, the transition from the antiferromagnetic to the paramagnetic state. Antiferromagnetic materials have zero net magnetic moment because the cooperative magnetic moments in different sublattices are oriented in opposite directions. Furthermore, in contrast to ferromagnetic materials, the magnetic moment increases with temperature in antiferromagnets.

The magnetic moment can be measured by the AC/DC Measurement System (ACMS) in a Quantum Design PPMS using the extraction method [142]. In the DC measurement, a constant external magnetic field is applied and the sample is moved quickly through four coils. According to Faraday's law, if a magnetic moves toward or away from a coil, a voltage is induced proportional to the magnetic flux ($V = -\frac{\Delta\Phi_B}{\Delta t}$ with Φ_B as the magnetic flux). The magnetic moment is determined from the integration of the voltage profile (from the translation of the sample through the coil) and fitting the resulting data to a known waveform for a dipole moving through the coils using a regression algorithm [142].

Further information about magnetic properties and the measurement technique can be found in references [73] and [142], respectively.

3.2.6.b Instruments

The magnetic moment measurements were performed with a Quantum Design PPMS with the assistance of Michel B. Johnson in the laboratory of Dr. Mary Anne White, Department of Chemistry, Dalhousie University, using the ACMS option. Before the measurement, the sample was polished and encapsulated in a polycarbonate capsule. The capsule was closed with Kapton® polyimide film tape which has the advantage of a small magnetic moment and good adhesivity, even at low temperature. The encapsulated sample was placed tightly in a holder and centered to a reference sample in terms of the sample position relative to the coils with the DC measurement software. Centering of the sample increases the accuracy for the magnetic moment determination. For the DC measurement, the sample was zero-field cooled to 2 K and the magnetic moment was measured at different set

temperatures. After several steps, the sample was re-centered by the software. At low temperature, a small magnetic field was applied (∼0.1 T) and the magnetic moment was measured on heating.

In addition to the temperature-dependent magnetic moment measurements, the magnetic moment also was obtained as function of the external magnetic field. The magnetic field was swept from 9 T to -9 T and back to 9 T with two different sweep rates. From 9 T to 1 T and -1 T to -9 T, the magnetic field was swept with a rate of 0.01 T s^{-1}. From 1 T to -1 T, the sweep rate was 0.002 T s^{-1} to get more accurate results in the important regions for ferromagnetic materials, such as remanent magnetic moment (the magnetic moment for zero magnetic field) and the coercive field (the magnetic field to restore zero magnetic moment).

3.2.7 Dilatometry

The coefficient of thermal expansion is an important parameter to determine the heat capacity at constant volume from heat capacity at constant pressure measurements (Equation 2.3) or to calculate the Grüneisen parameter (Equation 2.17). It is proportional to the change in volume or length over the change in temperature (see Equation 2.4 for linear coefficient of thermal expansion). While the thermal expansion of gases and liquids can be directly measured, it is challenging to measure the thermal expansion in solids due to the small change in length. The changes have to be amplified to get a strong signal to increase the signal-to-noise ratio. A potential way to measure even small thermal expansion is using a dilatometer. In addition to the linear coefficient of thermal expansion, subtle phase changes which might be difficult to detect by differential scanning calorimetry (see Section 3.1.8) can be indicated using dilatometry.

3.2.7.a Theory

The dilatometer consists of a heating chamber, a push-rod, thermoelements, and a displacement transducer. The displacement transducer can be based on a piezoelectric crystal or an inductive transducer. If a piezoelectric crystal is used, a spring is placed between the sample and the crystal. The piezoelectric voltage is proportional to the force on the contact area of the crystal and according to Hooke's law, the force has

a linear relationship with the change in length of the sample. For more accurate measurements, an inductive transducer is in general used. The inductive transducer consists of a solenoidal coil where a ferromagnetic core is moved through the coil. The ferromagnetic core is connected to the sample by a push-rod. If alternating current flows through the coil, the change in voltage in the coil is proportional to the induction and therefore, also to the thermal expansion. In this study, a linear variable differential transformer (LVDT) was used as the displacement transducer. It is similar to the inductive transducer except three solenoidal coils are used for the induction measurement. A primary coil in the center is linked to two secondary coils which are set parallel and the difference in the voltage between the secondary coils is measured. With this setup, also large thermal expansion can be measured (up to several cm) while the accuracy remains high.

The push-rod and the heating chamber are made from a low thermal expansion material. The thermal expansion should remain low even at high temperature to reduce the signal-to-noise ratio. To minimize the difference between the temperature of the sample and the recorded temperature, the thermoelement has to be placed close to the sample and the measurement has to be conducted under vacuum. Vacuum reduces both convection and surface oxidation.

3.2.7.b Instruments

The thermal expansion was obtained with the assistance of Dr. Julian O'Flynn and Addison Rayner in the laboratory of Dr. Stephen Corbin, Department of Civil and Resource Engineering, Dalhousie University, using a Netzsch DIL 402 C. Prior the thermal expansion measurement, the dilatometer was calibrated with a silica reference sample of similar thickness to the actual sample. Both the reference and sample were heated and cooled with the same scanning rate under high vacuum. For a uniform temperature through the sample, the scanning rate was chosen to be low (2-5 K min^{-1}) and at the highest set temperature the sample was kept isothermal for five minutes.

It is challenging to get a good estimation of the accuracy of the coefficient of thermal expansion. Although longer samples and large coefficient of thermal expansion would increase the accuracy due to a larger change in length, small

samples also can provide accurate results if the thickness of the reference is similar to that of the sample. Therefore, the thickness of the sample has to be measured with high accuracy and it is important that the ends of the sample are parallel. For this study, a thermal expansion uncertainty of $2 \cdot 10^{-6}$ K^{-1} was estimated for a sample thickness of >2 mm.

3.2.8 Ultrasound Measurements

Ultrasound measurements were performed to determine the speed of sound in solids. While in gases and liquids only longitudinal waves propagate, there are additionally transverse waves in solids where the atoms vibrate perpendicular to the propagation direction. From the speed of sound, the bulk and shear modulus can be calculated. Furthermore, the speed of sound can be used to determine the minimum thermal conductivity using the model by Cahill, Watson, and Pohl [66, 67]. In addition to the speed of sound, ultrasound measurements can also be performed to non-destructively detect defects.

3.2.8.a Theory

In the ultrasound measurements, a transducer generates a high-frequency pulse (100 kHz to several MHz) through the sample which is reflected on the back wall of the sample and detected by the same transducer. From the thickness of the sample and the time delay between the transmitted and received pulses, the speed of sound of the material is obtained ($v_s = \frac{2L}{\Delta t}$ where Δt is the time difference between the transmitted and received pulse). The transducer consists in general of a piezoelectric crystal which can be used as emitter and receiver. For a better contact, a coupling agent is applied between the transducer and the sample.

Two different transducers were used for the speed of sound measurement: A longitudinal and a shear transducer to determine the longitudinal and transverse speed of sound, respectively. The longitudinal speed of sound, $v_{s,L}$, is related to the bulk modulus, B, and shear modulus, G, by

$$v_{s,L} = \sqrt{\frac{B + \frac{4}{3}G}{\rho}} = \sqrt{\frac{Y(1-\nu)}{\rho(1+\nu)(1-2\nu)}} \tag{3.39}$$

while the transverse speed of sound, $v_{s,T}$, is given by [143]

$$v_{s,T} = \sqrt{\frac{G}{\rho}} = \sqrt{\frac{Y}{\rho \cdot 2(1+\nu)}}. \tag{3.40}$$

where Y is Young's modulus, ν is the Poisson's ratio which ranges between 0 and 0.5 for most materials [144] and therefore, $v_{s,T} > v_{s,L}$. For the detection of the transmitted and received pulse, the transducer is connected to an oscilloscope which shows the pulses as a function of time. For more information of the physics behind ultrasound measurements, reference [143] is recommended.

3.2.8.b Instruments

The ultrasound measurements were performed with the assistance of Saneyuki Ohno in the laboratory of Dr. William L. Johnson, Division of Engineering and Applied Science, California Institute of Technology, using a Panametrics NDT 5800 pulser/receiver and 5 MHz and 25 MHz shear and longitudinal transducers. The impulses were recorded with a Tektronix TDS 1012 digital oscilloscope. The low pass filter was set to 30 MHz and the high pass filter to 1 MHz. Honey is applied between the transducer and the sample as a coupling agent to improve the signal.

While the theoretical accuracy of the ultrasound measurement is related to the frequency of the pulse, the actual accuracy depends mainly on the quality of the sample. Defects, such as vacancies and cracks, can reflect the incoming pulse and overestimate the speed of sound. Therefore, low porosities are desirable to reduce the uncertainty in the measurement. Furthermore, the uncertainty in thickness can lead to a large uncertainties due to thin samples (<2 mm) and the speed of sound is proportional to twice the thickness. Therefore, an uncertainty of 5% is used for the speed of sound in the present study.

3.3 Thermal Transport Modeling

In addition to the experimental techniques used in this study, the thermal transport was simulated using the finite element method (FEM) embedded in the heat transfer module of the commercial software package *COMSOL Multiphysics*. With the heat transfer module thermal conduction, convection, and radiation of complex structures can be simulated.

FEM is a computational technique used to approximate physical problems in continuum mechanics where an analytical approach would fail. It is currently used in various fields, such as fluid dynamics, mechanical and electrical engineering. The approximation can be constructed based on the discretization with numerical model equations. In the discretization, a complex geometry is divided into a system of smaller finite elements interconnected to other elements or boundaries at multiple nodes [145]. Each of the elements can be described by a set of basis functions where the dependent variable, *e.g.*, temperature, is related to an independent variable, *e.g.*, time or space. For more information about FEM, the book '*The Finite Element Method: An Introduction with Partial Differential Equations*' by A. J. Davies is recommended [145].

For FEM simulation of thermal transport, first the geometry has to be defined. While more accurate geometries of the model provide a better understanding of the underlying physics, the real geometry could be too complex, requiring extensive amount of memory and time. Therefore, it is important to simplify the geometry without affecting the physics of the system. Further reduction in computational cost often can be obtained by introducing axis-symmetry. The geometry is discretized into a mesh which is related to the quality of the computation. The shape and size of the mesh elements can be chosen. Although a finer mesh provides more accurate results, the computation time increases exponentially with the mesh size. In addition to the geometry, the appropriate material parameters have to be defined for each geometry in the system, *e.g.*, the thermal conductivity, heat capacity, and density of the material have to be provided for heat transfer simulations.

After the geometry and material are defined, appropriate boundary conditions have to be applied to the system. The boundary on the surface can be thermally insulating or radiative or something else. For all systems in the present study, the temperature was fixed on one side and a heat flux was applied on the opposite side resulting in an increase in temperature on the heat flux side. From the heater power and the temperature gradient, the thermal conductance can be determined. Furthermore, the heat conduction in the solid and radiation were calculated from Equation 2.9 and Equation 2.10, respectively. In this study, convection is neglected because all thermal conductivity experiments were performed under high vacuum.

More details about modeling heat transfer can be found in reference [146].

All finite element analyses were performed with COMSOL v. 5.2a and the LiveLink™ for MATLAB. The accuracy of the model is highly dependent on the quality of the geometry, mesh size, as well as the boundary conditions. It is important to test that the system converges by changing mesh size. The computations were run on a two core processor (Intel® Core™ i3) with 6 GB RAM.

Chapter 4

Thermal Properties

An advanced understanding of the origins of low thermal conductivity can be used to discover and improve new thermoelectric and other materials. In this chapter, the origins of the ultralow thermal conductivity in [6,6]-phenyl-C_{61}-butyric acid methyl ester (PCBM) are delineated and the thermal as well as electrical conductivity of three-dimensional hierarchical microstructures of ZnO and carbon nanotubes (CNTs) are presented and discussed.

In the first section, the characterization and investigation of the thermal properties in PCBM are given and, based on the results, a new model of the minimum thermal conductivity is presented. The second section describes the investigation of the thermal conductivity of pure and metal oxide-coated ZnO tetrapods using a lab-developed powder cell. Furthermore, some ZnO tetrapods were coated with CNTs, enhancing the electrical conductivity.

4.1 Origins of Ultralow Thermal Conductivity in PCBM[1]

4.1.1 Introduction

Enhancement of the figure of merit in thermoelectric materials is strongly related to minimization of the thermal conductivity, as previously discussed. While several strategies can be applied to reduce the thermal conductivity, such as nanostructuring [18], point defect scattering, or alloy scattering [17], the reduction of the thermal conductivity is limited by the amorphous limit for the material [65, 66, 67].

[1]This section was adapted from: J.-H. Pöhls, M. B. Johnson and M. A. White, 'Origins of ultralow thermal conductivity in bulk [6,6]-phenyl-C_{61}-butyric acid methyl ester (PCBM)', *Physical Chemistry Chemical Physics*, 2016, **18**, 1185–1190, DOI: 10.1039/C5CP06575E - Reproduced by permission of the PCCP Owner Societies. Figures taken from the manuscript are labelled with reference [147]. The author's contribution was the characterization of the material, the development of the model, the measurement of the heat capacity and thermal conductivity, and writing the relevant sections of the manuscript. All measurements were performed in the laboratory of Dr. Mary Anne White, Department of Chemistry, Dalhousie University, unless stated otherwise.

The first concept of minimum thermal conductivity was introduced by Einstein in 1911 where he assumed that heat is transported between individual atoms [65]. However, this model did not agree with many materials. Cahill, Watson and Pohl modified Einstein's model of the minimum thermal conductivity with the assumption that heat is transported between entities of atoms over a wide range of temperature [66, 67]. This model agrees well for many materials, however, multilayered thin films of metals and oxides have shown lower thermal conductivity than the predicted minimum thermal conductivity of the material, giving rise to a property known as ultralow thermal conductivity [148, 149]. In particular, the disordered layered structure of WSe_2 has one of the lowest thermal conductivities ever measured ($\kappa = 0.048$ W m^{-1} K^{-1}) [149]. In addition to thin films, ultralow thermal conductivity also was reported in bulk materials, including SnSe [26, 27] and CdSe [150].

Recent studies by Duda *et al.* showed that thin films of PCBM have the lowest reported room-temperature thermal conductivity for a fully dense material ($\kappa = 0.030 \pm 0.0003$ W m^{-1} K^{-1}) [69]. The experimental thermal conductivity is about twenty times lower than the lowest limit of thermal conductivity predicted using the Cahill, Watson, and Pohl model ($\sim$0.61 W m^{-1} K^{-1}). The ultralow thermal conductivity in PCBM was verified by Wang *et al.* [151] and Guo *et al.* [152] but with slightly higher values ($\kappa = 0.057 \pm 0.007$ W m^{-1} K^{-1} and $\kappa = 0.070 \pm 0.007$ W m^{-1} K^{-1}, respectively). In addition to experimental studies, the phonon dispersion of PCBM was recently computed using molecular dynamics (MD) simulation and the room-temperature thermal conductivity was predicted to range from 0.050 to 0.075 W m^{-1} K^{-1} [153].

The large discrepancy between the experimental and theoretical minimum thermal conductivity could be a result of several factors. The thermal conductivity of the thin films was determined with the time-domain thermo-reflectance method in which a laser heats a spot on the surface and the thermal conductivity is determined by the change in reflectance due to thermal stress. This determination of the thermal conductivity requires knowledge of the heat capacity of the materials. For PCBM, Duda *et al.* assumed that the specific heat of PCBM is the same as for C_{60}/C_{70} fullerite which introduces uncertainty in the result [69]. Small changes in

the morphology can have a large effect on the heat capacity and in particular, the side chain of the PCBM molecule can affect the heat capacity. The calculated thermal conductivity is inversely proportional to the heat capacity and a decrease in heat capacity would increase the thermal conductivity. Furthermore, the accuracy of the thermal conductivity is lower in thin films due to their small dimensions. Additionally to the small dimensions, thin films could show lower thermal conductivity than their corresponding bulk material. Therefore, it was not clear if the low experimental value was intrinsic to PCBM or due to morphology.

In this section of the thesis, the bulk properties of PCBM including the heat capacity and thermal conductivity are reported and show that the ultralow thermal conductivity in PCBM is an intrinsic property. Based on heat capacity and thermal conductivity measurements to low temperatures, a new model of the minimum thermal conductivity was developed and compared to the minimum thermal conductivity models by Einstein as well as by Cahill, Watson and Pohl. In addition to the low-temperature physical properties, high-temperature properties of PCBM also were analyzed to determine the temperature stability of PCBM.

4.1.2 Background Concerning Minimum Thermal Conductivity

Before a new model of minimum thermal conductivity can be developed, a short background of the Einstein and the Cahill, Watson and Pohl models for minimum thermal conductivity are presented. Both models can be derived from a modified Callaway equation (see Equation 2.14) given by

$$\kappa_{min}(\omega, T) = \sum_{i}^{3} \int_{0}^{\infty} \frac{1}{3} D_i(\omega) \frac{1}{V} \frac{\mathrm{d}\langle U \rangle(\omega, T)}{\mathrm{d}T} v_i(\omega) \lambda(\omega) \mathrm{d}\omega \tag{4.1}$$

where the heat capacity was split into the density of states, $D_i(\omega)$, and the change of the average internal energy, $\langle U \rangle(\omega)$, over the absolute temperature, as also discussed in Section 2.1.

Einstein assumed in his model that heat is only transported between individual atoms, in particular, thermal energy is transferred between the first, second, third nearest neighbors [65]. Furthermore, he assumed that all atoms vibrate incoherently with a single frequency. The dispersion curve of a single frequency, ω_0, can be described by a delta (δ)-function resulting in a density of states of

$D_i(\omega) = N\delta(\omega - \omega_0)$. The average internal energy is calculated from the Bose-Einstein distribution to determine the average number of phonons per mode and the energy of a single mode ($\hbar\omega$), *i.e.*, $\langle U \rangle(\omega) = \frac{\hbar\omega}{e^{(\hbar\omega)/(k_B T)}-1}$.

The phonon mean free path is limited in Einstein's model by the atomic density $\left(\lambda = \left(\frac{V_{UC}}{N}\right)^{1/3}\right)$ where V_{UC} is the unit cell volume and N is the number of atoms in the unit cell. The phonon mean speed is given by $v_i = \frac{\lambda}{\tau_{rel}}$ where τ_{rel} is the time required to transfer thermal energy between first neighbor atoms [65]. Einstein showed in his study that the average total energy is of the same order as the energy fluctuations, using a relaxation time equal to half of the period of vibration ($\tau_{rel} = \frac{\pi}{\omega_0}$) [65]. A simpler way to show that the time is limited by half of the period of vibration is using the (minimum) phonon mean free path as shown in Figure 4.1 (a). The solid line shows that the phonon mean free path is limited by the interatomic distance, a_{dist}, where the interatomic distance is half of the wavelength. A smaller wavelength (dashed line) would show the same atomic pattern and would not have an effect on the (minimum) phonon mean free path. Therefore, the relaxation time is given by $\left(\tau_{rel} = \frac{a_{dist}}{v_i} = \frac{\lambda/2}{\omega\lambda/2\pi} = \frac{\pi}{\omega}\right)$. All parameters are inserted in Equation 4.1 and Einstein's minimum thermal conductivity is calculated from

$$\kappa_{min,Einstein} = \frac{k_B^2}{\pi\hbar}\left(\frac{V_{UC}}{N}\right)^2 \theta_E \frac{x_E^2 e^{x_E}}{\left(e^{x_E}-1\right)^2} \tag{4.2}$$

with $x_E = \frac{\theta_E}{T}$. For more information of the derivation of the minimum thermal conductivity, Einstein's original study is recommended [65]. The Einstein model for minimum thermal conductivity has been tested but does not agree with experimental thermal conductivities of many materials because heat is not transferred between individual atoms vibrating with a single frequency.

In 1988, the Einstein model was modified by Cahill and Pohl with the assumption that heat is transferred between entities of atoms vibrating coherently in a range of frequencies from 0 to a maximum frequency, ω_{max}, also known as the Debye frequency [66]. While the density of states of a single frequency can be represented by a δ-function, the density of states for a range of frequency in a three-dimensional solid can be described by the volumetric density of states ($D_i = V\frac{\omega^2}{2\pi^2 v_p^2 v_g}$ where $v_p = \frac{\omega}{k}$ is the phase velocity and $v_g = \frac{\partial\omega}{\partial k}$ is the group velocity). The phonon mean free path is given, similar to the Einstein model, by $\lambda = v_i \cdot \tau_{rel} = \frac{\pi v_i}{\omega}$ and the minimum thermal

conductivity according to the Cahill, Watson, and Pohl model can be calculated from

$$\kappa_{min,Cahill} = \left(\frac{\pi}{6}\right)^{1/3} k_B \left(\frac{N}{V_{UC}}\right)^{2/3} \sum_i v_i \left(\frac{T}{\theta_{D,i}}\right)^2 \int_0^{x_D} \frac{x^3 \mathrm{e}^x}{(\mathrm{e}^x - 1)^2} \mathrm{d}x \tag{4.3}$$

with $x_D = \frac{\theta_{D,i}}{T}$ [66, 67]. At high temperature, the minimum thermal conductivity model approaches a constant thermal conductivity and can be written as

$$\kappa_{min,Cahill,HT} = \frac{1}{2}\left(\frac{\pi}{6}\right)^{1/3} k_B \left(\frac{N}{V_{UC}}\right)^{2/3} (2v_{s,T} + v_{s,L}) \tag{4.4}$$

where $v_{s,T}$ and $v_{s,L}$ can be obtained from ultrasound measurements.

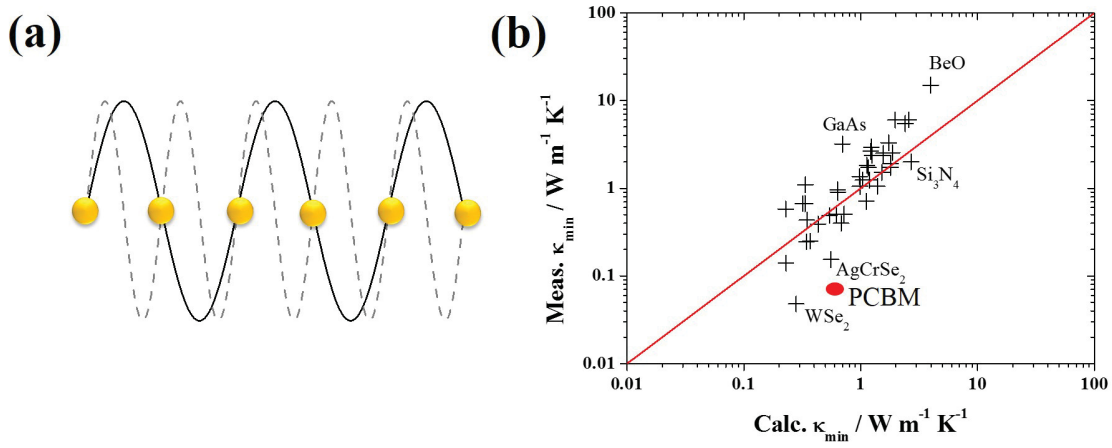

Figure 4.1: (a) Relaxation time is determined from the smallest phonon mean free path where the interatomic distance is half of the wavelength (solid line). A reduction in wavelength (dashed line) would not affect the phonon mean free path. (b) Experimental and theoretical minimum thermal conductivity using Cahill, Watson and Pohl model. The experimental thermal conductivity is the lowest thermal conductivity reported for the material above room temperature. Most of the materials agree well with the predicted minimum thermal conductivity. However, several materials have a lower thermal conductivity than the predicted theoretical minimum thermal conductivity. Adapted and reproduced from Ref. [35] with permission from The Royal Society of Chemistry.

The Cahill, Watson, and Pohl model is commonly used in the thermoelectric community to determine the lowest limit of thermal conductivity. It was found that the minimum thermal conductivity model agrees for many materials (see Figure 4.1 (b)). However, in recent years several materials have been found to have lower thermal

conductivity than the predicted lowest limit. In particular, the thermal conductivities in selenides, such as WSe_2 [149] and $AgCrSe_2$ [154], and even in elemental selenium [66] are lower than the Cahill-Watson-Pohl theoretical lowest limit. One of the largest discrepancies between the experimental and predicted minimum thermal conductivity was observed for PCBM, which is ten to twenty times lower than the amorphous limit [69]. This might be surprising because other carbon-based materials have extremely high thermal conductivity; examples include diamond [79] and carbon nanotubes [155]. However, the structure and bonding of carbon-based materials vary widely, leading to a large range in thermal conductivity. In the following section, PCBM is introduced and its chemical structure is compared to other carbon-based materials.

4.1.3 Materials

The most common carbon allotropes, graphite and diamond, have been known for thousands of years, although it was only in 1796 that Tennant proved that diamonds consist of pure carbon [156]. In recent decades, research in carbon-based materials increased rapidly and new carbon structures were discovered, such as Buckminsterfullerene (C_{60}) by Kroto *et al.* in 1985 [157], carbon nanotubes by Iijima in 1991 [158], and graphene by Novoselov *et al.* in 2004 [159]. Theoretical and experimental studies have shown that carbon-based materials have aesthetic chemical structures and unique chemical and physical properties [160]. While many carbon structures have only one specific phase, the crystal structure of fullerene can be tuned by pressure and temperature [161] leading to unusual properties, *e.g.*, ultra hardness [162] or superconductivity [163].

PCBM is the most common fullerene derivative to date due to its wide application range in organic electronics, *e.g.*, electron acceptor in bulk hetero-junction (BHJ) solar cells [164]. Although organic electronics containing PCBM are well investigated [165, 166, 167], the properties of pure PCBM are rarely explored. PCBM can be synthesized by different routes, *e.g.*, reaction of a diazone derivative with C_{60} at elevated temperatures [168] or a microwave-assisted synthesis [169]. The synthesis of PCBM is complex and the yield is normally low resulting in a high production cost. However, in contrast to C_{60}, PCBM has the advantage that it is highly soluble in organic solvents; PCBM is very soluble in chlorobenzene and forms nano-scale

networks with poly(3-hexylthiophene-2,5-diyl) (P3HT) [170].

The molecular structure of PCBM is shown in Figure 4.2 (b). Each PCBM molecule consists of a phenyl group and a butyric acid methyl ester group attached to a C_{60} fullerene. The fullerene core consists of 20 six-member rings and 12 five-member rings where the carbon atoms are sp^2-hybridized. Most carbon-based materials, such as diamond and graphene, have strong covalent bonds resulting normally in extremely high thermal conductivity. However, carbon-based materials can be categorized as three-dimensional (*e.g.*, diamond), two-dimensional (*e.g.*, graphene), one-dimensional (*e.g.*, CNT), and zero-dimensional structures (*e.g.*, fullerene and PCBM). While diamonds, graphene, and CNTs have at least one direction where the phonons can propagate, individual fullerene and PCBM molecules are only connected by weak van der Waals interactions. Both fullerene and PCBM have four individual molecules in each unit cell but the fullerene molecules are packed more tightly than PCBM due to its additional side chains [171, 172]. The side chain also leads to a reduction of the crystal symmetry. While C_{60} has a high-symmetry face-centered-cubic (fcc) structure [172], the crystal structure of PCBM is monoclinic [171]. In addition to the crystal structure, the electronic band structure of PCBM has also been investigated [173, 174]. Pristine PCBM has a relative large band gap energy ($E_g = 1.7 - 2.5$ eV) which is consistent with the red-brown color of the PCBM powder shown in Figure 4.2 (a).

PCBM powder ($> 99\%$; Solenne BV, Netherlands) was used as-received. It is important to note that the material has to be stored under vacuum in a dark container. PCBM was only briefly exposed to oxygen and light for sample preparation to avoid any change in the molecular structure. For the investigation of the bulk properties, PCBM powder was placed in a stainless steel die (5.08 mm) and consolidated with a pressure of 439 MPa for 15 min in air. Before the heat capacity and thermal conductivity of bulk PCBM were investigated, the crystal and molecular structure of bulk PCBM were compared to the powder to allay concerns with consolidation and photoreactivity.

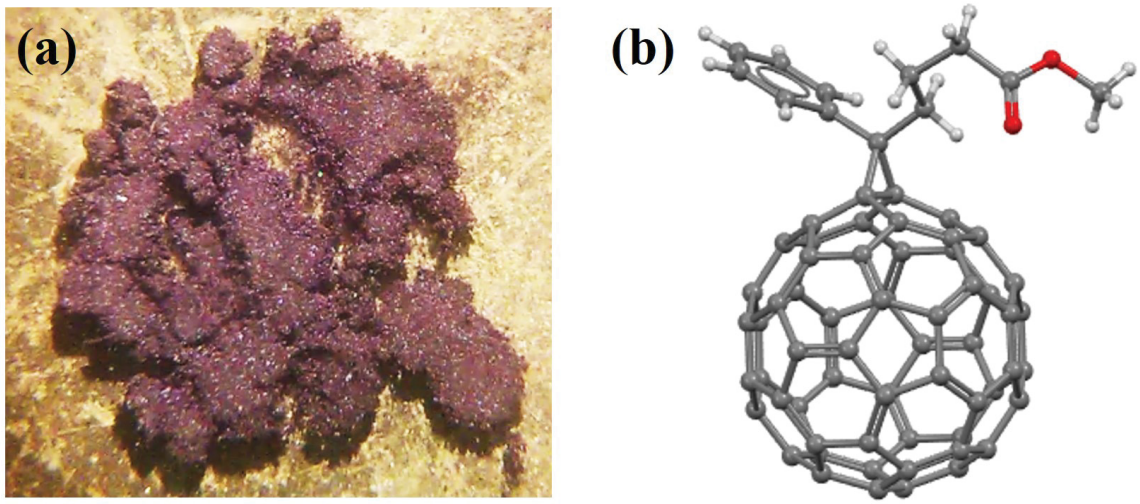

Figure 4.2: (a) PCBM powder (as-received) under an optical microscope. (b) Molecular structure of PCBM (•: carbon; •: oxygen; ∘: hydrogen). Figure from reference [147].

4.1.4 Characterization

4.1.4.a Powder X-ray Diffraction of PCBM

The PXRD pattern of as-received PCBM powder and consolidated pellet were acquired in the laboratory of Dr. Mark Obrovac, Department of Chemistry, Dalhousie University, are shown in Figure 4.3. No peak shifts or additional peaks were observed between the two samples, indicating that the crystal structure is intact after consolidation. The PXRD patterns are similar to the reported patterns for PCBM thin films [166, 171] and PCBM powder [167]. The pattern was refined with the Le Bail method and both samples were found to crystallize in the monoclinic phase with space group $P2_1/n$. However, a small reduction in the unit cell volume was observed with applied pressure ($V_{UC,thinfilm} \sim 3761$ Å^3 and $V_{UC,pellet} \sim 3752$ Å^3) which is slightly higher than the volume of solvent-free PCBM thin film ($V_{UC,powder} \sim 3733$ Å^3) [171]. The experimental mass density of the pellet determined from its dimensions was compared to the theoretical mass density from the Le Bail refinement indicating a porosity of 6%. It was not feasible to refine the PXRD pattern with the Rietveld method due to the large number of atoms in the unit cell.

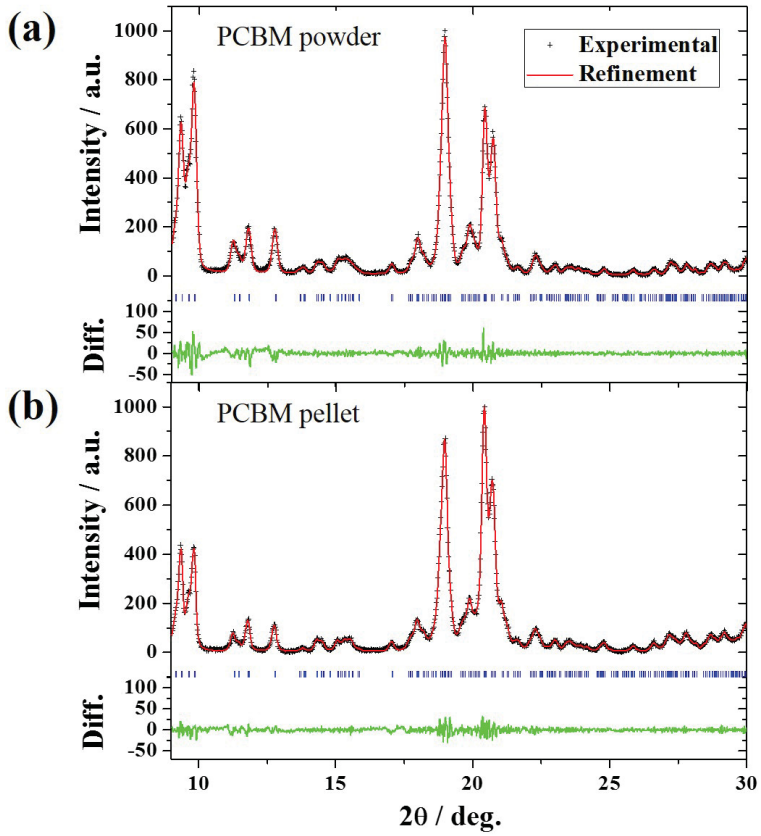

Figure 4.3: Le Bail refined PXRD pattern of (a) PCBM powder and (b) a consolidated PCBM pellet. Blue ticks indicate the computed reflection position and the green line is the residual of the refinement. The refinement data for PCBM powder and PCBM pellet are given in Table A.1 of Appendix A. Figure from reference [147].

The present PCBM powder and pellet have sharp peaks in the PXRD which point to large crystals (in µm range) with high crystallinity at room temperature. Mens *et al.* reported that the morphology of the PCBM crystal structure is dependent on the preparation method [175]. They heated the PCBM powder to 663 K for 10 minutes and quenched it with liquid nitrogen. The quenched samples had broader peaks than the as-received sample indicating smaller crystals with amorphous regions [175]. The temperature stability of the crystal structure was investigated here by heating a PCBM pellet to 493 K, 533 K, and 563 K, respectively, for one hour and recording the PXRD pattern at room temperature (see Figure 4.4 (a) and (b)). Additional peaks

were recorded after heating to 493 K, in particular, at $2\theta \sim 12.1°$ and 17.9°, indicating an irreversible change in crystal structure. The intensity of the peaks increased with temperature leading to the conclusion that more of the initial phase was transformed to a second phase. After heating to 563 K, the sample had been melted and two broad peaks were recorded, similar to the PXRD pattern of the thermally quenched PCBM powder reported by Mens *et al.* [175].

In addition to the measurement of heat treated samples, temperature-dependent PXRD measurements were performed in the laboratory of Andy George, Department of Physics and Atmospheric Science. With the temperature-modification stage in the X-ray diffractometer, the PXRD can be recorded in a temperature range from 123 K to 473 K (see Figure 4.4 (c) and (d)). Due to the irreversible change in crystal structure at high temperature the sample was first cooled from 300 K to 123 K and PXRD patterns were recorded at 123 K, 223 K, 300 K, 373 K, and 473 K.
The intensity of the peaks increased with temperature and the positions of the peaks shifted to lower angles (Figure 4.4 (c) and (d)). Similar to the heat-treated PCBM pellets, additional peaks were recorded at 473 K confirming the high-temperature change in crystal structure. The PXRD patterns were refined by the Le Bail method except for 473 K. (Data are given in Table A.2 of Appendix A). An increase in the unit cell volume was determined from 123 K to 223 K, and a nearly constant unit cell volume at 223 K, 298 K, and 373 K as shown in Table A.2 of Appendix A. This is not consistent with the density reported by Tummala *et al.* [176]. They found an increase in density from 150 K to 200 K for solvent-free PCBM molecules in the monoclinic phase. However, their calculated density is in the range of amorphous PCBM [176] while the present PCBM pellet showed high crystallinity at room temperature which might influence the temperature-dependence of PCBM.

It can be concluded that consolidation does not affect the crystal structure of PCBM. However, it was found that the crystal structure changed below 473 K and therefore the phase transition was further investigated (*vide infra*).

4.1.4.b Raman Spectroscopy of PCBM

In addition to the crystal structure, no significant change in molecular structure on pressing was observed using Raman spectroscopy (see Figure 4.5 (a) and (b)).

Due to the fact that no complete experimental Raman spectrum is available from the literature for PCBM, the Raman spectra were compared here to C_{60} powder (<99.5%; Sigma Aldrich) as shown in Figure 4.5 (c). C_{60} has 10 Raman modes (2 A_g and 8 H_g) as well as 4 infrared modes (F_{1u}) which are highly degenerate due to its high symmetry (I_h) [177].

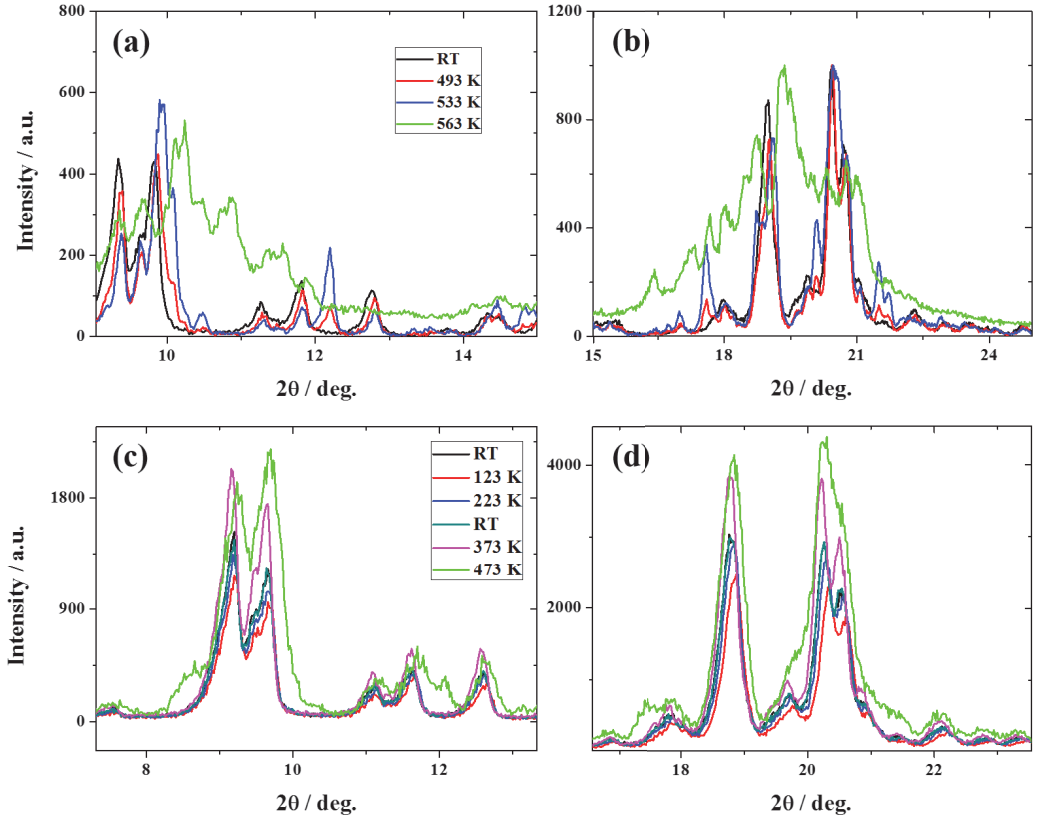

Figure 4.4: (a) and (b) PXRD pattern of a PCBM pellet at room temperature after different heat treatments. Additional peaks were observed after heating to 493 K, and increased in intensity with temperature. (c) and (d) Temperature PXRD measurements of a PCBM pellet indicating that the crystal structure changes at 473 K. The peak intensity increased with temperature. The refined data for room temperature (RT; 300 K), 123 K, 223 K, and 373 K are given in Table A.2 of Appendix A. Figure from reference [147].

The most important Raman modes are the two non-degenerate A_g modes. The $A_g(1)$ mode describes the breathing mode of the C_{60} molecule due to radial displacements, *i.e.*, all carbon atoms in the fullerene core expand and contract

simultaneously. The $A_g(2)$ mode, also known as pentagonal pinch mode, implies tangential displacements where the hexagonal rings expand and concurrently the pentagonal rings contract [177].

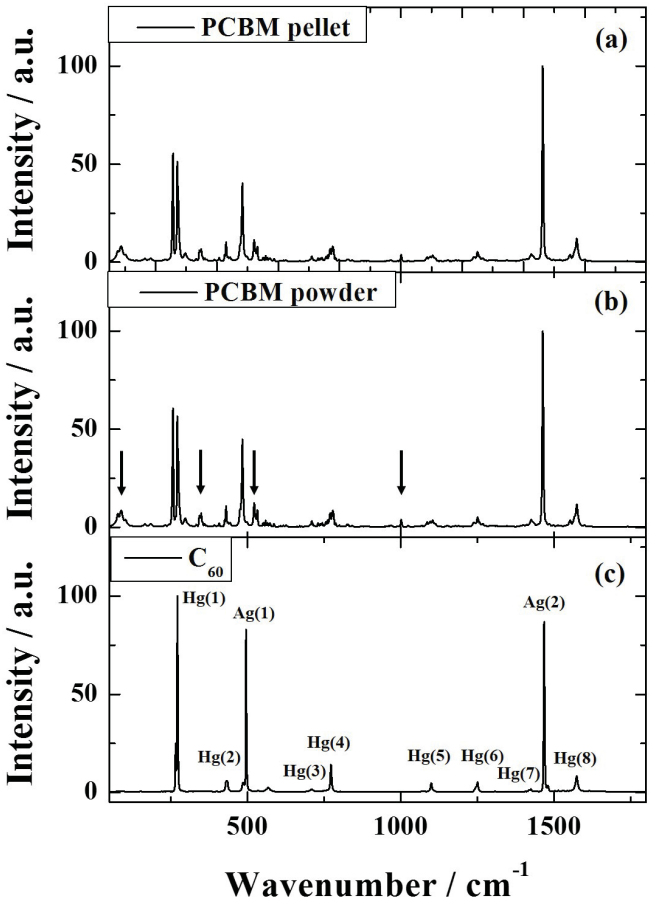

Figure 4.5: Experimentally determined Raman spectra of (a) PCBM powder, (b) consolidated PCBM pellet, and (c) C_{60} powder. No significant discrepancy between the PCBM powder and pellet spectra was observed. However, the number of modes increased from C_{60} to PCBM due to a reduction in symmetry. The frequencies of the modes for PCBM powder, PCBM pellet, and C_{60} powder are given in Table A.3 of Appendix A. Figure from reference [147].

The number of Raman peaks increases in PCBM relative to C_{60} because the icosahedral modes in the fcc structure of C_{60} are split into a partially broken symmetry (C_{2v}) for the fullerene core [178]. A shift of the $A_g(2)$ peak to lower wavenumbers was

observed from C_{60} to PCBM because the negative charge increased on the fullerene core due to the side chainl [179].

In addition to the Raman peaks of C_{60}, four major Raman peaks (88 cm^{-1}, 348 cm^{-1}, 521 cm^{-1}, and 1001 cm^{-1}) were recorded for PCBM. These Raman modes were assigned to the side chain of the PCBM molecule. The Raman peak at 521 cm^{-1} and 1001 cm^{-1} are most likely due to carbon-carbon stretching in the butyric acid methyl ester group and the breathing mode of the phenyl group [180], respectively. The low-frequency Raman peaks are most likely due to rotation and carbon-carbon stretching of the butyric acid methyl ester group and the rotation of the phenyl group. In particular, the low-frequency Raman peak at 88 cm^{-1} might be a reason for the low thermal conductivity in PCBM.

High-wavenumber Raman modes for PCBM thin films were reported by Falke *et al.* [179]. The frequencies of the published data for $H_g(7)$, $A_g(2)$, and $H_g(8)$ agree well with the present results. In addition to experimental data, the Raman spectra were also compared to calculated Raman spectra [181, 153]. However, the calculated Raman spectrum using first-principle calculations [181] and molecular dynamics simulations [153] do not fully represent the present spectrum.

The molecular structure was also investigated via temperature-dependent Raman spectroscopy (298 K, 348 K, 323 K, 273 K, and 198 K) (Figure 4.6). No shifts or new Raman peaks were recorded indicating that the molecular structure does not change with temperature in the temperature range from 198 K to 348 K. In addition to the temperature measurements, PCBM powder was heated to 553 K and 723 K and quenched to room temperature in liquid nitrogen. In contrast to the PXRD spectra, there was no change in the Raman spectra indicating an intact molecular structure also with heat treatment.

4.1.4.c Differential Scanning Calorimetry and Thermal Analysis

For a better understanding of the temperature behavior of PCBM, thermograms of PCBM powder ($m = 3.47 \pm 0.02$ mg) and pellet ($m = 4.85 \pm 0.02$ mg) were recorded with a scanning rate of 10 K min^{-1} as shown in Figure 4.7 (a) and (b), respectively. Three thermal cycles were performed where the sample was heated to 493 K (1. cycle), 533 K (2. cycle), or 573 K (3. cycle), each time cooled back to room temperature.

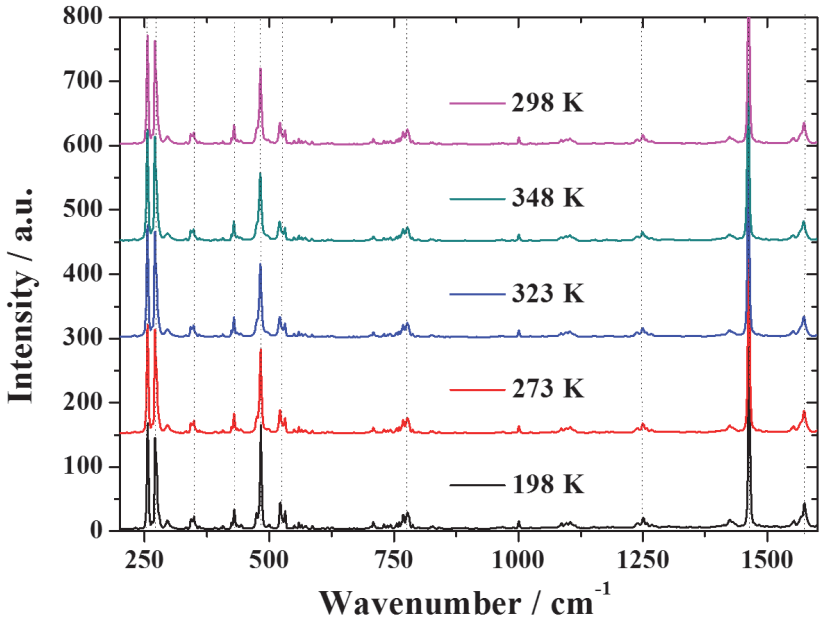

Figure 4.6: Experimentally determined Raman spectra of PCBM powder at various temperatures (298 K, 348 K, 323 K, 273 K, and 198 K). No shifts or new Raman peaks were observed with temperature. The dashed lines are guides to the eye. Figure from reference [147].

While no anomalous behavior was observed after heating to 493 K, two endothermic events were recorded at around 515 K and 550 K on heating, similar to reports in the literature [182, 175]. The endothermic peaks reported by Mens *et al.*, however, were shifted to higher onset temperatures (529 K and 561 K) which might be a result of their high scanning rate of 20 K min^{-1} [175]. While the onset temperatures are similar for PCBM powder and pellet, the change in enthalpy ($\Delta_{trs}H$) depended on the sample morphology and the prior thermal treatment. The lower-temperature phase transition was nearly suppressed in the PCBM pellet while the first thermal event in the PCBM powder had a larger change in enthalpy than the second event. The first event is most likely due to a polymorphic transition as no melting was observed after the second cycle. The second endothermic peak was due to melting and the change in enthalpy was slightly larger for the pellet than the powder. Ngo *et al.* claimed that the first peak is due to evaporation of the solvent in the sample [182], but the as-received PCBM powder should not contain any solvent, as confirmed

by the thermogravimetric analysis (*vide infra*). It is important to note that many samples with varying masses were measured here, all confirming the thermograms of the powder and the pellet.

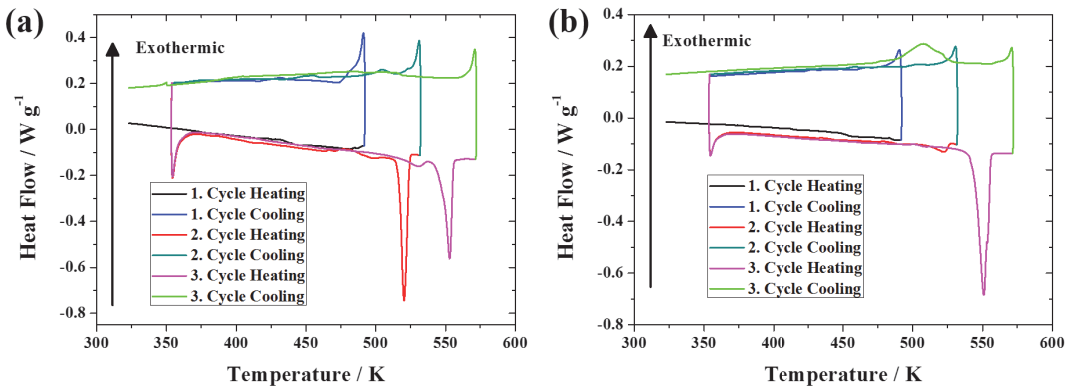

Figure 4.7: DSC thermograms for (a) PCBM powder and (b) PCBM pellet. Two irreversible phase transitions were observed for both samples. The lower-temperature phase transition in the PCBM pellet is almost suppressed in comparison to the powder. The thermogram data are given in Table A.4 of Appendix A. Figure from reference [147].

Although the scanning rate was rather high for highly accurate measurement of the onset temperature (see Section 3.1.8), the results indicate that the pellet undergoes a more substantial solid-solid transition than in the powder. However, the overall change in entropy from the low-temperature solid to the liquid is in the same magnitude for the powder and the pellet. The onset temperatures, changes in enthalpy, and changes in entropy are given in Table A.4 of Appendix A. The sum of both endotherms for both PCBM powder ($\Delta_{trs}H \sim 33$ J g^{-1} and pellet ($\Delta_{trs}H \sim 26$ J g^{-1}) is similar to the reported endotherm of the crystalline PCBM powder [175]. Mens *et al.* found that a reduction in the crystallinity also decreases the total change in enthalpy [175].

A broad exothermic peak was recorded for both samples on cooling, indicating sluggish crystallization. Mens *et al.* found only a cold crystallization in the thermally quenched and the doctor blade sample, while the as-received samples did not indicate any transition [175]. This is especially surprising due to the fact that Mens *et al.* used a higher scanning rate than in the present study.

In addition to the melting point, a glass transition temperature has also been observed by Ngo *et al.* at T_g = 391.5 K for quenched PCBM blends [182]. Consequently, one PCBM sample was heated in the present study to 623 K and quenched in liquid nitrogen (T = 77 K). However, the thermogram of the quenched sample showed no significant difference from the untreated pellet. Different scanning rates (5 - 20 K min^{-1}) were used but no thermal event was noted between 373 K to 473 K.

For a visible observation of the phase transformation, PCBM powder and a PCBM pellet were heated to 565 K under an optical microscope in air. No visible change was observed to a temperature of 550 K. While the powder was completely molten to a glassy/liquid state at 555 K after 2-3 minutes, the bottom part of the PCBM pellet was only molten at the same temperature. The top surface of the pellet was even stable at 565 K after 1 hour. The temperature of the surface of the PCBM pellet was measured with a blackbody thermometer which showed a temperature of 545 K where the temperature of the hot plate was 565 K. It is postulated that the low thermal conductivity of PCBM and black body radiation would maintain a constant temperature gradient even over a long period of time. Although the power radiated on the surface of the pellet ($\sim$454 mW) can be calculated, it is challenging to model the heat transfer through the pellet due to various unknown parameters, such as the thermal conductivity and heat capacity of the molten phase and the convective losses.

In addition to the thermal stability of the crystal structure tested by PXRD (*vide supra*), the thermal decomposition of PCBM was measured with a scanning rate of 10 K min^{-1} in air using a TGA in the laboratory of Dr. Jeff Dahn, Department of Physics and Atmospheric Science, Dalhousie University. Figure 4.8 shows the resulting thermogram which at first glance seems uneventful. Taking the derivative of the mass loss, two small peaks were observed at the same temperature as the onset temperature of the endothermic peaks in the DSC, which might be due to adsorbed air or water. The very small mass losses also disproves the claim by Ngo *et al.* that the first endothermic peak is due to the evaporation of solvent [182]. PCBM powder starts to decompose around 670 K and at 715 K the rate of the mass loss dramatically increased.

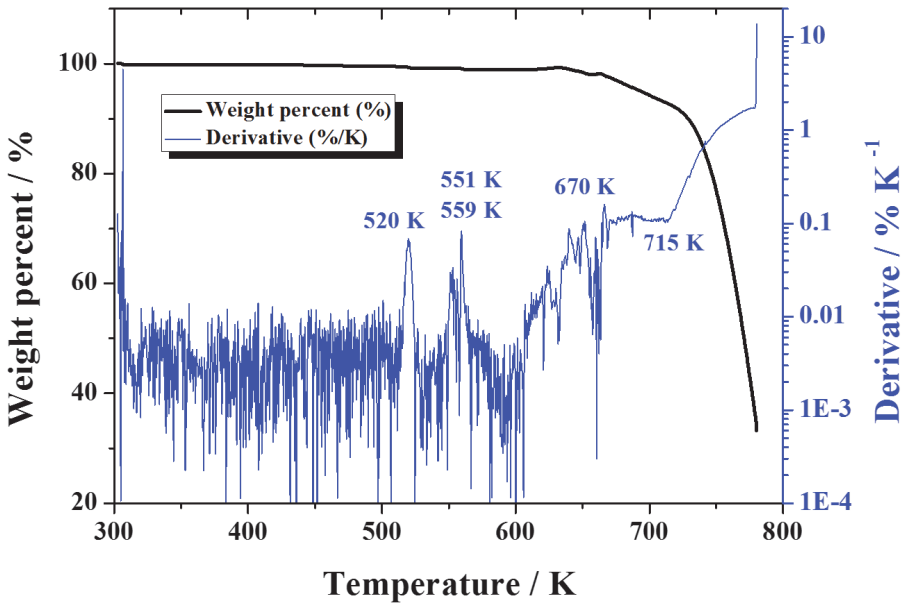

Figure 4.8: Thermogravimetric analysis of PCBM powder ($m = 2.2854 \pm 0.0001$ mg). Two small mass losses were detected at $\sim$ 520 K and$\sim$ 560 K and it starts to decompose at $\sim$ 670 K in air. Figure from reference [147].

4.1.4.d Thermal Expansion

Additionally to DSC, thermal expansion measurements can also identify phase transformations because a discontinuous volume change occurs at a first-order phase transition [73]. The thermal expansion of two PCBM pellets ($L_{0,1} = 1.194 \pm 0.003$ mm and $L_{0,2} = 1.213 \pm 0.002$ mm) was investigated in the laboratory of Dr. Stephen Corbin, Department of Civil and Resource Engineering, Dalhousie University.

On heating, nearly no thermal expansion was found in the temperature range from 298 K to 423 K, followed by a dramatic increase between 450 K and 480 K as shown in Figure 4.9. While the nearly constant length at lower temperature (300 K to 450 K) is consistent with the Le Bail refined unit cell volumes which only slightly increase from 298 K to 373 K (see Table A.2 of Appendix A), the relatively large thermal expansion (between 5-7%) at 450 K is surprising as no thermal event was observed with the differential scanning calorimeter. It is important to note that the length did not return to its initial value indicating that the thermal expansion at 450

K is irreversible, most likely due to an irreversible change in the crystal structure as found from PXRD measurements in Section 4.1.4.a. The change in crystal structure and the increase in length were indeed confirmed after the measurement by PXRD and thickness measurements with a Mitutoyo linear gage in the laboratory of Dr. Jeff Dahn, Department of Physics and Atmospheric Science, Dalhousie University, respectively.

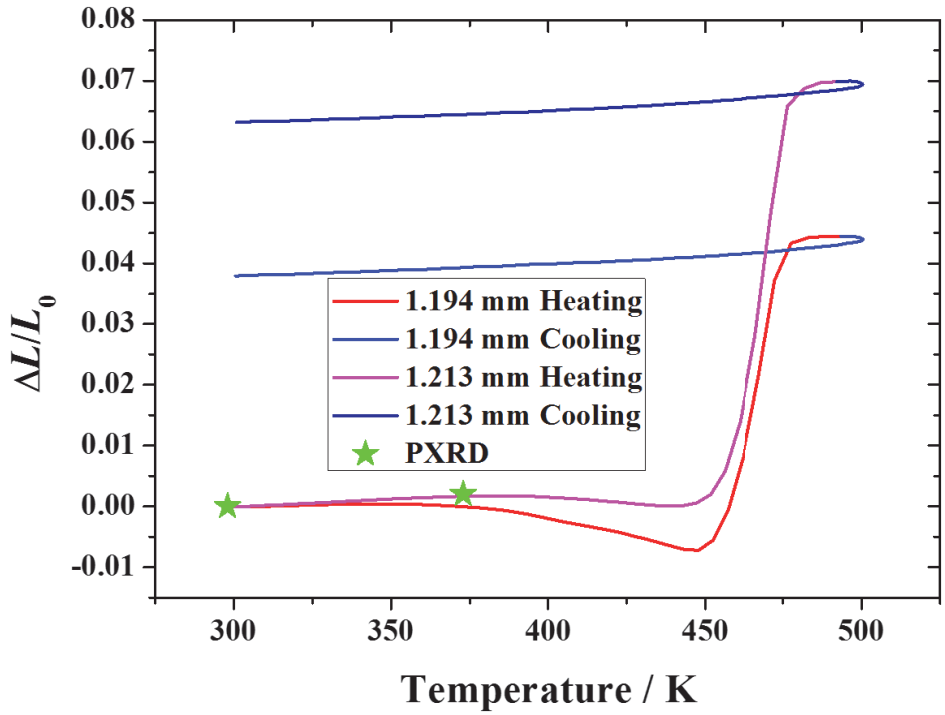

Figure 4.9: Strain of two PCBM pellets with thickness of 1.194 mm and 1.213 mm, respectively. An irreversible expansion was measured between 450 K and 480 K. The thermal expansion results agrees with the change in the unit cell volume determined from PXRD measurements. Figure from reference [147].

A similar irreversible expansion at this temperature range was found for polymerized C_{60} [183]. A 2D polymerized C_{60} sample was cycled between 200 K and 500 K and an irreversible expansion of 6.3% was observed after several hours ($>$ 6 h) at 500 K due to depolymerization [183]. However, the 2D polymerized C_{60} sample was sintered at 830 K for 5 h at a pressure of 2.0 GPa which is higher than the pressure applied for the consolidation of the PCBM pellets. Furthermore, no

change in Raman spectra and crystal structure were observed for PCBM after consolidation, so polymerization of PCBM was ruled out.

After the change in thermal expansion on heating, the coefficient of thermal expansion was measured on cooling, ranging from $(24 \pm 2) \cdot 10^{-6}$ K^{-1} for the 1.194 mm sample to $(26 \pm 2) \cdot 10^{-6}$ K^{-1} for the 1.213 mm sample. It is important to notice that this coefficient of thermal coefficient is not that of pristine PCBM due to the observed change in crystal structure. The measured coefficient of thermal expansion is similar to that of metals, such as Al ($\alpha = 23.2 \cdot 10^{-6}$ K^{-1}) and Ag ($\alpha = 19.3 \cdot 10^{-6}$ K^{-1}) at room temperature [73].

From the characterizations of PCBM, an irreversible change in the monoclinic crystal structure of PCBM was observed above 450 K. Although the change in length in the PCBM pellet was relatively large, no phase transformation was observed using DSC. Furthermore, the melting temperature and decomposition temperature were determined to be 550 K and 670 K, respectively.

4.1.5 Thermal Conductivity

In the previous sections, it was shown that no change in crystal and molecular structure of PCBM was observed with consolidation and exposure to temperatures under 450 K. Thus, the thermal conductivity of a consolidated sample should be the intrinsic value of PCBM. Several samples with varying thickness were measured in the temperature range from 2 K to 390 K using the steady-state method in a PPMS under high vacuum.

Figure 4.10 (a) shows the thermal conductivity of a PCBM pellet (diameter of 5.08 ± 0.02 mm, thickness of 0.90 ± 0.02 mm, mass density of 1.52 ± 0.02 g cm^{-3}) as a function of temperature. The thermal conductivity dramatically increased at low temperature ($T < 30$ K) and remained constant up to 300 K. At higher temperature, another erroneous increase in thermal conductivity was observed, most likely due to inaccurate accounting for blackbody radiation. Although an emissivity of one was assumed for the blackbody radiation in the sample, accurate assumption of the blackbody radiation is challenging at high temperature due to its T^4 behavior.

It is important to note that the measured thermal conductivity, κ_{porous}, was

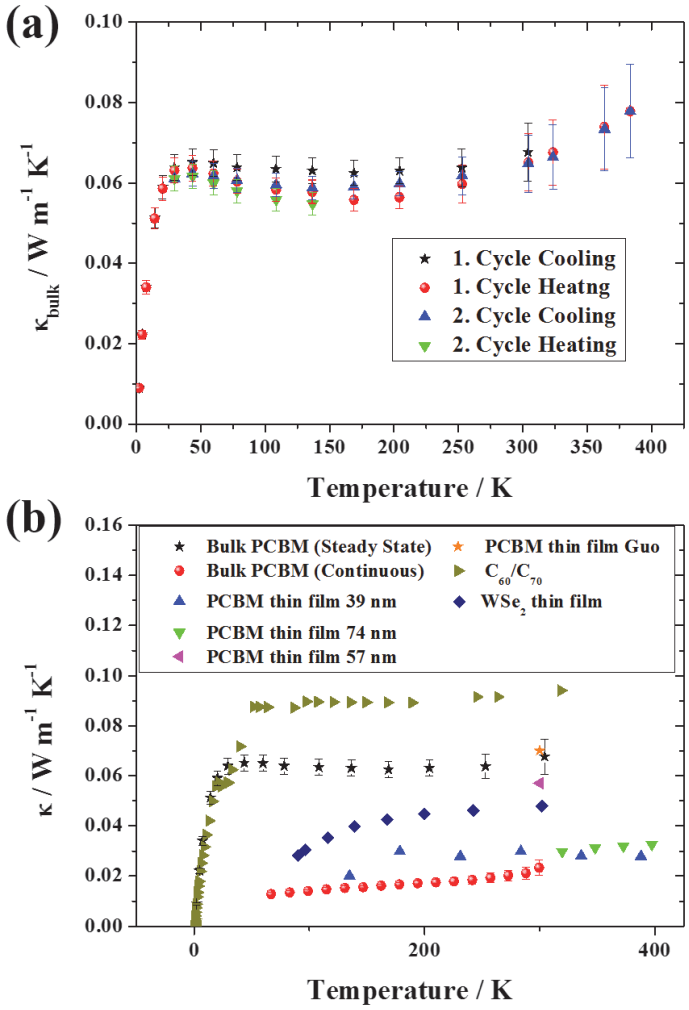

Figure 4.10: (a) Thermal conductivity of PCBM, corrected to zero porosity, determined by the steady-state method in a PPMS. The thermal conductivity in PCBM is ultralow and only a small hysteresis for two cooling/heating cycles was observed. The increase in thermal conductivity above 300 K likely is due to blackbody radiation. (b) The thermal conductivity of bulk PCBM is almost twice the value from Duda *et al.* (PCBM thin film of 39 nm (▲) and PCBM thin film of 74 nm (▼) [69] and in the range of Wang *et al.* (PCBM thin film of 54 nm (◀))[151], Guo *et al.* (PCBM thin film (★)) [152] and WSe_2 thin films [149]. Bulk PCBM using steady-state mode has a temperature behavior similar to C_{60}/C_{70} (mixture of C_{60} (85%) and C_{70} (15%)) [184]. A dramatic decrease in thermal conductivity was found using the continuous mode. The uncertainty was calculated from the uncertainty in geometry and from the measurement or 5%, whichever is greater. Figure from reference [147].

corrected to zero porosity using

$$\kappa_{bulk} = \frac{\kappa_{porous}}{1 - 4/3\Phi} \tag{4.5}$$

where Φ is the porosity of the material [185]. The measured PCBM pellet had a porosity of $\sim 6\%$ resulting in a $\sim 9\%$ increase in thermal conductivity on conversion to bulk ($\kappa_{bulk} = 0.068 \pm 0.007$ W m^{-1} K^{-1} at 300 K). The uncertainty of the measurement was calculated from the uncertainty in geometry and of the measurement or 5% of the measured value, whichever is greater. The room temperature thermal conductivity is within the uncertainty of solvent-free PCBM thin films reported by Wang *et al.* [151] and Guo *et al.* [152] and in the range of the computed thermal conductivity using molecular dynamics calculations [153] (see Figure 4.10 (b)). However, the measured bulk thermal conductivity is a factor of two larger than the thermal conductivity of PCBM thin film reported by Duda *et al.* [69].

For a more detailed comparison of the thermal conductivity in bulk PCBM with PCBM thin films, the sample preparation and the measuring method were compared as they provide the largest uncertainty. While the pellets were consolidated to pellets without using any solvent or elevated temperature in the present study, previous studies of PCBM thin films report results from samples prepared by solvent casting and thermal evaporation [69, 151]. Duda *et al.* used chlorobenzene as a solvent for the fabrication of the PCBM thin films [69]. Although Wang *et al.* reported that solvent-free thin films prepared by thermal evaporation have a lower thermal conductivity than the solvent-cast thin films [151] contradicting the lower thermal conductivity reported by Duda *et al.*, the thin films fabricated by Duda *et al.* and Wang *et al.* can have a different morphology which can explain the different thermal conductivities.

An unknown factor is, therefore, the crystal structure of the PCBM thin films because the morphology of PCBM can be dependent on the preparation method [175]. While the present crystal structure is highly crystalline, Mens *et al.* showed that solvents as well as temperature can lead to an amorphous structure [175]. It is not clear if an increase in disordering can explain the lower thermal conductivity in PCBM thin films. Another unknown factor of the PCBM thin films is the porosity. While the present thermal conductivity of the PCBM pellet was corrected to zero porosity, the porosity of the PCBM thin films described in the literature was not reported. An increase in porosity, *e.g.* due to the evaporation of the solvent, can

have a large decrease in thermal conductivity (see Equation 4.5). To reconcile the present thermal conductivity, a porosity of 35% is required for the PCBM thin film by Duda *et al.*

Additionally to the preparation method, the measurement technique for thermal conductivity also can introduce a large uncertainty, in particular, for temperature-dependent measurements. While Wang *et al.* and Guo *et al.* measured the thermal conductivity of PCBM at room temperature [151, 152], Duda *et al.* reported the thermal conductivity of PCBM thin films over a wide temperature from 135 K to 387 K [69]. Temperature-dependent thermal conductivity measurements can be dramatically influenced by non-steady-state conditions (*i.e.*, thermal equilibrium is not reached through the entire sample) because the temperature profile through the sample might not be uniform. To test the thermal conductivity in non-steady-state conditions, here a consolidated pellet (diameter of 5.00 ± 0.02 mm, thickness of 0.80 ± 0.02 mm, mass density of 1.50 ± 0.02 g cm^{-3}) was measured using the continuous mode in a PPMS (Figure 4.10 (b)). While the steady-state measurement has only a small hysteresis indicating that steady-state conditions were achieved, the thermal conductivity in the continuous mode was artificially a factor of three lower than the steady-state method and the measured thermal conductivity decreased with each temperature cycle. Due to the ultralow thermal conductivity in PCBM, thermal gradients in a PCBM pellet require a long time to reach steady state and non-steady-state conditions can severely affect the thermal conductivity results.

The anomalous decrease in thermal conductivity using the continuous mode can be the result of micro-cracking in the pellet due to thermal stress. Although the dilatometry results showed that PCBM has a coefficient of thermal expansion similar to silver in the temperature range from 300 K to 423 K (Section 4.1.4.d) and therefore, thermal stress is most likely negligible at the silver/PCBM interface at elevated temperature, thermal stress can occur within the PCBM pellet. In the continuous mode, the temperature changed constantly which could result in a non-uniform temperature profile through the sample due to its low thermal conductivity. Because the thermal expansion is dependent on the temperature, a thermal gradient in the pellet could lead to thermal stress and failure of the sample.

In particular, a large change in unit cell volume was obtained from temperature-dependent PXRD measurements (Section 4.1.4.a) between 123 K and 223 K, which might induce a large thermal stress. The change in temperature and the waiting time before the measurement of the PCBM thin films were not specified by Duda *et al.* [69], so micro-cracking in the thin film cannot be excluded.

Furthermore, the present steady-state experiments measure the thermal conductivity directly, while the thermal conductivity in PCBM thin films was determined by time-domain thermoreflectance (TDTR) and further parameters, such as the thickness, heat capacity, and thermal conductivity of an Al layer and the heat capacity of the PCBM thin film, are needed to calculate the thermal conductivity of PCBM thin films [151]. Since no PCBM specific heat data were available, Duda *et al.* and Guo *et al.* assumed that the specific heat for PCBM is the same as for C_{60}/C_{70} fullerite [184], which introduces further uncertainty [69, 152]. Wang *et al.* determined a slightly lower room-temperature heat capacity of PCBM from TDTR than that for C_{60}/C_{70} fullerite [151].

In addition to PCBM thin films, the bulk thermal conductivity was also compared to WSe_2 [149], and C_{60}/C_{70} [184] (Figure 4.10 (b)). While WSe_2 thin films are known for their low thermal conductivity, which is slightly lower than the thermal conductivity of bulk PCBM, the thermal conductivity in C_{60}/C_{70} fullerites is higher than bulk PCBM. As shown in Figure 4.10 the temperature behavior of C_{60}/C_{70} and PCBM are very similar as both thermal conductivities dramatically increase as temperature is increased at low temperature, following by nearly temperature-independent behavior to room temperature.

4.1.6 Heat Capacity

The specific heats of three PCBM pellets ($m = 3.67 \pm 0.18$ mg, $m = 3.22 \pm 0.16$ mg, and $m = 1.91 \pm 0.10$ mg) were determined using the relaxation calorimetry option of the PPMS from 300 K to 2 K as shown in Figure 4.11 (a). (For the accuracy of the mass an uncertainty of 5% was estimated due to handling of the brittle sample. The pellet was moved with tweezers from the balance to the heat capacity puck which can lead to mass loss.) While the heat capacities of the pellets with lower mass ($m = 3.22 \pm 0.03$ mg and $m = 1.91 \pm 0.03$ mg) are similar, a slightly larger specific

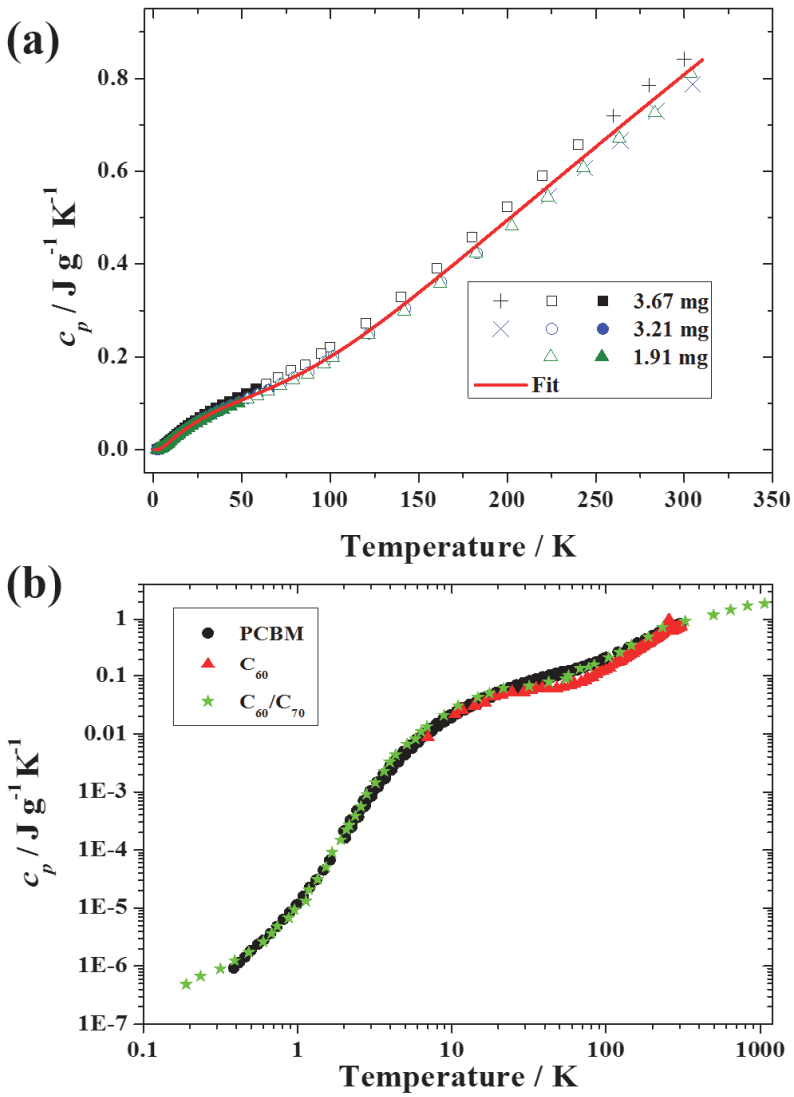

Figure 4.11: (a) Specific heat of several different PCBM pellets with masses as indicated; red curve is the fit (see Figure 4.12). (■, ●, and ▲) have a coupling constant above 90% and contribution of the sample heat capacity above 35% to the total heat capacity, for (□, ○, and △) the contribution of the sample heat capacity to the total heat capacity drops below 35%, and for (+ and ×) the coupling constant additionally drops below 90%. b) Specific heat of PCBM showing a shape similar to C_{60}/C_{70} fullerite [184] and C_{60} [186]. For the heat capacity curves in (b), the average C_p values for four PCBM pellets were used. Heat capacity of the PCBM pellets are given in Tables A.5-A.8 of Appendix A. Figure from reference [147].

heat was measured for the pellet with $m = 3.67 \pm 0.03$ mg. The uncertainty in heat capacity might be due to the low thermal coupling constant (*i.e*, the thermal resistance between the sample and platform) and the low ratio of specific heat to total specific heat, *i.e.*, specific heat of sample plus addendum. To obtain reliable data, the thermal coupling constant should be above 90% and the heat capacity of the sample should be at least 35% of the heat capacity of the addendum as discussed in Section 3.2.2 [127]. Figure 4.11 (a) shows the specific heat data of PCBM filtered with the above aforementioned constraints. Even though the data points fitting these criteria (filled symbols/ Figure 4.11 (a)) are only in a small temperature range, the heat capacity of PCBM can be determined with an uncertainty less than 9% from 300 K to 5 K and less than 16% from 5 K to 0.4 K (uncertainty in mass is included). The room-temperature specific heat can be, therefore, obtained with a reasonable accuracy ($c_p = 0.82 \pm 0.04$ J g^{-1} K^{-1}).

No temperature-dependent specific heat data were available from the literature for PCBM. Therefore, the specific heat of PCBM is compared to C_{60}/C_{70} fullerite [184] and C_{60} [186] (Figure 4.11 (b)). In addition to the three PCBM pellets in Figure 4.11 (a), the low temperature specific heat of a fourth PCBM pellet ($m = 3.89 \pm 0.01$ mg) was measured from 10 K to 0.4 K using ^{3}He cooling. The determined room-temperature specific heat of PCBM is in the range of the heat capacity of C_{60}/C_{70} fullerite ($c_p = 0.81$ J g^{-1} K^{-1}) [184] and considerably higher than the specific heat determined by Wang *et al.* for evaporated PCBM thin films ($c_p = 0.68$ J g^{-1} K^{-1}) [151]. Therefore, the extremely low thermal conductivity reported by Duda *et al.* [69] is most likely not an artifact of the conversion from TDTR results to thermal conductivity using the specific heat of C_{60}/C_{70} fullerite. Furthermore, the present results show that the specific heat of PCBM has trends similar to C_{60} and C_{60}/C_{70} fullerite except at very low temperature ($T < 0.5$ K) and in the temperature range from 30 K to 220 K. As shown in Figure 4.10 (b), the thermal conductivity of C_{60}/C_{70} fullerite has also a temperature behavior similar to the ultralow thermal conductivity in PCBM, suggesting a strong correlation between thermal conductivity and heat capacity. This is normally the case at low temperatures. However, if the phonon mean speed and the phonon mean free path are nearly temperature-independent, the thermal conductivity can be also

proportional to the heat capacity at elevated temperatures. For a better understanding of the origins of ultralow thermal conductivity in PCBM, the low temperature heat capacity was investigated further.

To analyze the heat capacity at low temperature the average values of C_pT^{-3} at a given temperature for the four PCBM pellets were plotted against T on a log scale (Figure 4.12 (a)). The uncertainty in the data is the spread of the four heat capacities and the uncertainty of the measurement or 9% from 300 K to 5 K and 16% from 5 K to 0.4 K, whichever is greater. The uncertainty in mass is included in the uncertainties of the heat capacity. A broad peak was observed at around $T = 4.5$ K suggesting the presence of low-frequency optical modes [187] or two-level states (TLS) where atoms can occupy two or more potential wells [188, 189]. Although the broad peak looks similar to a Boson peak [190] due to TLS in glassy and highly disordered materials at low temperatures, there is no evidence for TLS in PCBM. For systems with TLS, the low-temperature thermal conductivity increases with a T^2 behavior to a plateau at ~ 10 K and the low-temperature C_pT^{-3} peak is typically above 10 K [188]. This is not consistent with the heat capacity and thermal conductivity measured for bulk PCBM. The thermal conductivity increases at a much smaller rate ($T^{0.8}$) to a plateau at ~ 30 K. Furthermore, the C_pT^{-3} peak appears at 4.5 K (see Figure 4.12 (a)). Therefore, it is more likely that the low-temperature peak is due to presence of low-frequency optical modes, as a similar C_pT^{-3} peak and low-frequency optical modes were reported for the parent compound C_{60} [191, 192, 193].

Beyermann *et al.* showed that the low-temperature heat capacity of C_{60} can be well fit by the sum of two Debye terms, two Einstein terms, and a linear term [191]. The Debye model describes the acoustic vibrational modes in a crystal while the Einstein model is better for optical modes. In contrast to Beyermann *et al.*, only a single Debye term was used to model the acoustic modes of PCBM because it is assumed that the rotation of the molecules is hindered by the side chains [191]. It is important to note that each unit excites three acoustic modes and contains four PCBM molecules. Thus, ${n_D}^2$ was set to 0.25 in Equation 2.8 and the other parameters were fit. The best fit was achieved when four different Einstein terms ($n_{E1} = 0.0833$,

[2]In Section 2.1, the number of atoms in the Debye and Einstein model was labeled with N. However, to separate the two different terms, the number of atoms in the Debye model (Equation 2.8) is labeled n_D and in the Einstein model (Equation 2.7) is labeled n_E.

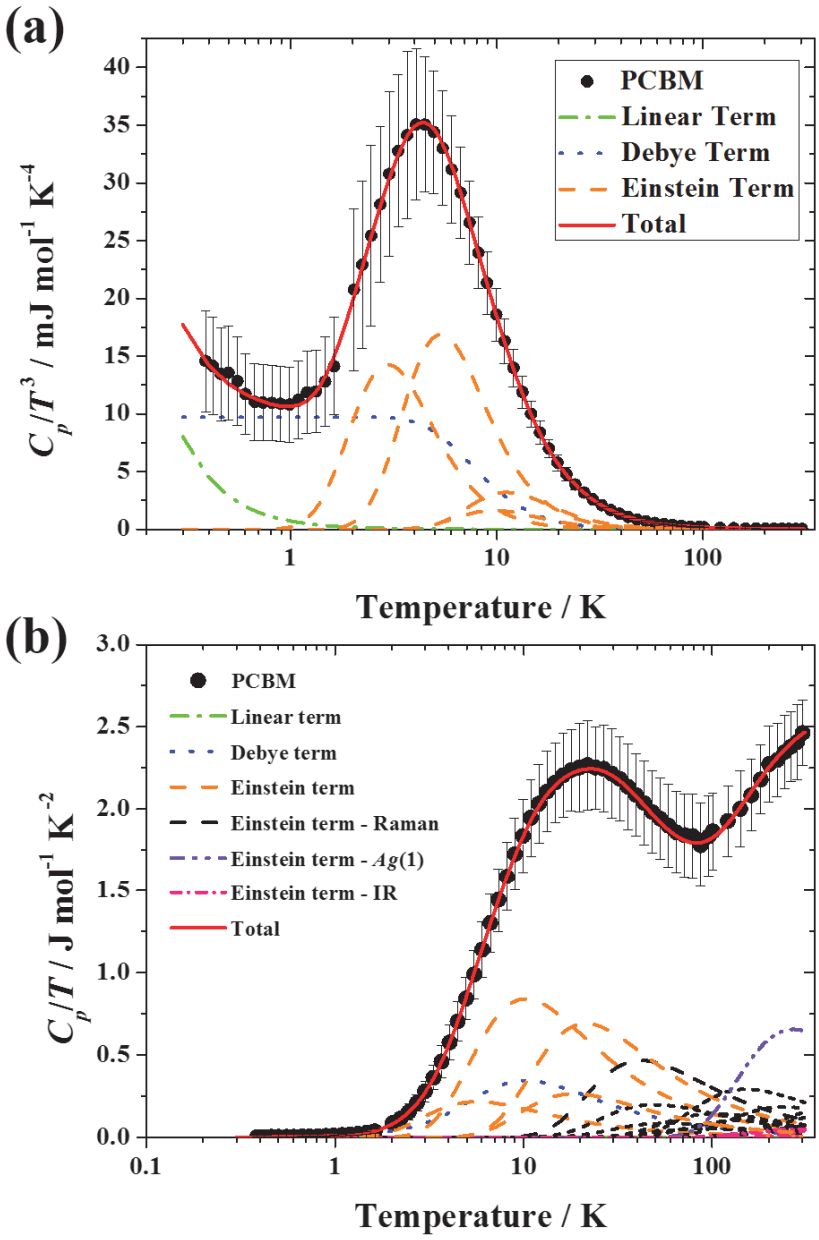

Figure 4.12: (a) C_pT^{-3} vs. T for PCBM fit with one Debye term, four Einstein terms, and one linear term. (b) C_pT^{-1} vs. T fit as in (a) with additional Einstein terms from Raman experiments and IR data. For the heat capacity curves in (a) and (b) the average C_p values for four PCBM pellets were used and the uncertainty shown in (a) and (b) is their standard deviation and the uncertainty in the measurement or 15% from 0.4 K to 5 K and 7% from 5 K to 300 K, whichever is greater. Figure from reference [147].

θ_{E1} = 14.6 K, n_{E2} = 0.583, θ_{E2} = 26.4 K, n_{E3} = 0.333, θ_{E3} = 47.8 K, n_{E4} = 1.00, θ_{E4} = 55.0 K) were applied (Figure 4.12 (a)).

The first two Einstein terms contain in total eight optical phonon modes per unit cell which means there would be exactly two modes per molecule. While Einstein terms are dispersionless, the optical modes at low frequency can have a large dispersion. Therefore, it was not clear if splitting of the Einstein modes is due to absence of dispersion in modelling of the optical modes or if one or more of these optical modes can be more easily excited than the others. The eight low-frequency optical modes (θ_{E1}= 14.6 K, θ_{E2} = 26.4 K) are most likely librational modes where the rigid PCBM molecules 'rock' at their equilibrium positions. Horoyski *et al.* reported two slightly higher librational modes for C_{60} (θ_E = 25.3 K and θ_E = 30.2 K) using Raman spectroscopy at 85 K [192], similar to the libration Einstein temperature of 32.5 K [193]. They also found that the energy of the librational modes decreases with decreasing pressure and increasing temperature which is most likely due to expansion of the unit cell. PCBM molecules are less densely packed in the unit cell than C_{60} (theoretical density from XRD: ρ_{PCBM} = 1.613 g cm^{-3}, $\rho_{C_{60}}$ = 1.678 g cm^{-3} [194]) which might result in lower intermolecular interaction energies and also in lower frequency modes. The temperature dependence of the librational modes in C_{60} was confirmed from neutron scattering experiments [195].

In addition to the low frequency librational modes in PCBM, two other Einstein terms were applied with higher frequencies (θ_{E3} = 47.8 K and θ_{E4} = 55.0 K). The optical modes with the lower frequency are most likely associated with librational modes which leads to a combined number of three librational modes per PCBM molecule. The higher frequency modes, on the other hand, are comparable to the Einstein modes found by Beyermann *et al.* (θ_E = 58 K) [191] and are in the range of intermolecular translational modes [177]. Olson *et al.* fit the low temperature heat capacity of C_{60}/C_{70} fullerite from 4 K to 40 K by a single Einstein term for three translational and three torsional modes (θ_E = 35 K) [184]. While the numbers of translational and librational modes are the same for PCBM, the optical modes in PCBM cannot be described by a single frequency.

In Figure 4.12 (b), C_pT^{-1} was plotted against T to analyze the heat capacity in the intermediate temperature range from 10 K to 300 K. An anomaly in the heat

capacity at $T \sim 90$ K was also observed for C_{60} [186] and C_{60}/C_{70} [184]. Matsuo *et al.* stated that the change in heat capacity of C_{60} is due to a glass transition associated with a molecular reorientation [186] while Olson *et al.* reported a modified Dulong-Petit specific heat for C_{60} above 40 K where the translational and torsional vibrations are fully excited with six degrees of freedom [184]. The heat capacity data in Figure 4.12 (b) were fit, in addition to the parameters used in the lower-temperature heat capacity (Figure 4.12 (a)), with Einstein terms from the Raman experiment (black line) (see Table A.3 of Appendix A) and infrared (IR) modes of C_{60} (pink lines) taken from reference [177]. The lower-temperature peak from 0.4 K to 90 K agrees well with the Debye term and Einstein terms from the C_pT^{-3} fit. However, three additional optical modes, recorded by Raman spectroscopy (Figure 4.5), contribute significantly to the heat capacity in the temperature range from ∼30 K to ∼200 K. These optical modes are most likely associated with vibrations of the side chain resulting in an increase of the heat capacity of PCBM compared to C_{60} reported by Matsuo *et al.* [186] (Figure 4.11 (b)). The large increase in the second peak occurs due to the excitation of intramolecular modes, *i.e.*, the vibration of the molecular bonds in the molecule. In particular, the breathing mode ($A_g(1)$) of the C_{60} moiety (purple line) has a large contribution to the increase in C_pT^{-1} due to the simultaneous expansion and contraction of 60 carbon atoms (see Figure 4.12 (b)). It is important to note that the silent modes (32 for C_{60} [177]) and IR modes of PCBM molecules were not considered for the fit and therefore the contribution for each mode does not represent the exact lattice dynamics. Although the analysis of the vibrational modes in PCBM is semi-quantitative, it indicates a large difference between the frequencies of intermolecular and intramolecular modes, as also found in C_{60} [177].

In addition to the optical modes, the Debye temperature ($\theta_D = 37$ K) and the slope of the linear term ($\gamma_{el} = 0.72$ mJ mol^{-1} K^{-2}) are both lower than the values for C_{60} ($\theta_{D1} = 49$ K, $\theta_{D2} = 67$ K, and $\gamma_{el} = 45$ mJ mol^{-1} K^{-2}) [191]. The low Debye temperature in PCBM is most likely due to lower interaction energies between the PCBM molecules than in C_{60} resulting in a softer PCBM lattice, as also observed from speed of sound measurements [69]. The value of γ_{el} in PCBM is in the range of glassy materials [196] and is about 2.5 times lower than the value for C_{60}/C_{70} fullerite

found by Olson *et al.* (γ_{el} = 1.8 mJ mol^{-1} K^{-2}) [184]. This is in good agreement with the low temperature specific heat data shown in Figure 4.11 (b).

The present heat capacity data also were compared to the calculated heat capacity of PCBM using the phonon density of states of molecular dynamics simulations [153] and a canonical partition function [197]. It is important to note that for the molecular dynamics study, the simplified lattice used, *i.e.*, hexagonal unit cell containing only one PCBM molecule, does not represent the present crystal structure of PCBM (monoclinic lattice with four molecules per unit cell). Although the predicted Debye temperature (θ_D = 99 K) is a factor of three higher than the Debye temperature determined from experiments, a higher calculated heat capacity was found at low temperatures. The high value of the calculated heat capacity is most likely due to the presence of low-frequency optical vibrational modes. At higher temperature (T > 20 K), the experimental and computed heat capacities converged. An *ab initio* study on the monoclinic unit cell would most likely enhance the heat capacity calculation but it is currently not feasible due to the large PCBM unit cell with 352 atoms.

For the comparison of the Debye temperature and the low-frequency optical modes of PCBM and C_{60}/C_{70} fullerite, the C_pT^{-3} curve of C_{60}/C_{70} fullerite was fit with the same approach as for PCBM (Figure 4.13). While the Einstein terms have even lower temperatures (n_{E1} = 0.083, θ_{E1} =14.0 K, n_{E2} = 0.583, θ_{E2} =24.2 K, n_{E3} = 0.333, θ_{E3} =39.8 K, n_{E4} = 1.000, θ_{E4} =56.0 K), the Debye temperature increased to θ_D = 54.0 K. The linear term of the heat capacity fit of C_{60}/C_{70} fullerite (γ_{el} = 1.80 mJ mol^{-1} K^{-2}) is more than twice that of PCBM.

As shown in Figure 4.10 (b), the thermal conductivity of C_{60}/C_{70} fullerite is higher than that for PCBM. Therefore, the origins of the low thermal conductivity cannot be explained with the Einstein model which uses only the optical vibrational modes [65] as described in Section 4.1.2. The Debye temperature also indicates a similar increase and thus solely acoustic phonons are considered for the new model of the minimum thermal conductivity. Based on that, Cahill *et al.* developed an approach to calculate the lower limit of the thermal conductivity in disordered crystals [66, 67].

4.1.7 Minimum Thermal Conductivity Model

A new model of minimum thermal conductivity was derived here from the modified Callaway equation (see Equation 4.1) which was also used to derive the Einstein model as well as the Cahill, Watson, and Pohl model for minimum thermal conductivity (for more details about the derivation of these models, see Section 4.1.2). As described above, the Einstein model cannot explain the low thermal conductivity in PCBM and C_{60}/C_{70} due to the opposite trends of thermal conductivity and low-frequency Einstein modes. However, a strong correlation between the thermal conductivity and the Debye temperature was noticed and therefore, a similar approach to the Cahill, Watson, and Pohl model [66, 67] was used. This new minimum thermal conductivity model considers only acoustic modes for the thermal transport and the Cahill, Watson, and Pohl model was modified with the following two new concepts.

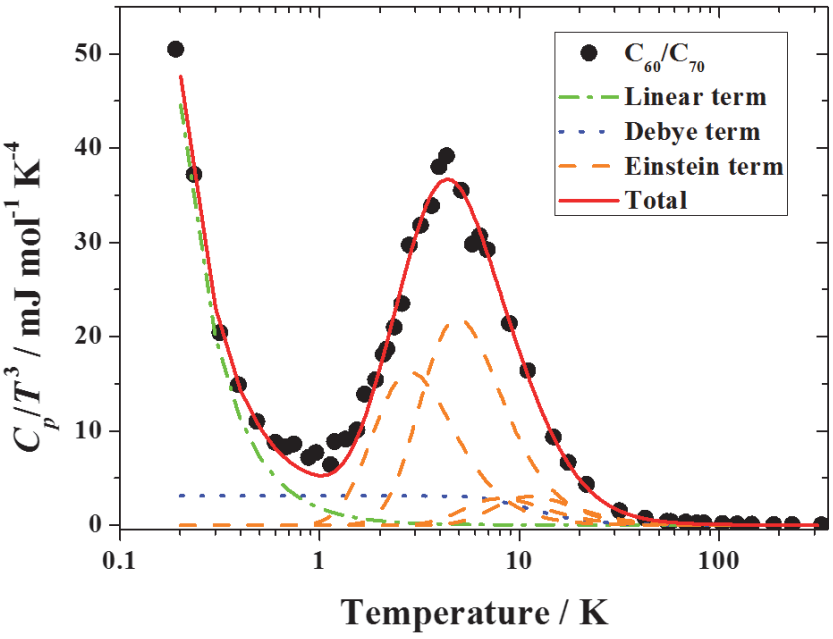

Figure 4.13: C_pT^{-3} vs. T of C_{60}/C_{70} extracted from Olson *et al.* [184] fit with one Debye term, four Einstein terms, and one linear term. Figure from reference [147].

The first modification is using an average phonon mean speed instead of the speed of sound. The difference between the speeds can be explained by a dispersion curve

of an acoustic phonon as shown in Figure 4.14. In the Debye approach, it is assumed that there is a linear dispersion between the angular frequency, ω, and the wave vector, k, with a constant velocity, *i.e.*, the speed of sound as indicated by the green line in Figure 4.14. In real crystals, however, the dispersion is not linear because the velocity decreases to the edge of the Brillouin zone, as indicated by Born and von Kármán [198].

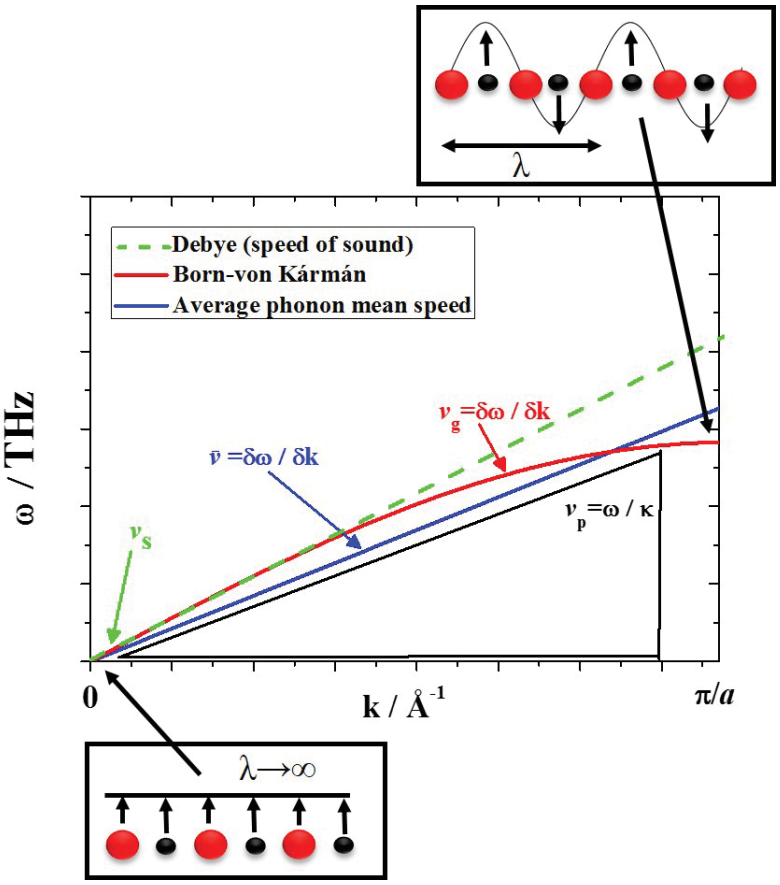

Figure 4.14: Dispersion diagram of acoustic phonons. Debye assumed a linear dispersion of the acoustic phonons in the first Brillouin zone (– – –) while the dispersion in the Born-von-Kármán model (—) is curved. The phonon mean free path goes to infinity at the Brillouin center and decreases with increasing wave vector, k, to give a phonon mean free path equal to the interatomic distance at the edge of the Brillouin zone.

Furthermore, the shortest possible phonon mean free path is inversely proportional to the wave vector ($\lambda = \frac{2\pi}{k}$). At the center of the Brillouin zone the phonon mean free path goes to infinity indicated by the linear diatomic chain in Figure 4.14. The

phonon mean free path, however, decreases with increasing wave vector until the phonon mean free path is proportional to the interatomic distance which both Einstein as well as Cahill, Watson and Pohl proposed as the limiting factor of the minimum thermal conductivity (see Section 4.1.2). Ultrasound measurements are normally in the range of MHz to GHz while phonons are excited in the THz range and therefore, the speed of sound (green dashed line in Figure 4.14) overestimates the phonon mean speed for small wavelengths at the edge of the Brillouin zone. Instead of using the speed of sound, the average phase velocity, $\langle v_p \rangle$, and average group velocity, $\langle v_g \rangle$, were considered for the calculation of the density of states in the present minimum thermal conductivity model. The average phonon mean speed, $\bar{v}$, is given by

$$\bar{v} = \left(\langle v_g \rangle \langle v_p \rangle^2 \right)^{1/3} = \frac{k_B \theta_D}{\hbar} \left(\frac{V}{6\pi^2 N} \right)^{1/3} \tag{4.6}$$

and thus, $D(\omega) = V \frac{\omega^2}{2\pi^2 \bar{v}^3}$. The volumetric density of states was also used to determine the Debye heat capacity and therefore, the Debye temperature from the heat capacity measurement can be used to calculate the lowest limit of thermal conductivity. As shown by the blue line in Figure 4.14, the average phonon mean speed is lower than the speed of sound in the Born-von-Kármán model (green dashed line).

The second new concept introduced in the new minimum thermal conductivity was the application of a constant mean free path $\left(\lambda = \left[\frac{\pi V_{UC}}{6N} \right]^{1/3} \right)$ instead of a frequency-dependent phonon mean free path $\left(\lambda_i = \frac{\pi}{\omega_i} \bar{v}_i \right)$ [66, 67]. The phonon mean free path can be limited by different mechanisms, such as phonon-phonon scattering, point defect scattering, and grain boundary scattering [82]. While phonon-phonon scattering and point defect scattering are frequency-dependent, the grain boundary scattering does not depend on the frequency and is only proportional to the grain size. The frequency-dependent phonon mean free path used in the Einstein model as well as in the Cahill, Watson and Pohl model contradicts the grain boundary limit as the phonon mean free path for low frequencies would go to infinity. Therefore, it is assumed here that the phonon mean free path is inversely proportional to the cube root of the atomic density in the unit cell. A similar assumption was made by Feser *et al.* where the mean free path is limited by the grain size [150]. Other studies have proposed that the grain boundary scattering is frequency-dependent and should not follow the gray model, *i.e.*, temperature-independent phonon mean

free path [199]. It is important to note that although the interatomic distances vary in and between the PCBM molecule(s), the cube root of the inverse atomic density can be taken as an average of the atomic distances. This is similar to using the average grain size as the limiting factor for grain boundary scattering.

Both new concepts were applied in Equation 4.1 and the average internal energy was taken from the Einstein model for the minimum thermal conductivity $\left(\langle U\rangle = \frac{\hbar\omega}{\mathrm{e}^{(\hbar\omega)/(k_B T)}-1}\right)$. Therefore, the new lowest limit of thermal conductivity is defined as

$$\kappa_{min,present} = \left(\frac{3}{6^{2/3}\pi^{1/3}}\right)\frac{k_B^2}{\hbar}\left(\frac{N}{V_{UC}}\right)^{1/3}\frac{\theta_D}{x_D^3}\int_0^{x_D}\frac{x^4\mathrm{e}^x}{\left(\mathrm{e}^x-1\right)^2}\mathrm{d}x \tag{4.7}$$

with $x_D = \frac{\theta_D}{T}$. The present minimum thermal conductivity model depends on the atomic density and the Debye temperature which are both available for PCBM ($\frac{N}{V_{UC}} = 9.36 \cdot 10^{22}$ cm^{-3}, $\theta_D = 37$ K) and C_{60}/C_{70} fullerite ($\frac{N}{V_{UC}} = 2.14 \cdot 10^{22}$ cm^{-3}, $\theta_D = 54$ K). The minimum thermal conductivity model was tested on the ultralow thermal conductivity of both PCBM and C_{60}/C_{70} fullerite [184], and it was found that the model could accurately represent the experimental data of both (see Figure 4.15). Equation 4.7 indicates a reciprocal relationship between minimum thermal conductivity and unit cell volume which in general changes with temperature. Therefore, information about the thermal expansion is required for more accurate prediction of the minimum thermal conductivity at a given temperature. From the temperature-dependent PXRD experiment for PCBM, a large increase in unit cell volume was determined between 123 K and 223 K suggesting a lower minimum thermal conductivity. This is consistent with experiments and thus, an explanation for the dip in the thermal conductivity between 40 K and 150 K can be provided from the new minimum thermal conductivity model.

Furthermore, the model was compared to both the Einstein and the Cahill, Watson and Pohl models for both materials. While the minimum thermal conductivity is overestimated for PCBM and C_{60}/C_{70} fullerite using the Cahill, Watson and Pohl model, the Einstein model agrees for PCBM. However, the Einstein model underestimates the thermal conductivity for C_{60}/C_{70} fullerite (Figure 4.15 (b)). Figure 4.15 (b) shows a change in thermal conductivity data of C_{60}/C_{70} which is most likely related to a change in the measurement method [184].

While the low-temperature thermal conductivity was measured with a DC method, the high-temperature thermal conductivity was acquired using the 3ω method. It is important to note that the Einstein and Debye temperatures were taken from the heat capacity fits for the calculation of the minimum thermal conductivity of the Einstein and the Cahill, Watson, and Pohl model, respectively. Otherwise, the speed of sound would show a larger discrepancy between the predicted minimum thermal conductivity and experimental data for PCBM and C_{60}/C_{70} fullerite.

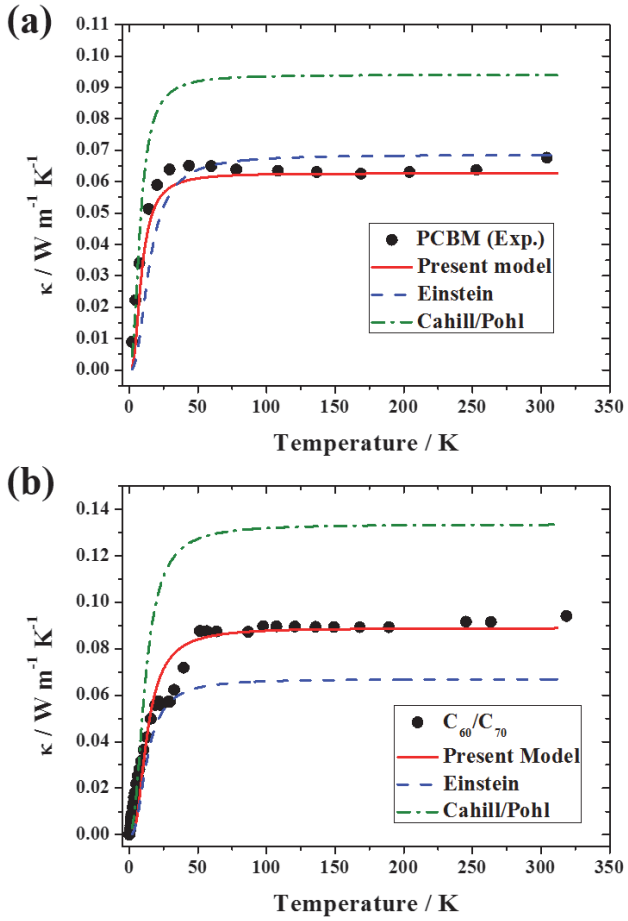

Figure 4.15: Present model for the minimum thermal conductivity agrees well for (a) PCBM and (b) C_{60}/C_{70} [184] using the atomic density and the Debye temperature from experiments. The local minimum of the thermal conductivity can be related to an increase in unit cell volume. While the Einstein model underestimates the minimum thermal conductivity, the amorphous limit is always overestimated by the Cahill, Watson and Pohl. Figure from reference [147].

4.1.8 Conclusions

In this section of the study, the ultralow thermal conductivity found in PCBM thin films was confirmed in bulk PCBM ($\kappa_{bulk} = 0.068 \pm 0.007$ W m^{-1} K^{-1} at 300 K). PCBM exhibits the lowest room-temperature thermal conductivity reported to date for a fully dense solid. Furthermore, a new model for the lowest limit of thermal conductivity was developed and it accurately represents the experimental data without using any fitting parameters (Figure 4.15). In this model it was assumed that heat is transported between entities of phonons oscillating in a range of frequencies and the energy transfer is limited by the atomic density and the average phonon mean speed determined from experimental Debye temperatures. No optical modes were contributing directly to the thermal transport resulting in a nearly temperature-independent thermal conductivity over a wide temperature range. The model developed here might be useful to describe the lowest limit of thermal conductivity for other materials, in particular for ultralow thermal conductivities, and it is used to delineate the thermal conductivities in the presented thermoelectric materials (see Chapter 5).

Furthermore, the heat capacity results indicate a distinct separation of the intra-and intermolecular modes in the lattice dynamics of PCBM. In particular, the $A_g(1)$ breathing mode of the fullerene core has a significant contribution to the intermolecular modes. A less distinct separation was observed for PCBM than C_{60} due to low-frequency modes assigned to the side chain of the PCBM molecule which were obtained from the Raman measurement.

The high-temperature results for PCBM suggest up to three phase transitions. A large irreversible thermal expansion was measured in the temperature range from 450 K and 480 K resulting in a change in the crystal structure. Above 550 K, PCBM melts and transforms into an amorphous phase on cooling as indicated by room-temperature PXRD.

4.2 ZnO Tetrapods as an Example of Unique Microstructure[3]

4.2.1 Introduction

In the previous section of this chapter, the origins of the ultralow thermal conductivity in PCBM were delineated and it was shown that PCBM has the lowest thermal conductivity reported to date for a fully dense bulk material. The low thermal conductivity of PCBM is an intrinsic property and does not depend on the morphology of the sample.

A variation in the morphology can have a large impact of the thermal conductivity. In particular, if the dimensions of the material are reduced, surface scattering events can dramatically decrease the thermal conductivity in the material. In recent years, research in 3D hierarchical microstructures has rapidly increased due to their wide range of applications, such as solar cells [200], supercapacitors [201], and batteries [202].

One unique microstructure is ZnO tetrapods where four arms radiate from a ZnO core with an angle of 109° to each other as shown in Figure 4.16 [203]. In a recent study, Mishra *et al.* synthesized ZnO tetrapods in sufficiently large quantity that the properties of consolidated ZnO tetrapods pellets now can be investigated [204]. While the electrical and mechanical properties of the ZnO tetrapods with and without metal oxide-coating have been already reported [205], the thermal conductivity in these materials was unknown.

In contrast to the consolidated PCBM pellet which had sufficient mechanical strength to be measured with the thermal transport option (TTO) in a PPMS, the ZnO tetrapods pellets are weakly interconnected and therefore it is challenging to measure the thermal conductivity with the TTO method. Although the TTO measurement has the advantage that the thermal conductivity can be measured directly from the applied power, temperature gradient, and the geometry of the sample, such measurements are limited to rigid samples as there is the need to support the heater and the thermometers. Furthermore, the wires of the heater and

[3]The author's contribution was the measurement of the Seebeck coefficient, the thermal and electrical conductivity as well as perform the finite element analysis. All measurements were performed in the laboratory of Dr. Mary Anne White, Department of Chemistry, Dalhousie University, unless stated otherwise.

thermometers can apply tension and shear forces on the sample. In particular, during the attachment of the TTO shoes to the sample leads, a large force can be induced on the sample which can lead to failure of the sample if it does not have a high tensile strength.

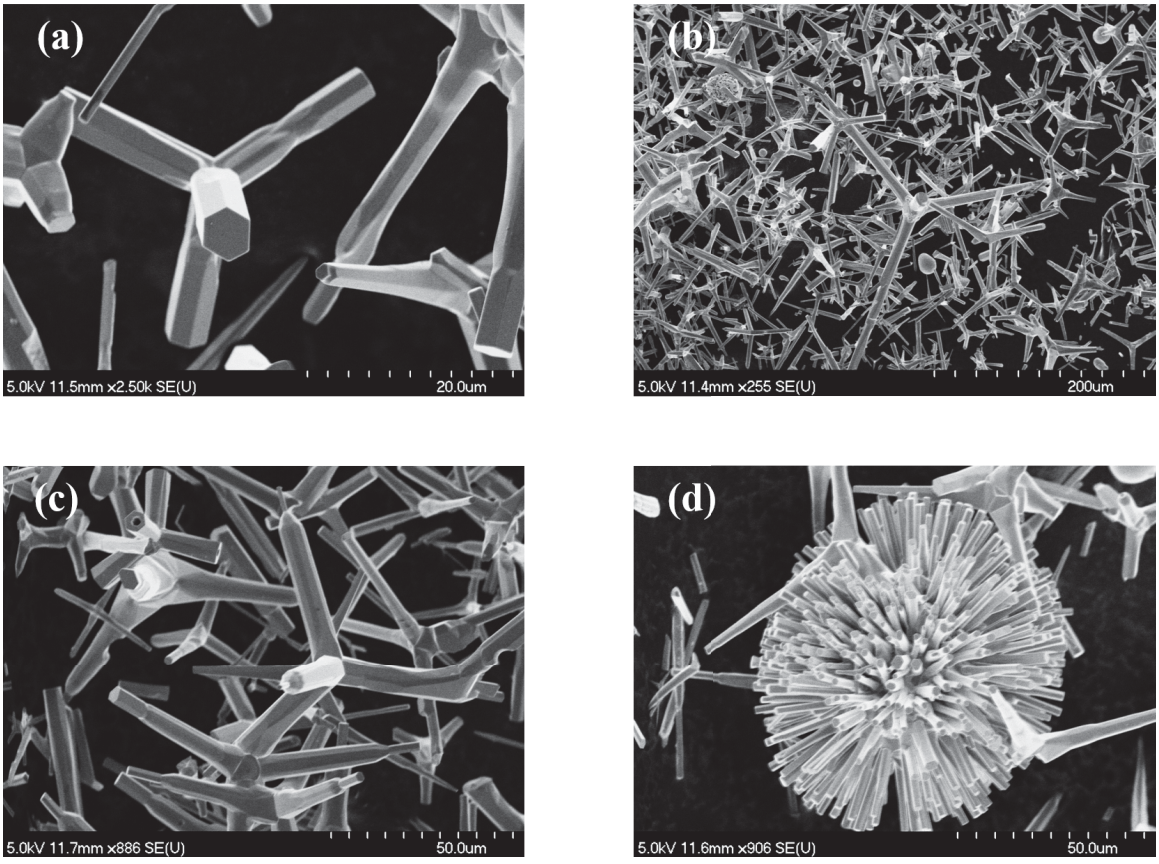

Figure 4.16: SEM image of Sn-coated ZnO tetrapods. (a) Each arm of the tetrapod has a similar length and the cross-section of the arm has a hexagonal facet. (b) Overview of distribution of the size and shape of ZnO tetrapods. (c) The arms of the tetrapods can form different shapes. Some arms have a pointed end while others can be hollow. (d) In addition to ZnO tetrapods, also other shapes were formed, *e.g.* ZnO 'Koosh balls'. SEM images were acquired with the assistance of Patricia Scallion in the laboratory of Dr. Kevin Plucknett, Faculty of Engineering, Dalhousie University.

For various applications it is important that the thermal conductivity can be measured for materials in different morphologies (*e.g.*, thin films, nanotubes) and over a large range of porosity (from consolidated materials to even powders) as well as for different phases (solid, liquid, and gas). For instance, in phase change materials energy can be stored as latent heat from a solid-liquid phase transition and these materials

can be used for the thermal regulation of buildings [206]. To optimize the design of the phase change materials in buildings, knowledge of the thermal conductivity of the solid and liquid phase is required. For determination of the thermal conductivity in fragile bulk samples as well as in thin films, nanotubes, fluids, and powders, different methods were developed and are discussed below.

In the present study, a new steady-state method was developed to measure the thermal conductivity in powders using a lab-developed powder cell. The powder cell was tested on pristine and metal oxide-coated ZnO tetrapods which cannot consolidated to a pellet without losing their unique microstructure. The thermal conductivity was compared to a computational study using a finite element method. Furthermore, the mechanical stability of the ZnO tetrapods was enhanced using CNTs. The pellets were rigid enough that the thermal and electrical conductivities of the ZnO tetrapods with varying CNT content were measured using the standard TTO method. CNT coating can enhance the electronic properties and reduce the heat transport as recently reported by Wang *et al.* [207].

4.2.2 ZnO Tetrapods

Bulk ZnO is a commonly investigated wide-band gap semiconductor ($E_g = 3.37$ eV) for thermoelectrics [208], optoelectronics [209], and biomedical applications [210]. In particular, the high exciton (*i.e.*, electron-hole pair) binding energy ($\sim$ 60 meV $> k_BT$ at room temperature), the potential to grow bulk single ZnO crystals, and to dope (p- and n-type) make the material very interesting for semiconductor research [209]. It was found that the morphology of ZnO depends on the synthesis and various microstructures were reported, such as single crystals, wires, bolts, and tetrapods [204]. A usual microstructure is the ZnO tetrapod structure which consists of a ZnO core from which four one dimensional arms radiate at a angle of $\sim$109° to each other [203] (see Figure 4.16 (a)). The arms have a hexagonal-wurtzite crystal structure, $P6_3mc$ space group, and grow preferentially along the [0001] direction with a hexagonal basal facet [203, 205]. While the growth of the arms is broadly understood, the structure of the ZnO core might be described by the octa twin model where eight tetrahedra form an octahedron consisting of eight [0001] basal planes [211]. However, this model has not been verified with experiments [212]. Ronning *et*

al. proposed a freestanding self-assembly nucleation where first small ZnO clusters are formed and then they collapse with further growth to a stable bulk structure [212].

ZnO tetrapods are in general prepared through the evaporation of zinc powder in an oxygen atmosphere [203, 212]. Recently, Mishra *et al.* described a flame transport synthesis to produce ZnO tetrapods in large quantities [204]. In the synthesis, a mixture of Zn powder, polyvinyl butyral (PVB), and ethanol was placed in a ceramic crucible and heated to 900 °C for 30 min under ambient atmosphere [204]. PVB and ethanol served as the oxygen source in the reaction.

For the present study, the same procedure was used to synthesize ZnO tetrapods, carried out by Jorit Gröttrup (metal oxide-coated ZnO tetrapods) and Fabian Schütt (ZnO tetrapods with CNTs) in the laboratory of Dr. Yogendra Mishra and Dr. Rainer Adelung, Faculty of Engineering, Christian-Albrechts-University. More details about the synthesis of the ZnO tetrapods can be found in reference [204].

4.2.3 Metal Oxide-Coated ZnO Tetrapods[4]

ZnO tetrapods were functionalized by coating them with metal particles which oxidized in the synthesis [205, 213, 214]. Good performance as selective gas sensors was observed for the metal oxide-coated tetrapods [213, 214]. The metal oxide-coated ZnO tetrapods were placed between two gold contacts and the change in current was measured over time of exposure to the gas. While Fe- and Cu-coated tetrapods show a good response to ethanol, the selectivity can change to hydrogen or methane depending on the concentration of Al in the ZnO tetrapods [214]. The gas sensitivity of hydrogen could be increased if the tetrapods were coated with Bi [213].

For the synthesis of metal oxide-coated ZnO tetrapods, the ZnO tetrapods were mixed with one of five different metals (Al, Bi, Sn, Cu, and Fe) in a mass ratio of 20:1 and compressed to a cylinder [205, 213, 214]. The metal-ZnO composites were heated to 1150 °C for 5 hours in air to form a 3D-interconnected network. More information

[4]Although ZnO tetrapods coated with metal oxides are referred to as 'alloyed ZnO tetrapods' in literature [205, 213, 214], the term can be misleading because the material does not contain any metal. Therefore, the present author will use the term 'metal oxide-coated ZnO tetrapods' henceforth.

about the synthesis and the materials is given in the references [205, 213, 214]. All samples were provided in powder form by Jorit Gröttrup, Faculty of Engineering, Christian-Albrechts-University.

The crystal structure and microstructure of metal oxide-coated ZnO tetrapods were reported for coatings with Cu, Al, and Sn [205], Bi [213] and Fe [214]. In addition to the crystal structure, the mechanical and electrical properties of Cu-, Al-, and Sn-coated ZnO tetrapods were investigated. The PXRD pattern of ZnO indicated that the tetrapods crystallized in the wurtzite structure with lattice constants $a = 3.249$ Å and $c = 5.206$ Å [205]. While only a small change in the PXRD pattern was found in the Cu-coated ZnO tetrapods, an additional phase was reported for the Al-coated and Sn-coated tetrapods [205]. The additional phases were assigned to zinc stannate (Zn_2SnO_4) and zinc aluminate ($ZnAl_2O_4$) for the Sn-coated and Al-coated ZnO tetrapods, respectively. The crystal structure of the Cu-coated sample also was investigated by Lupan *et al.* and they reported that copper oxide (CuO) was formed on the surface of the ZnO tetrapods [214]. Furthermore, the PXRD measurements of Bi-coated and Fe-coated tetrapods indicated that Bi_2O_3 [213] and Fe_2O_3 [214], respectively, were formed. Although the mass ratio of the metals to the tetrapods is low (1:20), oxides on the tetrapods can significantly influence the heat transfer.

Investigation with SEM revealed that Cu-coated tetrapods have an average size between 5 and 100 µm and the hexagonal basal facets are rounded because the copper oxide covers the tetrapods [205]. The Cu oxide-coating also created an interconnected network which can enhance the heat transport. Al-coated tetrapods also have a round basal facet but the interconnection between individual tetrapods is not as strong as for Cu-coated tetrapods. The size of the Al-coated ZnO tetrapods ranges from 5 to about 80 µm. Furthermore, microspherical particles of about 1 to 20 µm were connected to the ZnO tetrapods [205]. A similar morphology was found for Bi-coated ZnO tetrapods where the basal facets were rounded and the tetrapods are interconnected [213]. However, in contrast to Al-coated, no microparticles were found in the structure. EDX analysis of the Bi-coated tetrapods revealed that a Bi layer was formed around the ZnO tetrapod [213]. The size of Sn-coated tetrapods ranges from 5 to about 300 µm (see Figure 4.16 (a)). While Al- and Cu-coated ZnO tetrapods are interconnected, no interconnection was found for Sn-coated tetrapods. Furthermore,

different morphologies were found in Sn-coated sample, such as microparticles (Figure 4.16 (a)) and ZnO 'Koosh balls', also known as multipods (Figure 4.16 (d)). In the 'Koosh ball' structure, several arms radiating from the ZnO core and the 'Koosh ball' can be about 100 µm across. Moreover, the hexagonal basal facet as shown in Figure 4.16 (b) can be hollow or pointed (see Figure 4.16 (c)). In Fe-coated ZnO tetrapods, small microparticles of Fe_2O_3 were formed on the surface of the ZnO tetrapods as shown by Lupan *et al.* [214]. The sizes of these tetrapods range from 10-100 µm and the microparticles can have a size of 0.1-5 µm. These feature are summarized in Table 4.1.

Electrical measurements of consolidated metal oxide-coated pellets with the same mass density indicated that Cu-coated ZnO tetrapods are poor electrical conductors, in which the electrical conductivities were even below that of pristine ZnO tetrapods [205]. (Electrical conductance data are summarized in Table 4.1.) Although copper oxide, which has semiconducting behavior ($E_g = 1.35$ eV), was formed on the surface of the ZnO tetrapods [214], it is surprising that a higher electrical conductance, G, was found for the Al-coated tetrapods. $ZnAl_2O_4$ has a wider band gap ($E_g = 3.8$ eV) than CuO and pristine ZnO. Furthermore, the Sn-coated tetrapods have about one magnitude lower electrical conductance than the Al-coated samples and an order of magnitude higher conductance than the Cu-coated tetrapods. An increase in electrical conductance was observed with increasing density in all compressed pellets [205].

Table 4.1: Size, interconnection between tetrapods, electrical conductance, G, and Young's modulus, Y, of various metal oxide-coated ZnO tetrapods at room temperature. Electrical and mechanical properties were reported for metal-oxide coated ZnO tetrapods pellets with mass density of 500 kg m^{-3} except Y for Al-coated tetrapods ($\rho = 400$ kg m^{-3}).

Metal	Size of Tetrapods / µm	Interconnection	G / nS	Y / MPa
Sn [205]	5-300	None	6.00	0.025
Al [205]	5-80	Weak	52.00	0.81
Bi [213]	2-100	Average	N/A	N/A
Cu [205]	5-100	Strong	0.45	2.5
Fe [214]	10-100	Strong	N/A	N/A

In addition to the electrical properties, Gröttrup *et al.* also investigated the mechanical properties of Sn, Cu, and Al-coated ZnO tetrapods pellets [205].

(Mechanical data are summarized in Table 4.1.) While Al- and Sn-coated ZnO tetrapods have a smaller Young's modulus (∼0.81 MPa and ∼0.025 MPa for a sample density of 400 kg m^{-3} and 500 kg m^{-3}, respectively), the Young's modulus is about one order of magnitude higher for Cu-coated tetrapods (∼2.5 MPa for 500 kg m^{-3}). If the samples were compressed above their elastic limit, the samples were plastically deformed and then an increase in elastic limit was observed [205]. However, it is important to note that the mechanical properties of the metal oxide-coated tetrapods were determined under compression and no information is available from applying tension forces.

For the thermal conductivity measurement using the TTO method, tension and shear forces would be induced on the compressed pellet. Due to the weak mechanical stability of the metal oxide-coated ZnO samples, it was not feasible to measure the thermal conductivity using the TTO. Therefore, a lab-developed powder cell was used to measure the thermal conductivity of metal oxide-coated ZnO tetrapods. Before the powder cell is introduced, a short background of classical thermal conductivity measurement methods is presented.

4.2.4 Classical Thermal Conductivity Measurement Methods

Different methods have been developed to measure thermal conductivity in different phases as well as in various morphologies.

4.2.4.a Thin Films

The most common thermal conductivity method for thin films is the 3ω technique in which a metallic thin film is deposited on a substrate serving as resistance heater and thermometer [215]. An alternating current is applied with frequency ω to the sample, causing Joule heating at a frequency 2ω. The temperature oscillation generates an oscillation of the resistance in the heater at a frequency 2ω which is combined with the current at frequency ω to a measured voltage of frequency 3ω. The 3ω voltage is related to the thermal conductivity which can be determined from the measured voltage using various frequencies [215]. This measurement method has the advantage that the thermal conductivity can be measured in a wide temperature range and the blackbody radiation contribution is small compared to the total thermal conductance

($< 2\%$) [215]. However, the 3ω method does not take in account the thermal resistance of the interface between the heater and the sample, which can lead to uncertainties. Furthermore, the dimensions and the electrical properties of the thin film have to be exactly known to obtain accurate thermal conductivity.

More recently, the time-domain thermoreflectance (TDTR) technique has been established to determine the thermal conductivity in thin films [216, 217]. In TDTR, a laser produces sub-picosecond optical pulses which are split in two paths, denoted 'pump' and 'probe' paths [217]. Both beams are focussed on the surface of a metal transducer deposited on the sample. When the surface of the metal transducer is heated by the 'pump' pulses, the reflectivity of the metal transducer changes with temperature. The reflectivity is measured by the 'probe' pulses, which are delayed by the time to heat the metal layer [216]. The 'probe' pulses record the decay of the surface temperature which is fit to a heat transfer model for layered geometries to determine the thermal conductivity. As shown for PCBM thin films, the fitting of the thermal conductivity requires further parameters from the metal transducer, the sample, and the substrate which introduce uncertainty [69, 151]. In particular, it is challenging to model the interface between the metal transducer and the sample. It is assumed that the interface can be simulated with a radiative boundary condition which might lead to an error in the thermal conductivity [217]. Furthermore, the sample surface has to be smooth (surface roughness < 15 nm) to reduce diffuse scattering which can affect the thermal conductivity.

In addition to the 3ω method and TDTR, the thermal conductivity in thin films has also been measured using a laser flash analysis (LFA) [218]. (The measurement principle of LFA is described in Section 3.2.3.b.) The LFA method in thin films has the advantage that the in-plane thermal conductivity can be determined, even for materials with low thermal conductivity.

4.2.4.b Carbon Nanotubes

For the determination of the thermal conductivity in nanotubes, in particular CNTs, different small devices have been developed in which a single CNT is suspended across a trench and the thermal conductivity is calculated from Joule self-heating [155] or a thin film heater is placed on one side leading to a temperature gradient

[219]. Both measurement methods are performed under steady-state conditions. The measurements can be challenging due to the high thermal conductivity found in CNTs (κ = 3500 W $m^{-1}K^{-1}$ at room temperature) [155] and the small dimensions of the nanotubes.

In addition to individual CNTs, the thermal conductivity of different CNT based macroscopic materials, such as CNT arrays [220], yarns [221, 222] and sheets [223, 224], have been investigated. While the thermal transport in CNT arrays can be determined with a steady-state method (*e.g.*, TTO in a PPMS) [220], CNT yarns and sheets are not rigid enough to measure the thermal conductivity using the TTO. Therefore, the parallel thermal conductance method [225] was used for CNT yarns and sheets [221, 222, 223, 224]. This method is similar to the thermal conductivity measurements of individual CNTs where the CNT yarns or sheets are suspended across two stages. A thermally isolated stage contains a resistive heater to supply a heat flux and a brass stage serves as heat sink. The measurement of the thermal conductivity is time-consuming because three measurements are performed: background, sample and background, as well as background and radiation. Furthermore, a linear temperature gradient is assumed for the radiation loss which can introduce uncertainty [225].

4.2.4.c Liquids

The thermal conductivity in fluids is generally measured by the hot wire method [226]. The hot wire method is a transient method in which a thin wire with known resistance-temperature relation is placed in a fluid serving as heater and thermometer. A constant current applied for a short duration heats the wire. The thermal energy dissipates from the wire into the investigated fluid and the thermal conductivity can be determined from a temperature and time plot [226]. The measurements are very fast to avoid thermal loss through convection. However, the thermal resistance between the wire and the fluid cannot be separated from the measurement which can increase the error in the result. Furthermore, the sample cells have to be long to enhance the sensitivity in the measurements.

In addition to the hot wire method, the thermal conductivity in liquids can be measured with a lab-developed liquid cell with the TTO method [206]. The liquid

cell construction consists of two plates made out of a high thermal conductivity material (*e.g.*, Cu) closing the tube. The tube material is chosen such that the thermal conductivity is low to minimize the background thermal conductance. The empty and liquid-filled cell are measured using steady-state conditions and the sample thermal conductance is determined from the thermal conductance difference of the filled and empty cell.

4.2.4.d Powders

Powders can have a very low thermal conductivity and it was reported that powders can even suppress the thermal conductivity in a Dewar vessel compared to the 'true' vacuum by reducing convection and radiation [70, 71]. Several papers were published which conclude that powder can have similar thermal conductivities to the surrounding gas [227] and that the effective thermal conduction, *i.e.*, the conductive and radiative heat transfer, of glass microspheres can be lower than that of the 'true' vacuum [228]. The determination of the thermal conductivity in powders is challenging due to the low thermal conductivity as well as the lack of the comparison to standards. In recent years, DSC [227] and modified steady-state methods [228, 229] were developed to measure the thermal conductivity in powders.

For the reported thermal conductivity measurement using DSC, two samples were measured, a metal sphere with known radius and the investigated powder with a metal sphere on the top, both placed in hemispherical pans [227]. Both pans were heated with the same scanning rate to the melting point of the metal and the thermal conductivity was determined from the different slopes of the melting peak. As shown in the study by Rodriguez *et al.*, the onset temperature is shifted to higher temperatures when the powder is in contact with the metal sphere [227]. The change in onset temperature induces a temperature gradient which most likely influences the reported thermal conductivity of the powders. Furthermore, the metal has to be placed exactly in the center of the hemispherical pan and small displacements can introduce a large uncertainty in the measurements. Thus, the present author does not recommend this measurement technique to determine the thermal conductivity in powders.

The most common method to measure the thermal conductivity in powders is a

modified steady-state technique where a heater is placed in a cell and the temperature is measured at different radial displacements under high vacuum [229]. The thermal conductivity is determined from the heater power and the temperature gradient. This method has the advantage that the temperature gradient can be measured at different places. However, each thermocouple can act as a cold finger and influence the thermal conductivity measurements. Furthermore, a large amount of powder is required to reduce the axial heat losses and enhance the accuracy of distance measurements. Although many techniques have been developed to measure the thermal conductivity for materials of different sizes and phases, it is still challenging to determine thermal conductivity in powders.

4.2.5 Present Powder Cell

In the present study, a lab-developed cell was used to determine the thermal conductivity in metal oxide-coated ZnO tetrapods powder. The cell was constructed by Michel B. Johnson, Institute for Research in Materials, Dalhousie University, aimed initially for liquid samples, and consists of a polytetrafluoroethylene (PTFE) tube (length 11.66 mm; outer diameter 6.10 mm; inner diameter 4.46 mm) and two metallic caps (see Figure 4.17 (a) and (b)). PTFE was chosen due to its low thermal conductivity ($\sim$0.24 W $m^{-1}K^{-1}$) and simple handling. The caps were fabricated from a 2.80 mm section of 8-32 brass thread. The sections were soldered to gold-plated Cu disks from Quantum Design. For the liquid cell, a hole (diameter $\sim$0.80 mm) was drilled through the disk-screw assembly. For the present powder measurements, the hole was filled with epoxy (LePage® Speed Set™ Instant Mix™; mainly consisting of epoxy resin/ polycaptane and amine hardener) to avoid losing powder during the measurement. The caps were screwed into the PTFE tube but the cell was not tightly sealed as reported for liquid samples [206]. Therefore, the remaining air in the cell could most likely be removed during pumping to avoid heat transfer through the gas. Prior each measurement the sample cell was hold under high vacuum ($\sim 10^{-7}$ bar) for at least 10 min. The powder cell was also tested with isopropanol in a desiccator showing that isopropanol can off-gas from the powder cell.

A similar cell was used by Kahwaji *et al.* to determine the thermal conductivity

of the solid and liquid phases of fatty acids [206]. In the study, they compared the thermal conductivity of water measured with the liquid cell to the standard value at room temperature and found that the measurement was within 10%. (The thermal conductivity of isopropanol was also measured indicating good agreement with literature [Dr. Samer Kahwaji, unpublished work]). The thermal conductivity of water is generally higher than the thermal conductivity of loose powders. Furthermore, water was only measured at room temperature [206] and temperature-dependent measurements can influence the thermal conductivity due to different thermal expansions of the PTFE tube and the material. PTFE has a relatively high coefficient of thermal expansion of $2.0 \cdot 10^{-4}$ K^{-1} from 273 K to 298 K and $1.2 \cdot 10^{-4}$ K^{-1} from 298 K to 398 K [230] while the material in the powder cell has normally a lower coefficient of thermal expansion than PTFE resulting in a decrease in thermal contact with increasing temperature.

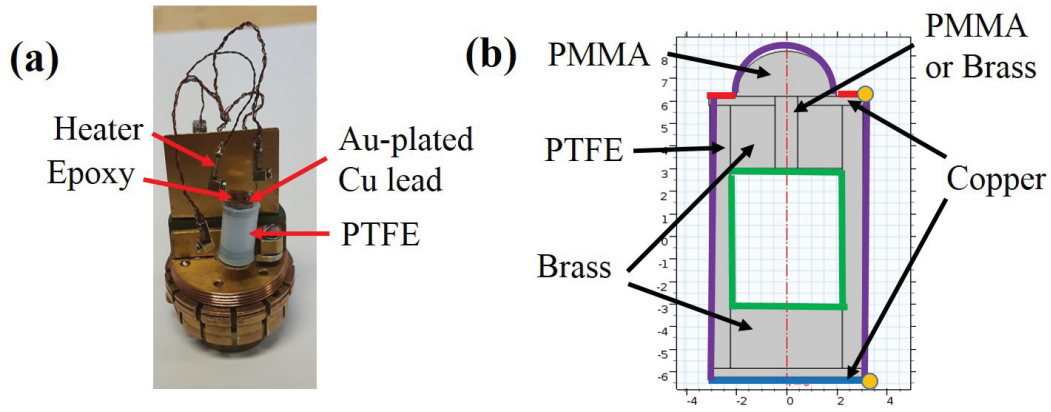

Figure 4.17: (a) Powder cell attached to the TTO puck. Heater and hot thermometer are attached to the top and heat sink and cold thermometer are attached to the bottom disk. (b) Longitudinal cross section of the empty powder cell for modelling the heat transfer using the software COMSOL (scale is in mm). A heater power of 10 mW (red line) was applied and the temperature of the opposite side was fixed to 300.9 K (blue line). Blackbody radiation (purple line) and surface-to-surface radiation (green line) were taken as the boundary condition for the cell. Temperature was recorded on the hot side and cold side (yellow circles).

Furthermore, it is important to cycle the temperature over the temperature range to see if hysteresis occurs. Hysteresis in the powder cell can mean that steady-state conditions were not fulfilled and/or there is a change in thermal contact due

to thermal expansion. The former effect can be minimized by increasing the waiting time. However, the temperature range is limited due to thermal expansion of the cell and the powder. In the present study, thermal conductivity was measured from 265 K to 330 K. There are currently no standard materials available for thermal conductivity in powders and therefore, an uncertainty of 20% was estimated for the powder cell. While the uncertainty of the liquid cell was 10% at room temperature, temperature-dependent measurements can increase the uncertainty due to non-steady state conditions. Furthermore, the thermal conductivity in powders depend on various factors, such as particle size and distribution, and/or porosity. It is important to note that the hot wire method is the standard method to measure thermal conductivities in powders [231].

To analyse the powder cell, the thermal conductance was computed with a finite element method using the software package COMSOL [232]. The longitudinal cross section of the powder cell is shown in Figure 4.17 (b). Although the epoxy was a mix of polycaptane and amine hardener, the properties to calculate the heat transfer in this epoxy (needed for Equation 2.9) are not given in literature and therefore, the epoxy was modelled with polymethyl methacrylate (PMMA). The parameters for the heat transfer for the materials used in the model are given in Table 4.2. For the boundary conditions, a heat flux was applied on the top copper disk with a heating power of 0.1 mW and the temperature of the opposite copper disk was set to 300.9 K (see red and blue lines, respectively, in Figure 4.17 (b)) which was the experimental temperature on the cold side using the TTO method. The outside of the cylinder had a radiative boundary condition (see purple line in Figure 4.17 (b)) and the blackbody radiation was modelled according to the Stefan-Boltzmann law ($-\vec{n}\cdot\vec{Q} = \varepsilon_T\sigma_T((300\text{ K})^4 - T^4)$, where $\vec{n}\cdot\vec{Q}$ is the dot product of the surface vector and the heat flux vector) [146].

The green line in Figure 4.17 (b) represents the surface-to-surface radiation in the powder cell. The surface-to-surface radiation is the difference between the absorbing and emitting radiation given by

$$-\vec{n}\cdot\vec{Q} = \varepsilon_T\left(G^* - n^2\sigma_T T^4\right) \tag{4.8}$$

where G^* is the absorbing radiation and n is the magnitude of the surface vector [146]. G^* can be separated in an external irradiation, G^*_{ext}, a mutual irradiation from other boundaries, G^*_m, and the ambient irradiation, G^*_{amb}. In the present study, no

external irradiation was applied.

An extra fine mesh (minimum element size 0.374 µm) was applied and the surface temperature was computed for the empty powder cell as shown in Figure 4.18 (a). While one side was fixed to a temperature of 300.9 K, the temperature of the heater side increased to 309.2 K. For better comparison, the temperatures of the hot and cold sides were taken at the same spot where the thermometers are attached (see yellow circles in Figure 4.17 (b)) in COMSOL. A temperature difference of 8.3 K was determined resulting in a thermal conductance of 1.2 mW K^{-1}. The importance of blackbody radiation was investigated by disabling blackbody radiation (purple line in Figure 4.17 (b)). Without blackbody radiation the temperature difference increased to 20 K and the thermal conductance dropped to 0.5 mW K^{-1}. In the finite element method, the hole was sealed with either PMMA or brass, with no significant difference observed in the thermal conductance of the cell.

Table 4.2: Thermal conductivity, κ, heat capacity, C_p, mass density, ρ, and the emissivity, ε_T, of the materials at room temperature for the finite element model. Parameters were provided from the COMSOL library [232], unless otherwise stated.

Material	κ / W m^{-1} K^{-1}	C_p / J kg^{-1} K^{-1}	ρ / kg m^{-3}	ε_T
Copper	400	385	8960	0.03 [233]
PTFE	0.24	1050	2200	0.92 [233]
Brass	125 [234]	385 [235]	8450 [234]	0.06 [233]
PMMA	0.19	1420	1190	0.90 [236]
Zinc Oxide	6	505 [237]	5676	0.92 [238]

The computed thermal conductance of the empty powder cell was compared to experimental results, shown in Figure 4.18 (b). In an experiment, the empty powder cell was cycled in the temperature range from 265 K to 330 K and an increase in the raw thermal conductance, *i.e.*, thermal conductance of the powder cell including blackbody radiation and thermal conductance of the leads (see Equation 3.24) was observed with increasing temperature (black line). For comparison with the computed data, the thermal conductance of the leads ($\sim$0.42 mW K^{-1} at room temperature) was removed from the total heat transfer and the thermal conductance was calculated with (red line) and without (blue line) blackbody radiation to evaluate the effect of blackbody radiation on the comparison. The

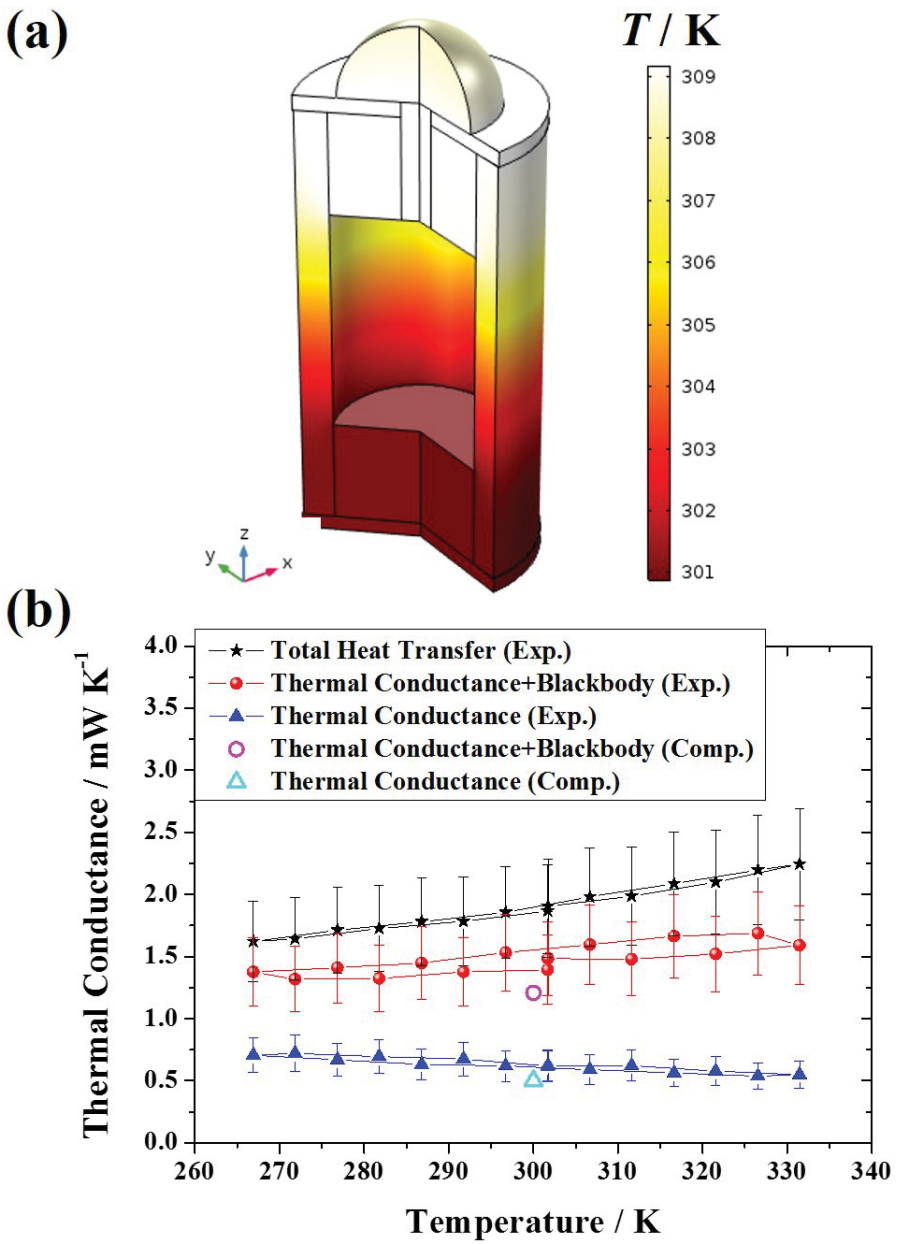

Figure 4.18: (a) Modeled heat flux in the empty powder cell including blackbody radiation using the software package COMSOL. (b) For the empty cell, the total heat transfer (*i.e.*, blackbody radiation, thermal conductance of the cell and the leads) (—), as well as thermal conductance of the empty powder cell with (—) and without blackbody radiation (—) correction is in agreement with the computed data with (○) and without (△) blackbody radiation.

experimental thermal conductance of the empty powder cell slightly decreases with temperature and shows only a small hysteresis with cycling. An increase in hysteresis was found for the thermal conductance with blackbody radiation which is nearly temperature-independent. The data for the experimental thermal conductance of the empty powder cell are given in Table B.1 of Appendix B.

The computed thermal conductance is within uncertainties of the experimental data. However, both computed values are lower than the experimental thermal conductance of the empty powder cell indicating that the discrepancy between simulation and experiment cannot be explained by inaccurate accounting of the blackbody radiation. The discrepancy between the computed and experimental data could be due to underestimation of the thermal conductance in the leads. The thermal conductance of the cell at room temperature ($\sim$0.62 mW K^{-1}) is slightly higher than the thermal conductance of the leads. Furthermore, the computed thermal conductance is limited by the low value of the thermal conductivity of PTFE used in the calculations (see Table 4.2). A slight increase in thermal conductivity of PTFE would have a large impact of the computed thermal conductance in the powder cell. It is important to note although it is challenging to model the blackbody radiation of the cell, the computed thermal conductance without blackbody radiation also was lower than the experimental value. Therefore, blackbody radiation most likely did not cause the discrepancy between computed and experimental values.

4.2.6 Thermal Conductivity in Metal Oxide-Coated ZnO Tetrapods

4.2.6.a Method

The thermal conductivities of the pristine and metal oxide-coated ZnO tetrapods were determined experimentally from the difference of the thermal conductance of the filled powder cell with ZnO tetrapods, K_{filled}, the thermal conductance of the empty powder cell, K_{empty}, and the geometry of the inner cell. The thermal conductivity was calculated by two different methods. For the measurements, the empty powder cell was weighed, following by filling the cell with the metal oxide-coated ZnO tetrapods and measuring the mass of the filled powder cell. It is important that the powder is packed in the cell to enhance the heat transfer through

the sample. To obtain comparable results, a similar mass of the pristine and metal oxide-coated ZnO tetrapods was filled in the powder cell ($m = 44.3 - 52.4$ mg) and the thermal conductance of the metal oxide-coated tetrapods was measured with the same sequence as for the empty powder cell. (The apparent mass densities of the compressed metal oxide-coated ZnO tetrapods are given in Table 4.3.)

Table 4.3: Thermal conductivity of pristine and various metal oxide-coated ZnO tetrapods at 300 K. The thermal conductivities were calculated from Equation 4.10 (difference of the thermal conductance of the cell of the filled and empty cell (κ_{cell})) and Equation 4.9 (difference of the total thermal conductance of the filled and empty cell (κ_{total})). Φ is the porosity.

Metal	ρ / kg m^{-3}	Φ	κ_{total} / W m^{-1} K^{-1}	κ_{cell} / W m^{-1} K^{-1}
Pristine	460±10	0.915±0.046	0.18±0.04	0.13±0.03
Pristine	460±10	0.915±0.046	0.16±0.03	0.09±0.02
Al	460±11	0.915±0.046	0.12±0.02	0.08±0.02
Al	420±10	0.922±0.046	0.10±0.02	0.12±0.02
Sn	420±10	0.923±0.046	0.06±0.01	0.07±0.01
Sn	500±12	0.909±0.045	0.13±0.03	0.11±0.02
Bi	440±10	0.920±0.046	0.10±0.02	0.12±0.02
Bi	440±10	0.920±0.046	0.12±0.02	0.07±0.01
Fe	440±10	0.919±0.046	0.15±0.03	0.13±0.03
Fe	460±11	0.915±0.046	0.13±0.03	0.11±0.02
Cu	440±10	0.919±0.046	0.13±0.03	0.14±0.03
Cu	430±10	0.921±0.046	0.13±0.03	0.09±0.02

On the one hand, the total thermal conductance of the filled, $K_{filled,total}$, and empty powder cell, $K_{empty,total}$, was used to determine the thermal conductivity of the powder. This approach assumes that the thermal conductance of the leads and the blackbody radiation of the cell were the same for the empty and filled powder cell. Therefore, the sample thermal conductivity is given by

$$\kappa_{total} = (K_{filled,total} - K_{empty,total}) \frac{L}{A_{cross}} \tag{4.9}$$

where $L = 6.06 \pm 0.04$ mm and $A_{cross} = 15.62 \pm 0.04$ mm^2 are the length and the cross-section area of the inner cell.

On the other hand, the thermal conductance of the leads and the black body radiation were subtracted from the total heat transfer and solely the thermal conductance of the filled, $K_{filled,cell}$, and empty powder cell, $K_{empty,cell}$, were applied

in the calculation and the sample thermal conductivity was calculated from

$$\kappa_{cell} = (K_{filled,cell} - K_{empty,cell}) \frac{L}{A_{cross}}. \quad (4.10)$$

4.2.6.b Experimental Results

As shown in Figure 4.19 all metal oxide-coated ZnO tetrapods samples exhibited low thermal conductivity (0.07-0.18 W $m^{-1}K^{-1}$) and both approaches (*i.e.*, Equation 4.9 and Equation 4.10) indicate similar thermal conductivities. (The thermal conductivity data of the metal oxide-coated ZnO tetrapods at 300 K are given in Table 4.3 and the data for the full temperature range are given in Tables B.2 and B.3 of Appendix B). Although the difference is small between the two calculations, it should be noted that using Equation 4.10 for the determination of the thermal conductivity would provide a more accurate result because for Equation 4.9 it was assumed that there is no change in blackbody radiation between the empty and filled cell. However, the thermal conductance is higher for the filled cell resulting in a decrease in the temperature difference and therefore different contributions to blackbody radiation. Although the temperature difference decreased for the ZnO tetrapod-filled cells, the blackbody radiation does not necessary decrease because the power loss due to blackbody radiation is proportional to $(T_{hot}^4 - T_{cold}^4)$ (see Equation 3.23). If the temperature of the hot side, for example, rose for the filled powder cell and the temperature difference slightly decreased, the blackbody radiation would increase for the filled powder cell. A small hysteresis was observed with cycling, within uncertainty of the experiment. The estimated uncertainty is similar to the uncertainty of the empty powder cell (20%), but can be even higher due to inhomogeneous shapes and sizes of ZnO tetrapods.

Although the thermal conductivity can change between samples, the thermal conductivities of the metal oxide-coated ZnO tetrapods slightly varied depending on the metal used (see Figure 4.19 (a) and Table 4.3). Cu-coated and Fe-coated tetrapods exhibited higher thermal conductivities whereas Sn-coated tetrapods have the lowest thermal conductivity of the investigated metal oxide coated ZnO tetrapods. The difference between the thermal conductivities can be systematic or an effect of the material used for the coating. For investigating the effect of the latter, the thermal conductivity of the metal-oxides formed on the coated ZnO

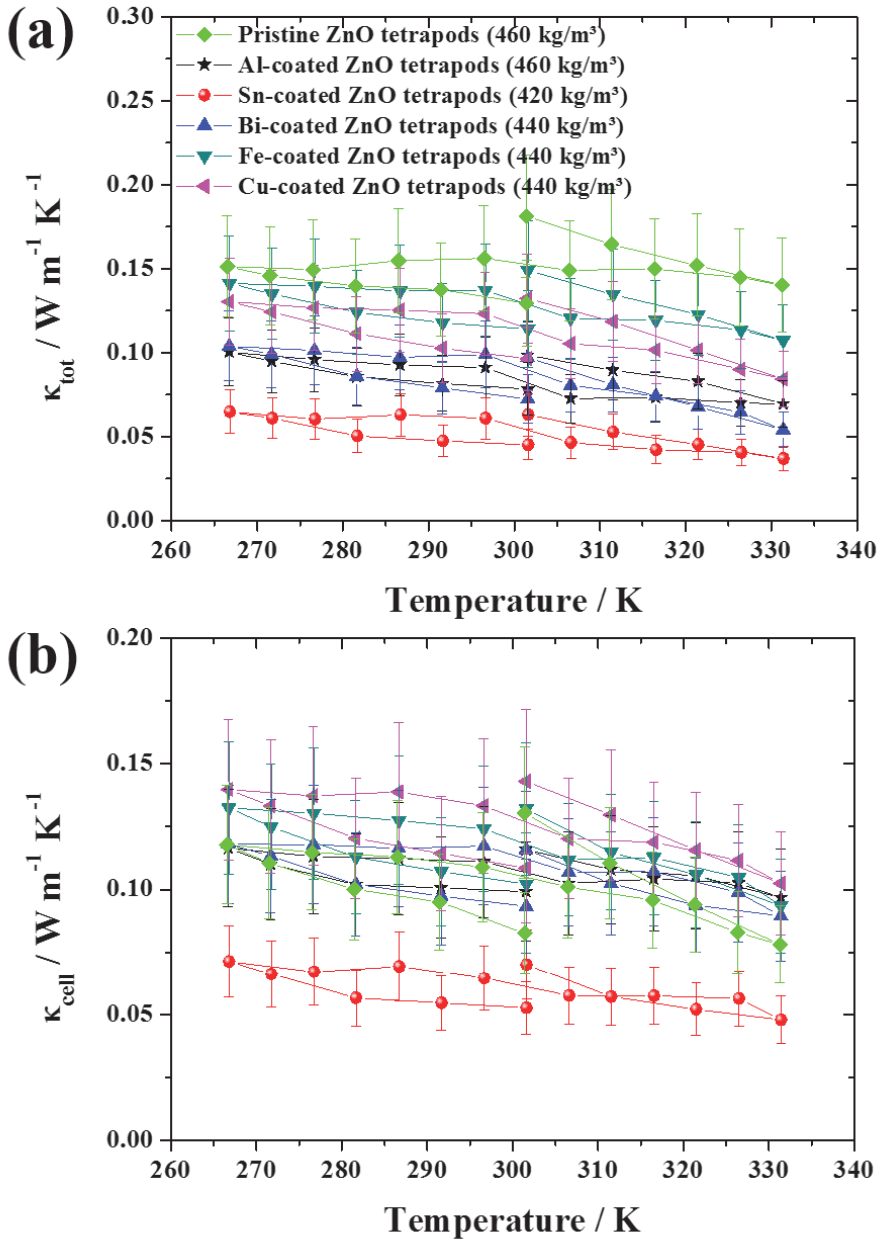

Figure 4.19: Thermal conductivity of the pristine and metal oxide-coated ZnO tetrapods calculated using (a) the total thermal conductance, κ_{total}, (Equation 4.9) and (b) the thermal conductance of the powder cell, κ_{cell} (Equation 4.10). No significant change was observed between the methods. An uncertainty of 20% was estimated due to the uncertainty in shape and size of ZnO tetrapods as well as in the measurement method. Data are given in Tables B.2 and B.3 of Appendix B.

tetrapods are compared. While bulk Fe_2O_3 and $ZnAl_2O_4$ have high thermal conductivities at room temperature ($\kappa \sim 15$ W m^{-1}K^{-1} [239] and 12-14 W m^{-1}K^{-1} [240], respectively), the thermal conductivity of CuO, Bi_2O_3, and Zn_2SnO_4 are relatively low ($\kappa \sim 3.7$ W m^{-1}K^{-1} [241], $\kappa \sim 3.5$ W m^{-1}K^{-1} [242], and $\kappa \sim 0.9$ W m^{-1}K^{-1} [243], respectively). Although zinc stannate has the lowest thermal conductivity and Fe_2O_3 has the highest thermal conductivity, the thermal conductivity of the metal oxides cannot fully describe the differences in thermal conductivity of the coated ZnO tetrapods. CuO has one third the thermal conductivity of zinc aluminate but Cu-coated tetrapods have a higher thermal conductivity than Al-coated tetrapods. Therefore, in addition to the thermal conductivities of the metal oxides, their morphologies on the ZnO tetrapods also have to be considered. Details of the morphologies of the metal oxide-coated tetrapods are given in Table 4.1. CuO forms a layer around the tetrapods creating a 3D interconnected network [205] enhancing the heat transfer while Sn-coated tetrapods are not interconnected (see Figure 4.16). Similar to Cu-coated tetrapods, Fe-coated tetrapods formed a layered structure around the tetrapods and the arms of the tetrapods are interconnected increasing the thermal conductivity [214]. Bi-coated and Al-coated tetrapods have also a layered structure. However, the interconnection between individual ZnO tetrapods is not as dominant as in Fe-coated and especially in Cu-coated tetrapods [205, 213, 214]. The weaker interconnection between the tetrapods would reduce the heat transfer through the sample.

4.2.6.c Finite Element Method - Thermal Conductance

The apparent mass densities of the pristine and metal oxide-coated ZnO tetrapods were slightly different as shown in Table 4.3. However, no correlation was found between density and room-temperature thermal conductivity, if the change in density was small. In general, the thermal conductivity is proportional to the density for randomly oriented and distributed voids as shown by Klemens [185] (see Equation 4.5). Although the model by Klemens was applied even below 60% theoretical density for $HfMo_2O_8$ [244], it fails for very porous samples. The extremely high porosity of ZnO tetrapods ($sim92\%$) would result in a negative thermal conductivity if the

porous thermal conductivity was calculated from the dense thermal conductivity using Equation 4.5. Therefore, the effect of the density on the thermal conductivity of ZnO tetrapods was modeled using a finite element method. Furthermore, it is shown in Table 4.3 that the porosity does not change significantly between various metal oxide-coated ZnO tetrapods indicating that all studied metal oxide-coated ZnO tetrapods have nearly the same void volume and therefore, the void volume should not have a large effect on the thermal conductivity.

In the finite element model, the heat transfer across randomly oriented ZnO tetrapods between two copper plates was calculated. To simulate randomly oriented ZnO tetrapods, the programming language Python 2.7 was used in the software package VPython. It is important to note that several assumptions were considered for the simulation of the tetrapods. While the synthesized tetrapods have different sizes and shapes, the calculated tetrapods were simplified to have the same size (arm length of 30 µm and arm diameter of 5 µm) and shape. For the tetrapod arms, a round basal facet was assumed, as observed for the Cu- and Al-coated tetrapods [205]. However, the cross-sectional areas of the arms normally decreased from the core to the end for the synthesized tetrapods whereas the simulated tetrapod arms have a constant cross-sectional area (see Figure 4.16). In the simulation, the tetrapods were randomly oriented in a row and moved together until the tetrapods slightly overlapped by less than 1 µm to assure contact between the tetrapods. For the present study, chains of four, six, and eight tetrapods were simulated using Python (see Figure 4.20). Note the Python script can simulate more tetrapods not only in one-dimension but also in two- and three-dimensions. However, it was not feasible to compute the heat transfer for more than eight tetrapods with COMSOL. The Python script produced a MATLAB output file which could integrate the geometry into the COMSOL software using the LiveLink™ for MATLAB.

The tetrapods were placed between two copper plates (width of 100 µm, length of 100 µm, and thickness of 20 µm) in the simulation. Although most of the ZnO tetrapods were coated with different metals, it is challenging to model the coated ZnO tetrapods due to lack of knowledge of the exact compositions and the thickness of the layer. Therefore, only the heat transfer of pure ZnO tetrapods was computed (the difference in thermal conductivities between pristine and metal oxide-coated ZnO

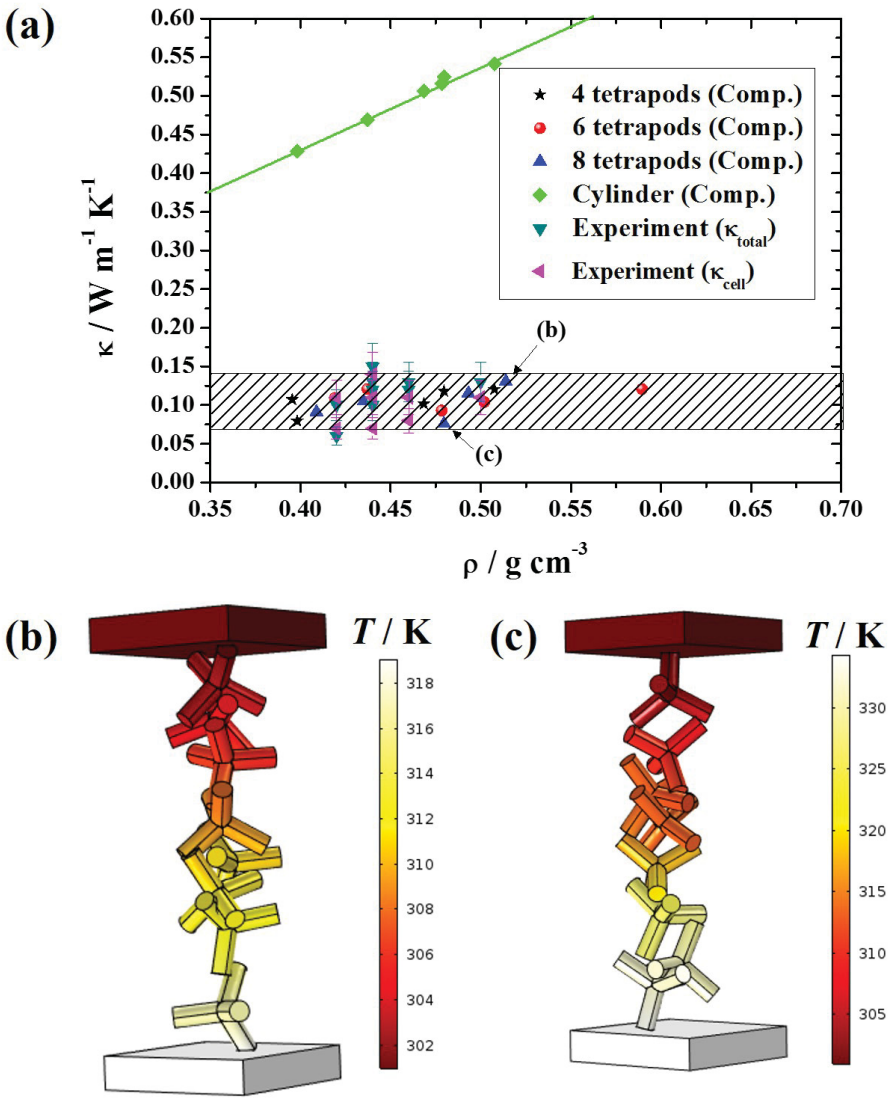

Figure 4.20: (a) Computed room-temperature thermal conductivity of various lengths of ZnO tetrapods using a finite element method. ZnO tetrapods have a range of thermal conductivities (shaded area) similar to the experimental values. A simulation of the heat transfer in ZnO tetrapods (b) for enhanced thermal conductivity (mass density of 257 kg cm^{-3}) and (c) low thermal conductivity (mass density of 240 kg cm^{-3}) indicated that there is no correlation between thermal conductivity and mass density of ZnO tetrapods. The thermal conductivity of a solid ZnO cylinder between two copper plates increased with mass density (line as guide for the eye).

tetrapods is small, as discussed above). For the boundary conditions a heater power of 50 µW was applied on one copper plate and the temperature of the opposite copper plate was fixed to 301 K generating a heat flux through the ZnO tetrapods. Open boundaries were assumed between the individual tetrapods and the tetrapod-copper interface. Although surface-to-surface radiation would enhance the model of the heat transfer, the computational cost was too expensive and the effect of the radiation on the measurement was separately modelled (*vide infra*).

The heat transfer was computed with an extra fine mesh (minimum element size 0.374 µm) and the thermal conductivities were calculated from the length of the tetrapod assemble (ranging from ∼120 and ∼300 µm) and the area of the Cu plate (2,500 μm^2). The mass density in the simulation was determined from the mass of the tetrapods (volume of the tetrapods times the mass density of ZnO given in Table 4.2) and the cuboid described by the area of the Cu plates and the length of the tetrapod assemble. Each assemble of four, six, and eight ZnO tetrapods was repeated five times with different configurations; results are shown in Figure 4.20 (a). It was found that even though the mass density (ranging from ∼380 to ∼600 kg m^{-3}) and the numbers of tetrapods are similar, the thermal conductivity can dramatically change (ranging from ∼0.08 to ∼0.14 W $m^{-1}K^{-1}$). For example, two assembles each of eight ZnO tetrapods with similar mass density (480 kg m^{-3} and 514 kg m^{-3}) showed a thermal conductivity of 0.08 and 0.13 W m^{-1} K^{-1}, respectively, as shown in Figure 4.20 (b) and (c). The thermal conductivity even decreased with increasing density as shown in Figure 4.20 (a). Therefore, the change in the computed thermal conductivity of the ZnO tetrapods cannot be solely explained by the mass density. Furthermore, due to the small sample size a huge fluctuation in the thermal conductivity is expected and the computed data should be considered as the upper and lower limits of the thermal conductivity. This is in contrast to a solid ZnO cylinder with the same mass density (*i.e.*, the mass of the cylinder was divided by the cuboid described by the copper plates) and length as the ZnO tetrapods. The cylinder was also placed between two copper plates and was computed with the same conditions as the tetrapods. The green line in Figure 4.20 indicates that the thermal conductivity of the ZnO cylinder increases with mass density and the thermal conductivity of the ZnO cylinder was more than three orders of magnitude higher than ZnO tetrapods. The discrepancy of

the thermal conductivity between the cylinder and the tetrapods is most likely due to the larger contact area of the cylinder enhancing the heat transfer between the two Cu plates. If the green line was extrapolated to the mass density of ZnO (see Table 4.2), the thermal conductivity would be 6 W m^{-1} K^{-1}.

Two features are important to obtain high thermal conductivities in ZnO tetrapods and powders. On the one hand, a direct path would enhance the heat transfer through the sample because the tetrapods act as thermal resistors in series such that the total thermal resistance is equal to the sum of the thermal resistances of each tetrapod, *i.e.*, a longer thermal path would thus increase the thermal resistance. Although the tetrapods have the same size and the heat has to travel through all tetrapods in the present simulation, the distance between the contacts on the ZnO tetrapods limits the thermal conductance. Figure 4.20 (c) shows that most ZnO tetrapods overlapped at the ends of the arms while the tetrapods in Figure 4.20 (b) touched closer to the ZnO core decreasing the thermal path and therefore, increasing the thermal conductance in the sample. The thermal path in experiments can change even more dramatically than in the present finite element simulations because heat can travel through a number of tetrapods in various three-dimensional directions reducing the thermal conductance in the measurement with increasing number of tetrapods.

The second feature which limits the thermal conductance might be the contact area between the individual tetrapods. With increasing contact areas the heat transfer between the tetrapods also increased as shown in Figure 4.20 (b) and (c). While the tetrapods in Figure 4.20 (c) only slightly touch, the arms of the tetrapods overlapped in Figure 4.20 (b) increasing the contact area as well as the thermal conductance of the assemble. The change in contact area, however, is most likely not very significant due to small changes in contact areas in comparison to the change in thermal path.

4.2.6.d Finite Element Method - Blackbody Radiation

In addition to the thermal conductance of the ZnO tetrapods, surface-to-surface radiation between the tetrapods might contribute to the heat transfer. To compute the effect of radiation, the surface area of ZnO was varied computationally inside the powder cell while keeping the volume constant (mass density of 220 kg m^{-3} in

the powder cell) and the thermal conductivity of ZnO was calculated with the same conditions as for the empty powder cell (see Figure 4.17). The surface area was varied by splitting the volume of bulk ZnO in a solid cylinder placed in the center of the powder cell and hollow cylinders around the solid cylinder. An example of four cylinders (one solid and three hollow) is shown in Figure 4.21 (a). Furthermore, the computations were performed for different cases. On the one side, the hole in the cap can be filled with PMMA or brass. While PMMA is more accurate to the 'real' powder cell, the computation would depend on the volume of the ZnO cylinders placed on the PMMA due to its lower thermal conductivity compared to the surrounding brass. In particular, the solid cylinder in the center contributed less to the heat transfer as shown in Figure 4.21 (c). Therefore, it is challenging to separate the effect from the PMMA and the surface area. To determine only the influence of the surface area, the hole filler was modelled with brass. Heat can travel through all cylinders with the same probability increasing the heat transfer through the center cylinder (see Figure 4.21 (d)). Furthermore, the boundary conditions of the ZnO cylinders were set to thermal insulation or surface-to-surface radiation to delineate the effect of blackbody radiation between ZnO tetrapods.

Figure 4.21 (b) indicates that the heat transfer through surface-to-surface radiation can be neglected. The differences between the thermal conductivity with and without surface-to-surface radiation are less than 2 mW $m^{-1}K^{-1}$ and did not increase with increasing surface area, $A_{surface,ZnO}$, per unit volume. The small variations for thermal conductivities for different surface areas are due to generating the exact geometry. However, the variations would not create a large change in the surface-to-surface radiation. Furthermore, the PMMA-filled powder cell had a lower thermal conductivity at small surface area per unit volume which increases with increasing surface area as shown in Figure 4.21 (b). This effect is related to how the surface area was modelled rather than the surface area per se. The lowest surface area is a solid cylinder in the center of the powder cell, so the solid cylinder modelled was only in contact with the PMMA. The thermal conductivity of PMMA is much lower than the thermal conductivity of brass (see Table 4.2) increasing the thermal resistance of the cell. With increasing surface area per unit volume the contribution of the heat transfer through PMMA decreased because the volume of

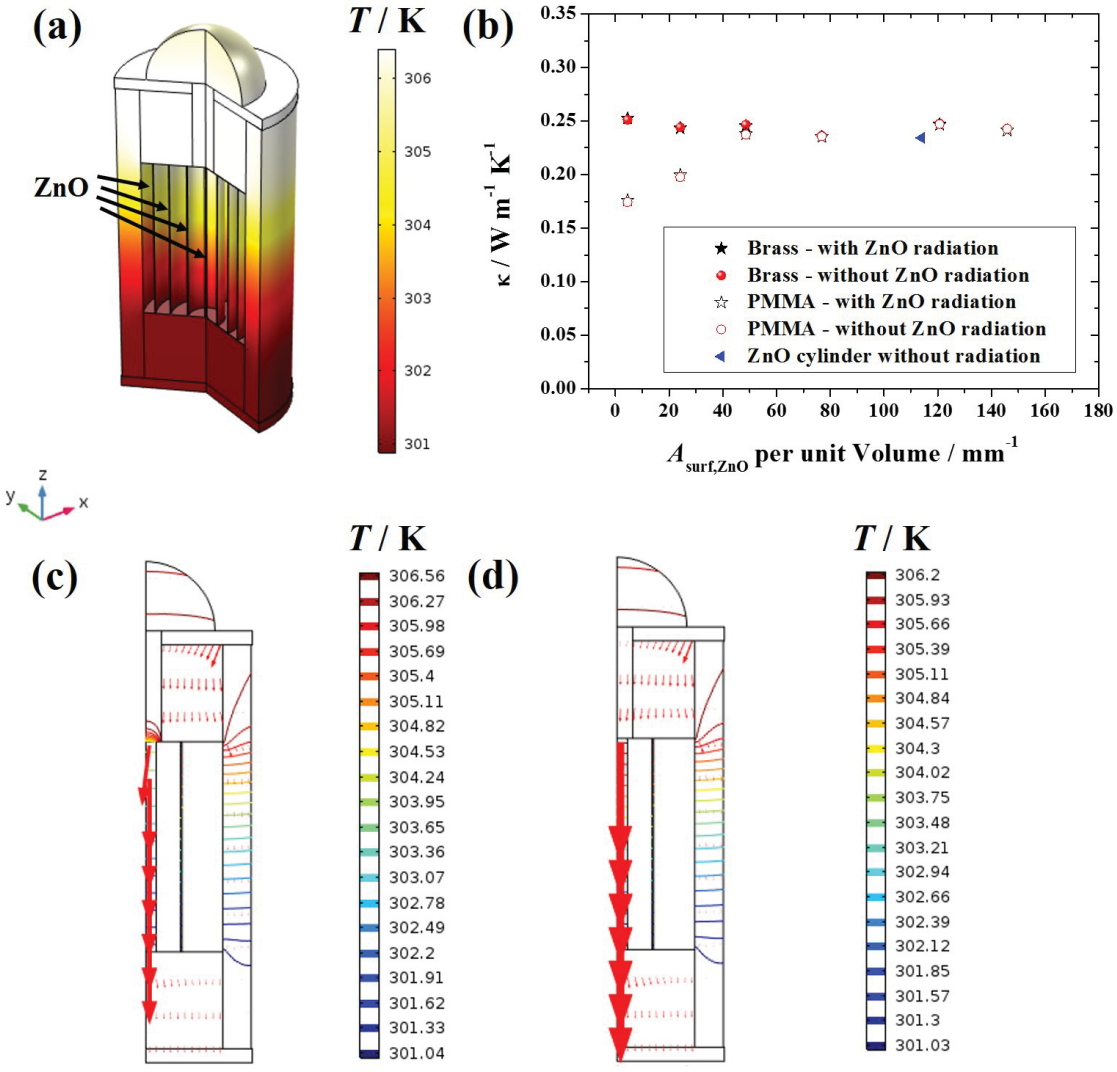

Figure 4.21: (a) Computation of surface-to-surface radiation in the powder cell using various numbers of ZnO cylinders inside the powder cell. The surface area of ZnO, $A_{surface,ZnO}$, per unit volume increases with the numbers of cylinders whereas the volume was kept constant. (b) The effect of surface-to-surface radiation in ZnO is negligible. While PMMA as a filler influenced the computed thermal conductivity, brass did not affect the computation. Isothermal contour plots of (c) PMMA-filled and (d) brass-filled hole. PMMA has a lower thermal conductivity than the surrounding brass, reducing the heat transfer through the solid ZnO cylinder in the center whereas a complete brass cap can transfer heat through all cylinders with the same likelihood.

the solid cylinders decreased and the volume of the hollow cylinders which are in contact with brass increased. Figure 4.21 (a) depicts that the thermal conductivity

increased with increasing surface area per unit volume until the thermal conductivity was similar to the brass-filled powder cell. Therefore, the composition of the plug (PMMA or brass) plays a role when heat is solely transferred through the center and does not influence uniformly distributed powder or ZnO tetragonal in the powder cell.

The effect of blackbody radiation was studied in a separate simulation in which the thermal conductance of the empty powder cell was calculated with and without surface-to-surface radiation in the inner cell. With surface-to-surface radiation an increase of $< 2\%$ was obtained and it can be concluded that the surface-to-surface radiation can be neglected. In particular, the contribution of radiation even decreased if powder was placed in the cell. Although the surface area in the powder increased, due to smaller temperature difference between the individual surfaces a similar radiation power was absorbed and emitted. This effect can reduce the heat transfer compared to the 'true' vacuum as reported by Smoluchowski [70, 71]. Moreover, the thermal conductivity also was compared to that of a free-standing ZnO cylinder with the same mass density as the cylinders in the cell and without powder cell and radiation. The thermal conductivity is slightly smaller than that of the cylinders in the powder cell indicating that the powder cell and radiation did not contribute significantly to the heat transfer. Therefore, the thermal conductance of the simulated ZnO tetrapods can describe the heat transfer well in the powder cell.

4.2.6.e Comparison of Experiments and Simulations

As shown by the shaded area in Figure 4.20 (a) the computed thermal conductivity ranges from 0.08 to 0.14 W $m^{-1}K^{-1}$ which is within uncertainty of the experimental thermal conductivity of the pristine and metal oxide coated ZnO tetrapods (see Table 4.3). However, the computed thermal conductivity of ZnO tetrapods depends on the bulk value for ZnO which ranges considerably (from 1.6 W $m^{-1}K^{-1}$ for micro-sized particles [corrected to the bulk thermal conductivity using Equation 4.5] to 37 - 54 W $m^{-1}K^{-1}$ for a fully sintered pellet [245, 246]). Due to the large range of thermal conductivities it is challenging to calculate accurate values for the heat transfer of ZnO tetrapods.

Furthermore, both experimental and computational studies indicated that the thermal conductivity of ZnO tetrapods could change between samples due to a change in heat transfer (*vide supra*). For example, a higher thermal conductivity was found in Fe-coated and Al-coated tetrapods with reduced mass density (see Table 4.3). A reason for the higher thermal conductivity might be a larger contribution of large ZnO tetrapods (length of arms > 100 µm) in the sample. Larger tetrapods might provide a longer phonon mean free path while the mass density in the powder cell can be simultaneously reduced. However, the thermal conductivity should in general increase with mass density because the probability to obtain a continuous path for heat transfer increases with mass density. For instance, the apparent mass density of Sn-coated was increased from 210 to 250 kg m^{-3} and the thermal conductivity increased from 0.07 to 0.11 W $m^{-1}K^{-1}$. It should be noted that the number of ZnO tetrapods in the experimental study is much larger ($\sim 10^5$ tetrapods) than in the simulation (8 ZnO tetrapods) and an increase in the number of tetrapods would enhance the computed thermal conductivity. Therefore, the finite element analysis should be considered as a semi-quantitative approach to calculate the thermal conductivity in ZnO tetrapods.

In conclusion, the thermal conductivity of pristine and various metal oxide-coated ZnO tetrapods was determined with a lab-developed powder cell. All ZnO tetrapods exhibited very low thermal conductivity and no correlation between mass density and thermal conductivity was found due to the small change in apparent mass density. The experimental thermal conductivity for the empty powder cell and for ZnO tetrapods were confirmed by a finite element method. However, it is important to note that the ZnO tetrapods have a range of thermal conductivities.

4.2.7 ZnO Tetrapods Coated with CNTs

The first step of the ZnO tetrapods with CNTs fabrication is similar to the metal oxide-coated ZnO tetrapods synthesis [205]. However, only pure ZnO tetrapods were compressed to a pellet (with a mass density of $\sim$0.3 g cm^{-3}) and sintered at 1150° C for 5 hours. After sintering, a 1 w% solution of multi-walled CNTs (MWCNTs) (CARBOBYK-9810 purchased from Byk Additives & Instruments) was infiltrated in the ZnO tetrapod pellet and the pellet was dried for one hour in air. The infiltration step was repeated one to six times to investigate the thermal and

electrical conductivity in relation to MWCNT content. All samples were provided by Fabian Schütt, Faculty of Engineering, Christian-Albrechts-University, as compressed pellets with a diameter of 6 mm and a height ranging from ∼2.2 mm to about ∼3.5 mm.

For the thermal and electrical conductivity measurements, three different infiltrations (FL) were studied (2 FL, 5 FL, and 7 FL). SEM images of these samples, acquired by Fabian Schütt, are shown in Figure 4.22. While the 2 FL tetrapods are lightly coated with MWCNTs, the MWCNT content increased rapidly with infiltrations. The 7 FL samples are completely coated with MWCNTs which enhanced the interconnection between individual ZnO tetrapods (see Figure 4.22 (e) and (f)). Although the MWCNTs are randomly oriented on the tetrapods, the MWCNTs overlapped creating a continuous path for electrical and thermal transport, even for the 2 FL samples.

The measurements of MWCNT-coated ZnO tetrapods will be compared here to pure CNT tubes (CNTTs) in which the ZnO tetrapods were removed from the 7 FL ZnO+CNT sample. The CNTTs were synthesized by Fabian Schütt and the thermal and electrical conductivities were measured by Catherine O'Neill at Dalhousie University [unpublished work, reproduced with permission]. The CNTTs consist of pure carbon, enhancing the electrical and thermal conductivities. The thermal and electrical conductivity of both ZnO tetrapods coated with MWCNTs and CNTTs could be measured with the standard TTO method in a PPMS. However, during the attachment of the wires of the TTO puck it was found that the mechanical stability was slightly reduced for CNTTs compared to ZnO tetrapods coated with MWCNTs and therefore, it is more likely that micro cracks could occur in the CNTTs, reducing the thermal and electrical performance.

4.2.8 Thermal and Electrical Conductivity of MWCNT-coated ZnO Tetrapods

The Seebeck coefficient, thermal and electrical conductivity of ZnO tetrapods coated with MWCNTs were measured as functions of temperature in the range from 2 K to 390 K. All samples were consolidated pellets with a diameter of 6 mm and various thicknesses. The transport properties were obtained using the standard

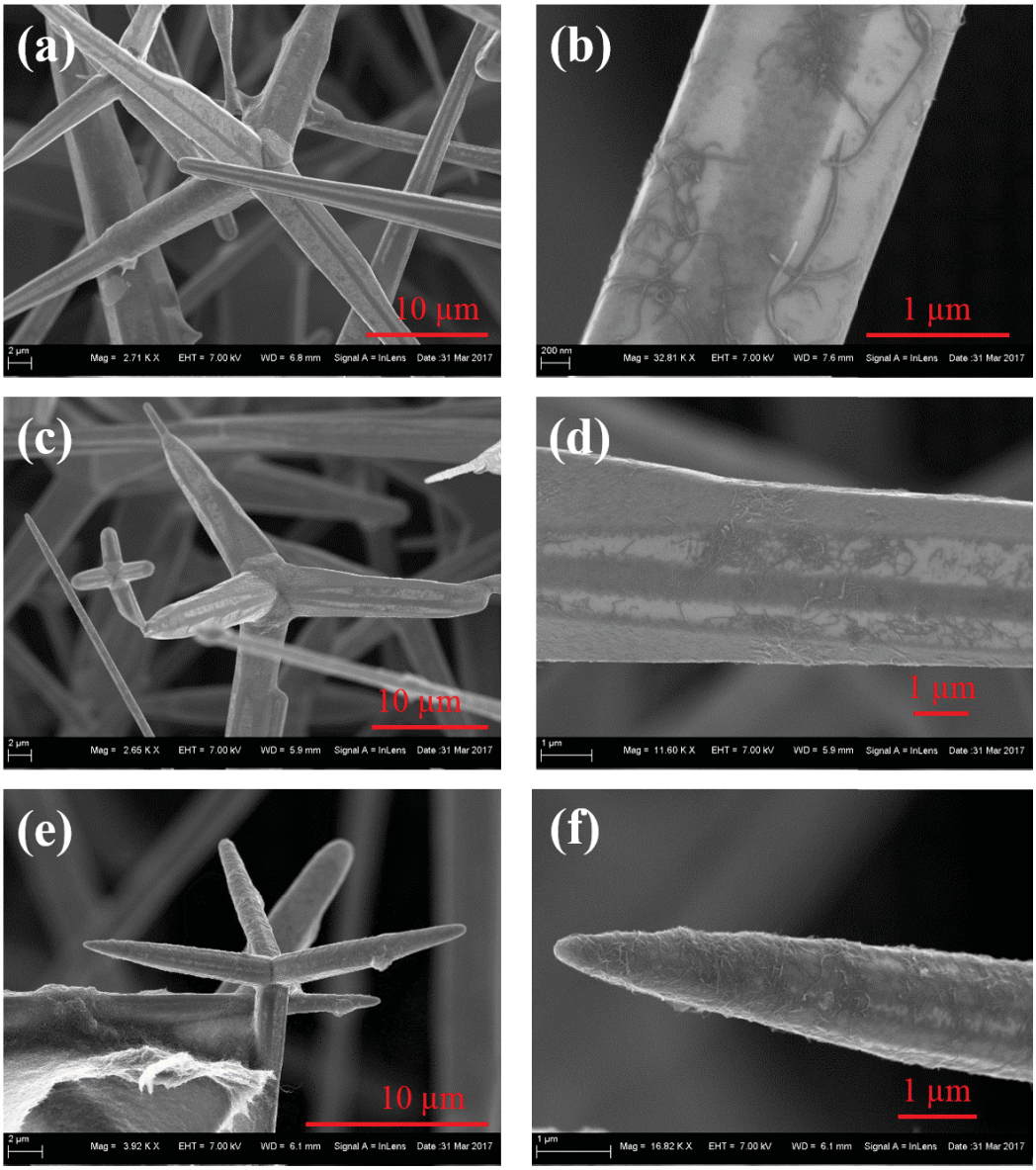

Figure 4.22: SEM image of ZnO tetrapods coated with MWCNTs with (a, b) 2 infiltrations (c, d) 5 infiltrations and (e, f) 7 infiltrations. SEM images of ZnO tetrapods with CNTs were taken by Fabian Schütt, Faculty of Engineering, Christian-Albrechts-University.

TTO method. (Room temperature thermal and electrical conductivity, thicknesses and mass densities of the pellets are given in Table 4.4 and temperature-dependent properties are given in Tables B.4-B.12 of Appendix B.) The uncertainty of the electrical conductivity and thermal conductivity was calculated from the uncertainty of the geometry and the measurement method or 5%, whichever was greater.

4.2.8.a Electrical Properties - Results

The electrical conductivities of ZnO tetrapods with various MWCNT content as well as CNTTs are shown as a function of temperature in Figure 4.23. All samples showed a similar temperature trend and the electrical conductivity increased with temperature indicating semiconducting behavior ($d\sigma_{el}/dT > 0$). The temperature trends of the ZnO tetrapods with MWCNTs is similar to CNTTs suggesting that the MWCNTs dominate the electron transfer in the sample over the entire temperature range. This is consistent with the wide band gap of undoped ZnO ($E_g = 3.37$ eV) [208] and the zero band gap of MWCNTs [223]. Although single-walled CNTs are mostly semiconducting and MWCNTs can be considered as stacked single-walled CNT shells, the statistical probability is high that one shell is metallic resulting in metallic behavior of the MWCNT. However, thermal energy is required for electrons to transfer between individual MWCNTs and therefore, the electrical conductivity increased with MWCNT content due to the increased probability of electrical connections. Furthermore, it was found that the electrical conductivity of all the ZnO tetrapods with MWCNTS samples and the CNTTs increased with a temperature dependence of $T^{0.2}$ from 50 K to 400 K. Below 50 K a dramatic decrease in electrical conductivity was observed and the electrical conductivity of all samples converged with decreasing temperature because the probability that electrons are transferred between inidividual MWCNTs decreased with temperature. Similar temperature trends in electrical conductivity were reported for CNT yarns [222] and CNT sheets [223]. However, the electrical conductivity increased linearly with temperature above 30 K for CNT yarns [222] and above 75 K for CNT sheets [223].

Table 4.4 indicates that the electrical conductivity can depend on the thickness and density of the pellet which is discussed below. Furthermore, it was recently found in CNT yarns that the electrical conductivity can change when the sample was first heated to 390 K in vacuum due to outgassing of absorbed oxygen or water [222].

No hysteresis in the electrical conductivity was found for the MWCNT-coated ZnO tetrapods and CNTTs between 2 and 300 K whereas the electrical conductivity showed a hysteresis at high temperature. When the pellet was heated from room temperature to 390 K and cooled to room temperature, the electrical conductivity

increased for all investigated samples in the present study. Water or oxygen might be absorbed in the porous structure of the ZnO tetrapod pellets and removed at 390 K increasing the electrical conductivity. The influence of water vapour in CNT was discussed by Lekawa-Raus *et al.* [247]. While they reported an increase in electrical conductivity with absorbing water, the electrical conductivity increased with degassing in the present study as shown in Figure 4.24 (a).

Table 4.4: Thickness, L, mass density, ρ, room-temperature electrical conductivity, σ_{el}, after annealing at 390 K and room-temperature thermal conductivity, κ, of ZnO tetrapods samples with various MWCNT content and CNTTs.

Sample	L / mm	ρ / kg m^{-3}	σ_{el} / S m^{-1}	κ / W m^{-1} K^{-1}
2 FL 2 mm	2.40±0.04	345±83	9.93±0.50	0.24±0.02
2 FL 3 mm	3.34±0.04	340±83	7.20±0.36	0.23±0.03
2 FL 3 mm (2)	3.38±0.04	345±83	4.23±0.21	0.28±0.03
5 FL 2 mm	2.20±0.04	396±84	20.90±1.05	0.34±0.02
5 FL 3 mm	3.40±0.04	432±82	31.37±1.57	0.41±0.04
5 FL 3 mm (2)	3.44±0.04	409±82	18.78±0.94	0.31±0.03
5 FL 3 mm (3)	3.34±0.04	405±83	21.47±1.07	0.36±0.03
7 FL 2 mm	2.20±0.04	432±84	49.00±2.45	0.43±0.02
7 FL 3 mm	3.50±0.04	448±82	42.34±2.12	0.45±0.04
7 FL 3 mm (2)	3.50±0.04	439±82	35.44±1.63	0.46±0.04
CNTTs	3.42±0.04	86±93	24.39±1.22	0.08±0.02

CNTs are generally p-doped as confirmed by the positive Seebeck coefficient at room temperature (see Figure 4.24 (b)). The temperature-dependent Seebeck coefficient also showed hysteresis when the samples were cycled between room temperature and 390 K. Note that the accuracy of the Seebeck coefficient might be low due to its small value and therefore, the Seebeck coefficient is only shown at high temperature. With decreasing temperature, the Seebeck coefficient decreased and fluctuated between positive and negative values. As shown in Figure 4.24, the Seebeck coefficient increased for all samples with temperature to about 350-375 K, following by a decrease in Seebeck coefficient to 390 K. On cooling the Seebeck coefficient decreased from 390 K to room temperature, reaching a lower Seebeck coefficient than the initial value indicating that the sample slightly changed. Based on Equation 2.29 the Seebeck coefficient is the sum of the p-type and n-type electronic properties. The removal of absorbed gas or water can increase more

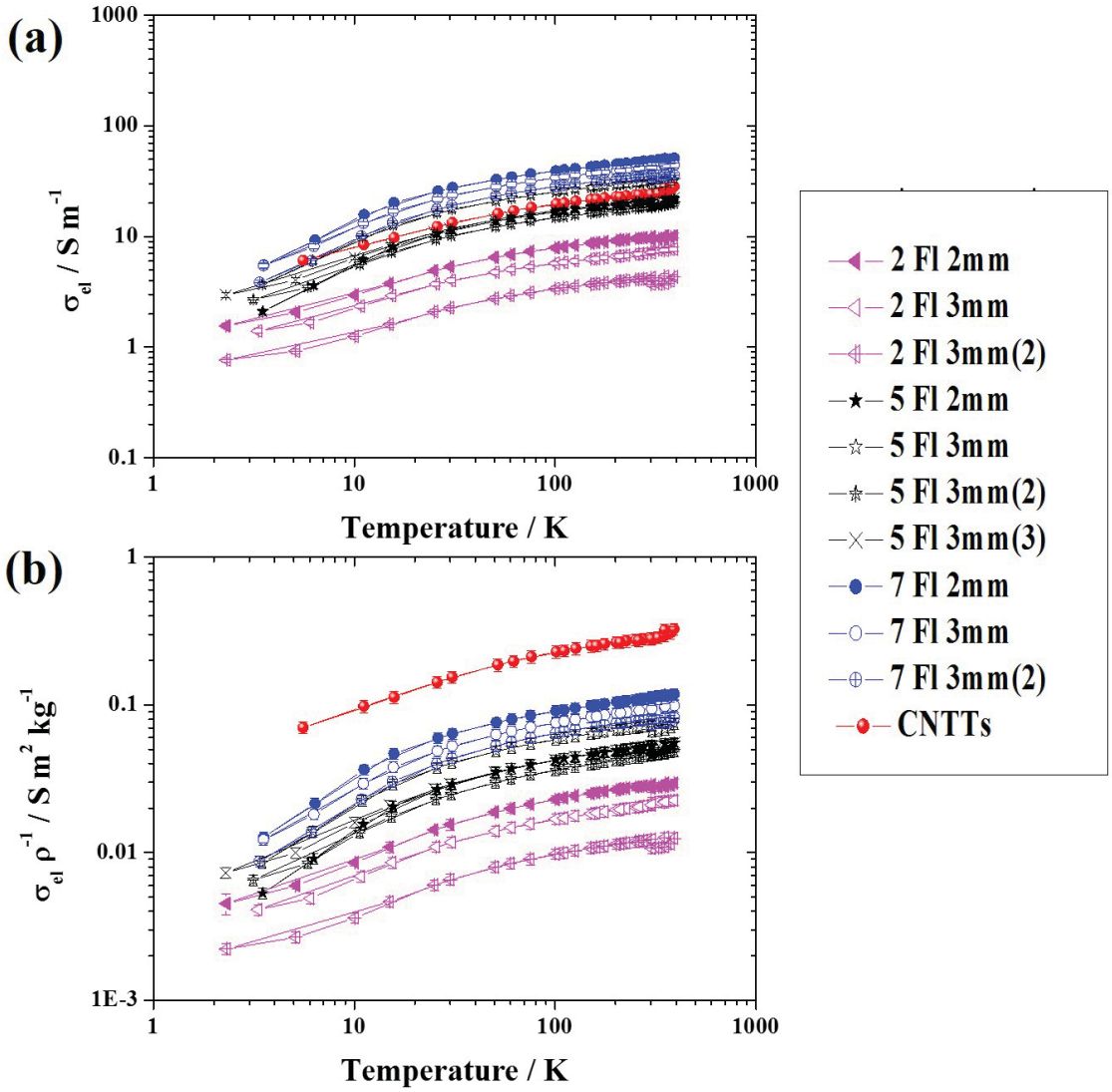

Figure 4.23: Electrical conductivity of ZnO tetrapods coated by MWCNTs and CNTTs. (a) The electrical conductivity increased with the MWCNT content and a nearly exponential increase in electrical conductivity was observed for all samples. (b) Specific electrical conductivity (*i.e.*, electrical conductivity per unit mass density) shows a similar trend to (a) except the specific electrical conductivity of the CNTTs was higher due to its low mass density. The uncertainty was calculated from the geometry and measurement methods or 5%, whichever is greater. Data given in Tables B.4-B.7 of Appendix B.

n-type behavior and therefore, the positive Seebeck coefficient would decrease. The temperature trend of the Seebeck coefficient is consistent with the electrical

conductivity measurement (see Figure 4.24 (a)). As described in Section 2.3 and Section 2.4, the electrical conductivity is proportional to the carrier concentration while the Seebeck coefficient decreased with carrier concentration. Further investigations of the electrical conductivity and Seebeck coefficient of CNTs on cycling are required at high temperature. For consistent electrical measurements, it is important to heat the samples to high temperature in vacuum prior the measurements to remove water or oxygen absorbed to the sample.

In addition to the electrical conductivity increase due to MWCNT content, thinner samples (<3 mm) exhibited higher electrical conductivity than the pellets with thickness >3 mm (see Figure 4.23 (a)). This is surprising because the electrical conductivity was measured with a 2-probe configuration so contact resistance could contribute significantly to the total resistance, and the ratio of the contact resistance to the total resistance would be lower for thicker samples. However, the MWCNT solution was infiltrated from the top of the pellet resulting in a concentration gradient of MWCNTs through the sample. The MWCNT content could be more uniformly distributed in thinner samples reducing the MWCNT concentration gradient and therefore, the electrical conductivity increased due to a uniform continuous path through the entire sample. Therefore, the more meaningful results are those for the thinnest samples.

As shown in Table 4.4, the mass density generally increased with the number of infiltration steps. The MWCNT content can be calculated from the difference between the mass density of the sample and the sintered ZnO pellets without infiltration (∼300 kg m^{-3}). While the MWCNT content increased only by a factor of three from the 2 FL samples to the 7 FL samples, the electrical conductivity increased five-fold at high temperature ($\sigma_{el,2FL}$ = 10.2±0.5 S m^{-1} and $\sigma_{el,7FL}$ = 51±3 S m^{-1} at 390 K). At low temperature, the difference between the electrical conductivities of 2 FL and 7 FL was reduced to a factor of 3.5 ($\sigma_{el,2FL}$ = 1.6±0.1 S m^{-1} and $\sigma_{el,7FL}$ = 5.5±0.3 S m^{-1} at 2 K). Although the mass densities in the 7 FL samples were about 25% higher than the ZnO pellets with five infiltration steps, the electrical conductivity was relative higher at low temperature ($\sigma_{el,5FL}$ = 2.1±0.1 S m^{-1} at 2 K). The high-temperature electrical conductivity of the 7 FL samples was slightly higher than for the 5 FL samples ($\sigma_{el,5FL}$ = 32.3±1.6 S m^{-1} at 390 K). Furthermore, the ZnO

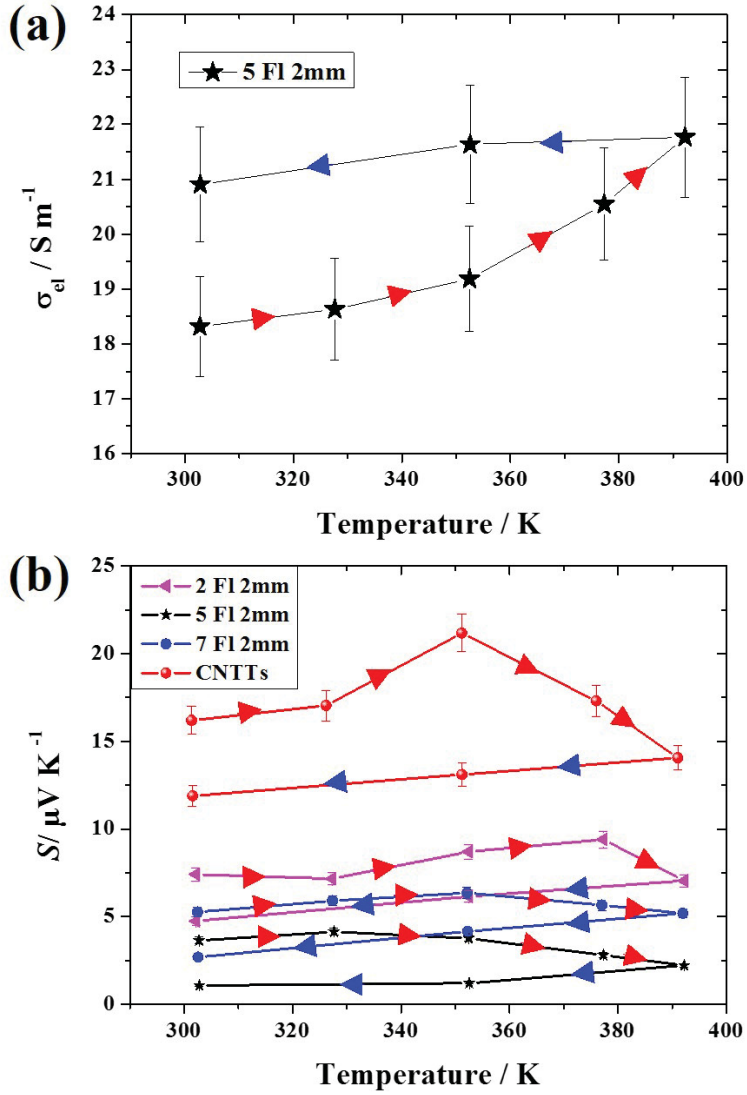

Figure 4.24: (a) Hysteresis of electrical conductivity. Electrical conductivity increased after heating to 390 K. (b) Seebeck coefficient, S, indicates p-type behavior for ZNO tetrapods with various MWCNT content and CNTTs. The Seebeck coefficient decreased at high temperature, most likely due to degassing, and a lower Seebeck coefficient was determined on cooling. The uncertainty was calculated from the uncertainty of geometry and measurement methods or 5%, whichever is greater. Data are given in Table B.8 of Appendix B.

tetrapods with MWCNTs were compared to pure CNTTs which were synthesized from the 7 FL samples by removing ZnO. The electrical conductivity of the CNTTs was slightly lower than the 7 FL samples as shown in Figure 4.23 (a). However, the

mass density varied even for samples with the same number of infiltration steps. For example, the sample '5 FL 3 mm' had a similar mass density to the 7 FL samples. The electrical conductivity was slightly lower than that of the 7 FL samples. Note that electrical conductivity requires a continuous path through the sample which might change between samples.

4.2.8.b Electrical Properties - Comparison to Literature

For a better comparison, the specific electrical conductivity, *i.e*, the electrical conductivity per unit mass density, was calculated (see Figure 4.23 (b)) and is compared here to literature values for CNT bulk materials. The electrical conductivity is affected by the mass density and with decreasing mass density the electrical conductivity should decrease as well. It is supposed that electrons flow only in the MWCNTs and the contribution of the electrical conductivity of ZnO can be neglected due to its relatively low electrical conductivity ($\sim$0.1 S m^{-1} for fully dense ZnO at 300 K [248]). The electrical conductivity in ZnO can increase with the impurity concentration, *i.e.*, doping level, which can lead to a wide range of electrical conductivities. A 40% lower specific electrical conductivity was measured for the ZnO tetrapods with MWCNTs compared to the specific electrical conductivity of CNTTs. CNTTs consists only of MWCNTs while ZnO contributes to the mass density but not significantly to the electrical conductivity. In comparison to literature values for bulk CNTs, ZnO tetrapods with CNTs indicated a lower room-temperature electrical conductivity than CNT arrays (23 S m^2 kg^{-1} [221]) and CNT sheets (51 S m^2 kg^{-1} [223]). (The specific electrical conductivities are given in Table 4.5.) The lower electrical conductivity in the present samples, in particular in the CNTTS, can be a result of the randomly orientation of the MWCNTs on the ZnO tetrapods whereas the CNT in CNT arrays and CNT sheets were aligned.

Niven *et al.* showed that defects in the MWCNTs can decrease the electrical conductivity as found for CNT yarns [222]. (When the CNT yarns were annealed to 2700 °C and the defect concentration in the CNTs decreased, the high electrical conductivity was twice that of the pristine sample [222].) The defect concentrations of the present MWCNTs on the ZnO tetrapods were determined using Raman

spectroscopy. The most important peaks to delineate the defect concentration in CNTs using Raman spectroscopy are the defect-induced D peak and the G peak at 1596 cm^{-1} where the label G refer to graphite [249]. The frequency of the D peak depends on the energy of the laser, E_{las}. A frequency of 1350 cm^{-1} was found for the D peak with a laser energy of 2.41 eV and the frequency changes with laser energy by 53 cm^{-1} eV [250]. A laser energy of 2.33 eV was used to acquire the Raman spectrum of MWCNT-coated ZnO with 7 FL. The frequencies of the D (1336 cm^{-1}) and G (1584 cm^{-1}) peaks were slightly lower than the expected values of 1345 cm^{-1} and 1596 cm^{-1}. For the quantification of the defect concentration in the MWCNTs the ratio of the intensities of G, I_G, and D, I_D, peaks was used. The ratio of the MWCNT-coated ZnO tetrapods was 0.8 which is lower than CNT sheets ($I_G/I_D \sim 1.3 - 2.5$ depending on E_{las}) [223] and CNT yarns ($I_G/I_D \sim 1.8 - 7.5$ with different annealing) [222]. Pimenta *et al.* have shown that the ratio depends on the laser energy in graphitic materials and for a more comparable analysis the crystallite size, L_c, can be calculated by [251]

$$L_c = \frac{560 \text{ nm eV}^{-4}}{E_{las}^4} \left(\frac{I_G}{I_D} \right). \tag{4.11}$$

A crystallite size of ∼15 nm was calculated which is lower than for CNT sheets ($L_c \sim$ 25-50 nm) [223] and CNT yarns ($L_c \sim$ 30-115 nm) [222]. Therefore, the small I_G/I_D ratio and crystallite sizes of the MWCNTs on the ZnO tetrapods indicate that the MWCNTs contain many defects resulting most likely in a decrease in the electrical conductivity.

It can be concluded that mostly the MWCNTs contribute to the electrical conductivity of the MWCNT-coated ZnO tetrapods whereas ZnO has insulating behavior. The electrical conductivity of the MWCNTs was not as high as in bulk CNT materials which might be due to randomly ordering of the MWCNTs and/or the high defect concentration in the MWCNTs.

4.2.8.c Thermal Conductivity - Results

In addition to the electrical conductivity, the thermal conductivity of ZnO tetrapods with various MWCNT content was investigated as a function of temperature (see Figure 4.25). While the electrical conductivity increased with the number of

Table 4.5: Specific electrical conductivity, σ_{el}/ρ, and specific thermal conductivity, κ/ρ of ZnO, various CNT bulk materials, and various ZnO tetrapods at room temperature.

Sample	σ_{el}/ρ / S m^2 kg^{-1}	κ/ρ W cm^2 kg^{-1} K^{-1}	Reference
Pure ZnO	0.15	2.8-95.1	[245, 246, 248]
CNT arrays	23	200	[221]
CNT sheets	51	650	[223]
CNT fibres	N/A	12,200	[224]
Pristine ZnO tetrapods	N/A	2.9-4.1	Present study
Metal oxide-coated ZnO tetrapods	N/A	1.6-3.2	Present study
ZnO tetrapods + MWCNTs (2 FL)	0.01-0.03	6.6-8.2	Present study
ZnO tetrapods + MWCNTs (5 FL)	0.05-0.07	7.6-9.4	Present study
ZnO tetrapods + MWCNTs (7 FL)	0.07-0.09	9.9-10.2	Present study
CNTTs	0.28±0.03	8.8±2.6	Present study

infiltration steps over the entire temperature range, the same trend was only observed for thermal conductivity at high temperature ($T > 300$ K). At low temperature, the thermal conductivity varied between samples with the same infiltrations indicating that the thermal conductivity of the ZnO tetrapods dominated at low temperature while the thermal conductivity of the MWCNTs contributed significantly to the thermal conductivity at high temperature. The low-temperature thermal conductivity showed that some samples were more crystalline than other samples, leading to a higher thermal conductivity for the former. Based on Equation 2.14, the thermal conductivity is a product of the heat capacity per unit volume, the group velocity, and the phonon mean free path. While the heat capacity increases with temperature and the group velocity is nearly temperature-independent, the phonon mean free path first dramatically increases due to the normal processes. However, with increasing temperature, longer phonon mean free paths can create phonons larger than the first Brillouin zone resulting in phonons with wave vectors opposite to that of the initial phonons. Reduction of the phonon mean free path would counteract the increase in heat capacity and therefore, the thermal conductivity generally decreases at high temperature. The increase of the thermal conductivity at low temperature is highly dependent on

crystallinity. The highest crystallinity was found for the '2 FL 3 mm(2)' sample as shown in Figure 4.25 (b). The thermal conductivity in this sample peaked at ∼80 K which is at a higher temperature than for the thermal conductivity of ZnO single-crystals ($T \sim 10$ K) [252]. Although some of the present samples showed high crystallinity, the phonon mean free path is most likely limited by the small dimensions of the tetrapods. Larger tetrapods or enhanced interconnection of the ZnO tetrapods might increase the crystallinity and hence the thermal conductivity at low temperature.

The thermal conductivity of the CNTTs increased linearly with temperature to about 300 K. Above 300 K, the thermal conductivity increased more rapidly, but that might be due to blackbody radiation. The low thermal conductivity of the CNTTs was most likely intrinsic and not caused by microcracks in the sample because the electrical conductivity is in the expected range similar to that of 7 FL samples (see Figure 4.23 (a)).

In the MWCNT-coated samples, the thermal conductivity of the MWCNTs add to the thermal conductivity of ZnO. In particular above 100 K, the ZnO tetrapods with MWCNTs presented different trends depending on the MWCNT content. While for $T > 100$ K, the thermal conductivity of the 2 FL samples decreased with temperature, the thermal conductivity of the 5 FL and 7 FL samples are nearly temperature-independent. Note that the thermal conductivity is not a simple sum of the thermal conductivity in the ZnO tetrapods and the MWCNTs. The difference between the thermal conductivities of the 2 FL and 7 FL samples was about twice as large as the thermal conductivity of the CNTTs; see Figure 4.25 (a).

4.2.8.d Thermal Conductivity - Comparison to Literature

To compare the thermal conductivity with literature values of CNT bulk materials and metal oxide-coated ZnO tetrapods, the specific thermal conductivity was calculated from the thermal conductivity and the mass density of the pellets (see Figure 4.25 (b)). Although the specific thermal conductivity was dominated by the MWCNT content at high temperature, the differences between the 7 FL samples and the 2 FL slightly decreased compared to the thermal conductivity shown in Figure 4.25 (a). Below 250 K CNTTs have a lower specific thermal conductivity than ZnO tetrapods

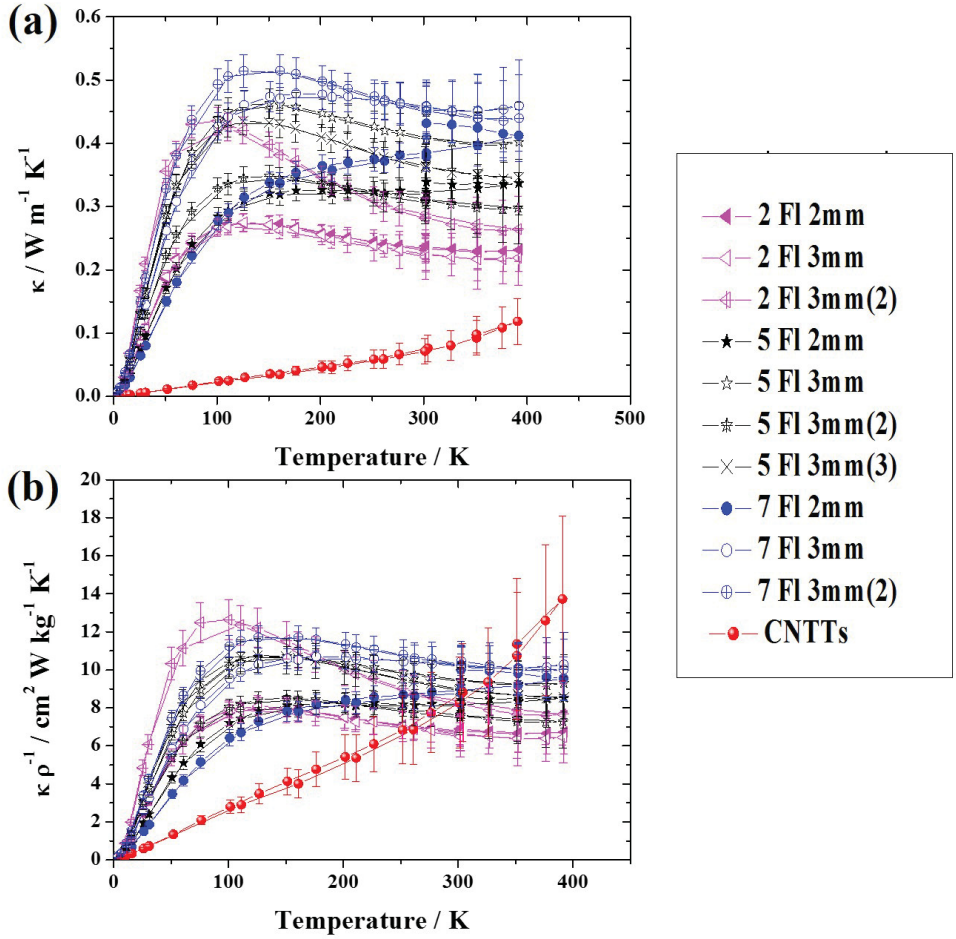

Figure 4.25: Thermal conductivity of ZnO tetrapods with MWCNTs and CNTTs. (a) Low-temperature thermal conductivity is nearly independent of the MWCNT content whereas high-temperature thermal conductivity increases with the number of infiltration steps. (b) Specific thermal conductivity (*i.e.*, thermal conductivity per unit mass density) indicates that the thermal conductivity of ZnO is dominant at low temperature. The uncertainty was calculated from the geometry and measurement methods or 5%, whichever is greater. Data are given in Tables B.9-B.12 of Appendix B.

with MWCNTs.

While the specific thermal conductivities for most ZnO samples were temperature-independent or even decreasing above 150 K, the specific thermal conductivity of CNTTs increased with temperature throughout the entire range and exceeded the specific thermal conductivity of ZnO tetrapods with MWCNTs at 350

K. In comparison to pure CNT bulk materials, the ZnO tetrapods with MWCNTs and CNTTs have many orders of magnitude lower room-temperature specific thermal conductivity than CNT arrays (200 W cm^2 kg^{-1} K^{-1} [221]), CNT sheets (650 W cm^2 kg^{-1} K^{-1} [223]) and CNT fibres (12,200 W cm^2 kg^{-1} K^{-1} [224]). The reduction of the specific thermal conductivity in the ZnO tetrapods with MWCNT might be due to the random orientation of the MWCNTs on the tetrapods which most likely also limited their electrical conductivity. The thermal conductivity might increase with alignment of the CNTs. The specific thermal conductivity of pure ZnO ranges between 2.8 to 95.1 W cm^2 kg^{-1} K^{-1} [245, 246] which encompasses the present experimental results. Furthermore, the specific thermal conductivities of 2 FL samples (6.6-8.2 W cm^2 kg^{-1} K^{-1}) were slightly higher than that of pristine (2.9-4.1 W cm^2 kg^{-1} K^{-1}) and metal oxide-coated ZnO tetrapods (1.6-3.2 W cm^2 kg^{-1} K^{-1}) demonstrating that thermal conductivity results from the powder cell were consistent with the thermal conductivity using the standard TTO method.

4.2.9 Conclusions

In the first part of this section, the thermal conductivity of pristine and metal oxide-coated ZnO tetrapods was presented. Due to their unique morphology and low stiffness, it was not feasible to use the standard TTO method and therefore, a lab-developed powder cell was used for the first time. The heat transfer of the empty powder cell was verified with finite element simulations. The thermal conductivity of the pristine and metal oxide-coated ZnO tetrapods range between 0.07 to 0.18 W m^{-1} K^{-1} which was in agreement with the computed thermal conductivity for randomly oriented ZnO tetrapods. The finite element simulations revealed that blackbody radiation in ZnO tetrapods does not significantly contribute to the heat transfer and that the thermal conductivity of the tetrapods was related to the arrangement of the tetrapods. Although the temperature range is limited with the powder cell due to the thermal expansion of the cell, the powder cell can be used to determine the thermal conductivity of various loosely packed powders. This can be applied to reduce the heat transfer in 'true' vacuum or in buildings due to a decrease in convection and blackbody radiation.

In addition to metal oxide-coated ZnO tetrapods measured in the powder cell,

the electrical and thermal conductivities of ZnO tetrapods coated with MWCNTs were measured with the standard TTO method due to an increase in stability of these samples. Low thermal and electrical conductivities were found for the ZnO tetrapods with MWCNTs. While the electrical conductivities were mostly dependent on the MWCNT content from 2 K to 390 K, the thermal conductivity was dominated by the crystallinity of the ZnO tetrapods. Furthermore, the electrical conductivity increased with mass density and reducing sample thickness due to an increase and homogeneous distribution of the MWCNTs in the ZnO tetrapods samples. The samples were also compared to CNTTs (prepared by ZnO-removal from MWCNT-coated ZnO tetrapods) indicating similar electrical conductivity to ZnO tetrapods with MWCNTs. However, CNTTs exhibited a lower thermal conductivity than the tetrapod samples indicating that ZnO is electrical insulating and thermally conductive. MWCNT coated ZnO tetrapods can enhance the mechanical and electrical properties compared to ZnO tetrapods. However, further enhancement of the MWCNT coating (*e.g.*, improved aligned CNT on the tetrapods and a reduction of the number of defects in the MWCNTs) is required for potential applications, such as thermistors due to their constant temperature behavior or gas sensors as reported for metal oxide-coated ZnO tetrapods [213, 214].

Chapter 5

Thermoelectric Materials

High-performance thermoelectric materials require enhanced electronic properties as well as low heat transport. Due to the fact that all thermoelectric properties are interdependent and linked by the carrier concentration, n, it is challenging to discover new high-performance thermoelectric materials. Computational investigations can accelerate the discovery and can also provide useful directions to enhance the properties of these thermoelectric materials. While the electrical properties can be calculated with a high accuracy, accurate prediction of heat transport is currently not feasible. However, insight concern in the heat transport can be given by computing the lowest limit of heat transport using the present minimum thermal conductivity (see Section 4.1). Using first-principle calculations, two potential high-performance thermoelectric classes, XYZ_2 with X, Y as rare earth or transition metals and Z as group VI element, and metal phosphides, were predicted by 'The Materials Project' [48].

The first section of this chapter describes three different compounds of the XYZ_2 class, $TmAgTe_2$, $YAgTe_2$, and $YCuTe_2$ with intrinsic and extrinsic doping, including synthesis and investigation of thermoelectric properties. However, for the calculated thermoelectric performance a constant relaxation time and a fixed thermal conductivity was assumed which might overestimate the performance of the thermoelectric materials.

In the second section, the computational approach to predict the thermoelectric performance of metal phosphide was modified. For the computation of the thermal conductivity, the present minimum thermal conductivity model and other models were used. Furthermore, the thermoelectric properties were computed with a variable relaxation time, enhancing the prediction of the properties at high temperature.

As an example of the metal phosphide class, NiP_2 in the cubic phase was synthesized and the physical properties were characterized.

In addition to the novel thermoelectric classes, germanium type II clathrates with partially sodium-filling were synthesized in a solid-gas reaction and the thermoelectric properties were investigated.

5.1 Novel Thermoelectric Class XYZ_2[1]

5.1.1 Introduction

The search for novel thermoelectric materials with high performance can be challenging using an experimental route due to the complex interdependency of the thermoelectric properties. In particular, the electronic properties are highly dependent on the carrier concentration and the electronic band structure. For enhanced thermoelectric properties, optimization of the carrier concentration and multiple valley degeneracy in the electronic band structure are required [253]. A potential way to reveal new high-performance thermoelectric materials is using first-principle calculations, *e.g.* based on density functional theory (DFT). In recent years, DFT has become a common technique to compute electronic band structures and with this approach several promising new materials have been already discovered for batteries [36, 37], photocatalysts [38], and solar cells [254]. With the exponential growth of computing power, it is getting more feasible to reveal new materials with unique electronic properties using first-principle calculations.

Several computational studies on various thermoelectric families, such half- [39]

[1]Parts of this section were adapted from: H. Zhu, G. Hautier, U. Aydemir, Z. M. Gibbs, G. Li, S. Bajaj, J.-H. Pöhls, D. Broberg, W. Chen, A. Jain, M. A. White, M. Asta, G. J. Snyder, K. Persson, and G. Ceder, 'Computational and experimental investigation of $TmAgTe_2$ and XYZ_2 compounds, a new group of thermoelectric materials identified by first-principles high-throughput screening', *Journal of Materials Chemistry C*, 2015, **3**, 10554–10565, DOI: 10.1039/C5TC01440A - Reproduced by permission of the Royal Society of Chemistry; and from U. Aydemir, J.-H. Pöhls, H. Zhu, G. Hautier, S. Bajaj, Z. M. Gibbs, W. Chen, G. Li, S. Ohno, D. Broberg, S. Dongmin Kang, M. Asta, G. Ceder, M. A. White, K. Persson, A. Jain, and G. Jeffrey Snyder, '$YCuTe_2$: a member of a new class of thermoelectric materials with $CuTe_4$-based layered structure', *Journal of Materials Chemistry A*, 2016, **4**, 2461–2472, DOI: 10.1039/C5TA10330D - Reproduced by permission of the Royal Society of Chemistry. The author's contributions were the synthesis, the characterization (PXRD, SEM, WDS), and the investigation of the thermoelectric properties at high temperature with the assistance of Dr. Umut Aydemir; DSC; heat capacity measurements; low-temperature transport properties; and writing the characterization sections of the manuscripts and the transport property in the $YCuTe_2$ manuscript. The synthesis and all measurements were performed in the laboratory of Dr. G. Jeffrey Snyder, California Institute of Technology, unless stated otherwise. Previously published diagrams are note by quoting the source; otherwise the information is based on the author's new analysis.

and full Heusler compounds [40], transition metal silicides [41], zinc antimonides [42, 43], and sulfides [44], have already been performed to predict their electronic properties. In addition to the thermoelectric families, the thermoelectric properties were predicted from high-throughput studies using first-principle calculation (*e.g.*, TE Design Lab [45, 46]) or machine learning (*e.g.*, Citrine [47]). While the TE Design Lab computes the electronic band structure and calculates a material-dependent beta-factor from the band structures (further discussed in Section 5.2.2), Citrine predicts the goodness of the thermoelectric properties based on the composition and comparing it to the properties of similar compounds reported in literature. However, thermoelectric properties depend on the crystal structure as well as the doping (level and *p*- or *n*-type) and a full electronic band structure analysis is required to enhance the prediction of the electronic properties.

'The Materials Project' computes the electronic band structure of inorganic compounds [48] and the electronic properties are calculated with the Boltzmann transport equations using the software BoltzTrap [49]. In a recent high-throughput screening of 'The Materials Project', the thermoelectric properties of over 9,000 inorganic compounds were computed with the assumption of constant relaxation time for electron scattering and a fixed phononic thermal conductivity ($\kappa_{pho} = 0.5$ W m^{-1} K^{-1}). From this screening, more than 500 candidates with the nominal composition of XYZ_2 (X, Y: rare earth or transition metals; Z: group VI element) revealed potential high thermoelectric performance. In a study separate from 'The Materials Project', Lin *et al.* reported enhanced thermoelectric properties in $TmCuTe_2$ with a thermoelectric figure of merit of 0.81 at 745 K [255].

In this section, the thermoelectric properties of three XYZ_2 materials, $TmAgTe_2$, $YAgTe_2$, and $YCuTe_2$, were investigated and compared to the computed data. Furthermore, the computational results were verified with experimental methods (*i.e.*, UPS/IPES for the electronic DOS, and heat capacity for the phononic DOS) to enhance the prediction of the thermoelectric properties for further studies.

5.1.2 Computation

5.1.2.a Methodologies

The electronic band structure calculations were performed by 'The Materials Project' [48] and by Dr. Hong Zhu and Zhe Luo, School of Materials Science and Engineering, Shanghai Jiao Tong University, using the Vienna Ab initio Simulation Package (VASP) [256] with the Perdew-Burke-Ernzerhof (PBE) generalized gradient approximation (GGA) [51] and projector augmented-wave (PAW) [52] method to model core electrons. For f-electrons in Tm, the valence electrons were set to 3 while modelling the other electrons with pseudopotentials. Electron occupation was smeared with a Gaussian smearing function. For the density of states (DOS), the tetrahedron method (*i.e.*, the Brillouin zone divided into irreducible tetrahedra to reduce the number of k points without changing the accuracy of the calculation) with Blöchl corrections was used [257]. To enhance the prediction of the band gap energy, the electronic band structures also were computed with the hybrid functional HSE06 [258, 259]. In the high-throughput screening, the electronic properties were computed with no spin orbit coupling (NSOC) which can introduce uncertainty, in particular for heavy elements, such as tellurium and lanthanides. Spin orbit coupling (SOC) is a relativistic correction for the interaction between the orbital angular momentum of the nucleus and the electron spin angular momentum. Including SOC in the electronic band structure calculations, degenerate electron bands can split which could have a significant effect of the electronic properties. All electronic properties were calculated by 'The Materials Project' using the Boltzmann transport equations in the software BoltzTrap [49] and a constant relaxation time of $\tau_{el} = 10^{-14}$ s. More information about the Boltzmann transport equations can be found in Section 2.6.

A 6 $\times$ 6 elastic tensor, c_{ij}, was calculated from first-principles calculations as described by de Jong *et al.* [260]. In the first step the crystal structure was relaxed to obtain zero stress, followed by deformation in six independent directions with four different magnitudes ($\pm$0.5% and $\pm$1 %). The stress tensor was calculated from the derivative of the total energy over the applied strain and the elastic tensor was fitted from the 24 stress-strain pairs with a linear least-square fit [260]. The bulk,

B_{VRH}, and shear moduli, G_{VRH}, were calculated from the elastic tensor using the Voigt-Reuss-Hill average [261] given by

$$B_{VRH} = \frac{([c_{11} + c_{22} + c_{33}] + 2[c_{12} + c_{23} + c_{31}])/9}{2} + \frac{([s_{11} + s_{22} + s_{33}] + 2[s_{12} + s_{23} + s_{31}])^{-1}}{2} \tag{5.1}$$

and

$$G_{VRH} = \frac{([c_{11} + c_{22} + c_{33}] - [c_{12} + c_{23} + c_{31}] + 3[c_{44} + c_{55} + c_{66}])/15}{2} + \frac{(4[s_{11} + s_{22} + s_{33}] - 4[s_{12} + s_{23} + s_{31}] + 3[s_{44} + s_{55} + s_{66}])^{-1} \cdot 15}{2}, \tag{5.2}$$

respectively [260]. The elements $s_{ij} = c_{ij}^{-1}$ give the compliance. More information about the calculation of mechanical properties using first-principle calculations can be found in reference [260].

The thermodynamic stability was computed by comparing the total energy of the phase to the total energy of other phases at absolute zero temperature and zero pressure. The decomposition energy, E_{decomp}, was defined as the difference in computed ground state energy between the compound and competing phases. In this sense, the ground state energy is connected to all ground state phases in an energy-composition diagram [48]. A decomposition energy equal to zero would correspond to stable compounds whereas large decomposition energies point to unstable compounds. However, it is important to note that small decomposition energies can be stabilized at elevated temperature by entropy effects or by metastable synthesis methods. All computations and data analyse were carried out using the high-throughput calculation software developed in Python: pymatgen [262], FireWorks [263, 264], and atomate (available at https://github.com/hackingmaterials/atomate).

For the computation of the defect formation energy, $\Delta H_{d,q}$, (*i.e.*, the energy of a defect with charge, q) in $TmAgTe_2$, the Zhang-Northrup supercell formalism [265] was used

$$\Delta H_{d,q} = |E_{d,q} - E_b| + \sum_{\alpha} n_{\alpha}(\mu_{\alpha}^0 + \Delta\mu_{\alpha}) + q(E_{VBM} + V_{PA} + \mu) + \Delta E_{IC} \tag{5.3}$$

where the first term is the total energy difference between the defect containing supercell, $E_{d,q}$, and the ideal supercell, E_b. The second term describes the crystal

growth conditions with μ_α^0 and $\Delta\mu_\alpha$ as the chemical potential of an element in its standard reference state ($T = 0$ K; $P = 0$ Pa) and the change in chemical potential of an element with reference to its standard state, respectively. The parameter n_α can be +1 (removing an atom) or -1 (adding an atom to the host supercell in the formation of a defect). The energy to remove an electron from the top of the valence band is described in the third term, where E_{VBM} is the valence band maximum energy, μ is the chemical potential of the removed electron, and V_{PA} is the correction of the alignment of the electrostatic potential. The parameter E_{IC} is the image-charge correction energy which can be calculated together with the electrostatic potential alignment correction with the method of Freysoldt, Neugebauer, and Van de Walle [266]. In their scheme, electrons are added or removed from a defect state introducing a charge in a single defect. The other electrons are frozen to avoid polarization but the electrons are allowed to screen the charge of the defect leading to a change in electrostatic potential with respect to the neutral defect [266]. Furthermore, a homogeneous background charge is introduced over the volume of the supercell. The electrostatic potential alignment can be determined from the electrostatic potential difference between a 'bulk-like' region (*i.e.*, a region far away from the point defect) and the perfect crystal [267].

The defect formation energy calculations of $TmAgTe_2$ in the trigonal phase (space group $P\bar{3}m1$) were performed on a $3 \times 3 \times 2$ supercell with 72 atoms. For the computation, the calculated dielectric constant of 23.15 was applied in the Freysoldt, Neugebauer, and Van de Walle scheme. It is important to note that the f-electrons were not considered as valence electrons due to high computational cost. The f-electrons might reduce the defect formation energy. However, the trend was confirmed for $YAgTe_2$ which does not contain f-electrons.

The phononic dispersion curves were calculated by Dr. Hong Zhu and Zhe Luo, School of Materials Science and Engineering, Shanghai Jiao Tong University, using the frozen phonon method implemented in the software package Phonopy [60]. Long range van der Waals interactions in the layered structure of $TmAgTe_2$ and $YAgTe_2$ were corrected with the DFT-D3 method [268]. The lack of inter-layer interactions can result in an overestimation of the inter-layer distance reducing the accuracy of the computations. The importance of inter-layer interactions is reported in several papers

[269, 270]. While the lattice parameters of $YAgTe_2$ and $TmAgTe_2$ were computed with van der Waals interaction, the lattice constants of $YCuTe_2$ were taken from experiments and no van der Waals interactions were considered.

In a high-throughput screening within 'The Materials Project', more than 500 candidates of a novel thermoelectric class were revealed, namely trigonal and tetragonal XYZ_2 where X and Y are rare-earth or transition metals and Z is a group VI element, such as oxygen, sulphur, selenium, or tellurium (see Figure 5.1 and Figure 5.2). In the high-throughput screening, the thermoelectric figure of merit, zT, was calculated from the electronic results using the BoltzTrap code [49] and the phononic contribution of the thermal conductivity was set to an arbitrary value of 0.5 W $m^{-1}K^{-1}$. Although set to a relative low value, extremely low thermal conductivity was reported for various selenides, such as CdSe ($\kappa \sim 0.2$ W m^{-1} K^{-1}) [150] and SnSe ($\kappa \sim 0.23$ W m^{-1} K^{-1}) [26, 27]. In addition to the selenides, low thermal conductivity, similar to the amorphous limit [66, 67], has also been reported for some silver chalcogenides, *e.g.*, Ag_2Te [271], AgCrSe [154], and $AgSbTe_2$ [272], as well as copper chalcogenides, *e.g.*, $CuGaTe_2$ [273], Cu_2Se [274], Cu_2S [275], and $CuInTe_2$ [276]. The set thermal conductivity was verified with experiments where the phononic contribution of the thermal conductivity in all investigated XYZ_2 compounds was found to be equal or lower than 0.5 W $m^{-1}K^{-1}$ (*vide infra*).

5.1.2.b High-Throughput Screening Results

The crystal structures of XYZ_2 are all anisotropic, and reported zT values were averaged over three crystallographic directions. Figure 5.1 and Figure 5.2 show the theoretical p-type zT and n-type zT, respectively, of various sulfides, selenides, and tellurides XYZ_2 compounds at 600 K and a carrier concentration of 10^{20} cm^{-3}. In both figures it is shown that the trigonal phase had a higher predicted zT than the tetragonal phase. The discrepancy between the thermoelectric properties of the trigonal and tetragonal phase can be described by the crystal structure. While X and Y occupy octahedral (oh) interstices in the trigonal phase, represented as $X^{oh}Y^{oh}Te_2$, Y fills tetrahedral (th) interstices in the tetragonal phase, represented as $X^{oh}Y^{th}Te_2$ in the present study. It is important to note that Y atoms can occupy a tetrahedral interstices in the trigonal phase (*e.g.*, for Y = Cu; as discussed further below). The

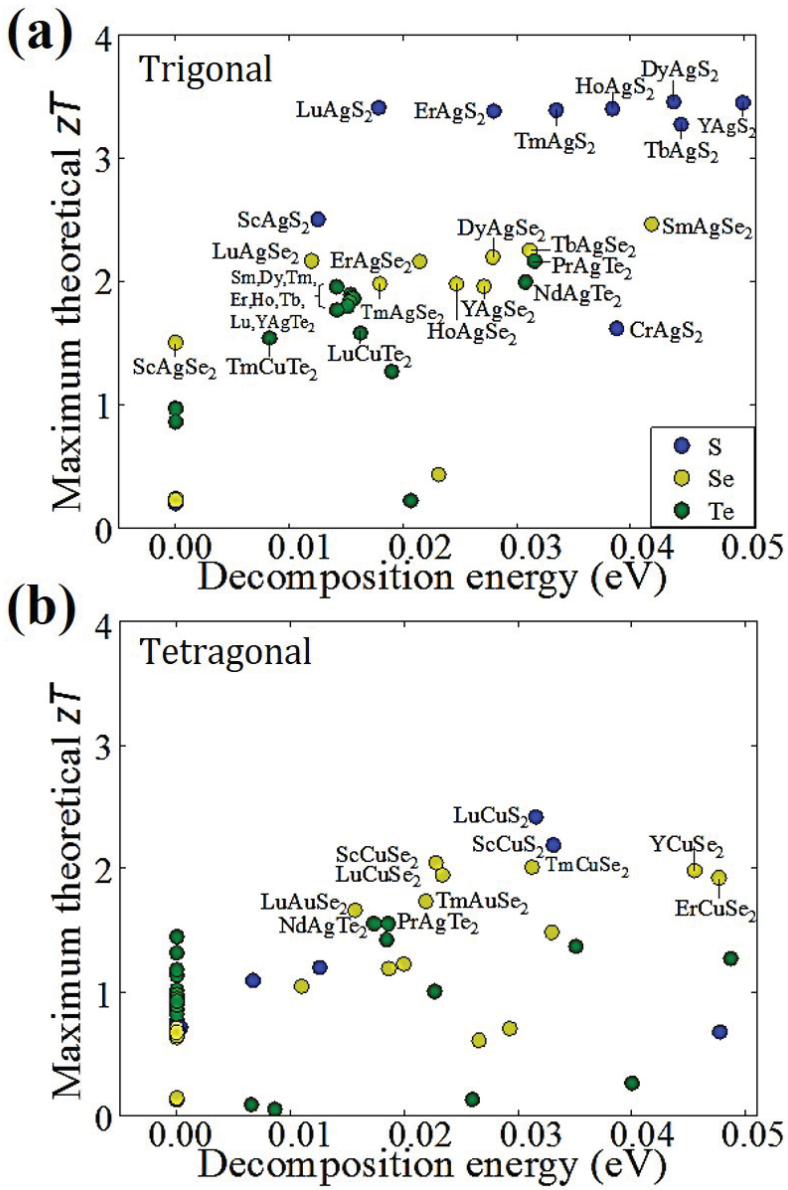

Figure 5.1: Estimated thermoelectric figure of merit, zT, using a carrier concentration of 10^{20} cm^{-3} at 600 K and decomposition energy per atom for p-type XYZ_2 compounds in the (a) trigonal phase and (b) tetragonal phase. Sulfides showed a higher zT than the corresponding selenides and tellurides but the decomposition energy increased from tellurides to sulfides indicating that sulfides are less stable). For clarity, solely the compositions of compounds with zT above 1.5 are shown and the decomposition energy was limited to 0.5 eV per atom. The electronic properties were calculated with a constant relaxation time of 10^{-14} s and the phononic contribution of the thermal conductivity was set to 0.5 W m^{-1}K^{-1}. Figure from reference [277].

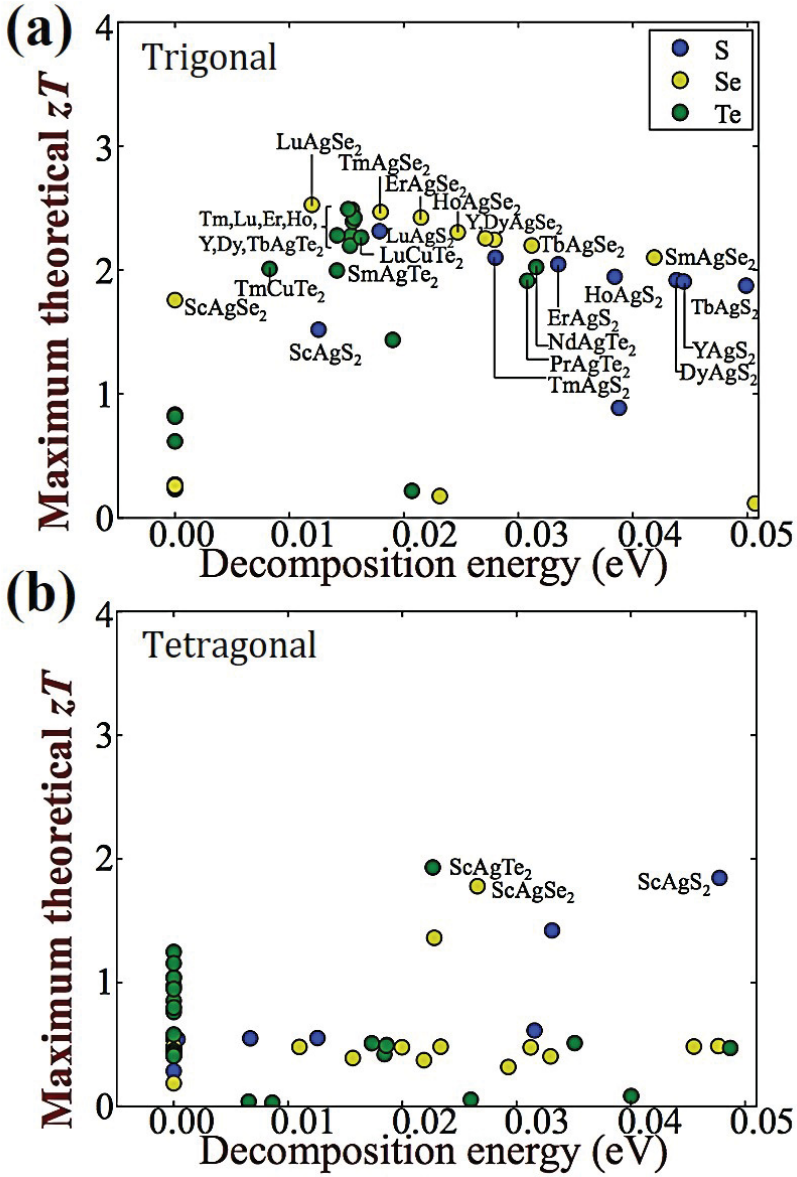

Figure 5.2: Estimated thermoelectric figure of merit, zT, using a carrier concentration of 10^{20} cm^{-3} at 600 K in relation to the decomposition energy per atom for n-type XYZ_2 compounds in the (a) trigonal phase and (b) tetragonal phase. In average, n-type zT is lower than p-type zT shown in Figure 5.1. The electronic properties were calculated with a constant relaxation time of 10^{-14} s and the phononic contribution of the thermal conductivity was set to 0.5 W m^{-1}K^{-1}. Figure from reference [277].

trigonal phase has a higher symmetry than the tetragonal phase resulting in more degenerate bands at the valence band maximum (VBM). Multiple band degeneracy

generally enhance the thermoelectric performance due to an increase in the density of state (DOS) effective mass, m^*_{DOS}, while keeping the band effective mass, m^*_b, constant [253]. As discussed in Section 2.3, the Seebeck coefficient is in general proportional to the DOS effective mass, and the electrical conductivity, in particular the mobility, is inversely proportional to the band effective mass. The relation between the DOS effective mass and band effective mass is given by the band degeneracy; see Equation 2.28. The band degeneracy does not have a large effect on the mobility, other than that the relaxation time can be limited by inter-valley scattering [278].

In addition to the higher symmetry, hybridization can influence the band degeneracy. In the case of *p*-type XYZ_2 compounds, it was found that the VBM mostly consists of $Y-d$ and $Z-p$ orbitals. If X contains *d*-orbitals, the orbitals can contribute to the $p-d$ hybridization and the band structure can change at the VBM. As shown in Figure 5.3 (a), the predicted zT largely depends on the VBM band structure. If the energy difference between the two highest VBM decreased, the thermoelectric performance improves due to an increase in band degeneracy. A higher band degeneracy at VBM was found if the hybridization of the $X-d$ and $Z-p$ orbitals in the trigonal phase and the $Y-d$ and $Z-p$ orbitals of the tetragonal phase was reduced. The VBM of XYZ_2 compounds in the tetragonal phase is dominated by the hybridization of the $Y-d$ and $Z-p$ orbitals because the hybridization is stronger in YZ_4 tetrahedra than in XZ_6 octahedra resulting in lower band degeneracies at the VBM compared to the trigonal phase. As an example, trigonal $\mathrm{Lu^{oh}Ag^{oh}}Z_2$ and $\mathrm{Lu^{oh}Cu^{oh}}Z_2$ were compared to their corresponding tetragonal compounds (see Figure 5.3 (b)). The highest zT was estimated for the sulfides, followed by selenides and tellurides of $\mathrm{Lu^{oh}Ag^{oh}}Z_2$ and $\mathrm{Lu^{oh}Cu^{th}}Z_2$. The relative positions of the atomic orbitals are given in Figure 5.3 (b) indicating a larger energy difference between the Lu-*d* and S-*p* orbitals than the other group VI elements. This leads to higher band degeneracy in the trigonal phase and therefore, the theoretical zT increases. For the tetragonal phase, Ag-*d* and Te-*p* orbitals as well as Cu-*d* and S-*p* have the weakest hybridization resulting in enhanced thermoelectric performance (see Figure 5.3 (b)). Therefore, weak $p-d$ hybridization is preferable in XYZ_2 compounds to enhance the thermoelectric performance.

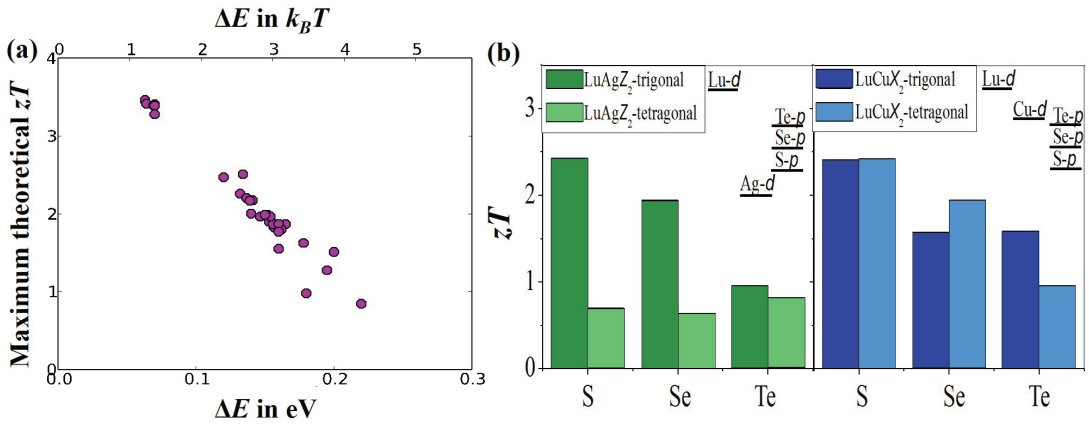

Figure 5.3: (a) Maximum theoretical p-type zT in relation to the energy difference between the two highest VBM for XYZ_2 in the trigonal phase with non-zero band gap energy. The maximum predicted zT decreases linearly with increasing energy difference between the two highest VBM. (b) Maximum estimated p-type zT of trigonal and tetragonal LuAgZ_2 and LuCuZ_2 (Z = S, Se, and Te). The relative positions of the computed orbitals for Lu-d, Ag-d, Cu-d, Te-p, Se-p, and S-p are provided to show the effect of hybridization. All zT were calculated for a carrier concentration of 10^{20} cm^{-3} at 600 K and the phononic contribution of the thermal conductivity was set to 0.5 W m^{-1}K^{-1}. Figures from reference [277].

In addition to the thermoelectric performance, the crystal structure provides information about the thermodynamic stability of the compounds. According to Pauling's first rule, the thermodynamic stability depends on the ratio of the ionic radii [279]. A smaller ionic radius ratio prefers a tetrahedral environment while an ionic radius ratio above 0.414 favors octahedral interstices [280]. The ionic radii for Ag^+ and Cu^+ are 1.00 Å and 0.60 Å, respectively, for a coordination number (CN) of four and 1.15 Å and 0.77 Å, respectively, for a CN of six [281]. The ionic radii of the group VI elements increase with increasing atomic number (S^{2-} 1.84 Å, Se^{2-} 1.98 Å, and Te^{2-} 2.21 Å) [281]. Therefore, the ionic radii ratio decreases with increasing atomic number of the group VI elements indicating that tetrahedral environment is preferable. In particular for Cu compounds, the ionic radius ratio is below the minimum ratio for octahedral environments (except for S with CN of four) and therefore, Cu generally occupies the tetrahedral interstices as shown for the trigonal $Tm^{oh}Cu^{th}Te_2$ [255] and trigonal $Y^{oh}Cu^{th}Te_2$ (*vide infra*). It is important to consider the ionic radii rather than the atomic radii for the analysis of

the thermodynamic stability. While the atomic radii of Ag and Au are the same (1.35 and 1.35 Å, respectively)[282] the ionic radius of Au^+ (1.37 Å) is about twice the ionic radius of Ag^+ (1.00 Å) [281].

It is important to note that the *p*-type theoretical zT in Figure 5.1 was even higher for XYZ_2 in the trigonal phase than the current best thermoelectric material (SnSe with a zT of ∼2.6 [26, 27]). However, all electronic properties in the high-throughput screening were computed with NSOC which can introduce uncertainty. In particular, the inclusion of SOC can dramatically influence the top of the valence band as shown in Figure 5.4. While the trigonal phase of $Tm^{oh}Ag^{oh}Te_2$ has doubly degenerate valence bands at the A symmetry point with NSOC (Figure 5.4 (a)), these bands split by 0.2 eV with the inclusion of SOC (Figure 5.4 (b)). Furthermore, SOC leads also to an increase in energy difference between the two highest valence bands (at symmetry points A and Λ) by ∼0.15 eV compared to the NSOC band structure resulting in a reduction of the thermoelectric performance as depicted in Figure 5.3 (a). A smaller valence band splitting was observed for tetragonal $Tm^{oh}Ag^{th}Te_2$ at the Γ point (∼0.1 eV compared to the NSOC electronic band structure).

The influence of the inclusion of SOC in selenides (*e.g.*, $Pr^{oh}Ag^{oh}Se_2$) is smaller than in tellurides. The valence bands at the A symmetry point split by ∼0.2 eV with SOC compared to NSOC band structure (see Figure 5.4 (c) and (d), respectively) resulting in an increase of the energy difference of the valence band maxima at the A and Γ symmetry point by 0.06 eV. The effect of SOC is negligible for the valence band maxima in sulfides as shown by the example of $Y^{oh}Ag^{oh}S_2$ in Figure 5.4 (e) and (f).

It can be concluded that high thermoelectric performance was predicted for XYZ_2 compounds in a high-throughput screening. High thermoelectric performance was obtained when the $p-d$ hybridization was weak at the valence band maximum. In particular, trigonal XYZ_2 compounds revealed high theoretical zTs due to degenerate bands computed with NSOC. However, SOC can influence the band degeneracy, especially for *p*-type tellurides, and therefore, the thermoelectric performance might be reduced. For example in $Tm^{oh}Ag^{oh}Te_2$, the predicted power factors reduced with the inclusion of SOC. Whereas a predicted average power factor of ∼6.7 mW $m^{-1}K^{-2}$ was calculated for NSOC band structures with a carrier

concentration of 10^{20} cm^{-3} at 600 K, the estimated power factor is reduced by more than a third to ∼4.2 mW m^{-1}K^{-2}. The predicted value is still high but it has to be considered that a constant relaxation time (set to 10^{-14} s) was used for the calculations of the electronic properties which most likely overestimates the thermoelectric performance at high temperature. The relaxation time generally decreases with temperature due to increasing electron-phonon interactions.

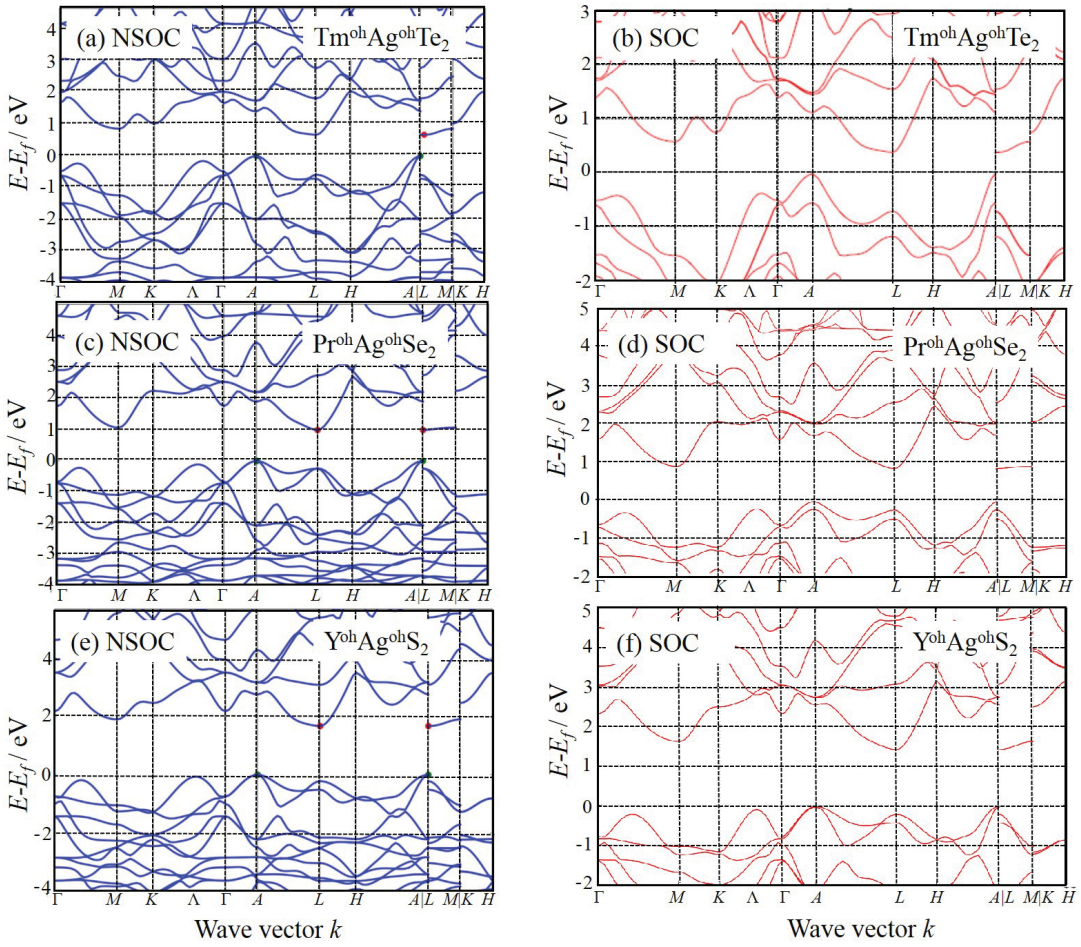

Figure 5.4: Electronic band structure calculations using PBE-GGA with spin orbit coupling (SOC) and no spin orbit coupling (NSOC) for (a,b) Tm^{oh}Ag^{oh}Te$_2$, (c,d) Pr^{oh}Ag^{oh}Se$_2$, and (e,f) Y^{oh}Ag^{oh}S$_2$. While a large split of the valence bands at symmetry point A was observed for tellurides with the inclusion of SOC, the SOC effect is reduced with decreasing atomic numbers. Figures from reference [277].

5.1.3 Synthesis

For the present study, three different tellurides of the XYZ_2 class were synthesized. Although a higher thermoelectric performance was predicted for sulfides (see Figure 5.1), tellurides have several advantages. On the one hand, tellurides can be easier to synthesize with solid state methods due to the high vapor pressure of sulfur which might result in large pressures at elevated temperature. Furthermore, it is less challenging to dope smaller band gap materials than large band gap materials [58]. In a large high-throughput screening it was found that the band gap decreases on average from sulfides to tellurides indicating preferable dopability in tellurides [35]. In addition to the synthesis and the dopability, the thermal conductivity was assumed to be lower than in sulfides [35] because lighter atoms generally have higher thermal conductivity than heavy atoms resulting in lower zTs [57]. As described above, the phononic contribution of the thermal conductivity was set to a constant value and was not computed in this part of the study.

The three XYZ_2 tellurides, $TmAgTe_2$, $YAgTe_2$, and $YCuTe_2$, were synthesized by a solid-state method similar to the synthesis route previously reported by Gulay *et al.* [283, 284]. Furthermore, they were intrinsically (*i.e.*, changing the composition of the compound) and extrinsically (*i.e.*, substituting an element of the XYZ_2 compound with another element) doped to add or remove free carriers and enhancing, therefore, the carrier concentration.

5.1.3.a $TmAgTe_2$

Polycrystalline $TmAgTe_2$ and extrinsically Mg-doped and Zn-doped $TmAgTe_2$ were synthesized with the assistance of Dr. Umut Aydemir in the laboratory of Dr. G. Jeffrey Snyder, California Institute of Technology, by sealing stoichiometric amounts of the elements (Tm pieces [99.9% purity, metal basis, Alfa Aesar]; Ag pieces [99.999% purity, metal basis, Alfa Aesar]; Te pieces [99.999% purity, metal basis, Alfa Aesar]; Mg slug [99.95% purity, metal basis, Alfa Aesar]; and Zn shot [99.999% purity, metal basis, Alfa Aesar]) with a total mass of 3.5 g in quartz ampoules ($\sim$30 cm length, 12.8 mm in diameter, and wall thickness of 1.1 mm) under high vacuum ($\sim 10^{-6}$ mbar). The elements were placed in the ampoule with decreasing melting point (*i.e.*, the element with the lowest melting point on the top) to avoid outgassing of

elements with high vapor pressures, *e.g.* Zn, and to enhance mixing of the elements. The ampoule was slowly heated in a vertical tube furnace to 1443 K over 30 h and annealed at that temperature for 15 h. The ampoule was slowly cooled to 873 K over 30 h and annealed at that temperature for one week. The ampoule was quenched in water to room temperature and was opened in an argon-filled glovebox. The ingots were hand-ground to get a ∼1.5 g fine powder which was filled into a 1.27 cm diameter high-density graphite die (POCO). The powder was sintered in a rapid hot press using RF induction heating [285] at 973 K under a pressure of 40 MPa for 1 hour and cooled to room temperature over 2 h. The rapid hot press has the advantages that it has a fast heating rate and the system size is relatively small. More information about the rapid hot press can be found in reference [285]. All steps were performed under argon atmosphere to avoid oxidation of the elements or the compressed pellet.

5.1.3.b $YAgTe_2$

Polycrystalline $YAgTe_2$ and an intrinsically doped sample ($Y_{0.98}Ag_{1.02}Te_{1.98}$) were synthesized with the assistance of Dr. Umut Aydemir in the laboratory of Dr. G. Jeffrey Snyder, California Institute of Technology, using a procedure similar to $TmAgTe_2$. Stoichiometric amounts of the elements (Y pieces [99.9% purity, metal basis, Alfa Aesar]; Ag pieces [99.999% purity, metal basis, Alfa Aesar]; Te pieces [99.999% purity, metal basis, Alfa Aesar]) with a total mass of 3.5 g were sealed in an quartz ampoule (∼30 cm length, 12.8 mm in diameter, and wall thickness of 1.1 mm) under high vacuum (∼10^{-6} mbar). The ampoule was heated in a vertical tube furnace to 1443 K in 40 h and annealed at that temperature for 15 h. The ampoule was slowly cooled to 473 K over 45 h and then the tube furnace was turned off. The sample was hand-ground to fine powder in a glove box and ∼1.5 g powder was filled into a 1.27 cm diameter high-density graphite die (POCO), followed by sintering to 873 K under a pressure of 80 MPa for 1 h in a rapid hot press and annealing at 673 K for 1 h in the rapid hot press. The consolidated sample was cooled to room temperature over two hours.

5.1.3.c $YCuTe_2$

Polycrystalline $YCuTe_2$ and various intrinsically doped samples ($YCu_{0.96}Te_2$, $YCu_{1.04}Te_2$, $YCu_{1.08}Te_2$, $Y_{0.96}Cu_{1.08}Te_2$, and $Y_{0.98}CuTe_2$) were synthesized with the assistance of Dr. Umut Aydemir in the laboratory of Dr. G. Jeffrey Snyder, California Institute of Technology, using a solid-state method. For the synthesis of the compounds, stoichiometric amounts of the elements (Y pieces [99.9% purity, metal basis, Alfa Aesar]; Cu slug [99.995% purity, oxygen was removed using a reduction furnace (*i.e.*, copper was placed in a tube furnace with a continuous flow of Ar with 2% H_2 at $\sim$ 950 K) and provided by Stephen Dongmin Kang, Alfa Aesar]; Te pieces [99.999% purity, metal basis, Alfa Aesar]) with a total mass of 3.5 g were vacuum sealed in a carbon-coated fused silica ampoule ($\sim$30 cm length, 12.8 mm in diameter, and wall thickness of 1.1 mm). Prior the carbon-coating, oxygen in the silica ampoule was removed by heating the tube with a torch under dynamic vacuum. For the carbon-coating, acetone was spread over the inside of the ampoule and the ampoule was heated with a torch, starting from the closed end to half way to the opening, while constantly rotating to obtain a homogeneous coating. The coating procedure was repeated and the tube was cleaned with acetone, followed by isopropanol to remove any residuals.

The ampoule was heated in a vertical tube furnace to 648 K over 10 h, then to 1073 K over 15 h, and eventually to 1443 K over 15 h, followed by annealing at that temperature for 15 h. The sample was slowly cooled to 1073 K over 15 h, to 673 over 15 h, and finally to 373 K over 15 h. At 373 K, the furnace was turned off and the sample cooled in the furnace. It is important to note that the carbon-coating was gone after the high-temperature treatment. The resulting ingots were hand-ground to a fine powder and $\sim$1.5 g of the powder was filled in a 1.27 cm diameter high-density graphite die (POCO). The samples were sintered at 873 K in a rapid hot press under a pressure of 80 MPa in argon atmosphere. The consolidated samples were cooled to room temperature over two hours.

5.1.4 Characterization

5.1.4.a Crystal Structures [2]

All three parent compositions, $TmAgTe_2$, $YAgTe_2$, and $YCuTe_2$, display at least two polymorphs, a low-temperature (LT) phase and a high-temperature (HT) phase. The LT and HT phases were detected by PXRD measurements and the patterns were refined using the LeBail method [103].

$TmAgTe_2$ At low temperatures, $TmAgTe_2$ crystallizes in a tetragonal phase with space group $P\bar{4}2_1m$ as shown in Figure 5.5 (a). Based on a computational study, Ag atoms occupy tetrahedral interstices in the tetragonal phase whereas Tm atoms fill the octahedral interstices and the crystal structure is composed of a mixture of distorted $TmTe_6$ octahedra and $AgTe_4$ tetrahedra. Furthermore, the view on the basal planes indicates that Cu and Te atoms form ladder-like structure in which Tm atoms can fill the large channels (see Figure 5.5 (a)).

At elevated temperatures ($T > 740$ K as determined by DSC [*vide infra*]), the tetragonal phase transforms to the high-temperature trigonal phase with space group $P\bar{3}m1$ where Ag and Tm occupy each half of the octahedral interstices as shown in the third panel of Figure 5.5 (b). The trigonal phase has a smaller unit cell volume than the tetragonal phase. Whereas the mixture of the octahedra and tetrahedra in the tetragonal phase was disordered as shown in the third panel of Figure 5.5 (a), the octahedra in the trigonal phase are ordered showing a layered crystal structure similar to that of classic Li-ion battery electrodes, such as CoO_2 [286]. According to the notation by Delmas *et al.* for layered structures the trigonal structure can be referred to an O1-type structure because the unit cell consists only of a single-layer $AgTe_2$ [287].

Although the tetragonal phase is considered as the low-temperature phase as it has a lower symmetry and the energy of the tetragonal phase was predicted to be ∼15 meV per atom lower than the energy than the trigonal phase, an experimental study by Gulay *et al.* showed that the trigonal phase was obtained at room temperature if the samples were annealed at 870 K and quenched in air [284]. The trigonal phase was also obtained in the present study if $TmAgTe_2$ was quenched from 870 K in water,

[2] All compositions discussed in this section are nominal.

as confirmed by PXRD (see Figure 5.6 (c)). However, it was found that the trigonal phase slowly transformed to the tetragonal phase at temperatures slightly below the phase transition (650 K $< T <$ 740 K). (The phase transition in $TmAgTe_2$ is further discussed below). The quenched sample was, therefore, sealed in a quartz ampoule under high vacuum (10^{-6} mbar) and heated at 673 K for three days. After three days the trigonal phase completely transformed to the tetragonal phase as confirmed by PXRD shown in Figure 5.6 (d). In a similar experiment, the trigonal sample was annealed for one day and only a small contribution of the tetragonal was found in the PXRD pattern suggesting that the transformation is a slow process and that the trigonal phase might be metastable at low temperature. Therefore, the transport properties of the tetragonal phase were solely determined below the phase transition.

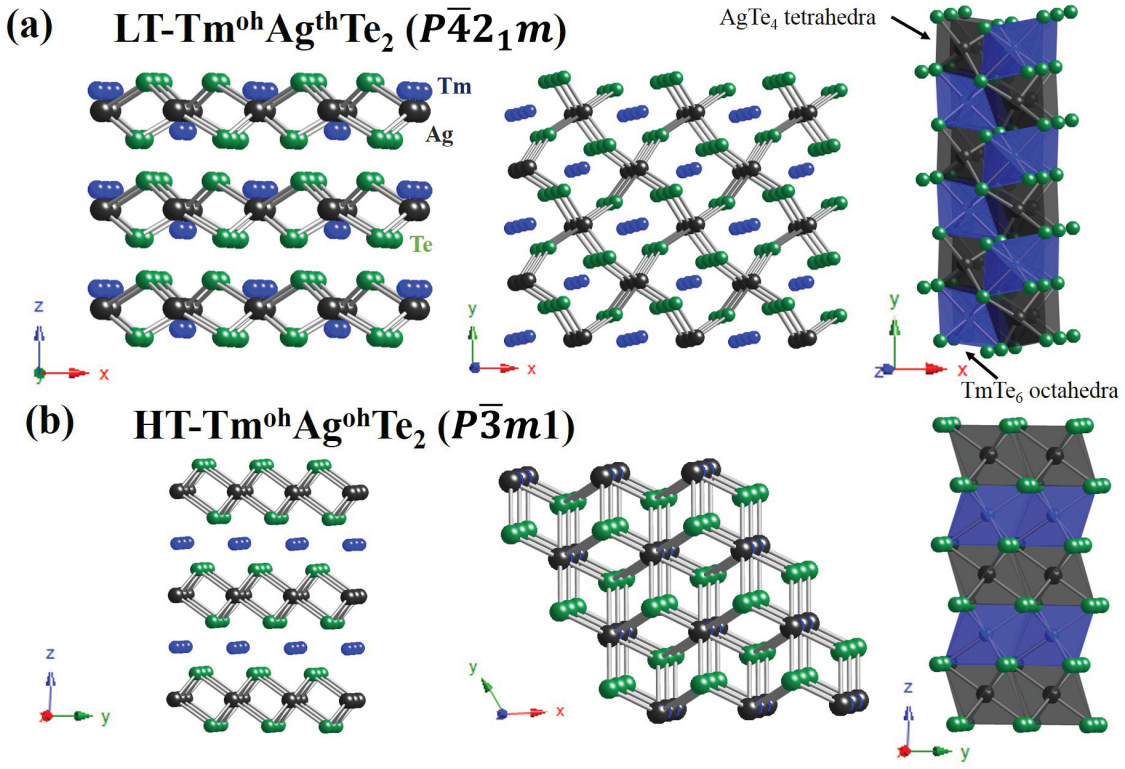

Figure 5.5: Crystal structure of $TmAgTe_2$ in (a) the low-temperature (LT) tetragonal phase ($P\bar{4}2_1m$) and (b) the high-temperature (HT) trigonal phase ($P\bar{3}m1$). While Tm (●) and Ag (●) are in octahedral environments surrounded by Te atoms (●) in the trigonal phase, Ag atoms occupy tetrahedral interstices in the tetragonal phase.

.

The PXRD pattern of the tetragonal and trigonal phase was refined with the Le Bail method. Note that the PXRD data could not be directly imported in the software package Rietica due to irregular step size of the scattering angle. Therefore, the data were modified to obtain regular steps with linear interpolation between two values using the programming language Python in the software package Canopy. With the interpolation the step size was increased from $\sim$0.004° to 0.05°, as was also used for the PXRD acquirement for PCBM. The χ^2 and the R_{wp} values are relatively high and the Le Bail refined data have to be considered as a semi-quantitative analysis due to the low goodness of the fit.

The tetragonal phase has a larger unit cell volume ($a = b = 7.091$ Å and $c = 4.526$ Å, $V_{UC} = 228$ Å^3) than the trigonal phase ($a = b = 4.286$ Å and $c = 7.016$ Å, $V_{UC} = 112$ Å^3). However, while the trigonal cell is composed of one unit formula, the tetragonal unit cell contains two formula units, resulting in similar theoretical densities (see Table C.1 of Appendix C). Furthermore, the lattice parameters of the trigonal phase are in agreement with the parameters reported by Gulay *et al.* ($a = b = 4.292$ Å and $c = 7.003$ Å) [284]. The lattice parameters of the LT and HT phase were also calculated using first-principle calculations without the inclusion of van der Waals interactions. The calculated lattice parameters for the LT phase were $a = b = 7.072$ Å and $c = 4.684$ Å and for the HT phase were $a = b = 3.497$ Å and $c = 6.992$ Å. In particular, a larger value was calculated in the c direction (*i.e*, perpendicular to the lattice planes) due to an underestimation of the binding forces. Underestimation of binding energy is a typical problem for PBE-GGA calculations, especially in layered structures [288, 289]. Therefore, the lattice parameters of the LT phase also were calculated with the inclusion of van der Waals interaction using the dispersion correction DFT-D3 in VASP. The computed lattice parameters with the inclusion of van der Waals interactions ($a = b = 7.061$ Å and $c = 4.532$ Å) show better agreement with experiments than without van der Waals interactions. (Computed and experimental lattice parameters for the compounds are given in Table 5.1.) In addition to the crystal structure of the parent compound, the PXRD pattern of the Zn-doped and Mg-doped $TmAgTe_2$ are shown in Figure 5.6 (a) and (b), respectively. Both compounds crystallized in the high-temperature trigonal phase, even if they were annealed at the same temperature as the parent compound, and no evidence of

the low-temperature phase was found using PXRD. Therefore, doping might stabilize the material in the high-temperature phase. (The Le Bail refined PXRD are shown in Figures C.1-C.4 and the refined data are given in Table C.1 of Appendix C.)

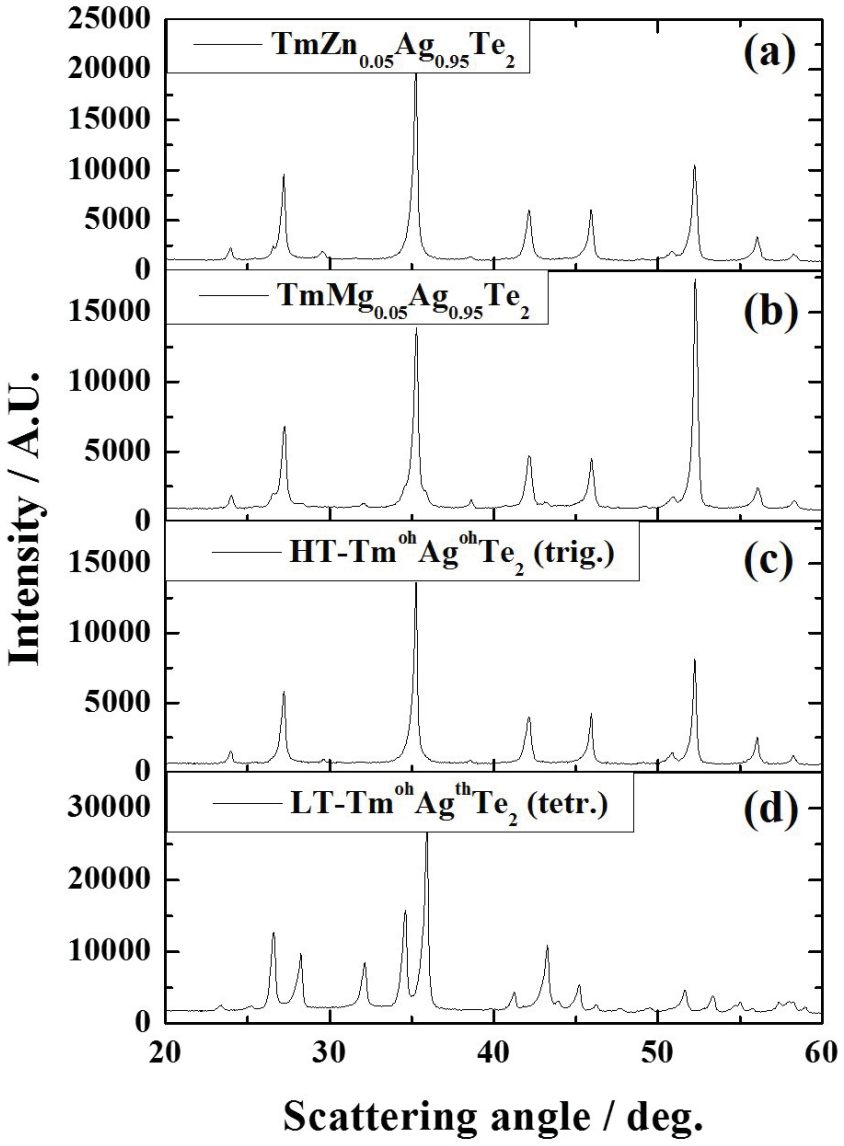

Figure 5.6: PXRD pattern (a) $TmZn_{0.05}Ag_{0.95}Te_2$, (b) $TmMg_{0.05}Ag_{0.95}Te_2$, (c) $Tm^{oh}Ag^{oh}Te_2$ in the high-temperature trigonal phase, and (d) $Tm^{oh}Ag^{th}Te_2$ in the low-temperature tetragonal phase. Extrinsically doped $TmAgTe_2$ samples prepared here all crystallized in the trigonal phase.

Table 5.1: Computational and experimental lattice parameters of $TmAgTe_2$, $YAgTe_2$, and $YCuTe_2$. Computational parameters were calculated with PBE-GGA with and without van der Waals interaction (DFT-D3). Computations were performed by Zhe Luo and Dr. Hong Zhu, School of Materials Science and Engineering, Shanghai Jiao Tong University [unpublished work presented with permission]. Experimental results were determined using the Le Bail refinement method. However, a weak goodness of fit can produced uncertainty in the refinement.

Compound	Space group	PBE-GGA	PBE-GGA with DFT-D3	Exp.
$TmAgTe_2$	$P\bar{4}2_1m$	$a = 7.072$ Å $c = 4.684$ Å	$a = 7.061$ Å $c = 4.532$ Å	$a = 7.091$ Å $c = 4.526$ Å
$TmAgTe_2$	$P\bar{3}m1$	$a = 4.342$ Å $c = 6.998$ Å		$a = 4.286$ Å $c = 7.016$ Å
$TmMg_{0.05}Ag_{0.95}Te_2$	$P\bar{3}m1$			$a = 4.305$ Å $c = 7.037$ Å
$TmZn_{0.05}Ag_{0.95}Te_2$	$P\bar{3}m1$			$a = 4.298$ Å $c = 7.021$ Å
$YAgTe_2$	$P\bar{4}2_1m$	$a = 7.126$ Å $c = 4.742$ Å	$a = 7.120$ Å $c = 4.580$ Å	$a = 7.149$ Å $c = 4.593$ Å
$Y_{0.98}Ag_{1.02}Te_{1.98}$	$P\bar{4}2_1m$			$a = 7.154$ Å $c = 4.604$ Å
$YCuTe_2$	$P\bar{3}m1$	$a = 8.614$ Å* $c = 13.829$ Å*		$a = 8.606$ Å $c = 13.837$ Å
$Y_{0.98}CuTe_2$	$P\bar{3}m1$			$a = 8.628$ Å $c = 13.867$ Å
$YCu_{0.96}Te_2$	$P\bar{3}m1$			$a = 8.658$ Å $c = 13.908$ Å
$YCu_{1.04}Te_2$	$P\bar{3}m1$			$a = 8.634$ Å $c = 13.865$ Å
$YCu_{1.08}Te_2$	$P\bar{3}m1$			$a = 8.629$ Å $c = 13.871$ Å
$Y_{0.96}Cu_{1.08}Te_2$	$P\bar{3}m1$			$a = 8.649$ Å $c = 13.841$ Å

* Lattice parameters could not be computed for $YCuTe_2$ and the Rietveld refined parameters were used for the computation of the electronic and phononic dispersion curves.

$YAgTe_2$ $YAgTe_2$ crystallizes in a tetragonal phase with space group $P\bar{4}2_1m$ at low temperature as reported by Gulay *et al.* [283] and Pardo *et al.* [290]. Similar to the LT phase of $TmAgTe_2$, the tetragonal phase of $YAgTe_2$ is a mixture of distorted YTe_6

octahedra and $AgTe_4$ tetrahedra and the Y atoms fill the large channels consisting of Ag and Te atoms as shown in Figure 5.7 (a). At high temperature ($T > 753$ K as shown in the DSC thermogram [*vide infra*]), the crystal structure transforms from the tetragonal structure to a trigonal structure with space group $P\bar{3}$ as also reported by Pardo *et al.* [290]. The $AgTe_4$ tetrahedra and YTe_6 octahedra are ordered in the crystal structure (see Figure 5.7 (b)) and the layered structure can be described as an O1-type structure, similar to the HT-trigonal phase of $Tm^{oh}Ag^{oh}Te_2$. Furthermore, the high-temperature phase of $Y^{oh}Ag^{th}Te_2$ consists of honeycomb-like channels formed of Ag and Te atoms which are occupied by Y atoms in the center. The lower coordination number of Ag in the high-temperature phase of $Y^{oh}Ag^{th}Te_2$ compared to the high-temperature phase of $Tm^{oh}Ag^{oh}Te_2$ might be a result of the larger ionic radius in Y^{3+} (0.90 Å) than Tm^{3+} (0.88 Å) [281].

The low-temperature structure was confirmed by PXRD as shown in Figure C.5 of Appendix C and refined with the Le Bail method (see Figures C.6 and C.7 of Appendix C). (The refined data are given in Table C.2 of Appendix C.) The refined lattice parameters of the tetragonal phase of $Y^{oh}Ag^{th}Te_2$ ($a = b = 7.149$ Å and $c = 4.593$) are in good agreement with the reported parameters by Pardo *et al.* ($a = b = 7.126$ Å and $c = 4.581$ Å) [290] and Gulay *et al.* ($a = b = 7.140$ Å and $c = 4.594$ Å) [283]. While Pardo *et al.* recorded the crystal structure of the high-temperature phase of $Y^{oh}Ag^{th}Te_2$ [290], the PXRD pattern of the high-temperature phase of $YAgTe_2$ was not recorded in the present study. The lattice parameters of the LT phase of $YAgTe_2$ were also computed with and without van der Waals interactions. Whereas the computed lattice parameters without van der Waals interactions are overestimated in the c direction ($a = b = 7.126$ Å and $c = 4.742$ Å), with inclusion of van der Waals interactions the lattice parameters agree well with the refined parameters ($a = b = 7.120$ Å and $c = 4.580$ Å) as shown in Table 5.1. Additionally to the parent compound, the PXRD pattern of an intrinsically doped sample ($Y_{0.98}Ag_{1.02}Te_{1.98}$) was recorded, indicating an increase in the crystallinity as deduced by the sharpness of the PXRD peaks and the purity of the phase (see Figure C.5 (b) of Appendix C). $Y_{0.98}Ag_{1.02}Te_{1.98}$ crystallized in the same crystal structure ($P\bar{4}2_1m$) as the parent compound at low temperature.

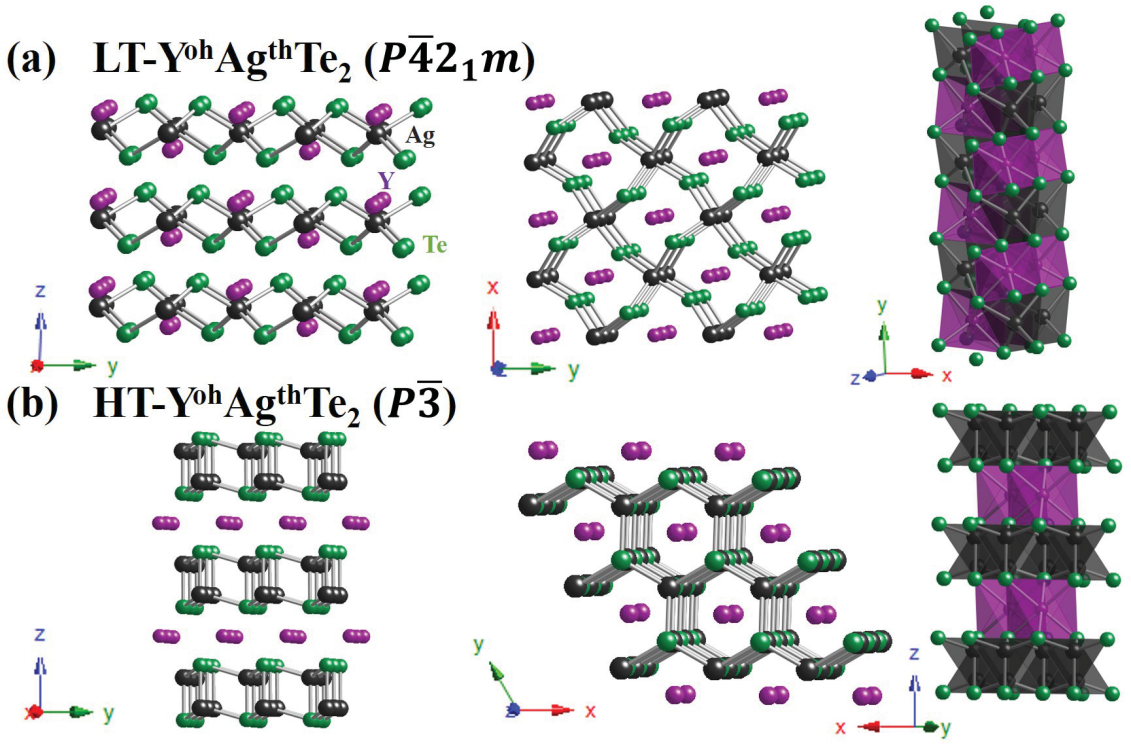

Figure 5.7: Crystal structure of $YAgTe_2$ in (a) the low-temperature (LT) tetragonal phase ($P\bar{4}2_1m$) and (b) the high-temperature (HT) trigonal phase ($P\bar{3}$). While Y atoms (•) fill the octahedral environments formed by Te atoms (•), Ag atoms (•) occupy tetrahedral interstices in the LT and in the HT phase.

.

$YCuTe_2$ The low-temperature phase of $Y^{oh}Cu^{th}Te_2$ is isotypic to the trigonal $DyCuTe_2$ crystal structure with space group $P\bar{3}m1$ [291]. In the LT crystal structure, there are two Y ($2c$, $6i$), three Cu ($2d$, $2\times$ $6i$) and four Te ($2 \times 2d$, $2 \times 6i$) Wyckoff sites. While all Y and Te positions as well as the Cu $2d$ sites are fully occupied, the Cu $6i$ sites are partially occupied. In contrast to the low-temperature phase of $Tm^{oh}Ag^{th}Te_2$ and $Y^{oh}Ag^{th}Te_2$, the $AgTe_6$ octahedra and YTe_4 tetrahedra are ordered as shown in Figure 5.8 (a) which is similar to the high-temperature structure of $Y^{oh}Ag^{th}Te_2$.

Whereas the HT phase of $Y^{oh}Ag^{th}Te_2$ was stacked in a O1-type structure, the unit cell of the LT $Y^{oh}Cu^{th}Te_2$ phase consists of two layers (A-B-A stacking) due to the two types of $CuTe_4$ tetrahedra. One layer consists of $CuTe_4$ tetrahedra with disordered Cu occupying the $6i$ site, where the other layer comprises $CuTe_4$ tetrahedra with

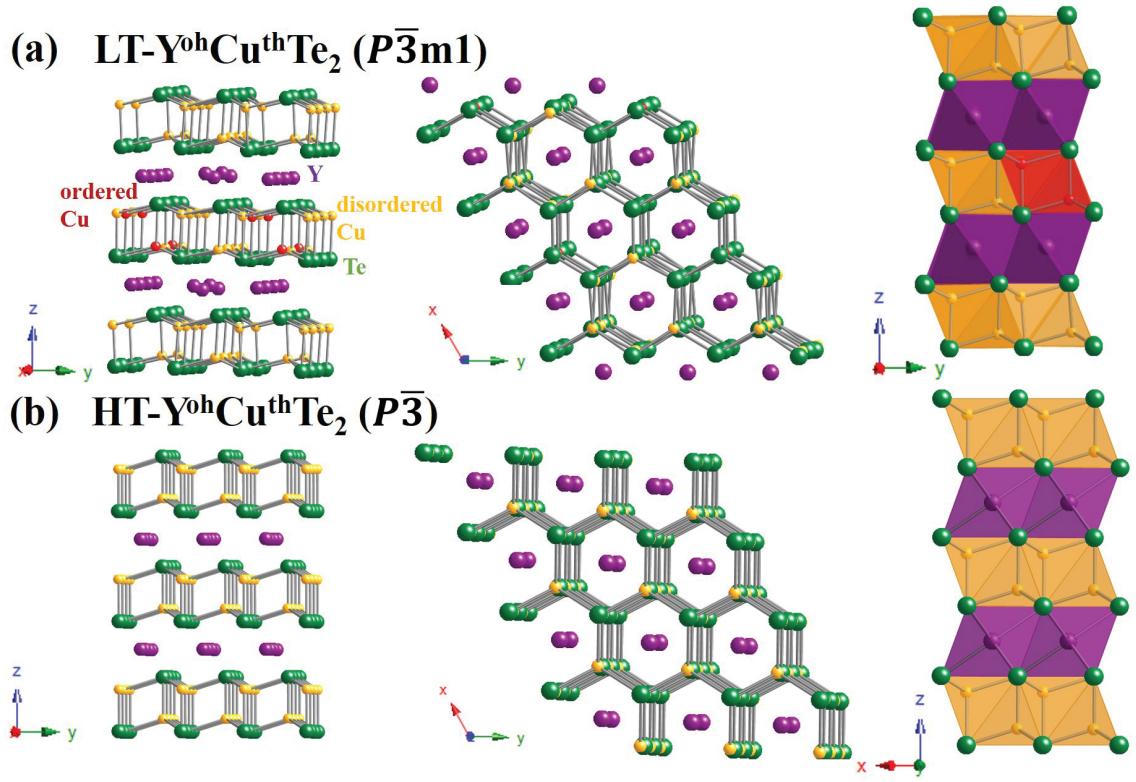

Figure 5.8: Crystal structure of $YCuTe_2$ in (a) the low-temperature (LT) trigonal phase ($P\bar{3}m1$) and (b) the high-temperature (HT) phase ($P\bar{3}$). The LT phase has a layered structure with A-B-A stacking where Y atoms (•) occupy octahedral interstices and Cu atoms (disordered: •; ordered: •) are tetrahedrally coordinated by Te atoms (•). While the Cu atoms are partially disordered in the LT crystal structure, the Cu atoms are completely disordered at high temperature. Figure from reference [292].

.

ordered Cu atoms occupying the $2d$ site and disordered Cu at the $6i$ site. Cu and Te form a honeycomb-like shape which is partially destroyed by unoccupied Cu positions. At elevated temperature, the partially ordered Cu atoms are completely disordered and $YCuTe_2$ crystallizes in the space group $P\bar{3}$. The LT and HT phases were also investigated by DFT calculations where six configurations each for the LT and HT phase were ranked based on the electrostatic energy as determined by the Ewald sum. The energy difference between the LT phase and HT phase was calculated to be ~0.7 meV per atom for all computed models, which is within the numerical tolerance of the calculations which can explain the HT phase stabilization with increasing Cu content

and temperature. It is important to note that $P\bar{3}m1$ is a subgroup of $P\bar{3}$ and the unit cell of the LT phase is a $2 \times 2 \times 2$ supercell of the HT phase.

The LT phase structure of $YCuTe_2$ was investigated by PXRD (see Figure 5.9) and the patterns were refined with the Le Bail method (see Figures C.9-C.13; refined data are given in Table C.3 of Appendix C). The LT trigonal phase of $YCuTe_2$ has lattice parameters $a = b = 8.606$ Å and $c = 13.837$ Å. Furthermore, supercell reflections peaks (*i.e.*, peaks of the $P\bar{3}m1$ structure) with low intensity were observed at room temperature for the parent compound (see arrows in Figure 5.9 (f)). It is shown that the supercell reflection peaks decreased with increasing Cu content from $YCuTe_2$ to $YCu_{1.08}Te_2$ suggesting that a small increase in Cu content might stabilize the HT phase ($P\bar{3}$). A similar behavior was found from temperature-dependent PXRD measurements as shown in Figure 5.10 (a). With increasing temperature a decrease in the supercell peaks was observed which might lead to completely disordered Cu atoms at the $2d$ site in the HT phase.

The thermal expansion of $YCu_{1.04}Te_2$ was additionally determined from its lattice parameters at various temperatures measured by PXRD and using Rietveld refinement (see Figure 5.10 (b)). The Rietveld refinements were performed on the raw PXRD data by Dr. Umut Aydemir using the software WinCSD [293]. The lattice parameter c has almost a linear increase with temperature whereas the lattice parameter a has a constant rate of increase to ∼350 K, a slight jump to the phase transition, then increasing again with approximately the same temperature trend found between room temperature and ∼350 K. The change of the lattice parameter a might indicate reorganization of the Cu atoms during the phase transition. Furthermore, the c/a ratio is 1.605 which is lower than the ideal value for a hcp structure (c/a=1.633). Although all PXRD pattern point to a pure $YCuTe_2$ crystal structure using PXRD, small secondary phases, such as YCu_xTe_{3-x} [294], could be formed during the synthesis. If the percentage of the secondary phase is low, it is challenging to detect that phase using PXRD and therefore, SEM and WDS can provide more information about additional phases. (Determination of the actual composition of $YCuTe_2$ using SEM and WDS can be found in Section C.1 of Appendix C.)

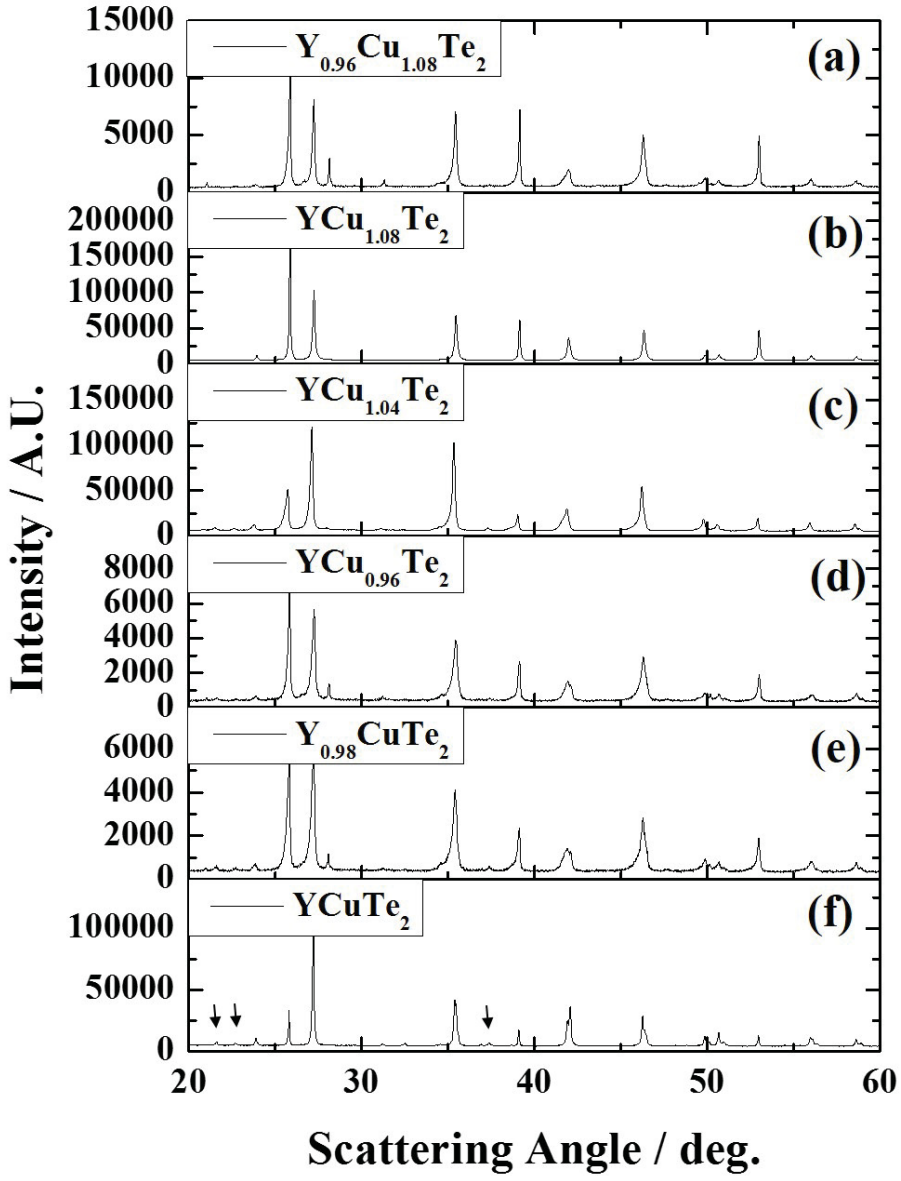

Figure 5.9: PXRD pattern of (a) $Y_{0.96}Cu_{1.08}Te_2$, (b) $YCu_{1.08}Te_2$, (c) $YCu_{1.04}Te_2$, (d) $YCu_{0.96}Te_2$, (e) $Y_{0.98}CuTe_2$ and (f) $YCuTe_2$ in the low-temperature trigonal phase ($P\bar{3}m1$). All intrinsic doped samples crystallized in the low-temperature phase. Arrows mark the peaks of the supercell reflections which decrease with increasing Cu content. Figures from reference [292].

.

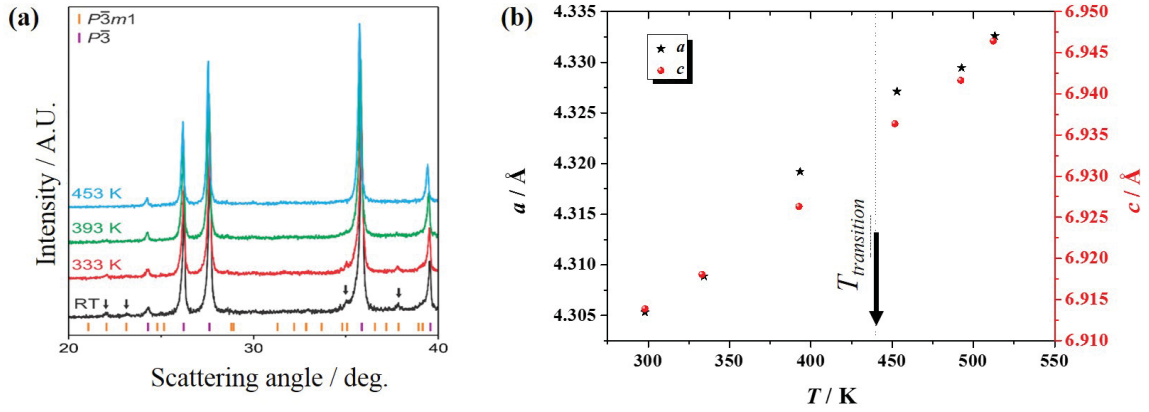

Figure 5.10: Temperature-dependent PXRD of $YCu_{1.04}Te_2$ sample. (a) With increasing temperature, the intensities of the supercell reflections (as shown by the arrow) were reduced and vanished above the phase transition at 453 K. (b) The lattice parameters a and c increased with temperature. While the increase in the lattice parameter c was nearly linear, the lattice parameter a has a change in temperature behavior through the phase transition, $T_{transition}$, possible indicating reorganization of the Cu atoms in the crystal structure. Lattice parameters were refined with the Rietveld method. Figures from reference [292].
.

5.1.4.c Differential Scanning Calorimetry

The transport properties are strongly related to the crystal structure of the investigated compounds and therefore it is necessary to determine the temperature range for each phase. Differential scanning calorimetry (DSC) can detect phase transitions by a change in the heat flux. In this section, the parent compounds, $TmAgTe_2$, $YAgTe_2$, and $YCuTe_2$, were investigated by DSC in the laboratory of Dr. Mary Anne White, Department of Chemistry, Dalhousie University (see Figure 5.11). All samples were scanned from 373 K to 773 K with a scanning rate of 10 K min^{-1} under nitrogen atmosphere and finned air cooling. $YCuTe_2$ was additionally scanned with a scanning rate of 1 K min^{-1} under helium atmosphere with liquid nitrogen cooling to analyze the phase transition at ∼440 K (see Figure 5.11 (c)).

$TmAgTe_2$ As discussed above $TmAgTe_2$ can crystallize at room temperature in one of two phases, a tetragonal phase ($P\bar{4}2_1m$) and a trigonal phase ($P\bar{3}m1$), depending

on the thermal history. If the material was quenched at high temperature (∼850 K), the compound crystallized in the trigonal phase. If the material was annealed at 453 K for a long time (several days), the material transformed from the trigonal phase to the tetragonal phase which was found to be more stable in a computational study. It is important that $TmAgTe_2$ is in the tetragonal phase prior the DSC run to detect the phase transition. The thermogram of $TmAgTe_2$ ($m = 7.88 \pm 0.01$ mg) is shown in Figure 5.11 (a) and two reversible phase transitions were obtained. A strong first-order phase transition from the tetragonal and trigonal phase was found with an onset temperature of 736 K and a change in enthalpy of 14.0 ± 1.4 J g^{-1}. The change in entropy was calculated from the change in enthalpy and the onset temperature ($\Delta S = \frac{\Delta H}{T_{onset}}$) and the uncertainty was determined from the uncertainty of the change in enthalpy (10%) and the uncertainty of the onset temperature (1.5 K). (Thermodynamic properties of all three parent compounds are given in Table 5.2.) In additional to the strong first-order transition, a subtle phase transition was recorded at 651 K ($\Delta H = 2.7 \pm 0.3$ J g^{-1}). Both solid-solid phase transitions were reversible but the onset temperature of each phase transition on cooling was lower than the corresponding transition on heating indicating supercooling behavior (see Table 5.2). Doped $TmAgTe_2$ compounds showed only a weak phase transition at 705 K, *i.e.* at a temperature between the temperatures of both phase transitions of the parent compound (see Table 5.2).

Due to the fact that no thermograms of $XAgZ_2$ are available from literature the thermogram of $TmAgTe_2$ was here compared to the thermodynamic properties of various Ag chalcogenides [295, 296, 297]. The phase transition temperatures of Ag_2S ($T_{transition} \sim 448$ K) [295], Ag_2Se ($T_{transition} \sim 408$ K) [296], and Ag_2Te ($T_{transition} \sim 400 - 430$ K) [296, 297] are all lower than observed for $TmAgTe_2$. A similar hysteresis as in $TmAgTe_2$ was found for Ag_2Te where the phase transition supercooled from ∼420 K to ∼330 K [296]. Supercooling indicates that the dynamics through the phase transition in these compounds are slow and it takes a long time to form the LT phase. This would be in agreement with the PXRD recorded after the DSC measurement where the trigonal phase was not completely transformed back to the tetragonal phase. Furthermore, Aliev *et al.* reported that the phase transition in Ag_2Te from the LT phase to the HT phase was going to an additional phase region [297] which

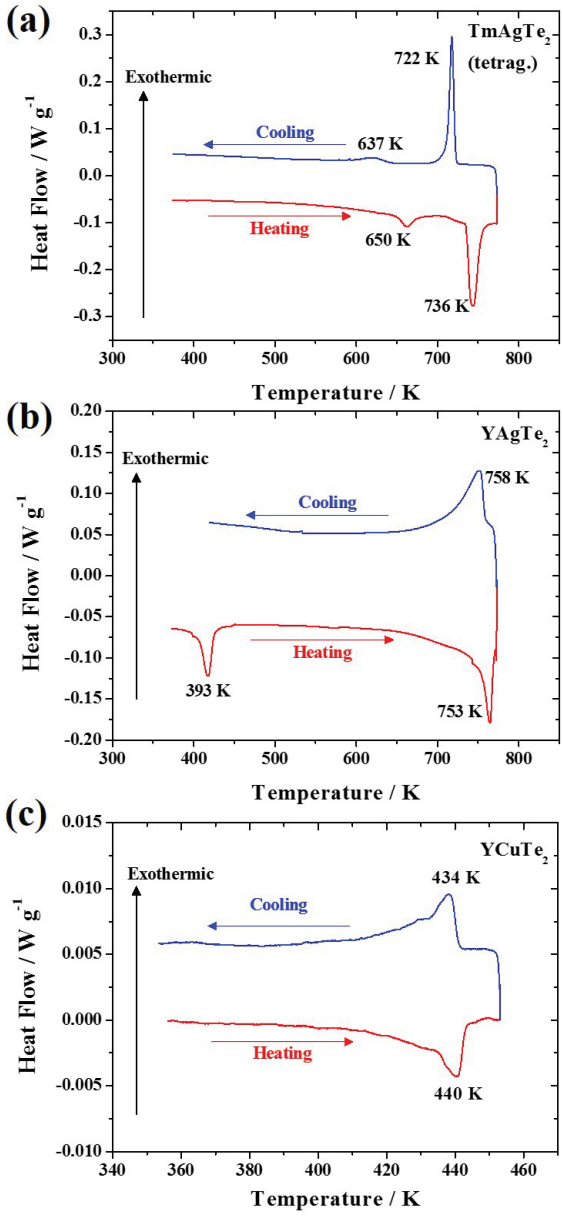

Figure 5.11: DSC thermograms of (a) $TmAgTe_2$, (b) $YAgTe_2$, and (c) $YCuTe_2$. The initial phase of $TmAgTe_2$ was the tetragonal phase ($P\bar{4}2_1m$). The phase transitions in all compounds were reversible. Temperature range shown for $YCuTe_2$ is smaller than the other two compounds to emphasize the anomalous shape of the transition peak. Thermodynamic properties of all three parent compounds are given in Table 5.2. Figures (a) and (c) were taken from references [277] and [292], respectively.

.

might also appear in the present study of $TmAgTe_2$ indicated by the smaller peak at 650 K. For enhanced understanding of the thermodynamics of $TmAgTe_2$ further investigation with a more detailed structural analysis is required. In addition to the phase transition temperature, Aliev *et al.* determined also the change in enthalpy for Ag_2Te ($\Delta H \sim 8.4$ kJ mol^{-1} for the sum of the three phase transition peaks) which is less than the sum of two phase transition peaks in the present study ($\Delta H \sim 12.3$ kJ mol^{-1}).

$YAgTe_2$ Similar to $TmAgTe_2$ the thermogram of $YAgTe_2$ ($m = 7.88 \pm 0.01$ mg) has two reversible first-order phase transitions (see Figure 5.11 (b)). While the high-temperature phase transition of $YAgTe_2$ at ∼753 K was slightly higher than $TmAgTe_2$, the low-temperature phase transition was recorded at ∼393 K. PXRD showed that the tetragonal phase ($P\bar{4}2_1m$) is the LT phase of $YAgTe_2$ and Pardo *et al.* reported a phase transition to the trigonal phase ($P\bar{3}$) at 793 K [290]. The phase transition temperature is higher than that obtained in the present study. The lower phase transition temperature in the present study might be due to slightly different compositions of $YAgTe_2$ used by Pardo *et al.* and in the present study. While Pardo *et al.* reported a single phase transition, the present composition has two phase transitions. The phase in the intermediate temperature region is unknown and further studies of the thermodynamic behavior of $YAgTe_2$ are required to perform a complete phase diagram analysis. Furthermore, the transitions of $YAgTe_2$ are weaker than for $TmAgTe_2$ indicated by the smaller change in enthalpy (see Table 5.2). No hysteresis was found on cooling which shows faster dynamics of the phases compared to $TmAgTe_2$. That is reasonable because Ag fills the tetrahedral interstices in the LT and HT of YAgTe while the Ag atoms switch from the tetrahedral interstices in the LT phase of $TmAgTe_2$ to an octahedral environment in the HT phase.

$YCuTe_2$ The thermogram of $YCuTe_2$ ($m = 12.20 \pm 0.01$ mg) indicates a broad phase transition from the low-temperature partially ordered phase to the high-temperature completely disordered phase as shown in Figure 5.11 (c). Due to the broad peak it is challenging to determine the onset temperature and therefore, the peak temperature, which would not be the actual transition temperature, can be

Table 5.2: Thermodynamic parameters of $TmAgTe_2$, $YAgTe_2$, and $YCuTe_2$. Onset temperatures, T_{onset}, peak temperature, T_{peak}, change in enthalpy, ΔH, and change in entropy, ΔS, of the phase transitions on heating and cooling. $Y_{0.96}Cu_{1.08}Te_2$ showed a broad peak, not a sharp transition. LT peak and HT peak referred to the lower temperature phase transition and higher temperature phase transition, respectively. The thermograms were recorded with a scanning rate of 10 K min^{-1} from 373 K to 773 K.

Compound	T_{onset} / K	T_{peak} / K	ΔH / kJ mol^{-1}	ΔS / J K^{-1} mol^{-1}
Heating				
$TmAgTe_2$ (LT peak)	649.5 ± 1.5	662.1 ± 1.5	1.4 ± 0.1	2.2 ± 0.2
$TmAgTe_2$ (HT peak)	735.6 ± 1.5	743.5 ± 1.5	7.4 ± 0.7	10.1 ± 1.0
$TmAg_{0.95}Zn_{0.05}Te_2$	704.8 ± 1.5	719.1 ± 1.5	0.8 ± 0.1	1.1 ± 0.1
$YAgTe_2$ (LT peak)	393.3 ± 1.5	413.3 ± 1.5	0.6 ± 0.1	0.9 ± 0.1
$YAgTe_2$ (HT peak)	752.7 ± 1.5	765.4 ± 1.5	2.1 ± 0.2	2.8 ± 0.3
$YCuTe_2$	430.2 ± 1.5	440.2 ± 1.5	1.7 ± 0.2	3.9 ± 0.4
$Y_{0.96}Cu_{1.08}Te_2$	340.9 ± 1.5	376.6 ± 1.5	0.4 ± 0.1	1.2 ± 0.1
Cooling				
$TmAgTe_2$ (LT peak)	636.7 ± 1.5	616.5 ± 1.5	0.6 ± 0.1	1.0 ± 0.1
$TmAgTe_2$ (HT peak)	721.8 ± 1.5	717.5 ± 1.5	6.2 ± 0.6	8.6 ± 0.9
$TmAg_{0.95}Zn_{0.05}Te_2$	685.2 ± 1.5	670.1 ± 1.5	1.0 ± 0.1	1.4 ± 0.1
$YAgTe_2$ (LT peak)	400.7 ± 1.5	389.2 ± 1.5	0.8 ± 0.1	2.0 ± 0.2
$YAgTe_2$ (HT peak)	758.1 ± 1.5	751.7 ± 1.5	2.4 ± 0.2	3.2 ± 0.3
$YCuTe_2$	439.2 ± 1.5	434.2 ± 1.5	1.7 ± 0.2	3.9 ± 0.4
$Y_{0.96}Cu_{1.08}Te_2$	392.8 ± 1.5	365.5 ± 1.5	0.5 ± 0.1	1.3 ± 0.1

more accurately determined in this study ($T_{peak} \sim 440$ K). Figure 5.11 (c) shows an anomaly in the phase transition and the breadth of the anomaly in $YCuTe_2$ could be a result of an intrinsic double transition with the second (minor) phase transition at slightly lower temperature, or a transition from a single-phase region to a two-phase region with change in phase fractions over a temperature range indicating discontinuous phase transition as reported for $Cu_{2-x}Se$ [298]. A broad exothermic peak also appears in the cooling cycle, pointing to a reversible phase transition(s). It is important to note that no additional peaks were recorded for $YCuTe_2$ in the temperature range from 300 K to 773 K. The change at the phase transition is rather subtle with $\Delta H = 1.7 \pm 0.2$ J mol^{-1} slightly lower to $YAgTe_2$ (see Table 5.2). A first-order phase transition was also shown for $TmCuTe_2$ at around 600 K [255].

The change in enthalpy was not reported by Lin *et al.* [255]. Cu chalcogenides, in comparison, undergo several phase transitions as reported for Cu_2S ($T_{transition} \sim 370$ K and ∼700 K) [299], Cu_2Se ($T_{transition}$ ∼414 K) [274, 298, 300], and Cu_2Te ($T_{transition}$ ∼450 K, ∼550 K, ∼590 K, ∼640 K, and ∼850 K) [300, 301]. The large number of phase transitions in Cu_2Te is particularly surprising as both $YCuTe_2$ and $TmCuTe_2$ have only a single phase transition.

It is challenging to reveal the order of the phase transition in $YCuTe_2$ due to the broad peak. If the space group of the low-temperature phase is a subgroup of the space group of the high-temperature phase, which is always the case for an order-disorder phase transition, a second-order (continuous) phase transition can appear [302]. To exclude a second-order phase transition Landau's criteria were applied [302, 303, 304]. According to Landau, the necessary conditions for a second-order transition are continuity and a minimum Helmholtz energy, $F(\eta_F)$, with an order parameter of $\eta_F = 0$ [303]. The Taylor expansion of the Helmholtz energy is given by

$$F(\eta_F) = F_0 + A\eta_F^2 + B\eta_F^3 + C\eta_F^4. \tag{5.4}$$

In a second-order transition the free energy at $\eta_F = 0$ moves from a minimum to a maximum and therefore, B has to be zero [304]. The third term can be described by a star, k_0, (*i.e.*, a set of unique wave vectors of superlattice reflections) [302]. Therefore, the excluding principle of the second-order transition can be determined from supercell reflections of the ordering wave vectors. If any three ordering wave vectors of the star can be combined to give a reciprocal lattice vector, G, (*i.e.*, $k_{0j1} + k_{0j2} + k_{0j3} = G$) it is not a second-order phase transition [302].

The coordinates of the star were taken from the disordered phase. However, in a order-disorder phase transition, the coordinates can be found in the ordered phase and set equivalent to the coordinates of the disordered phase. The ordered phase in $YCuTe_2$ is a $2 \times 2 \times 2$ supercell and therefore, the coordinates $\{1\,1\,1\}$ of the ordered phase are equivalent to $\left\{\frac{1}{2}\,\frac{1}{2}\,\frac{1}{2}\right\}$ in the disordered phase. Three stars were detected for $YCuTe_2$: $\left[\left\{0\,0\,\frac{1}{2}\right\},\left\{0\,\frac{1}{2}\,0\right\},\left\{\frac{1}{2}\,0\,0\right\}\right]$, $\left[\left\{0\,\frac{1}{2}\,\frac{1}{2}\right\},\left\{\frac{1}{2}\,0\,\frac{1}{2}\right\},\left\{\frac{1}{2}\,\frac{1}{2}\,0\right\}\right]$, and $\left\{\frac{1}{2}\,\frac{1}{2}\,\frac{1}{2}\right\}$. It was found that three wave vectors can be combined to a reciprocal lattice vector, *e.g.*, $\left\{0\,\frac{1}{2}\,\frac{1}{2}\right\}+\left\{0\,0\,\frac{1}{2}\right\}+\left\{0\,\frac{1}{2}\,0\right\}=\{0\,1\,1\}$ which is a reciprocal lattice vector of the disordered phase, and therefore, the necessary conditions for a second-order phase transition are not fulfilled. Although the phase transition can be a higher-order

phase transition, the phase transition in $YCuTe_2$ is more likely a first-order transition, as also reported for $TmCuTe_2$ [255]. The lattice parameter anomaly in $YCu_{1.04}Te_2$ (Figure 5.10 (b) also indicates most likely a first-order transition.

In conclusion, both Ag-based compounds show two first-order phase transitions while a single first-order (according to Landau's criteria) phase transition was found for $YCuTe_2$. The phase transition in $TmAgTe_2$ supercooled by ∼15 K and the trigonal phase did not transform completely back to the tetragonal phase. For additional information about the phases, the thermal expansion was measured for the parent compounds.

5.1.4.d Thermal Expansion

The thermal expansion measurements on the parent compounds were performed with the assistance of Dr. Julian O'Flynn and Addison Rayner in the laboratory of Dr. Stephen Corbin, Department of Civil and Resource Engineering, Dalhousie University. The strain and the coefficient of the linear thermal expansion of $TmAgTe_2$ ($L = 0.946 \pm 0.002$ mm), $YAgTe_2$ ($L = 1.371 \pm 0.002$ mm), and $YCuTe_2$ ($L = 1.218 \pm 0.002$ mm) are shown in Figure 5.12. All samples were heated from 350 K to 675 K. Prior the thermal expansion measurements, $TmAgTe_2$ was first annealed at 473 K for one week to obtain the tetragonal phase as confirmed by PXRD.

On heating, the coefficient of linear thermal expansion of $TmAgTe_2$ is nearly constant to ∼675 K with a value of $(20 \pm 2) \cdot 10^{-6}$ K^{-1} as shown in Figure 5.12 (a). The coefficient of linear thermal expansion indicates a phase transition on cooling where an increase in the coefficient of linear thermal expansion was observed at around 625 K. This temperature is slightly lower than the low-temperature phase transition temperature of $TmAgTe_2$ at 637 K observed in DSC (see Table 5.2). Cooling through the phase transition, the thickness of the $TmAgTe_2$ pellet decreased, followed by a linear change in thickness with a similar coefficient of thermal expansion ($(19 \pm 2) \cdot 10^{-6}$ K^{-1}) to that found on heating. After the measurement, a reduction of the thickness in the $TmAgTe_2$ pellet was obtained suggesting that the phase transition did not fully reverse. The coefficients of linear thermal expansion for the compounds are given in Table 5.3.

The thermal expansion of $YAgTe_2$ is more complex. A phase transition was

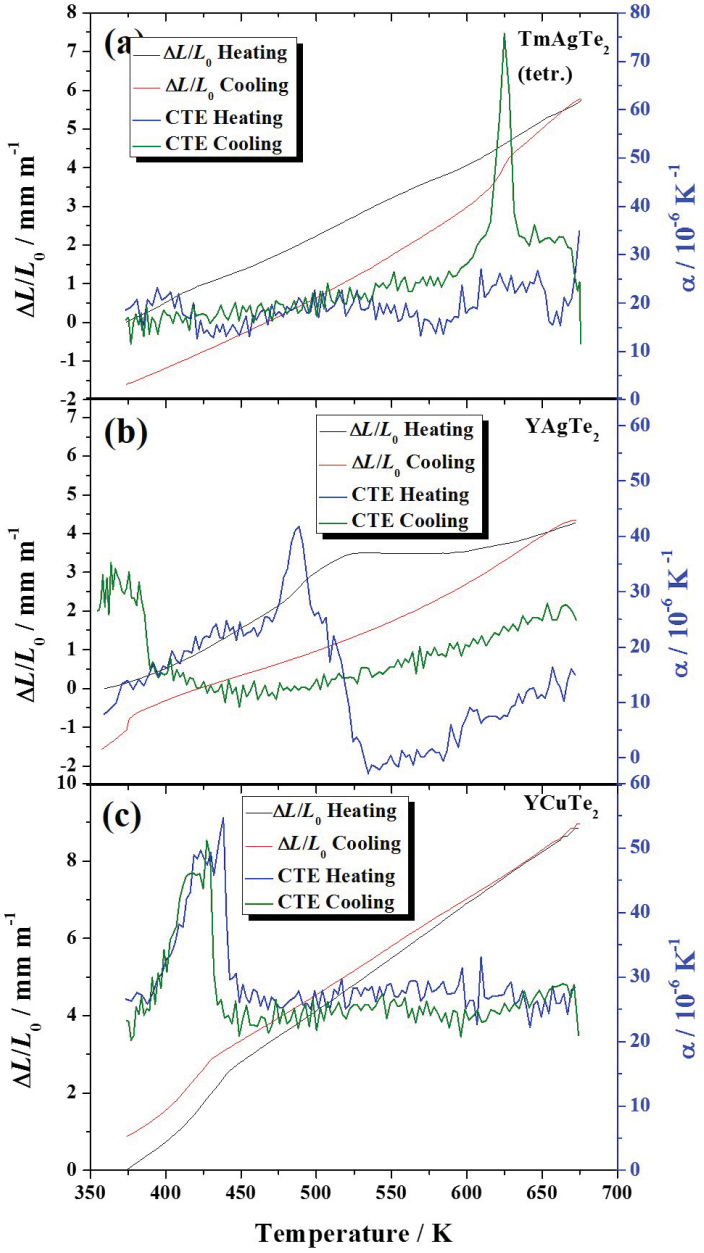

Figure 5.12: Strain and coefficient of linear thermal expansion, α, of (a) $TmAgTe_2$, (b) $YAgTe_2$, and (c) $YCuTe_2$. Constant α values were found for $TmAgTe_2$ and $YCuTe_2$ over a wide range of temperature, while the coefficient of linear thermal expansion of $YAgTe_2$ changes constantly. The average α values on heating and cooling are given in Table 5.3.

.

observed at ∼490 K on heating (see Figure 5.12 (b)), higher than the phase transition determined by DSC (see Table 5.2). The thermal expansion is nearly constant above 525 K and the coefficient of linear thermal expansion increased from $\sim 0 \pm 2$ to $(\sim 15 \pm 2) \cdot 10^{-6}$ K^{-1} in the temperature range from 525 K to 675 K which might be due to thermal expansion through a mixed phase region. On cooling, the coefficient of linear thermal expansion decreased from $(\sim 27 \pm 2) \cdot 10^{-6}$ K^{-1} to $(\sim 13 \pm 2) \cdot 10^{-6}$ K^{-1} in the temperature range from 675 K to 550 K, followed by a nearly constant coefficient of linear thermal expansion ($(\sim 13 \pm 2) \cdot 10^{-6}$ K^{-1}) from 550 K to 425 K (see Figure 5.12 (b)). At lower temperatures, the thermal expansion dramatically increased at 375 K which is lower than the phase transition temperature determined from DSC measurements.

The thermal expansion of $YCuTe_2$ was similar on heating and cooling where a phase transition appeared at around 435 K (see Figure 5.12 (c)) which is in agreement with the phase transition temperature reported from DSC measurements as shown in Table 5.2. Above the phase transition, the coefficient of linear thermal expansion is nearly constant above 450 K ($(\sim 27 \pm 2) \cdot 10^{-6}$ K^{-1} on heating and $(\sim 25 \pm 2) \cdot 10^{-6}$ K^{-1} on cooling, *i.e* the same within uncertainty). The coefficient of linear thermal expansion is higher than that of $TmAgTe_2$ which might due to tetrahedral interstices in $YCuTe_2$ in contrast to the octahedrally coordinated structure. However, an opposite trend was reported by Zeier *et al.* where tetrahedrally coordinated structures have a lower Grüneisen parameter than octahedrally coordinated structures [305]. The Grüneisen parameter is proportional to the coefficient of volumetric thermal expansion (Equation 2.17) and based on this trend a higher coefficient of linear thermal expansion could have been expected for $TmAgTe_2$.

No literature values of thermal expansion were available of XYZ_2 compounds and therefore the thermal expansion was compared to Ag and Cu chalcogenides. The linear coefficient of thermal expansion of $YCuTe_2$ and $TmAgTe_2$ is comparable to the coefficient of linear thermal expansion of $Cu_{2-x}Se$ with a value of $23 \cdot 10^{-6}$ K^{-1} from room-temperature to 773 K [274]. Honma and Iida determined the coefficient of linear thermal expansion of silver chalcogenides [306]. The low-temperature phase of Ag_2S, Ag_2Se, and Ag_2Te had a coefficient of linear thermal expansion ranging from

$16.2 \cdot 10^{-6}$ K^{-1} to $24.7 \cdot 10^{-6}$ K^{-1} from 300 K to ∼450 K, similar to those determined for $TmAgTe_2$ and $YCuTe_2$. However, the coefficients of the high-temperature phase of Ag_2S ($45.8 \cdot 10^{-6}$ K^{-1}), Ag_2Se ($34.7 \cdot 10^{-6}$ K^{-1}), and Ag_2Te ($35.7 \cdot 10^{-6}$ K^{-1}) were larger than the present XYZ_2 [306].

Table 5.3: Average coefficient of linear thermal expansion, α, of $TmAgTe_2$, $YAgTe_2$, and $YCuTe_2$, on heating (H) and cooling (C).

Compound	Temperature range (H) / K	α (H) / 10^{-6} K^{-1}	Temperature range (C) / K	α (C) / 10^{-6} K^{-1}
$TmAgTe_2$	350-675	19 ± 2	350-625	20 ± 2
$YAgTe_2$	525-595	0 ± 2	425-550	13 ± 2
$YCuTe_2$	450-675	27 ± 2	450-675	25 ± 2
$Cu_{2-x}Se$ [274]	300-773	23		
Ag_2S [306]	300-450	16.2	300-430	16.2
Ag_2S [306]	450-575	45.8	430-575	45.8
Ag_2Se [306]	300-410	17.7	300-390	17.7
Ag_2Se [306]	410-575	34.7	390-575	34.7
Ag_2Te [306]	300-420	24.7	300-410	24.7
Ag_2Te [306]	430-575	35.7	420-575	35.7

It can be concluded that the thermal expansion is nearly constant for $TmAgTe_2$ and $YCuTe_2$ over a wide range of temperature (see Table 5.3) and in the range of Cu and Ag chalcogenides. The thermal expansion of $YAgTe_2$, on the other hand, indicated a complex behavior in the temperature range from 350 K to 675 K.

5.1.5 Electronic Properties

With the understanding of the temperature range for the various phases of the XYZ_2 compounds, the thermoelectric properties can be investigated. High-throughput screening predicted that the XYZ_2 compounds have enhanced electronic properties pointing to promising thermoelectric materials. The electronic properties were calculated from the electronic band structures and using Boltzmann transport equations. While the Boltzmann transport equations are limited to the constant relaxation time, an accurate calculation of the electronic band structure is required to improve the prediction of the electronic properties in thermoelectrics. Therefore, the computed electronic band structure are compared to experimental density of states (DOS).

5.1.5.a Electronic Band Structure - Computation

The electronic band structures of the LT phases of $Tm^{oh}Ag^{th}Te_2$ (space group $P\bar{4}2_1m$), $Y^{oh}Ag^{th}Te_2$ (space group $P\bar{4}2_1m$), and the HT phase of $Y^{oh}Cu^{th}Te_2$ (space group $P\bar{3}$) were computed with and without the inclusion of spin orbit coupling using PBE-GGA as shown in Figure 5.13. The colors in the electronic band structures represent the projections of the wave function onto the different elements.

$TmAgTe_2$ The LT phase of $Tm^{oh}Ag^{th}Te_2$ has an indirect band gap with band gap energy of 0.91 eV (with no spin orbit coupling (NSOC); Figure 5.13 (a)) and 0.67 eV (with spin orbit coupling (SOC); Figure 5.13 (b)). Multiple bands close to VBM and the conduction band minimum (CBM) were observed which contribute to the electronic transport. The valence band has a maximum at the Γ symmetry point where four bands are degenerate in the NSOC structure. Additionally, two valence bands at the A point can contribute to the electronic properties at elevated temperature suggesting enhanced p-type electronic properties in the LT phase of $TmAgTe_2$. With the inclusion of SOC, the valence bands at Γ point split by about 0.1 eV pointing to a reduction in the thermoelectric performance.

The conduction band has a minimum between the M and Γ symmetry points with NSOC and several conduction bands can contribute to the electronic transport at elevated temperature (between Γ and Z as well as between Γ and X). For the SOC band structure, the conduction bands are flatter which decreases the electron mobility and hence, the electrical conductivity. In addition to the LT tetragonal phase of $TmAgTe_2$, the electronic band structure of the HT trigonal phase ($P\bar{3}m1$) was computed to have multiple bands at the symmetry point A and along Σ and Λ with multiplicities of 1, 6, and 6, respectively. The trigonal phase of $TmAgTe_2$ also has an indirect band gap with band gap energy of 0.69 eV and 0.40 eV, with NSOC and SOC, respectively. The conduction bands have minima at L, K, and M which can contribute to the n-type electron properties. With the inclusion of SOC the doubly-degenerate valence bands at A split by around 0.5 eV which increases the separation of the valence band maxima at A and Λ by $\sim$0.2 eV resulting in a reduction of the predicted thermoelectric performance (see Figure 5.3 (a)).

The electronic band structures of both phases indicate that there is only a weak

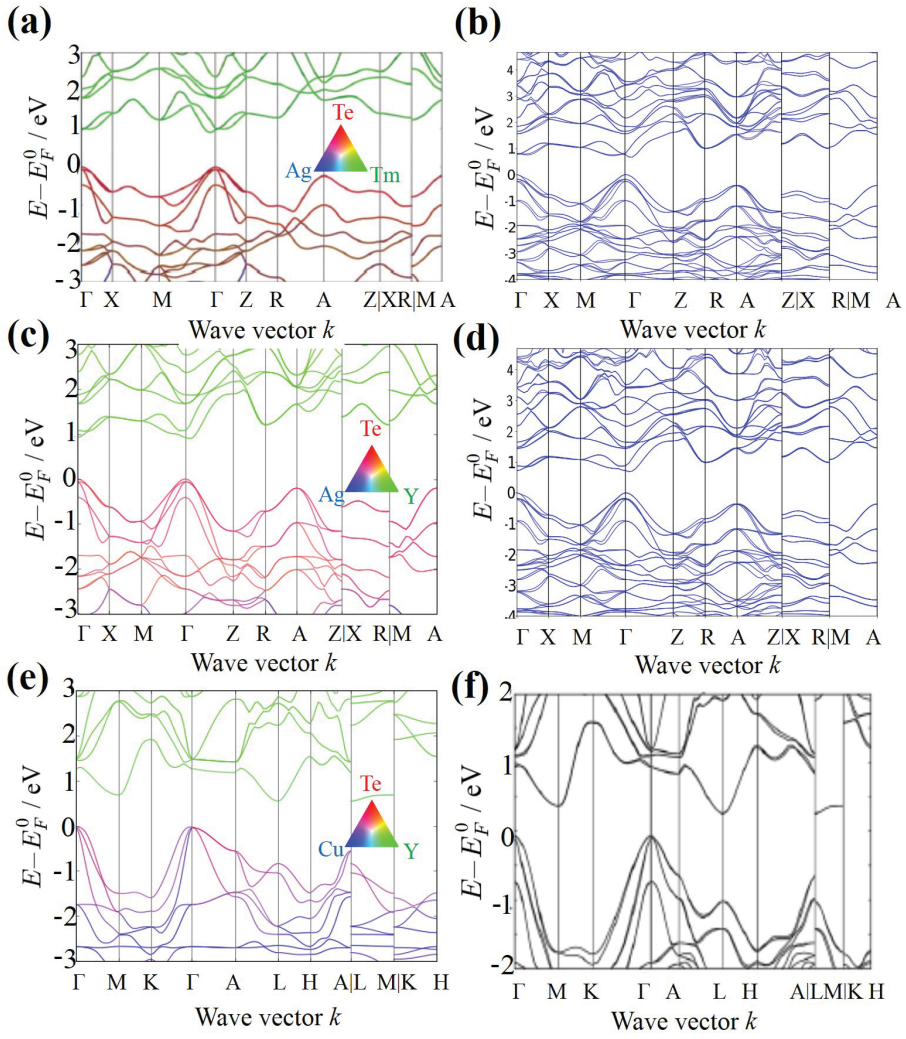

Figure 5.13: Electronic band structure with and without the inclusion of spin orbit coupling using PBE-GGA. The low-temperature phase of (a) $Tm^{oh}Ag^{th}Te_2$ (space group $P\bar{4}2_1m$), (c) $Y^{oh}Ag^{th}Te_2$ (space group $P\bar{4}2_1m$), and the high-temperature phase of (e) $Y^{oh}Cu^{th}Te_2$ (space group $P\bar{3}$) without spin orbit coupling. The corresponding electronic band structure of (b) $Tm^{oh}Ag^{th}Te_2$, (c) $Y^{oh}Ag^{th}Te_2$, and (f) $Y^{oh}Cu^{th}Te_2$ with the inclusion of spin orbit coupling indicates a splitting of the bands at the valence band maxima. The colors in the electronic band structure without spin orbit coupling represent the contribution of the elements onto the various bands. Figures of NSOC are from 'The Materials Project' and SOC were provided by Dr. Hong Zhu and Zhe Luo, School of Materials Science and Engineering, Shanghai Jiao Tong University (unpublished work shown with permission). Figure (f) from reference [292].

.

hybridization of Te-p and Ag-d orbitals as shown in Figure 5.13 (a). This is reasonable because the position of the computed Ag-d and Te-p orbitals are far apart (see Figure 5.3 (b)) and the thermoelectric performance enhanced with a reduction in the hybridization of $Y - d$ and $Z - p$ orbitals of the tetragonal phase (see Figure 5.3 (b)). A similar weak hybridization of Ag-d and Te-p was obtained in the LT phase of $Y^{oh}Ag^{th}Te_2$ (see Figure 5.13 (c)).

$YAgTe_2$ The electronic band structure of $YAgTe_2$ is similar to the LT band structure of $TmAgTe_2$. Four degenerate valence bands are at Γ symmetry point and a doubly-degenerate valence band is at the symmetry point A. The energy difference between the A and Γ was determined to be $\sim$0.21 eV. $YAgTe_2$ has an indirect band gap with a band gap energy of 0.90 eV (with NSOC; Figure 5.13 (c)) and 0.68 eV (with SOC; Figure 5.13 (d)). The conduction bands of the LT phase of $YAgTe_2$ have a minimum along Z and Γ. The valence bands at the Γ point slightly split with the inclusion of SOC with an energy difference of $\sim$0.19 eV. Furthermore, the SOC band structure has a larger energy separation between the valence bands at Γ and A of roughly 0.35 eV.

$YCuTe_2$ In addition to the LT phases of $Tm^{oh}Ag^{th}Te_2$ and $Y^{oh}Ag^{th}Te_2$ which are both in the tetragonal phase (space group $P\bar{4}2_1m$), the electronic band structure of the HT phase of $Y^{oh}Cu^{th}Te_2$ indicates an indirect band gap with band gap energy of 0.58 eV (with NSOC; Figure 5.13 (e)) and 0.36 eV (with SOC; Figure 5.13 (f)). Note that the space group of the LT phase is a subgroup of the space group of the HT phase of $YCuTe_2$ and the change between the LT and HT electronic band structure is most likely not very significant. Furthermore, a large band separation between the light and heavy hole band appeared at the Γ symmetry point with SOC ($\sim$0.7 eV). The conduction bands of $YCuTe_2$ have a minimum at M and L which contribute to the n-type electronic properties which are separated by an energy difference of 0.13 eV with NSOC. The energy difference slightly decreased to 0.11 eV with the inclusion of SOC suggesting that $YCuTe_2$ has good p- and n- type electronic behavior. In contrast to the Ag-based compounds, the Cu$-d$ and Te$-p$ orbitals hybridized at the VBM. However, for XYZ_2 compounds in the trigonal phase, it was found that reduced hybridization of the Y-d and Te-p orbitals is more important for multiple

degeneracy than weak hybridization of the Cu$-d$ and Te$-p$ orbitals as found for tetragonal compounds (*vide supra*).

5.1.5.b Electronic Band Structure - Experiments

The computed electronic band structures were confirmed by experimentally determined density of states (DOS). The experimental DOS was acquired using ultraviolet photoelectron spectroscopy (UPS) below the Fermi energy and inverse photoemission spectroscopy (IPES) above the Fermi energy by Jon-Paul Sun in the laboratory of Dr. Ian Hill, Department of Physics and Atmospheric Science, Dalhousie University [307]. UPS measurements was performed with a He discharged lamp which has two energies, 21.21 eV for HeI and 40.82 eV for HeII. Although the HeII indicated more features at the valence band maximum, the signal-to-noise ratio was, in some samples, too large and therefore, HeI was used for the measurement as indicated in Figure 5.14. The computed DOS was calculated using PBE-GGA [51] with the inclusion of SOC to enhance the estimation of the separated valence bands.

TmAgTe$_2$ The experimental DOS of $TmAgTe_2$ agrees well with the computed DOS as shown in Figure 5.14 (a). The experimental DOS was recorded for the LT and HT phase as well as the Mg-doped sample. It is important to note that the Zn-doped could not be investigated because the measurements were performed under high vacuum which increased evaporation of high vapor pressure elements. Furthermore, the surface of the parent compound and the Mg-doped sample were sputtered for 60 min and 10 min, respectively, to remove contamination and surface oxide layer.

Below the Fermi Energy, all three $TmAgTe_2$ compounds show two distinct peaks which can be assigned to Te ($E - E_F^0 = -10.3$ eV) and the hybridization of Te-p and Ag-d ($E - E_F^0 = -6$ eV). While the parent compounds have a shoulder at the VBM, no feature was observed for the Mg-doped sample (see Figure 5.14 (a)). Note that the Mg-doped compound crystallized in the trigonal phase and the DOS of the Mg-doped is nearly the same to a binding energy of $E - E_F^0 = -3.8$ eV. The tetragonal phase, on the other hand, shows another peak at $E - E_F^0 = -12.3$ eV and the peak of the hybridization Te-p and Ag-d was suppressed. Above the Fermi energy, the DOS of the parent is nearly the same for the tetragonal and trigonal phase. However, the

Mg-doped compound has a distinct peak around $E - E_F^0 = 2$ eV.

The computed DOS of Te and Ag for the trigonal phase were shifted to lower binding energies than for the tetragonal phase. However, it is important to note that Tm-f electrons were calculated as core electrons using a pseudo-potential. The inclusion of Tm-f valence electrons can affect the position of the Te-p and Ag-d DOS. It is challenging to include f electrons in the calculations. A fit of the experimental DOS, however, indicated that there might be another DOS peak between the Te-p and the Ag-d peaks which can be assigned to Tm-f electrons.

It can be concluded that both phases of the parent compound have the same DOS at the VBM and CBM resulting in similar electronic behavior, although the electronic band structure was different for the tetragonal and trigonal phases. The Mg-doped compound has a different DOS than the corresponding parent compound and the electronic properties are most likely different than the parent compound.

$YAgTe_2$ The experimental DOS of the tetragonal phase of $YAgTe_2$ is shown in Figure 5.14 (b). The UPS spectrum was acquired with HeI and after 15 min sputtering to remove surface contamination and oxidation. Although the DOS increased with increasing binding energy, a peak was observed at around $E - E_F^0 = -10.8$ eV which is at a slightly higher binding energy than for $TmAgTe_2$. A higher binding energy was also computed for the Te-p peak of $YAgTe_2$ compared to the peak of $Tm^{oh}Ag^{th}Te_2$ in the tetragonal phase. A small shoulder appeared around $E - E_F^0 = -7$ eV which can be assigned to the Ag-d peak. Above the Fermi energy, the experimental DOS showed a large increase followed by a plateau which is found at an energy similar to the computed Tm peak.

$YCuTe_2$ In addition to the Ag-based compounds, the experimental DOS of $YCuTe_2$ and an intrinsically doped compound, $Y_{0.96}Cu_{1.08}Te_2$, were recorded using HeI and HeII, respectively (see Figure 5.14 (c)). Prior the recording of the UPS and IPES spectra, the parent compound and the intrinsically doped sample were sputtered for 30 min and 10 min, respectively. Two peaks of the DOS were found below the Fermi energy where the peak at $E - E_F^0 = -10.6$ eV can be assigned to the Te-p DOS. The DOS is similar to the computed DOS using PBE-GGA with the inclusion of SOC ($E - E_F^0 = -10.7$ eV) as shown in Figure 5.14 (c). The intrinsically doped compound

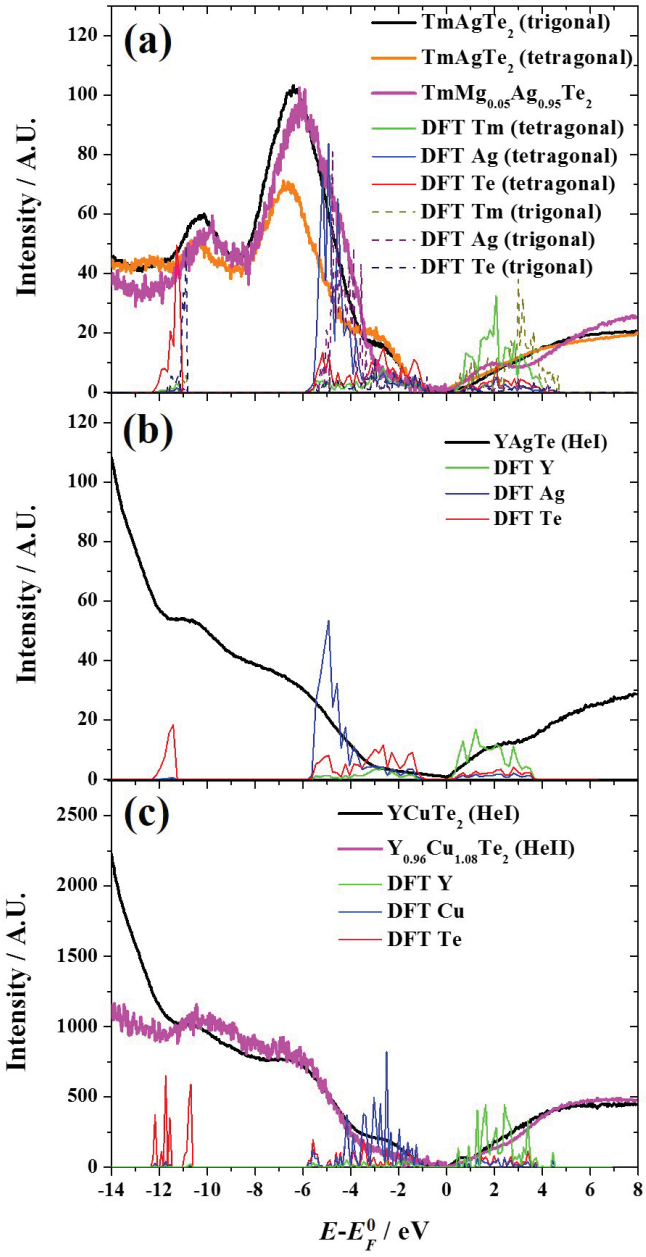

Figure 5.14: Comparison of computational and experimental density of states (DOS) of (a) $TmAgTe_2$ and Mg-doped sample, (b) $YAgTe_2$, and (c) $YCuTe_2$ and an intrinsically doped compound, $Y_{0.96}Cu_{1.08}Te_2$. Computed DOS of elements were calculated using PBE-GGA with SOC and experimental DOS were acquired with ultraviolet photoelectron spectroscopy (UPS) and inverse photoemission spectroscopy (IPES). Experimental DOS agrees well with the computed DOS of the elements.
.

has a DOS similar to the parent compound. However, the DOS of $Y_{0.96}Cu_{1.08}Te_2$ is lower at the band gap than the parent compound which might point to an increase in electrical conductivity whereas the Seebeck coefficient would be smaller.

It is important to note that the electronic band structure of $TmAgTe_2$, $YAgTe_2$, and $YCuTe_2$ were calculated with PBE-GGA which normally underestimates the band gap energy [53]. A better approach would be the hybrid functional HSE06 which predicts the band gap energy more accurately. However, HSE06 with the inclusion of SOC was too computationally expensive to compute with f-electrons or the large supercell of $YCuTe_2$. With exponential growth of computing power the first-principles calculations of these structures will be feasible to calculate with the HSE functional and the inclusion of SOC in future.

It can be concluded that the first-principle calculations agree well with experiments. The Te-p peak was observed in the experimental DOS for all compounds. However, with extrinsic and intrinsic doping the DOS can be changed at the band gap and that might influence the electronic properties of the compounds.

5.1.5.c Electrical Resistivity

The electrical resistivities, ρ_{el}, of $TmAgTe_2$, $YAgTe_2$, $YCuTe_2$ and the corresponding doped compounds were measured from room-temperature to high temperatures (see Section 3.2.5.c). (The low-temperature electrical resistivity was measured with the TTO method and the DC resistivity option in a PPMS. However, the electrical resistivity was, by several orders of magnitude, higher than the electrical resistivity determined at high temperature or the resistance was out of range for the measurement, likely due to surface oxidation and/or the 2Ω method.) In addition to the electrical resistivity, the Hall coefficient was measured with a magnetic field of ±2 T (see Section 3.2.5.c) and the Hall mobility, μ_H, as well as the Hall carrier concentration, n_H, was calculated from Equation 2.49 and Equation 2.48, respectively. (Electrical resistivity, Hall mobility, and Hall carrier concentration data of $TmAgTe_2$, $YAgTe_2$, $YCuTe_2$ parent compounds and their corresponding doped compounds are given in Tables C.5-D.14 of Appendix C).

$TmAgTe_2$ Temperature-dependent resistivities of the $TmAgTe_2$ parent compound and extrinsically doped compounds are shown in Figure 5.15 (a). While both tetragonal and trigonal phases of $TmAgTe_2$ and the Mg-doped compound had a similar resistivity at room-temperature, the temperature dependence of these compounds was different. The electrical resistivity of the tetragonal phase increased with temperature to ∼440 K, followed by a decrease in resistivity ($\rho_{el} \sim 230$ mΩ cm at 675 K). The trigonal phase resistivity decreased with increasing temperature from room-temperature to ∼575 K ($\rho_{el} \sim 140$ mΩ cm) indicating intrinsic semiconducting behavior and the resistivity slightly increased with temperature above 575 K. The difference between the temperature dependence of both phases can be explained by the Hall mobility and Hall carrier concentration. The Hall mobility decreased for both phases but the Hall carrier concentration of the trigonal phase increased with temperature to ∼480 K whereas the Hall carrier concentration of the tetragonal phase is nearly constant to 450 K resulting in an increase in the electrical resistivity as shown in Figure 5.15. Above 450 K the Hall carrier concentration of the tetragonal phase increased with temperature from $4 \cdot 10^{17}$ h^+ cm^{-3} to $5 \cdot 10^{18}$ h^+ cm^{-3}. The temperature behavior of the trigonal phase changed above ∼480 K where the Hall mobility increased while the Hall carrier concentration decreased with temperature, most likely due to a bipolar effect (*i.e.*, electrons and holes contribute to the electrical conductivity). The Hall mobility is relatively high indicating potential for enhanced thermoelectric performance if the Hall carrier concentration increased.

The electrical resistivity of Mg-doped $TmAgTe_2$ compound decreased with temperature pointing to intrinsic semiconducting behavior. The electrical resistivity is similar to that of the parent compound at 700 K. A slight increase in Hall mobility and Hall carrier concentration were observed. It is important to note that the Hall carrier concentration is relatively low at room-temperature suggesting that Mg enhanced impurity scattering. The Zn-doped compound had the lowest electrical resistivity at room temperature of all $TmAgTe_2$ compounds ($\rho_{el} \sim 750$ mΩ cm). While the Hall mobility decreased with a similar trend than the tetragonal phase, the Hall carrier concentration increased continuously with temperature to $\sim 10^{19}$ h^+ cm^{-3} which is in the region of good thermoelectric materials. Further

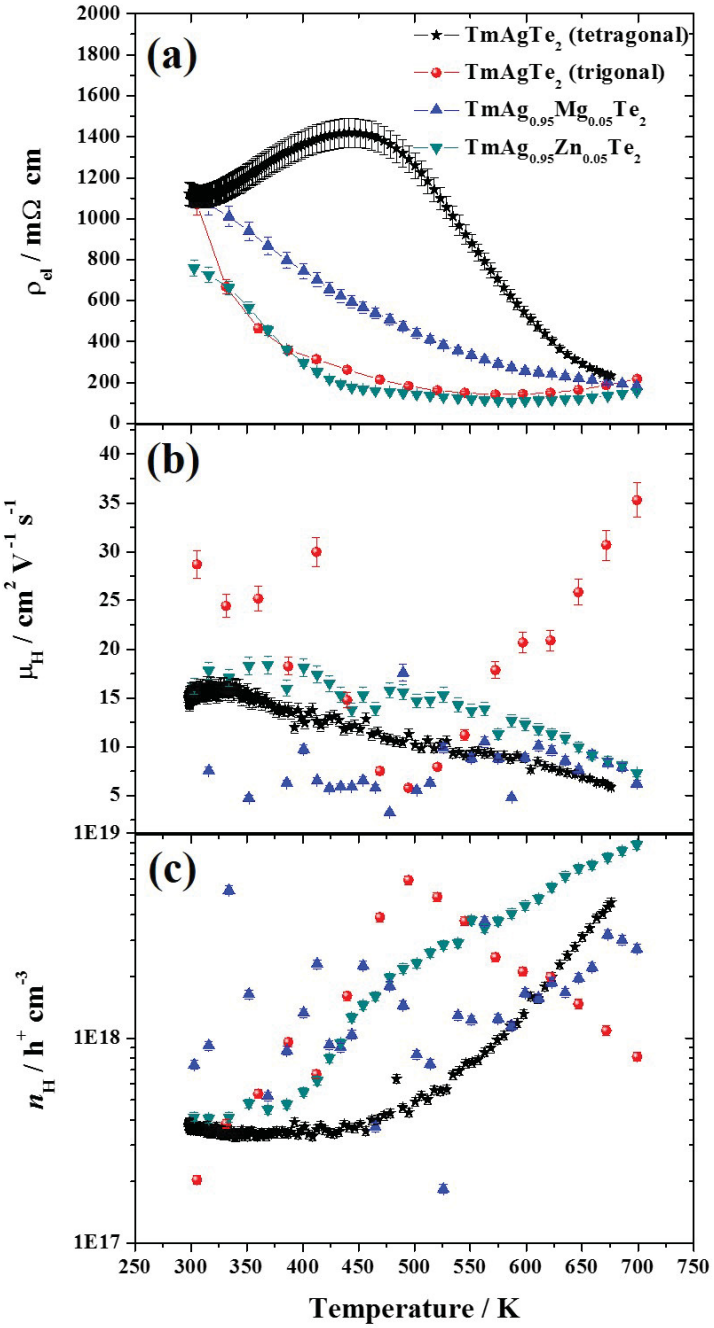

Figure 5.15: Temperature dependence of (a) electrical resistivity, ρ_{el}, (b) Hall mobility, μ_H, and (c) Hall carrier concentration, n_H, of $TmAgTe_2$ parent compound and extrinsically doped. An uncertainty of 5% was estimated for ρ_{el}, μ_H, and n_H. Figure (a) was partially taken from reference [277].

.

studies with an increased Zn-doping to $Zn_{0.1}$ were performed but no increase in carrier concentration was observed. It is important to note that all $TmAgTe_2$ compounds showed a positive Hall coefficient resulting in *p*-type semiconducting behavior.

The resistivity in the $TmAgTe_2$ parent compounds is relatively high for enhanced thermoelectric materials due to the low carrier concentration. For a better understanding of the carrier concentration, the defects were calculated for the trigonal phase of $Tm^{oh}Ag^{oh}Te_2$ in four different regions in the Tm - Ag - Te phase diagram (see Figure 5.16). Figure 5.16 (a) depicts the calculated ternary ground state phase diagram and the numbers indicate the four different regions in which $TmAgTe_2$ can appear by slight changes of the optimum composition. The defect formation enthalpies are plotted as a function of the Fermi level in Figure 5.16 (b). For *p*-type behavior, the lowest defect formation enthalpies were found for cation antisite defects (Tm_{Ag}, *i.e.*, Tm sits on Ag site) in region 2 and 4 and for cation vacancy defect (V_{Ag}, *i.e.*, a vacancy on Ag site) in region 1 and 3. Whereas V_{Ag} defects enhanced the *p*-type carrier concentration, Tm_{Ag} antisite defects result in *n*-type behavior decreasing the hole carrier concentration of the compounds. Therefore, the carrier concentration could be low in the synthesized $TmAgTe_2$ compounds due to Tm_{Ag} antisite defects. With Mg- and Zn-doping, an increase of the Hall carrier concentration was observed in contrast to the trigonal phase, in particular, at high temperatures. Ag has an oxidization number of +1 and Tm has an oxidization of +3 resulting in two electrons for each Tm_{Ag} antisite defect, whereas Mg and Zn have oxidization numbers of +2 reducing the number of electrons per antisite defect.

In conclusion, a low carrier concentration in $TmAgTe_2$ due to Tm_{Ag} antisite defects resulted in high electrical resistivity. With extrinsic doping, the effect of the Tm_{Ag} antisite defects might be reduced which would increase the carrier concentration and hence reduce the electrical resistivity.

$YAgTe_2$ The electrical resistivity of $YAgTe_2$ and $Y_{0.98}Ag_{1.02}Te_{1.98}$ as a function of temperature is shown in Figure 5.17 (a). Higher resistivity was found for the parent compound at room temperature than for the extrinsically doped compound or the

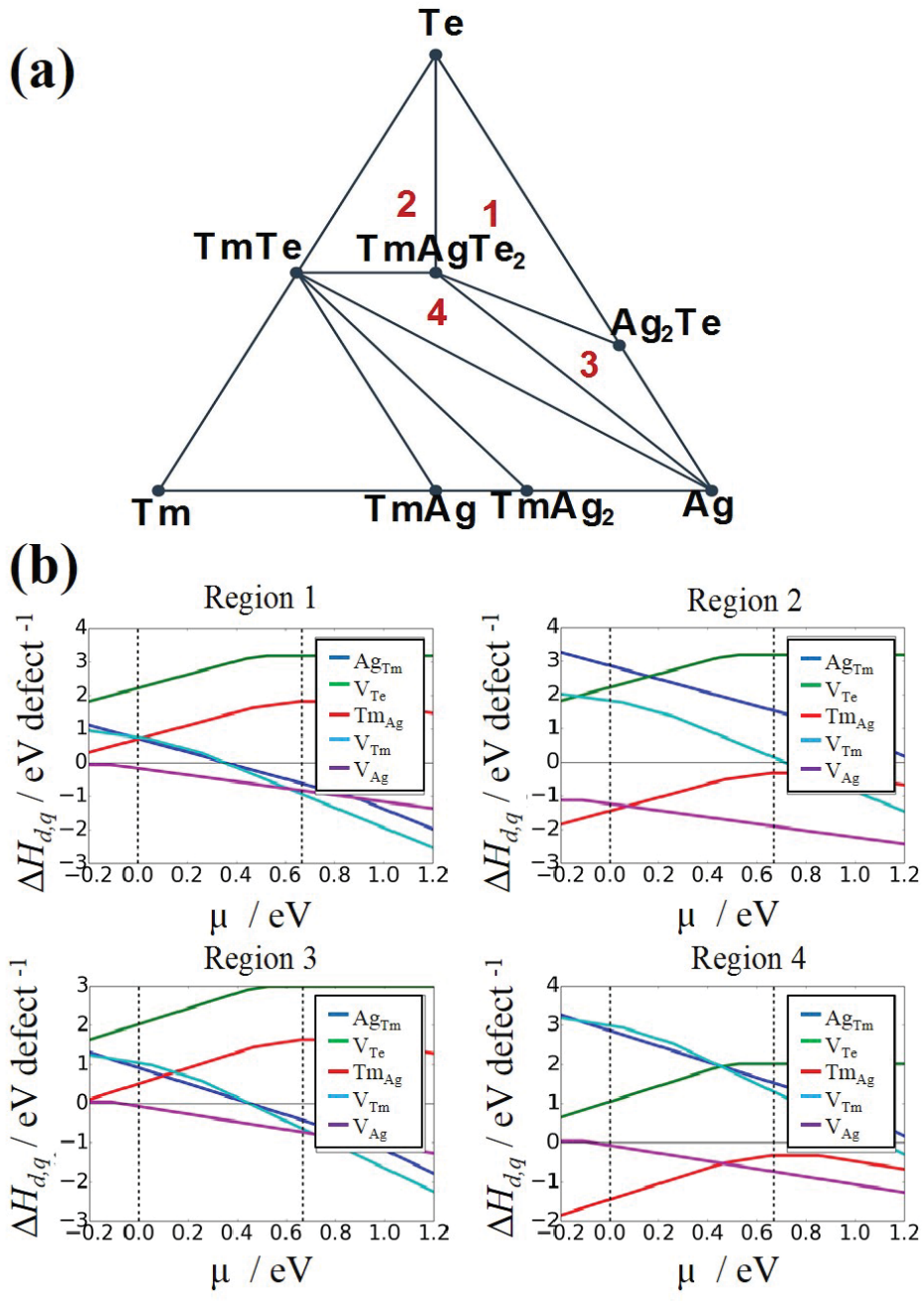

Figure 5.16: (a) Ground state phase diagram of Tm - Ag - Te from the Materials Project Database [48]. Different synthesis regions of $TmAgTe_2$ are denoted by the numbers which have slightly different compositions than the three-phase equilibrium of $TmAgTe_2$. (b) Computed defect formation enthalpies, $\Delta H_{d,q}$, in the trigonal phase of $Tm^{oh}Ag^{oh}Te_2$ as a function of the Fermi level, μ. Vertical lines represent the calculated band gap edges. Figures from reference [277].

$TmAgTe_2$ compounds. At high temperature, however, the electrical resistivity of the parent compound decreased to about 100 mΩ cm at 800 K which is lower than the resistivity measured in $TmAgTe_2$ (see Figure 5.15 (a)). While the resistivity in the intrinsically doped compound decreases nearly exponentially with temperature, the resistivity in the parent $YAgTe_2$ compound dramatically decreased from 300 K to 530 K, followed by a slight reduction of the resistivity. A similar change was also observed in thermal expansion of $YAgTe_2$ (see Figure 5.12 (b)).

The Hall mobility of the $YAgTe_2$ parent compound shows positive and negative values whereas the mobility of $Y_{0.98}Ag_{1.02}Te_{1.98}$ is positive at room-temperature and changed to negative at ∼425 K as shown in Figure 5.17 (b). The negative mobility indicates that electrons are the dominant carriers at high temperature. However, this is contradictory to the positive Seebeck coefficient, as discussed below. Furthermore, the Hall carrier concentration of both $YAgTe_2$ phases has positive and negative values indicating that holes or electrons can be the dominant carriers at a given temperature (see Figure 5.17 (c)). The absolute values of the carrier concentration, plotted on a log scale, show continuous curves suggesting that the sign of the Hall coefficient cannot be accurately measured. The raw Hall coefficient which is proportional to the Hall voltage is relatively high and the changing signs cannot be explained with the uncertainty of the instrument. However, the contact resistances of the individual leads were high (∼10,000 Ω) and different (up to a factor of three) introducing uncertainty in the measurement and therefore, the dominant charge carriers can be more precisely delineated by the Seebeck coefficient. While the Hall carrier concentration is relatively low at room temperature ($\sim 10^{16}$ cm^{-3}) it increased to $\sim 5 \cdot 10^{18}$ cm^{-3} for the parent compound and $\sim 2 \cdot 10^{18}$ cm^{-3} for the doped compound. Further doping might enhance the carrier concentration and hence, the electronic properties of the material. Furthermore, the carrier concentration of the doped compound peaks twice (at ∼410 K and ∼700 K). While the low-temperature peak is similar to the phase transition temperature determined in DSC (∼ 400 K), the second peak is lower than the high-temperature phase transition at ∼750 K (see 5.11 (b)). This phase transition temperature is consistent with the change in Hall mobility and Hall carrier concentration of the parent compound as shown in Figure 5.17. However, due to change in signs of the Hall

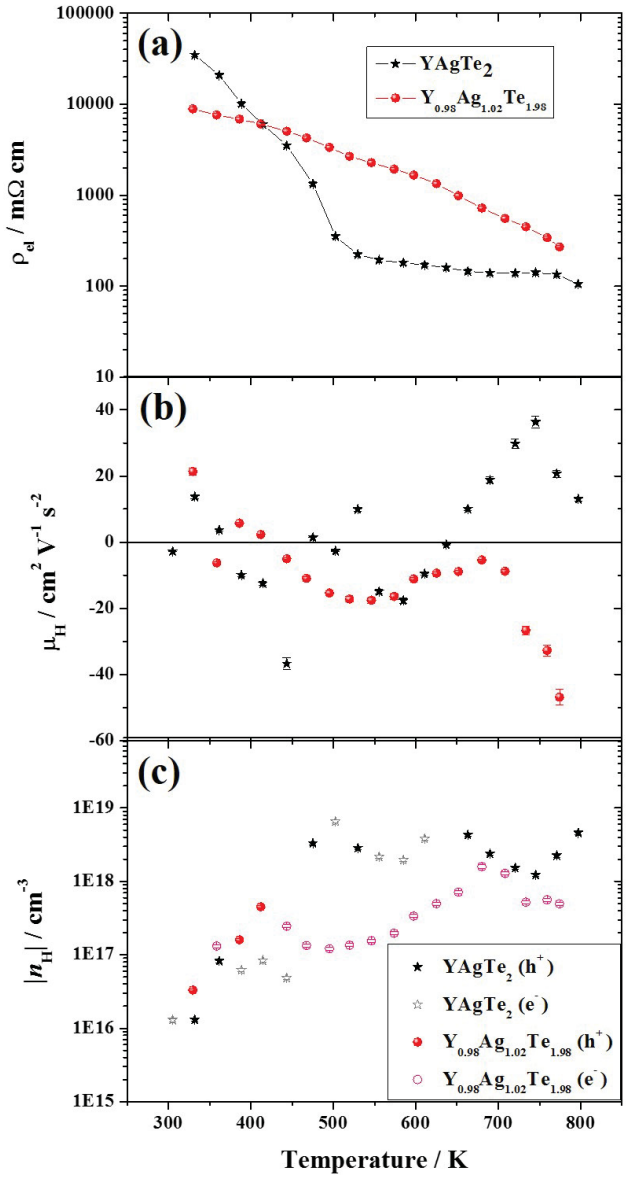

Figure 5.17: Temperature dependence of (a) electrical resistivity, ρ_{el}, (b) Hall mobility, μ_H, and (c) the absolute value of the Hall carrier concentration, $|n_H|$, of $YAgTe_2$ parent compound and intrinsically doped compound. Note that the electrical resistivity is shown on a log-scale to emphasize the discrepancy between the compounds at high temperature, $Y_{0.98}Ag_{1.02}Te_{1.98}$. Holes ($h^+$, solid symbols) and electrons (e^-, hollow symbols) can be the major carrier concentration in both compounds depending on the temperature. An uncertainty of 5% was estimated for ρ_{el}, μ_H, and n_H.

.

coefficient and the high contact resistances the values of the Hall mobility and Hall carrier concentration should be treated with due cautions.

The $YAgTe_2$ parent compound had a lower resistivity than $TmAgTe_2$ at high temperature whereas the room-temperature resistivity is over one order of magnitude higher. Two distinct resistivity regions were observed for the parent compound. The intrinsically doped compound had a lower resistivity at room temperature which nearly continuously decreased with temperature. The Hall data suggest p- and n-type behavior which might be an artifact of the sample. Further experiments would be required.

$YCuTe_2$ In addition to $TmAgTe_2$ and $YAgTe_2$ compounds, the electronic transport properties of $YCuTe_2$ and the intrinsically doped samples were measured from room-temperature to 775 K as shown in Figure 5.18. The electrical resistivity increased with temperature indicating heavily doped semiconducting behavior (Figure 5.18 (a)). The lowest room-temperature electrical resistivity was observed for the Cu excess samples ($\rho_{el} \sim 4$ mΩ cm) which increased to $\sim$16 mΩ cm at 800 K. A slightly higher resistivity was measured for $YCuTe_2$ with lower Cu content. The electrical resistivities in all $YCuTe_2$ compounds were more than two orders of magnitude higher than $TmAgTe_2$ and $YAgTe_2$ at room temperature and nearly an order of magnitude higher at 775 K. However, $YCuTe_2$ has a higher electrical resistivity than Cu_2Te ($\rho_{el} = 0.18$ mΩ cm at 300 K) [300] and $TmCuTe_2$ ($\rho_{el} = 0.99$ mΩ cm at 300 K) [255]. The higher electrical conductivity of $YCuTe_2$ might be a result of the larger band gap energy ($E_g \sim 0.58$ eV from PBE-GGA NSOC calculations) compared to Cu_2Te $E_g \sim 0$ eV from PBE-GGA NSOC calculations) and $TmCuTe_2$ ($E_g \sim 0.23$ eV from PBE-GGA NSOC calculations) [255]. A smaller band gap energy might result in a higher carrier concentration and hence in a lower electrical resistivity.

The Hall mobility indicates two distinct regions where the mobility decreased more rapidly from room temperature to 440 K as shown in Figure 5.18 (b). This is consistent with the temperature of the phase transition observed from DSC (see Figure 5.11 (c)). Above the phase transition, the Hall mobility decreased with temperature and is nearly proportional to $T^{-1.5}$, suggesting that acoustic phonons are most likely the dominant source of charge carrier scattering in $YCuTe_2$. While the mobility at

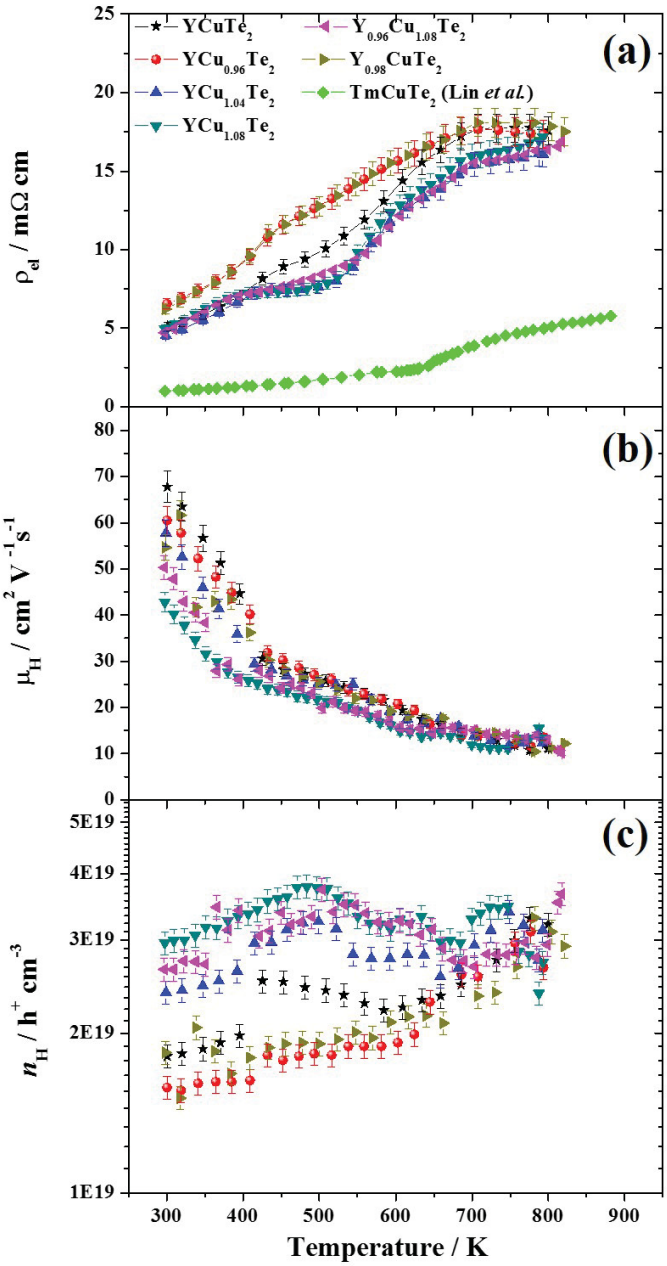

Figure 5.18: Temperature dependence of (a) electrical resistivity, ρ_{el}, (b) Hall mobility, μ_H, and (c) Hall carrier concentration, n_H, of $YCuTe_2$ parent compound and intrinsically doped compound. Resistivity of $YCuTe_2$ compounds was compared to $TmCuTe_2$ [255]. An uncertainty of 5% was estimated for ρ_{el}, μ_H, and n_H. Figure from reference [292].

.

room temperature depends on the Cu content and increased from 43 cm^2 $V^{-1}s^{-1}$ for $YCu_{1.08}Te_2$ to 67 cm^2 $V^{-1}s^{-1}$ for $YCuTe_2$, the mobility of all $YCuTe_2$ samples approached a similar value at high temperature ($\mu_H \sim 12$ cm^2 $V^{-1}s^{-1}$ at 775 K). The room-temperature mobility of all $YCuTe_2$ compounds is higher than that of $TmAgTe_2$ and $YAgTe_2$.

A similar temperature behavior was found for the Hall carrier concentration compared to the mobility as presented in Figure 5.18 (c). In contrast to the mobility which decreased with Cu content, the room-temperature carrier concentration increased with Cu content which is highest for $YCu_{1.08}Te_2$. This is consistent with Cu_2Te which has a lower Hall mobility ($\mu_H = 13$ cm^2 $V^{-1}s^{-1}$ at 300 K) but a larger Hall carrier concentration ($n_H = 2.77 \cdot 10^{21}$ h^+ cm^{-3} at 300 K) than $YCuTe_2$ [300]. This behavior is expected if the actual compositions of the $YCuTe_2$ compounds are considered (see Table C.4). Y-deficient and slightly Cu-excess compositions were observed for $YCu_{1.08}Te_2$ and $Y_{0.96}Cu_{1.08}Te_2$ whereas compounds with Cu < 1.08 have excess Y. Although the Cu content slightly increases, Y-deficiency results in an overall increase of p-type carrier concentration because Y is a trivalent cation whereas Cu is monovalent.

The Hall carrier concentration of $YCuTe_2$ ($(1.5 - 4) \cdot 10^{19}$ h^+ cm^{-3}) is higher than for $TmAgTe_2$ and $YAgTe_2$ and nearly temperature-independent. At high temperature, all $YCuTe_2$ compounds had comparable Hall carrier concentrations of $\sim 3 \cdot 10^{19}$ h^+ cm^{-3} as also observed for the Hall mobility. Furthermore, the Hall carrier concentration showed a phase transition between 400 K and 440 K (except for $YCu_{1.08}Te_2$) depicted by discontinuous curves in Figure 5.18 (c). The change in the carrier concentration at the phase transition is most likely due to a slight shift in compositions during the phase transition from a single phase to a phase-mixture region.

It can be concluded that all $YCuTe_2$ compounds had the lowest electrical resistivity of all investigated XYZ_2 compounds in the present study and slightly higher than $TmCuTe_2$. The low electrical conductivity is a result of a high Hall carrier concentration and Hall mobility. Intrinsic doping slightly changed the electrical resistivity in which the compounds with a higher Cu content had a lower mobility and a higher carrier concentration resulting in lower electrical resistivity.

The carrier concentrations of $TmAgTe_2$ compounds were lower than $YCuTe_2$ most likely due to Tm_{Ag} antisite defects which can act as hole killers[3]. The antisite defect might be reduced by extrinsically doping with divalent atoms (Mg and Zn) leading to a slight increase in carrier concentration. The resistivity of $YAgTe_2$ had a complex temperature trend leading to a dramatic decrease of electrical resistivity with temperature.

5.1.5.d Seebeck Coefficient

The Seebeck coefficients of $TmAgTe_2$, $YAgTe_2$, and $YCuTe_2$ parent compounds and their corresponding doped compounds were measured from low temperature (∼50 K for $TmAgTe_2$ and $YAgTe_2$ compounds; ∼2 K for $YCuTe_2$) to high temperature (∼800 K). The low-temperature Seebeck coefficient measurements were performed in the laboratory of Dr. Mary Anne White, Department of Chemistry, Dalhousie University, using a PPMS. The Seebeck coefficients of the Ag-based compounds changed at low-temperature (<50 K) from negative to positive and over several orders of magnitude suggesting systematic errors due to single-point measurements. Therefore, these Seebeck coefficients were excluded below 50 K. Similarly, erratic individual data points which have a large discrepancy to the temperature trend were also removed. (The Seebeck coefficients of the various XYZ_2 compounds are given in Tables C.14-C.16 of Appendix C.)

The Seebeck coefficients of all investigated XYZ_2 show a positive Seebeck coefficient indicating that holes are the majority carriers in these compounds (see Figure 5.19). The temperature dependence of the Seebeck coefficient of $TmAgTe_2$ compounds is shown in Figure 5.19 (a). All $TmAgTe_2$ compounds have a high Seebeck coefficient enhancing the thermoelectric figure of merit. At low temperature, the Seebeck coefficient of the trigonal phase increased with temperature to about 200 K, followed by a nearly constant Seebeck coefficient to ∼300 K. However, a large discrepancy between the low-temperature and high-temperature measurements was observed which might be due to a slight transformation from the trigonal to the tetragonal phase in the parent compound

[3]The term 'hole killer' is referred to anti-site defects which provide free electrons, *e.g.*, Tm^{3+} on Ag^{+} site can provide two free electrons/atom. These free electrons can combine with holes leading to a reduction in hole concentration.

over time. The Seebeck coefficient of the Zn-doped compound also was measured at low temperature and showed a slightly higher Seebeck coefficient than the trigonal phase from 100 K to 300 K. The low-temperature Seebeck coefficient of $TmZn_{0.05}Ag_{0.95}Te_2$ agrees well with the high-temperature measurements which are similar to the trigonal phase of the parent compound. It is important to note that the extrinsically doped compounds crystallized in the trigonal phase and all trigonal phases show a similar temperature trend in Seebeck coefficient over the entire temperature range. A dip in the Seebeck coefficient was observed between 500 K and 550 K. The Seebeck coefficient of the trigonal phase of the parent compound is consistent with the Hall carrier concentration which maximized around 500 K (see Figure 5.15 (c)). However, the Hall carrier concentration of the extrinsically doped compounds cannot explain the temperature trend of the Hall carrier concentration.

Mg-doped $TmAgTe_2$ had a lower room-temperature Seebeck coefficient than the other two compounds in the trigonal phase which is similar to the Seebeck coefficient of the trigonal parent compound from the low-temperature measurements. The lower Seebeck coefficient of $TmMg_{0.05}Ag_{0.95}Te_2$ compared to the parent compound might be due to a reduced DOS at the valence band edge as shown in Figure 5.14 (a). At high temperature, the Seebeck coefficient of the Mg-doped compound approached the value of the other trigonal $TmAgTe_2$.

The tetragonal phase of $TmAgTe_2$ showed a different temperature trend than the trigonal compounds which is similar to the temperature trend of the electrical resistivity which increases with temperature, followed by a decrease to the phase transition (Figure 5.15 (a)). Furthermore, the tetragonal phase had the highest Seebeck coefficient among all $TmAgTe_2$ compounds ($S \sim 600$ µV K^{-1} at 475 K).

The temperature dependence of the Seebeck coefficient of $YAgTe_2$ and $Y_{0.98}Ag_{1.02}Te_{1.98}$ is presented in Figure 5.19 (b). The low-temperature Seebeck coefficient of the parent compound increased from 50 K and 300 K. The Seebeck coefficient from the low-temperature measurement agrees well with the high-temperature measurement. At elevated temperature, a complex temperature behavior was observed, consistent with the two phase transitions recorded by DSC at ∼400 K and ∼750 K (see Figure 5.11 (b)). The Seebeck coefficient is, in particular, high at the phase transition ($S \sim 600$ µV K^{-1} at 395 K and $S \sim 545$ µV

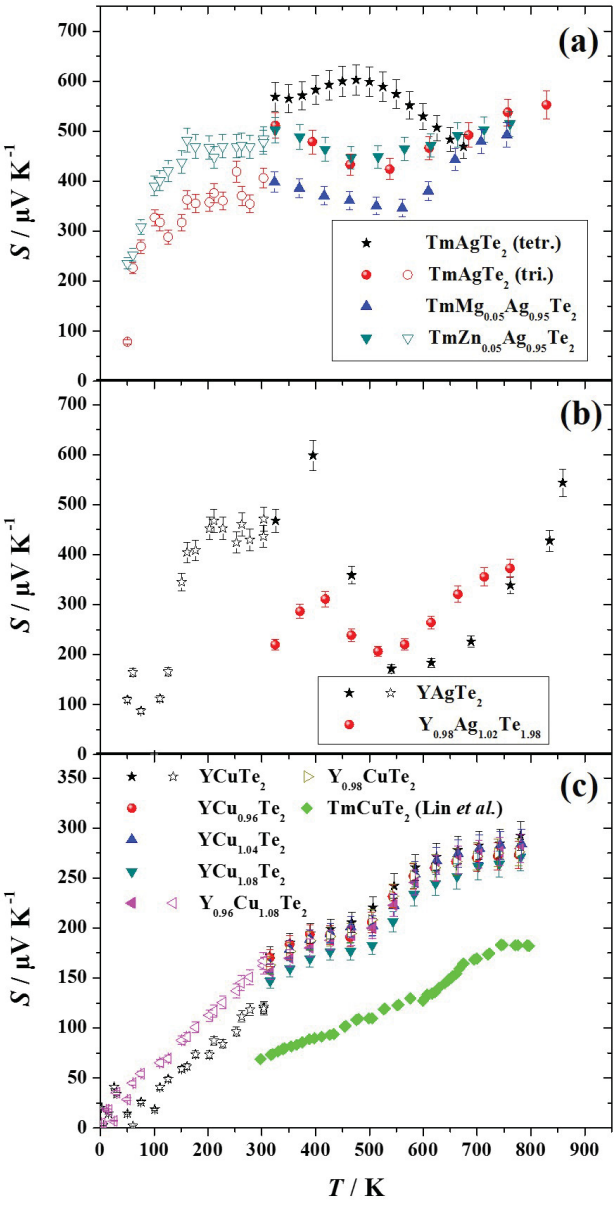

Figure 5.19: Seebeck coefficient, S, as a function of temperature of (a) $TmAgTe_2$, (b) $YAgTe_2$, and (c) $YCuTe_2$ parent compounds and their corresponding doped compounds. Seebeck coefficient of $YCuTe_2$ compounds was compared to $TmCuTe_2$ [255]. Low-temperature Seebeck coefficients (hollow symbols) are similar to high-temperature Seebeck coefficients (solid symbols) at room temperature. An uncertainty of 5% was estimated for S. Figures (a) and (c) from reference [277] and [292].

.

K^{-1} at 860 K). Although the electrical resistivity of $YAgTe_2$ was higher than $TmAgTe_2$ at 800 K, the Seebeck coefficients of both compounds are similar indicating enhanced thermoelectric performance in $YCuTe_2$.

The intrinsically doped compound has a temperature dependence similar to the parent compound with a lower Seebeck coefficient ($S \sim 225$ µV K^{-1} at 325 K and $S \sim 375$ µV K^{-1} at 760 K). It is important to note that Seebeck coefficient is positive indicating holes are the dominant charge carrier over the entire temperature range whereas the Hall coefficient switched between positive and negative values. The Hall coefficient was determined using only two data points at ±2 T, while the Seebeck coefficient was calculated from the slope of voltage versus temperature difference for at least twenty data points at a given temperature.

The Seebeck coefficient of the $YCuTe_2$ parent compound and intrinsically doped compounds is shown as a function of temperature in Figure 5.19 (c). The Seebeck coefficient increased with temperature, with a similar temperature behavior for all samples, to a maximum Seebeck coefficient of ∼285 µV K^{-1} for the parent compound at 775 K. The low-temperature Seebeck coefficient increased nearly linearly with temperature from 2 K to 300 K. While the Seebeck coefficient of $Y_{0.96}Cu_{1.08}Te_2$ from the low-temperature measurements agrees well with the high-temperature measurements at room temperature, the parent compound had a lower room-temperature Seebeck coefficient determined by the TTO method than using the high-temperature measurement.

The highest Seebeck coefficient was measured for the parent compound while the Seebeck coefficient decreased with increasing Cu content which can be attributed to its higher carrier concentration. $YCu_{1.08}Te_2$ had a slightly lower Seebeck coefficient at high temperature ($S \sim 270$ µV K^{-1}). However, a higher Seebeck coefficient was measured for all Ag-based XYZ_2 compounds and correlated with lower carrier concentrations, as expected. For comparison to literature, Cu_2Te and $TmCuTe_2$ both exhibited higher carrier concentrations than $YCuTe_2$, and all $YCuTe_2$ compounds had larger Seebeck coefficients than Cu_2Te (∼57 µV K^{-1} at 780 K) [300] and $TmCuTe_2$ (∼185 µV K^{-1} at 745 K) [255].

In conclusion, high Seebeck coefficients were found for all $TmAgTe_2$ compounds where the Seebeck coefficients for the compounds in the trigonal phase decreased

with temperature due to an increase in carrier concentration. However, the high electrical resistivity in these compounds reduced the thermoelectric performance due to the low carrier concentration. Extrinsic doping increased the carrier concentration indicating a decrease in electrical resistivity whereas their Seebeck coefficients were comparable to the trigonal phase at high temperature. The $YAgTe_2$ parent compound had a lower resistivity than $TmAgTe_2$ at high temperature while the Seebeck coefficient was similar to that of the $TmAgTe_2$ compounds indicating enhanced thermoelectric performance for $YAgTe_2$. The most promising electronic properties for thermoelectrics was observed for the $YCuTe_2$ compounds, showing one order of magnitude lower electrical resistivity than the Ag-based XYZ_2 compounds. Although the Seebeck coefficient of the $YCuTe_2$ compounds was about half of the Seebeck coefficient determined for $TmAgTe_2$ and $YAgTe_2$ at 775 K due to the higher carrier concentration, the power factor (*i.e.*, the product of the electrical conductivity and the square of the Seebeck coefficient) was the largest for the $YCuTe_2$. However, with optimization of the carrier concentration in $TmAgTe_2$ and $YAgTe_2$, the electronic properties likely can be enhanced.

5.1.6 Thermal Properties

In addition to the electronic properties, the thermal properties of $TmAgTe_2$, $YAgTe_2$, and $YCuTe_2$ compounds also were investigated, in order to better understand the potential of those materials as thermoelectrics. For the high-throughput screening, the phononic contribution of the thermal conductivity was set to a constant value ($\kappa_{pho} = 0.5$ W m^{-1} K^{-1}). However, the phononic contribution of thermal conductivity depends on many factors, *e.g*, crystal structure, crystallinity, and temperature. It is not feasible to predict the thermal conductivity in a high-throughput screening. However, the lowest limit of the thermal conductivity can provide insight of the phononic contribution of the thermal conductivity. In Section 4.1, a new model of minimum thermal conductivity was developed to estimate the lowest limit of the thermal conductivity. The Debye temperature can be determined from low-temperature heat capacity and from phononic dispersion curves.

5.1.6.a Phononic Dispersion Curves

The phononic dispersion curves of the low-temperature phases of $TmAgTe_2$, $YAgTe_2$, and $YCuTe_2$ were calculated by Zhe Luo and Dr. Hong Zhu, School of Materials Science and Engineering, Shanghai Jiao Tong University, using the lattice parameters given in Table 5.1. For $TmAgTe_2$ and $YAgTe_2$, van der Waals interactions were included to obtain more accurate results for the lattice parameters. It is important to note that the phononic dispersion curve was calculated for the monoclinic $YCuTe_2$ crystal structure with space group $C2/m$ instead of the $P\bar{3}m1$ crystal structure, as observed from experiments. The disordering of the Cu atoms can be better simulated in less symmetric space groups and the monoclinic cell with space group $C2/m$ had the lowest energy of all primitive (triclinic/monoclinic) cells. The disordered structure of $YCuTe_2$ was approximated by setting occupations of the $6i$ sites far from the $2d$ sites to 2/3 and the occupation of the $6i$ sites near the $2d$ site to 1/3. Although the change in crystal structure introduce uncertainty, the experimental heat capacity results agree well with the computed heat capacity from the monoclinic structure (*vide infra*).

All three phononic dispersion curves indicate low-frequency optical modes which might suppress the frequency of the acoustic modes, as shown in Figure 5.20. The acoustic modes increase nearly linearly from the center of the Brillouin zone for all phononic dispersion curves and therefore the thermal conductivity of the acoustic modes can be modeled with the Debye model. Furthermore, a large split between the transverse and longitudinal acoustic modes was observed along the Γ and Z direction for $TmAgTe_2$ and $YAgTe_2$ (see Figure 5.20 (a) and (b), respectively). No phononic band gap was observed in any of the three phononic dispersion curves due to the large number of modes (three acoustic modes and 21 optical modes for the tetragonal phases of $TmAgTe_2$ and $YAgTe_2$; three acoustic modes and 93 optical modes for the monoclinic phase of $YCuTe_2$). The maximum frequency of the optical modes in the three investigated XYZ_2 compounds was $\sim$180 cm^{-1}, suggesting a low thermal conductivity. Furthermore, most of the optical phonon modes were nearly constant over the entire Brillouin zone resulting in low group velocity and hence, the contribution of the optical phonons to the thermal conductivity would be insignificant.

The phononic dispersion curves of the $TmAgTe_2$ and $YAgTe_2$ are similar,

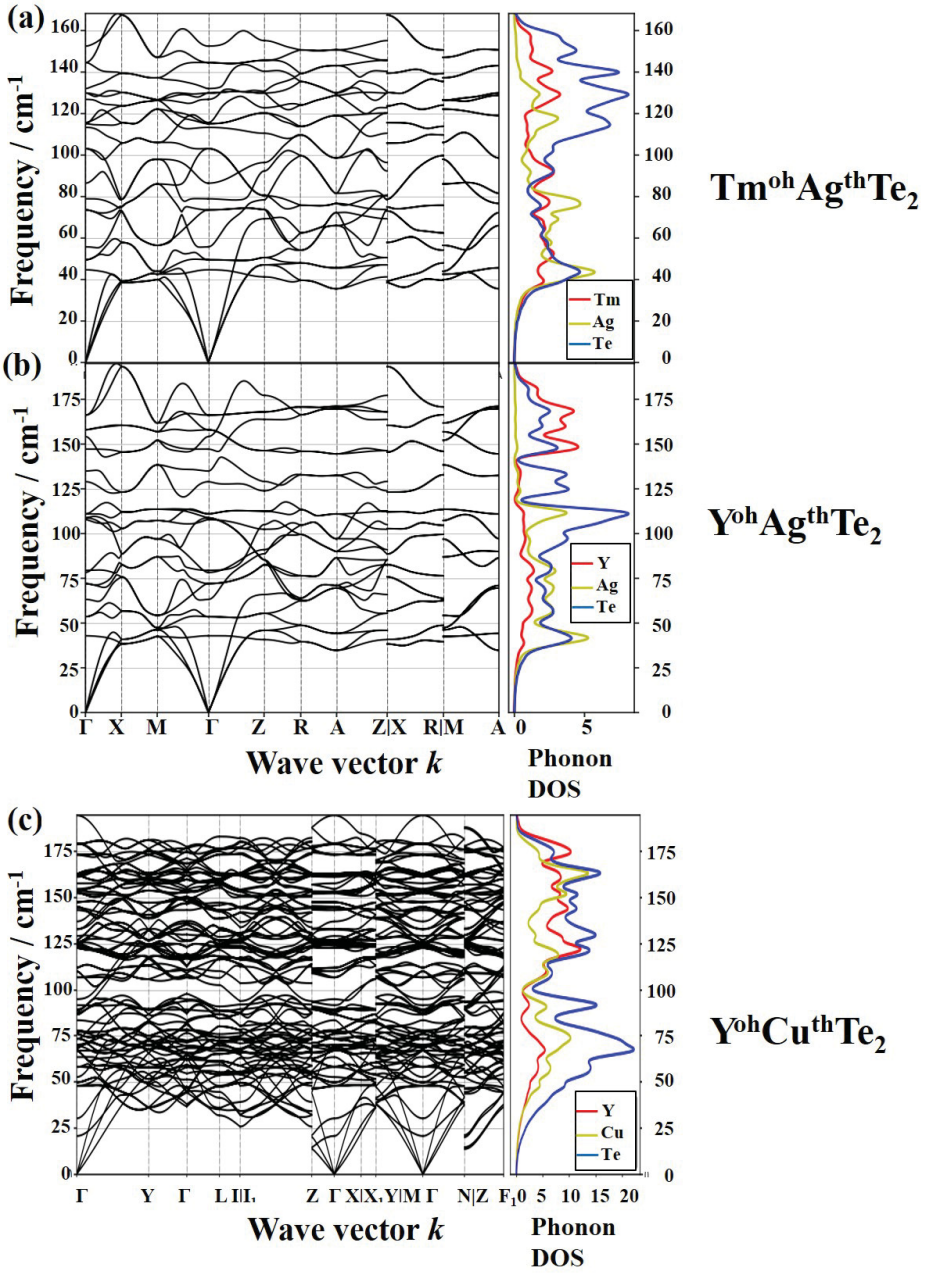

Figure 5.20: Computed phononic dispersion curves of the tetragonal phases of (a) $Tm^{oh}Ag^{th}Te_2$ and (b) $Tm^{oh}Ag^{th}Te_2$ as well as the monoclinic phase of (c) $YCuTe_2$. The phonon density of states (DOS) of the individual elements are provided to depict the contributions of the elements to the bands. Phononic dispersion curves were computed by Zhe Luo and Dr. Hong Zhu, School of Materials Science and Engineering, Shanghai Jiao Tong University (unpublished work shown with permission).

especially at low frequencies. However, slightly higher frequencies were calculated for the tetragonal phase of $YAgTe_2$ than in $TmAgTe_2$ (see Figure 5.20 (a) and (b)). While 24 phonons were calculated for the Ag-based compounds, the number of phonons increased to 96 for $YCuTe_2$ due to the larger $2 \times 2 \times 2$ supercell (see Figure 5.20 (c)). The frequency of the acoustic phonons of $YCuTe_2$ was slightly higher than $TmAgTe_2$ and $YAgTe_2$ as observed from the phononic dispersion curves (Figure 5.20) suggesting a higher thermal conductivity in $YCuTe_2$.

In addition to the phononic dispersion curve, the phonon DOS is also presented in Figure 5.20. At low frequency, the total phonon DOS increased exponentially with frequency for all three compounds where Te and Ag/Cu mostly contribute to the phonon DOS. At high frequencies, Y also significantly contributed to the phonon DOS. While the phonon DOS of Ag-based XYZ_2 compounds peaks at $\sim$40 cm^{-1} and $\sim$110 cm^{-1}, the phonon DOS of $YCuTe_2$ peaks around 70 cm^{-1} and 120 cm^{-1}.

It can be concluded that the phononic dispersion curves of the three compounds all had low-frequency phonon modes suggesting low thermal conductivity. In particular, low-frequency optical modes might suppress the frequency of the acoustic modes. $TmAgTe_2$ showed slightly lower frequencies than the Y-based compounds and therefore, a lower thermal conductivity would be expected for $TmAgTe_2$. The phonon DOS was compared to Raman spectra (see Section C.2) which confirm the trends observed in the computed band structures. Because Raman spectra were not calculated, the experimental Raman spectra cannot provide a quantitative conclusion concerning the accuracy of the phononic dispersion curve calculations. Therefore, the heat capacity calculated from the phononic dispersion curve was compared to the experimental heat capacity of the investigated XYZ_2 compounds.

5.1.6.b Heat Capacity

The heat capacity, C_p, was measured from 0.4 K to 300 K using the ^{3}He and ^{4}He option in a PPMS and the high-temperature capacity was determined with the enthalpy method using a DSC. Both measurements were performed in the laboratory of Dr. Mary Anne White, Department of Chemistry, Dalhousie University. (Heat capacity data are given in Tables C.18-C.25 of Appendix C.) The heat capacity determined with the enthalpy method was empirically corrected to

the heat capacity measured with the PPMS at a temperature of 323 K. Uncertainty in PPMS heat capacity was estimated to be 5% from 0.4 K to 5 K and 1% from 5 K to 300 K whereas the uncertainty of the enthalpy method was estimated to be 10%. The computed heat capacity was calculated from the phononic dispersion curves using a canonical partition function [197]. The heat capacity of $YAgTe_2$ was calculated with and without the inclusion of van der Waals interactions to depict the influence of van der Waals interactions on the calculation of thermal properties.

$TmAgTe_2$ The experimental molar heat capacities of the $TmAgTe_2$ parent compound in the tetragonal phase and the extrinsically doped compounds are shown as a function of temperature in Figure 5.21. All $TmAgTe_2$ compounds have a similar temperature trend: C_p increased with temperature to about 200 K, followed by a nearly constant heat capacity (see Figure 5.21 (a)). The heat capacity is slightly higher than the Dulong-Petit value most likely due to work resulting from the thermal expansion as the heat capacity was measured at constant pressure, C_p, while the Dulong-Petit value assumes constant volume, C_V. Higher experimental heat capacities were also observed for all the other investigated XYZ_2 compounds; see Figure 5.22 (a) and 5.23 (a). Furthermore, a higher heat capacity was observed for the tetragonal phase of the parent compound in contrast to the extrinsically doped compounds. The heat capacity of both extrinsically doped compounds are nearly the same over the entire temperature range suggesting that the difference between the heat capacity of the parent compound and the extrinsically doped compounds is related to the crystal structure. As discussed above, the extrinsically doped compounds crystallized in the trigonal crystal structure where Tm and Ag occupy octahedral interstices.

In addition to the experimental heat capacity, the heat capacity, C_V, was computed from the phononic dispersion curve. It is important to note that van der Waals interactions between the layers was included, enhancing the computation of the lattice parameters as well as the interatomic forces. The calculated heat capacity was lower than the experimental heat capacity over the entire temperature range. Intermediate and low temperature range are emphasized by plots of $C_{\mathrm{mol}}T^{-1}$ and $C_{\mathrm{mol}}T^{-3}$ (Figure 5.21 (b) and (c), respectively). The discrepancy between the

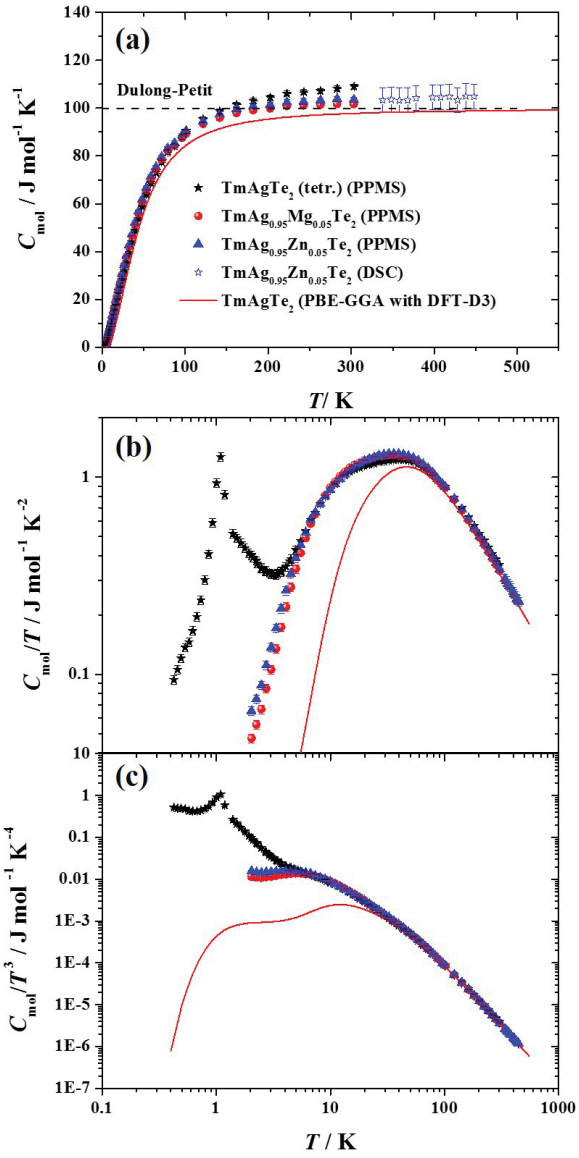

Figure 5.21: Comparison of experimental and computational heat capacities, C_{mol}, of $TmAgTe_2$ parent compound and extrinsically doped compounds. (a) Experimental heat capacities (C_p) of $TmAgTe_2$ compounds are higher than the corresponding computational heat capacity (C_V; —) and Dulong-Petit value (- - -) at high temperature most likely due to the work of thermal expansion. (b) $C_{\mathrm{mol}}T^{-1}$ versus T indicates a phase transition at ∼1 K. (c) $C_{\mathrm{mol}}T^{-3}$ versus T shows that low-temperature heat capacity exhibits a large difference between experiment and computation.

experimental and computed heat capacity might be a result of several factors. For example, Figure 5.21 (b) indicates a low-temperature phase transitions at $\sim$ 1 K which is most likely a second-order phase transition as observed in other related systems [308]. The second-order phase transition can increase the heat capacity at low temperatures (<40 K) as observed for $Er_2Ti_2O_7$ [309]. In $Er_2Ti_2O_7$, the magnetic contribution to the heat capacity was separated from the total heat capacity indicating a broad peak whereas the phase transition appeared at $\sim$1.5 K. In the present study, the magnetic heat capacity was not separated from the heat capacity of the phonon vibrations. Therefore, it was not feasible to determine the Debye temperature and the electronic contribution of the heat capacity from the present experimental heat capacity. For the calculation of the minimum thermal conductivity, the computed Debye temperature (*i.e.*, the function $D(\omega) = a\omega^2$ was fitted to the phonon DOS from 0 to 1/4 of the maximum phonon frequency) was used. The trigonal phase has a slightly lower Debye temperature ($\theta_D \sim 126$ K) than the tetragonal phase ($\theta_D = 150$ K), which is consistent with the lower heat capacity of the extrinsically compounds. (Computed and experimental Debye temperatures and Sommerfeld constants [to calculate the electronic contribution of the heat capacity (Equation 2.5)] are given in Table 5.4.) Further discussions of the origins of the low-temperature phase transition are given in Section C.3 of Appendix C.

Figure 5.21 (b) also reveals that the broad peak in $C_{\mathrm{mol}}T^{-1}$ versus T from experiments does not agree with computation. The discrepancy could be reduced with lower frequencies for the phonon modes in the phononic dispersion curve calculation. As mentioned above, most of the f electrons in Tm were treated as core electrons in the calculations which might increase the binding energy and hence, the phonon frequencies. In addition to the accuracy of the calculations, it has to be noted that the experimental heat capacity consists of the heat capacity at constant volume, the electronic heat capacity, and the heat capacity due to work of thermal expansion, whereas the computed heat capacity is solely the heat capacity at constant volume. The two neglected terms are both temperature-dependent (see Equation 2.3 and 2.5) and can significantly contribute, especially to the heat capacity at high temperature. The heat capacity due to work of thermal expansion ($C_p - C_V$) was estimated at room temperature using Equation 2.3 for the tetragonal

phase. The unit cell volume, V_{UC}, and the coefficient of volumetric thermal expansion, $\alpha_V = 3 \cdot \alpha$, were taken from experiments and the isothermal compressibility was calculated from the PBE-GGA-DFT-D3 computed elastic properties with a bulk modulus of 60.7 GPa using the method described by de Jong *et al.* [260]. The resulting $C_p - C_V = 9.0$ J mol^{-1} K^{-1} is smaller than the difference between experiments and computation for the tetragonal $TmAgTe_2$ phase ($C_p - C_V \sim 10.7$ J mol^{-1} K^{-1}). A similar $C_p - C_V$ is estimated for the other XYZ_2 compounds.

$YAgTe_2$ The temperature-dependence of the heat capacity of $YAgTe_2$ is shown in Figure 5.22. The heat capacity increased less rapidly than $TmAgTe_2$ suggesting that the crystal structure of $YAgTe_2$ is slightly stiffer than $TmAgTe_2$. While the low-temperature heat capacity is similar to $TmAgTe_2$, the high-temperature heat capacity of $YAgTe_2$ continued to increase with temperature. The increase in heat capacity at elevated temperature might be related to the phase transition at 408 K which is consistent with the phase transition recorded by DSC (see Figure 5.11 (b)).

Similar to $TmAgTe_2$, a peak was observed by plotting $C_{\text{mol}}T^{-1}$ versus T (see Figure 5.22 (b)). However, the peak is less broad than for $TmAgTe_2$ and no phase transition was observed at low temperature suggesting that the phase transition in the latter is most likely related to Tm. A similar low-temperature phase transition was observed in thulium boride due to magnetic ordering [310]. Furthermore, Figure 5.22 (b)) shows that the experimental heat capacity agrees well with the computed heat capacity with the inclusion of van der Waals interactions whereas the heat capacity was slightly overestimated without the consideration of van der Waals interactions. It is important to note that the electronic contribution of the heat capacity ($\gamma_{el} \sim$0.7 mJ mol^{-1}K^{-2}) which was determined by fitting the experimental heat capacity was added to the computed heat capacity (see Equation 2.5).

The plot of $C_{\text{mol}}T^{-3}$ versus T reveals the contribution of the acoustic phonons to the heat capacity as shown in Figure 5.22 (c). The acoustic phonons were slightly under- estimated if van der Waals interactions were included in the calculation whereas a small increase in computed heat capacity was observed if van der Waals interactions were not considered. The underestimation of the heat capacity is most

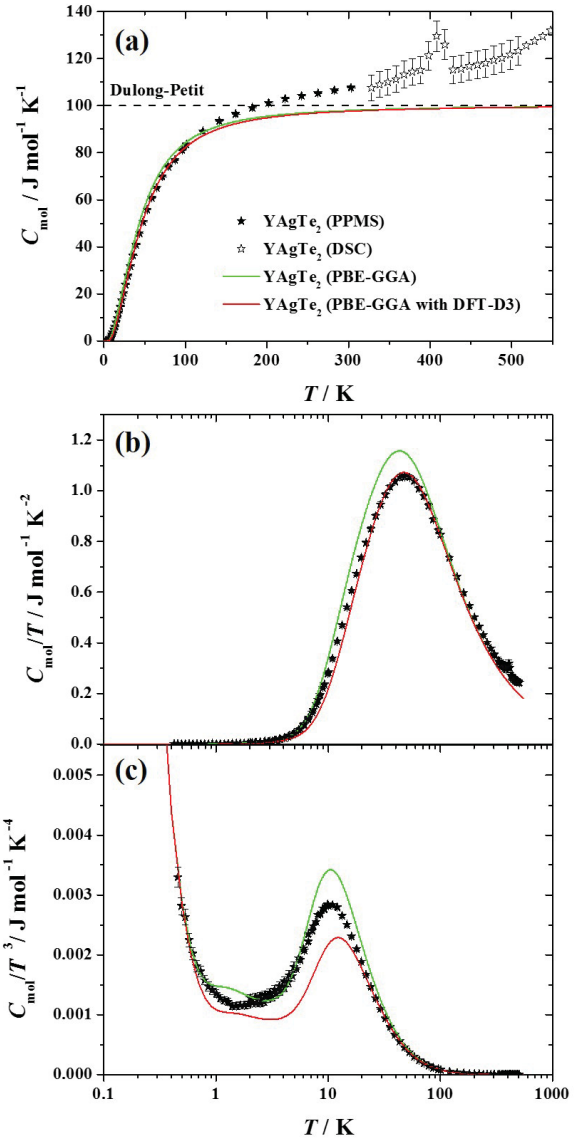

Figure 5.22: Comparison of experimental and computational heat capacity, C_{mol}, of $YAgTe_2$ parent compound. (a) Experimental heat capacities (C_p) of $YAgTe_2$ are higher than the computational heat capacity ($C_V + \gamma_{el}T$; — and —) and Dulong-Petit value (- - -) at high temperature most likely due to the work of thermal expansion. (b) $C_{\mathrm{mol}}T^{-1}$ versus T shows good agreement between computation and experiment with the inclusion of van der Waals interactions in the calculations using DFT-D3. (c) $C_{\mathrm{mol}}T^{-3}$ versus T reveals that the heat capacity is over-/underestimated with/without the inclusion of van der Waals interactions. Note that the electronic contribution was added to the computed heat capacity.

likely related to an overestimation of the interatomic forces due to the inclusion of van der Waals interactions. However, the discrepancy is small and within uncertainty of the calculation. The computed Debye temperature was also compared to the experimental fitted Debye temperature. The computed Debye temperature was 107 K and 125 K without and with the inclusion of van der Waals interactions, respectively. The fitted Debye temperature from experiments agrees well with the computed Debye temperature ($\theta_D = 122$ K).

Table 5.4: Comparison of computational and experimental Debye temperature, θ_D, and the Sommerfeld constant, γ_{el}, for $TmAgTe_2$, $YAgTe_2$, and $YCuTe_2$.
* θ_D and γ_{el} of $TmAgTe_2$ could not be determined from experiments due to the low-temperature phase transition.

Compound	γ_{el} / mJ mol^{-1} K^{-2}	θ_D (Exp.) / K	θ_D (Comp.) / K
$TmAgTe_2$ (tetr.)	NA*	NA*	150 (with DFT-D3)
$TmAgTe_2$ (tri.)	NA*	NA*	126 (with DFT-D3)
$YAgTe_2$	0.7	122	107 (with DFT-D3) 125 (without DFT-D3)
$YCuTe_2$	0.5	131	172 (without DFT-D3)

$YCuTe_2$ The heat capacities of $YCuTe_2$ and $Y_{0.96}Cu_{1.08}Te_2$ are shown as a function of temperature from 2 K to 525 K in Figure 5.23. Both $YCuTe_2$ compounds show a similar temperature trend in which the heat capacity increased with temperature to the phase transition at ∼440 K, followed by a nearly constant heat capacity above the phase transition. The phase transition is in accord with DSC (Figure 5.11 (c)) and PXRD (Figure 5.10). The doped compound has a slightly higher heat capacity and the phase transition was suppressed in comparison to the parent compound. PXRD showed that the peaks of the LT phase are more suppressed in $Y_{0.96}Cu_{1.08}Te_2$ (see Figure 5.9) and therefore, the transition to the HT phase requires less energy.

In binary copper chalcogenides, such as Cu_2S [299], Cu_2Se [274, 298, 300], and Cu_2Te [300, 301], Cu ions are kinetically disordered and distributed throughout possible vacancy positions whereas the anions maintain a rigid sub-lattice. The superionic Cu ions with liquid-like mobilities reduce the heat capacity as well as the thermal conductivity [274]. However, the nearly temperature-independent heat capacity above the phase transition indicates that superionic behavior is not present

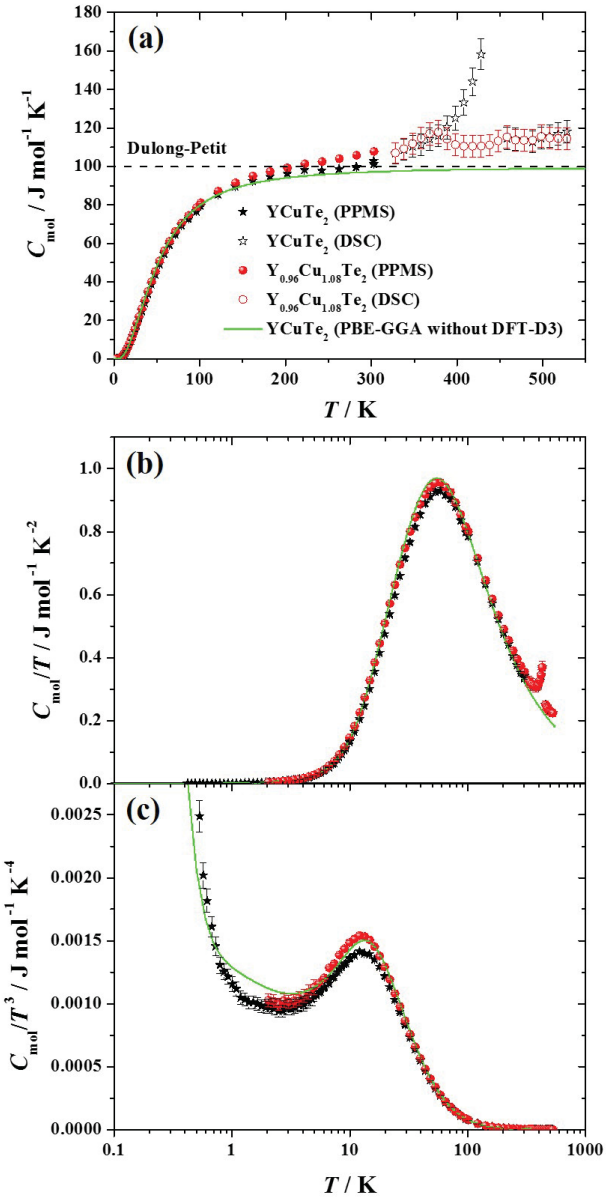

Figure 5.23: Comparison of experimental and computational heat capacity of $YCuTe_2$ parent compound and $Y_{0.96}Cu_{1.08}Te_2$. (a) Experimental heat capacities (C_p) of $YCuTe_2$ compounds show a phase transition at ∼440 K which is reduced with intrinsic doping. (b) Experimental $C_{\mathrm{mol}}T^{-1}$ versus T indicates good agreement with computation ($C_V + \gamma_{el}T$). (c) $C_{\mathrm{mol}}T^{-3}$ versus T emphasizes the experimental low-temperature heat capacity which agrees well with computation although van der Waals interactions were not included. Figure (a) is partially taken from reference [292].

in the current $YCuTe_2$ compounds. Corroborating the heat capacity results, a subtle change in enthalpy and entropy was determined at the phase transition and therefore, the Cu atoms in $YCuTe_2$ should not be considered as superionic.

The computed heat capacity including the electronic contribution of the heat capacity ($C_V + \gamma_{el}T$) agrees well with experiment below room-temperature as shown in Figure 5.23 (b) and (c). $C_{\mathrm{mol}}T^{-3}$ versus T showed a behavior similar to $YAgTe_2$ whereas the Debye temperature of $YCuTe_2$ slightly increased to 131 K. A higher Debye temperature was calculated from the computed heat capacity ($\theta_D = 171$ K). The difference between experimental and computed Debye temperature can be a result of the different methodologies to calculate the Debye temperature. While the fitted Debye temperature describes an average value over the entire Brillouin zone, the computed Debye temperature is calculated from the phonon DOS near the center of the Brillouin zone which can overestimate the phonon mean velocity. The Sommerfeld constant of $YCuTe_2$ ($\gamma_{el} = 0.5$ mJ mol^{-1} K^{-1}) was slightly lower than for $YAgTe_2$.

It can be concluded that the computed heat capacities of $YAgTe_2$ and $YCuTe_2$ agree well with experiments whereas the computed heat capacity of $TmAgTe_2$ was underestimated, in particular at low temperature. The discrepancy between experiment and computation might be the computational treatment of the f electrons as core electrons. Furthermore, a low-temperature phase transition was observed in $TmAgTe_2$ which would influence the low-temperature heat capacity. It was shown for $YAgTe_2$ that the inclusion of van der Waals interactions between the layers can enhance the calculation. The high-temperature heat capacity is nearly temperature-independent or increases with temperature and therefore, superionic behavior as shown in some other Cu compounds was not observed in the present study.

5.1.6.c Thermal Conductivity

The thermal conductivity was measured from 2 K to 300 K in the laboratory of Dr. Mary Anne White, Department of Chemistry, Dalhousie University, using the TTO method in a PPMS. The high-temperature thermal conductivity was determined from the thermal diffusivity using laser-flash method measured with the assistance of Dr. Umut Aydemir, the mass density, and the experimental heat capacity as

shown in Figures 5.21 - 5.23. Although the Dulong-Petit value is generally used in the thermoelectric community for the calculation of the thermal conductivity from thermal diffusivity, it can underestimate the heat capacity as shown for the investigated compounds and hence thermoelectric performance can be overestimated due to the lower thermal conductivity. Therefore, experimental heat capacities were used here. For the doped compounds the same heat capacity as the parent compound was assumed. An uncertainty of 5% for the low-temperature thermal conductivity and an uncertainty of 15% for the high-temperature thermal conductivity were estimated. As mentioned in Section 2.2, thermal conductivity has an electronic and phononic (+bipolar) contribution. The electronic contribution was calculated from the effective Lorenz number (see Equation 2.23) which was determined using the single-parabolic band model as discussed in Section 2.5. Due to the fact that the Hall carrier concentration is required for the single-parabolic band model the separation of the electronic and phononic contribution was only performed above room temperature where Hall carrier concentrations had been determined (see Section 5.1.5.c). (Thermal conductivity data of XYZ_2 compounds are given in Tables C.26-C.28 of Appendix C.)

$TmAgTe_2$ The temperature-dependence of the thermal conductivity of $TmAgTe_2$ parent compounds and extrinsically doped compounds is shown in Figure 5.24. The low-temperature thermal conductivity determined with the PPMS TTO method is slightly lower than the thermal conductivity determined from the laser flash method. Each method has its drawback to determine the thermal conductivity. For the thermal conductivity measurement using the TTO method, the contact thermal resistance was neglected and for the blackbody radiation, an emissivity of one was assumed which introduced uncertainty. On the other hand, the heat capacity and the mass density had to be known to determine the thermal conductivity from the laser flash method, each introducing uncertainty.

The low-temperature thermal conductivity increased dramatically at low temperature until about 110 K, followed by a decrease in thermal conductivity with increasing temperature until ∼700 K (see Figure 5.24 (a)). The high-temperature reduction in thermal conductivity is most likely due to phonon-phonon interactions.

While the trigonal phase of the parent compound and the Zn-doped compound have similar thermal conductivities the thermal conductivity of the Mg-doped compound and the tetragonal phase of the parent compound have higher thermal conductivities. In particular, the tetragonal phase of $TmAgTe_2$ has about 50% higher thermal conductivity than the trigonal phase. This is consistent with the heat capacity which was higher for the tetragonal phase than the trigonal phase (see Figure 5.21 (a)).

Above 700 K, the thermal conductivity increased with temperature which could be an indication of bipolar thermal conductivity. However, the electronic contribution generally increases with temperature which can also be the reason for the increase in thermal conductivity at high temperature. The electronic contribution of the thermal conductivity was calculated using Equation 2.23 where the effective Lorenz number was determined from the single parabolic band (SPB) model (see Section 2.5). To delineate the origins of the increase in thermal conductivity above 700 K, the electronic contribution (Figure 5.24 (b)) was removed from the total thermal conductivity and the phononic (+bipolar) contribution is shown as a function of temperature in Figure 5.24 (c). The phononic (+bipolar) contribution also increased slightly above 700 K, suggesting a bipolar contribution at low temperature. The bipolar behavior was not observed in the Seebeck measurement as the Seebeck coefficient increased continuously above 700 K (see Figure 5.19 (a)).

The electronic contribution of the thermal conductivity shows that the trigonal phases of $TmAgTe_2$ and the Zn-doped samples have similar temperature trends which increased with temperature to $\sim$600 K, followed by a reduction in electronic thermal conduction. The Mg-doped compound did not increase as rapidly as the other compounds in the trigonal phase whereas $TmAgTe_2$ in the tetragonal phase increased nearly exponentially with temperature. The temperature trend is consistent with the electrical resistivity measurements in which $TmAgTe_2$ in the trigonal phase and the Zn-doped compound had nearly the same temperature trend (see Figure 5.15 (a)).

The present minimum thermal conductivity model (Equation 4.7) was tested on the $TmAgTe_2$ compound and compared to the amorphous limit of the thermal

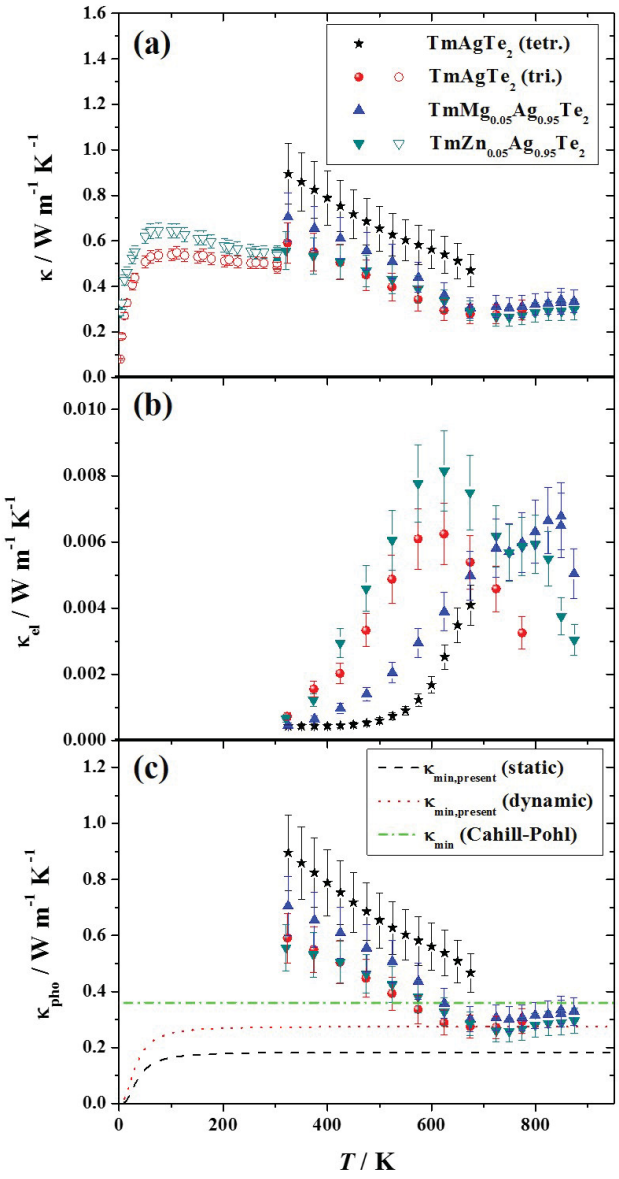

Figure 5.24: Thermal conductivity of $TmAgTe_2$ parent compounds and extrinsically doped compounds using TTO method (hollow symbols) and the laser flash method (solid symbols). (a) Thermal conductivities of $TmAgTe_2$ and related compounds in the trigonal phase have similar low thermal conductivity at high temperature. (b) Electronic contribution of the thermal conductivity, κ_{el}, indicates similar temperature trends of the Zn-doped compound and the trigonal phase of the parent compound. (c) Phononic contribution of the thermal conductivity is lower than the amorphous (Cahill-Pohl) limit, approaching the dynamic limit of the minimum thermal conductivity. Figure (a) is partially taken from reference [277].

conductivity [66, 67]. Generally the Debye temperature taken from the fit of the experimental heat capacity provides a better approximation of the average phonon mean speed, but here the heat capacity could not be fit due to a low-temperature phase transition. Therefore, the minimum thermal conductivity was calculated with the computed Debye temperature given in Table 5.4. In addition to the model of minimum thermal conductivity presented for PCBM in Section 4.1, a modified model of the minimum thermal conductivity is presented here. In the derivation of the minimum thermal conductivity model, the phonon mean free path was limited by the atomic density. While a constant phonon mean free path can represent the limit for disordered structure (*i.e.*, static disordering) a frequency-depending mean free path can more accurately describe the thermal conductivity where dynamical disordering (*i.e.*, disordering due to phonon-phonon interactions with a relaxation time of $\tau_{rel,U} \propto \omega^{-2}$ [82]; see Equation 2.15) is the limiting factor. The phonon mean free paths as per Einstein [65] and Cahill, Watson, and Pohl [66, 67], were applied in their minimum thermal conductivity models ($\lambda_i = \frac{\bar{v}_i}{\omega}$). The modified (dynamic) minimum thermal conductivity is calculated from

$$\kappa_{min,dyn} = \left(\frac{3}{6^{2/3}\pi^{1/3}}\right)\frac{k_B^2}{\hbar}\left(\frac{N_{UC}}{V_{UC}}\right)^{1/3}\frac{\theta_D}{x_D^2}\int_0^{x_D}\frac{x^3 \mathrm{e}^x}{\left(\mathrm{e}^x-1\right)^2}\mathrm{d}x. \tag{5.5}$$

(The model of Section 4.1 is hereafter referred to as $\kappa_{min,static}$.) The phononic contribution of the thermal conductivity in $TmAgTe_2$ compounds was lower than the minimum thermal conductivity model of Cahill, Watson, and Pohl ($\kappa_{min,Cahill,HT} = 0.36$ W m^{-1}K^{-1}) whereas the present static minimum thermal conductivity is lower than the experimental thermal conductivity. However, the minimum thermal conductivity limited by dynamic disordering agrees well with the lowest phononic contribution of thermal conductivity at ∼700 K. This is reasonable as phonon-phonon interactions reduce the thermal conductivity and therefore, a frequency-dependent phonon mean free path better represents the minimum thermal conductivity in this compound. It is important to note that the minimum thermal conductivity using the Cahill, Watson, and Pohl model was calculated from the bulk and shear modulus in Figure 5.24 (c). First, the longitudinal and transverse speeds of sound were calculated from Equations 3.39 and 3.40, respectively, and with the speeds of the sound the minimum thermal conductivity of

Cahill, Watson, and Pohl was determined using Equation 4.4. A similar minimum thermal conductivity was determined from experimental longitudinal and transverse speed of sound for both the tetragonal phase ($v_{L,s}$ = 2810 m s^{-1}, $v_{T,s}$ = 1625 m s^{-1}, and $\kappa_{min,Cahill,HT}$ = 0.36 W m^{-1}K^{-1}) and the trigonal phase ($v_{L,s}$ = 3520 m s^{-1}, $v_{T,s}$ = 1390 m s^{-1}, and $\kappa_{min,Cahill,HT}$ = 0.38 W m^{-1}K^{-1}). The speeds of sound were measured with the assistance of Saneyuki Ohno using ultrasound measurements in the laboratory of Dr. William L. Johnson, Division of Engineering and Applied Science, California Institute of Technology. The minimum thermal conductivities of the various models are given in Table 5.5.

Table 5.5: Minimum thermal conductivities calculated from the present model limited by static disordering, $\kappa_{min,static}$, or dynamic disordering,$\kappa_{min,dyn}$, as well as the Cahill, Watson, and Pohl model. The latter minimum thermal conductivity was calculated from speed of sounds measurements, $\kappa_{min,CP,s}$, or elastic constants, $\kappa_{min,CP,E}$ using Equation 4.4. (Longitudinal and transverse speed of sounds were calculated from Equations 3.39 and 3.40, respectively.) The lowest experimental phononic contribution of the thermal conductivity, $\kappa_{min,pho}$, is provided for comparison.

Compound	$\kappa_{min,static}$ / W m^{-1} K^{-1}	$\kappa_{min,dyn}$ / W m^{-1} K^{-1}	$\kappa_{min,CP,s}$ / W m^{-1} K^{-1}	$\kappa_{min,CP,E}$ / W m^{-1} K^{-1}	$\kappa_{min,pho}$ / W m^{-1} K^{-1}
$TmAgTe_2$ (tetr.)	0.18	0.27	0.36	0.36	0.47±0.07
$TmAgTe_2$ (tri.)				0.38	0.26±0.04
$YAgTe_2$	0.15	0.22	0.40	NA	0.36±0.05
$YCuTe_2$	0.16	0.24	0.43	0.43	0.39±0.06

The phononic contribution of the minimum thermal conductivity is extremely low ($\kappa_{min,pho}$ = 0.26±0.04 W m^{-1}K^{-1}) at high temperature enhancing the thermoelectric performance in these compounds. Similar low thermal conductivity was found for Ag_2Te which goes even down to 0.14 W m^{-1}K^{-1} [271]. Furthermore, SnSe which has currently the highest figure of merit (zT = 2.6±0.3 at 923 K) showed a similar low thermal conductivity at high temperature (κ = 0.20 W m^{-1}K^{-1} at 973 K) [26, 27]. However, the present minimum thermal conductivity model with dynamic disordering predicts that the thermal conductivity in $TmAgTe_2$ cannot be reduced further.

$YAgTe_2$ The thermal conductivities of $YAgTe_2$ and $Y_{0.98}Ag_{1.02}Te_{1.98}$ are shown as a function of temperature in Figure 5.25. In the temperature range measured, the

thermal conductivity peaks at around 60 K ($\kappa = 1.29 \pm 0.06$ W m^{-1}K^{-1}) and decreased as temperature increased further most likely due to phonon-phonon interactions. The thermal conductivity was the lowest at ∼725 K for the parent compound ($\kappa = 0.36 \pm 0.05$ W m^{-1}K^{-1}). At high temperature the thermal conductivity increased due the presence of a phase transition at $T \sim 750$ K and the resulting increase in heat capacity. The intrinsically doped compound has a thermal conductivity similar to the parent compound. As for the $TmAgTe_2$ compounds, the electronic contribution of the thermal conductivity (calculated from Equation 2.23 with the effective Lorenz number from SPB model and depicted in Figure 5.25 (b)) was subtracted from the total thermal conductivity to analyze the phononic contribution. The electronic contribution increased with temperature as expected for intrinsic semiconductors. Due to the lower resistivity of the $YAgTe_2$ parent compound as shown in Figure 5.17 (a), a lower electronic contribution was calculated for the intrinsically doped compound, where the latter was in the same range as for the $TmAgTe_2$ compounds.

The phononic contribution of the thermal conductivity in $YAgTe_2$ is not as low as the thermal conductivity in $TmAgTe_2$ but it is lower than the amorphous limit (see Figure 5.25 (c)). However, the lattice thermal conductivity is higher than the minimum thermal conductivity calculated from the present minimum thermal conductivity limited by either static or dynamic disordering.

$YCuTe_2$ The temperature dependence of the thermal conductivity of the $YCuTe_2$ parent compound and intrinsically doped compounds is plotted in Figure 5.26. The thermal conductivity increased dramatically at low temperature and peaked at ∼60 K, similar to $YAgTe_2$. Above 60 K, the thermal conductivity decreased with increasing temperature due to phonon-phonon interactions. Furthermore, the room-temperature thermal conductivity decreased with increasing Cu content which stabilizes the high-temperature phase. The high-temperature phase displays a higher Cu disorder compared to the low-temperature phase resulting in lower thermal conductivity as observed for $YCu_{1.08}Te_2$ ($\kappa = 0.89$ W m^{-1}K^{-1}) and for $Y_{0.96}Cu_{1.08}Te_2$ ($\kappa = 0.82$ W m^{-1}K^{-1}). All $YCuTe_2$ compounds show a higher thermal conductivity at high temperature than $TmAgTe_2$ and $YAgTe_2$ compounds

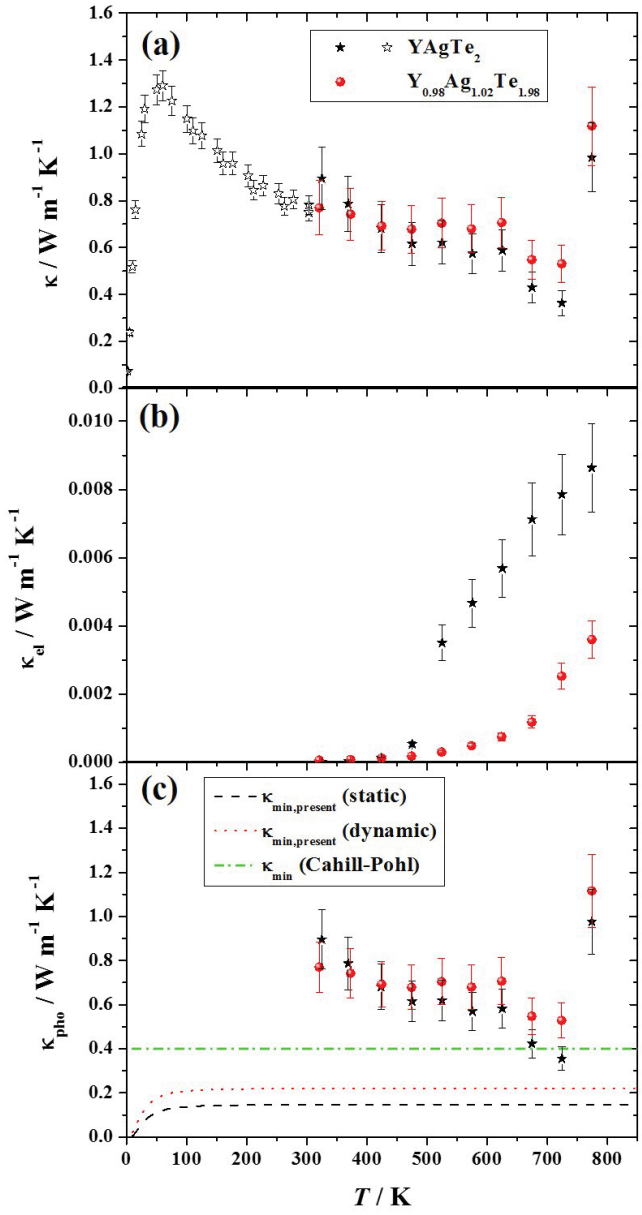

Figure 5.25: Thermal conductivity of $YAgTe_2$ parent compound and $Y_{0.98}Ag_{1.02}Te_{1.98}$. (a) Thermal conductivity of both $YAgTe_2$ compounds decreased from 60 K to the phase transition. (b) The electronic contribution of the thermal conductivity, κ_{el}, increased with temperature for both compounds due to an increase in electrical conductivity with temperature. (c) Phononic contribution of the thermal conductivity is slightly lower than the amorphous limit (Cahill-Pohl) but higher than present (static and dynamic) minimum thermal conductivities.

whereas $TmCuTe_2$ had a higher thermal conductivity than the present $YCuTe_2$ over the entire temperature range.

The electronic contribution of thermal conductivity is nearly temperature-independent for most $YCuTe_2$ compounds except the parent compound and the Cu-excess compounds (see Figure 5.26 (b)). While the electronic contribution decreased for the parent compound, the Cu-excess samples have a maximum electronic contribution above the phase transition. At high temperature, all $YCuTe_2$ compounds have a similar electronic contribution to the thermal conductivity.

The resulting phononic contribution of the thermal conductivity for $YCuTe_2$ compounds decreased with temperature as shown in Figure 5.26 (c). The phononic contribution of the thermal conductivity in the YCu_xTe_2 compounds with $x \leq 1$ is proportional to T^{-1} in the temperature range from 320 K to 780 K, indicating that phonon-phonon interactions are the limiting scattering factor. Cu-excess compounds, on the other hand, have a T^{-1} dependence above the phase transition at 440 K. No evidence of a bipolar contribution was observed up to 780 K.

The lowest phononic contribution to thermal conductivity was determined for $YCu_{1.08}Te_2$ ($\kappa \sim 0.39 \pm 0.06$ W m^{-1}K^{-1}) which is even lower than the amorphous limit determined from elastic properties using Equations 3.39, 3.40, and 4.4 ($\kappa_{min,Cahill,HT} = 0.43$ W m^{-1} K^{-1}). This is consistent with the amorphous limit calculated from speed of sound measurements ($v_{L,s} = 3420$ m s^{-1} and $v_{T,s} = 1870$ m s^{-1} at room-temperature). The speeds of sound were measured from ultrasound measurements with the assistance of Saneyuki Ohno in the laboratory of Dr. William L. Johnson, Division of Engineering and Applied Science, California Institute of Technology. The minimum thermal conductivity calculated from the present models is lower than experimental results. However, the phononic contribution of the thermal conductivity is already below the amorphous limit and the temperature trend suggests that the phononic contribution might decrease further with temperature. Therefore, the present minimum thermal conductivity limited by dynamic disordering might better represent the lowest limit of thermal conductivity than the amorphous limit model.

In conclusion, the thermal conductivities of all investigated XYZ_2 compounds exhibited low thermal conductivity at high temperature ($\kappa < 0.5$ W m^{-1}K^{-1}). In

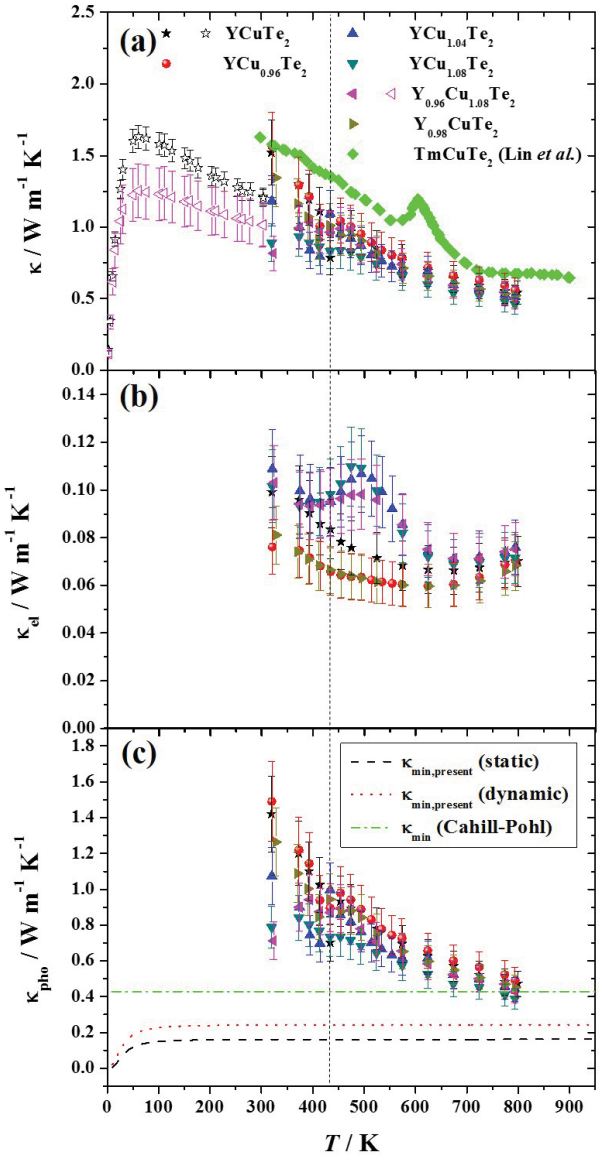

Figure 5.26: Thermal conductivity of $YCuTe_2$ parent compounds and intrinsically doped compounds. (a) Thermal conductivity of $YCuTe_2$ compounds decreased with increasing temperature. The room-temperature thermal conductivity decreased with increasing Cu content and decreasing Y content. All compounds displayed lower thermal conductivity than $TmCuTe_2$ [255]. (b) The electronic contribution of the thermal conductivity, κ_{el}, indicates a peak for Cu-excess (YCu_xTe_2, $x > 1$) samples above the phase transition (vertical dashed line). (c) Phononic contribution of the thermal conductivity is slightly lower than the amorphous (Cahill-Pohl) limit. Figures from reference [292].

particular, the trigonal phase of the $TmAgTe_2$ parent compound as well as the corresponding extrinsically doped compounds have low thermal conductivities, comparable to the thermal conductivity of the current best thermoelectrics. Furthermore, the thermal conductivity peaks at low temperature, followed by a decrease in thermal conductivity with increasing temperature, most likely due to phonon-phonon interactions. The phononic contribution of the thermal conductivity for most investigated XYZ_2 compounds are below the amorphous limit of thermal conductivity. However, the thermal conductivity approached the minimum thermal conductivity as limited by dynamic disordering. This model assumes that the phonon mean free path is frequency-dependent which is in accord with the relaxation time of phonon-phonon interactions ($\tau_{rel,U} \propto \omega^{-2}$) [82].

5.1.7 Thermoelectric Figure of Merit

The thermoelectric figure of merit, zT, was calculated using Equation 1.15 from polynomial fits of the experimental electronic and thermal data. The uncertainty in zT is generally 25% but for clarity, only a few uncertainties are shown in the figures here.

$TmAgTe_2$ Thermoelectric figures of merit zT for $TmAgTe_2$ compounds as a function of temperature are displayed in Figure 5.27 (a). An increase of zT with temperature was observed for all $TmAgTe_2$ compounds. While zT of the parent compound in the trigonal phase and Zn-doped sample peaked at ∼650 K (zT ∼0.35±0.09) and at 700 K (zT ∼0.47±0.12), zT for the tetragonal $TmAgTe_2$ compound and the Mg-doped sample was still increasing even at the highest measurement temperature. Due to the irreversible phase transition, the tetragonal compound was measured only to 675 K and a relatively low zT was observed ((zT ∼0.14±0.03). The Mg-doped sample might be promising at high temperature as it already shows a zT of 0.35±0.09 at 750 K. (Maximum values of zT and the peak temperatures are given in Table 5.6.) The peak figure of merit is only ∼30% of that for the binary compound Ag_2Te ($zT \sim 1$) [271]. The lower zT in $TmAgTe_2$ is most likely a result of the low carrier concentration.

The optimum carrier concentration can be calculated by applying the single

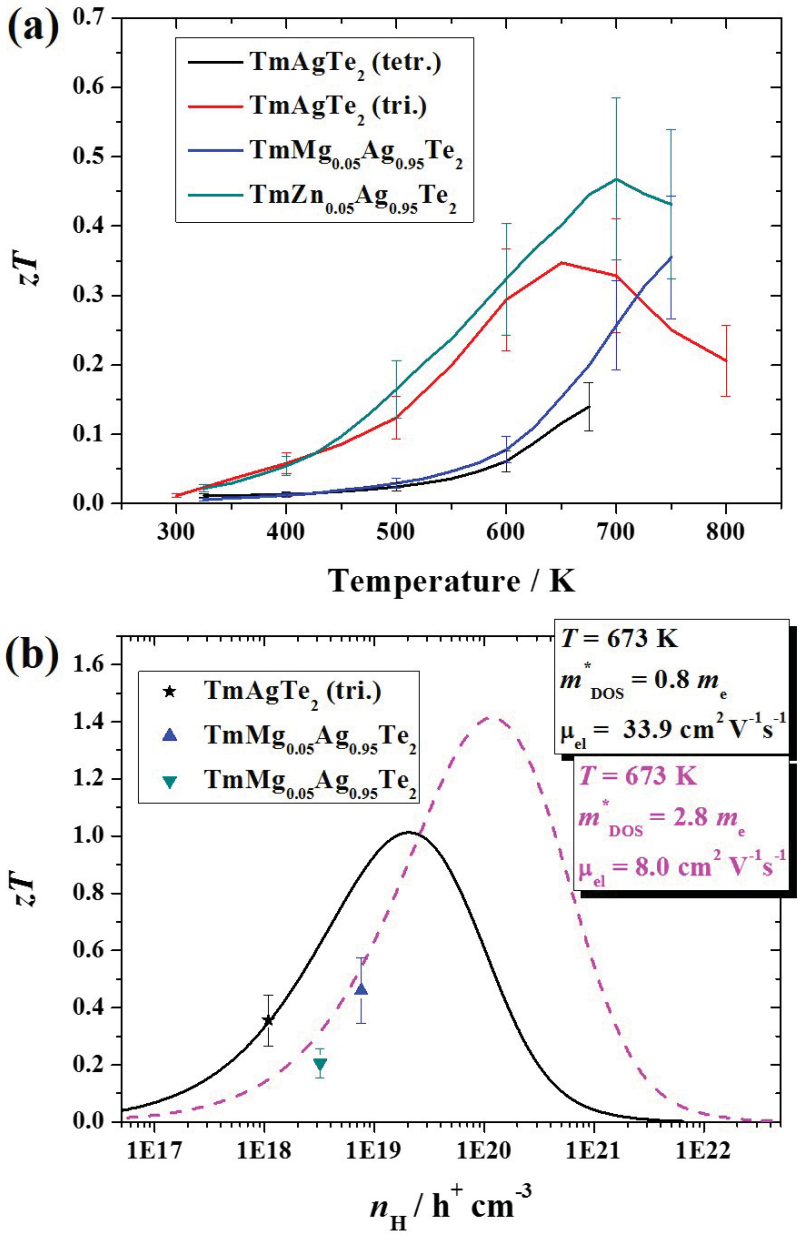

Figure 5.27: Thermoelectric figure of merit, zT, for the $TmAgTe_2$ parent compound and extrinsically doped samples. Extrinsic doping enhanced zT to ~0.5 at 700 K due to an increase in carrier concentration. (b) The single parabolic band model indicates that optimizing the carrier concentration can dramatically enhance zT. With extrinsic doping an increase in the effective mass was revealed resulting in potentially higher zT with optimized carrier concentration. Figure (a) was partially taken from reference [277].

parabolic band (SPB) model [90] as discussed in Section 2.5. Assuming that the phononic contribution to the thermal conductivity is independent of the carrier concentration, zT is plotted as a function of the Hall carrier concentration at 673 K in Figure 5.27 (b). Using the parameters of the parent compound in the trigonal phase, an optimum carrier concentration would be about $3 \cdot 10^{19}$ h^+ cm^{-3} which could increase zT to ∼1.0, similar to Ag_2Te [271]. However, the zT of the extrinsically doped compounds do not agree with the SPB model. A higher density of states effective mass, m^*_{DOS}, was calculated for the extrinsically doped samples from the SPB model which increased from $0.8 \cdot m_e$ for the parent compound to $2.8 \cdot m_e$ for the Zn-doped sample. With a higher m^*_{DOS} and a lower mobility, µ, the SPB model predicts that zT could be increased to ∼1.4 with an optimized carrier concentration of $\sim 10^{20}$ h^+ cm^{-3} (see Figure 5.27 (b)).

Table 5.6: Maximum experimental zT and peak temperature, T_{peak}, of various $TmAgTe_2$, $YAgTe_2$, and $YCuTe_2$ compounds. An uncertainty of 25% and 10 K were estimated for zT and T_{peak}, respectively.

Compound	T_{peak} / K	zT
$TmAgTe_2$ (tetr.)	675±10	0.14±0.03
$TmAgTe_2$ (tri.)	650±10	0.35±0.09
$TmMg_{0.05}Ag_{0.95}Te_2$	750±10	0.35±0.09
$TmZn_{0.05}Ag_{0.95}Te_2$	700±10	0.47±0.12
$YAgTe_2$	725±10	0.11±0.03
$Y_{0.98}Ag_{1.02}Te_{1.98}$	750±10	0.05±0.01
$YCuTe_2$	780±10	0.69±0.17
$YCu_{0.96}Te_2$	780±10	0.57±0.14
$YCu_{1.04}Te_2$	780±10	0.66±0.16
$YCu_{1.08}Te_2$	780±10	0.70±0.18
$Y_{0.96}Cu_{1.08}Te_2$	780±10	0.73±0.18
$Y_{0.98}CuTe_2$	780±10	0.61±0.15

$YAgTe_2$ The temperature-dependence of zT for $YAgTe_2$ and $Y_{0.98}Ag_{1.02}Te_2$ is shown in Figure 5.28. The parent compound had higher zT over the entire temperature range compared to the intrinsically doped sample. Both compounds showed zT increases to ∼725 K, followed by a decrease. The reduction in zT is most likely due to the increase in heat capacity at the phase transition and hence,

an increase in thermal conductivity. It is important to note that using the Dulong-Petit value to determine the thermal conductivity would overestimate zT at the phase transition by a factor of three. zT of both $YAgTe_2$ and $Y_{0.98}Ag_{1.02}Te_2$ are lower than the for all $TmAgTe_2$ compounds although the Hall carrier concentrations of $YAgTe_2$ and $TmAgTe_2$ is similar.

The SPB model of the parent compound indicates that zT can be slightly increased by optimizing the carrier concentration to $\sim 10^{19}$ h^+ cm^{-3}. However, the optimization would only improve zT to 0.13. The low zT in $YAgTe_2$ might be a result of the lower DOS effective mass compared to that of $TmAgTe_2$. Furthermore, the intrinsically doped sample does not fit the same curve as the parent compound because the mobility (29.9 cm^2 V^{-1} s^{-1}) and DOS effective mass (0.15 m_e) can change with intrinsic doping.

$YCuTe_2$ The values of zT for all $YCuTe_2$ compounds increased with temperature to 780 K as shown in Figure 5.29. The maximum zT was observed for $Y_{0.96}Cu_{1.08}Te_2$ ($zT = 0.73 \pm 0.11$ at 780 K). Furthermore, the maximum zT increased with increasing Cu content and decreasing Y content. The electronic properties increased with a decrease in Y whereas an increase in Cu increased the electrical conductivity and reduced the thermal conductivity, as shown in Figure 5.18 and 5.26.

All $YCuTe_2$ compounds studied showed higher thermoelectric performance than $YAgTe_2$ and $TmAgTe_2$ compounds over the entire temperature range. Furthermore, the maximum zT is about eight times higher than Cu_2Te [300] and about only 15% smaller than $TmCuTe_2$ [255]. However, the thermal conductivity of $TmCuTe_2$ was calculated from the Dulong-Petit heat capacity [255] which might overestimate the thermoelectric figure of merit; using the Dulong-Petit value for the thermal conductivity calculation for $YCuTe_2$ compounds would increase the peak zT ($\sim$0.85 at 780 K) above the zT for $TmCuTe_2$.

The SPB model using the parameters of the parent compound predicts that the thermoelectric performance could be enhanced by increasing the carrier concentration to $\sim 10^{20}$ h^+ cm^{-3}. The optimized zT at 775 K would be $\sim$0.75 which is similar to that observed for $Y_{0.96}Cu_{1.08}Te_2$. Although the carrier concentration could not be increased significantly, intrinsic doping could change the mobilities and DOS effective

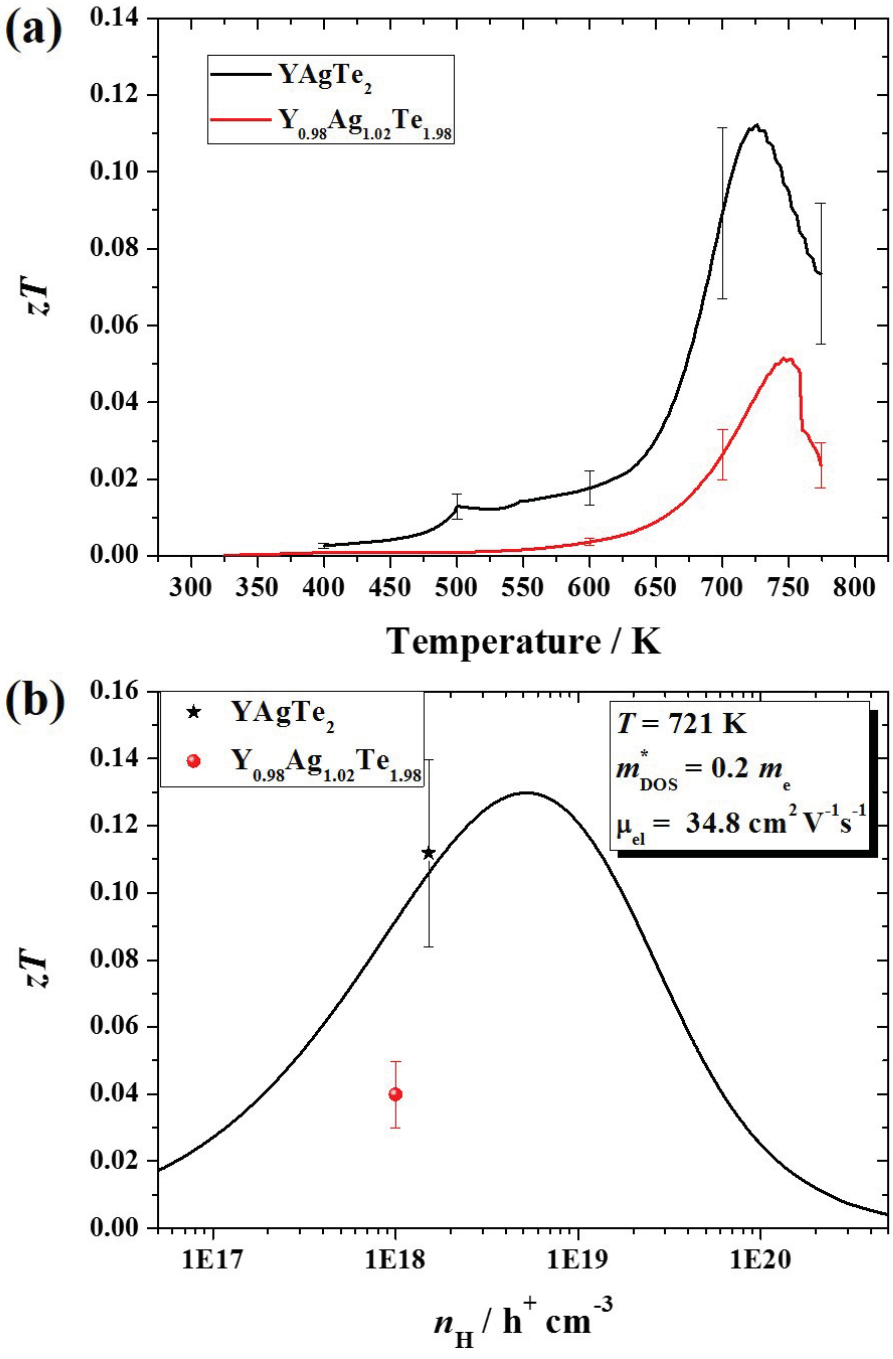

Figure 5.28: (a) Thermoelectric figure of merit, zT, for $YAgTe_2$ and $Y_{0.98}Ag_{1.02}Te_2$. The parent has a higher zT. (b) The single parabolic band model reveals that zT can only slightly increased with optimization of the carrier concentration.

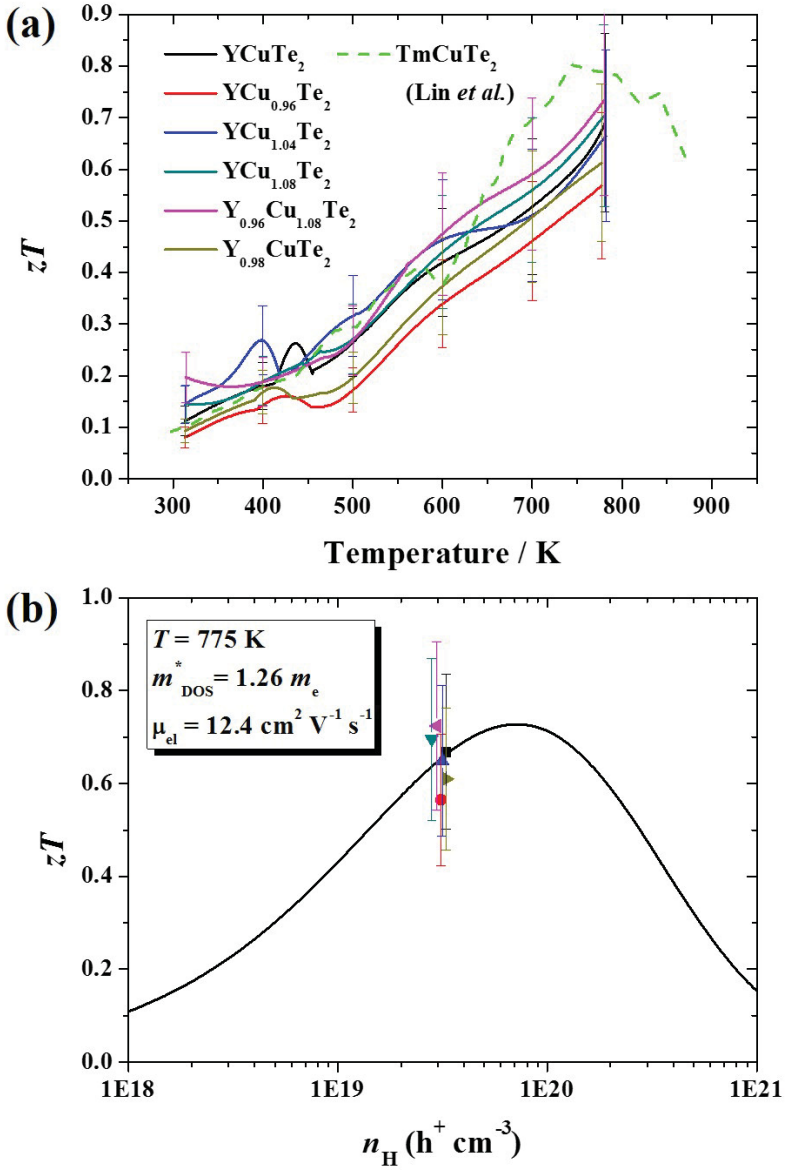

Figure 5.29: (a) Thermoelectric figure of merit, zT, for the $YCuTe_2$ parent compound and intrinsically doped samples. The parent has a higher zT. (b) The single parabolic band model indicates that intrinsically doping with Cu can enhance zT. Figure was taken from reference [292].

mass resulting in higher zT.

In comparison to the computed figures of merit, all studied XYZ_2 compounds exhibit lower experimental thermoelectric performance. While the theoretical figure of merit of $YCuTe_2$ is only slightly higher ($zT \sim 1.05$), the experimental thermoelectric

figures of merit of $TmAgTe_2$ and $YAgTe_2$ are lower than the predicted ones ($zT \sim 1.8$ for $TmAgTe_2$ and $zT \sim 1.6$ for $YAgTe_2$). The computed thermoelectric performance can be overestimated due to an overestimation of the electronic properties. The overestimation of the electronic properties can be a result of several factors, such as using a constant relaxation time and NSOC. While the valence band maxima are degenerate with NSOC, SOC splits the valence band maxima and therefore, the thermoelectric performance decreases. Furthermore, the constant relaxation time approach using $\tau_{el} = 10^{-14}$ s typically overestimates the electrical conductivity at high temperature. The large discrepancy between the experimental and computed zTs of $YAgTe_2$ and $TmAgTe_2$ is also related to the low carrier concentration. While $YAgTe_2$ does not show a significant increase in thermoelectric performance with optimization of the carrier concentration based on the SPB model, optimized carrier concentration can increase the thermoelectric figure of $TmAgTe_2$ to ∼1.0 and ∼1.4 for the parent and the extrinsically doped compounds, respectively. It should be noted that the estimated phononic contribution to the thermal conductivity ($\kappa_{pho} = 0.5$ W m^{-1} K^{-1}) in all studied XYZ_2 compounds was also overestimated leading to an underestimation of the thermoelectric figure of merit.

It can be concluded that the best thermoelectric performance was observed here for $YCuTe_2$ compounds over the entire temperature range. The high zT can be related to the high carrier concentration (∼10^{19} h$^+$ cm^{-3}) giving a maximum zT of ∼0.73 at 780 K for $Y_{0.96}Cu_{1.08}Te_2$. Lower zTs were determined for $TmAgTe_2$ compounds where the trigonal phase had a higher zT than the tetragonal phase due to higher carrier concentration. However, the carrier concentration was low for the $TmAgTe_2$ parent compounds due to Tm_{Ag} antisite defects acting as hole killers. Enhancement in the carrier concentration was observed for Mg- and Zn-doped compounds resulting in an increase in zT to ∼0.47 at 700 K. The poorest thermoelectric performance of the investigated XYZ_2 compounds was revealed for $YAgTe_2$ compounds. Although the carrier concentration of $YAgTe_2$ was similar to the parent compounds of $TmAgTe_2$, the lower Seebeck coefficient due to a reduction of the DOS effective mass and the higher thermal conductivity in $YAgTe_2$ compounds led to a low zT.

5.1.8 Conclusions

In a high-throughput screening of ∼9000 inorganic compounds, a novel class of high-potential thermoelectric materials with the nominal formula XYZ_2 (X, Y = rare-earth or transition metals; Z = group VI element) was revealed. From the first-principle calculations, a strong correlation between band degeneracy and maximum figure of merit was observed. The electronic and phononic dispersion curves agree well with the experimental DOS recorded by UPS/IPES and experimental heat capacity, respectively.

Three different XYZ_2 parent compounds and several corresponding doped samples were synthesized indicating enhanced thermoelectric performance with a maximum thermoelectric figure of merit of ∼0.73±0.18 at 780 K for $Y_{0.96}Cu_{1.08}Te_2$. Thermoelectric properties were improved with intrinsic and extrinsic doping in $YCuTe_2$ and $TmAgTe_2$, respectively. In particular, the thermoelectric performance in $TmAgTe_2$ was increased with Zn-doping due to an increase in carrier concentration whereas Tm_{Ag} antisite defects act as hole killer in the parent compound. $YAgTe_2$ has a low figure of merit although the carrier concentration was similar to that of $TmAgTe_2$. The SPB model indicates that the thermoelectric figure of merit in $TmAgTe_2$ could be significantly increased with optimizing the carrier concentration.

All investigated XYZ_2 compounds exhibited extremely low thermal conductivity, even lower than the (Cahill, Watson, and Pohl) amorphous limit [66, 67]. The present minimum thermal conductivity model was modified to account for phonon mean free paths limited by dynamic disordering (*i.e.*, phonon-phonon interactions) whereas the thermal conductivity in PCBM was limited by static disordering in the crystal structure. Both (static and dynamic) models predict even lower thermal conductivity than the present experimental phononic contribution to the thermal conductivity. The low thermal conductivity can be attributed to the low Debye temperature, as determined from heat capacity at low temperature except for $TmAgTe_2$ where there is a low-temperature magnetic phase transition.

Although the computational approach to predict the electronic properties can accelerate the search for novel high-performance thermoelectric materials, the electronic properties are typically overestimated due to the exclusion of SOC and

using the constant relaxation time approach. However, with optimization of the carrier concentration the experimental thermoelectric figure of merits might be in the same order of magnitude to the computed values. The computational approach should be considered as qualitative rather than quantitative.

These new thermoelectric materials are likely to have enhanced thermoelectric performance compared to the well-investigated binary silver and copper chalcogenides due to the high band degeneracy at the band edge and the extremely low thermal conductivity. However, the carrier concentration needs to be optimized to improve the thermoelectric figure of merit, and that could likely be accomplished through a joint effort of experimental studies and theoretical defect calculations.

5.2 Metal Phosphides[4]

5.2.1 Introduction

In the previous section of this chapter, the electronic properties of ∼9,000 inorganic compounds were calculated using the electronic band structure and Boltzmann transport equations with a constant relaxation time of 10^{-14} s. In a recent study, the high-throughput screening of electronic properties within 'The Materials Project' was extended to over 48,000 inorganic compounds [35]. From this screening, a potential class of high-performance thermoelectric materials with enhanced electrical properties was revealed: metal phosphides. Although metal phosphides have been investigated for thermoelectrics indicating enhanced electronic properties and thermodynamic stability at elevated temperatures [311, 312, 313, 314], they had not been further considered due to their expected high thermal conductivity.

In a recent computational study, the thermoelectric properties of two-dimensional black phosphorous were calculated, showing promising electronic properties but high thermal conductivity [315]. It was predicted that the lattice thermal conductivity could be reduced by the substitution of Sb for P resulting in an estimated increase of zT to 5.4 at 800 K. Low thermal conductivity was also found in some metal phosphides

[4]The author's contribution in this section was the development of the variable relaxation time, the synthesis of nickel diphosphide, the characterization (PXRD, SEM, TGA), heat capacity measurements and the investigation of the thermoelectric properties at low temperature. The synthesis and all measurements were performed in the laboratory of Dr. Mary Anne White, Department of Chemistry, Dalhousie University, unless stated otherwise.

but high electrical resistivity limited their thermoelectric performance [316].

Therefore, for a more complete prediction of the thermoelectric performance in metal phosphides, the lattice thermal conductivity was predicted here by different methods. On the one one hand, the theoretical minimum thermal conductivity was computed using the Cahill, Watson, and Pohl model [66, 67] and the present models. For more crystalline samples, the minimum thermal conductivity underestimates the phononic contribution of the thermal conductivity and therefore, the lattice thermal conductivity was predicted using a recent semi-empirical approach by Miller *et al.* [68]. While the lattice thermal conductivity approaches the minimum thermal conductivity at high temperature or at small grain size and should be considered as a lower bound, an average thermal conductivity can be calculated using the semi-empirical approach [68]. It was recently shown that the lattice thermal conductivity in Zn_3P_2 can be dramatically reduced by nanostructuring, even below the (Cahill,Watson, and Pohl) amorphous limit [66, 67], whereas the electrical conductivity was not affected by the grain size [317, 318].

In addition to the prediction of the lattice thermal conductivity, the electronic properties were calculated here with a variable relaxation time using the Boltzmann transport approach. While a constant relaxation time can overestimate the electrical thermal conductivity, in particular, at high-temperature, a variable relaxation time considers the crystal structure as well as the energy- and temperature-dependence of the relaxation time. The variable relaxation time was computed from the mobility which was calculated with a semi-empirical approach reported by Yan *et al.* [46]. For the energy- and temperature-dependence of the relaxation time acoustic scattering was assumed, as it is generally the limiting scattering factor in thermoelectrics.

Combining the predicted electronic properties with constant and variable relaxation times with the phononic properties, several metal phosphides would be predicted to have higher figures of merit than the current best thermoelectric materials (PbTe and Bi_2Te_3). The thermoelectric figure of merit is compared here to the beta-factor [46]. As an example of the metal phosphides, nickel diphosphide in the cubic phase was synthesized and the present results show thermal conductivity below the amorphous limit yet high electrical conductivity.

5.2.2 Computation

5.2.2.a Methodologies

All computations were performed by the 'Materials Project' [48]. The electronic band structures were computed using VASP [256] with PBE-GGA [51] and PAW [52] for the pseudopotentials. To enhance the prediction of the band gaps, the electronic band structures were also computed with the hybrid functional HSE06 [258, 259]. The electronic transport properties were calculated using the PBE-GGA and HSE band structures and Boltzmann transport equations in the software package BoltzTrap [49]. The electronic properties were computed both with a constant relaxation time set to 10^{-14} s and a variable relaxation time (*vide infra*). The force constants were obtained using the Alloy Theoretic Automated Toolkit (ATAT) code [264].

The elastic properties, including the 6×6 elastic tensor, shear and bulk moduli were calculated using density functional theory (DFT) [260]. More information on the elastic properties can be found in Section 5.1.2. The Bader charges were calculated with the code developed by the Henkelman group where the steepest ascent in the charge density gradient between the grid point was taken to determine the atom's Bader volume [319]. The charge density was integrated to calculate the charge of the atom via DFT. More information concerning the Bader charges can be found in reference [319].

Phononic dispersion curves and thermodynamic properties were computed by Dr. Guido Petretto and Dr. Gian-Marco Rignanese, Institute of Condensed Matter and Nanosciences - Nanoscopic Physics, Université catholique de Louvain, using the ABINIT software package [320] within the framework of density functional perturbation theory (DFPT) [197, 321, 322]. For the calculation, norm-conserving pseudopotentials [323] were employed and long-range exchange correlations were considered using the PBE-GGA approximation [51].

5.2.2.b Variable Relaxation Time Approach

The electronic properties of the XYZ_2 class were first calculated from the electronic band structures and the Boltzmann transport equations using a constant relaxation time, set to 10^{-14} s. This value is typical for metals at room temperature and has

the advantage of providing the electrical conductivity and Seebeck coefficient for comparison with experiment. In the constant relaxation time approach, the Seebeck coefficient is treated as independent of the relaxation time, while both the electrical conductivity and the electronic contribution to the thermal conductivity scale linearly with the relaxation time. However, it is important to note that the relaxation time can differ between materials/samples as it depends on diverse scattering mechanisms such as grain boundaries, electron-phonon interactions, and impurities. In particular, electron-phonon scattering can have a large influence on the relaxation time at high temperature. In this sense, the relaxation time is not independent of temperature and energy and normally decreases dramatically with temperature. Thus, the constant relaxation time approach most likely overestimates the electrical conductivity and the electronic contribution of the thermal conductivity at high temperature.

Due to the fact that it is not feasible to calculate the relaxation from first-principle calculations in a high-throughput screening because of the high computing cost, the constant relaxation time is a common approach to compute the electronic properties in the thermoelectric community. The relaxation time is typically set to a fix value, in general $\tau_{el} = 10^{-14}$ s [35, 277], or the electrical conductivity is represented as a function of the relaxation time [41, 42, 43]. In the latter approach, the figure of merit is estimated with the assumption that the lattice thermal conductivity divided by the relaxation time is a constant value ($\kappa_{pho}\tau_{el}^{-1} = 10^{14}$ W m^{-1} K^{-1} s^{-1} [41, 42, 43]) and it has been shown that the relaxation time has a temperature behavior similar to the lattice thermal conductivity. In the present study, a variable relaxation time is postulated where the temperature-dependent relaxation was limited by acoustic scattering.

Yan *et al.* reported a semi-empirical approach to calculate the electron mobility, μ_{el}, from first-principle calculations [46]. The electron mobility is generally limited by acoustic and optical phonons at elevated temperatures and the mobility decreases with $T^{-1.5}$ as observed for $YCuTe_2$. The charge carrier scattering in semiconductors can be described by four scattering mechanisms: (a) acoustic deformation scattering, (b) optical deformation potential scattering, (c) polar optical phonon scattering, and (d) piezoelectric scattering. While the piezoelectric effect is significant at low temperatures, deformation potential and polar optical

scattering mechanisms contribute at room temperature and above. Because the semi-empirical approach for the electron mobility prediction was performed at room temperature, piezoelectric scattering was not considered [46]. The three remaining scattering mechanisms have in common that phonons displace the ions in the crystal leading to a change in the dispersion in the electronic band structures and hence in the deformation potentials. Furthermore, the dipole moment between the atoms can be perturbed by phonons in noncentrosymmetric crystals, resulting in a nonzero polarization in the material and induced fields [46]. Therefore, stiffening of the crystal lattice would reduce the electron-phonon scattering mechanisms and it is reasonable to deduce that the electron mobility would increase with increasing bulk modulus, B (in Pa).

In addition to the elastic properties, the Drude model proposes that the electron mobility is inversely proportional to the band effective mass, m_b^* (in m_0^*), (see Equation 2.42) and the electron mobility can be described by

$$\mu_{el} = A_0 B^s (m_b^*)^{-t} \tag{5.6}$$

where A_0, s, and t are empirical parameters. The band effective mass in Equation 5.6 can be calculated from the DOS effective mass, m_{DOS}^* and the band degeneracy, N_v (see Equation 2.28). However, it is important to note that Equation 2.28 is only valid if the effective mass is symmetric in all crystal directions and the hole pockets/electron valleys are spherical [50] (see Section 2.4 for further discussion). Furthermore, the calculation of the DOS effective mass can introduce uncertainty. The calculated DOS from DFT can be fit to a DOS with parabolic bands given by

$$DOS(E) = \frac{1}{2\pi^2}\left(\frac{2m_{DOS}^*}{\hbar^2}\right)^{1.5} E^{0.5} \tag{5.7}$$

where the energy, E, is limited to 100 meV from the valence and conduction band edges [46]. The fitted DOS effective masses are typically underestimated and therefore, were adjusted by an exponent of 0.6 [46]. The band degeneracy is determined by identifying the Fermi surface pockets inside the first Brillouin zone and summing up the number of individual bands inside each pocket for the valence band and the conduction band, respectively [46].

Equation 5.6 was fitted to a learning set of 31 materials, including oxides and common thermoelectric materials, at room temperature and the best fit was obtained

for $A_0 = 1.2 \cdot 10^{-14}$ kg^2 A^{-1} s^{-4}, $s = 1$, and $t = 1.5$. It is important to note that t varies from the reported $t = 2.5$ [46] [private communication with Dr. Prashun Gorai and Dr. Eric Toberer]. With this semi-empirical approach, the electron mobility can be calculated with a relative low computational cost and good accuracy; most materials had an uncertainty in mobility of less than half an order of magnitude [46]. For more details about the calculation of the electron mobility, the study by Yan *et al.* is recommended [46].

From the electron mobility, the relaxation time at room temperature can be calculated with the Drude model using Equation 2.42 and the band effective mass calculated from the Boltzmann transport equations in BoltzTrap,

$$M_{\beta u}^{-1}(i,k) = \frac{1}{\hbar^2} \frac{\partial^2 \varepsilon_{i,k}}{\partial k_\beta \partial k_u}. \tag{5.8}$$

This approach is more computationally expensive than the calculation of the band effective mass for the electron mobility but enhances the accuracy of the band effective mass. Using Equation 5.8 for the band effective mass, the relaxation time is given by

$$\tau_{el,300\mathrm{K}} = \frac{\mu_{el} m_b^*}{q}. \tag{5.9}$$

For the energy- and temperature-dependence of the relaxation time, it is postulated that the carriers are solely scattered by acoustic phonons (see Equation 2.43). Therefore, the variable relaxation time is proportional to the inverse temperature and $E^{-0.5}$ and given by

$$\tau_{el,variable} = \tau_{el,300\mathrm{K}} \left(\frac{T}{T_0} \right)^{-1.5} \left(\frac{E - E_{edge}}{k_B T} \right)^{-0.5} \tag{5.10}$$

with $T_0 = 300$ K as the initial temperature and E_{edge} as the energy of the band edge. Equation 5.10 was employed in the software package BoltzTrap by Dr. Guodong Yu with three conditions. If the energy is lower than the valence band maximum (VBM,) $\tau_{el,300\mathrm{K}}$ and E_{edge} were set to the variable relaxation time of the holes ($\tau_{el,300\mathrm{K,p-type}}$) and the energy of the VBM ($E_{edge} = E_{VBM}$), respectively. Similarly, if the energy is larger than the conduction band minimum (CBM), the computed variable relaxation time of the electrons ($\tau_{el,300\mathrm{K,p-type}}$) was used for $\tau_{el,300\mathrm{K}}$ and $E_{edge} = E_{CBM}$ with E_{CBM} as the energy of the conduction band minimum. At the band gap, $\tau_{el,variable}$ was set to zero. However, it is important to know that although the relaxation

time can be calculated at 300 K, exact definitions of T_0 and E_{edge} are unknown, which can introduce uncertainty. The present variable relaxation time approach was tested on the metal phosphides for the first time and further investigations of the variable relaxation time are required. (The relaxation times of the investigated metal phosphides at room temperature are given in Table D.1 in Appendix D.)

The electrical conductivity of metal phosphides as well as for PbTe and Bi_2Te_3 were calculated with the variable relaxation time approach and compared to that calculated with a fixed relaxation time of 10^{-14} s (see Figure 5.30). The electrical conductivity from both approaches is similar at 300 K whereas at high temperature nearly all electrical conductivities are overestimated. An overestimation of the electrical conductivity would show a higher thermoelectric performance. Therefore, the present variable relaxation time approach would most likely enhance the search not only for thermoelectric materials but also for high-temperature electrical conductors. (The data for the electrical conductivity with the inclusion of a constant relaxation time or the present variable relaxation time approach are given in Tables D.2-D.5 of Appendix D.)

5.2.2.c Electronic Band Structures

From the high-throughput screening of 48,000 inorganic compounds using the Boltzmann transport approach with constant relaxation time approach, several metal phosphides with enhanced electronic properties were revealed; the present study focuses on 26 metal phosphides. The compounds can be separated in different subclasses: XP, XYP, XP_2, and X_3P_2 where X is a metal and Y is an alkali metal. For the calculations of the electronic properties, the carrier concentration was set to 10^{20} cm^{-3}. The electronic band structures were calculated with PBE-GGA and the electronic properties were calculated with both constant relaxation time and variable relaxation time. The data for the electronic band structures were taken from 'The Materials Project' database. The data were plotted with a script written in Python where the electron bands are color-coded using the elemental DOS to show the contribution of the individual elements to the electronic band structure.

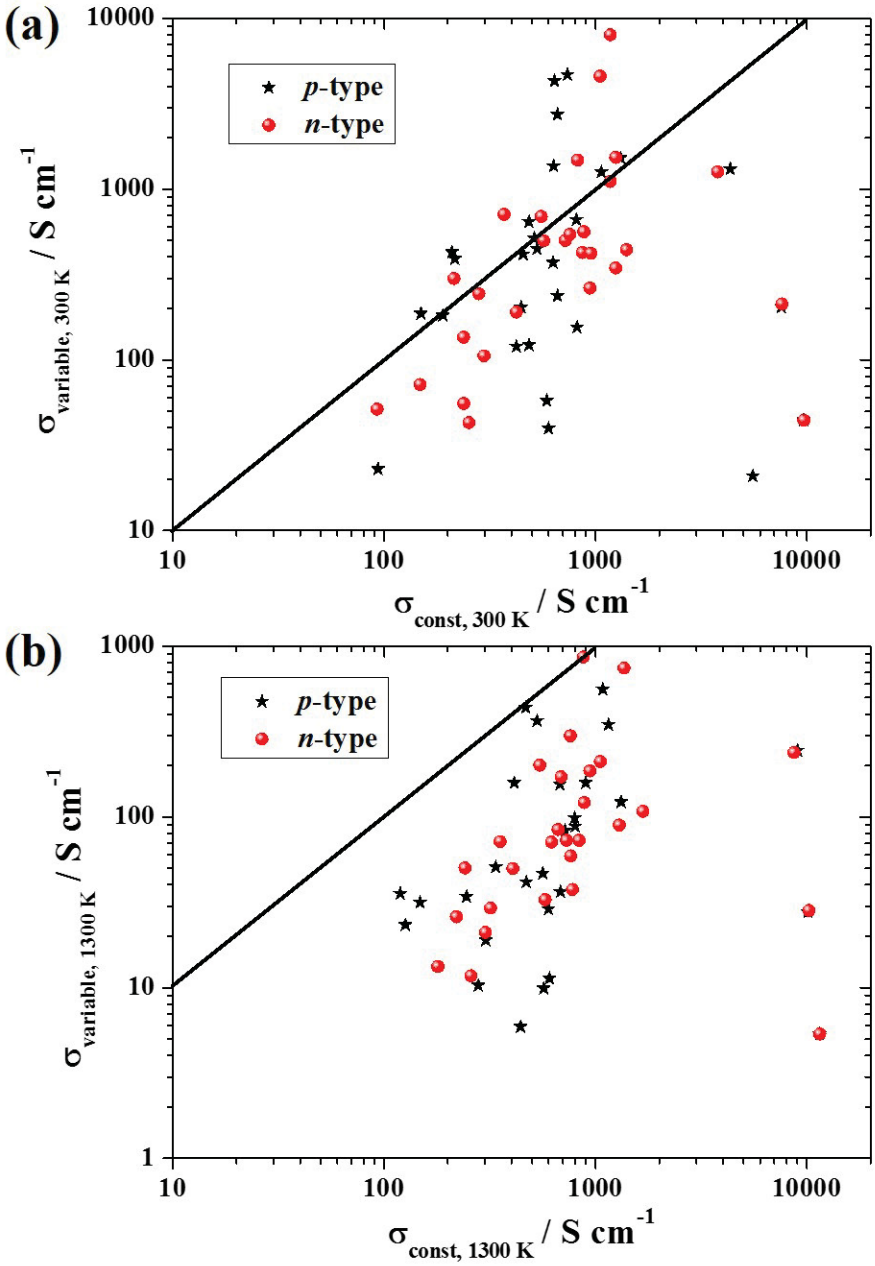

Figure 5.30: Comparison of the computed electrical conductivity with constant, σ_{const}, and variable, $\sigma_{variable}$, relaxation time at (a) 300 K and (b) 1300 K. At high temperature, the electrical conductivity is overestimated using a constant relaxation time. The black lines indicate the optimum correlation for both approaches and are shown as a guide for the eye.

$X\mathbf{P}$ In the XP group where X is a metal, the p-type power factor ($p-PF_{const}$) and n-type power factor ($n-PF_{const}$) of GaP and BP using a constant relaxation time are relatively high within the class of isotropic band structures due to the parabolic band cuves (see Figure 5.31). The valence bands in BP are multi-degenerate at the Brillouin center leading to high $p-PF_{const}$ (see Figure 5.31 (a)). On the other hand, GaP also has multiple band degeneracy in the conduction at the L symmetry point (which is the CBM) with a valley degeneracy of 4 and a second minimum was observed along $\Gamma-X$ which is 0.054 eV higher in energy than the CBM. The second minimum had a valley degeneracy of 6 as shown in Figure 5.31 (b). Furthermore, it was found that the predicted $n-PF_{const}$ in GaP and BP is relatively high due to a predicted high electrical conductivity (1040 and 766 S cm^{-1}, respectively, at 600 K) using a constant relaxation time. A high electrical conductivity in both compounds also was observed using the present variable relaxation time (3011 and 569 S cm^{-1} for GaP and BP, respectively, at 600 K). In particular, the electrical conductivity of GaP increased with the present approach due to a long relaxation time at room temperature ($\tau_{el,300\text{K}} \sim 10^{-13}$ s; see Table D.1 of Appendix D). High electrical conductivities are typically observed for most III-V semiconductors where the Fermi surface is often spherical leading to uniformly low effective mass [50]. However, a high electrical conductivity increases the electrical contribution of the thermal conductivity at high temperature ($\kappa_{el} > 1$ W m^{-1}K^{-1}) which might reduce the thermoelectric performance.

$XY\mathbf{P}$ The most interesting characteristic of the XYP group where X is a metal and Y is an alkali metal is the highly anisotropic electrical conduction, in particular, the p-type electrical conductivity can vary by a factor of 20 in different crystal directions as shown in Table 5.7. It was found that anisotropy can result in high PF due to the distortion of electron/hole pockets [50]. Although the DOS effective mass remains nearly the same leading to a nearly isotropic Seebeck coefficient, the band effective mass changes in different directions. Lower effective mass increases the electrical conductivity and the PF is, thus, improved in certain direction(s). Furthermore, at high temperature multiple valleys in the electronic band structure contribute to the carrier transport leading to an increase in the Seebeck coefficient as extreme as -400/-370 and 394/365 µV K^{-1} in BaLiP/NaZnP, respectively,

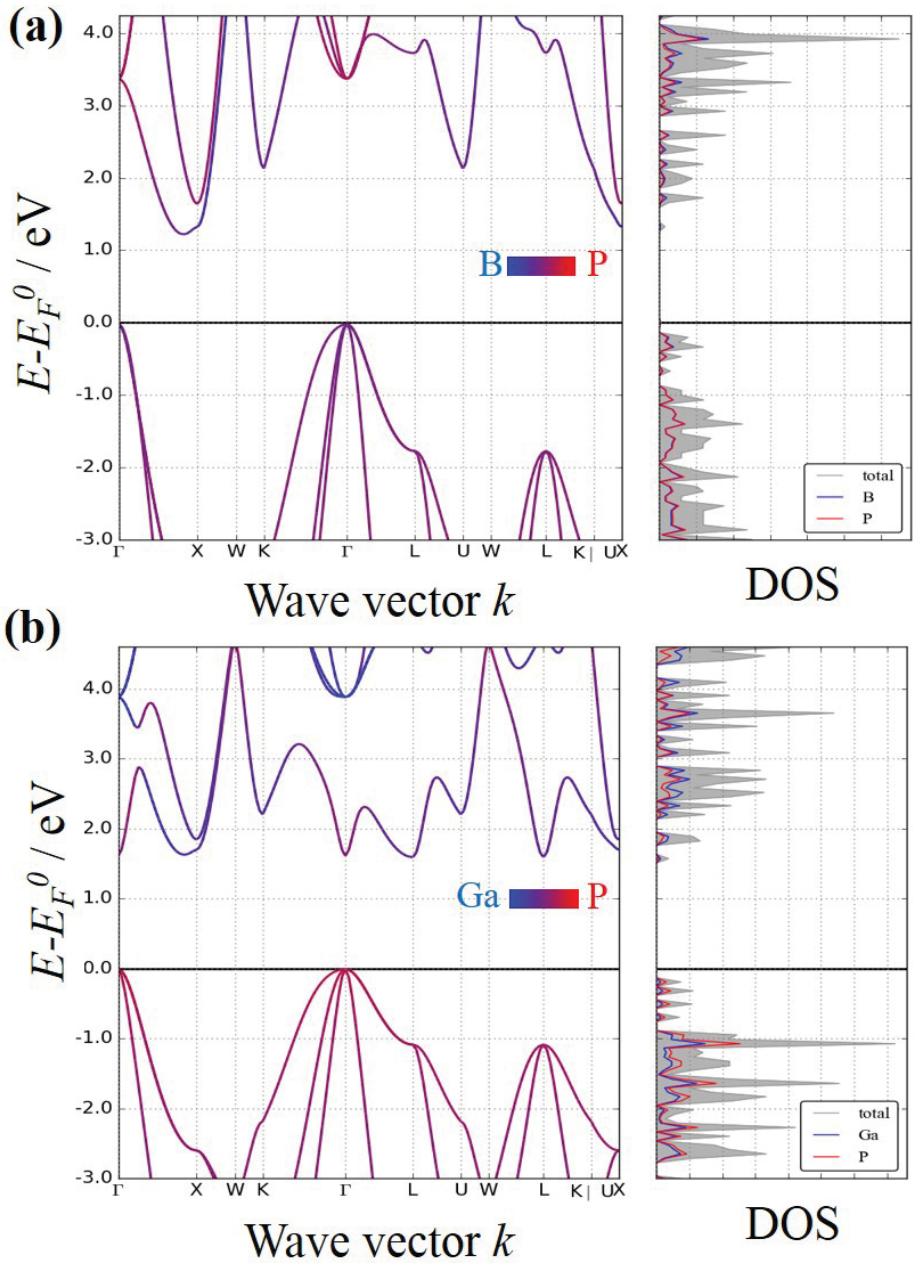

Figure 5.31: Electronic band structure and DOS of (a) BP and (b) GaP computed using PBE-GGA. Parabolic band structures and multiple valley degeneracy enhance the electronic properties of these compounds.

whereas curvature of the bands increases the electrical conductivity (see Figure 5.32). However, if the variable relaxation time approach is employed, a reduction in

electrical conductivity was observed due to low electron mobility and hence short relaxation times for most XYP compounds ($\sim 10^{-15}$ s). Therefore, the constant relaxation time approach overestimates the PF of the XYP compounds by almost one order of magnitude at high temperature. (Predicted power factors using the constant relaxation time and variable relaxation times are compared in Table 5.8.)

XP$_2$ The XP$_2$ compounds (X=metal) show high calculated $p - PF$ for the monoclinic phase of NiP$_2$ (m-NiP$_2$) while the cubic phase (c-NiP$_2$) has up to two orders of magnitude lower $p - PF$ using the electronic properties from the variable relaxation time approach. The low power factor is mostly a result of the zero band giving a magnified bipolar effect and therefore, the predicted magnitude of the Seebeck coefficient is low. (The electronic structure of c-NiP$_2$ calculated with PBE-GGA and HSE is further discussed below.) m-NiP$_2$ has a relatively high computed Seebeck coefficient at low temperature indicating that it is a potential candidate for low-temperature thermoelectrics.

Other XP$_2$ monoclinic, including BeP$_2$ and PdP$_2$, also have a multiple valley degeneracy. However, the PdP$_2$ band structure is much more anisotropic than that of BeP$_2$ and predicts, therefore, a larger $n - PF$ and $p - PF$. The discrepancy between the compounds can be related to the crystal structure. Although both PdP$_2$ and BeP$_2$ crystallize in the same space group ($C2/c$), PdP$_2$ crystallizes in a layered structure resulting in an anisotropic band structure similar to m-NiP$_2$, whereas the atoms in BeP$_2$ are more ordered leading to more isotropic properties. In the variable relaxation time approach, the electron relaxation time of PdP$_2$ is almost an order of magnitude higher than the constant relaxation approach. Due to the multi-valley degenerate electron bands in the conduction bands in PdP$_2$ a relative high n-type Seebeck coefficient (-227 µV K^{-1} at 800 K) was calculated whereas the curvature leads to low effective mass and hence, high electrical conductivity (1153 S cm^{-1}).

It should be noted that the conduction bands of CoP$_2$ and AgP$_2$ as well as the valence bands of CuP$_2$, IrP$_2$, and RhP$_2$ are also multi-valley degenerate. Consequently, these compounds have relatively high predicted $n - PF$ or $p - PF$. In particular, due to the high hole relaxation time in IrP$_2$ and RhP$_2$ ($\sim 10^{-13}$ s) in the variable relaxation approach these compounds are predicted to possess high

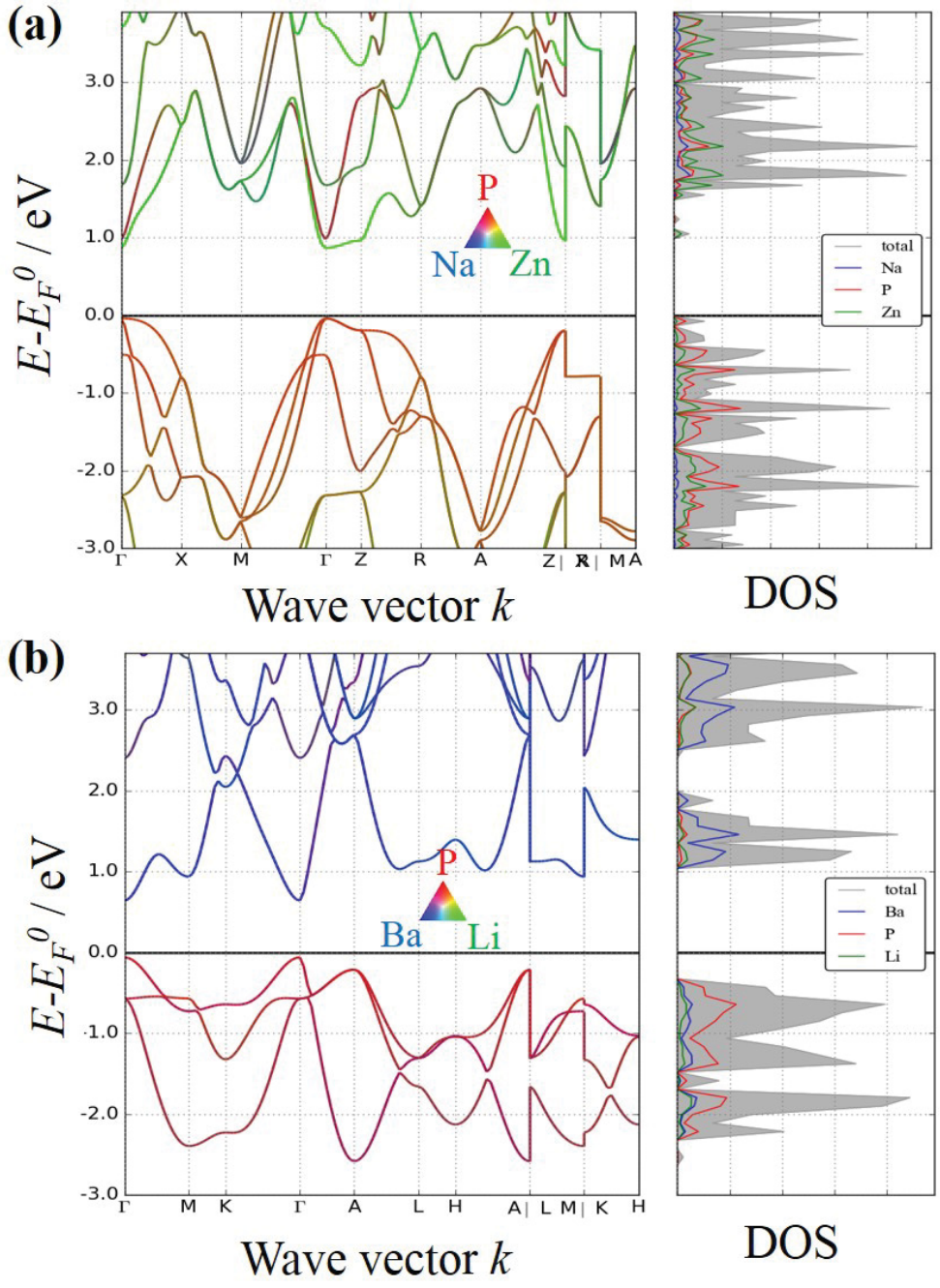

Figure 5.32: Electronic band structure and DOS of (a) NaZnP and (b) BaLiP computed using PBE-GGA. Lower bands can contribute at high temperature to the carrier transport resulting in an increase in Seebeck coefficient.

Table 5.7: Calculated power factors in x, y, and z-direction in the units mW m^{-1} K^{-2} at $n = 10^{20}$ cm^{-3} and $T = 600$ K and a constant relaxation time of 10^{-14} s.

Material	SrLiP	NaSnP	NaZnP	BaLiP	m-NiP_2	CoP_2	PdP_2	RuP_2
$n - PF_x$	1.66	2.72	2.28	1.37	1.36	1.54	2.71	2.04
$n - PF_y$	1.66	4.18	2.28	1.37	6.67	3.48	3.99	2.83
$n - PF_z$	3.28	4.18	0.33	2.21	2.48	5.35	6.06	1.15
$p - PF_x$	2.38	0.84	6.39	1.57	1.37	2.01	2.73	3.05
$p - PF_y$	2.38	0.84	6.39	1.57	5.73	2.89	4.87	3.51
$p - PF_z$	6.90	7.70	0.36	3.14	5.08	2.97	3.25	4.86

$p - PF$ with 5.1 and 6.6 mW m^{-1}K^{-2} for RhP_2 and IrP_2. It was also noted that although both valence and conduction bands in ZnP_2 and the valence band in FeP_2 have multiple valley degeneracies, the flatness of the bands increases the band effective mass in the conduction bands according to Equation 5.8, limiting the thermoelectric performance due to the very low electrical conductivity (<100 S cm^{-1} at high temperature with variable relaxation time).

$X_3\mathbf{P}_2$ Most of the X_3P_2 compounds (X = metal) have a direct band gap with high degeneracy in the valence bands at the Γ symmetry point. In particular, Zn_3P_2 has curved bands with some slightly lower-energetic valley which increase the Seebeck coefficient leading to high calculated $p - PF$ at ambient temperatures using the constant-relaxation time approach (4.4 mW m^{-1} K^{-2} at 900 K). However, an extremely low hole relaxation time was calculated for Zn_3P_2 with the present variable relaxation time approach ($\sim 6 \cdot 10^{-16}$ s) limiting the electrical conductivity and hence, the thermoelectric performance in Zn_3P_2. In general, these X_3P_2 compounds have parabolic conduction bands leading to high electrical conductivity while at high temperature multi-valleys contribute to the carrier transport enhancing the Seebeck coefficients. For instance, a high $n - PF$ was calculated for Mg_3P_2 at 1300 K with the constant relaxation time which in general is overestimated at high temperature. Using the variable relaxation time approach the $n - PF$ of Mg_3P_2 decreased by more than one order of magnitude compared to the constant relaxation time. However, it is surprising that a higher $p - PF$ was computed for Mg_3P_2 at 300 K with the variable relaxation time approach ($\sim$2.5

Table 5.8: Calculated power factors [in mW m^{-1} K^{-2}] calculated from the Boltzmann transport equation using a constant relaxation time, set to 10^{-14} s, PF_{const}, or the present variable relaxation time approach, $PF_{variable}$, at T = 600 K and $n = 10^{20}$ cm^{-3}.

Material	Space Group	$n - PF_{const}$	$p - PF_{const}$	$n - PF_{variable}$	$p - PF_{variable}$
NiP_2	$Pa\bar{3}$	2.01	3.21	0.07	0.05
NiP_2	$C2/c$	4.10	4.61	0.27	1.98
ZnP_2	$P4_32_12$	0.96	2.04	0.17	0.77
ZnP_2	$P4_12_12$	0.96	2.04	0.17	0.77
AgP_2	$P2_1/c$	2.94	1.86	1.09	1.17
TiP_2	$Pnnm$	0.55	0.44	0.01	0.01
CuP_2	$P2_1/c$	2.04	3.74	0.28	1.26
RuP_2	$Pnnm$	2.08	3.78	1.12	6.31
CoP_2	$P2_1/c$	3.45	3.78	0.23	0.79
IrP_2	$P2_1/c$	1.08	3.56	0.27	7.02
BeP_2	$C2/c$	2.97	2.65	0.76	0.44
RhP_2	$P2_1/c$	1.58	3.59	0.09	4.62
PdP_2	$C2/c$	4.92	3.85	6.66	0.02
FeP_2	$Pnnm$	1.81	1.38	0.74	0.04
Zn_3P_2	$P4_2/nmc$	1.14	3.59	0.18	0.03
Mg_3P_2	$Pn\bar{3}m$	2.07	3.05	0.30	1.44
Cd_3P_2	$P4_2/nmc$	0.70	2.54	0.08	0.12
NaZnP	$P4/nmm$	2.23	3.91	0.09	0.11
SrLiP	$P\bar{6}m2$	2.18	3.55	0.21	0.50
BaLiP	$P\bar{6}m2$	2.26	3.18	0.30	0.21
NaSnP	$P6_3mc$	3.76	3.91	0.61	0.07
MnP_4	$P\bar{1}$	0.88	0.96	0.16	0.35
MnP_4	$P\bar{1}$	2.89	1.91	0.14	0.55
FeP	$Pnma$	0.75	0.74	0.00	0.00
Mg_3P_2	$Ia\bar{3}$	1.44	2.09	0.28	1.42
BP	$F\bar{4}3m$	4.19	4.07	2.16	0.89
GaP	$F\bar{4}3m$	6.45	3.88	13.37	0.37
PbTe	$Fm\bar{3}m$	3.07	10.52	1.06	3.90
Bi_2Te_3	$R\bar{3}m$	3.47	3.33	0.38	0.03

mW m^{-1} K^{-2}).

All these band structures were calculated with the PBE-GGA exchange functional which underestimates the experimental band gap energies [324, 325]. Some of the metal phosphide band structures were also calculated with the more accurate HSE06

exchange functional indicating an increase in the band gap energies as shown in Table D.6 in Appendix D. The average increase in band gap energy of the metal phosphides using the HSE functional compared to the PBE-GGA was 0.76 eV. This agrees with the study by Chan and Ceder which reported that PBE-GGA exchange functional underestimated the band gap energy on average by 0.73 eV compared to experimentally determined band gap energies [53]. It is important to note that the HSE functional slightly overestimates the band gap energy compared to experimental band structures which even reduced the discrepancy between the present study and the study by Chan and Ceder. Setyawan *et al.* reported a relative uncertainty of 42% between PBE-GGA and experimental band gap energies in large band gap systems [54], which is consistent with the relative error for metal phosphides (∼48%), although the band gap energies are in the range of 0.3 to 1.6 eV (1.1 to 2.2 eV) for PBE-GGA (HSE). For most compounds investigated with PBE-GGA and HSE functionals, the underestimation of the band gap energy has only a small effect on the predicted electronic properties. While the PFs in AgP_2 are decreased for p-type and n-type, the $p-PF$ and $n-PF$ increases for ZnP_2 at 600 K. In other materials, an increase in the PF was observed for p- or n-type, while the PF of the opposite type decreases. The electronic properties of the HSE band structures were calculated with the constant relaxation time and it is planned to calculate the electronic properties of the HSE structure with the variable relaxation time approach in future.

5.2.2.d Phononic Dispersion Curves

In addition to the electronic band structures, the phononic dispersion curves of 10 metal phosphides were computed to provide information about the thermal conductivity. The phononic dispersion curves revealed that more complex unit cells (*i.e.*, large number of atoms per unit cell) possess low-frequency acoustic modes which can be suppressed by optical modes and avoided band crossing, as shown for AgP_2 and Zn_3P_2 in Figure 5.33.

Figure 5.34 presents the phonon band structures of BP and GaP which are similar to that of diamond structures, such as Si and Ge [326], and III-V semiconductors, *e.g.* GaAs [327]. A phononic band gap appears between the acoustical and optical modes leading typically to an increase in the frequency of the

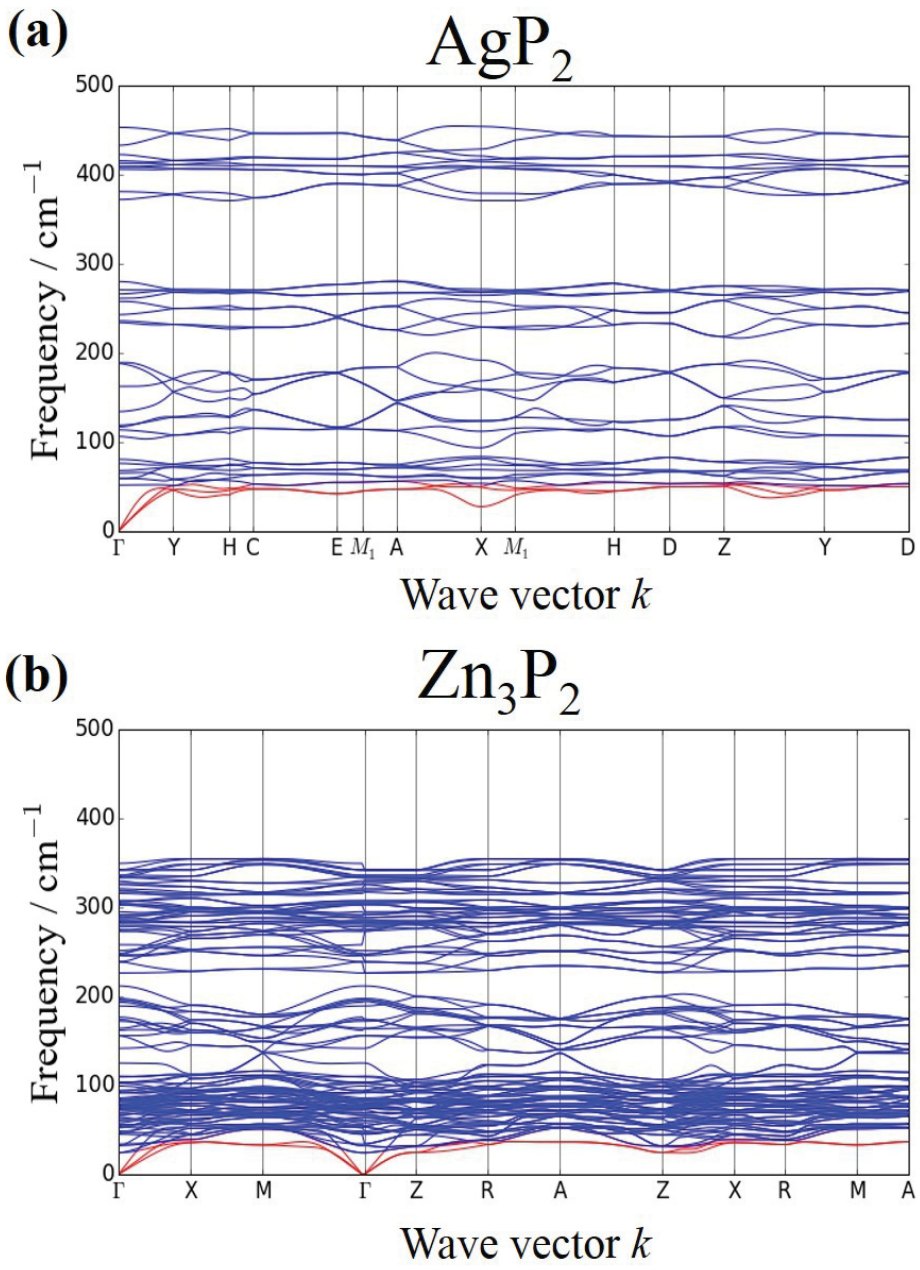

Figure 5.33: Calculated PBE-phononic dispersion curves of (a) AgP_2 and (b) Zn_3P_2. Low-frequency acoustic modes were observed for both compounds.

acoustic phonons and hence, high thermal conductivity. Furthermore, phononic dispersion curves of III-V semiconductors have a large split between the longitudinal and transverse acoustical modes. Although the transverse modes have zero group

velocity at the Brillouin zone edge, the speed of sound for all transverse and longitudinal acoustic modes is nearly the same at the Brillouin zone center, leading to high thermal conductivities for samples with long phonon mean free paths (*e.g.*, single crystals). Furthermore, all optical modes are nearly flat in all metal phosphide phononic dispersion curves and therefore, the optical modes do not contribute significantly to the thermal conductivity.

Currently, it is not feasible to determine the thermal conductivity from the phononic dispersion curves in a high-throughput screening and therefore, the thermal conductivity was estimated from the minimum thermal conductivity using the Cahill, Watson, and Pohl model [66, 67] and the present models for minimum thermal conductivity (see Equations 4.7 and 5.5). In an earlier study, it was revealed that the computed amorphous limit of the thermal conductivity has a strong correlation with the experimental thermal conductivity (see Figure 4.1) [35]. However, some materials have lower thermal conductivities than the amorphous limit as reported for PCBM (see Section 4.1) and XYZ_2 compounds (see Section 5.1). These compounds were tested using the present models for minimum thermal conductivities which are limited by static and dynamic disordering, respectively.

All three models for the minimum thermal conductivity (Cahill, Watson, Pohl; static; dynamic) were tested on Zn_3P_2 because an extremely low thermal conductivity was reported for the compound [317]. The longitudinal and transverse speed of sounds for the Cahill, Watson, and Pohl model were determined from the bulk and shear modulus using Equations 3.39 and 3.40, respectively ($v_{s,L} = 5406$ m s^{-1}; $v_{s,T} = 3155$ m s^{-1}). Lower average phonon mean speeds for the acoustic phonons were calculated using the entire Brillouin zone ($v_{s,L} = 2755$ m s^{-1}, $v_{s,T1} = 1951$ m s^{-1}, and $v_{s,T2} = 2097$ m s^{-1}) resulting in lower minimum thermal conductivity than the amorphous limit as shown in Figure 5.35. The amorphous limit of the thermal conductivity described by the Cahill, Watson, and Pohl model overestimated the experimental thermal conductivity of Zn_3P_2 whereas the minimum thermal conductivity using the present model with static disordering is lower than the experimental conductivity. However, the minimum thermal conductivity using a frequency-dependent phonon mean free path (dynamic model) agrees well with the experimental data.

Although the minimum thermal conductivity limited by dynamic disordering has

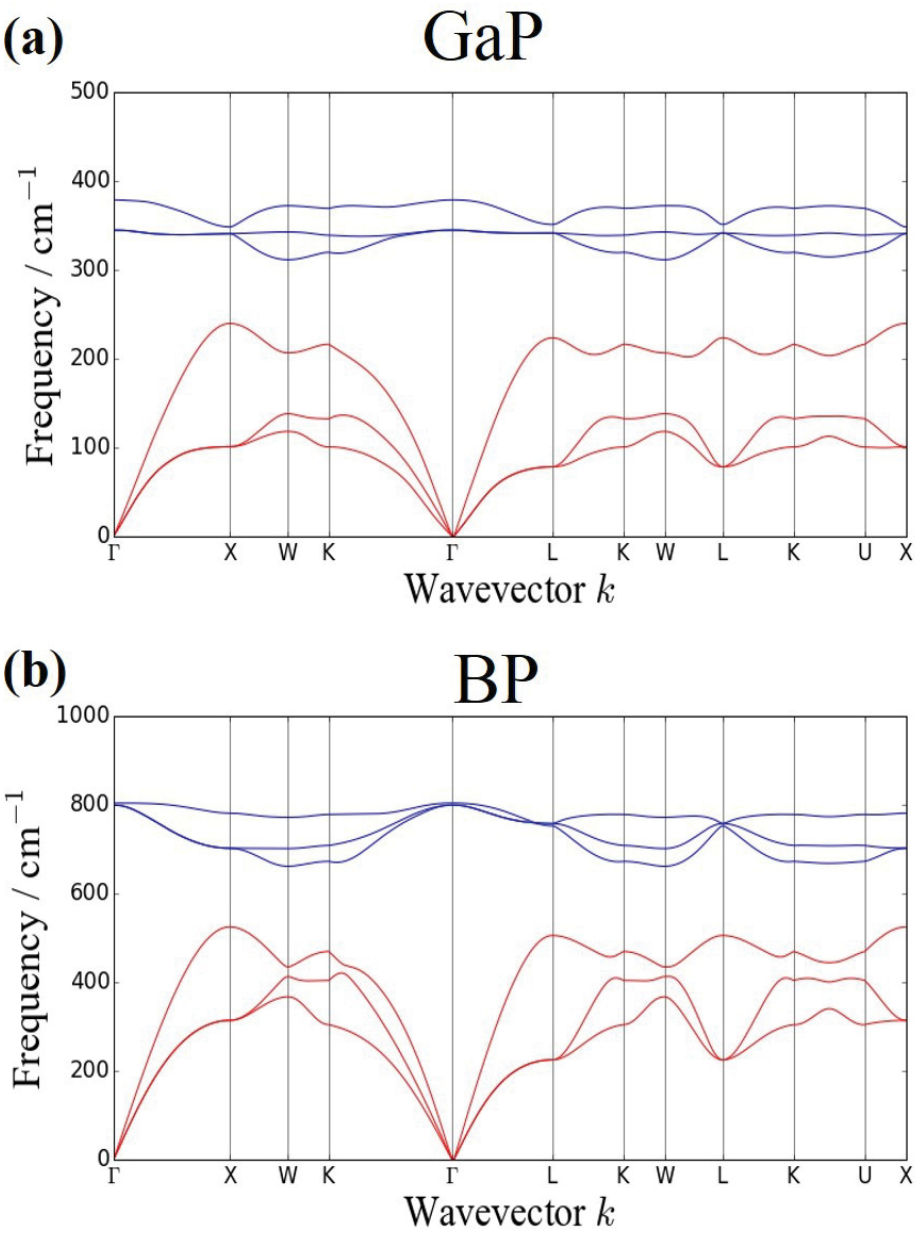

Figure 5.34: Calculated PBE-phononic dispersion curves of (a) GaP and (b) BP. The phononic band gap increases the frequency of the acoustic phonons and therefore, a high thermal conductivity is expected in these compounds.

a strong correlation with the experimental thermal conductivity, static disordering is more likely the reason for the ultralow thermal conductivity in Zn_3P_2 due to the small grain size and the lack of a peak in thermal conductivity at low temperature. The static disordering approach proposed that the phonon mean free path is limited by

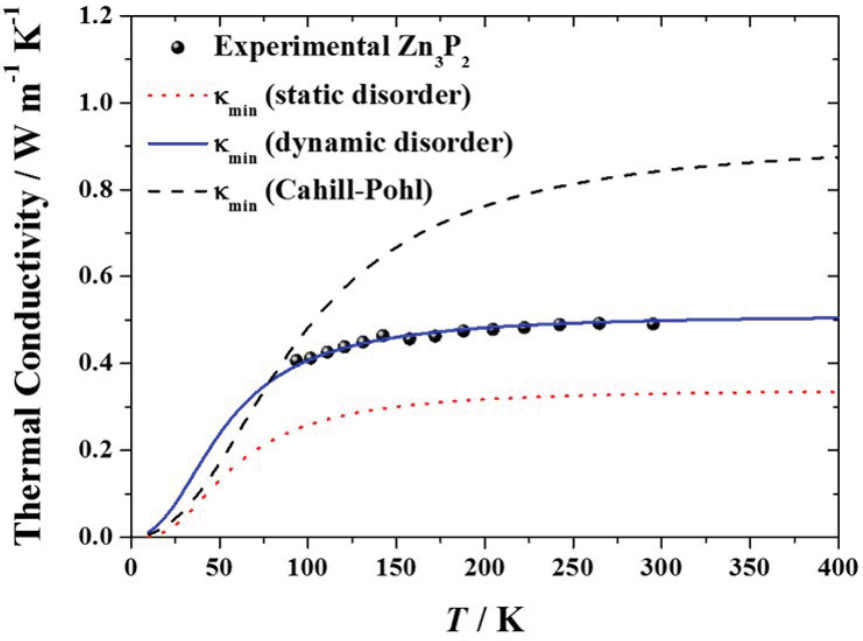

Figure 5.35: Ultralow thermal conductivity in Zn_3P_2 [317] can be explained using an average phonon mean speed from phonon band calculations. While static disordering predicts a lower thermal conductivity, dynamic disordering agrees well with the experiments.

the atomic density, which would be smaller than the grain size (∼2.9-6.3 nm) [317]. The grain size in Zn_3P_2 can be most likely further reduced leading to an even lower thermal conductivity, similar to the limit of static disordering. Therefore, it is not yet clear if the low thermal conductivity is due to dynamic or static disordering.

Several materials, such as AgP_2, GaP, and Mg_3P_2, with high predicted PFs reveal low minimum thermal conductivity, similar to Zn_3P_2, indicating potential for high-performance of thermoelectric materials as shown in Table D.7 of Appendix D. In particular, GaP is a promising thermoelectric material due to its predicted low minimum thermal conductivity and excellent electrical properties, if n can be increase to 10^{20} cm^{-3}. In addition to the described models, the minimum thermal conductivity also was calculated using the linear slope of the acoustic phonons at the Brillouin center and the Cahill, Watson, and Pohl model where the speed of sound was average for the longitudinal and transverse phonons (see Table D.7 of

Appendix D).

In addition to the amorphous limit, the thermal conductivity of the metal phosphides was computed with a semi-empirical model as recently reported by Miller *et al.* [68]. In this approach, the lattice thermal conductivity was separated into acoustic and optic terms in which the acoustic term is temperature-dependent ($\propto T^{-1}$) [68]. The acoustic term is typically the dominant one in thermal conductivity and can be model by the Callaway model (see Equation 2.14). It was assumed that the phonon mean free path is limited by phonon-phonon scattering as described in Equation 2.15. Thus, the acoustic term of the thermal conductivity can be calculated from

$$\kappa_{pho,aco} = A_1 \frac{\bar{M} v_s^y}{T \gamma^2 V^z n^{x-z}} \tag{5.11}$$

where A_1, x, y, and z are fitting parameters, $\bar{M} = V\rho N^{-1}$ is the average atomic mass, $v_s = B\rho^{-1}$ is the speed of sound, and N is the number of atoms. Here γ is the Grüneisen parameter which was relatively accurately estimated at room temperature with a semi-empirical approach using only the average coordination number, CN, as

$$\gamma = \gamma_0 \left[1 - \mathrm{e}^{-a(CN - CN_0)}\right] \tag{5.12}$$

where $\gamma_0 = 7.33688$, $CN_0 = 2.13647$, and $a = 0.05868$ [68]. This semi-empirical approach does not require any computation and the Grüneisen parameter can be determined using solely the crystal structure. However, the approach is not based on fundamental theory and has to be treated with due caution.

Optical modes are more important for systems with few atoms because in these systems the optical modes are more curved leading to an increase in the group velocity of the phonons. Miller *et al.* define the optical contribution by the amorphous limit using the model by Cahill, Watson, and Pohl [66, 67]. This could be misleading because the amorphous limit is calculated from the speed of sound which is determined from acoustic phonons. Therefore, the present author defines the optical contribution as the minimum thermal conductivity of the acoustic modes, $\kappa_{pho,aco,min}$, which is given by

$$\kappa_{pho,aco,min} = A_2 \frac{v_s n^z}{V^z} \left(1 - \frac{1}{n^{2/3}}\right) \tag{5.13}$$

and approaches the amorphous limit with increasing number of atoms. Note that although A_2 should be equal to $\frac{3k_B}{2}\left(\frac{\pi}{6}\right)$ it was treated as a fitting parameter by Miller *et al.* [68] to get the correct units (W m^{-1} K^{-1}) and order of magnitude for $\kappa_{pho,aco,min}$. The present calculation of the acoustic and $\kappa_{pho,aco,min}$ contribution varies from the reported approach [68] and was provided by the authors of the study [private communications with Dr. Eric Toberer and Sam Miller]. The acoustic (Equation 5.11) and the minimum acoustic contribution of the thermal conductivity (Equation 5.13) were combined and the resulting total thermal conductivity, κ_{SE}, was fitted to 63 experimental lattice thermal conductivities to determine the fitting parameters ($A_1 = 12.0265$ m$^{2.43027}$ s$^{-1.43483}$, $A_2 = 1.50296 \cdot 10^{-13}$ J K^{-1} m$^{-0.995444}$, $x = 1.0477825$, $y = 4.4348273$, and $z = 0.334852$) [68].

The minimum thermal conductivity, κ_{min}, using the Cahill, Watson, and Pohl model [66, 67] calculated with the computed elastic properties was compared to the semi-empirical model, κ_{SE}, as shown in Figure 5.36. It is shown that the thermal conductivity from the semi-empirical approach is nearly an order of magnitude higher than the amorphous limit for most metal phosphides. An increase of more than one order of magnitude was observed for GaP ($\kappa_{SE} = 48$ W m^{-1} K^{-1}) and BP ($\kappa_{SE} = 244$ W m^{-1} K^{-1}). This is consistent with the high thermal conductivity reported in literature for GaP (77 W m^{-1} K^{-1} at 300 K [328]) and BP ($\kappa_{SE} \sim 400$ W m^{-1} K^{-1} at 300 K [329]). The high thermal conductivity in these compounds is reasonable as the semi-empirical approach predicts the thermal conductivity at 300 K and provides an average thermal conductivity whereas the amorphous limit described the lower bound of the thermal conductivity. On the other hand, if the predicted amorphous limit of the thermal conductivity is already high, such as in BeP_2, the thermal conductivity of the semi-empirical approach is similar to the minimum thermal conductivity (see Figure 5.36). (Minimum thermal conductivities and room-temperature thermal conductivity using the semi-empirical approach are given in Table D.8 of Appendix D.)

5.2.2.e Computed Thermoelectric Performance

The electrical and phononic properties were combined to predict the thermoelectric performance of metal phosphides, and compare to current-best thermoelectric

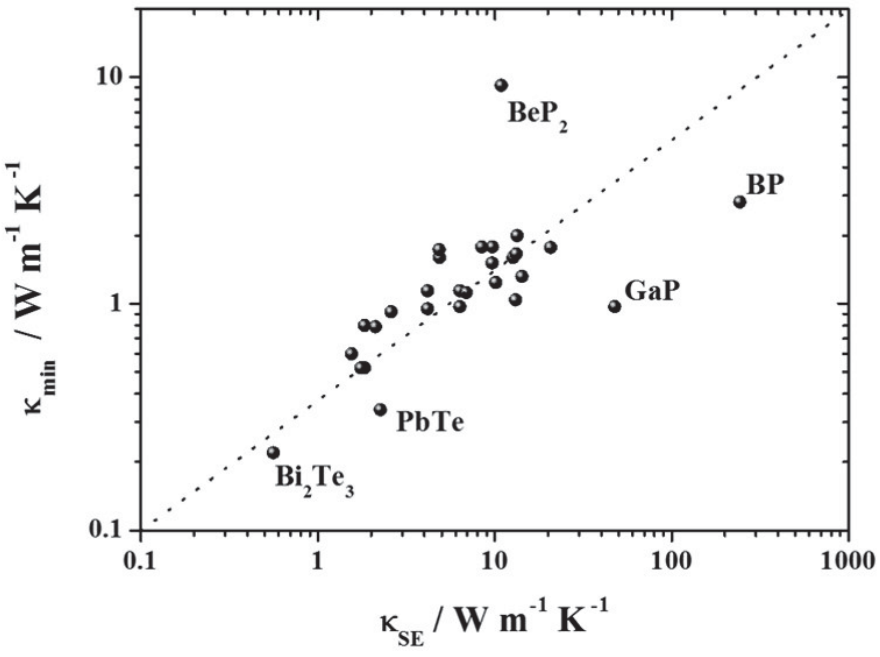

Figure 5.36: Minimum thermal conductivity using the Cahill, Watson, Pohl model was compared to the thermal conductivity from a semi-empirical approach [66, 67]. The black dashed line indicates the optimum correlation and is shown as a guide for the eye.

materials (PbTe and Bi_2Te_3). For the calculation of the thermoelectric figure of merit using Equation 1.15, the electronic properties were computed using a constant relaxation time set to 10^{-14} s, and also the variable relaxation time approach, whereas the lattice thermal conductivity was estimated by the minimum thermal conductivity using the Cahill, Watson, and Pohl model [66, 67]. Additionally, the electronic properties calculated from the variable relaxation time approach were combined with the lattice thermal conductivity using the semi-empirical approach [68]. The latter approach has the advantage that the relaxation time and the lattice thermal conductivity are both inversely proportional to the temperature which is consistent with the experimental relaxation time and lattice thermal conductivity for zinc antimonides [43]. The constant and variable relaxation time approaches are compared in Figure 5.37.

The figures of merit are higher for the electronic properties calculated from the

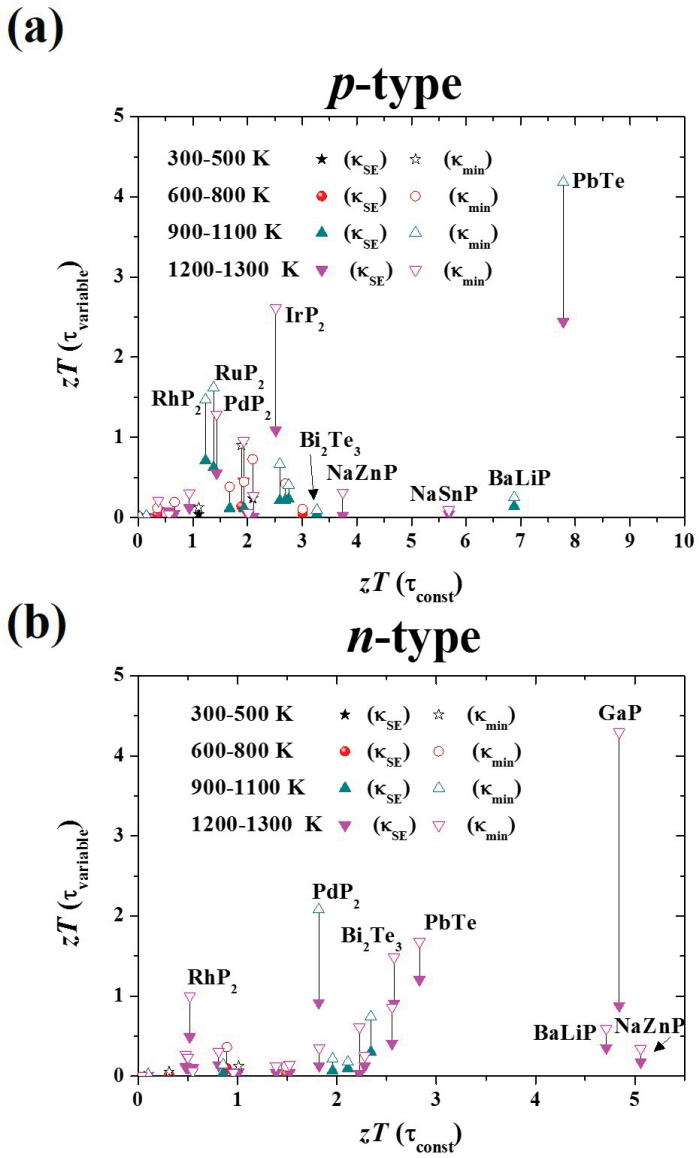

Figure 5.37: Comparison of the computed thermoelectric figures of merit of (a) p-type and (b) n-type metal phosphides sorted by the peak temperature (*i.e.*, temperature where zT is the maximum). The electronic properties were calculated with constant ($zT(\tau_{\text{const}})$) and variable ($zT(\tau_{\text{variable}})$) relaxation time approaches and the lattice thermal conductivity was predicted by the minimum thermal conductivity, κ_{min}, using the Cahill, Watson, and Pohl model [66, 67]. Additionally, the electronic properties from the variable relaxation time approach were combined with the thermal conductivity using a semi-empirical approach, κ_{SE} [68]. Black lines connect the same compounds using different estimated thermal conductivities (κ_{min} and κ_{SE}) to calculate $zT(\tau_{\text{variable}})$).

constant relaxation time approach. In particular, high zTs were computed for XYP compounds due to their high Seebeck coefficients and relatively low thermal conductivities. The n-type thermoelectric performance of the XYPs is almost twice as high as the predicted zT of PbTe and the current best experimental zT (SnSe with a zT of $\sim$2.6 [26, 27]). However, the thermoelectric performance in the XYP compounds is reduced in the variable relaxation time approach as the relaxation time was approximately one order of magnitude lower than the constant relaxation time. Using the variable relaxation time approach and the minimum thermal conductivity, high zTs were predicted for several XP_2, such as IrP_2, PdP_2, and RhP_2 (see Figure 5.37). Furthermore, high n-type thermoelectric performance was found for GaP with the constant and variable relaxation time approach as long as the lattice thermal conductivity was calculated with the minimum thermal conductivity model. The thermoelectric performance in GaP decreased by almost a factor of five using the semi-empirical model for the calculation of the lattice thermal conductivity.

Figure 5.37 reveals that zT of PbTe is high, independent of the approach used for the calculation. However, the most reasonable zTs were calculated using the variable relaxation time approach for the electronic properties and the semi-empirical approach for the lattice thermal conductivity ($p - zT = 2.44$ and $n - zT = 1.21$). The experimental p-type and n-type zTs are in the range of the computed figure of merit ($p - zT \sim 2.20$ [31] and $n - zT \sim 1.30$ [330]). To obtain the high experimental thermoelectric figures of merit in PbTe, the compounds were heavily doped which can affect the effective mass and the elastic properties of PbTe. Therefore, although the variable relaxation time approach combined with the semi-empirical approach for the lattice thermal conductivity is reasonable to predict the thermoelectric performance more accurately than the other current models, the model has to be tested on a larger set of thermoelectric materials to make a statement about the goodness of this approach.

In addition to the thermoelectric figure of merit using Boltzmann transport equations, the thermoelectric performance can be quantified by the beta-factor [46]. The beta-factor, β, is a material-dependent parameter that is independent of charge

carrier concentration and is calculated from

$$zT = \frac{u\beta}{v\beta + 1} \tag{5.14}$$

with u and v as functions depending on the chemical potential and charge carrier scattering [46]. Therefore, the beta-factor is given by

$$\beta = \left(\frac{k_B}{q}\right)^2 \frac{2q(k_B T)^{1.5} T}{(2\pi)^{1.5}\hbar^3} \frac{\mu_{el}(m^*_{\mathrm{DOS}})^{1.5}}{\kappa_{SE}} \tag{5.15}$$

where μ_{el} was calculated from Equation 5.6 [46].

The beta-factor was compared to the computed thermoelectric figure of merit where the electronic properties were calculated from the variable relaxation time approach and the lattice thermal conductivity with the semi-empirical approach (see Figure 5.38). No correlation between the predicted maximum zTs from the semi-empirical approaches and the beta-factor at 300 K was found. Figure 5.38 shows that zero band gap materials (*e.g.*, FeP and TiP_2, and *c*-NiP_2) have a high beta-factor whereas the maximum predicted zT is relatively low. It is challenging to determine the effective mass and the degeneracy in zero band gap materials and therefore, their predicted thermoelectric performance should be treated with due caution. Furthermore, a high beta-factor is observed for *p*-type IrP_2 which is even higher than PbTe as shown in Figure 5.38. This is consistent with the computed zT and therefore, IrP_2 might be a promising high-performance thermoelectric material. Other *p*-type XP_2 compounds, such as CoP_2, RhP_2, and RuP_2, possess higher beta-factors than PbTe and experimental studies are recommended on these compounds. It is important to note that the same computed lattice thermal conductivity and electron mobility were used for both approaches and therefore, the present approach, in which the electronic properties were calculated from a variable relaxation time approach and the lattice thermal conductivity was estimated from a semi-empirical approach [68], is a combination of the beta-factor and the Boltzmann transport approach to estimate zT.

In conclusion, the theoretical studies of the electronic and thermal properties reveal that metal phosphides could have thermoelectric performance similar to or higher than the current best thermoelectrics. The prediction of the thermoelectric figure of merit can most likely be enhanced by the inclusion of a variable relaxation

time approach and a semi-empirical approach to determine the thermal conductivity. The thermal conductivity and relaxation time have similar temperature behavior and are dependent on the crystallinity of the compound as experimentally reported for zinc antimonides [43].

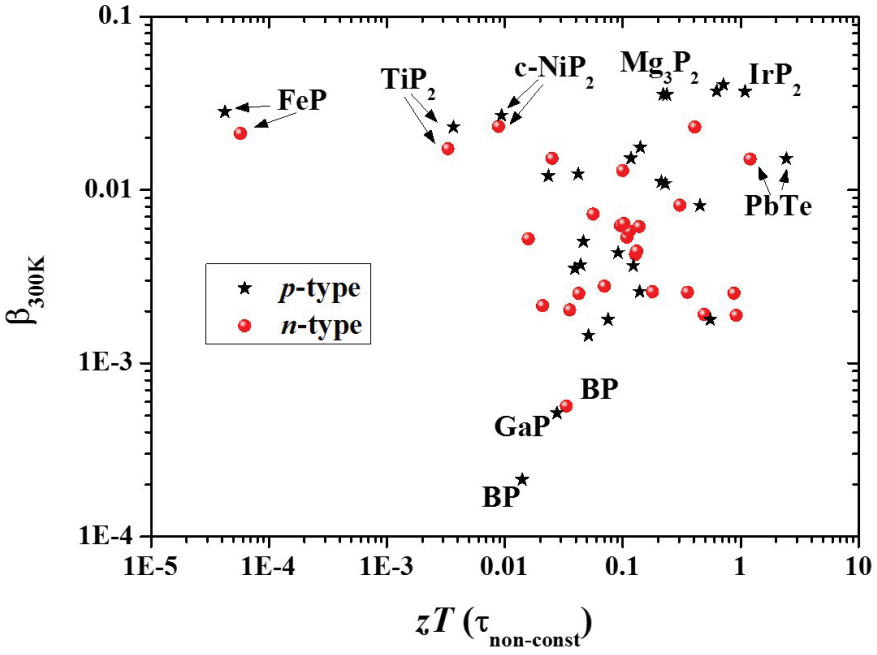

Figure 5.38: Comparison of the computed maximum thermoelectric figures of merit using the variable relaxation time approach and the semi-empirical approach to calculate the lattice thermal conductivity to give the beta factor at 300 K, β_{300K}.

5.2.3 Nickel Diphosphide

As an example of metal phosphides, the cubic phase of nickel diphosphide (c-NiP_2) was synthesized. Although the thermoelectric performance in c-NiP_2 is lower than other metal phosphides, it has several advantages. c-NiP_2 is a simple binary metal phosphide with excellent intrinsic properties due to its small band gap energy (thereby avoiding the matter of doping). Furthermore, c-NiP_2 can be synthesized by solid-state synthesis and is stable in oxidative conditions.

5.2.3.a Synthesis

The cubic phase of nickel diphosphide, which is stable at low temperatures and high pressures, was synthesized using high-energy ball milling, similar to the procedure described in reference [331]. Elemental Ni (0.97 g, <150 micron, 99.99%, Sigma Aldrich) and red P (1.153 g [6 mass% more than the stoichiometric requirement], 99.7%, Sigma Aldrich) were placed in a hardened steel vial with six 1.27 cm in diameter, hardened steel balls (total of ∼33 g) under argon atmosphere. The milling time was set to 6 hours and 15 minutes in a SPEX model 8000-D and the vial was opened in argon atmosphere. Lower milling times were used but peaks of by-products were observed in PXRD spectra. The product was a black powder, yield >90% determined by weighing the powder after ball milling. The powder was consolidated to a pellet using a pressure of ∼1.1 GPa for 15 minutes at room temperature and under air atmosphere. For the low-temperature transport properties measurements, the consolidated pellet was annealed in a sealed quartz tube under vacuum at 873 K for 2 hours, followed by slowly cooling to room temperature. The crystal structure of c-NiP_2 was confirmed after the heat treatment by PXRD.

5.2.3.b Characterization

Nickel diphosphide can crystallize in a cubic phase with space group $Pa\bar{3}$ or a monoclinic phase (m-NiP_2) with space group $C2/c$. According to PBE-GGA, the cubic phase is predicted to be more stable thermodynamically (13 meV/atom) at absolute zero and zero pressure [48]. The PBE-GGA exchange correlation functional indicates band gap energies of 0 eV and 0.53 eV for c-NiP_2 and m-NiP_2, respectively. Increases in band gap energies to 0.13 eV and 1.15 eV were found for c-NiP_2 and m-NiP_2, respectively, by adopting the more accurate HSE functional (see Figure 5.39).

The m-NiP_2 crystal structure is highly anisotropic with pseudo-planes of Ni_2P_4 along the c-axis connected through Ni-Ni bonds, leading to a higher PF along the b-axis than in other directions. The pyrite c-NiP_2 structure, on the other hand, is isotropic and the electronic band structure of NiP_2, shown in Figure 5.39 (a), reveals three degenerate valleys in the conduction band and twelve valleys in the

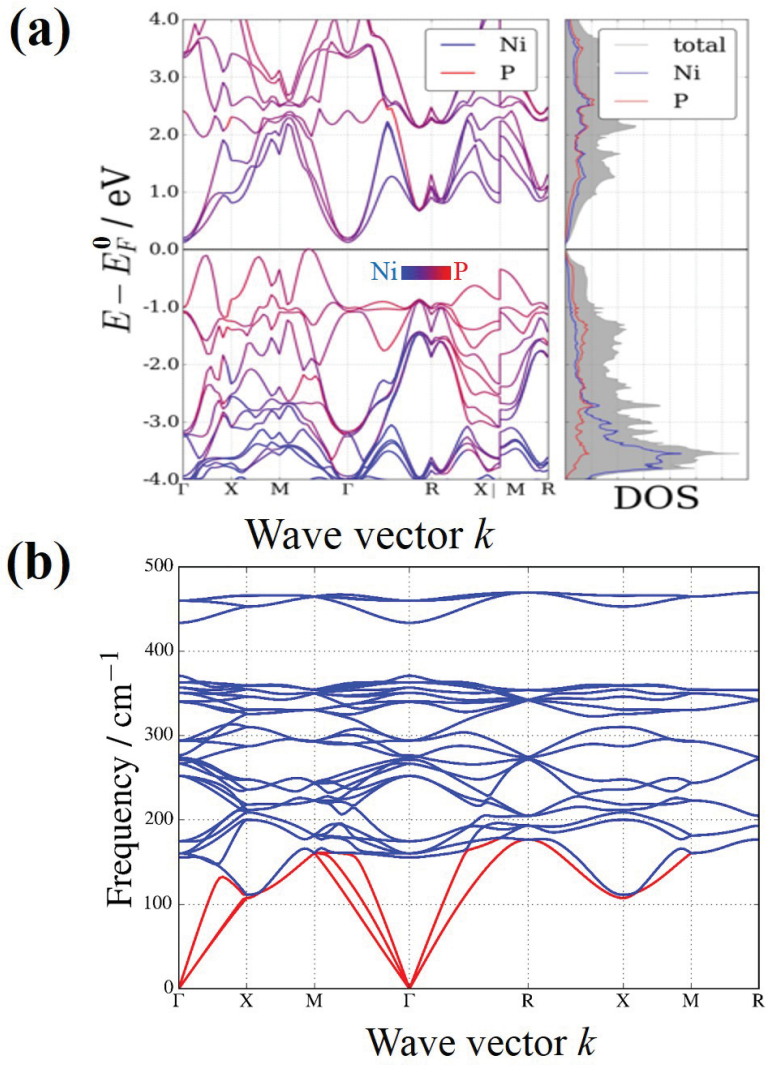

Figure 5.39: (a) HSE-electronic band structure and (b) PBE-phononic dispersion curve of c-NiP_2. The electronic structure reveals enhanced properties whereas the optical phonon modes (blue) possess relatively low frequencies and suppress the acoustic phonons (red).

valence bands that contribute to the electrical properties resulting in high p - and n-type PFs (6.1/4.4 mW m^{-1} K^{-2} calculated using a constant relaxation time of 10^{-14} s and a carrier concentration of 10^{20} cm^{-3}). However, the thermoelectric performance is expected to be limited by the high electronic contribution of the thermal conductivity. The predicted electronic properties are significantly decreased in the variable relaxation time approach due to a reduction in the relaxation time

($\sim 2.5 \cdot 10^{-15}$ s). While the monoclinic phase of NiP_2 is predicted to have better thermoelectric performance than the cubic phase, the synthesis of the former using a solid-state approach [331] was not successful here and toxic phosphine gas was produced.

In the pyritic crystal structure of *c*-NiP_2 Ni and P occupy octahedral and tetrahedral environments, respectively, as shown in Figure 5.40. The tetrahedral and octahedral environments are slightly disordered which could be expected to reduce the thermal conductivity, as for the low-temperature phase of $TmAgTe_2$. Each P is bonded to one P and three Ni, while Ni is surrounded by six P atoms. Electron localization function calculations showed share electrons for Ni-P bonds indicating polar covalent bonding. This is consistent with the Bader charge analysis which demonstrated that the charge transfer between Ni (+0.11) and P (-0.04; -0.07) is subtle, due to the similar electronegativity of Ni (1.91) and P (2.19).

The crystal structure of *c*-NiP_2 was confirmed by PXRD, acquired in the laboratory of Dr. Mark Obrovac, Department of Chemistry, Dalhousie University. The PXRD spectrum was refined with the Rietveld method as shown in Figure 5.41 (a). The refined lattice parameter of the cubic structure (a = 5.469 Å) is close to the reported value of 5.4706 Å [332] and to the computed structure with a = 5.453 Å. The PXRD pattern in Figure 5.41 (a) shows broad peaks indicating small grain size. From the Rietveld refinement it was found that the PXRD peaks can be fitted solely with Lorentzian functions and therefore, the grain size can be determined using a Hall-Williamson plot [95], as described in Section 3.1.1. From the intercept and the slope of the Hall-Williamson plot, a grain size of 19±1 nm and an inhomogeneous strain of (2.6-3.6)·10^{-3} was calculated using Equations 3.3 and 3.4.

This result is consistent with the SEM images taken with the assistance of Patricia Scallion in the laboratory of Dr. Kevin Plucknett, Faculty of Engineering, Dalhousie University. A grain size of 10 to 20 nm was determined from the SEM images as shown in Figure 5.42. In addition to the grain size, SEM shows that the *c*-NiP_2 sample contains pores in the range of 10 to 30 nm resulting in low mass density (4.04±0.20 g cm^{-3} measured by Archimedes principle) compared to the computed theoretical density (4.94 g cm^{-3}). The low mass density and small grain size can reduce the electrical and thermal conductivity due to boundary scattering.

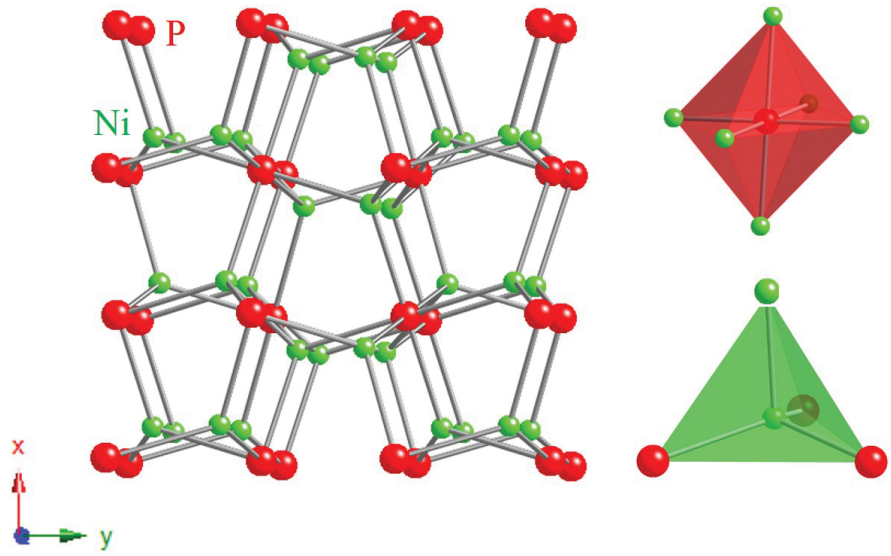

Figure 5.40: Crystal structure of cubic NiP_2, space group $Pa\bar{3}$. Ni occupies octahedral interstices where P is surrounded by three Ni atoms and one P atom.

In addition to the crystal structure and the electronic band structure, the phononic dispersion curve of *c*-NiP_2 was computed (see Figure 5.39 (b)), predicting relatively low minimum thermal conductivity, from 0.8 to 1.4 W m^{-1} K^{-1} determined by the present minimum thermal conductivity models (static and dynamic) and the (Cahill, Watson, and Pohl) amorphous limit of thermal conductivity [66, 67]. Using the semi-empirical approach [68], the theoretical thermal conductivity increased to 12.7 W m^{-1} K^{-1} at 300 K. A low thermal conductivity as observed here experimentally (*vide infra*), could be a result of the large voids in the crystal structure due to distorted pentagonal channels and/or low-frequency phonon modes which can reduce the acoustic phonon modes due to avoided crossings. Figure 5.39 (b) displays a splitting of the optical phonon modes which can be assigned to the weak Ni-P bonds (with a force constant of 4.63 eV $Å^{-2}$) and strong P-P bond stretching modes (with a force constant of 10.28 eV $Å^{-2}$). The computed values of the force constants agree well with the computed Ni-P (2.29 Å) and P-P (2.19 Å) bond lengths of the relaxed crystal structure, both smaller than the sum of the covalent radii (P: 1.10 Å, Ni: 1.23 Å [331]). Together with the small transfer between Ni and P, a weak interaction and low-frequency

modes were proposed, lowering the frequency of the acoustic phonon modes and hence, reducing the minimum thermal conductivity.

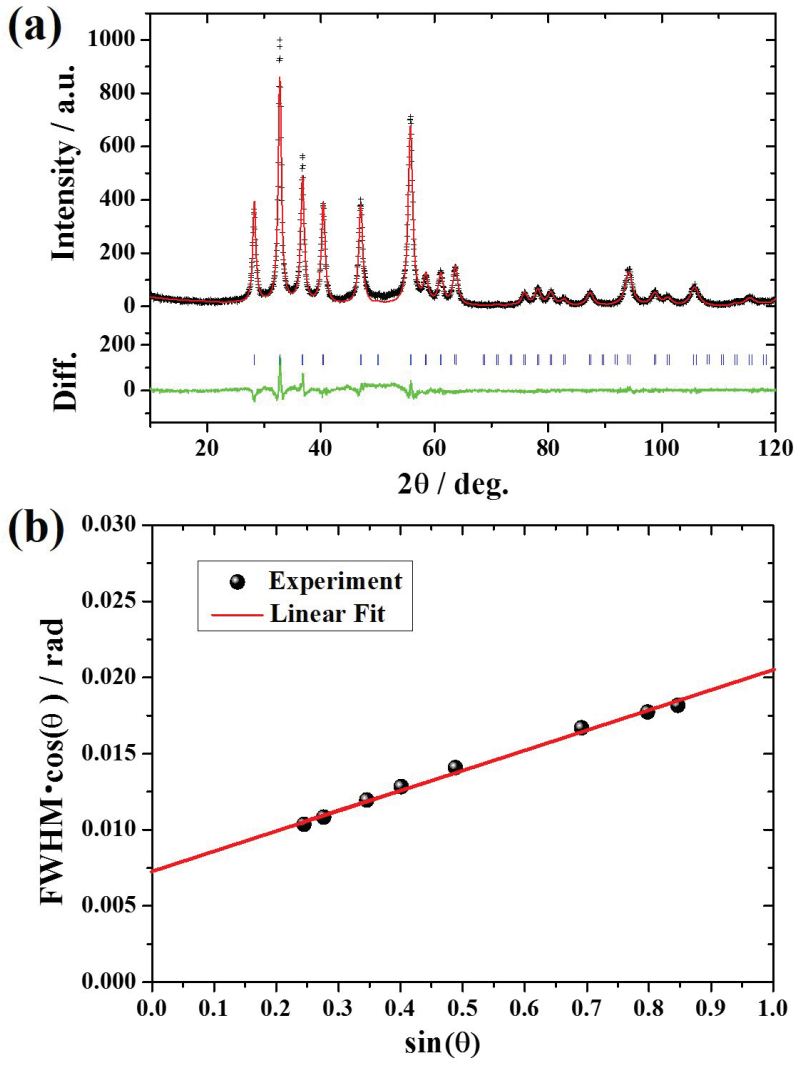

Figure 5.41: (a) Rietveld refinement pattern of cubic NiP_2 (space group: $Pa\bar{3}$). Blue tick marks show the calculated reflections and the green line corresponds to the residuals of the Rietveld refinement. (b) Hall-Williamson plot gives a grain size of 19±1 nm. Refined data are given in Table D.9 of Appendix D.

The phononic dispersion curves were consistent with the experimental heat capacity, as shown in Figure 5.43. (The heat capacity of a ∼21 mg sample was measured from 0.4 K to 300 K in a PPMS. Heat capacity data are given in Tables

D.10 and D.11 of Appendix D.) The experimental heat capacity agrees well to the computed heat capacity from the phononic dispersion curves when the electronic contribution of the heat capacity, C_{el}, was added to the computed heat capacity. The electronic contribution of the heat capacity was taken from fitting of the experimental heat capacity at low temperature with a Sommerfeld constant of 100 mJ mol^{-1} K^{-2} as shown in Figure 5.43 (b). It is important to note that the experimental heat capacity (C_p) is generally higher than the computational heat capacity ($C_V + \gamma_{el}T$) due to the work of thermal expansion which could in principles be estimated from Equation 2.3. However, the coefficient of the volumetric thermal expansion is unknown and therefore, $C_p - C_V$ cannot be predicted.

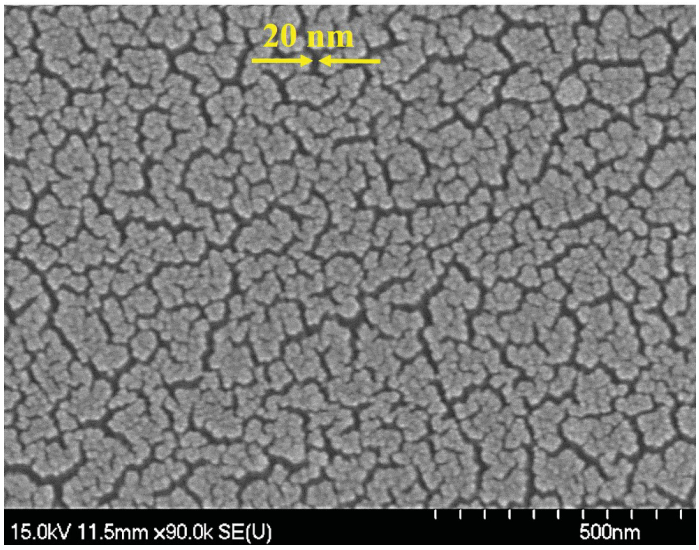

Figure 5.42: SEM image of the surface of a consolidated NiP_2 pellet, showing grains in the range of 10 to 20 nm. Red arrows indicate a pore size of 20 nm.

The low-temperature experimental heat capacity suggest that the acoustic modes and the low-frequency optical modes of the calculated phononic dispersion curves should be shifted to slightly lower frequencies. However, above 100 K the computed heat capacity agrees well with the experimental heat capacity when the electronic contribution of the heat capacity was included. Note that the heat capacity was computed with a harmonic approach and anharmonicity can play a significant role at high temperature, increasing the heat capacity. The estimated Grüneisen parameter from Equation 5.12 is relatively low ($\gamma \sim 1$) which is typical for structures containing

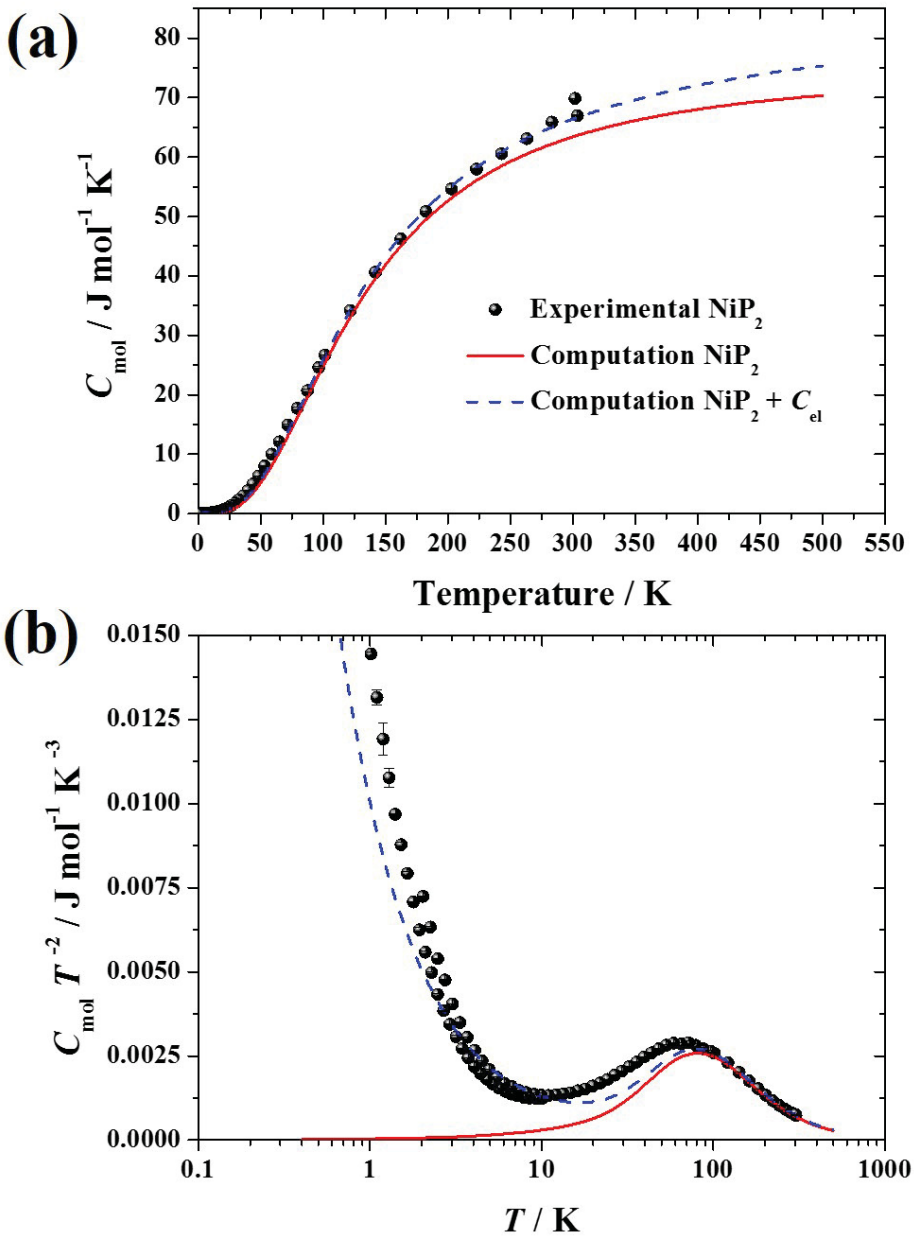

Figure 5.43: Comparison of experimental and computed heat capacity, C_{mol}, of *c*-NiP_2. Experimental results, C_p, agree with the calculated heat capacity, C_V, when the electronic contribution of the heat capacity, C_{el}, was included. (b) CT^{-2} *vs* T indicates low frequency optical modes. A slight discrepancy between the calculated and experimental heat capacity appears at very low temperature.

both tetrahedral and octahedral environments [305]. Zeier *et al.* showed that most tetrahedral structures (*e.g.*, ZnS or Si) have a Grüneisen parameter around 0.5 to 0.7 at room temperature whereas binary systems with octahedral environments have Grüneisen parameters between 1.5 to 2 [305]. Although the Grüneisen parameter in *c*-NiP_2 is slightly higher than for GaP, the low Grüneisen parameter cannot explain the low minimum thermal conductivity calculated for *c*-NiP_2.

The thermodynamically stability of *c*-NiP_2 (m = 12 mg) was investigated by TGA with the assistance of Sarah Ellis in the laboratory of Dr. Mark Obrovac, Department of Chemistry, Dalhousie University. Figure 5.44 (a) depicts distinct features in the thermograms on heating: a mass increase from 743 K to 843 K, followed by a mass decrease from 843 K to ∼1000 K. No change in mass was observed on cooling indicating that the decomposition was complete at 1000 K. Although the measurements were performed under inert (nitrogen) atmosphere, the mass increase can be assigned to oxidation of NiP_2 to $Ni(PO_3)_2$ as shown by the minor phase in the PXRD spectrum which was acquired after the measurement (see Figure 5.44 (b)). At higher temperature ($T > 843$ K), P vaporizes from the material that was not oxidized until it is completed converted to $Ni_{12}P_5$ as shown in Figure 5.44.

5.2.3.c Transport Properties

Transport properties were determined for a *c*-NiP_2 (pellet diameter = 5.10±0.02 mm; thickness ∼ 1.12±0.04) from 2 K to 725 K. The low-temperature transport properties were measured with the TTO option whereas the high-temperature transport properties were measured on a different consolidated sample from the same batch and with similar dimensions (diameter = 5.10±0.02 mm; thickness ∼ 1.35±0.04) by Dr. Umut Aydemir in the laboratory of Dr. G. Jeffrey Snyder, Faculty of Materials Science & Engineering, Northwestern University. Note that the sample was annealed at 873 K for 2 h under vacuum for the low-temperature measurement while the Seebeck coefficient was measured on the untreated sample. The Seebeck coefficient can change with grain size due to grain size effects and is only nearly constant at large grain sizes (>3 µm) [333]. In an experimental study, it was shown that the Seebeck coefficient of *n*-type PbTe can increase by a factor of two with a decrease in grain size from 4 µm to 0.7 µm [334]. However, it was found

in a computational study that the difference in Seebeck coefficient is almost constant over the temperature range from 300 K to 800 K [333]. To determine the effect of annealing and the corresponding change in grain size, the Seebeck coefficients of both the untreated (high temperature) and annealed (low temperature) sample were measured between 300 K and 390 K. The high-temperature Seebeck coefficient measurement annealed the sample (measured up to 773 K) and therefore, the sample for the high-temperature electrical and thermal conductivity measurements is predicted to have the same crystallinity as for the low-temperature measurements.

The low-temperature electrical resistivity was measured with the two-probe method (2Ω) whereas the high-temperature resistivity was determined by the van der Pauw method. The latter method is preferable to measure low electrical resistivity because the contribution from the contact resistance is negligible. In the two-probe method, however, the total resistance is a sum of the sample resistance and the contact resistance between the sample and the contacts. Due to the small dimensions of the *c*-NiP_2 pellet, it was not be feasible to obtain accurate electrical conductivity results using a four-probe method. Therefore, the room-temperature electrical resistivity of the TTO measurement was compared to that from the van der Pauw method and the difference of 24 mΩ cm (resistance difference of 10 mΩ) was attributed to the contact resistance. The low-temperature electrical resistivity was empirically corrected to the van der Pauw measurement at 312 K and it was assumed that the contact resistance does not change with temperature.

The electrical resistivity of *c*-NiP_2 is plotted as a function of temperature in Figure 5.45 (a). The resistivity decreases with temperature over the entire temperature range indicating semiconducting behavior. From the curved conduction bands at the band edges a high mobility, μ_H, is expected due to their low effective mass. However, using the variable relaxation time approach (see Equation 5.6), the mobility is reduced due to a higher predicted average band effective mass in the energy window of 0.1 eV from the band edges ($\mu_H = 63$ cm^2 V^{-1} s^{-1}). The experimental Hall mobility was about two orders of magnitude lower than the mobility computed using variable relaxation time and was nearly temperature-independent as shown in Figure 5.45 (b). Therefore, the low experimental mobility cannot be explained by the variable relaxation time

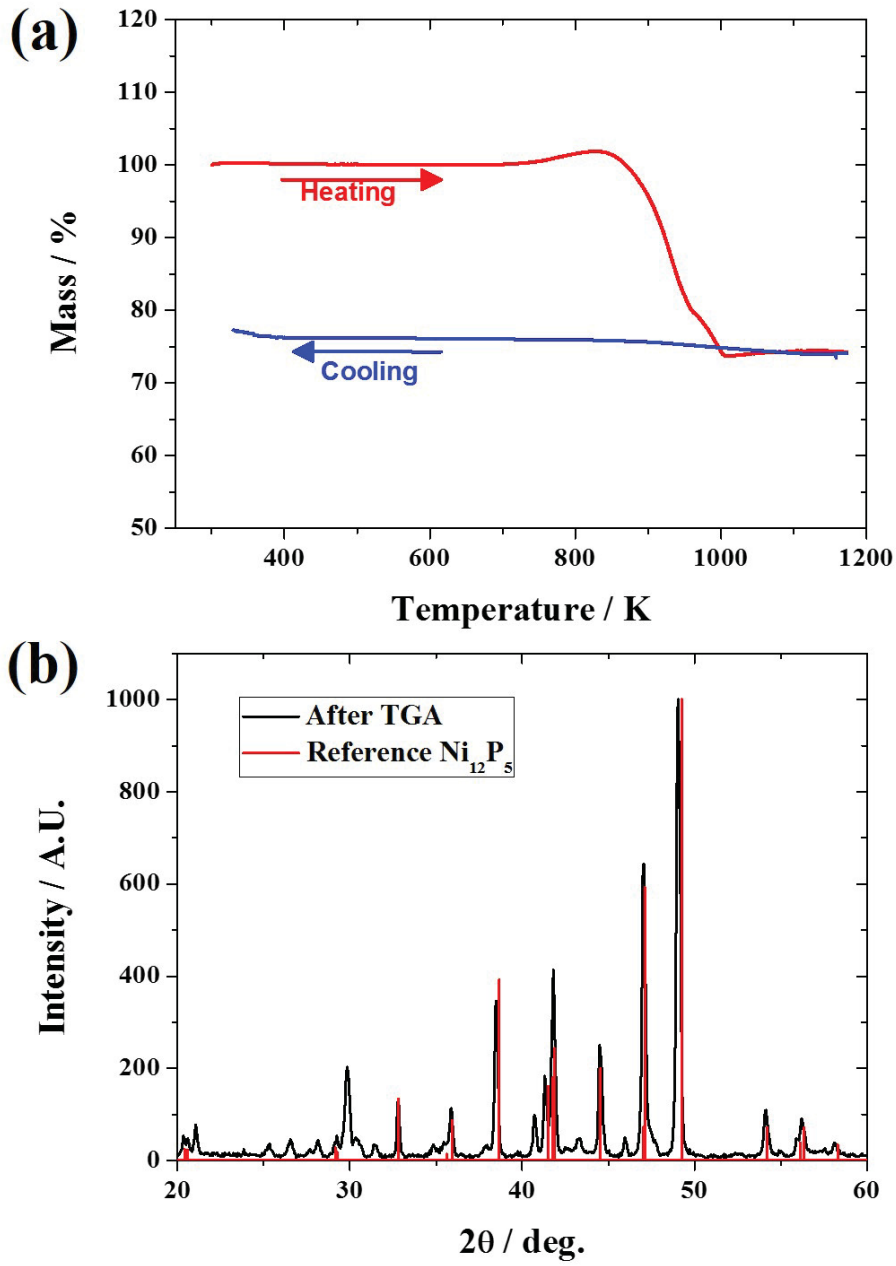

Figure 5.44: (a) Thermogravimetric analysis of c-NiP_2 indicates that major decomposition sets in at 843 K. (b) PXRD pattern of the sample after TGA shows that the major phase is $Ni_{12}P_5$ with a minor phase of $Ni(PO_3)_2$.

but it is most likely a result of the small grain size and the nanoporous structure. Due to the small band gap (computed band gap energy of 0.13 eV with HSE functional),

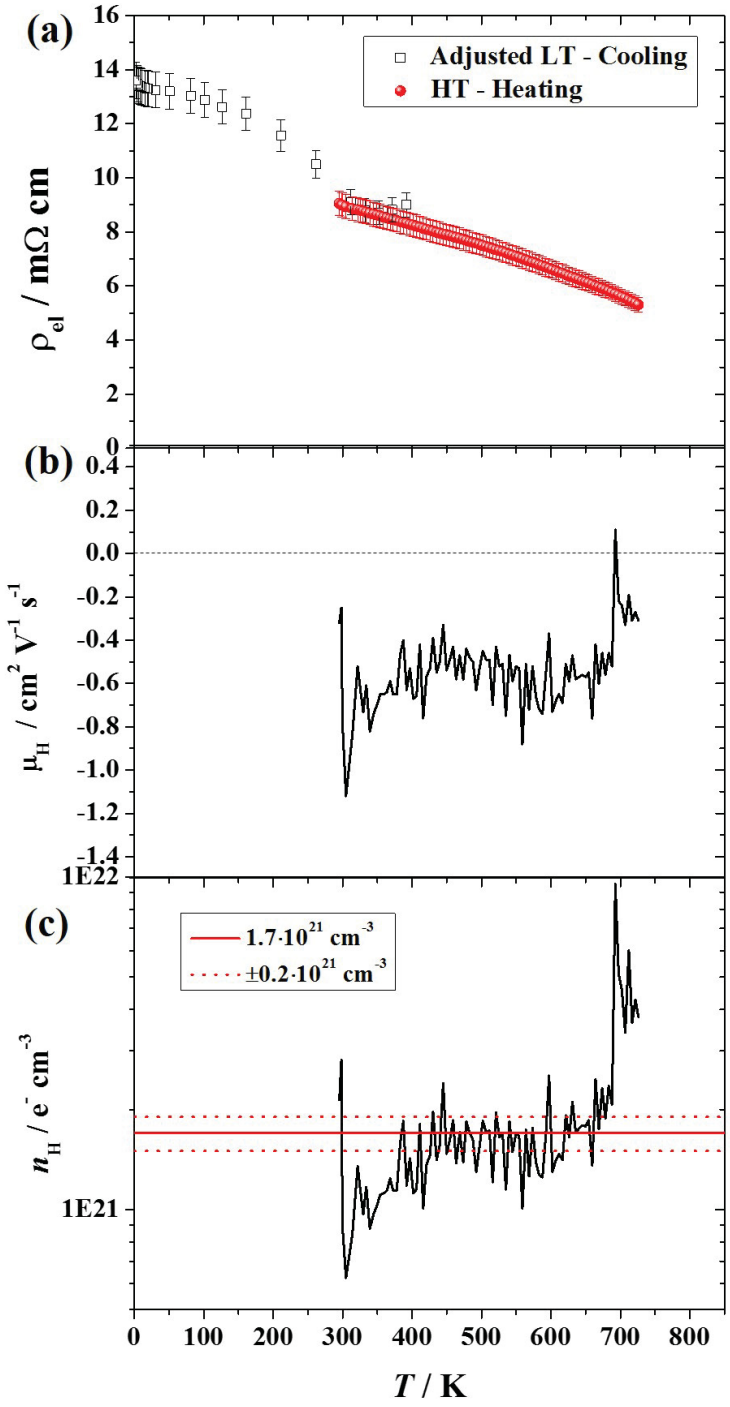

Figure 5.45: (a) Electrical resistivity, ρ_{el}, (b) Hall mobility, μ_H, and (c) Hall carrier concentration of c-NiP_2. Resistivity decreases with temperature indicating intrinsic semiconducting behavior.

c-NiP_2 has without doping a high carrier concentration ($[1.7\pm0.2] \cdot 10^{21}$ e^- cm^{-3}) as shown in Figure 5.45 (c). It is important to note that the increase in Hall mobility and Hall carrier concentration at high temperature might be due to oxidation as observed in the TGA experiment.

The temperature-dependence of the Seebeck coefficient is shown in Figure 5.46. The Seebeck coefficients of the untreated and annealed sample are in uncertainties indicating that the larger grain size has no effect on the Seebeck coefficient. Due to the low effective mass, small band gap energy, and high carrier concentration, the Seebeck coefficient is small, as typically observed for small band gap thermoelectric materials [335]. The magnitude of the Seebeck coefficient increases with temperature to ∼57 µV K^{-1} at 600 K, followed by a decrease in the magnitude of the Seebeck coefficient most likely due to the excitation of minority carriers. The negative sign of the Seebeck coefficient indicates that electrons are the dominant charge carriers, consistent with the negative Hall coefficient. While the magnitude of the Seebeck coefficient at 650 K is only slightly lower than at 600 K, a large drop in the magnitude was observed at 700 K due to a dramatic increase in carrier concentration (see Figure 5.45 (b)).

The band gap energy can also be calculated using the Goldsmid-Sharp approach ($E_{g,GS} = 2|S|_{max}T_{max}$) [86] giving 0.07 eV, which is lower than the HSE band gap energy (0.13 eV). Although it is known that HSE generally overestimated the band gap energy [336], it has to be noted that the Goldsmid-Sharp approach is not valid for small band gap semiconductors ($E_g \leq 6k_BT$) [86]. Together they provide semi-quantitative information about the band-gap energy.

In addition to the electronic properties, the thermal conductivity of c-NiP_2 was determined and is shown as a function of temperature in Figure 5.47 (a). (Data for the transport properties of c-NiP_2 are given in Tables D.12-C.28 of Appendix D.) The experimental thermal conductivity at high temperatures was determined from the measured thermal diffusivity, the mass density, and the computed heat capacity including the electronic contribution of the heat capacity. (No high-temperature experimental heat capacity data were available.)

The thermal conductivities from low- and high-temperature measurements have a mis-match at room temperature, just within their uncertainties. It is important to note that the uncertainty for the high temperature results is due to the additive

uncertainties of the thermal diffusivity, mass density, and heat capacity. However, for the low-temperature thermal conductivity measurements in the TTO method, the blackbody radiation correction can lead to a substantial error due to the assumption of the emissivity ($\varepsilon_T = 1$), in particular at high temperatures due to the T^4 relationship of the blackbody radiation (see Equation 3.23).

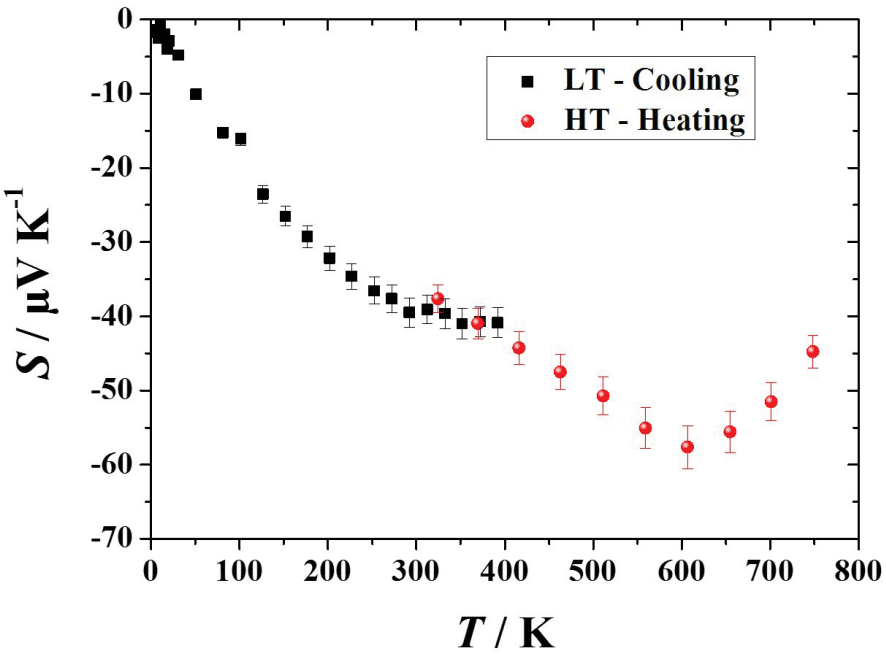

Figure 5.46: Magnitude of the Seebeck coefficient of c-NiP_2 increased with temperature to 600 K, and reduced at higher temperatures most likely due to a bipolar contribution.

The thermal conductivity of c-NiP_2 increased over the entire temperature range, similar to glassy materials. The increase in thermal conductivity at high temperature is due to the large electronic contribution in thermal conductivity as shown in Figure 5.47 (b). The electronic contribution of the thermal conductivity was calculated from Equation 2.23 which required the effective Lorenz number, as estimated by the single-parabolic model using carrier concentration and therefore, only the high temperature electronic contribution of the thermal conductivity is shown.

The electronic contribution of the thermal conductivity was subtracted from the total thermal conductivity to obtain the phononic contribution of the thermal

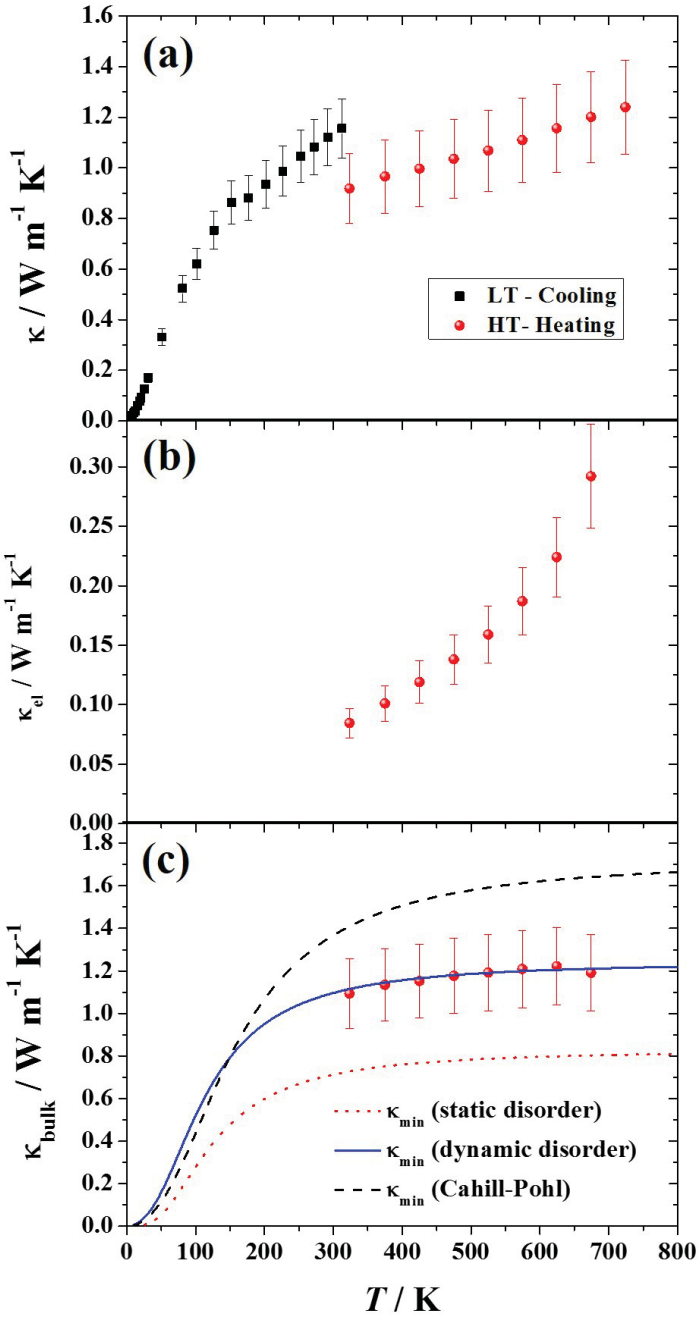

Figure 5.47: (a) Thermal conductivity increases with temperature indicating glass-like behavior. (b) High electronic contribution of the thermal conductivity was observed which increased with temperature. (c) Lattice thermal conductivity, corrected to zero porosity (Equation 4.5), agrees well with the present minimum thermal conductivity model limited by dynamic disordering.

conductivity. The phononic contribution was corrected to zero-porosity using Equation 4.5 and plotted as a function of temperature in Figure 5.47 (c). It is important to porosity-correct the phononic contribution of the thermal conductivity rather than the total thermal conductivity because the relationship between the porosity and the electronic contribution of the thermal conductivity is unknown. The phononic contribution of the thermal conductivity is nearly temperature-independent above 300 K and lower than the Cahill, Watson, and Pohl amorphous limit of the thermal conductivity [66, 67]. The lattice thermal conductivity, however, agrees well with the minimum thermal conductivity using an average phonon mean speed and a frequency-dependent phonon mean free path (*i.e.*, dynamic disordering), as also found for the ultralow thermal conductivity in Zn_3P_2 (see Figure 5.35). In both cases, the thermal conductivity is most likely limited by the nano-sized grains which scatter the acoustic phonons. Reducing the grain size further might lower the thermal conductivity in NiP_2, approaching the minimum thermal conductivity limited by static disordering.

The electronic and thermal properties of *c*-NiP_2 were polynomial fitted to calculate the thermoelectric figure of merit using Equation 1.15. The figure of merit increases to 0.03 in the temperature range from 2 K to 650 K as shown in Figure 5.48 (a). The SPB model predicts that a reduction of the carrier concentration to 10^{20} e^- cm^{-3} would improve zT to 0.07 given the same effective mass, electron mobility and phononic contribution of the thermal conductivity. Another potential approach to increase efficiency is reduction of the porosity by further consolidation of the sample. A denser sample would enhance the mobility and most likely increase the figure of merit. However, the prediction of the thermoelectric performance of *c*-NiP_2 does not reveal a high thermoelectric figure of merit.

5.2.4 Conclusions

From a high-throughput screening of 48,000 inorganic compounds [35], metal phosphides were revealed as a potential new class of high-performance thermoelectric materials. The electronic properties were calculated from the Boltzmann transport equations and a constant relaxation time. To enhance the prediction of the thermoelectric performance, a variable relaxation time approach

was developed, which depends on the bulk modulus and the band effective mass and the carrier scattering is limited to acoustic phonons. In addition to the electronic properties, the thermal conductivity was estimated using the minimum thermal conductivity and a semi-empirical models [68].

High thermoelectric performance was predicted for *p*-type XYP compounds using the constant relaxation time approach, indicating predicted zTs similar to or even higher than the current-best thermoelectric materials (*e.g.*, PbTe). However, the variable relaxation time approach predicts a low relaxation time for the XYP group. High zTs from the variable relaxation time approach were calculated for $X\mathrm{P}_2$ compounds, such as IrP_2, RhP_2, and RuP_2.

As an example of metal phosphides, *c*-NiP_2 was synthesized and the thermoelectric properties were investigated indicating high electrical conductivity and low thermal conductivity even at high temperature. The thermal conductivity of *c*-NiP_2 agrees well with the present minimum thermal conductivity model in which the phonon mean free path is limited by dynamic disordering, as also shown for $\mathrm{Zn}_3\mathrm{P}_2$. Further studies of other metal phosphides with high predicted zTs are required to reveal their potential for high-performance thermoelectrics. Furthermore, the variable relaxation time approach should be tested on various classes of thermoelectric materials to determine its validity.

5.3 Germanium Clathrates with Partial Filling by Sodium[5]

5.3.1 Introduction

In the last section of this chapter, the thermal properties of clathrates, which are another important family of thermoelectric materials, are presented. Clathrates are cage compounds with including guests in which the electrical and thermal conductivities satisfy the requirements of the phonon glass-electron crystal (PGEC) approach [72], as discussed in Chapter 1. The PGEC approach can improve the efficiencies of thermoelectric materials by tailoring of physical properties [337, 338].

[5]The author's contribution in this section was the synthesis of the precursor and the germanium type II clathrates, the characterization, heat capacity measurements and the investigation of the thermal conductivity at low temperature. The synthesis and all measurements were performed in the laboratory of Dr. Mary Anne White, Department of Chemistry, Dalhousie University, unless stated otherwise.

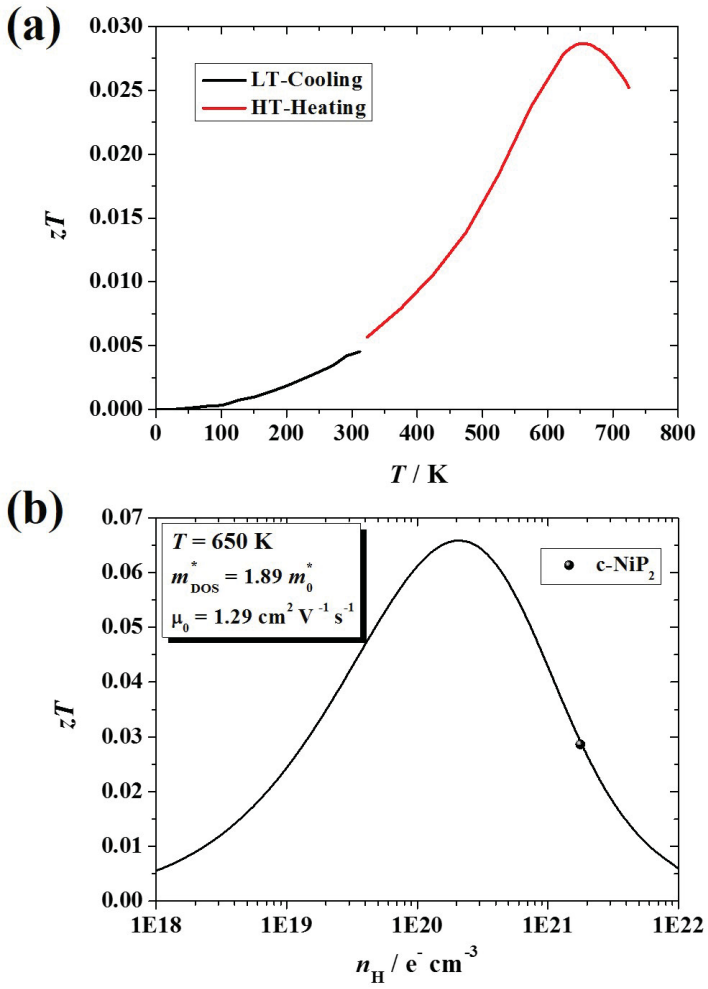

Figure 5.48: (a) Thermoelectric figure of merit, zT, of c-NiP_2 as a function of temperature with a peak zT of $\sim$0.03 at 650 K. (b) The single parabolic model suggests that zT could be increased to 0.07 by reducing the carrier concentration to $\sim 10^{20}$ e^- cm^{-3}.

This is particularly true in clathrates since, in some instances, occupancy of the cages can be varied [339, 340, 341].

In a recent study, the thermal conductivity [341] and electronic properties [342] of Si type II clathrates with varying occupancies of Na guests (Na_xSi_{136}) were reported. All Na atoms were in the larger Si_{28} cages in Na_xSi_{136} when $x < 8$ [341]. Within this range, increasing Na content decreased thermal conductivity. However, when $x > 8$, Na atoms also occupied the smaller Si_{20} cages, result in increasing thermal conductivity with increasing Na content. The electrical conductivity increases and

the Seebeck coefficient decreases with increasing Na content, from $x = 0$ to 24 [342].

Although the thermoelectric properties of Na_xSi_{136} materials have been found to change dramatically with Na content [341, 342], the thermoelectric properties of partially filled Ge type II clathrates have not yet been explored. This is especially surprising because the unit cells of Ge type II clathrates [343] are larger than those of Na_xSi_{136} [341, 342] and it is thus expected that guest atoms in Ge clathrates would have more significant effects on lattice dynamics.

The opportunity exists to investigate Ge clathrates in more detail, as a window into the structure-property relationships in these interesting materials. In addition to a fully occupied Ge type II clathrate, Guloy *et al.* synthesized the empty Ge type II clathrate (Ge_{136}) [344], but X-ray diffraction data indicated that an amorphous impurity was included. Böhme *et al.* improved on the method [345] and several $(K,Na)_xGe_{136}$ clathrates have been synthesized but their properties not reported [346, 347, 348]. In the present study a solid-gas reaction was used to synthesize partially filled germanium type II clathrates (Na_xGe_{136}) [345]. The thermal conductivity and the heat capacities of the Na_xGe_{136} clathrates were determined and considered in the context of other type II semiconductor clathrates [341, 342] and partially Na-filled Ge clathrates synthesized by a solid-liquid reaction [344].

5.3.2 Synthesis

The NaGe precursor used in the solid-gas reaction was produced by melting Ge chips (99.9999%, Sigma-Aldrich) and one large chunk of Na (Fisher Scientific) in a 1:1 mass ration with a total mass of 0.7 g in an arc furnace under argon. The oxide-layer of the Na chunk was removed prior the synthesis and the material was handled under inert conditions at all times. For the synthesis it is important to melt the Ge chips first to produce a pellet and place the Ge pellet on the Na chunk. The arc was used to heat germanium above its melting point without heating the Na chunk because Na has a lower boiling point than the melting point of Ge. Preparation and handling of the precursor had to be done solely under inert atmosphere because NaGe is highly air sensitive.

The solid-gas synthesis of partially filled Ge clathrates was achieved by reaction of the NaGe precursor with the decomposition products of an ionic liquid as described

by Böhme *et al.* [345]. In the first step, the reactants of the ionic liquid (IL), dodecyltrimethylammonium chloride (DTAC) ($m \sim 250$ mg; ≥99%, Sigma-Aldrich) and aluminum chloride ($AlCl_3$) ($m \sim 125$ mg; anhydrous, ≥ 98%, Sigma-Aldrich), were dried in evacuated sealed glass ampoules for two days at room temperature. The reactants (white powder) were then placed in one of two connected glass ampoules (1:1 molar ratio) whereas the other glass ampoule was filled with the NaGe precursor ($m \sim 250$ mg; black powder) and the glass system was sealed as shown in inset of Figure 5.49. These steps were carried out in an Ar-filled glove box. The glass system was placed in an aluminum box to achieve a homogeneous thermal environment and the aluminum box was heated to 553 K for 10 days in a box furnace. During the reaction, the IL changed color from white to yellow as a result of decomposition (inset Figure 5.49). NaCl was washed away with water and the clathrate product was dried in air at room temperature.

5.3.3 Characterization

For the present study, NaGe has been has been produced for the first time in an arc furnace, a method which has the advantages of reducing both synthesis time (from two days to approximately five minutes) and cost, *i.e.*, no Ta tube is required as was previously used for the synthesis [349]. The PXRD data indicate that crystalline NaGe was produced; see Figure E.1 of Appendix E. The NaGe precursor crystallized in a monoclinic lattice with space group $P2_1/c$ with lattice parameters $a = 12.37$ Å, $b = 6.658$ Å, $c = 11.47$ Å, and $\beta = 120.2°$, as determined from the Rietveld refinement (Figure E.1 of Appendix E). The refined data agree well with the parameters previously determined by Wang *et al.* ($a = 12.43$ Å, $b = 6.667$ Å, $c = 11.59$ Å, and $\beta = 119.9°$) [350].

The Na_xGe_{136} clathrates were produced by a polymerization-oxidation reaction of Ge anions from the NaGe precursor, following the Hofmann elimination mechanism [351]. Böhme *et al.* found that in the solid-gas reaction this involved the oxidation of NaGe by the gaseous decomposition products of the ionic liquid, mainly HCl, CH_3Cl, and NH_3, to give partially Na-filled Ge clathrates and NaCl [345]. The PXRD patterns of the synthesized clathrate samples were refined using the Rietveld method and showed crystallization in a cubic crystal structure with space group $Fd\bar{3}m$ and

a lattice constant of $a = 15.219$ Å (see Figure 5.49 (b)). This is consistent with the calculated [352] and reported lattice parameter of $Na_{3.0(2)}Ge_{136}$ ($a = 15.218$ Å) [347]. In addition to the clathrate peaks, unreacted polycrystalline Ge peaks were also recorded, *e.g.*, the peak at $\sim 28°$ (shown as $\star$ in Figure 5.49 (b)).

Figure 5.50 shows the crystal structure of Na_xGe_{136} in which the framework comprises eight hexakaidecahedra (cages of 28 atoms with twelve pentagonal and four hexagonal faces $[5^{12}6^4]$) and sixteen dodecahedra (cages of 20 atoms with twelve pentagonal faces $[5^{12}]$). The framework atoms occupy the $96g$, $32e$, and $8a$ Wyckoff positions with each $8a$ atom connected to four $32e$ atoms and each $32e$ atom connected to one $8a$ and three $96g$ atoms. The guest atoms in the Ge_{20} and Ge_{28} cages occupy the $16c$ and $8a$ Wyckoff positions, respectively [353].

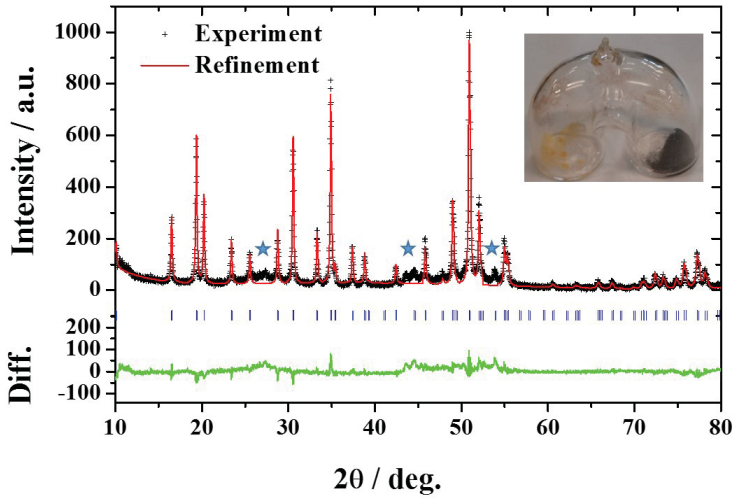

Figure 5.49: Rietveld refined PXRD pattern partially Na-filled Ge type II clathrate. Blue ticks mark the calculated position of the reflections. Polycrystalline Ge peaks are marked with $\star$. Inset: Glass system after the solid-gas reaction. The ionic liquid changed color from white to yellow (left); the right ampoule contains the solid-gas synthesized product.

For a quantitative analysis of the Na content, the pattern of the Na_xGe_{136} clathrate was refined using the Rietveld method indicating a Na content of 3.4. (The refined data are given in Table E.2 of Appendix E.) In addition, because the sample produced was small (<100 mg) the Rietveld-determined Na content was

checked with WDS. WDS data were taken from multiple sites on the cold pressed samples by Dan MacDonald in the Robert M. MacKay Electron Microprobe Laboratory, Department of Earth Sciences, Dalhousie University, and indicated average Na content of 3.1±1.6 for the solid-gas synthesized clathrates. These results are similar to those obtained from the Rietveld refinements. WDS is, however, a more quantitative method and therefore, the synthesized Na_xGe_{136} clathrates will hereafter be referred to as $Na_{3.1}Ge_{136}$. It is important to note that the WDS results showed significant variations in Na content throughout both samples (±50%). The measured physical properties of the Na_xGe_{136} samples, therefore, represent averages of clathrates with a range of Na loadings, between 1.6 and 4.7 Na for $Na_{3.1}Ge_{136}$.

The solid-gas synthesized $Na_{3.1}Ge_{136}$ clathrates were compared to solid-liquid synthesized clathrates with a WDS-determine Na content of 9.0±1.4 (referred as Na_9Ge_{136} hereafter) by Dr. Andrew Ritchie in the laboratory of Dr. Mary Anne White, Department of Chemistry, Dalhousie University [349]. Despite the significant variances in Na content, the present samples occupy distinct and discrete Na loading regions and can be used to obtain insight into how Na occupation influences the thermal properties of Na_xGe_{136} clathrates.

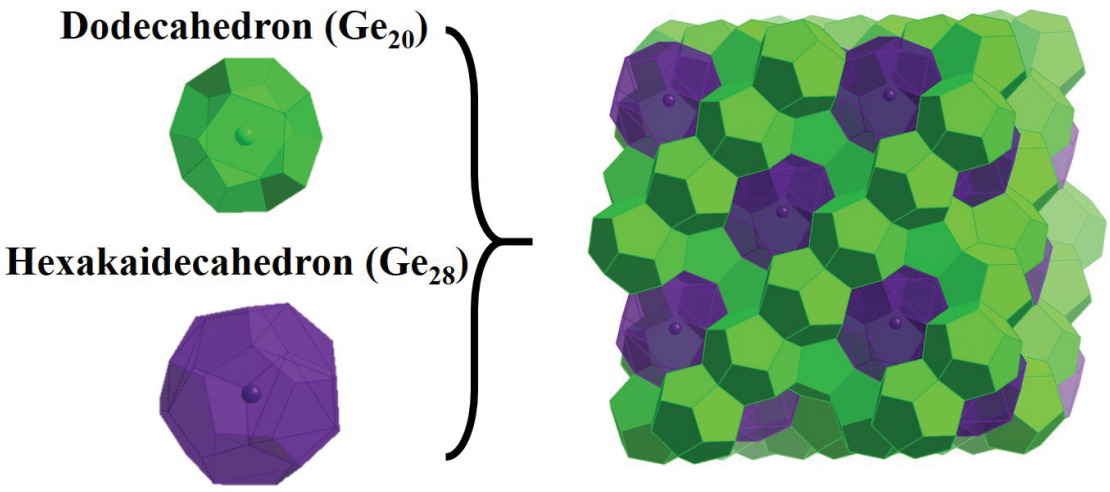

Figure 5.50: Dodecahedron (Ge_{20}) and hexakaidecahedron (Ge_{28}) each with a guest atom as shown on the left, pack to fill space. In the $2 \times 2 \times 2$ supercell of Na_8Ge_{136} shown on the right, Na atoms occupy the Ge_{28} cages while the Ge_{20} cages are empty.

5.3.4 Heat Capacity

The clathrate powders were cold pressed into pellets for the heat capacity, electrical conductivity, and thermal conductivity measurements. The maximum applied pressure for the consolidations ($p \sim 0.5$ - 1.5 GPa) was far lower that of the pressure-induced phase transformation ($p \sim 7.6$ GPa) [354]. However, the pellets were found to be highly porous (with a porosity of $\Phi = 19\%$ for Na_9Ge_{136} and $\Phi = 40\%$ for $Na_{3.1}Ge_{136}$) and therefore, the measured thermal conductivities underestimate the intrinsic values of the materials (which can, however, be corrected to zero porosity using Equation 4.5). Even in highly porous systems (up to 43%) it has been found that this correction is valid as long the phonon mean free path is short [244].

Heat capacity data for both partially Na-filled Ge clathrates are shown in Figure 5.51 and the data are given in Table E.3 in Appendix E. (The heat capacities and thermal conductivities of Na_9Ge_{136} were from reference [349].)$Na_{3.1}Ge_{136}$ has a higher molar heat capacity than Na_9Ge_{136} (Figure 5.51 (a)) which is consistent with the trend previously observed in the Na_xSi_{136} system [341]. At low Na loadings, $x \leq 8$, only the large Ge_{28} cages are occupied and the host lattice relaxes in relation to the empty clathrates, resulting in a reduction in lattice stiffness and an increase in heat capacity. However, when $x > 8$, the Ge_{28} cages are completely filled, the smaller Ge_{20} cages are partially occupied and the host lattice stiffens with increasing Na content. Lattice stiffening results in lower heat capacities, as observed in the Na_9Ge_{136} sample. In the case of Si clathrates, $Na_{1.3}Si_{136}$ exhibited an increase in stiffness even compared to the empty clathrate Si_{136} and therefore, its molar heat capacity was lower than that of the empty clathrate [341]. Furthermore, the experimental heat capacities of both Ge clathrates are higher than those calculated using the Neumann-Kopp law which indicates that the host lattices of the prepared Ge clathrates are less stiff, and that the clathrates have more low-frequency modes, than their elemental constituents. This is consistent with the low temperature C_pT^{-2} *vs* T peaks centered between 20 and 30 K which are the result of low-frequency optical modes; see Figure 5.51 (b).

For a better understanding of the low-frequency modes, C_pT^{-3} *vs* T plots were produced and fitted for both clathrates as shown in Figure 5.51 (c) and Figure E.2 of Appendix E. There are different approaches for fitting the heat capacities of type

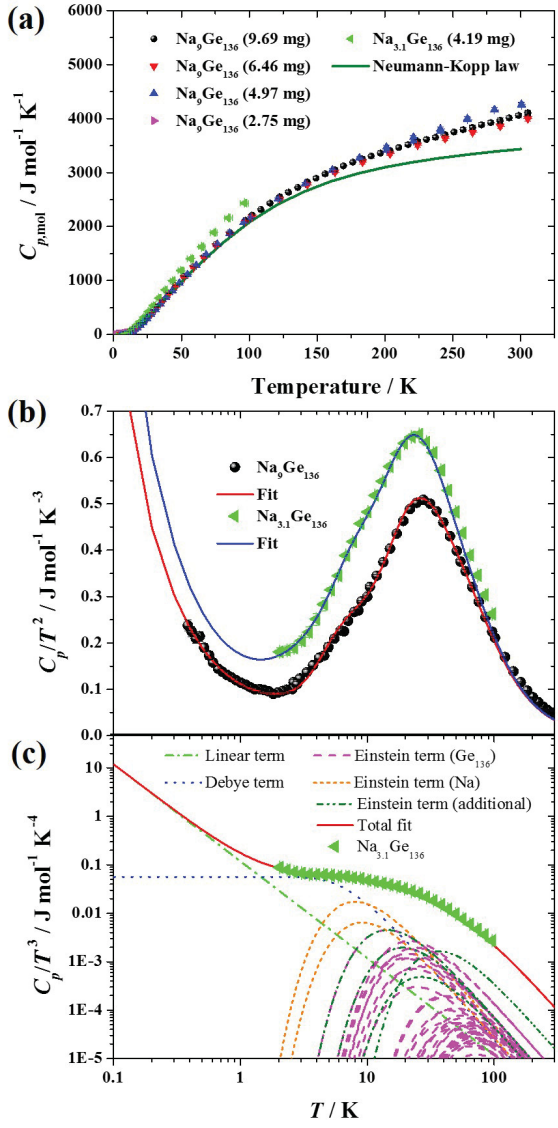

Figure 5.51: Heat capacities of partially Na-filled Ge clathrates. (a) $Na_{3.1}Ge_{136}$ has a higher heat capacity than Na_9Ge_{136} (data taken from reference [349]) and the estimated heat capacity using the Neumann-Kopp law. (b) The C_pT^{-2} curve indicates the presence of more low-intermediate optical phonon modes where $Na_{3.1}Ge_{136}$ has a broader peak than Na_9Ge_{136}. Fitted lines are taken from the heat capacity fits in (c) and C_pT^{-3} fit of Na_9Ge_{136}. C_pT^{-3} *vs* T fits of $Na_{3.1}Ge_{136}$ including three Debye modes, a linear electronic term, and Einstein modes for Ge_{136} and Na. Additional Einstein modes were applied to compensate for the softening of the optical Ge_{136} modes. Uncertainty in experimtal values of C_p was estimated to be 5% from 0.4 K to 5 K and 1% from 5 K to 300 K.

II clathrates using various numbers of Debye modes (n_D = 288 to 480) [341, 355]. However, in the first Brillouin zone the acoustic modes are highly dispersed (and can be described by the Debye model) while most of the optical modes are nearly frequency independent (and can be described by the Einstein model) [356, 343]. Therefore, the present heat capacity data were fit using three Debye modes, a linear electronic term and Einstein terms for 297 Ge_{136} and $3N_{Na}$ Na optical modes where N_{Na} is the number of Na atoms per unit cell (see Figure 5.51 (c)). The Einstein terms describing the optical modes of the Ge_{136} framework were taken from the computed phonons at the Brillouin center where the symmetries A_{xx}, B_{xx}, and T_{xx} have degeneracies of one, two, and three, respectively [356]. Nolas *et al.* computed the Raman modes of the completely filled $Cs_8Na_{16}Ge136$ clathrate [343] and found that the frequencies of its optical modes are significantly lower than those of the empty Ge_{136} clathrate [356]. Therefore, additional Einstein terms were included in the fit to accommodate for the stiffness changes, and accompanying optical mode softening, that occurs with Na guests present.

The Debye temperature, as determined from the heat capacity curves in Figure 5.51 (c), increased with increasing Na content, as expected ($\theta_{D,Na_{3.1}Ge_{136}}$ = 33 K, and $\theta_{D,Na_9Ge_{136}}$ = 44 K). The effective Debye temperature previously calculated for $Na_{8.8}Si_{136}$ ($\theta_{D,Na_{8.8}Si_{136}}$ = 250 K) is higher than $\theta_{D,Na_9Ge_{136}}$ as Ritchie *et al.* assumed that all atoms contribute to the Debye heat capacity [341] while the present approach assumes that only three acoustic modes contribute to the Debye heat capacity as described above. If only three Debye modes are considered for $Na_{8.8}Si_{136}$, a Debye temperature of 48 K is obtained from the published heat capacity data, *i.e.*, similar to that calculated for Na_9Ge_{136} here. Similarly, the reported Debye temperature for $Cs_8Na_{16-x}Tl_xGe_{136}$ decreases from 225 K to 41.4 K if only three Debye modes are used instead of 480 [355]. The Debye temperature for $Na_{3.1}Ge_{136}$ is one of the lowest reported, even lower than that of PCBM here ($\theta_{D,PCBM}$ = 37 K). The low Debye temperature and low atomic density in the clathrates reduce the predicted minimum thermal conductivity dramatically as described by Equation 4.7. Moreover, the linear electronic heat capacity decreases from 109 mJ mol^{-1} K^{-2} for $Na_{3.1}Ge_{136}$ to 89 mJ mol^{-1} K^{-2} for Na_9Ge_{136} with increasing Na content. The linear heat capacity is in the same range as other type II clathrates (100 mJ mol^{-1} K^{-2} for $Na_{21.5}Si_{136}$ [341]

and 114 mJ mol^{-1} K^{-2} for $Cs_8Na_{9.94}Tl_{6.06}Ge_{136}$ [355]). Refined Debye temperatures, Sommerfeld constants, and calculated minimum thermal conductivity from the Debye temperature are given in Table 5.9.

In addition to having low Debye temperatures, low-frequency optical modes would be excited by the oscillations of the Na atoms within the cages of these Ge clathrates (Figure 5.51 (c) and Figure E.2 of Appendix E). While all of the Na atoms of $Na_{3.1}Ge_{136}$ had low Einstein temperatures ($\theta_{E1,Na_{3.1}Ge_{136}}$ = 40 K and $\theta_{E2,Na_{3.1}Ge_{136}}$ = 45 K with $n_{E1,Na_{3.1}Ge_{136}}$ = 6 and $n_{E2,Na_{3.1}Ge_{136}}$ = 3.3 where n_E is the number of Einstein modes), the Einstein temperatures for the Na atoms in Na_9Ge_{136} varied more ($\theta_{E1,Na_9Ge_{136}}$ = 28 K, $\theta_{E2,Na_9Ge_{136}}$ = 60 K, $\theta_{E3,Na_9Ge_{136}}$ = 118 K, and $\theta_{E4,Na_9Ge_{136}}$ = 150 K with $n_{E1,Na_9Ge_{136}}$ = 2, $n_{E2,Na_9Ge_{136}}$ = 6, $n_{E3,Na_9Ge_{136}}$ = 6, and $n_{E4,Na_9Ge_{136}}$ = 13). These values are in good agreement with those of the guest atoms of the fully occupied clathrate $Cs_8Na_{16}Ge_{136}$, which have Einstein temperatures of ∼28 K for the Cs atoms, occupying the Ge_{28} cages, and 120 K for Na atoms, occupying the Ge_{20} cages [357]. The low-frequency optical modes are in the frequency region of the acoustic modes and, therefore, would efficiently scatter acoustic phonons to reduce phononic thermal conductivity. Note that this analysis is semi-quantitative since the optical modes of the Ge_{136} framework soften with increased Na content and therefore, additional Einstein terms were used for the fit. Furthermore, the frequencies and symmetries of the Na atoms in the cages are unknown.

Table 5.9: Debye temperature, θ_D, Sommerfeld constant, γ_{el}, and minimum thermal conductivity, $\kappa_{min,static}$, computed with the present minimum phononic thermal conductivities models for Na_xGe_{136} with various Na content.

Na content	θ_D / K	γ_{el} / mJ mol^{-1} K^{-2}	$\kappa_{min,static}$ / W m^{-1} K^{-1}
3.1±1.6	32.5	109	0.04-0.06
9.0±1.4	44.1	89	0.06-0.09

The experimental heat capacity is ∼15% higher than the heat capacity from the Neumann-Kopp law at room temperature. Oxidation of the compound can also increase the heat capacity and therefore, the heat capacity of the partially Na-filled germanium type II clathrates has to be treated with caution. As discussed earlier, the Neumann-Kopp law enhanced the prediction compared to the Dulong-Petit value but the electronic heat capacity and the heat capacity due to work of thermal

expansion can vary from the individual elements to the compound.

5.3.5 Thermal Conductivity

The experimental thermal conductivities of both Ge clathrates were adjusted to zero porosity and plotted as a function of temperature in Figure 5.52. (The thermal conductivity data for $Na_{3.1}Ge_{136}$ is given in Table E.4 in Appendix E.) The thermal conductivity of the germanium clathrates was also compared to the silicon clathrates with similar Na content [341]. The thermal conductivity of $Na_{3.1}Ge_{136}$ is approximately twice that of Na_9Ge_{136}. This is in contrast to the thermal conductivity behavior found in Si clathrates, which demonstrate increased thermal conductivity from $Na_{5.5}Si_{136}$ to $Na_{8.8}Si_{136}$ at room temperature [341].

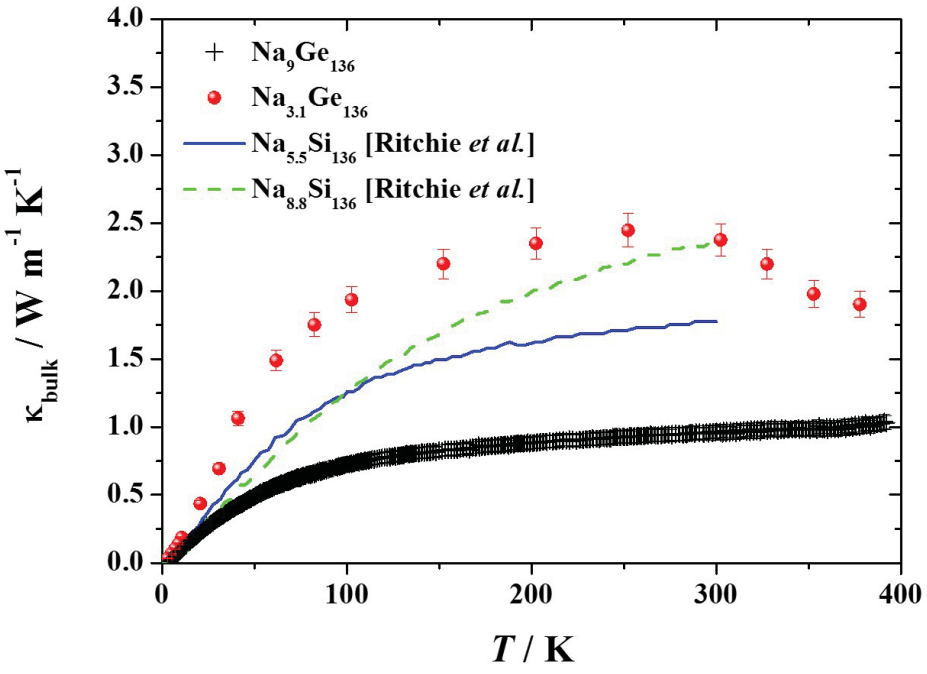

Figure 5.52: Thermal conductivity of $Na_{3.1}Ge_{136}$, Na_9Ge_{136}, $Na_{5.5}Si_{136}$, and $Na_{8.8}Si_{136}$ [341]; corrected to zero porosity. While $Na_{3.1}Ge_{136}$ demonstrates a crystalline behavior, Na_9Ge_{136} exhibits glassy behavior.

Thermal conductivity is a product of heat capacity per unit volume, phonon mean speed, and phonon mean free path as described by the Callaway model (see

Equation 2.14). On the one hand, the heat capacity of $Na_{3.1}Ge_{136}$ is higher than that of Na_9Ge_{136}, as shown in Figure 5.51. But, on the other hand, the phonon mean speed, which is proportional to the Debye temperature, would be lower and hence give lower thermal conductivity for $Na_{3.1}Ge_{136}$. The higher thermal conductivity observed in $Na_{3.1}Ge_{136}$, therefore, is most likely the result of a longer phonon mean free path. This is consistent with the PXRD patterns which indicate a lower proportion of the secondary polycrystalline Ge contaminant phase in the $Na_{3.1}Ge_{136}$ sample (Figure 5.49). Furthermore, the temperature-dependent thermal conductivity of Na_9Ge_{136} shows an increase in thermal conductivity with temperature indicating glassy behavior, while the thermal conductivity of $Na_{3.1}Ge_{136}$ has a more crystalline character, reaching a maximum thermal conductivity of 2.5 W m^{-1} K^{-1} at 250 K. Above 250 K the thermal conductivity of $Na_{3.1}Ge_{136}$ decreases, most likely as a result of Umklapp scattering, which also indicates higher crystallinity. Other potential sources of the shorter phonon mean free path in Na_9Ge_{136} might be grain surface oxidation, surface defects, and/or smaller grain size. In particular, the higher heat capacity than the Neumann-Kopp heat capacity might be the result of surface oxidation.

Na_9Ge_{136} has lower thermal conductivity than any reported Na_xSi_{136} clathrate [341]. Stefanoski *et al.* reported the thermal conductivities of monocrystalline Na_xSi_{136} clathrates and found [342] that the lowest thermal conductivity is more than three times higher than that of $Na_{3.1}Ge_{136}$. Furthermore, the thermal conductivities of both clathrates in the present study are significantly lower than the thermal conductivity of $Cs_8Na_{16}Ge_{136}$ [355]. The high thermal conductivity observed in $Cs_8Na_{16}Ge_{136}$ is assumed to be due to a large electronic contribution, which is proportional to a material's electrical conductivity. It was not feasible to measure the electrical conductivity of the present Na_xGe_{136} sample due to a high electrical resistivity and therefore, it is assumed that the electronic contribution of the thermal conductivity is negligible and the reported thermal conductivity is similar to the phononic contribution of the thermal conductivity. The minimum thermal conductivities of the clathrates also were calculated from the present models using Equations 4.7 and 5.5. Both clathrates have a low minimum thermal conductivity similar to that of PCBM where $Na_{3.1}Ge_{136}$ has a slightly lower

minimum thermal conductivity (0.04-0.06 W m^{-1} K^{-1}) than $Na_{9.0}Ge_{136}$ (0.06-0.09 W m^{-1} K^{-1}). Therefore, a reduction in thermal conductivity might be observed at high temperature due to an increase in dynamic disordering.

5.3.6 Conclusions

Ionic liquids have been successfully used to produce type II Ge clathrate materials from NaGe precursors. The NaGe precursors were synthesized using arc melting, which reduced synthesis time and cost, compared to a previously reported solid state method that required a Ta tube. Partially Na-filled Ge type II clathrates with low Na content were synthesized using a solid-gas reaction. Heat capacity data indicated that the Ge clathrates produced have very low Debye temperatures, most likely due to the low-frequency modes of the intercalated Na atoms. The thermal conductivities decreased with increasing Na content which is in contrast to the behavior observed in silicon type II clathrates. Furthermore, the observed inhomogeneity and the uncertainty regarding the positions of Na atoms within these structures make it apparent that further structure and synthesis investigations and Na content control are needed in order to fully understand the dynamics of the physical properties that govern the transport properties of type II Ge clathrates.

Chapter 6

Conclusion

6.1 Conclusions

Thermoelectric materials are currently not widely used in domestic applications due to their low thermoelectric efficiency. The search for new high-performance thermoelectric materials can be challenging because they require enhanced electrical properties and low heat transport. A potential way to accelerate the search can be established by first-principles calculations where thousands of compounds can be investigated simultaneously. Computational studies also have the advantage of requiring less energy and especially less material than experimental 'trial-and-error' methods. However, accurate models are required to obtain qualitative and quantitative prediction of the thermoelectric properties. The present study focused on the understanding of the underlying physics in thermoelectric properties. The electronic properties were predicted with the Boltzmann transport approach using a constant relaxation time and a novel variable relaxation time method. The lowest limit of the thermal conductivity was delineated by a new model for minimum thermal conductivity, which accurately described the ultralow thermal conductivity (*i.e.*, thermal conductivity lower than the predicted Cahill, Watson, and Pohl amorphous limit [66, 67]) for various materials.

In the present model of minimum thermal conductivity, an average phonon mean speed was determined from experimental Debye temperatures and the phonon mean free path was limited by static (frequency-independent) or dynamic (frequency-dependent) disordering. While thermal conductivity limited by static disordering represented the ultralow thermal conductivity of [6,6]-phenyl-C_{61}-butyric acid methyl ester (PCBM) and of C_{60}/C_{70} fullerite well, the low thermal conductivity of $TmAgTe_2$ at high temperature agreed well with the estimated thermal conductivity limited by dynamic disordering.

With the new concepts of variable relaxation time and minimum thermal

conductivity, two new classes of thermoelectric materials (XYZ_2 [X,Y: rare earth or transition metal; Z: group VI element] and metal phosphides), were revealed from a high-throughput screening of ∼48,000 inorganic compounds within 'The Materials Project', and were investigated herein. Three different parent compounds of the XYZ_2 class, $TmAgTe_2$, $YAgTe_2$, and $YCuTe_2$, and the corresponding intrinsically and extrinsically doped compounds were synthesized. All investigated XYZ_2 compounds had at least one phase transition. The electronic and phononic band structures of the XYZ_2 compounds were confirmed by experimental DOS from UPS/IEPS studies and experimental heat capacity from 0.4 K to 500 K. Furthermore, thermal transport properties, measured from 2 K up to 900 K, indicated extremely low lattice thermal conductivity ($\kappa_{pho} < 0.5$ W m^{-1}K^{-1}) at high temperature.

All XYZ_2 compounds possess promising thermoelectric figures of merit with a maximum zT of 0.73±0.18 at 780 K for $Y_{0.96}Cu_{1.08}Te_2$. The thermoelectric figure of merit in $TmAgTe_2$ was low most likely due to Tm_{Ag} antisite defects acting as hole killers. The thermoelectric performance measured in these compounds was enhanced by intrinsic doping and it was predicted from the single parabolic band model that the thermoelectric figure of merit of $TmAgTe_2$ could reach a value of 1.4 by optimizing the charge carrier concentration.

Metal phosphides were investigated with the variable relaxation time method, developed from a semi-empirical approach depending on just the elastic properties and the electronic band structure of the compound. For the energy and temperature dependence, it was assumed that the electron scattering is limited by acoustic phonons. Whereas, for the phosphides, high thermoelectric performance was predicted for XYP compounds using a constant relaxation time approach, the variable relaxation time approach predicted higher thermoelectric figures of merit for XP_2 compounds. In addition to metal phosphides, the thermoelectric figures of merit of some of the best current thermoelectric materials (PbTe and Bi_2Te_3) were computed with the variable relaxation time and a semi-empirical model for thermal conductivity [68] showing good agreement with experiments. As an example for metal phosphides, NiP_2 in the cubic phase was synthesized and found to exhibit relatively low thermal conductivity and high electrical conductivity.

In addition to the thermoelectric materials, other materials were investigated which possess extremely low intrinsic thermal conductivity. In particular, ultralow thermal conductivity measured for a consolidated PCBM pellet, presents the lowest thermal conductivity ever reported for a fully dense solid at room temperature ($\kappa_{bulk} = 0.068 \pm 0.007$ W m^{-1} K^{-1}). In addition to the ultralow thermal conductivity, a distinct separation of the intra- and intermolecular modes was observed in the heat capacity of PCBM which has additional low-frequency intermolecular modes compared to C_{60}. The low-frequency modes were assigned to the side chain of the PCBM molecule, and observed from Raman measurements. Furthermore, it was found that the $A_g(1)$ breathing mode, which is due to the expansion and contraction of all carbon-carbon bonds in the fullerene core, has a significant contribution to the heat capacity at elevated temperatures ($T > 90$ K).

The determination of the thermal conductivity for low thermal conductivity materials can be challenging, in particular, for less stiff samples (*e.g.*, powder samples). The thermal conductivity of pristine and metal oxide-coated ZnO tetrapods, which could not be consolidated to a pellet due to their unique and fragile morphology, was measured in a lab-developed powder cell. Low thermal conductivity was found for the pristine and metal oxide-coated ZnO tetrapods, ranging from 0.07 to 0.18 W m^{-1} K^{-1}. The heat transfer in the empty powder cell and randomly oriented ZnO tetrapods was confirmed with finite element simulations. The simulations indicate that the blackbody radiation in ZnO tetrapods can be neglected and the thermal conductivity is strongly related to the arrangement of the tetrapods. Furthermore, the electrical and thermal properties of ZnO tetrapods coated with MWCNTs were investigated with the standard steady-state method in a PPMS. In comparison to the pristine and metal oxide-coated ZnO tetrapods, an increase in thermal ($\kappa = 0.24 - 0.46$ W m^{-1} K^{-1} at 300 K) and electrical conductivities ($\sigma_{el} = 4 - 49$ S m^{-1} at 300 K) was obtained. Whereas the electrical conductivities increase with increasing MWCNT content from 2 K to 390 K, the thermal conductivity is strongly related to the crystallinity of the ZnO tetrapods at low temperatures ($T < 100$ K).

Finally, the thermal properties of germanium type II clathrates with partial Na filling were analyzed. For the synthesis of the Ge clathrates, a NaGe precursor

produced in an arc furnace reacted with the products of an ionic liquid in a solid-gas reaction. A low Debye temperature was found for the clathrates which could be the result of low-frequency optical modes and avoided band crossing.

To conclude, the new concepts introduced here for the prediction of thermoelectric properties could be potential game changers in the search of high-performance thermoelectric properties using first-principles calculations and, hence, could reduce the time and material compared to using a purely experimental route.

6.2 Future Work

Although the novel concepts of minimum thermal conductivity limited by static and dynamic disordering and the variable relaxation time showed strong correlation with experiments in the present study, further studies with larger test sets are required to reveal the accuracy of these models.

For the minimum thermal conductivity calculation, the average phonon speed in ultralow thermal conductivity materials could be obtained from experimental heat capacity data or phononic band structures and the resulting estimated minimum thermal conductivity could be compared to reported thermal conductivity. Several materials with ultralow thermal conductivity were already reported [26, 27, 148, 149, 150, 154], which could be used as a test set for the minimum thermal conductivity. For instance, ultralow thermal conductivity was reported in single-crystalline SnSe at high temperature [26, 27]. The experimental low-temperature heat capacity could be determined in a PPMS using the ^{3}He option and the minimum thermal conductivity limited by dynamic disordering could be compared to the experimental lattice thermal conductivity. Because the present minimum thermal conductivity model is only dependent on the Debye temperature and the atomic density, an advanced understanding of the Debye temperature is required to search for materials with low thermal conductivity.

In addition to the minimum thermal conductivity, electronic properties calculated from the electronic band structures with the variable relaxation time were only tested on the experimental data of two optimized thermoelectric compounds (*i.e.*, PbTe and Bi_2Te_3). However, for a quantitative analysis of the accuracy of the model a

larger test set is required. The test set reported by Wei *et al.* [35] with 31 entries could be compared to the predicted electronic properties using the variable relaxation time. Furthermore, the electron mobility to calculate the variable relaxation time was determined here from a constant band effective mass. However, the band effective mass can depend on the carrier concentration and temperature. For an enhanced variable relaxation time, the band effective mass needs to be calculated from the Boltzmann transport band effective mass.

The high-throughput screening revealed that several metal phosphides have enhanced electronic properties and relatively low thermal conductivities. In particular, XP_2 compounds, such as IrP_2, RhP_2, and RuP_2, showed an estimated thermoelectric performance similar to the current best thermoelectric materials (*i.e.* PbTe and Bi_2Te_3). Experimental studies of these materials would be required to determine their actual thermoelectric figures of merit.

In addition to metal phosphides, various XYZ_2 compounds reveal high predicted thermoelectric performance. However, the thermoelectric properties were determined from PBE-GGA electronic band structures without spin-orbit coupling and Boltzmann transport equations with a constant relaxation time. Electronic band structures determined using the hybrid functional HSE and spin orbit coupling as well as Boltzmann transport equations using the present variable relaxation time approach could enhance the prediction of the thermoelectric properties. Note that although it was predicted that $TmAgTe_2$ can be optimized to a thermoelectric figure of merit of 1.4, such a potentially high figure of merit does not justify the use of rare-earth elements because alternative thermoelectrics without rare-earth elements show higher thermoelectric performance than the predicted figure of merit.

In addition to thermoelectric materials, a lab-developed powder cell was used in the present study to determine the thermal conductivity of ZnO tetrapods. It is proposed that powder can reduce the thermal conductivity, even below the thermal conductivity of 'true' vacuum [70, 71]. To test the hypothesis, the thermal conductivities of different powders with various sizes could be determined [70, 71]. However, a large temperature difference between the cold and hot side is required, so that the contribution of the blackbody radiation ($\propto T^4$) is larger than the thermal conduction ($\propto T$) of the powder.

The thermal conductivity of pristine and metal oxide-coated ZnO tetrapods was investigated, and these materials were typically coated with oxides due to the synthesis at high temperature under oxygen atmosphere. Oxides have low thermal conductivity but also low electrical conductivity and hence, all investigated metal oxide-coated samples were insulators. A potential way to enhance the electrical properties in these materials could be achieved by the use of noble metals, such as Ag, and/or the change to inert synthesis conditions. In particular, Ag has, in addition to its high electrical conductivity, anti-bacterial effects which could make the material desirable for *in vivo* medical devices. Furthermore, the electrical and thermal properties of MWCNT-coated ZnO tetrapods could be improved by aligning the MWCNTs in the sample.

In conclusion, high-throughput screening, *e.g.*, as currently performed by 'The Materials Project', can provide a potential way to accelerate the search for new materials with a wide range in application. In particular, with the growth in computing power and the enhancement of the theoretical models, high-throughput approaches can calculate the electrical and thermal properties of billions of compounds on an annual basis and can be considered as a major direction of future research. While experimental studies require many resources, *e.g.*, material, energy, and time, computational studies used only a fraction of the resources. Especially in the search of thermoelectric materials, high-throughput approaches can help to identify new promising materials due to their complex interdependent properties. While the Seebeck coefficient and the heat capacity can be already computed with high accuracy as shown in the present study, the prediction of the electrical and thermal conductivity are not yet feasible in a high-throughput screening due to the unknown relaxation time. The present variable relaxation time approach can enhance the prediction of the electrical conductivity but further enhancements of the variable relaxation time approach are required, including the role of optical phonon/electron interactions and the dielectric constant. In addition to identifying materials with enhanced electronic properties, computations also can help to optimize the electronic properties in these materials. The electronic properties are strongly related to the Fermi level, *i.e.*, carrier concentration, and a computational study can indicate the optimum carrier concentration to optimize the electronic

properties, a matter which is challenging using just an experimental approach. However, it is important to note that doping is required in experiments to optimize the carrier concentration, and this can affect the electronic and phononic dispersion curves.

The prediction of the thermal conductivity by calculation is more expensive than for the electrical conductivity and new approaches are required to calculate the thermal conductivity using high-throughput screenings. However, research in the area of thermal conductivity prediction has dramatically increased in the last decade and it should be feasible to calculate the thermal conductivity of a majority of materials in the next decade if the enhancement of the thermal conductivity prediction increases with the same rate. Therefore, computational studies are an important tool to search for new materials and to optimize the physical properties in these materials. However, the theoretical models have to be further improved before computational studies alone can be completely relied upon to identify new materials.

Appendix A

Origins of Ultralow Thermal Conductivity in PCBM

Table A.1: Refined PXRD data for PCBM powder and PCBM pellet using the Le Bail method. The diffractograms of PCBM powder and pellet are shown in Figure 4.3.

Parameter	PCBM Powder	PCBM Pellet
Space group	$P2_1/n$ (No. 14)	$P2_1/n$ (No. 14)
a / Å	13.529	13.503
b / Å	15.203	15.199
c / Å	19.117	19.119
α / °	90.000	90.000
β / °	106.960	107.013
γ / °	90.000	90.000
Number of molecules per unit cell, Z	4	4
Volume / Å^3	3761	3752
Calculated density / g cm^{-3}	1.609	1.613
R_p	4.950	4.512
R_{wp}	8.121	8.816
χ^2	0.604	0.676

Table A.2: Refined PXRD data for PCBM pellet at various temperatures using the Le Bail method. The diffractograms of the PCBM pellet are shown in Figure 4.4.

Parameter	123 K	223 K
Space group	$P2_1/n$ (No. 14)	$P2_1/n$ (No. 14)
a / Å	13.423	13.538
b / Å	15.148	15.299
c / Å	18.954	19.153
α / °	90.000	90.000
β / °	106.839	107.026
γ / °	90.000	90.000
Number of molecules per unit cell, Z	4	4
Volume / Å^3	3686	3794
Calculated density / g cm^{-3}	1.641	1.595
R_p	6.545	6.308
R_{wp}	11.025	9.683
χ^2	3.042	2.760
Parameter	300 K	373 K
Space group	$P2_1/n$ (No. 14)	$P2_1/n$ (No. 14)
a / Å	13.512	13.530
b / Å	15.265	15.270
c / Å	19.139	19.153
α / °	90.000	90.000
β / °	107.039	107.032
γ / °	90.000	90.000
Number of molecules per unit cell, Z	4	4
Volume / Å^3	3775	3784
Calculated density / g cm^{-3}	1.603	1.599
R_p	6.146	5.335
R_{wp}	10.115	8.510
χ^2	3.092	2.677

Table A.3: Wavenumbers of Raman peaks in C_{60}, PCBM powder, and PCBM pellet. The corresponding Raman spectra are shown in Figure 4.4.

C_{60} / cm^{-1} [177]	PCBM powder / cm^{-1}	PCBM pellet/ cm^{-1}
	75	75
	88	88
	103	103
	163	163
	182	184
266	255	255
273 ($H_g(1)$)	271	271
	348	348
433 ($H_g(2)$)	429	429
496 ($A_g(1)$)	481	483
568	531	531
709 ($H_g(3)$)	709	709
771 ($H_g(4)$)	768	768
	776	778
1101 ($H_g(5)$)	1104	1104
1251 ($H_g(6)$)	1249	1251
1424 ($H_g(7)$)	1424	1424
1469 ($A_g(2)$)	1461	1463
1574 ($H_g(8)$)	1573	1575

Table A.4: Change in enthalpy, ΔH, onset temperature, T_{onset}, and change in entropy, ΔS, at the phase transitions of PCBM powder and PCBM pellet. The corresponding DSC thermograms are shown in Figure 4.7.

Peak	ΔH / J g^{-1}	T_{onset} / K	ΔS / mJ g^{-1} K^{-1}
Powder			
Heating 1. peak (endothermic)	18	517	35
Heating 2. peak (endothermic)	15	548	27
Cooling 1. peak (exothermic)	1.2	479	2.5
Pellet			
Heating 1. peak (endothermic)	1.7	513	3.3
Heating 2. peak (endothermic)	24	551	44
Cooling 1. peak (exothermic)	11	525	20

Table A.5: Heat capacity data: 3.210 mg with ^{4}He option; in order of data collection. The heat capacity is plotted as function of temperature in Figure 4.11.

T / K	C_p / J mol^{-1} K^{-1}	T / K	C_p / J mol^{-1} K^{-1}	T / K	C_p / J mol^{-1} K^{-1}
304.698	718±50	48.516	93.4±6.5	9.071	15.3±1.07
284.248	665±47	43.956	86.9±6.1	8.220	12.8±0.90
264.044	607±42	39.826	80.6±5.6	7.442	10.5±0.74
243.773	553±39	36.085	74.9±5.2	6.756	8.69±0.61
223.530	498±35	32.697	69.2±4.8	6.118	6.90±0.48
183.004	385±27	29.624	63.8±4.5	5.536	5.47±0.38
162.709	329±23	26.851	58.2±4.1	5.008	4.20±0.29
142.429	277±19	24.336	53.3±3.7	4.535	3.22±0.48
122.142	228±16	22.041	48.4±3.4	4.108	2.40±0.36
101.905	184±13	19.971	43.7±3.1	3.719	1.76±0.26
96.823	172±12	18.075	39.3±2.7	3.369	1.26±0.19
87.696	152±11	16.388	35.2±2.5	3.050	0.88±0.13
79.467	142±10	14.863	31.3±2.2	2.760	0.60±0.09
72.020	129±9	13.463	27.7±1.9	2.498	0.41±0.06
65.238	118±8	12.203	24.2±1.7	2.260	0.27±0.04
59.103	109±8	11.057	21.0±1.5	2.047	0.18±0.03
53.552	101±7	10.022	17.9±1.3	1.995	0.19±0.03
48.516	93.4±6.5	9.071	15.3±1.1		

Table A.6: Heat capacity data: 3.670 mg with ^{4}He option; in order of data collection. The heat capacity is plotted as function of temperature in Figure 4.11.

T / K	C_p / J mol^{-1} K^{-1}	T / K	C_p / J mol^{-1} K^{-1}	T / K	C_p / J mol^{-1} K^{-1}
299.993	766±53	52.454	110±8	9.742	19.2±1.3
280.004	715±50	47.506	102±7.	8.820	16.4±1.2
260.003	655±46	43.021	94.5±6.6	7.988	13.7±1.0
239.999	598±42	38.961	87.5±6.1	7.233	11.3±0.8
220.002	537±38	35.286	81.2±5.7	6.558	9.30±0.65
199.996	477±33	31.956	75.0±5.3	5.931	7.39±0.52
179.996	417±29	28.942	69.1±4.8	5.373	5.82±0.41
159.996	356±25	26.205	63.5±4.4	4.865	4.52±0.68
139.998	300±21	23.746	57.3±4.0	4.406	3.44±0.52
119.989	248±17	21.504	52.6±3.7	3.990	2.57±0.39
99.995	201±14	19.476	47.2±3.3	3.613	1.87±0.28
95.000	189±13	17.636	42.3±3.0	3.273	1.34±0.20
86.050	166±12	15.978	37.8±2.6	2.965	0.947±0.142
77.942	155±11	14.475	33.5±2.3	2.685	0.646±0.097
70.607	141±10	13.111	29.6±2.1	2.432	0.441±0.066
63.951	129±9	11.877	25.9±1.8	2.202	0.296±0.044
57.918	119±8	10.759	22.5±1.6	1.995	0.194±0.029

Table A.7: Heat capacity data: 1.908 mg with ^{4}He option; in order of data collection. The heat capacity is plotted as function of temperature in Figure 4.11.

T / K	C_p / J mol^{-1} K^{-1}	T / K	C_p / J mol^{-1} K^{-1}	T / K	C_p / J mol^{-1} K^{-1}
303.742	738±52	53.258	98.4±6.9	9.936	17.3±1.2
283.425	661±46	48.245	91.0±6.4	9.002	14.7±1.0
263.267	611±43	43.708	84.8±5.9	8.159	12.2±0.9
243.019	553±39	39.595	78.8±5.5	7.394	10.0±0.7
222.820	496±35	35.867	73.1±5.1	6.709	8.26±0.58
202.579	438±31	32.498	67.8±4.7	6.079	6.47±0.45
182.290	386±27	29.442	62.1±4.3	5.504	5.09±0.36
162.068	326±23	26.678	57.3±4.0	4.982	3.95±0.59
141.864	272±19	24.173	52.1±3.6	4.513	2.97±0.45
121.633	225±16	21.903	47.4±3.3	4.087	2.17±0.33
101.424	180±13	19.839	42.6±3.0	3.701	1.55±0.23
96.351	168±12	17.977	38.5±2.7	3.350	1.12±0.17
87.255	147±10	16.288	34.2±2.4	3.033	0.773±0.116
79.065	137±10	14.755	30.5±2.1	2.746	0.523±0.078
71.644	125±9	13.367	26.8±1.9	2.485	0.338±0.051
64.889	115±8	12.107	23.4±1.6	2.251	0.225±0.034
58.784	106±7	10.968	20.3±1.4	2.037	0.145±0.022
53.258	98.4±6.9	9.936	17.2±1.2		

Table A.8: Heat capacity data: 3.890 mg with ^{3}He option; in order of data collection. The heat capacity is plotted as function of temperature in Figure 4.11.

T / K	C_p / J mol^{-1} K^{-1}	T / K	C_p / mJ mol^{-1} K^{-1}	T / K	C_p / mJ mol^{-1} K^{-1}
10.048	18.6±1.3	3.300	1100±165	0.895	7.77±1.17
9.082	15.6±1.1	2.984	754±113	0.812	5.85±0.88
8.203	13.0±0.9	2.698	500±75	0.736	4.37±0.66
7.412	10.7±0.7	2.437	333±50	0.670	3.32±0.50
6.699	8.51±0.60	2.200	219±33	0.604	2.58±0.39
6.059	6.80±0.48	1.625	60.6±9.1	0.553	2.17±0.33
5.475	5.27±0.37	1.472	40.8±6.1	0.500	1.69±0.25
4.946	4.01±0.60	1.327	27.9±4.2	0.458	1.29±0.19
4.471	2.99±0.45	1.203	20.7±3.1	0.419	1.04±0.16
4.041	2.20±0.33	1.090	14.5±2.2	0.387	0.843±0.127
3.647	1.58±0.24	0.988	10.4±1.6		

Appendix B

ZnO Tetrapods

Table B.1: Thermal conductance of the empty cell with blackbody radiation, K_{empty}, without the thermal conductance of the shoes, K_{empty}-K_{shoes}, and without the thermal conductance of the shoes and blackbody radiation, $K_{empty,cell}$; in order of data collection. The thermal conductance is plotted as function of temperature in Figure 4.18.

T / K	K_{empty} / mW K^{-1}	K_{empty}-K_{shoes} / mW K^{-1}	$K_{empty,cell}$ / mW K^{-1}
301.721	1.90±0.38	1.48±0.30	0.625±0.125
311.628	1.99±0.40	1.48±0.30	0.625±0.125
321.549	2.10±0.42	1.52±0.30	0.577±0.115
331.463	2.24±0.45	1.59±0.32	0.550±0.110
326.543	2.20±0.44	1.69±0.34	0.538±0.108
316.629	2.09±0.42	1.66±0.33	0.564±0.113
306.698	1.98±0.40	1.60±0.32	0.591±0.118
296.764	1.86±0.37	1.53±0.31	0.620±0.124
286.811	1.78±0.36	1.45±0.29	0.633±0.127
276.857	1.71±0.34	1.41±0.28	0.669±0.134
266.912	1.62±0.32	1.38±0.28	0.708±0.142
271.852	1.64±0.33	1.32±0.26	0.722±0.144
281.771	1.73±0.35	1.32±0.26	0.695±0.139
291.746	1.78±0.36	1.38±0.28	0.676±0.135
301.690	1.87±0.37	1.40±0.28	0.619±0.124

Table B.2: Thermal conductivity of the pristine and alloyed ZnO tetrapods calculated using the total thermal conductance, κ_{total}; in order of data collection. The thermal conductivity is plotted as function of temperature in Figure 4.19 (a).

T / K	κ_{total} / mW m^{-1} K^{-1} (Al-alloyed ZnO)	T / K	κ_{total} / mW m^{-1} K^{-1} (Sn-alloyed ZnO)
301.581	98.5±19.7	301.627	63.0±12.6
311.519	89.5±17.9	311.561	52.6±10.5
321.453	82.8±16.6	321.500	45.4±9.1
331.384	69.5±13.9	331.423	36.9±7.4
326.452	70.1±14.0	326.496	40.5±8.1
316.526	73.4±14.7	316.575	42.2±8.4
306.584	72.7±14.5	306.635	46.4±9.3
296.637	91.0±18.2	296.692	60.9±12.2
286.670	92.7±18.5	286.730	63.0±12.6
276.703	95.9±19.2	276.766	60.4±12.1
266.742	100±20	266.809	64.9±13.0
271.697	94.8±19.0	271.761	61.0±12.2
281.633	85.7±17.1	281.692	50.4±10.1
291.619	81.7±16.3	291.674	47.4±9.5
301.578	78.3±15.7	301.631	45.2±9.0
T / K	κ_{total} / mW m^{-1} K^{-1} (Fe-alloyed ZnO)	T / K	κ_{total} / mW m^{-1} K^{-1} (Cu-alloyed ZnO)
301.591	149±30	301.571	132±26
311.529	135±27	311.508	118±24
321.471	122±25	321.450	102±20
331.404	107±21	331.391	84.2±16.8
326.473	113±23	326.456	90.1±18.0
316.544	119±24	316.526	102±20
306.603	120±24	306.582	105±21
296.653	137±27	296.628	123±25
286.690	137±27	286.660	125±25
276.724	140±28	276.694	127±25
266.766	141±28	266.732	131±26
271.718	135±27	271.686	124±25
281.655	124±25	281.628	111±22
291.640	118±24	291.618	103±21
301.601	114±23	301.582	96.3±19

T / K	κ_{total} / mW m^{-1} K^{-1} (Bi-alloyed ZnO)	T / K	κ_{total} / mW m^{-1} K^{-1} (Pristine ZnO)
301.573	97.1±19.4	301.404	181±36
311.516	81.0±16.2	311.360	164±33
321.457	67.8±13.6	321.329	152±30
331.387	54.1±10.8	331.295	140±28
326.453	64.4±12.9	326.348	145±29
316.526	74.1±14.8	316.403	150±30
306.583	80.5±16.1	306.443	149±30
296.634	98.9±19.8	296.471	156±31
286.670	97.2±19.5	286.489	155±31
276.704	101±20	276.507	150±30
266.746	104±21	266.534	151±30
271.697	99.0±19.8	271.502	146±29
281.636	86.1±17.2	281.457	140±28
291.626	78.9±15.8	291.456	138±28
301.588	72.4±14.5	301.445	129±26

Table B.3: Thermal conductivity of the pristine and alloyed ZnO tetrapods calculated using the thermal conductance of the powder cell, κ_{cell}; in order of data collection. The thermal conductivity is plotted as function of temperature in Figure 4.19 (b).

T / K	κ_{cell} / mW m^{-1} K^{-1} (Al-alloyed ZnO)	T / K	κ_{cell} / mW m^{-1} K^{-1} (Sn-alloyed ZnO)
301.581	116±23	301.627	70.0±14.0
311.519	108±22	311.561	57.0±11.4
321.453	105±21	321.500	52.0±10.4
331.384	96.8±19.4	331.423	47.8±9.6
326.452	102±20	326.496	56.3±11.3
316.526	104±21	316.575	57.3±11.5
306.584	102±20	306.635	57.5±11.5
296.637	111±22	296.692	64.5±12.9
286.670	112±22	286.730	69.3±13.9
276.703	113±23	276.766	67.1±13.4
266.742	116±23	266.809	71.3±14.3
271.697	110±22	271.761	66.2±13.2
281.633	102±20	281.692	56.6±11.3
291.619	101±20	291.674	54.5±10.9
301.578	99.1±19.8	301.631	52.5±10.5

T / K	κ_{cell} / mW m^{-1} K^{-1} (Fe-alloyed ZnO)	T / K	κ_{cell} / mW m^{-1} K^{-1} (Cu-alloyed ZnO)
301.591	132±26	301.571	143±29
311.529	115±23	311.508	130±26
321.471	106±21	321.450	116±23
331.404	93.5±18.7	331.391	102±20
326.473	105±21	326.456	112±22
316.544	113±23	316.526	119±24
306.603	112±22	306.582	120±24
296.653	124±25	296.628	133±27
286.690	127±25	286.660	139±28
276.724	130±26	276.694	137±27
266.766	132±26	266.732	140±28
271.718	125±25	271.686	133±27
281.655	113±23	281.628	120±24
291.640	107±21	291.618	114±23
301.601	102±20	301.582	108±22
T / K	κ_{cell} / mW m^{-1} K^{-1} (Bi-alloyed ZnO)	T / K	κ_{cell} / mW m^{-1} K^{-1} (Pristine ZnO)
301.573	116±23	301.404	130±26
311.516	102±20	311.360	111±22
321.457	93.8±18.8	321.329	93.9±18.8
331.387	89.4±17.9	331.295	78.0±15.6
326.453	98.8±19.8	326.348	82.8±16.6
316.526	107±21	316.403	95.8±19.2
306.583	107±21	306.443	101±20
296.634	117±23	296.471	109±22
286.670	116±23	286.489	113±23
276.704	118±24	276.507	115±23
266.746	118±24	266.534	118±24
271.697	113±23	271.502	111±22
281.636	102±20	281.457	100±20
291.626	97.3±19.5	291.456	95.0±19.0
301.588	93.2±18.6	301.445	82.5±16.5

Table B.4: Electrical conductivity of MWCNTs coated ZnO with 2 infiltrations; in order of data collection. The electrical conductivity is plotted as function of temperature in Figure 4.23.

T / K	σ_{el} / S m^{-1} (2 FL 2 mm)	T / K	σ_{el} / S m^{-1} (2 FL 3 mm)	T / K	σ_{el} / S m^{-1} (2 FL 3 mm (2))
301.603	9.44±0.47	301.987	7.40±0.37	301.708	3.69±0.18
302.153	9.45±0.47	326.877	7.53±0.38	326.641	3.73±0.19
327.261	9.59±0.48	351.749	7.58±0.38	351.554	3.78±0.19
352.449	9.67±0.48	376.572	7.64±0.38	376.463	3.96±0.20
377.275	9.88±0.49	391.579	7.70±0.39	391.421	4.31±0.22
392.255	10.2±0.5	351.797	7.48±0.37	351.602	4.36±0.22
352.510	10.2±0.5	302.001	7.20±0.36	301.712	4.23±0.21
302.192	9.93±0.50	276.673	7.06±0.35	276.414	4.16±0.21
276.345	9.77±0.49	251.719	6.92±0.35	251.426	4.09±0.20
251.364	9.59±0.48	226.326	6.78±0.34	226.077	4.02±0.20
226.022	9.42±0.47	201.384	6.63±0.33	201.090	3.93±0.20
201.066	9.22±0.46	175.981	6.46±0.32	175.765	3.83±0.19
175.732	8.98±0.45	150.677	6.26±0.31	150.233	3.71±0.19
150.204	8.69±0.43	125.720	6.02±0.30	125.264	3.56±0.18
125.247	8.35±0.42	100.597	5.73±0.29	100.276	3.37±0.17
100.206	7.91±0.40	75.439	5.34±0.27	75.265	3.12±0.16
75.184	7.33±0.37	50.504	4.77±0.24	50.105	2.75±0.14
50.103	6.48±0.32	25.580	3.72±0.19	25.060	2.09±0.10
25.077	4.92±0.25	10.782	2.35±0.12	10.058	1.25±0.06
10.072	2.94±0.15	6.058	1.67±0.08	5.112	0.921±0.046
5.127	2.06±0.10	3.324	1.40±0.07	2.309	0.768±0.038
2.307	1.55±0.08	15.426	2.92±0.15	15.028	1.60±0.08
15.036	3.76±0.19	30.463	4.01±0.20	30.041	2.26±0.11
30.056	5.34±0.27	60.446	5.03±0.25	60.028	2.92±0.15
60.079	6.87±0.34	110.549	5.84±0.29	110.206	3.44±0.17
110.391	8.09±0.40	160.571	6.32±0.32	160.242	3.75±0.19
160.381	8.80±0.44	210.897	6.66±0.33	210.630	3.95±0.20
210.639	9.28±0.46	261.603	6.93±0.35	261.307	4.10±0.20
261.232	9.63±0.48	301.921	7.16±0.36	301.655	4.20±0.21
301.548	9.89±0.49				

Table B.5: Electrical conductivity of MWCNTs coated ZnO with 5 infiltrations; in order of data collection. The electrical conductivity is plotted as function of temperature in Figure 4.23.

T / K	σ_{el} / S m^{-1} (5 FL 2 mm)	T / K	σ_{el} / S m^{-1} (5 FL 3 mm)	T / K	σ_{el} / S m^{-1} (5 FL 3 mm (2))
302.769	18.3±0.9	302.779	28.5±1.4	301.649	18.7±0.9
327.653	18.6±0.9	327.637	28.9±1.5	326.573	19.0±1.0
352.491	19.2±1.0	352.463	29.5±1.5	351.486	19.2±1.0
377.340	20.6±1.0	377.287	30.7±1.5	376.410	19.6±1.0
392.247	21.8±1.1	392.190	32.3±1.6	391.377	19.8±1.0
352.591	21.6±1.1	352.515	32.4±1.6	351.549	19.4±1.0
302.843	20.9±1.1	302.742	31.4±1.6	301.684	18.8±0.9
277.410	20.5±1.0	277.301	30.8±1.5	276.392	18.4±0.9
252.46	20.2±1.0	252.345	30.3±1.5	251.404	18.1±0.9
226.942	19.8±1.0	226.826	29.8±1.5	226.068	17.7±0.9
202.036	19.4±1.0	201.914	29.2±1.5	201.112	17.3±0.9
176.508	18.9±0.9	176.401	28.5±1.4	175.787	16.8±0.8
151.070	18.3±0.9	150.999	27.6±1.4	150.542	16.3±0.8
126.126	17.6±0.9	126.061	26.6±1.3	125.585	15.7±0.8
100.919	16.7±0.8	100.867	25.3±1.3	100.493	14.8±0.7
75.702	15.6±0.8	75.645	23.6±1.2	75.383	13.8±0.7
50.788	13.8±0.7	50.739	21.0±1.1	50.432	12.2±0.6
25.902	10.6±0.5	25.844	16.3±0.8	25.484	9.41±0.47
11.063	6.17±0.31	11.003	9.75±0.49	10.632	5.59±0.28
6.286	3.60±0.18	6.238	6.00±0.30	5.874	3.48±0.17
3.503	2.10±0.10	3.480	3.68±0.18	3.150	2.68±0.13
15.635	8.09±0.40	15.592	12.6±0.6	15.345	7.23±0.36
30.733	11.5±0.6	30.687	17.6±0.9	30.392	10.2±0.5
60.700	14.6±0.7	60.663	22.2±1.1	60.384	12.9±0.7
110.749	17.1±0.9	110.776	25.8±1.3	110.440	15.1±0.8
160.774	18.5±0.9	160.878	27.9±1.4	160.423	16.4±0.8
211.391	19.5±1.0	211.324	29.4±1.5	210.698	17.3±0.9
262.344	20.2±1.0	262.266	30.4±1.5	261.282	18.0±0.9
302.739	20.7±1.0	302.687	31.2±1.6	301.589	18.6±0.9

Table B.6: Electrical conductivity of MWCNTs coated ZnO with 5 infiltration and carbon nanotubes tubes (CNNTs); in order of data collection. The electrical conductivity is plotted as function of temperature in Figure 4.23.

T / K	σ_{el} / S m^{-1} (5 FL 3 mm (2))	T / K	σ_{el} / S m^{-1} (CNTTs)
301.982	21.0±1.1	304.131	24.4±1.2
327.095	21.3±1.1	276.312	24.1±1.2
352.271	21.6±1.1	251.576	23.8±1.2
377.156	22.0±1.1	226.367	23.4±1.2
392.111	22.4±1.1	201.739	23.0±1.2
352.334	22.2±1.1	176.381	22.4±1.1
302.008	21.5±1.1	151.355	21.7±1.1
276.231	21.1±1.1	126.790	20.9±1.0
251.235	20.7±1.0	101.628	19.8±1.0
225.918	20.3±1.0	76.255	18.3±0.9
200.959	19.9±1.0	51.897	16.1±0.8
175.650	19.4±1.0	25.892	12.3±0.6
150.171	18.8±0.9	11.176	8.45±0.42
125.212	18.1±0.9	5.566	6.07±0.30
100.186	17.2±0.9	15.803	9.74±0.49
75.176	16.0±0.8	30.730	13.4±0.7
50.095	14.2±0.7	62.231	17.1±0.9
25.065	10.9±0.6	111.181	20.1±1.0
10.065	6.45±0.32	160.897	21.8±1.1
5.117	4.04±0.20	211.097	22.9±1.2
2.291	2.95±0.15	261.024	23.7±1.2
15.032	8.40±0.42	301.381	24.3±1.2
30.052	11.8±0.6	326.192	24.7±1.2
60.073	15.0±0.8	351.216	25.4±1.3
110.364	17.5±0.9	376.025	26.5±1.3
160.341	19.0±1.0	391.058	28.3±1.4
210.569	20.1±1.0	351.264	27.8±1.4
261.137	20.8±1.0		
301.410	21.4±1.1		

Table B.7: Electrical conductivity of MWCNTs coated ZnO with 7 infiltrations; in order of data collection. The electrical conductivity is plotted as function of temperature in Figure 4.23.

T / K	σ_{el} / S m^{-1} (7 FL 2 mm)	T / K	σ_{el} / S m^{-1} (7 FL 3 mm)	T / K	σ_{el} / S m^{-1} (7 FL 3 mm (2))
302.497	49.0±2.5	302.787	40.9±2.1	302.660	32.5±1.6
327.365	49.7±2.5	327.617	41.6±2.1	327.549	32.9±1.7
352.229	50.1±2.5	352.470	42.4±2.1	352.436	33.4±1.7
377.074	50.3±2.5	377.248	43.2±2.2	377.256	34.3±1.7
392.017	51.2±2.6	392.219	44.2±2.2	392.212	36.0±1.8
352.331	50.7±2.5	352.538	43.8±2.2	352.470	36.4±1.8
302.594	49.0±2.5	302.781	42.3±2.1	302.649	35.4±1.8
277.195	48.0±2.4	277.358	41.5±2.1	277.209	34.9±1.7
252.269	47.1±2.4	252.415	40.8±2.0	252.250	34.3±1.7
226.807	46.2±2.3	226.904	40.0±2.0	226.753	33.7±1.7
201.921	45.2±2.3	202.013	39.2±2.0	201.841	33.0±1.7
176.447	44.1±2.2	176.508	38.2±1.9	176.329	32.1±1.6
151.036	42.8±2.1	151.079	37.1±1.9	125.906	29.9±1.5
126.131	41.3±2.1	126.145	35.7±1.8	100.740	28.4±1.4
100.954	39.3±2.0	100.945	33.9±1.7	75.553	26.3±1.3
75.738	36.7±1.8	75.705	31.6±1.6	50.622	23.2±1.2
50.905	32.9±1.6	50.800	28.2±1.4	25.700	17.6±0.9
26.080	25.8±1.3	25.918	21.9±1.1	10.870	10.1±0.50
11.202	15.8±0.8	11.079	13.1±0.7	6.120	6.03±0.30
6.376	9.32±0.47	6.309	8.12±0.41	3.385	3.85±0.19
3.546	5.53±0.28	3.535	5.45±0.27	15.497	13.3±0.7
15.744	20.2±1.0	15.647	16.9±0.9	30.567	19.2±1.0
30.879	27.7±1.4	30.744	23.6±1.2	60.566	24.6±1.2
60.799	34.6±1.7	60.694	29.8±1.5	110.695	29.0±1.5
110.893	40.0±2.0	110.799	34.6±1.7	160.790	31.5±1.6
160.946	43.2±2.2	160.890	37.5±1.9	211.232	33.2±1.7
211.338	45.5±2.3	211.366	39.5±2.0	262.146	34.4±1.7
262.178	47.1±2.4	262.283	40.9±2.0	302.577	35.3±1.8
302.529	48.5±2.4	302.682	42.0±2.1		

Table B.8: Seebeck coefficient of MWCNTs coated ZnO with various infiltrations and CNTTs; in order of data collection. The Seebeck coefficient is plotted as function of temperature in Figure 4.24.

T / K	S / µV K^{-1} (2 FL 2 mm)	T / K	S / µV K^{-1} (5 FL 2 mm)
302.153	7.42±0.37	302.769	3.64±0.18
327.261	7.17±0.36	327.653	4.14±0.21
352.449	8.70±0.43	352.491	3.77±0.19
377.275	9.41±0.47	377.340	2.81±0.14
392.255	7.05±0.35	392.247	2.23±0.11
352.510	6.15±0.31	352.591	1.22±0.06
302.192	4.75±0.24	302.843	1.09±0.05
T / K	S / µV K^{-1} (7 FL 2 mm)	T / K	S / µV K^{-1} (CNTTs)
302.497	5.26±0.26	301.381	16.2±0.8
327.365	5.91±0.30	326.192	17.0±0.9
352.229	6.36±0.32	351.216	21.2±1.1
377.074	5.66±0.28	376.025	17.3±0.9
392.017	5.19±0.26	391.058	14.1±0.7
352.331	4.16±0.21	351.264	13.1±0.7
302.594	2.70±0.13	301.605	11.9±0.6

Table B.9: Thermal conductivity of MWCNTs coated ZnO with 2 infiltrations; in order of data collection. The thermal conductivity is plotted as function of temperature in Figure 4.25.

T / K	κ / mW m^{-1} K^{-1} (2 FL 2 mm)	T / K	κ / mW m^{-1} K^{-1} (2 FL 3 mm)	T / K	κ / mW m^{-1} K^{-1} (2 FL 3 mm (2))
301.603	238±20	301.987	226±30	301.708	283±32
302.153	237±20	326.877	221±30	326.641	272±37
327.261	233±24	351.749	217±34	351.554	265±43
352.449	230±28	376.572	217±39	376.463	262±48
377.275	229±32	391.579	219±44	391.421	264±52
392.255	232±34	351.797	217±47	351.602	273±43
352.510	228±28	302.001	224±39	301.712	288±32
302.192	234±20	276.673	232±29	276.414	296±27
276.345	239±17	251.719	239±25	251.426	311±22
251.364	245±14	226.326	247±20	226.077	329±17
226.022	251±13	201.384	256±16	201.090	347±17
201.066	258±13	175.981	266±13	175.765	373±19
175.732	267±13	150.677	272±14	150.233	398±20
150.204	271±14	125.720	275±14	125.264	421±21
125.247	274±14	100.597	269±13	100.276	436±22
100.206	266±13	75.439	245±12	75.265	431±22
75.184	242±12	50.504	190±9	50.105	356±18
50.103	186±9	25.580	86.4±4.3	25.060	167±8
25.077	84.8±4.2	10.782	20.3±1.0	10.058	30.3±1.5
10.072	17.4±0.9	6.058	7.37±0.37	5.112	6.54±0.33
5.127	4.28±0.21	3.324	3.09±0.15	2.309	1.31±0.07
2.307	0.932±0.047	15.426	37.5±1.9	15.028	68.4±3.4
15.036	37.2±1.9	30.463	109±5	30.041	209±10
30.056	108±5	60.446	216±11	60.028	384±19
60.079	218±18	110.549	268±13	110.206	426±21
110.391	273±14	160.571	262±13	160.242	382±19
160.381	273±14	210.897	247±12	210.630	337±17
210.639	256±13	261.603	234±13	261.307	300±24
261.232	241±15	301.921	220±22	301.655	281±32
301.548	231±20				

Table B.10: Thermal conductivity of MWCNTs coated ZnO with 5 infiltrations; in order of data collection. The thermal conductivity is plotted as function of temperature in Figure 4.25.

T / K	κ / mW m^{-1} K^{-1} (5 FL 2 mm)	T / K	κ / mW m^{-1} K^{-1} (5 Fl 3 mm)	T / K	κ / mW m^{-1} K^{-1} (5 FL 3 mm (2))
302.769	339±22	302.779	408±37	301.649	311±34
327.653	334±26	327.637	401±44	326.573	303±40
352.491	336±30	352.463	398±513	351.486	298±46
377.340	335±35	377.287	397±58	376.410	296±52
392.247	337±38	392.190	402±63	391.377	298±56
352.591	329±30	352.515	400±51	351.549	303±46
302.843	324±21	302.742	409±37	301.684	312±34
277.410	325±18	277.301	418±30	276.392	318±28
252.460	324±16	252.345	427±24	251.404	324±22
226.942	326±16	226.826	438±22	226.068	331±18
202.036	326±16	201.914	448±22	201.112	338±17
176.508	326±16	176.401	458±23	175.787	346±17
151.070	321±16	150.999	463±23	150.542	348±17
126.126	310±15	126.061	460±23	125.585	345±17
100.919	285±14	100.867	439±22	100.493	329±16
75.702	241±12	75.645	386±19	75.383	293±15
50.788	172±9	50.739	287±14	50.432	223±11
25.902	75.9±3.8	25.844	130±7	25.484	103±5
11.063	20.4±1.0	11.003	34.4±1.7	10.632	25.3±1.3
6.286	8.41±0.42	6.238	13.8±0.7	5.874	9.05±0.45
3.503	3.85±0.19	3.480	6.19±0.30	3.150	3.66±0.18
15.635	34.3±1.7	15.592	58.9±2.9	15.345	46.6±2.3
30.733	95.1±4.8	30.687	163±8	30.392	130±6
60.700	202±10	60.663	334±17	60.384	256±13
110.749	294±15	110.776	450±23	110.440	336±17
160.774	319±16	160.878	461±23	160.423	345±17
211.391	321±16	211.324	441±22	210.698	333±17
262.344	322±16	262.266	420±27	261.282	317±25
302.739	320±21	302.687	406±37	301.589	307±34

Table B.11: Thermal conductivity of MWCNTs coated ZnO with 5 infiltration and carbon nanotubes tubes (CNTTs); in order of data collection. The thermal conductivity is plotted as function of temperature in Figure 4.25.

T / K	κ / mW m^{-1} K^{-1} (5 FL 3 mm (3))	T / K	κ / mW m^{-1} K^{-1} (CNTTs)
301.982	364±35	304.131	76.1±21.2
327.095	354±42	276.312	66.9±17.1
352.271	352±48	251.576	59.1±14.2
377.156	344±55	226.367	52.7±11.5
392.111	346±59	201.739	46.8±9.2
352.334	350±48	176.381	41.2±7.0
302.008	363±35	151.355	35.7±5.1
276.231	375±29	126.790	30.1±3.5
251.235	385±23	101.628	24.2±2.1
225.918	399±20	76.255	18.0±1.1
200.959	410±20	51.897	11.6±0.6
175.650	424±21	25.892	5.18±0.26
150.171	433±22	11.176	2.01±0.10
125.212	435±22	5.566	0.831±0.042
100.186	422±21	15.803	2.89±0.14
75.176	380±19	30.730	6.23±0.20
50.095	289±14	111.181	25.0±2.6
25.065	128±6	160.897	34.6±5.6
10.065	26.7±1.3	211.097	46.4±9.8
5.117	6.61±0.33	261.024	59.3±14.9
2.291	1.40±0.07	301.381	71.5±19.8
15.032	56.5±2.8	326.192	80.8±23.3
30.052	164±8	351.216	92.9±27.5
60.073	334±17	376.025	109±33
110.364	432±22	391.058	119±36
160.341	431±22	351.264	98.1±28.5
210.569	405±20		
261.137	378±25		
301.410	360±35		

Table B.12: Thermal conductivity of MWCNTs coated ZnO with 7 infiltrations; in order of data collection. The thermal conductivity is plotted as function of temperature in Figure 4.25.

T / K	κ / mW m^{-1} K^{-1} (7 FL 2 mm)	T / K	κ / mW m^{-1} K^{-1} (7 FL 3 mm)	T / K	κ / mW m^{-1} K^{-1} (7 FL 3 mm (2))
302.497	432±25	302.787	454±42	302.660	459±41
327.365	430±29	327.617	451±50	327.549	450±48
352.229	424±34	352.470	452±58	352.436	441±56
377.074	415±38	377.248	454±66	377.256	436±64
392.017	413±41	392.219	460±72	392.212	440±68
352.331	397±32	352.538	450±57	352.470	439±55
302.594	385±23	302.781	455±42	302.649	452±40
277.195	381±19	277.358	462±34	277.209	464±33
252.269	375±19	252.415	467±27	252.250	474±27
226.807	370±19	226.904	474±24	226.753	487±24
201.921	364±18	202.013	477±24	201.841	498±25
176.447	354±18	176.508	479±24	176.329	510±25
151.036	338±17	151.079	474±24	125.906	515±26
126.131	315±16	126.145	461±23	100.740	494±25
100.954	277±14	100.945	427±21	75.553	437±22
75.738	222±11	75.705	364±18	50.622	328±16
50.905	150±8	50.800	262±13	25.700	150±7
26.080	64.5±3.2	25.918	116±6	10.870	38.5±1.9
11.202	18.4±0.9	11.079	31.4±1.6	6.120	14.9±0.8
6.376	8.02±0.40	6.309	13.1±0.7	3.385	6.52±0.33
3.546	3.79±0.19	3.535	6.02±0.30	15.497	67.5±3.4
15.744	29.8±1.5	15.647	52.7±2.6	30.567	188±9
30.879	80.5±4.0	30.744	145±7	60.566	381±19
60.799	181±9	60.694	308±15	110.695	506±25
110.893	290±14	110.799	442±22	160.790	515±26
160.946	337±17	160.890	471±24	211.232	491±25
211.338	358±18	211.366	473±24	262.146	466±29
262.178	372±19	262.283	468±30	302.577	450±40
302.529	379±23	302.682	458±42		

Appendix C

Thermoelectric Properties of XYZ_2 Compounds

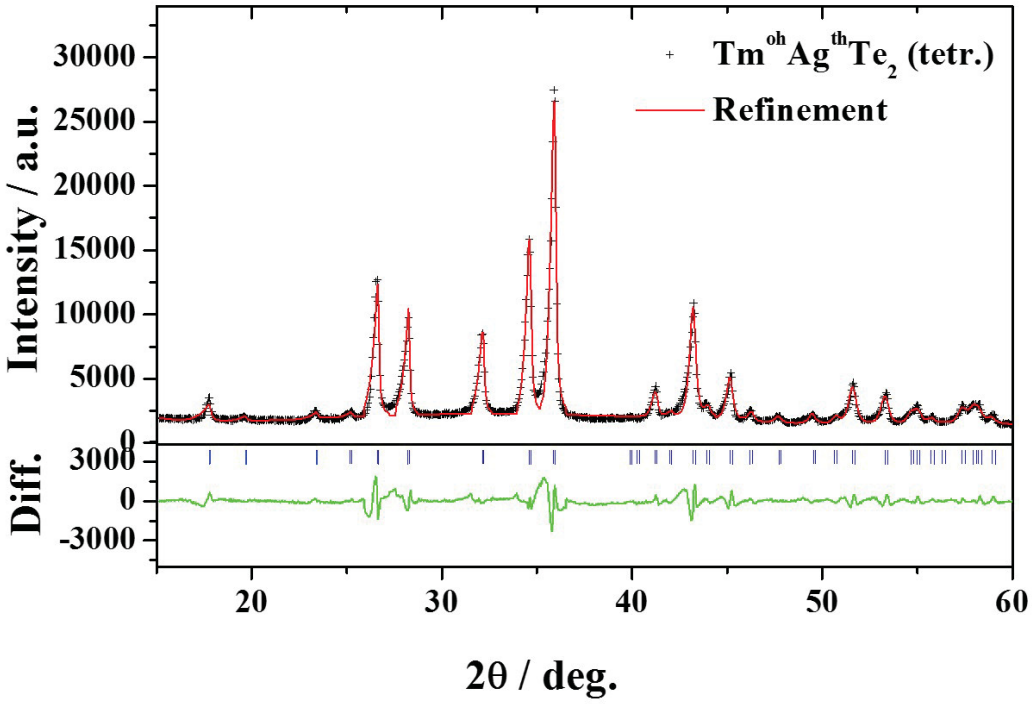

Figure C.1: Le Bail refined PXRD pattern of tetragonal $Tm^{oh}Ag^{th}Te_2$ (see Section 5.1). Blue ticks mark the calculated position of the reflections. Refined data are given in Table C.1.

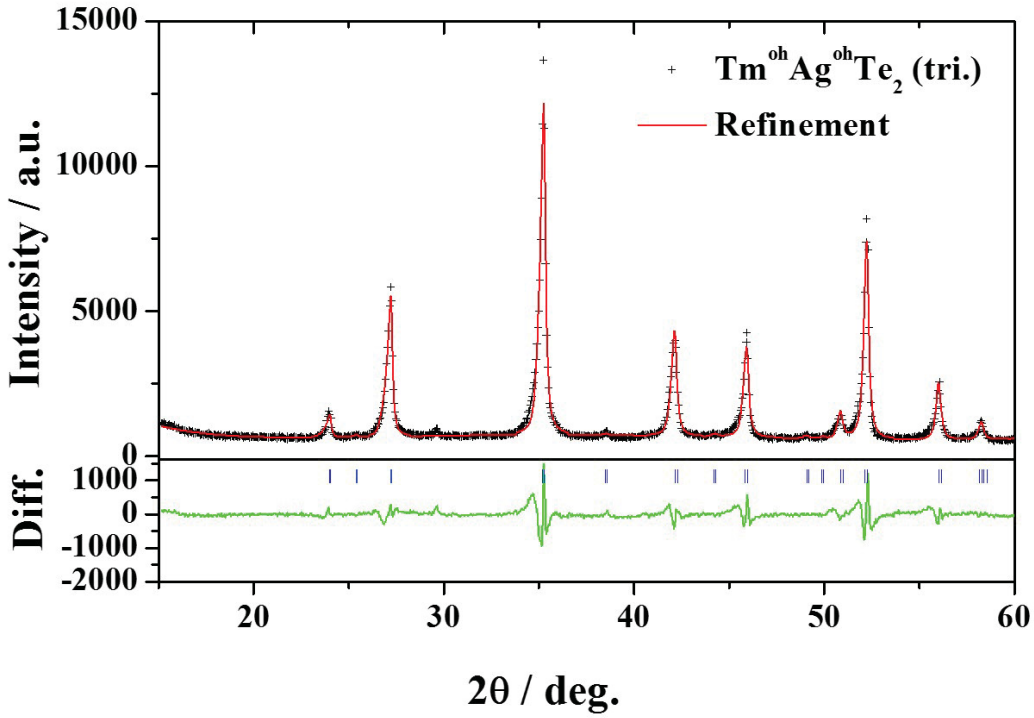

Figure C.2: Le Bail refined PXRD pattern of trigonal $Tm^{oh}Ag^{oh}Te_2$ (see Section 5.1). Blue ticks mark the calculated position of the reflections. Refined data are given in Table C.1.

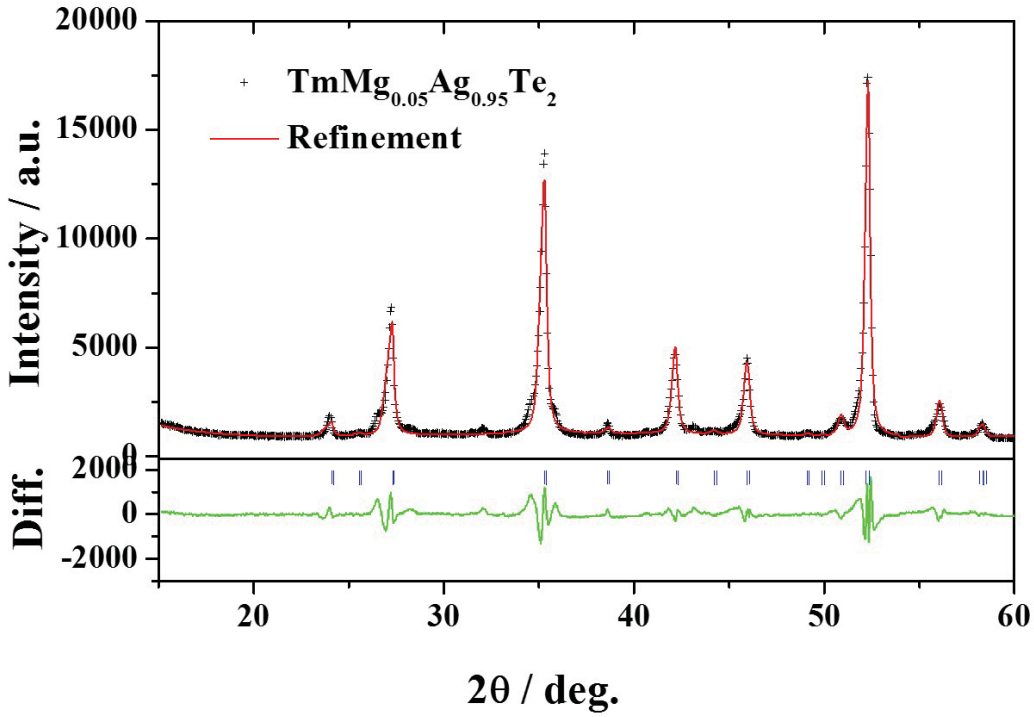

Figure C.3: Le Bail refined PXRD pattern of trigonal $TmMg_{0.05}Ag_{0.95}Te_2$ (see Section 5.1). Blue ticks mark the calculated position of the reflections. Refined data are given in Table C.1.

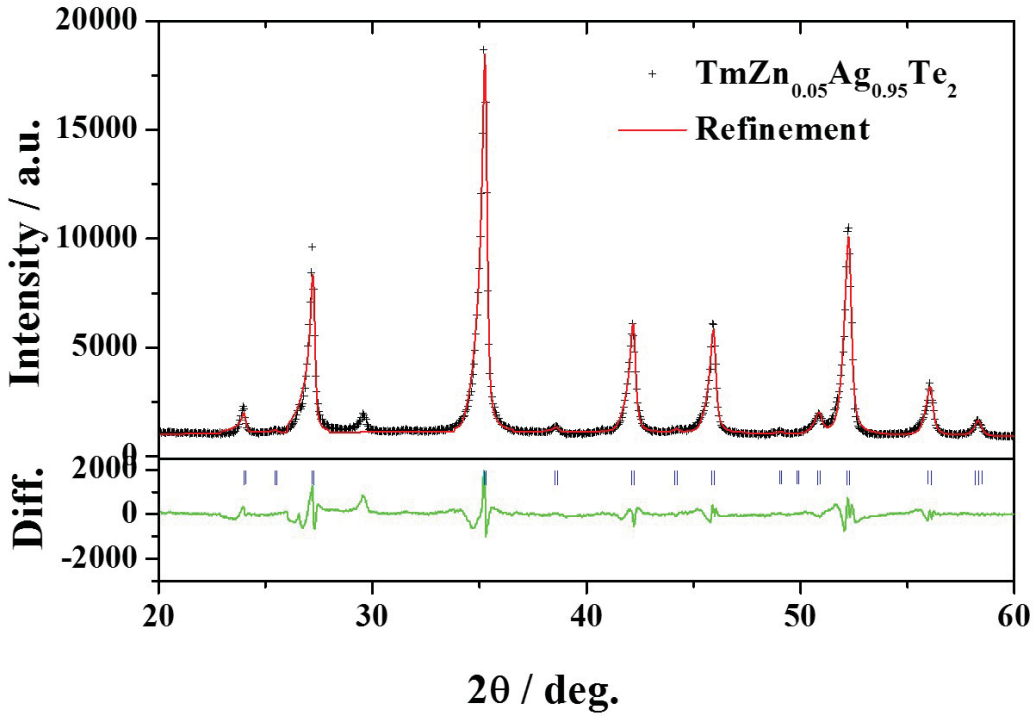

Figure C.4: Le Bail refined PXRD pattern of trigonal $TmZn_{0.05}Ag_{0.95}Te_2$ (see Section 5.1). Blue ticks mark the calculated position of the reflections. Refined data are given in Table C.1.

Table C.1: Refined PXRD data for $TmAgTe_2$ parent compounds and extrinsically doped compounds using the Le Bail method. The diffractograms of the $TmAgTe_2$ compounds are shown in Figures C.1-C.4.

Parameter	$Tm^{oh}Ag^{th}Te_2$	$Tm^{oh}Ag^{oh}Te_2$
Space group	$P\bar{4}2_1m$ (No. 113)	$P\bar{3}m1$ (No. 164)
a / Å	7.091	4.286
b / Å	7.091	4.286
c / Å	4.526	7.016
α / °	90.000	90.000
β / °	90.000	90.000
γ / °	90.000	120.000
Number of molecules per unit cell, Z	2	1
Volume / Å^3	228	112
Calculated density / g cm^{-3}	7.75	7.89
R_p	6.99	7.54
R_{wp}	9.47	9.75
χ^2	25.19	9.73
Parameter	$TmMg_{0.05}Ag_{0.95}Te_2$	$TmMg_{0.05}Ag_{0.95}Te_2$
Space group	$P\bar{3}m1$ (No. 164)	$P\bar{3}m1$ (No. 164)
a / Å	4.305	4.298
b / Å	4.305	4.298
c / Å	7.037	7.021
α / °	90.000	90.000
β / °	90.000	90.000
γ / °	120.000	120.000
Number of molecules per unit cell, Z	1	1
Volume / Å^3	113	112
Calculated density / g cm^{-3}	7.76	7.85
R_p	7.88	6.20
R_{wp}	10.71	8.08
χ^2	17.32	11.44

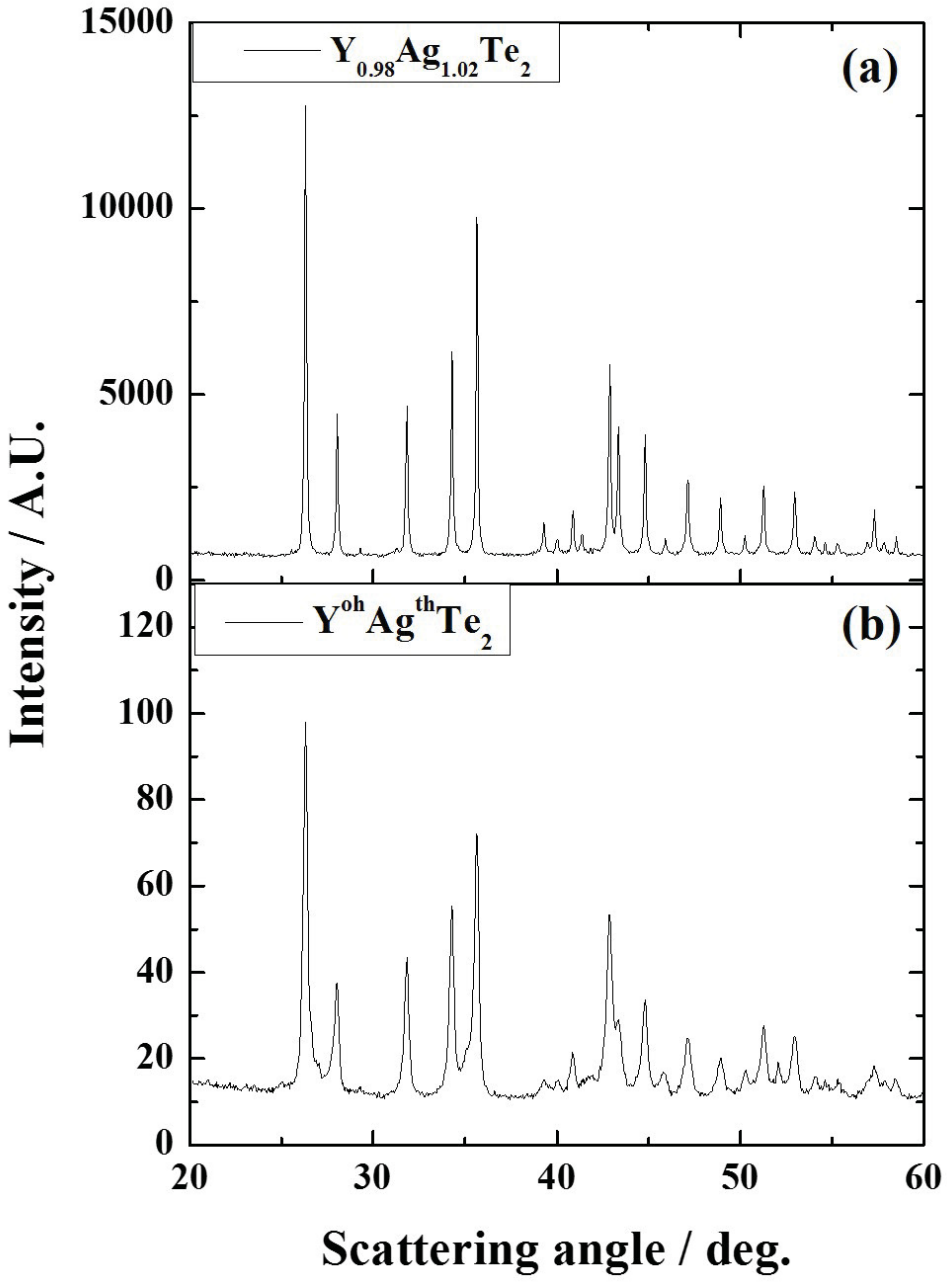

Figure C.5: PXRD pattern of (a) $Y_{0.98}Ag_{1.02}Te_{1.98}$, and (b) $Y^{oh}Ag^{th}Te_2$ in the low-temperature tetragonal phase. The crystallinity of $YAgTe_2$ was enhanced with intrinsic doping as judged by the sharpness of the peaks.

.

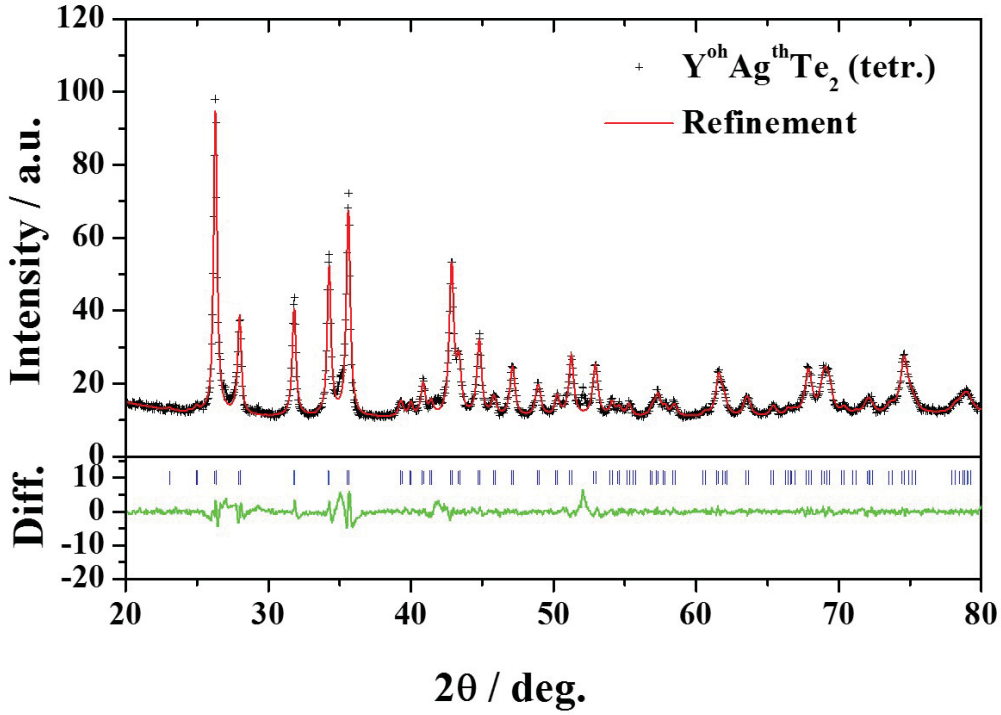

Figure C.6: Le Bail refined PXRD pattern of the low-temperature phase of $YAgTe_2$ (see Section 5.1). Blue ticks mark the calculated position of the reflections. Refined data are given in Table C.2.

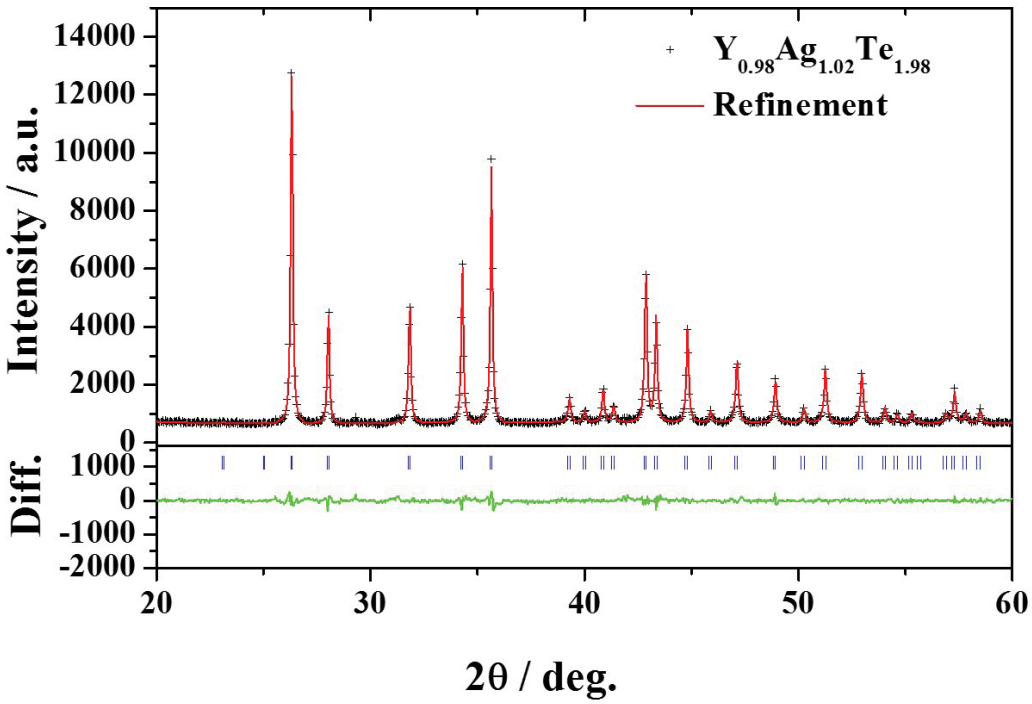

Figure C.7: Le Bail refined PXRD pattern of the low-temperature phase of $Y_{0.98}Ag_{1.02}Te_{1.98}$ (see Section 5.1). Blue ticks mark the calculated position of the reflections. Refined data are given in Table C.2.

Table C.2: Refined PXRD data for $YAgTe_2$ parent and intrinsically doped compounds using the Le Bail method. The diffractograms of PCBM powder and pellet are shown in Figure C.6 and C.7.

Parameter	$YAgTe_2$	$Y_{0.98}Ag_{1.02}Te_{1.98}$
Space group	$P\bar{4}2_1m$ (No. 113)	$P\bar{4}2_1m$ (No. 113)
a / Å	7.149	7.154
b / Å	7.149	7.154
c / Å	4.593	4.604
α / °	90.000	90.000
β / °	90.000	90.000
γ / °	90.000	90.000
Number of molecules per unit cell, Z	2	2
Volume / Å^3	235	236
Calculated density / g cm^{-3}	6.39	6.33
R_p	3.90	3.49
R_{wp}	5.69	4.57
χ^2	0.05	2.01

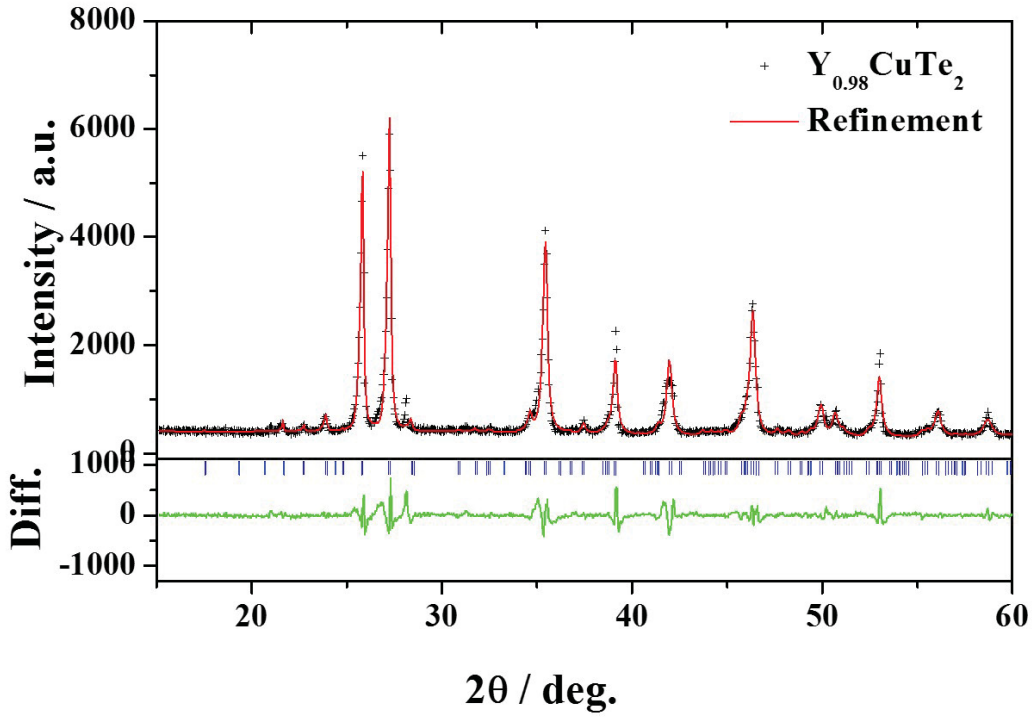

Figure C.8: Le Bail refined PXRD pattern of $Y_{0.98}CuTe_2$ (see Section 5.1). Blue ticks mark the calculated position of the reflections. Refined data are given in Table C.3.

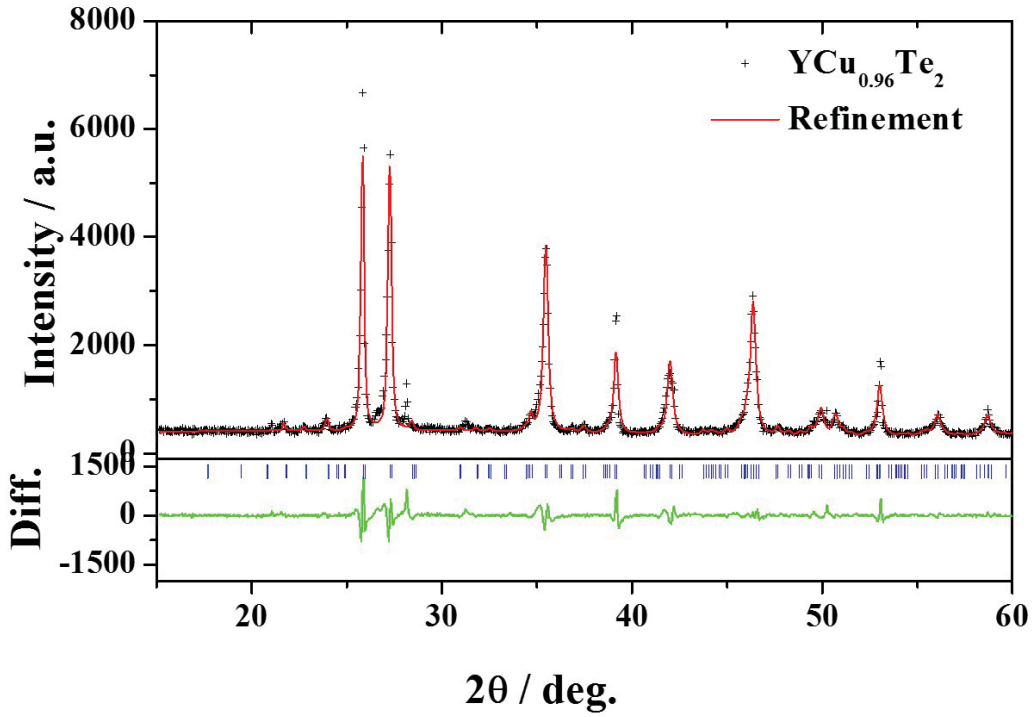

Figure C.9: Le Bail refined PXRD pattern of $YCu_{0.96}Te_2$ (see Section 5.1). Blue ticks mark the calculated position of the reflections. Refined data are given in Table C.3.

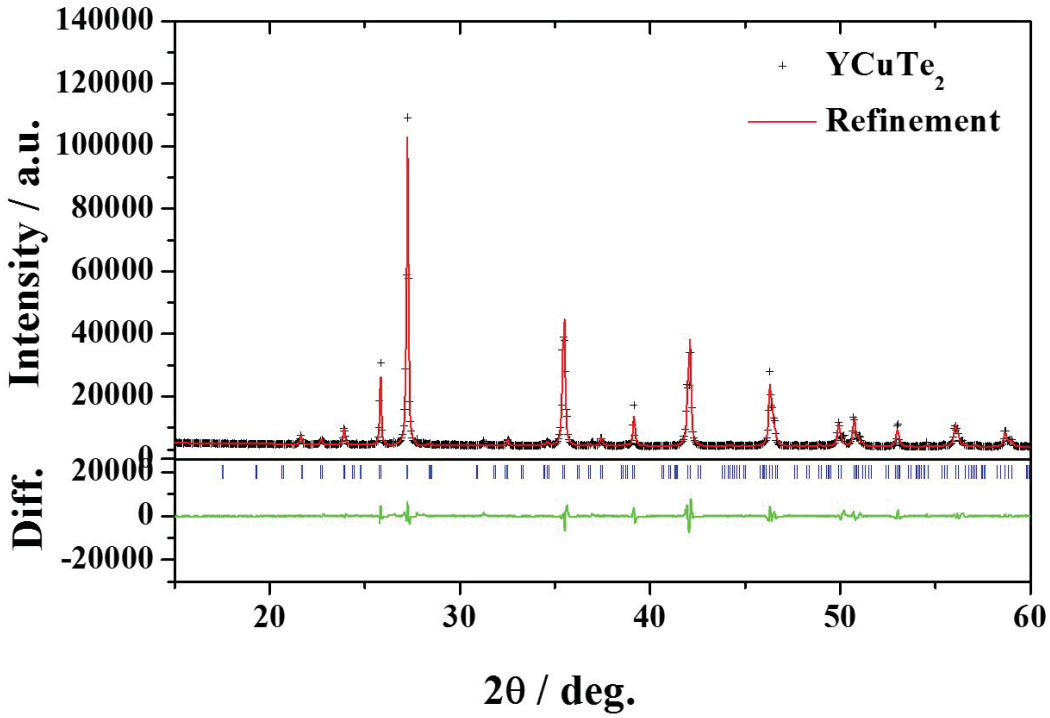

Figure C.10: Le Bail refined PXRD pattern of $YCuTe_2$ (see Section 5.1). Blue ticks mark the calculated position of the reflections. Refined data are given in Table C.3.

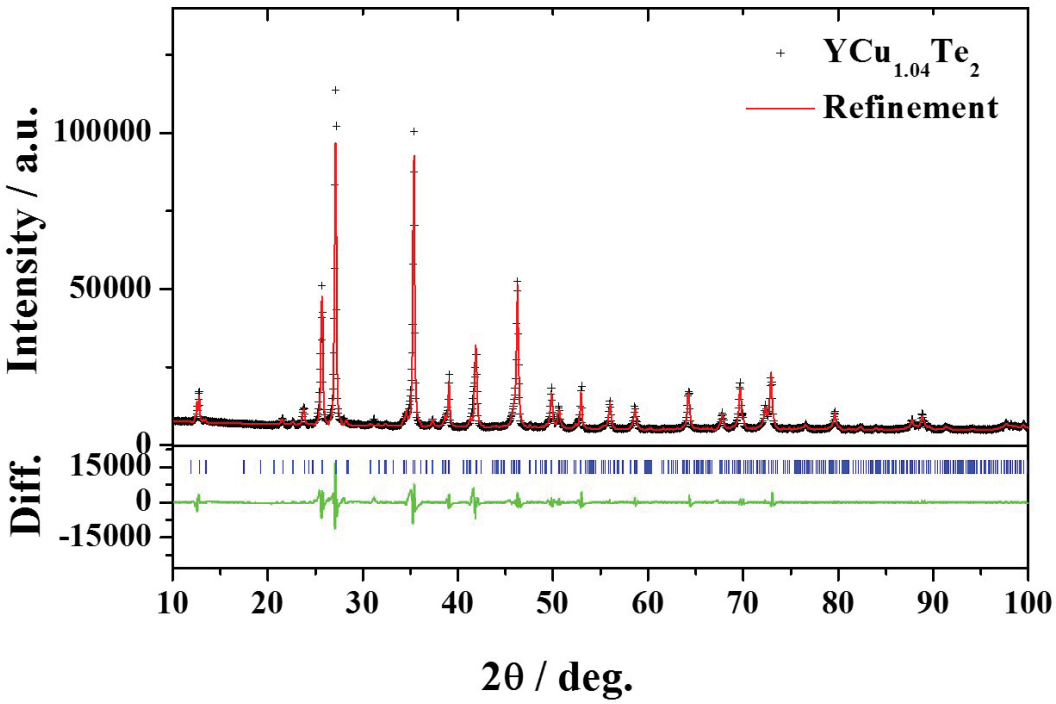

Figure C.11: Le Bail refined PXRD pattern of $YCu_{1.04}Te_2$ (see Section 5.1). Blue ticks mark the calculated position of the reflections. Refined data are given in Table C.3.

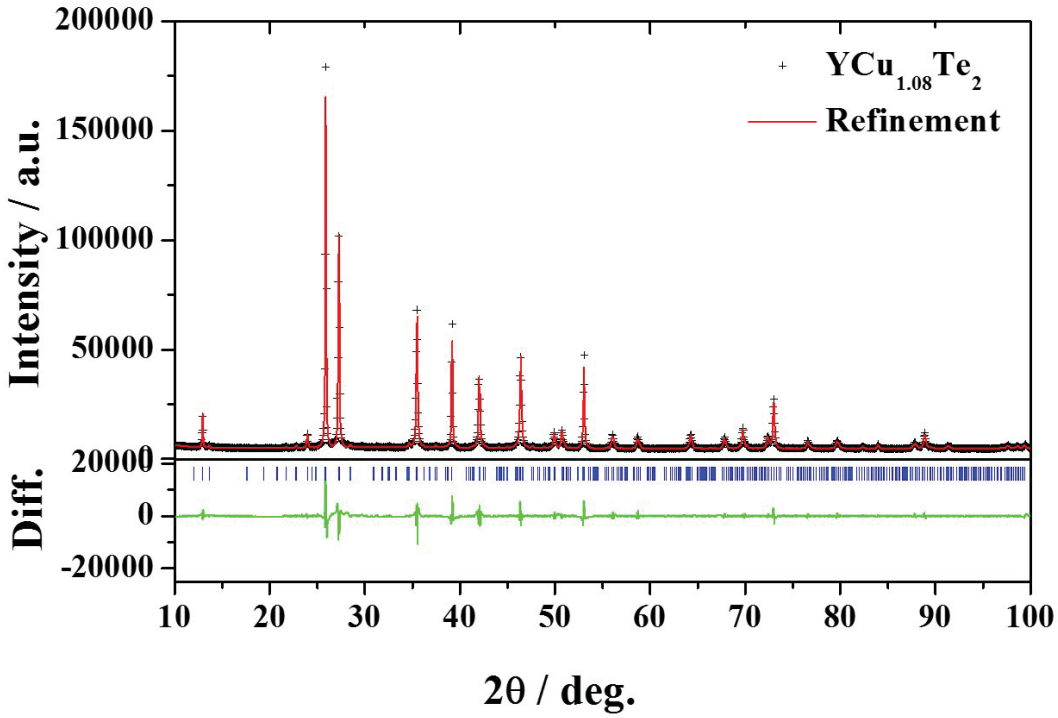

Figure C.12: Le Bail refined PXRD pattern of $YCu_{1.08}Te_2$ (see Section 5.1). Blue ticks mark the calculated position of the reflections. Refined data are given in Table C.3.

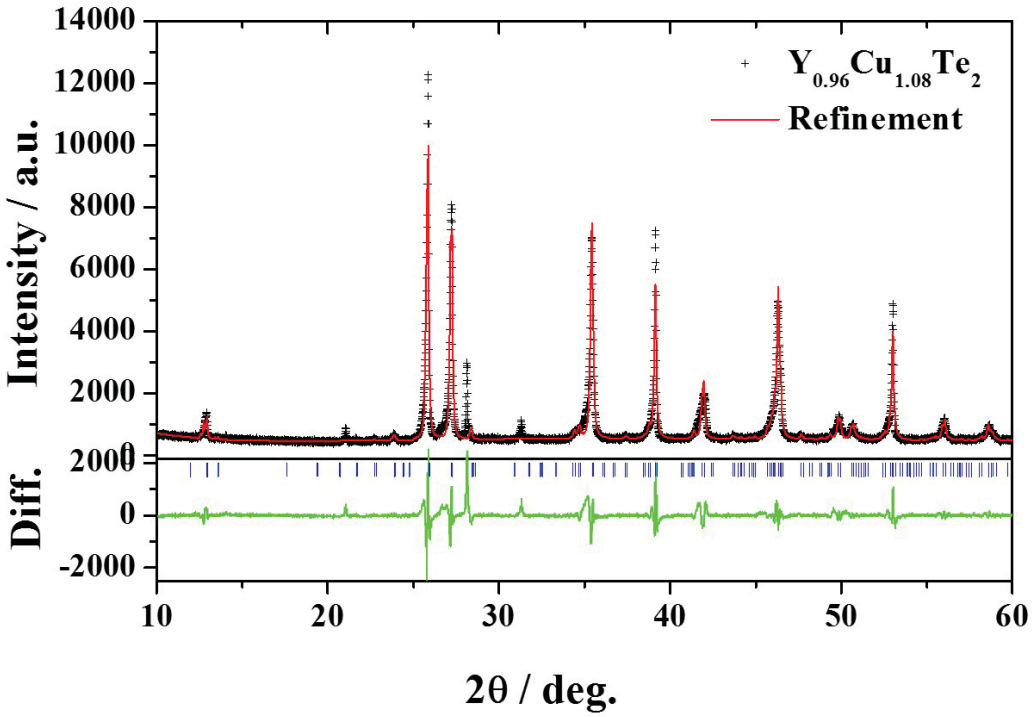

Figure C.13: Le Bail refined PXRD pattern of $Y_{0.96}Cu_{1.08}Te_2$ (see Section 5.1). Blue ticks mark the calculated position of the reflections. Refined data are given in Table C.3.

Table C.3: Refined PXRD data for $YCuTe_2$ parent compounds and intrinsically doped compounds using the Le Bail method. The diffractograms of the $YCuTe_2$ compounds are shown in Figures C.8-C.13.

Parameter	$Y^{oh}Cu^{th}Te_2$	$Y_{0.98}CuTe_2$
Space group	$P\bar{3}m1$ (No. 164)	$P\bar{3}m1$ (No. 164)
a / Å	8.606	8.628
b / Å	8.606	8.628
c / Å	13.837	13.867
α / °	90.000	90.000
β / °	90.000	90.000
γ / °	120.000	120.000
Number of molecules per unit cell, Z	8	8
Volume / Å^3	887	894
Calculated density / g cm^{-3}	6.10	6.01
R_p	4.46	7.67
R_{wp}	7.55	10.87
χ^2	30.58	6.84
Parameter	$YCu_{0.96}Te_2$	$YCu_{1.04}Te_2$
Space group	$P\bar{3}m1$ (No. 164)	$P\bar{3}m1$ (No. 164)
a / Å	8.662	8.634
b / Å	8.662	8.634
c / Å	13.922	13.865
α / °	90.000	90.000
β / °	90.000	90.000
γ / °	120.000	120.000
Number of molecules per unit cell, Z	8	8
Volume / Å^3	905	895
Calculated density / g cm^{-3}	5.94	6.00
R_p	8.82	5.00
R_{wp}	12.23	8.05
χ^2	8.81	48.68

Parameter	$YCu_{1.08}Te_2$	$Y_{0.96}Cu_{1.08}Te_2$
Space group	$P\bar{3}m1$ (No. 164)	$P\bar{3}m1$ (No. 164)
a / Å	8.629	8.649
b / Å	8.629	8.649
c / Å	13.871	13.841
α / °	90.000	90.000
β / °	90.000	90.000
γ / °	120.000	120.000
Number of molecules per unit cell, Z	8	8
Volume / Å^3	895	897
Calculated density / g cm^{-3}	6.00	5.99
R_p	3.96	9.59
R_{wp}	6.01	14.83
χ^2	23.82	16.66

C.1 Scanning Electron Microscopy and Wavelength-Dispersive Spectroscopy of $YCuTe_2$

The microstructures and compositions of all $YCuTe_2$ samples were investigated with scanning electron microscopy (SEM) (see Figure C.14) and wavelength-dispersive spectroscopy (WDS) (see Table C.4). SEM images and WDS analysis were acquired with the assistance of Dr. Chi Ma, Analytical Facility, California Institute of Technology. The SEM images indicate that $YCuTe_2$ was formed either almost as single phase or together with YTe_2 (as determined by energy-dispersive spectroscopy [EDS] function in the SEM) with YCu_xTe_{3-x} as by-products (see Figure C.14). SEM images were taken in the backscattered electron imaging mode which can provide more information concerning the composition as the number of generated backscattered secondary electrons is proportional to the average atomic number of the compound (*i.e.*, compounds with an average higher atomic number appear brighter). The formation of YCu_xTe_{3-x} was reported by Pardo and Flahaut [294] whereas YTe_2 has not been reported in the literature and was only observed by EDS.

A lower Cu content enhanced the formation of a secondary phase as shown for $YCu_{0.96}Te_2$ in Figure C.14. With increasing Cu content, the secondary phase decreased and a nearly single phase was observed for $YCu_{1.04}Te_2$ (Figure C.14 (d)) and $Y_{0.96}Cu_{1.08}Te_2$ (Figure C.14 (d)). It was also noted that the secondary phase precipitated within large grains in samples with lower Cu contents (see SEM image of $YCu_{0.96}Te_2$ in Figure C.14 (a)) whereas with increasing Cu content the secondary phase precipitated at the grain boundaries as observed for $YCu_{1.08}Te_2$ (Figure C.14 (e)).

The actual overall composition was determined by WDS as shown in Table C.4. The actual composition has higher Y content than the nominal composition at lower Cu content. With increasing Cu content, the Y content decreased resulting in Y-deficient compositions with a nominal Cu content of 1.08. All compositions except $Y_{0.96}Cu_{1.08}Te_2$ were Te-deficient and Cu-deficient compared to the nominal composition. Although it was reported for Cu chalcogenides that Cu precipitation was observed on the surfaces of the pellet after hot pressing due to the superionic behavior of Cu [358], no higher Cu concentration at the surface was detected using

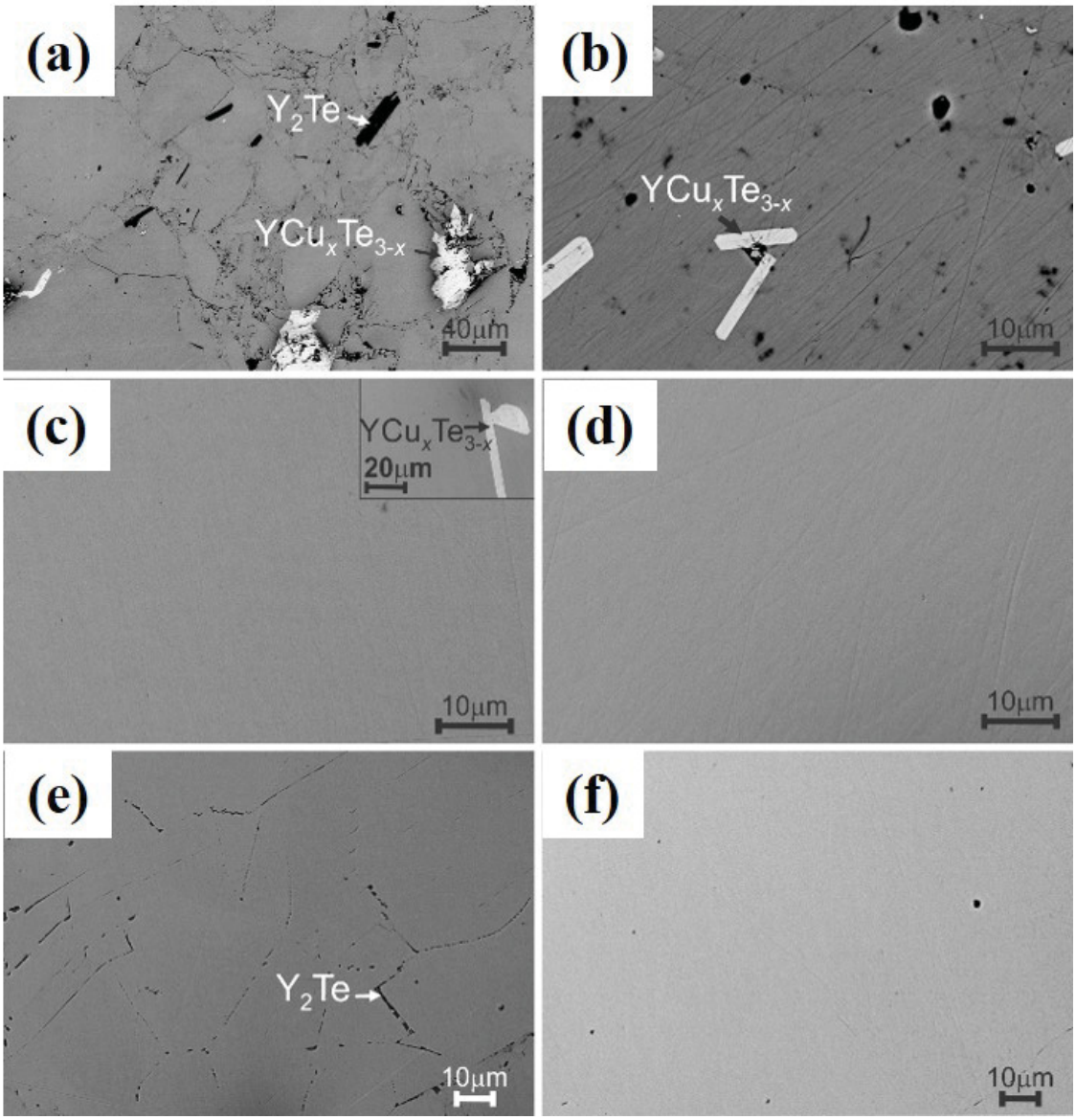

Figure C.14: Backscattering SEM images of intrinsic doped $YCuTe_2$ samples. (a) $YCu_{0.96}Te_2$, (b) $Y_{0.98}CuTe_2$, (c) $YCuTe_2$, (d) $YCu_{1.04}Te_2$, (e) $YCu_{1.08}Te_2$, and (f) $Y_{0.96}Cu_{1.08}Te_2$. YTe_2 (from EDS analysis) and YCu_xTe_{3-x} were formed as by-products which decrease with increasing Cu content. Figures from reference [292].
.

WDS. The Cu and Te content might be lower in the actual composition than in the nominal as the precursor might contain oxygen, even though oxygen was removed from Cu prior the solid-state synthesis. Thin oxide layers might also explain the removal of the carbon-coating in the sealed ampoules during the synthesis where

carbon might react with the oxygen in the material to give carbon dioxide gas.

It can be concluded that $YCuTe_2$ with low Cu content contained additional phases while the samples with higher Cu content crystallized almost as a single phase. Furthermore, the actual Cu and Te content is mostly lower than the nominal content. It is acknowledged that the actual composition is more accurate than the nominal composition to describe the compounds but for simplicity the $YCuTe_2$ compounds are labeled with the nominal composition in the following sections.

Table C.4: Nominal and actual composition of intrinsic doped $YCuTe_2$ compounds using wavelength-dispersive spectroscopy (WDS). Brackets indicate the standard uncertainty.

Nominal Composition	Actual (WDS) composition
$YCu_{0.96}Te_2$	$Y_{1.075(4)}Cu_{0.948(5)}Te_{1.974(6)}$
$Y_{0.98}CuTe_2$	$Y_{1.080(4)}Cu_{0.957(5)}Te_{1.962(6)}$
$YCuTe_2$	$Y_{1.052(4)}Cu_{0.971(5)}Te_{1.977(6)}$
$YCu_{1.04}Te_2$	$Y_{1.043(4)}Cu_{0.983(5)}Te_{1.973(6)}$
$YCu_{1.08}Te_2$	$Y_{0.971(4)}Cu_{1.031(5)}Te_{1.998(6)}$
$Y_{0.96}Cu_{1.08}Te_2$	$Y_{0.973(4)}Cu_{1.0121(5)}Te_{2.015(6)}$

Table C.5: Electrical resistivity of $TmAgTe_2$ parent compounds and extrinsically doped compounds; in order of data collection. The electrical resistivity is plotted as function of temperature in Figure 5.15 (a).

T / K	ρ_{el} / mΩ cm ($TmAgTe_2$ [tetr.])	T / K	ρ_{el} / mΩ cm ($TmAgTe_2$ [tetr.])	T / K	ρ_{el} / mΩ cm ($TmAgTe_2$ [tetr.])
676.1	232±12	478.4	1360±60	359.5	1240±60
673.0	235±12	472.8	1380±70	357.7	1230±60
668.6	243±12	467.3	1390±70	355.9	1230±60
663.1	255±13	461.9	1400±70	354.2	1220±60
656.9	271±14	456.6	1410±70	352.5	1210±60
650.4	290±15	451.5	1420±70	350.9	1210±60
643.6	312±16	446.5	1420±70	349.4	1200±60
636.8	336±17	441.7	1420±70	347.9	1200±60
630.0	365±18	437.1	1420±70	346.4	1190±60
623.3	402±20	432.6	1410±70	345.0	1190±60
616.8	439±22	428.3	1410±70	343.6	1180±60
610.4	474±24	424.1	1410±70	342.2	1180±60
604.1	509±25	420.1	1400±70	340.9	1170±60
598.0	545±27	416.2	1400±70	339.7	1170±60
591.9	583±29	412.5	1390±70	338.4	1170±60
586.0	623±31	408.9	1380±70	337.2	1160±60
580.1	664±33	405.4	1370±70	336.1	1160±60
574.3	706±35	402.0	1370±70	335.0	1160±60
568.6	748±37	398.8	1360±70	333.8	1150±60
562.8	791±40	395.7	1350±70	332.8	1150±60
557.1	835±42	392.7	1340±70	331.8	1150±60
551.5	879±44	389.7	1330±70	330.8	1140±60
545.9	923±46	386.9	1330±70	329.8	1140±60
540.2	967±48	384.2	1320±70	328.9	1140±60
534.6	1010±50	381.6	1310±70	328.0	1140±60
528.9	1050±50	379.0	1300±70	326.3	1130±60
523.3	1100±60	376.6	1300±60	324.6	1130±60
517.7	1140±60	374.2	1290±60	322.3	1120±60
512.0	1180±60	371.9	1280±60	319.6	1120±60
506.3	1220±60	369.6	1270±60	317.1	1110±60
500.7	1260±60	367.5	1270±60	314.5	1110±60
495.2	1290±60	365.4	1260±60	312.1	1110±60
489.6	1320±70	363.4	1250±60	309.4	1110±60
484.0	1340±70	361.4	1250±60	307.4	1110±60

T / K	ρ_{el} / mΩ cm ($TmAgTe_2$ [tri.)	T / K	ρ_{el} / mΩ cm ($TmMg_{0.05}Ag_{0.95}Te_2$)	T / K	ρ_{el} / mΩ cm ($TmZn_{0.05}Ag_{0.95}Te_2$)
305.55	1070±50	303.0	1110±60	303.0	758±38
331.51	667±33	316.0	1070±50	316.0	725±36
360.25	465±23	334.0	1010±50	334.0	662±33
387.16	358±18	352.0	938±47	352.0	566±28
412.43	313±16	369.0	867±43	369.0	455±23
439.95	262±13	386.0	797±40	386.0	361±18
469.20	214±11	401.0	744±37	401.0	295±15
494.66	183±9	413.0	701±35	413.0	252±13
520.53	161±8	424.0	655±33	424.0	216±11
544.98	149±7	434.0	622±31	434.0	192±10
572.66	141±7	444.0	594±30	444.0	176±9
597.13	143±7	454.0	567±28	454.0	167±8
621.82	150±8	465.0	538±27	465.0	160±8
646.85	164±8	478.0	508±25	478.0	155±8
671.75	187±9	490.0	474±24	490.0	149±7
699.27	218±11	502.0	440±22	502.0	143±7
		514.0	411±21	514.0	136±7
		526.0	383±19	526.0	130±7
		539.0	357±18	539.0	124±6
		551.0	333±17	551.0	119±6
		563.0	312±16	563.0	114±6
		575.0	292±15	575.0	111±6
		587.0	274±14	587.0	108±5
		599.0	258±13	599.0	110±6
		611.0	249±12	611.0	113±6
		623.0	241±12	623.0	115±6
		635.0	231±12	635.0	118±6
		647.0	220±11	647.0	121±6
		659.0	211±11	659.0	127±6
		673.0	203±10	673.0	135±7
		686.0	194±10	686.0	145±7
		699.0	183±9	699.0	156±8

Table C.6: Hall mobility of $TmAgTe_2$ parent compounds and extrinsically doped compounds; in order of data collection. The Hall mobility is plotted as function of temperature in Figure 5.15 (b).

T / K	μ_H / cm^2 V^{-1} s^{-1} ($TmAgTe_2$ [tetr.])	T / K	μ_H / cm^2 V^{-1} s^{-1} ($TmAgTe_2$ [tetr.])	T / K	μ_H / cm^2 V^{-1} s^{-1} ($TmAgTe_2$ [tetr.])
676.1	5.9±0.3	478.4	11±1	359.5	15±1
673.0	6.1±0.3	472.8	11±1	357.7	15±1
668.6	6.3±0.3	467.3	11±1	355.9	15±1
663.1	6.3±0.3	461.9	11±1	354.2	15±1
656.9	6.7±0.3	456.6	13±1	352.5	15±1
650.4	6.9±0.3	451.5	12±1	350.9	16±1
643.6	7.2±0.4	446.5	12±1	349.4	15±1
636.8	7.4±0.4	441.7	12±1	347.9	15±1
630.0	7.5±0.4	437.1	12±1	346.4	15±1
623.3	7.8±0.4	432.6	13±1	345.0	15±1
616.8	8.1±0.4	428.3	13±1	343.6	16±1
610.4	8.5±0.4	424.1	13±1	342.2	16±1
604.1	7.7±0.4	420.1	13±1	340.9	16±1
598.0	8.9±0.4	416.2	12±1	339.7	16±1
591.9	9.1±0.5	412.5	13±1	338.4	16±1
586.0	8.8±0.4	408.9	14±1	337.2	16±1
580.1	9.1±0.5	405.4	13±1	336.1	15±1
574.3	9.1±0.5	402.0	12±1	335.0	16±1
568.6	9.4±0.5	398.8	13±1	333.8	16±1
562.8	9.3±0.5	395.7	14±1	332.8	16±1
557.1	9.6±0.5	392.7	12±1	331.8	16±1
551.5	9.5±0.5	389.7	13±1	330.8	16±1
545.9	9.1±0.5	386.9	14±1	329.8	16±1
540.2	9.4±0.5	384.2	14±1	328.9	16±1
534.6	9.3±0.5	381.6	14±1	328.0	16±1
528.9	11±1	379.0	14±1	326.3	16±1
523.3	10±1	376.6	14±1	324.6	16±1
517.7	9.9±0.5	374.2	14±1	322.3	16±1
512.0	11±1	371.9	14±1	319.6	16±1
506.3	9.9±0.5	369.6	14±1	317.1	16±1
500.7	10±1	367.5	15±1	314.5	16±1
495.2	11±1	365.4	15±1	312.1	16±1
489.6	10±1	363.4	15±1	309.4	16±1
484.0	11±1	361.4	15±1	307.4	16±1

T / K	μ_H / cm^2 V^{-1} s^{-1} ($TmAgTe_2$ [tri.)	T / K	μ_H / cm^2 V^{-1} s^{-1} ($TmMg_{0.05}Ag_{0.95}Te_2$)	T / K	μ_H / cm^2 V^{-1} s^{-1} ($TmZn_{0.05}Ag_{0.95}Te_2$)
305.55	29±1	316.0	7.6±0.4	303.0	16±1
331.51	24±1	352.0	4.8±0.2	316.0	18±1
360.25	25±1	386.0	6.3±0.3	334.0	17±1
387.16	18±1	401.0	9.8±0.5	352.0	18±1
412.43	30±2	413.0	6.5±0.3	369.0	18±1
439.95	15±1	424.0	5.8±0.3	386.0	16±1
469.20	7.5±0.4	434.0	5.9±0.3	401.0	18±1
494.66	5.8±0.3	444.0	5.9±0.3	413.0	17±1
520.53	7.9±0.4	454.0	6.6±0.3	424.0	17±1
544.98	11±1	465.0	5.8±0.3	434.0	15±1
572.66	18±1	478.0	3.3±0.2	444.0	14±1
597.13	21±1	490.0	18±1	454.0	15±1
621.82	21±1	502.0	5.5±0.3	465.0	14±1
646.85	26±1	514.0	6.3±0.3	478.0	16±1
671.75	31±2	526.0	9.9±0.5	490.0	16±1
699.27	35±2	551.0	8.9±0.4	502.0	15±1
		563.0	11±1	514.0	15±1
		575.0	8.8±0.4	526.0	15±1
		587.0	4.8±0.2	539.0	14±1
		599.0	8.9±0.4	551.0	14±1
		611.0	10±1	563.0	14±1
		623.0	9.6±0.5	575.0	11±1
		635.0	8.6±0.4	587.0	13±1
		647.0	7.7±0.4	599.0	12±1
		659.0	9.2±0.5	611.0	12±1
		673.0	8.3±0.4	623.0	11±1
		686.0	7.9±0.4	635.0	11±1
		699.0	6.2±0.3	647.0	10±1
				659.0	9.1±0.5
				673.0	8.6±0.4
				686.0	8.1±0.4
				699.0	7.3±0.4

Table C.7: Hall carrier concentration of $TmAgTe_2$ parent compounds and extrinsically doped compounds; in order of data collection. The Hall carrier concentration is plotted as function of temperature in Figure 5.15 (c).

T / K	n_H / 10^{17} h^+ cm^{-3} ($TmAgTe_2$ [tetr.])	T / K	n_H / 10^{17} h^+ cm^{-3} ($TmAgTe_2$ [tetr.])	T / K	n_H / 10^{17} h^+ cm^{-3} ($TmAgTe_2$ [tetr.])
676.1	46±2	478.4	4.3±0.2	359.5	3.3±0.2
673.0	44±2	472.8	4.2±0.2	357.7	3.3±0.2
668.6	41±2	467.3	4.0±0.2	355.9	3.4±0.2
663.1	39±2	461.9	4.0±0.2	354.2	3.5±0.2
656.9	34±2	456.6	3.5±0.2	352.5	3.5±0.2
650.4	31±2	451.5	3.8±0.2	350.9	3.3±0.2
643.6	28±1	446.5	3.7±0.2	349.4	3.4±0.2
636.8	25±1	441.7	3.7±0.2	347.9	3.4±0.2
630.0	23±1	437.1	3.8±0.2	346.4	3.5±0.2
623.3	20±1	432.6	3.5±0.2	345.0	3.5±0.2
616.8	18±1	428.3	3.4±0.2	343.6	3.3±0.2
610.4	16±1	424.1	3.5±0.2	342.2	3.4±0.2
604.1	16±1	420.1	3.6±0.2	340.9	3.3±0.2
598.0	13±1	416.2	3.7±0.2	339.7	3.3±0.2
591.9	12±1	412.5	3.6±0.2	338.4	3.5±0.2
586.0	11±1	408.9	3.3±0.2	337.2	3.3±0.2
580.1	10±1	405.4	3.4±0.2	336.1	3.5±0.2
574.3	9.8±0.5	402.0	3.7±0.2	335.0	3.5±0.2
568.6	9.0±0.5	398.8	3.6±0.2	333.8	3.4±0.2
562.8	8.5±0.4	395.7	3.4±0.2	332.8	3.4±0.2
557.1	7.8±0.4	392.7	3.9±0.2	331.8	3.5±0.2
551.5	7.6±0.4	389.7	3.5±0.2	330.8	3.5±0.2
545.9	7.5±0.4	386.9	3.4±0.2	329.8	3.4±0.2
540.2	6.9±0.3	384.2	3.5±0.2	328.9	3.4±0.2
534.6	6.6±0.3	381.6	3.5±0.2	328.0	3.5±0.2
528.9	5.6±0.3	379.0	3.4±0.2	326.3	3.4±0.2
523.3	5.5±0.3	376.6	3.5±0.2	324.6	3.4±0.2
517.7	5.6±0.3	374.2	3.5±0.2	322.3	3.6±0.2
512.0	5.0±0.3	371.9	3.4±0.2	319.6	3.6±0.2
506.3	5.3±0.3	369.6	3.4±0.2	317.1	3.5±0.2
500.7	4.9±0.2	367.5	3.3±0.2	314.5	3.4±0.2
495.2	4.3±0.2	365.4	3.4±0.2	312.1	3.6±0.2
489.6	4.6±0.2	363.4	3.5±0.2	309.4	3.6±0.2
484.0	6.3±0.3	361.4	3.4±0.2	307.4	3.6±0.2

T / K	n_H / 10^{17} h$^+$ cm^{-3} ($TmAgTe_2$ [tri.)	T / K	n_H / 10^{17} h$^+$ cm^{-3} ($TmMg_{0.05}Ag_{0.95}Te_2$)	T / K	n_H / 10^{17} h$^+$ cm^{-3} ($TmZn_{0.05}Ag_{0.95}Te_2$)
305.55	2.0±0.1	303.0	7.4±0.4	303.0	4.1±0.2
331.51	3.9±0.2	316.0	9.2±0.5	316.0	4.1±0.2
360.25	5.3±0.3	334.0	53±3	334.0	4.1±0.2
387.16	9.6±0.5	352.0	16±1	352.0	4.8±0.2
412.43	6.7±0.3	369.0	5±0.3	369.0	4.5±0.2
439.95	16±1	386.0	8.7±0.4	386.0	4.8±0.2
469.20	39±2	401.0	13±1	401.0	5.4±0.3
494.66	59±3	413.0	23±1	413.0	6.2±0.3
520.53	49±2	424.0	9.3±0.5	424.0	8.0±0.4
544.98	37±2	434.0	9.0±0.5	434.0	9.5±0.5
572.66	25±1	444.0	10±1	444.0	13±1
597.13	21±1	454.0	23±1	454.0	15±1
621.82	20±1	465.0	3.7±0.2	465.0	16±1
646.85	15±1	478.0	18±1	478.0	20±1
671.75	11±1	490.0	15±1	490.0	22±1
699.27	8.1±0.4	502.0	8.3±0.4	502.0	23±1
		514.0	7.5±0.4	514.0	26±1
		526.0	1.8±0.1	526.0	28±1
		539.0	13±0.7	539.0	29±1
		551.0	12±0.6	551.0	38±2
		563.0	37±2	563.0	34±2
		575.0	13±1	575.0	37±2
		587.0	12±1	587.0	41±2
		599.0	17±1	599.0	44±2
		611.0	16±1	611.0	48±2
		623.0	19±1	623.0	55±3
		635.0	17±1	635.0	62±3
		647.0	20±1	647.0	67±3
		659.0	22±1	659.0	70±4
		673.0	32±2	673.0	76±4
		686.0	30±2	686.0	82±4
		699.0	27±1	699.0	88±4

Table C.8: Electrical resistivity of $YAgTe_2$ and $Y_{0.98}Cu_{1.02}Te_{1.98}$; in order of data collection. The electrical resistivity is plotted as function of temperature in Figure 5.17 (a).

T / K	ρ_{el} / mΩ cm ($YAgTe_2$)	T / K	ρ_{el} / mΩ cm ($Y_{0.98}Cu_{1.02}Te_{1.98}$)
332.12	34800±1700	329.68	8890±440
361.62	20800±1000	358.55	7590±380
388.65	10100±500	386.23	6860±340
414.74	6010±300	412.19	6070±300
443.51	3520±180	443.53	5060±250
475.34	1340±70	467.58	4270±210
502.58	352±18	495.52	3360±170
529.76	223±11	519.80	2680±130
555.55	194±10	546.26	2280±110
585.04	180±9	573.76	1930±100
610.76	172±9	597.72	1660±80
637.10	159±8	625.34	1340±70
663.18	146±7	651.69	986±49
690.12	139±7	680.25	723±36
720.76	138±7	708.30	554±28
745.36	141±7	733.51	450±23
770.91	135±7	759.46	342±17
797.11	105±6	774.27	270±13

Table C.9: Hall mobility of $YAgTe_2$ and $Y_{0.98}Cu_{1.02}Te_{1.98}$; in order of data collection. The Hall mobility is plotted as function of temperature in Figure 5.17 (b).

T / K	μ_H / cm^2 V^{-1} s^{-1} ($YAgTe_2$)	T / K	μ_H / cm^2 V^{-1} s^{-1} ($Y_{0.98}Cu_{1.02}Te_{1.98}$)
305.26	-2.8±0.1	329.68	21±1
332.12	14±1	358.55	-6.3±0.3
361.62	3.6±0.2	386.23	5.7±0.3
388.65	-10±1	412.19	2.3±0.1
414.74	-12±1	443.53	-5.0±0.3
443.51	-37±2	467.58	-11±1
475.34	1.4±0.1	495.52	-15±1
502.58	-2.7±0.1	519.80	-17±1
529.76	9.9±0.5	546.26	-18±1
555.55	-15±1	573.76	-16±1
585.04	-18±1	597.72	-11±1
610.76	-9.6±0.5	625.34	-9.4±0.5
637.10	-0.81±0.04	651.69	-8.9±0.4
663.18	10±1	680.25	-5.4±0.3
690.12	19±1	708.30	-8.8±0.4
720.76	30±1	733.51	-27±1
745.36	36±2	759.46	-33±2
770.91	21±1	774.27	-47±2
797.11	13±1		

Table C.10: Hall carrier concentration of $YAgTe_2$ and $Y_{0.98}Cu_{1.02}Te_{1.98}$; in order of data collection. The Hall carrier concentration is plotted as function of temperature in Figure 5.17 (c).

T / K	n_H / 10^{17} h^+ cm^{-3} ($YAgTe_2$)	T / K	n_H / 10^{17} h^+ cm^{-3} ($Y_{0.98}Cu_{1.02}Te_{1.98}$)
305.26	-0.13±0.01	329.68	0.33±0.02
332.12	0.13±0.01	358.55	-1.3±0.1
361.62	0.82±0.04	386.23	1.6±0.1
388.65	-0.62±0.03	412.19	4.5±0.2
414.74	-0.83±0.04	443.53	-2.5±0.1
443.51	-0.48±0.02	467.58	-1.3±0.1
475.34	33±2	495.52	-1.2±0.1
502.58	-65±3	519.80	-1.4±0.1
529.76	28±1	546.26	-1.6±0.1
555.55	-22±1	573.76	-2.0±0.1
585.04	-20±1	597.72	-3.4±0.2
610.76	-38±2	625.34	-5.0±0.3
663.18	43±2	651.69	-7.1±0.4
690.12	24±1	680.25	-16±1
720.76	15±1	708.30	-13±1
745.36	12±1	733.51	-5.2±0.3
770.91	22±1	759.46	-5.6±0.3
797.11	46±2	774.27	-4.9±0.3

Table C.11: Electrical resistivity of $YCuTe_2$ parent compound and intrinsically doped compounds; in order of data collection. The electrical resistivity is plotted as function of temperature in Figure 5.18 (a).

T / K	ρ_{el} / mΩ cm ($YCuTe_2$)	T / K	ρ_{el} / mΩ cm ($YCu_{0.96}Te_2$)	T / K	ρ_{el} / mΩ cm ($YCu_{1.04}Te_2$)
300.89	5.10±0.26	300.61	6.56±0.33	299.09	4.54±0.23
320.01	5.38±0.27	319.09	6.93±0.35	320.02	4.94±0.25
347.41	5.89±0.29	341.13	7.42±0.37	347.13	5.52±0.28
370.39	6.37±0.32	364.37	7.99±0.40	368.45	6.03±0.30
395.62	7.09±0.35	385.08	8.60±0.43	392.41	6.65±0.33
425.45	8.14±0.41	409.30	9.53±0.48	415.06	7.20±0.36
452.81	8.90±0.45	432.22	10.8±0.5	437.30	7.47±0.37
481.10	9.39±0.47	452.32	11.6±0.6	457.39	7.42±0.37
508.23	10.1±0.5	473.42	12.1±0.6	478.55	7.46±0.37
531.96	10.9±0.5	493.30	12.6±0.6	499.08	7.60±0.38
559.10	11.9±0.6	516.08	13.2±0.7	522.20	7.99±0.40
584.48	13.1±0.7	538.09	13.9±0.7	544.24	8.88±0.44
609.13	14.4±0.7	558.64	14.5±0.7	568.31	10.4±0.5
634.33	15.6±0.8	581.42	15.1±0.8	592.46	11.7±0.6
658.80	16.4±0.8	602.71	15.7±0.8	615.08	12.7±0.6
685.78	17.2±0.9	624.67	16.2±0.8	637.18	13.3±0.7
707.88	17.7±0.9	644.88	16.7±0.8	658.47	13.9±0.7
732.41	17.7±0.9	665.13	17.1±0.9	682.67	14.8±0.7
755.40	17.7±0.9	686.17	17.5±0.9	702.98	15.4±0.8
775.96	17.7±0.9	708.08	17.7±0.9	724.79	15.6±0.8
799.65	17.6±0.9	734.64	17.6±0.9	748.48	15.8±0.8
		756.51	17.5±0.9	767.62	15.9±0.8
		777.19	17.4±0.9	787.42	16.1±0.8
		793.80	17.3±0.9	792.78	16.1±0.8

T / K	ρ_{el} / mΩ cm ($YCu_{1.08}Te_2$)	T / K	ρ_{el} / mΩ cm ($Y_{0.96}Cu_{1.08}Te_2$)	T / K	ρ_{el} / mΩ cm ($Y_{0.98}CuTe_2$)
297.64	4.94±0.25	297.04	4.71±0.24	298.56	6.21±0.31
309.22	5.20±0.26	308.86	4.95±0.25	317.75	6.70±0.33
323.04	5.51±0.28	321.83	5.31±0.27	338.52	7.30±0.36
337.37	5.89±0.29	337.37	5.64±0.28	363.22	7.87±0.39
351.14	6.24±0.31	350.65	6.03±0.30	383.89	8.57±0.43
365.75	6.60±0.33	365.44	6.45±0.32	409.05	9.62±0.48
379.98	6.90±0.35	380.47	6.82±0.34	433.72	11.0±0.6
393.57	7.09±0.35	394.47	7.02±0.35	455.26	11.6±0.6
406.96	7.20±0.36	408.41	7.18±0.36	477.92	12.2±0.6
419.04	7.26±0.36	421.13	7.32±0.37	499.89	12.8±0.6
432.08	7.29±0.36	434.75	7.47±0.37	523.70	13.5±0.7
445.55	7.33±0.37	449.79	7.61±0.38	547.35	14.2±0.7
457.83	7.36±0.37	462.78	7.76±0.39	569.31	14.9±0.7
470.61	7.40±0.37	475.94	7.95±0.40	593.35	15.5±0.8
483.72	7.50±0.37	489.99	8.16±0.41	616.48	16.0±0.8
497.03	7.63±0.38	503.75	8.42±0.42	640.10	16.5±0.8
510.52	7.86±0.39	518.27	8.69±0.43	662.42	17.0±0.9
523.97	8.22±0.41	532.62	8.99±0.45	684.37	17.6±0.9
537.25	8.89±0.44	546.49	9.32±0.47	707.72	18.1±0.9
550.53	9.80±0.49	560.49	9.77±0.49	730.50	18.1±0.9
565.78	10.9±0.5	576.45	10.6±0.5	758.55	18.1±0.9
579.69	11.7±0.6	590.99	11.4±0.6	781.99	18.1±0.9
593.19	12.4±0.6	605.22	12.2±0.6	803.91	17.8±0.9
605.78	12.9±0.6	618.50	12.7±0.6	821.36	17.5±0.9
618.53	13.3±0.7	632.00	13.2±0.7		
633.74	13.8±0.7	648.05	13.7±0.7		
646.00	14.1±0.8	661.21	14.1±0.7		
658.82	14.6±0.7	674.82	14.6±0.7		
671.62	15.1±0.8	688.54	15.1±0.8		
684.81	15.7±0.8	702.90	15.5±0.8		
699.42	15.9±0.8	719.50	15.6±0.8		
710.89	16.0±0.8	732.07	15.7±0.8		
723.26	16.1±0.8	745.05	15.8±0.8		
735.00	16.2±0.8	757.41	15.9±0.8		
747.02	16.3±0.8	769.49	16.0±0.8		
761.11	16.5±0.8	784.25	16.3±0.8		
774.84	16.8±0.8	798.69	16.4±0.8		
787.83	16.9±0.9	812.62	16.6±0.8		
792.93	17.2±0.9	817.56	16.9±0.8		

Table C.12: Hall mobility of $YCuTe_2$ parent compound and intrinsically doped compounds; in order of data collection. The Hall mobility is plotted as function of temperature in Figure 5.18 (b).

T / K	μ_H / cm^2 V^{-1} s^{-1} ($YCuTe_2$)	T / K	μ_H / cm^2 V^{-1} s^{-1} ($YCu_{0.96}Te_2$)	T / K	μ_H / cm^2 V^{-1} s^{-1} ($YCu_{1.04}Te_2$)
300.89	68±3	300.61	61±3.	299.09	58±3
320.01	63±3	319.09	58±3	320.02	53±3
347.41	57±3	341.13	52±3	347.13	46±2
370.39	51±3	364.37	48±2	368.45	41±2
395.62	45±2	385.08	45±2	392.41	36±2
425.45	31±2	409.30	40±2	415.06	29±1
452.81	28±1	432.22	32±2	437.30	28±1
481.10	27±1	452.32	30±2	457.39	27±1
508.23	26±1	473.42	29±1	478.55	26±1
531.96	24±1	493.30	27±1	499.08	25±1
559.10	23±1	516.08	26±1	522.20	25±1
584.48	22±1	538.09	24±1	544.24	25±1
609.13	19±1	558.64	23±1	568.31	22±1
634.33	17±1	581.42	22±1	592.46	19±1
658.80	16±1	602.71	21±1	615.08	18±1
685.78	15±1	624.67	19±1	637.18	17±1
707.88	14±1	644.88	16±1	658.47	18±1
732.41	13±1	686.17	14±1	682.67	16±1
755.40	12±1	708.08	14±1	702.98	14±1
775.96	11±1	756.51	12±1	724.79	13±1
799.65	11±1	777.19	12±1	748.48	12±1
		793.80	14±1	767.62	12±1
				787.42	14±1
				792.78	12±1

T / K	μ_H / cm^2 V^{-1} s^{-1} ($YCu_{1.08}Te_2$)	T / K	μ_H / cm^2 V^{-1} s^{-1} ($Y_{0.96}Cu_{1.08}Te_2$)	T / K	μ_H / cm^2 V^{-1} s^{-1} ($Y_{0.98}CuTe_2$)
297.64	43±2	297.04	50±3	298.56	55±3
309.22	40±2	308.86	48±2	317.75	62±3
323.04	38±2	321.83	43±2	338.52	42±2
337.37	35±2	337.37	41±2	363.22	43±2
351.14	32±2	350.65	38±2	383.89	43±2
365.75	30±2	365.44	28±1	409.05	36±2
379.98	28±1	380.47	29±1	433.72	30±2
393.57	27±1	394.47	26±1	455.26	28±1
406.96	26±1	421.13	28±1	477.92	27±1
419.04	25±1	434.75	27±1	499.89	26±1
432.08	24±1	449.79	24±1	523.70	24±1
445.55	24±1	462.78	25±1	547.35	22±1
457.83	23±1	475.94	24±1	569.31	22±1
470.61	22±1	489.99	23±1	593.35	19±1
483.72	22±1	503.75	20±1	616.48	18±1
497.03	22±1	518.27	21±1	640.10	18±1
510.52	21±1	532.62	20±1	662.42	18±1
523.97	21±1	546.49	19±1	707.72	15±1
537.25	20±1	560.49	19±1	730.50	14±1
550.53	19±1	576.45	18±1	758.55	13±1
565.78	18±1	590.99	17±1	781.99	10±1
579.69	17±1	605.22	16±1	803.91	11±1
593.19	16±1	618.50	15±1	821.36	12±1
605.78	15±1	632.00	15±1		
618.53	15±1	648.05	15±1		
633.74	14±1	661.21	15±1		
646.00	14±1	674.82	16±1		
658.82	14±1	688.54	15±1		
671.62	14±1	702.90	15±1		
684.81	14±1	719.50	14±1		
699.42	12±1	732.07	14±1		
710.89	12±1	745.05	14±1		
723.26	11±1	757.41	14±1		
735.00	11±1	769.49	13±1		
747.02	11±1	784.25	14±1		
761.11	13±1	798.69	13±1		
774.84	13±1	812.62	11±1		
787.83	15±1	817.56	10±1		
792.93	13±1				

Table C.13: Hall carrier concentration of $YCuTe_2$ parent compound and intrinsically doped compounds; in order of data collection. The Hall carrier concentration is plotted as function of temperature in Figure 5.18 (c).

T / K	n_H / 10^{19} h^+ cm^{-3} ($YCuTe_2$)	T / K	n_H / 10^{19} h^+ cm^{-3} ($YCu_{0.96}Te_2$)	T / K	n_H / 10^{19} h^+ cm^{-3} ($YCu_{1.04}Te_2$)
300.89	1.8±0.1	300.61	1.6±0.1	299.09	2.4±0.1
320.01	1.8±0.1	319.09	1.6±0.1	320.02	2.4±0.1
347.41	1.9±0.1	341.13	1.6±0.1	347.13	2.5±0.1
370.39	1.9±0.1	364.37	1.6±0.1	368.45	2.5±0.1
395.62	2.0±0.1	385.08	1.6±0.1	392.41	2.6±0.1
425.45	2.5±0.1	409.30	1.6±0.1	415.06	3.0±0.2
452.81	2.5±0.1	432.22	1.8±0.1	437.30	3.0±0.2
481.10	2.4±0.1	452.32	1.8±0.1	457.39	3.1±0.2
508.23	2.4±0.1	473.42	1.8±0.1	478.55	3.2±0.2
531.96	2.4±0.1	493.30	1.8±0.1	499.08	3.3±0.2
559.10	2.3±0.1	516.08	1.8±0.1	522.20	3.2±0.2
584.48	2.2±0.1	538.09	1.9±0.1	544.24	2.8±0.1
609.13	2.2±0.1	558.64	1.9±0.1	568.31	2.8±0.1
634.33	2.3±0.1	581.42	1.9±0.1	592.46	2.8±0.1
658.80	2.4±0.1	602.71	1.9±0.1	615.08	2.8±0.1
685.78	2.5±0.1	624.67	2.0±0.1	637.18	2.8±0.1
707.88	2.6±0.1	644.88	2.3±0.1	658.47	2.6±0.1
732.41	2.8±0.1	686.17	2.6±0.1	682.67	2.7±0.1
755.40	3.0±0.2	708.08	2.6±0.1	702.98	2.9±0.2
775.96	3.3±0.2	756.51	3.0±0.2	724.79	3.1±0.2
799.65	3.2±0.2	777.19	3.1±0.2	748.48	3.4±0.2
		793.80	2.7±0.1	767.62	3.2±0.2
				787.42	2.8±0.1
				792.78	3.1±0.2

T / K	n_H / 10^{19} h$^+$ cm^{-3} ($YCu_{1.08}Te_2$)	T / K	n_H / 10^{19} h$^+$ cm^{-3} ($Y_{0.96}Cu_{1.08}Te_2$)	T / K	n_H / 10^{19} h$^+$ cm^{-3} ($Y_{0.98}CuTe_2$)
297.64	3.0±0.2	297.04	2.6±0.1	298.56	1.8±0.1
309.22	3.0±0.2	308.86	2.6±0.1	317.75	1.5±0.1
323.04	3.0±0.2	321.83	2.7±0.1	338.52	2.1±0.1
337.37	3.1±0.2	337.37	2.7±0.1	363.22	1.9±0.1
351.14	3.2±0.2	350.65	2.7±0.1	383.89	1.7±0.1
365.75	3.2±0.2	365.44	3.5±0.2	409.05	1.8±0.1
379.98	3.3±0.2	380.47	3.1±0.2	433.72	1.9±0.1
393.57	3.3±0.2	394.47	3.4±0.2	455.26	1.9±0.1
406.96	3.4±0.2	421.13	3.1±0.2	477.92	1.9±0.1
419.04	3.4±0.2	434.75	3.1±0.2	499.89	1.9±0.1
432.08	3.6±0.2	449.79	3.4±0.2	523.70	2.0±0.1
445.55	3.6±0.2	462.78	3.2±0.2	547.35	2.0±0.1
457.83	3.6±0.2	475.94	3.2±0.2	569.31	2.0±0.1
470.61	3.8±0.2	489.99	3.3±0.2	593.35	2.1±0.1
483.72	3.8±0.2	503.75	3.7±0.2	616.48	2.2±0.1
497.03	3.8±0.2	518.27	3.4±0.2	640.10	2.2±0.1
510.52	3.8±0.2	532.62	3.5±0.2	662.42	2.1±0.1
523.97	3.6±0.2	546.49	3.5±0.2	707.72	2.4±0.1
537.25	3.5±0.2	560.49	3.4±0.2	730.50	2.4±0.1
550.53	3.3±0.2	576.45	3.2±0.2	758.55	2.7±0.1
565.78	3.2±0.2	590.99	3.2±0.2	781.99	3.3±0.2
579.69	3.2±0.2	605.22	3.3±0.2	803.91	3.1±0.2
593.19	3.1±0.2	618.50	3.2±0.2	821.36	2.9±0.2
605.78	3.3±0.2	632.00	3.1±0.2		
618.53	3.2±0.2	648.05	3.1±0.2		
633.74	3.3±0.2	661.21	2.9±0.1		
646.00	3.2±0.2	674.82	2.8±0.1		
658.82	3.0±0.2	688.54	2.7±0.1		
671.62	3.0±0.2	702.90	2.7±0.1		
684.81	3.0±0.2	719.50	2.8±0.1		
699.42	3.3±0.2	732.07	2.8±0.1		
710.89	3.4±0.2	745.05	2.8±0.1		
723.26	3.5±0.2	757.41	2.8±0.1		
735.00	3.5±0.2	769.49	3.0±0.2		
747.02	3.5±0.2	784.25	2.8±0.1		
761.11	2.9±0.1	798.69	2.9±0.2		
774.84	2.8±0.1	812.62	3.5±0.2		
787.83	2.4±0.1	817.56	3.7±0.2		
792.93	2.7±0.1				

Table C.14: Seebeck coefficient of $TmAgTe_2$ parent compounds and extrinsically doped compounds; in order of data collection. The Seebeck coefficient is plotted as function of temperature in Figure 5.19 (a).

T / K	S / µV K^{-1} ($TmAgTe_2$ [tetr.])	T / K	S / µV K^{-1} ($TmAgTe_2$ [tri.])	T / K	S / µV K^{-1} ($TmAgTe_2$ [tri.])
325.0	568±28	325.09	511±26	278.025	355±18
350.0	565±28	393.85	479±24	253.067	419±21
375.0	571±29	464.27	433±22	227.639	361±18
400.0	582±29	537.77	424±21	202.714	358±18
425.0	592±30	610.99	466±23	176.889	356±18
450.0	600±30	684.34	492±25	151.140	317±16
475.0	603±30	757.06	537±27	125.934	289±14
500.0	599±30	828.85	553±28	100.780	327±16
525.0	589±29			75.619	269±13
550.0	574±29			50.385	78.9±3.9
575.0	551±28			60.379	227±11
600.0	529±26			110.896	318±16
625.0	507±25			161.021	363±18
650.0	483±24			211.356	376±19
675.0	469±23			262.550	371±19
				303.311	406±20

T / K	S / µV K^{-1} ($TmMg_{0.05}Ag_{0.95}Te_2$)	T / K	S / µV K^{-1} ($TmZn_{0.05}Ag_{0.95}Te_2$)	T / K	S / µV K^{-1} ($TmZn_{0.05}Ag_{0.95}Te_2$)
323.45	398±20	324.69	502±25	303.107	484±24
369.64	386±19	370.42	488±24	277.730	469±23
416.08	371±19	417.68	464±23	252.759	470±23
462.95	361±18	465.75	447±22	227.363	470±23
512.60	351±18	515.96	449±22	202.407	467±23
561.16	346±17	565.16	465±23	176.650	469±23
609.48	381±19	614.16	472±24	150.984	438±22
659.01	443±22	664.17	492±25	125.815	421±21
707.18	479±24	712.86	503±25	100.664	391±20
755.70	492±25	761.17	515±26	75.534	309±15
				50.326	236±12
				60.315	253±13
				110.762	402±20
				160.869	482±24
				211.195	448±22
				262.294	472±24
				303.011	478±24

Table C.15: Seebeck coefficient of $YAgTe_2$ and $Y_{0.98}Cu_{1.02}Te_{1.98}$; in order of data collection. The Seebeck coefficient is plotted as function of temperature in Figure 5.19 (b).

T / K	S / µV K^{-1} ($YAgTe_2$)	T / K	S / µV K^{-1} ($YAgTe_2$)	T / K	S / µV K^{-1} ($Y_{0.98}Ag_{1.02}Te_{1.98}$)
325.60	468±23	303.422	471±24	324.94	220±11
394.98	598±30	277.991	430±21	370.98	287±14
467.19	359±18	252.992	424±21	417.97	311±16
541.12	172±9	227.534	452±23	466.52	239±12
614.90	184±9	202.557	452±23	516.15	207±10
688.97	226±11	176.731	408±20	565.57	220±11
762.19	338±17	151.024	345±17	614.52	264±13
835.18	427±21	125.817	166±8	664.36	321±16
859.12	544±27	100.664	-1.12±0.06	713.30	356±18
		75.514	87.9±4.4	761.34	373±19
		50.300	110±5		
		60.296	165±8		
		110.772	112±6		
		160.923	404±20		
		211.326	467±23		
		262.571	460±23		
		303.376	436±22		

Table C.16: Seebeck coefficient of $YCuTe_2$ parent compound and intrinsically doped compounds; in order of data collection. The Seebeck coefficient is plotted as function of temperature in Figure 5.19 (c).

T / K	S / µV K^{-1} ($YCuTe_2$)	T / K	S / µV K^{-1} ($YCuTe_2$)	T / K	S / µV K^{-1} ($YCu_{0.96}Te_2$)
314.97	172±9	303.492	121±6	314.96	170±9
352.15	185±9	278.067	118±6	351.89	184±9
390.20	195±10	253.086	96.4±4.8	389.37	194±10
428.16	199±10	227.638	84.1±4.2	426.69	193±10
467.12	205±10	202.679	73.3±3.7	464.34	191±10
506.59	221±11	176.835	73.7±3.7	504.12	206±10
545.92	242±12	151.093	59.0±3.0	543.02	231±12
585.44	260±13	125.890	48.8±2.4	581.85	252±13
624.79	271±14	100.736	18.7±0.9	621.43	260±13
664.47	278±14	75.579	26.1±1.3	660.76	266±13
703.58	282±14	50.344	14.7±0.7	699.49	270±14
742.50	284±14	25.241	41.1±2.1	738.18	272±14
781.02	292±15	5.226	2.85±0.14	777.38	273±14
		2.404	20.3±1.0		
		15.119	14.6±0.7		
		30.213	34.1±1.7		
		60.348	2.15±0.11		
		110.864	40.8±2.0		
		160.997	61.8±3.1		
		211.367	87.2±4.4		
		262.589	112±6		
		303.415	119±6		

T / K	S / µV K^{-1} ($YCu_{1.04}Te_2$)	T / K	S / µV K^{-1} ($YCu_{1.08}Te_2$)	T / K	S / µV K^{-1} ($Y_{0.96}Cu_{1.08}Te_2$)
314.69	164±8	315.45	147±7	315.24	156±8
351.70	179±9	352.11	159±8	351.76	170±8
389.36	189±9	389.49	169±8	389.55	180±9
427.31	194±10	426.82	176±9	427.73	188±9
465.36	201±10	465.07	177±9	466.24	193±10
506.05	202±10	504.92	183±9	505.96	200±10
545.61	222±11	544.00	206±10	545.28	223±11
585.28	254±13	583.18	234±12	584.70	246±12
624.71	267±13	622.83	245±12	624.11	260±13
664.96	274±14	662.73	252±13	664.34	268±13
704.49	279±14	702.02	261±13	703.41	274±14
743.39	283±14	741.15	264±13	742.45	276±14
782.54	284±14	780.88	271±14	780.93	279±14

T / K	S / µV K^{-1} ($Y_{0.96}Cu_{1.08}Te_2$)	T / K	S / µV K^{-1} ($Y_{0.98}CuTe_2$)
303.210	162±8	314.74	163±8
277.823	151±8	352.01	177±9
252.865	137±7	389.30	187±9
227.463	126±6	426.64	192±10
202.533	113±6	464.52	195±10
176.745	101±5	504.16	208±10
151.119	87.7±4.4	543.00	232±12
125.952	69.7±3.5	581.98	252±13
75.645	54.4±2.7	621.31	260±13
50.418	28.5±1.4	660.70	266±13
25.351	7.10±0.35	699.55	272±14
10.716	18.6±0.9	738.40	275±14
5.361	1.33±0.07	777.74	276±14
2.307	4.77±0.24		
15.095	17.8±0.9		
30.186	35.3±1.8		
60.307	45.0±2.3		
110.770	65.4±3.3		
160.776	91.3±4.6		
210.921	117±6		
261.752	145±7		
302.694	167±8		

C.2 Raman Spectroscopy of XYZ_2

The phonon DOS of the three XYZ_2 compounds was compared to Raman spectra which were acquired with the assistance of Christopher Lee in the laboratory of Dr. Kevin Hewitt, Department of Physics and Atmospheric Science, Dalhousie University. It is important to note that the Raman spectrum of the $TmAgTe_2$ parent compound had broad background and therefore, the Raman spectrum of the Zn-doped compound was used instead of the parent compound. While four Raman peaks were recorded for $YCuTe_2$ and $Y_{0.96}Cu_{1.08}Te_2$, the Raman spectra of $TmAg_{0.95}Zn_{0.05}Te_2$ and $YAgTe_2$ showed two peaks (see Figure C.15 and Table C.17). Although Raman spectra were not calculated from the phononic dispersion curves and thus, the experimental Raman peaks cannot be assigned, the phononic dispersion curves show several optical bands at the frequencies where the experimental Raman peaks appeared. Furthermore, the computed phonon DOS indicates a trend similar to the experimental Raman spectra. Two low-frequency peaks were observed in the Cu-based compounds which were not detected in the Ag-based compounds. Similarly, the phonon DOS of $YCuTe_2$ is higher than $TmAgTe_2$ and $YAgTe_2$ in the frequency region between 50 cm^{-1} and 100 cm^{-1} with two peak at $\sim$ 68 cm^{-1} and $\sim$ 91 cm^{-1}. The high-frequency experimental Raman peaks of $TmAg_{0.95}Zn_{0.05}Te_2$ had a lower frequency than the other investigated compounds. The same trend was observed in the calculated phononic dispersion curve in which $TmAgTe_2$ had slightly lower frequencies than $YAgTe_2$ and $YCuTe_2$.

Table C.17: Frequency of Raman peaks for $TmAg_{0.95}Zn_{0.05}Te_2$, $YAgTe_2$, $YCuTe_2$, and $Y_{0.96}Cu_{1.08}Te_2$. $TmAgTe_2$ parent compounds show a broad fluorescence peak. 10 cm^{-1} uncertainty was estimated from the breadth of the peak.

Compound	Frequency / cm^{-1}
$TmAg_{0.95}Zn_{0.05}Te_2$	118±10; 138±10
$YAgTe_2$	122±10; 139±10
$YCuTe_2$	70±10; 92±10; 122±10; 139±10
$Y_{0.96}Cu_{1.08}Te_2$	71±10; 91±10; 122±10; 139±10

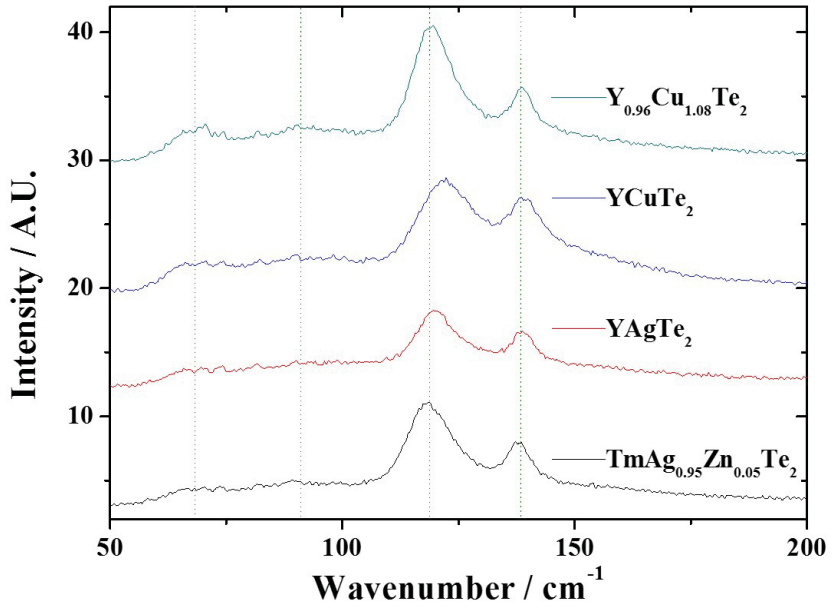

Figure C.15: Raman spectra of $Y_{0.96}Cu_{1.08}Te_2$, $YCuTe_2$, $YAgTe_2$, and $TmAg_{0.95}Zn_{0.05}Te_2$. Four peaks were observed for $Y_{0.96}Cu_{1.08}Te_2$ and $YCuTe_2$ whereas the Ag-based compounds have only two distinct Raman spectra (vertical dashed lines as guide for the eyes). No additional peaks were observed above 200 cm^{-1}.

Table C.18: Heat capacity data of $TmAgTe_2$ in the tetragonal phase measured in a PPMS: 19.262 mg; in order of data collection. The heat capacity is plotted as function of temperature in Figure 5.21.

T / K	C_p / J mol^{-1} K^{-1}	T / K	C_p / J mol^{-1} K^{-1}	T / K	C_p / J mol^{-1} K^{-1}
303.584	109±1	21.913	25.4±0.3	2.826	0.930±0.009
283.184	108±1	19.843	22.7±0.2	2.643	0.879±0.009
263.039	107±1	17.986	20.1±0.2	2.473	0.859±0.009
242.835	107±1	16.286	17.8±0.2	2.314	0.841±0.008
222.679	106±1	14.756	15.7±0.2	2.163	0.830±0.008
202.484	105±1	13.369	13.7±0.1	2.024	0.816±0.008
182.233	103±1	12.111	11.9±0.1	1.894	0.794±0.008
162.016	101±1	10.971	10.1±0.1	1.772	0.778±0.008
141.791	98.7±1.0	9.938	8.6±0.09	1.658	0.766±0.008
121.575	95.3±1.0	9.003	7.2±0.07	1.551	0.744±0.007
101.359	90.4±0.9	8.157	6.0±0.06	1.451	0.728±0.007
96.342	88.0±0.9	7.388	4.9±0.05	1.358	0.718±0.007
87.206	84.2±0.8	6.708	4.1±0.04	1.272	0.747±0.007
79.028	81.6±0.8	6.077	3.2±0.03	1.189	0.968±0.010
71.617	77.4±0.8	5.499	2.6±0.03	1.114	1.36±0.01
64.865	72.9±0.7	4.980	2.1±0.02	1.043	1.18±0.01
58.770	68.7±0.7	4.510	1.7±0.02	0.977	0.742±0.007
53.252	63.8±0.6	4.084	1.4±0.01	0.915	0.489±0.005
48.247	58.6±0.6	3.698	1.2±0.01	0.858	0.345±0.003
43.714	53.6±0.5	3.347	1.1±0.01	0.805	0.248±0.002
39.610	48.7±0.5	3.027	0.970±0.010	0.754	0.192±0.002
35.889	43.9±0.4	2.742	0.921±0.009	0.708	0.155±0.002
32.518	39.6±0.4	2.484	0.862±0.009	0.666	0.124±0.001
29.460	35.5±0.4	2.248	0.845±0.008	0.619	0.107±0.001
26.691	31.9±0.3	2.035	0.817±0.008	0.620	0.108±0.001
24.184	28.4±0.3	4.028	1.40±0.01		

Table C.19: Heat capacity data of $TmMg_{0.05}Ag_{0.95}Te_2$ measured in a PPMS: 44.266 mg; in order of data collection. The heat capacity is plotted as function of temperature in Figure 5.21.

T / K	C_p / J mol^{-1} K^{-1}	T / K	C_p / J mol^{-1} K^{-1}	T / K	C_p / J mol^{-1} K^{-1}
303.358	102±1	53.255	65.7±0.7	9.941	8.78±0.09
283.114	102±1	48.249	60.8±0.6	9.005	7.29±0.07
262.964	101±1	43.717	56.0±0.6	8.158	5.98±0.06
242.774	101±1	39.612	51.2±0.5	7.390	4.80±0.05
222.614	101±1	35.891	46.5±0.5	6.710	3.89±0.04
202.422	99.9±1	32.518	42.1±0.4	6.080	2.98±0.03
182.221	99.1±1.0	29.459	37.9±0.4	5.503	2.27±0.02
162.012	98.0±1.0	26.696	34.3±0.3	4.983	1.71±0.02
141.794	96.1±1.0	24.189	30.4±0.3	4.514	1.25±0.01
121.571	93.4±0.9	21.913	27.1±0.3	4.087	0.897±0.009
101.367	89.5±0.9	19.853	24.2±0.2	3.702	0.641±0.006
96.334	87.6±0.9	17.990	21.3±0.2	3.350	0.451±0.005
87.215	84.4±0.8	16.298	18.8±0.2	3.030	0.320±0.003
79.041	82.2±0.8	14.762	16.5±0.2	2.745	0.232±0.002
71.630	78.5±0.8	13.373	14.2±0.1	2.486	0.165±0.002
64.877	74.2±0.7	12.116	12.3±0.1	2.250	0.125±0.001
58.778	70.3±0.7	10.975	10.4±0.1	2.036	0.0963±0.0010

Table C.20: Heat capacity data of $TmZn_{0.05}Ag_{0.95}Te_2$ measured in a PPMS (low temperature): 41.378 mg; and DSC (high temperature): 18.790 mg; in order of data collection. The heat capacity is plotted as function of temperature in Figure 5.21.

T / K	C_p / J mol^{-1} K^{-1}	T / K	C_p / J mol^{-1} K^{-1}	T / K	C_p / J mol^{-1} K^{-1}
303.373	104±1	53.251	66.8±0.7	9.935	8.58±0.09
283.126	104±1	48.242	61.8±0.6	9.000	7.20±0.07
262.977	103±1	43.709	56.9±0.6	8.154	5.99±0.06
242.791	103±1	39.605	52.1±0.5	7.385	4.90±0.05
222.635	103±1	35.883	47.2±0.5	6.702	4.09±0.04
202.450	102±1	32.512	42.8±0.4	6.074	3.18±0.03
182.248	101±1	29.454	38.3±0.4	5.496	2.49±0.02
162.042	99.7±1	26.689	34.4±0.3	4.978	1.94±0.02
141.788	97.5±1.0	24.180	30.5±0.3	4.510	1.46±0.01
121.559	94.6±0.9	21.914	27.2±0.3	4.083	1.08±0.01
101.358	90.5±0.9	19.845	24.0±0.2	3.698	0.795±0.008
96.338	88.7±0.9	17.981	20.9±0.2	3.347	0.573±0.006
87.210	85.4±0.9	16.287	18.4±0.2	3.028	0.413±0.004
79.036	83.3±0.8	14.755	16.0±0.2	2.743	0.304±0.003
71.626	79.6±0.8	13.367	13.8±0.1	2.485	0.219±0.002
64.872	75.3±0.8	12.109	11.9±0.1	2.249	0.168±0.002
58.771	71.4±0.7	10.969	10.1±0.1	2.036	0.133±0.001
448.15	105±5	408.15	105±5	358.15	103±5
438.15	105±5	398.15	104±5	348.15	104±5
428.15	103±5	378.15	104±5	338.15	103±5
418.15	105±5	368.15	103±5		

Table C.21: Heat capacity data of $YAgTe_2$ measured in a PPMS (low temperature): 12.502 mg; and in a DSC (high temperature): 17.650 mg; in order of data collection. The heat capacity is plotted as function of temperature in Figure 5.22.

T / K	C_p / J mol^{-1} K^{-1}	T / K	C_p / J mol^{-1} K^{-1}	T / K	C_p / J mol^{-1} K^{-1}
303.064	108±1	53.059	55.9±0.6	9.892	2.75±0.03
282.760	107±1	48.065	50.7±0.5	8.961	2.00±0.02
262.619	105±1	43.539	45.8±0.5	8.121	1.43±0.01
242.435	104±1	39.443	40.9±0.4	7.357	0.987±0.010
222.273	103±1	35.731	36.3±0.4	6.672	0.696±0.007
202.076	101±1	32.377	31.9±0.3	6.046	0.466±0.005
181.871	99.2±1.0	29.331	27.7±0.3	5.471	0.318±0.003
161.669	96.5±1.0	26.580	23.9±0.2	4.955	0.218±0.002
141.476	93.5±0.9	24.078	20.4±0.2	4.488	0.150±0.002
121.290	89.2±0.9	21.807	17.3±0.2	4.064	0.105±0.001
101.089	83.6±0.8	19.764	14.6±0.1	3.681	0.0736±0.0007
96.080	81.1±0.8	17.906	12.1±0.1	3.333	0.0524±0.0005
86.947	77.1±0.8	16.213	9.84±0.10	3.018	0.0376±0.0004
78.775	74.1±0.7	14.689	7.94±0.08	2.732	0.0272±0.0003
71.388	69.9±0.7	13.304	6.24±0.06	2.473	0.0198±0.0002
64.648	65.2±0.7	12.051	4.89±0.05	2.240	0.0145±0.0001
58.565	60.9±0.6	10.920	3.69±0.04	2.026	0.0106±0.0001
328.15	108±5	478.15	119±6	628.15	142±7
338.15	109±5	488.15	120±6	638.15	142±7
348.15	110±6	498.15	122±6	648.15	137±7
358.15	111±6	508.15	123±6	658.15	135±7
368.15	113±6	518.15	126±6	668.15	130±7
378.15	114±6	528.15	128±6	678.15	118±6
388.15	115±6	538.15	129±6	688.15	118±6
398.15	121±6	548.15	132±7	698.15	124±6
408.15	130±6	558.15	135±7	708.15	126±6
418.15	126±6	568.15	136±7	718.15	129±6
428.15	115±6	578.15	138±7	728.15	136±7
438.15	116±6	588.15	138±7	738.15	148±7
448.15	117±6	598.15	140±7	748.15	169±8
458.15	117±6	608.15	141±7	758.15	261±13
468.15	118±6	618.15	141±7		

Table C.22: Heat capacity data of $YAgTe_2$ measured in a PPMS: 6.636 mg; in order of data collection. The heat capacity is plotted as function of temperature in Figure 5.22.

T / K	C_p / mJ mol^{-1} K^{-1}	T / K	C_p / mJ mol^{-1} K^{-1}	T / K	C_p / mJ mol^{-1} K^{-1}
302.165	106000±5000	3.445	55.0±2.8	1.091	1.66±0.08
10.040	2850±140	3.172	41.4±2.1	1.007	1.38±0.07
9.250	21840±110	2.924	31.7±1.6	0.928	1.13±0.06
8.517	1660±80	2.691	23.6±1.2	0.857	0.924±0.046
7.845	1230±60	2.481	18.2±0.9	0.790	0.779±0.039
7.224	906±45	2.279	14.2±0.7	0.730	0.669±0.033
6.651	653±33	2.102	11.1±0.6	0.676	0.559±0.028
6.130	478±24	1.937	8.51±0.43	0.621	0.483±0.024
5.651	345±17	1.784	6.60±0.33	0.575	0.428±0.021
5.203	249±12	1.643	5.15±0.26	0.532	0.396±0.020
4.792	181±9	1.514	3.98±0.20	0.491	0.334±0.017
4.414	132±7	1.396	3.10±0.16	0.455	0.311±0.016
4.066	97.6±4.9	1.285	2.58±0.13	0.423	0.246±0.012
3.740	72.8±3.6	1.185	2.06±0.10		

Table C.23: Heat capacity data of $YCuTe_2$ measured in a PPMS (low temperature): 22.234 mg; and in a DSC (high temperature): 13.410 mg; in order of data collection. The heat capacity is plotted as function of temperature in Figure 5.23.

T / K	C_p / J mol^{-1} K^{-1}	T / K	C_p / J mol^{-1} K^{-1}	T / K	C_p / J mol^{-1} K^{-1}
302.955	101±1	53.076	49.18±0.5	9.889	1.31±0.01
282.616	99.6±1.0	48.071	43.8±0.4	8.958	0.944±0.009
262.510	98.6±1.0	43.544	38.7±0.4	8.118	0.681±0.007
242.348	97.9±1.0	39.445	33.7±0.3	7.355	0.483±0.005
222.208	98.3±1.0	35.731	29.1±0.3	6.668	0.355±0.004
202.036	96.4±1.0	32.375	24.8±0.2	6.044	0.249±0.002
181.837	94.8±0.9	29.333	21.0±0.2	5.469	0.178±0.002
161.648	92.5±0.9	26.567	17.5±0.2	4.953	0.130±0.001
141.437	89.5±0.9	24.063	14.4±0.1	4.486	0.0935±0.0009
121.240	85.4±0.9	21.803	11.7±0.1	4.062	0.0678±0.0007
101.098	79.4±0.8	19.756	9.39±0.09	3.679	0.0496±0.0005
96.054	76.6±0.8	17.892	7.41±0.07	3.332	0.0364±0.0004
86.969	72.7±0.73	16.210	5.76±0.06	3.016	0.0271±0.0003
78.802	69.3±0.7	14.683	4.41±0.04	2.731	0.0199±0.0002
71.419	64.6±0.6	13.299	3.29±0.03	2.472	0.0149±0.0001
64.671	59.3±0.6	12.047	2.47±0.02	2.239	0.0111±0.0001
58.584	54.5±0.5	10.915	1.8±0.02	2.025	0.00821±0.0001
328.15	107±5	398.15	125±6	478.15	114±6
338.15	109±5	408.15	133±7	488.15	113±6
348.15	110±6	418.15	144±7	498.15	115±6
358.15	111±6	428.15	158±8	508.15	116±6
368.15	114±6	458.15	115±6	518.15	117±6
378.15	116±6	468.15	114±6	528.15	118±6
388.15	120±6				

Table C.24: Heat capacity data of $Y_{0.96}Cu_{1.08}Te_2$ measured in a PPMS (low temperature): 22.234 mg; and in a DSC (high temperature): 10.790 mg; in order of data collection. The heat capacity is plotted as function of temperature in Figure 5.23.

T / K	C_p / J mol^{-1} K^{-1}	T / K	C_p / J mol^{-1} K^{-1}	T / K	C_p / J mol^{-1} K^{-1}
303.166	108±1	53.214	50.8±0.5	9.927	1.45±0.01
282.955	106±1	48.211	45.4±0.5	8.989	1.04±0.01
262.834	104±1	43.680	40.1±0.4	8.142	0.749±0.007
242.669	103±1	39.578	35.1±0.4	7.372	0.528±0.005
222.531	101±1	35.861	30.3±0.3	6.688	0.384±0.004
202.366	99.2±1.0	32.490	26.0±0.3	6.061	0.268±0.003
182.168	97.3±1.0	29.434	22.0±0.2	5.485	0.192±0.002
161.966	95.0±1.0	26.675	18.6±0.2	4.968	0.138±0.001
141.759	91.5±0.9	24.167	15.3±0.2	4.500	0.100±0.001
121.544	87.1±0.9	21.892	12.5±0.1	4.075	0.0720±0.0007
101.323	81.2±0.8	19.831	10.1±0.1	3.690	0.0524±0.0005
96.330	78.6±0.8	17.972	8.00±0.08	3.340	0.0381±0.0004
87.157	74.5±0.7	16.271	6.26±0.06	3.022	0.0280±0.0003
79.026	70.6±0.7	14.744	4.83±0.05	2.738	0.0211±0.0002
71.581	66.2±0.7	13.356	3.65±0.04	2.481	0.0152±0.0002
64.833	61.0±0.6	12.098	2.73±0.03	2.247	0.0116±0.0001
58.740	56.1±0.6	10.958	1.99±0.02	2.034	0.00865±0.00009
328.15	107±5	398.15	111±6	468.15	114±6
338.15	109±5	408.15	110±6	478.15	114±6
348.15	112±6	418.15	110±6	488.15	114±6
358.15	115±6	428.15	111±6	498.15	116±6
368.15	117.±6	438.15	111±6	508.15	115±6
378.15	118±6	448.15	113±6	518.15	114±6
388.15	114±6	458.15	115±6	528.15	114±6

Table C.25: Heat capacity data of $YCuTe_2$ measured in a PPMS: 8.660 mg; in order of data collection. The heat capacity is plotted as function of temperature in Figure 5.23.

T / K	C_p / mJ mol^{-1} K^{-1}	T / K	C_p / mJ mol^{-1} K^{-1}	T / K	C_p / mJ mol^{-1} K^{-1}
302.323	104000±1000	3.446	39.7±2.0	1.092	1.45±0.07
10.046	1380±10	3.173	30.7±1.5	1.007	1.18±0.06
9.256	1050±10	2.924	24.0±1.2	0.928	0.971±0.049
8.523	799±8	2.692	18.4±0.9	0.857	0.788±0.039
7.848	604±6	2.481	14.4±0.7	0.790	0.643±0.032
7.225	456±5	2.281	11.4±0.6	0.729	0.563±0.028
6.654	342±3	2.101	9.00±0.45	0.675	0.494±0.025
6.127	261±3	1.937	7.05±0.35	0.617	0.426±0.021
5.650	198±2	1.784	5.56±0.28	0.572	0.377±0.019
5.204	150±2	1.643	4.43±0.33	0.531	0.373±0.019
4.793	114±6	1.514	3.51±0.18	0.488	0.327±0.017
4.415	87.4±4.4	1.395	2.75±0.14	0.454	0.288±0.014
4.066	66.9±3.3	1.285	2.19±0.11	0.421	0.262±0.013
3.739	51.6±2.6	1.184	1.74±0.09		

C.3 Magnetic Properties of $TmAgTe_2$

The low-temperature phase transition in $TmAgTe_2$ was investigated further to delineate the origins of the transition. The low-temperature heat capacity measurements revealed a phase transition at around 1.1 K. The phase transition might be attributed to a second-order magnetic transition as reported for other systems, such as TmB_{50} [310] and $Er_2Ti_2O_7$ [308, 309]. The heat capacity and magnetic measurements were performed in the laboratory of Dr. Mary Anne White, Department of Chemistry, Dalhousie University, using a PPMS.

The heat capacity of $TmAgTe_2$ ($m = 21.86 \pm 0.01$ mg) was measured under the influence of various applied magnetic fields as shown in Figure C.16. The heat capacity under an applied magnetic field of 0 T (before), 2 T, and 9 T was measured on cooling and under an applied magnetic field of 1 T, 5 T, and 0 T (after) was determined on heating. While a decrease in the intensity of the phase transition at $\sim$1.1 K was observed with increasing magnetic field, another peak in heat capacity appeared at $\sim$1.7 K. The heat capacity at 1.7 K was the highest for 2 T and reduced with increasing magnetic field. At 1 T, two distinct heat capacity peaks were observed. The heat capacity was reproducible as shown by the zero-field heat capacity before (cooling) and after (heating) the high-field measurements indicating that the phase transition is most likely of first-order. It is important to note that for the background heat capacity, the zero-field background was used for all heat capacity at various fields which can introduce uncertainty.

For a better analysis of the magnetic phase transition, the inverse magnetic susceptibility, χ, was determined and is plotted as a function of temperature in Figure C.17. The susceptibility (Equation 3.38) was calculated from the magnetic moment, M, which was measured using in a PPMS, and the magnetic field strength, H, assuming a relative permeability of $\mu_r = 1$. For the measurement, the external magnetic field was set to 0.2 T and χ^{-1} versus T showed a linear response which is typically for paramagnetic behavior. The low-temperature magnetic phase can be determined with the Curie-Weiss law given by

$$\chi = \frac{C}{T - T_C} \tag{C.1}$$

where C is the Curie constant and T_C is the Curie temperature [73]. Above the Curie

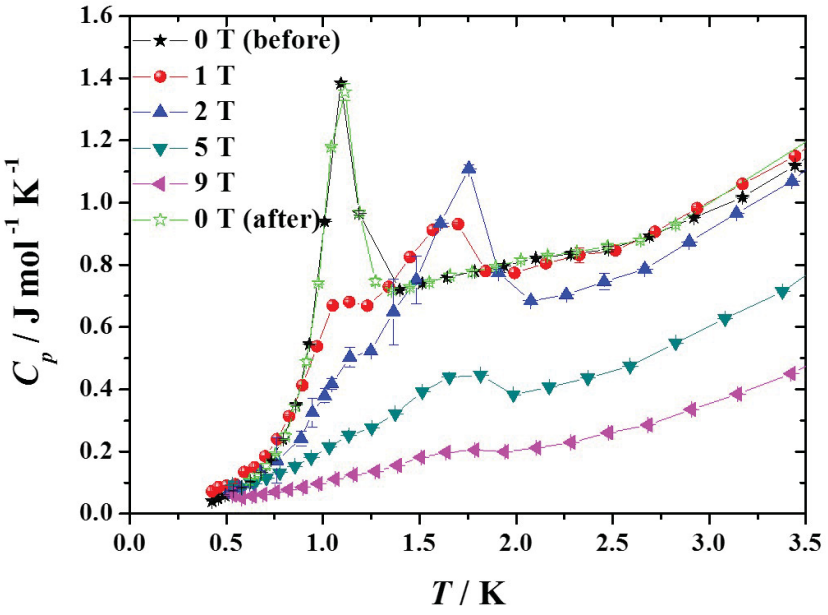

Figure C.16: Heat capacity of $TmAgTe_2$ in various magnetic fields from 0 T to 9 T. Intensity of the peak decreased shifted and with increasing magnetic field. Lines are a guide to the eye.

temperature, a material changes from ferromagnetic to paramagnetic. Similar to the Curie-Weiss law, the transition temperature from antiferromagnetic to paramagnetic behavior, also known as the Néel temperature, T_N, can be predicted by [73]

$$\chi = \frac{C}{T + T_N}. \tag{C.2}$$

Figure C.17 shows that the extrapolated fit intersects with the temperature axis at -6.5 K indicating that the low-temperature phase is antiferromagnetic with a Néel temperature of 6.5 K. The Néel temperature is higher than the recorded transition temperature from heat capacity measurements. The susceptibility was measured on heating and cooling and the phase transition in the magnetic susceptibility was only observed on heating whereas no phase transition was detected on cooling. The present author acknowledges that the relative permeability is an unknown, but the assumption to set the relative permeability to one would not change the intercept with the temperature axis.

The low-temperature magnetic properties of $TmAgTe_2$ were further investigated.

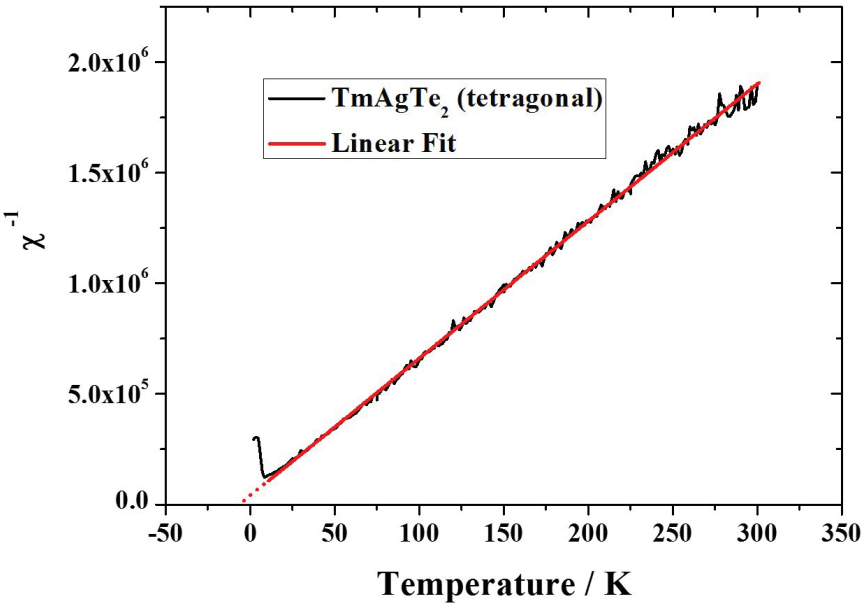

Figure C.17: Inverse magnetic susceptibility versus temperature with a magnetic field of 0.2 T indicates a magnetic phase transition from antiferromagnet to paramagnet for $TmAgTe_2$.

The sample was cooled to in zero-field 2 K and the magnetic hysteresis loop was recorded with a maximum magnetic field of 1 T (see Figure C.18 (a)). After the hysteresis, the magnetic moment was recorded as a function of temperature from 2 K to 10 K and back to 2 K in a magnetic field of 1 T (Figure C.18 (b)). The magnetic field was increased to 2 T and the procedure was repeated for 2 T, 5 T and 9 T (without cooling to 2 K). The magnetic hysteresis indicates that the initial magnetic moment was higher for all applied magnetic fields than the final moment. The lower magnetic moment after magnetic cycling might indicate that the spin states were frozen in the paramagnetic phase even below the Néel temperature. However, applying an opposite magnetic field rotates the spins in the thermodynamically stable antiferromagnetic phase at 2 K. This is consistent with the temperature cycling where an increase in magnetic moment was observed above the Néel temperature whereas no reduction in magnetic moment was detected from 10 K to 2 K (see Figure C.17 (b)). The temperature behavior of the magnetic moment also agrees with an antiferromagnetic state (*i.e.*, magnetic moment

increased with temperature to the phase transition) and paramagnetic (*i.e.*, magnetic moment decreased with temperature above the phase transition) phase. Further experiments would be required to fully understand the low-temperature magnetic phase transition(s).

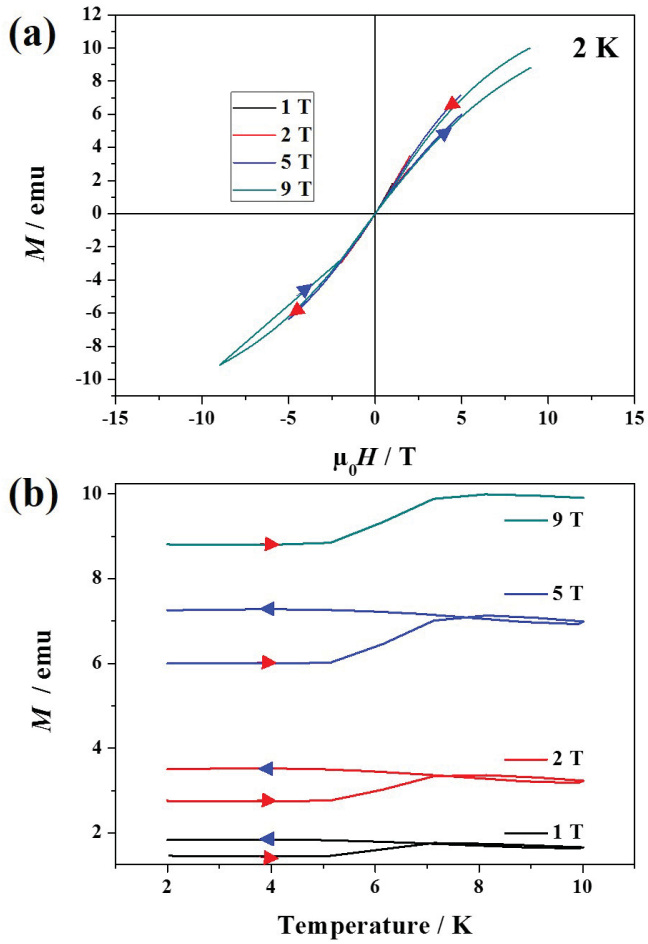

Figure C.18: (a) Magnetic moment, M, as a function of magnetic field, $\mu_0 H$, at 2 K indicates that moment decreased after cycling. (b) Temperature-cycling of the magnetic moment between 2 K and 10 K under various applied magnetic fields. A change in magnetic moment was observed on heating while the moment is nearly constant with cooling which might indicate a supercooled magnetic phase transition.

In conclusion, the peak in heat capacity at ∼1.1 K can be suppressed with increasing magnetic fields. However, another heat capacity peak appeared in a magnetic field of 2 T at slightly higher temperature. The temperature-dependent

magnetic susceptibility suggests a phase transition from antiferromagnetic to paramagnetic at ∼6.5 K. The paramagnetic phase might be supercooled and can be transformed to the antiferromagnetic phase by cycling the magnetic moment as a function of magnetic field.

Table C.26: Thermal conductivity of $TmAgTe_2$ parent compounds and extrinsically doped compounds; in order of data collection. The thermal conductivity is plotted as function of temperature in Figure 5.24.

T / K	κ / W m^{-1} K^{-1} ($TmAgTe_2$ [tetr.])	κ_{el} / mW m^{-1} K^{-1} ($TmAgTe_2$ [tetr.])	κ_{pho} / W m^{-1} K^{-1} ($TmAgTe_2$ [tetr.])
325.00	0.90±0.13	0.43±0.06	0.90±0.13
350.00	0.86±0.13	0.44±0.07	0.86±0.13
375.00	0.82±0.12	0.44±0.07	0.82±0.12
400.00	0.79±0.12	0.44±0.07	0.79±0.12
425.00	0.75±0.11	0.45±0.07	0.75±0.11
450.00	0.72±0.11	0.48±0.07	0.72±0.11
475.00	0.69±0.10	0.53±0.08	0.69±0.10
500.00	0.65±0.10	0.61±0.09	0.65±0.10
525.00	0.63±0.09	0.73±0.11	0.63±0.09
550.00	0.60±0.09	0.91±0.1	0.60±0.09
575.00	0.58±0.09	1.2±0.2	0.58±0.09
600.00	0.56±0.08	1.7±0.3	0.56±0.08
625.00	0.54±0.08	2.5±0.4	0.54±0.08
650.00	0.51±0.08	3.5±0.5	0.51±0.08
675.00	0.47±0.07	4.1±0.6	0.47±0.07

T / K	κ / W m^{-1} K^{-1} ($TmAgTe_2$ [tri.])	κ_{el} / mW m^{-1} K^{-1} ($TmAgTe_2$ [tri.])	κ_{pho} / W m^{-1} K^{-1} ($TmAgTe_2$ [tri.])
323.25	0.59±0.09	0.73±0.11	0.59±0.09
373.85	0.55±0.08	1.6±0.2	0.55±0.08
423.95	0.51±0.08	2.0±0.3	0.50±0.08
473.95	0.45±0.07	3.3±0.5	0.45±0.07
523.95	0.40±0.06	4.9±0.7	0.39±0.06
574.05	0.34±0.05	6.1±0.9	0.34±0.05
623.95	0.30±0.04	6.2±0.9	0.29±0.04
674.05	0.28±0.04	5.4±0.8	0.28±0.04
724.05	0.28±0.04	4.6±0.7	0.27±0.04
774.05	0.30±0.04	3.3±0.5	0.29±0.04

T / K	κ / W m^{-1} K^{-1} ($TmMg_{0.05}Ag_{0.95}Te_2$)	κ_{el} / mW m^{-1} K^{-1} ($TmMg_{0.05}Ag_{0.95}Te_2$)	κ_{pho} / W m^{-1} K^{-1} ($TmMg_{0.05}Ag_{0.95}Te_2$)
324.35	0.71±0.11	0.46±0.07	0.71±0.11
375.15	0.66±0.10	0.65±0.10	0.66±0.10
425.05	0.61±0.09	0.97±0.15	0.61±0.09
475.05	0.56±0.08	1.4±0.2	0.56±0.08
524.65	0.51±0.08	2.1±0.3	0.51±0.08
574.55	0.44±0.07	3.0±0.4	0.44±0.07
624.35	0.36±0.05	3.9±0.6	0.36±0.05
674.15	0.31±0.05	5.0±0.8	0.30±0.05
724.05	0.31±0.05	5.8±0.9	0.31±0.05
748.85	0.31±0.05	5.7±0.9	0.30±0.05
773.85	0.31±0.05	6.0±0.9	0.31±0.05
798.85	0.32±0.05	6.3±1.0	0.32±0.05
823.75	0.33±0.05	6.6±1.0	0.32±0.05
848.75	0.33±0.05	6.8±1.0	0.32±0.05
873.75	0.33±0.05	5.0±0.8	0.33±0.05
848.15	0.34±0.05	6.5±1.0	0.33±0.05

T / K	κ / W m^{-1} K^{-1} ($TmZn_{0.05}Ag_{0.95}Te_2$)	κ_{el} / mW m^{-1} K^{-1} ($TmZn_{0.05}Ag_{0.95}Te_2$)	κ_{pho} / W m^{-1} K^{-1} ($TmZn_{0.05}Ag_{0.95}Te_2$)
320.25	0.56±0.08	0.66±0.10	0.56±0.08
372.85	0.53±0.08	1.2±0.2	0.53±0.08
424.35	0.51±0.08	3.0±0.4	0.51±0.08
474.35	0.47±0.07	4.6±0.7	0.46±0.07
524.25	0.43±0.06	6.1±0.9	0.43±0.06
574.25	0.39±0.06	7.8±1.2	0.38±0.06
624.15	0.34±0.05	8.1±1.2	0.33±0.05
673.95	0.29±0.04	7.5±1.1	0.29±0.04
723.95	0.27±0.04	6.2±0.9	0.26±0.04
748.95	0.27±0.04	5.7±0.9	0.26±0.04
773.85	0.27±0.04	5.9±0.9	0.27±0.04
798.95	0.29±0.04	5.9±0.9	0.28±0.04
823.95	0.29±0.04	5.5±0.8	0.29±0.04
848.95	0.29±0.04	3.8±0.6	0.29±0.04
873.85	0.30±0.04	3.0±0.5	0.30±0.04

T / K	κ / W m^{-1} K^{-1} ($TmAgTe_2$ [tri.])	T / K	κ / W m^{-1} K^{-1} ($TmZn_{0.05}Ag_{0.95}Te_2$)
303.520	0.48±0.02	303.058	0.55±0.03
303.524	0.48±0.02	303.089	0.55±0.03
303.404	0.50±0.03	303.107	0.55±0.03
278.025	0.50±0.03	277.730	0.55±0.03
253.067	0.50±0.03	252.759	0.56±0.03
227.639	0.51±0.03	227.363	0.57±0.03
202.714	0.51±0.03	202.407	0.58±0.03
176.889	0.52±0.03	176.650	0.60±0.03
151.140	0.53±0.03	150.984	0.61±0.03
125.934	0.54±0.03	125.815	0.63±0.03
100.780	0.54±0.03	100.664	0.64±0.03
75.619	0.54±0.03	75.534	0.65±0.03
50.385	0.51±0.03	50.326	0.62±0.03
25.261	0.41±0.02	25.207	0.52±0.03
10.166	0.27±0.01	10.113	0.43±0.02
5.170	0.18±0.01	5.104	0.33±0.02
2.304	0.081±0.004	3.434	0.29±0.01
15.118	0.33±0.02	15.085	0.46±0.02
30.239	0.44±0.02	30.192	0.55±0.03
60.379	0.53±0.03	60.315	0.64±0.03
110.896	0.55±0.03	110.762	0.64±0.03
161.021	0.54±0.03	160.869	0.61±0.03
211.356	0.52±0.03	211.195	0.58±0.03
262.550	0.51±0.03	262.294	0.55±0.03
303.311	0.50±0.03	303.011	0.54±0.03

Table C.27: Thermal conductivity of $YAgTe_2$ parent and $Y_{0.98}Ag_{1.02}Te_{1.98}$; in order of data collection. The thermal conductivity is plotted as function of temperature in Figure 5.25.

T / K	κ / W m^{-1} K^{-1} ($YAgTe_2$)	κ_{el} / mW m^{-1} K^{-1} ($YAgTe_2$)	κ_{pho} / W m^{-1} K^{-1} ($YAgTe_2$)
325.00	0.90±0.13	0.01±0.00	0.90±0.13
369.05	0.79±0.12	0.04±0.01	0.79±0.12
423.55	0.68±0.10	0.12±0.02	0.68±0.10
475.25	0.62±0.09	0.53±0.08	0.62±0.09
525.05	0.62±0.09	3.5±0.5	0.62±0.09
575.45	0.57±0.09	4.7±0.7	0.57±0.09
625.05	0.59±0.09	5.7±0.9	0.58±0.09
674.65	0.43±0.06	7.1±1.1	0.42±0.06
724.35	0.36±0.05	7.9±1.2	0.36±0.05
774.05	0.98±0.15	8.6±1.3	0.98±0.15

T / K	κ / W m^{-1} K^{-1} ($Y_{0.98}Ag_{1.02}Te_{1.98}$)	κ_{el} / mW m^{-1} K^{-1} ($Y_{0.98}Ag_{1.02}Te_{1.98}$)	κ_{pho} / W m^{-1} K^{-1} $Y_{0.98}Ag_{1.02}Te_{1.98}$)
320.65	0.77±0.12	0.06±0.01	0.77±0.12
373.05	0.74±0.11	0.08±0.01	0.74±0.11
424.45	0.69±0.10	0.12±0.02	0.69±0.10
474.35	0.68±0.10	0.18±0.03	0.68±0.10
524.25	0.70±0.11	0.30±0.04	0.70±0.11
574.15	0.68±0.10	0.49±0.07	0.68±0.10
624.15	0.71±0.11	0.75±0.11	0.71±0.11
674.05	0.55±0.08	1.2±0.2	0.55±0.08
724.05	0.53±0.08	2.5±0.4	0.53±0.08
774.05	1.1±0.2	3.6±0.5	1.1±0.2

T / K	κ / W m^{-1} K^{-1} ($YAgTe_2$)
303.422	0.78±0.04
277.991	0.80±0.04
252.992	0.83±0.04
227.534	0.87±0.04
202.557	0.91±0.05
176.731	0.96±0.05
151.024	1.0±0.1
125.817	1.1±0.1
100.664	1.2±0.1
75.514	1.2±0.1
50.300	1.3±0.1
25.192	1.1±0.1
10.141	0.52±0.03
5.158	0.24±0.01
2.270	0.073±0.004
15.089	0.76±0.04
30.168	1.2±0.1
60.296	1.3±0.1
110.772	1.1±0.1
160.923	0.96±0.05
211.326	0.84±0.04
262.571	0.78±0.04
303.376	0.75±0.04
262.550	0.51±0.03
303.311	0.50±0.03

Table C.28: Thermal conductivity of $YCuTe_2$ parent compounds and intrinsically doped compounds; in order of data collection. The thermal conductivity is plotted as function of temperature in Figure 5.26.

T / K	κ / W m^{-1} K^{-1} ($YCuTe_2$)	κ_{el} / mW m^{-1} K^{-1} ($YCuTe_2$)	κ_{pho} / W m^{-1} K^{-1} ($YCuTe_2$)
319.35	1.5±0.2	99±15	1.4±0.2
372.75	1.3±0.2	96±14	1.2±0.2
392.55	1.2±0.2	90±14	1.1±0.2
413.45	1.1±0.2	86±13	1.0±0.2
433.95	0.78±0.12	84±13	0.70±0.11
454.05	1.0±0.2	78±124	0.93±0.14
474.25	0.97±0.15	76±11	0.89±0.13
524.15	0.85±0.13	71±11	0.78±0.12
573.95	0.76±0.11	68±10	0.69±0.10
623.95	0.69±0.10	67±10	0.63±0.09
674.05	0.64±0.10	66±10	0.57±0.09
724.05	0.59±0.09	67±10	0.52±0.08
774.05	0.55±0.08	70±10	0.48±0.07
798.95	0.54±0.08	70±11	0.47±0.07

T / K	κ / W m^{-1} K^{-1} ($YCu_{0.96}Te_2$)	κ_{el} / mW m^{-1} K^{-1} ($YCu_{0.96}Te_2$)	κ_{pho} / W m^{-1} K^{-1} ($YCu_{0.96}Te_2$)
320.25	1.6±0.2	76±11	1.5±0.2
373.15	1.3±0.2	75±11	1.2±0.2
393.15	1.2±0.2	72±11	1.1±0.2
413.75	1.0±0.2	68±10	0.94±0.14
434.05	0.96±0.14	66±10	0.90±0.13
453.95	1.0±0.2	64±10	0.98±0.15
474.05	1.0±0.2	64±10	0.94±0.14
494.05	0.95±0.14	63±10	0.89±0.13
514.05	0.89±0.13	62±9	0.83±0.12
534.05	0.84±0.13	61±9	0.78±0.12
554.05	0.80±0.12	61±9	0.74±0.11
573.85	0.79±0.12	60±9	0.73±0.11
623.95	0.72±0.11	60±9	0.66±0.10
673.95	0.66±0.10	60±9	0.60±0.09
723.95	0.63±0.09	63±10	0.56±0.08
773.95	0.59±0.09	69±10	0.52±0.08
793.95	0.56±0.08	71±11	0.49±0.07

T / K	κ / W m^{-1} K^{-1} ($YCu_{1.04}Te_2$)	κ_{el} / mW m^{-1} K^{-1} ($YCu_{1.04}Te_2$)	κ_{pho} / W m^{-1} K^{-1} ($YCu_{1.04}Te_2$)
320.25	1.2±0.2	110±20	1.1±0.2
374.25	1.0±0.2	100±20	0.90±0.13
394.35	0.84±0.13	96±14	0.74±0.11
413.95	0.79±0.12	94±14	0.70±0.10
433.95	1.1±0.2	95±14	1.0±0.2
454.05	0.95±0.14	99±14	0.86±0.13
474.05	0.92±0.14	100±20	0.82±0.12
493.95	0.87±0.13	110±20	0.76±0.11
513.95	0.81±0.12	100±20	0.70±0.11
533.95	0.76±0.11	99±15	0.67±0.10
554.15	0.73±0.11	92±14	0.63±0.09
574.15	0.70±0.10	85±13	0.61±0.09
623.95	0.69±0.10	74±11	0.62±0.09
673.95	0.60±0.09	71±11	0.52±0.08
723.95	0.57±0.09	72±11	0.50±0.07
773.95	0.53±0.08	74±11	0.46±0.07
793.85	0.52±0.08	76±11	0.44±0.07

T / K	κ / W m^{-1} K^{-1} ($YCu_{1.08}Te_2$)	κ_{el} / mW m^{-1} K^{-1} ($YCu_{1.08}Te_2$)	κ_{pho} / W m^{-1} K^{-1} ($YCu_{1.08}Te_2$)
319.85	0.89±0.13	100±20	0.79±0.12
372.95	0.93±0.14	93±14	0.84±0.13
392.95	0.89±0.13	93±14	0.80±0.12
412.85	0.86±0.13	95±14	0.77±0.11
433.35	0.83±0.12	98±15	0.73±0.11
453.45	0.84±0.13	100±20	0.73±0.11
473.65	0.82±0.12	110±20	0.71±0.11
493.75	0.79±0.12	110±20	0.68±0.10
523.85	0.74±0.11	100±15	0.64±0.10
573.95	0.66±0.10	82±12	0.57±0.09
623.85	0.60±0.09	72±11	0.53±0.08
673.85	0.54±0.08	69±10	0.47±0.07
723.95	0.52±0.08	70±10	0.45±0.07
773.75	0.48±0.07	72±11	0.41±0.06
793.65	0.46±0.07	72±11	0.39±0.06

T / K	κ / W m^{-1} K^{-1} ($Y_{0.96}Cu_{1.08}Te_2$)	κ_{el} / mW m^{-1} K^{-1} ($Y_{0.96}Cu_{1.08}Te_2$)	κ_{pho} / W m^{-1} K^{-1} ($Y_{0.96}Cu_{1.08}Te_2$)
323.75	0.82±0.12	100±20	0.71±0.11
373.85	0.99±0.15	94±14	0.90±0.13
393.85	1.0±0.2	93±14	0.94±0.14
413.85	0.97±0.15	94±14	0.87±0.13
433.95	0.96±0.14	95±14	0.87±0.13
453.95	0.99±0.15	96±14	0.89±0.13
474.05	0.98±0.15	98±15	0.88±0.13
493.95	0.88±0.13	98±15	0.78±0.12
523.95	0.80±0.12	96±14	0.71±0.11
573.95	0.74±0.11	85±13	0.66±0.10
623.85	0.66±0.10	75±11	0.58±0.09
673.85	0.59±0.09	71±11	0.52±0.08
723.85	0.57±0.09	71±11	0.50±0.07
773.75	0.54±0.08	74±11	0.47±0.07
793.75	0.50±0.08	75±11	0.43±0.06

T / K	κ / W m^{-1} K^{-1} ($Y_{0.98}CuTe_2$)	κ_{el} / mW m^{-1} K^{-1} ($Y_{0.98}CuTe_2$)	κ_{pho} / W m^{-1} K^{-1} ($Y_{0.98}CuTe_2$)
327.95	1.3±0.2	81±12	1.3±0.2
370.25	1.2±0.2	74±11	1.1±0.2
390.45	1.1±0.2	71±11	1.0±0.2
411.45	0.91±0.14	68±10	0.84±0.13
432.95	1.0±0.2	66±10	0.94±0.14
454.65	0.94±0.14	65±10	0.88±0.13
474.85	0.94±0.14	64±10	0.88±0.13
494.35	0.90±0.14	63±9	0.84±0.13
524.75	0.81±0.12	61±9	0.75±0.11
575.25	0.71±0.11	60±9	0.65±0.10
624.85	0.66±0.10	60±9	0.60±0.09
674.65	0.61±0.09	60±9	0.55±0.08
724.75	0.57±0.09	62±9	0.51±0.08
774.15	0.54±0.08	66±10	0.47±0.07
794.05	0.52±0.08	68±10	0.45±0.07

T / K	κ / W m^{-1} K^{-1} ($YCuTe_2$)	T / K	κ / W m^{-1} K^{-1} ($Y_{0.96}Cu_{1.08}Te_2$)
303.492	1.2±0.06	303.210	1.0±0.2
278.067	1.3±0.06	277.823	1.0±0.2
253.086	1.3±0.06	252.865	1.1±0.2
227.638	1.3±0.07	227.463	1.1±0.2
202.679	1.4±0.07	202.533	1.1±0.2
176.835	1.4±0.07	176.745	1.2±0.2
151.093	1.5±0.07	151.119	1.2±0.2
125.890	1.5±0.08	125.952	1.2±0.2
100.736	1.6±0.08	100.806	1.2±0.2
75.579	1.6±0.08	75.645	1.2±0.2
50.344	1.6±0.08	50.418	1.2±0.2
25.241	1.3±0.06	25.351	1.0±0.2
10.193	0.66±0.03	10.716	0.62±0.09
5.226	0.34±0.02	5.361	0.34±0.05
2.404	0.14±0.01	2.307	0.11±0.02
15.119	0.91±0.05	15.095	0.84±0.13
30.213	1.4±0.07	30.186	1.1±0.2
60.348	1.6±0.08	60.307	1.3±0.2
110.864	1.6±0.08	110.770	1.2±0.2
160.997	1.5±0.07	160.776	1.2±0.2
211.367	1.4±0.07	210.921	1.1±0.2
262.589	1.3±0.06	261.752	1.1±0.2
303.415	1.2±0.06	302.694	1.01±0.2

Appendix D

Metal Phosphides

Table D.1: Variable relaxation time of metal phosphides at room temperature.

Compound	Space group	$p-\tau_{el,variable}$ / s	$n-\tau_{el,variable}$ / s
NiP_2	$Pa\bar{3}$	$2.48{\cdot}10^{-15}$	$2.67{\cdot}10^{-15}$
NiP_2	$C2/c$	$1.64{\cdot}10^{-14}$	$5.96{\cdot}10^{-15}$
ZnP_2	$P4_32_12$	$1.58{\cdot}10^{-14}$	$7.09{\cdot}10^{-15}$
ZnP_2	$P4_12_12$	$1.58{\cdot}10^{-14}$	$7.10{\cdot}10^{-15}$
AgP_2	$P2_1/c$	$5.30{\cdot}10^{-14}$	$2.50{\cdot}10^{-14}$
TiP_2	$Pnnm$	$1.63{\cdot}10^{-16}$	$2.39{\cdot}10^{-16}$
CuP_2	$P2_1/c$	$1.79{\cdot}10^{-14}$	$8.47{\cdot}10^{-15}$
RuP_2	$Pnnm$	$9.81{\cdot}10^{-14}$	$3.24{\cdot}10^{-14}$
CoP_2	$P2_1/c$	$2.06{\cdot}10^{-14}$	$3.19{\cdot}10^{-15}$
IrP_2	$P2_1/c$	$1.12{\cdot}10^{-13}$	$1.62{\cdot}10^{-14}$
BeP_2	$C2/c$	$1.09{\cdot}10^{-14}$	$1.47{\cdot}10^{-14}$
RhP_2	$P2_1/c$	$6.61{\cdot}10^{-14}$	$7.41{\cdot}10^{-15}$
PdP_2	$C2/c$	$4.00{\cdot}10^{-15}$	$8.86{\cdot}10^{-14}$
FeP_2	$Pnnm$	$3.31{\cdot}10^{-15}$	$2.12{\cdot}10^{-14}$
Zn_3P_2	$P4_2/nmc$	$5.87{\cdot}10^{-16}$	$1.86{\cdot}10^{-14}$
Mg_3P_2	$Pn\bar{3}m$	$2.69{\cdot}10^{-14}$	$1.71{\cdot}10^{-14}$
Cd_3P_2	$P4_2/nmc$	$3.87{\cdot}10^{-15}$	$1.57{\cdot}10^{-14}$
NaZnP	$P4/nmm$	$1.48{\cdot}10^{-15}$	$6.76{\cdot}10^{-15}$
SrLiP	$P\bar{6}m2$	$8.29{\cdot}10^{-15}$	$5.22{\cdot}10^{-15}$
BaLiP	$P\bar{6}m2$	$4.52{\cdot}10^{-15}$	$1.33{\cdot}10^{-14}$
NaSnP	$P6_3mc$	$8.54{\cdot}10^{-16}$	$1.13{\cdot}10^{-14}$
MnP_4	$P\bar{1}$	$1.99{\cdot}10^{-14}$	$7.58{\cdot}10^{-15}$
MnP_4	$P\bar{1}$	$1.58{\cdot}10^{-14}$	$2.81{\cdot}10^{-15}$
FeP	$Pnma$	$4.85{\cdot}10^{-17}$	$2.64{\cdot}10^{-17}$
Mg_3P_2	$Ia\bar{3}$	$2.79{\cdot}10^{-14}$	$1.72{\cdot}10^{-14}$
BP	$F\bar{4}3m$	$1.47{\cdot}10^{-14}$	$3.03{\cdot}10^{-14}$
GaP	$F\bar{4}3m$	$6.03{\cdot}10^{-15}$	$1.28{\cdot}10^{-13}$
PbTe	$Fm\bar{3}m$	$2.51{\cdot}10^{-14}$	$2.86{\cdot}10^{-14}$
Bi_2Te_3	$R\bar{3}m$	$6.16{\cdot}10^{-16}$	$1.07{\cdot}10^{-14}$

Table D.2: Computed p-type electrical conductivity using constant relaxation time, $\sigma_{el,const}$, and variable relaxation time, $\sigma_{el,variable}$, at 300 K. Electrical conductivity is shown in Figure 5.30 (a).

Compound	Space group	$p-\sigma_{el,const}$ / S cm^{-1}	$p-\sigma_{el,variable}$ / S cm^{-1}
NiP_2	$Pa\bar{3}$	4350	1310
NiP_2	$C2/c$	84.0	642
ZnP_2	$P4_32_12$	455	416
ZnP_2	$P4_12_12$	454	416
AgP_2	$P2_1/c$	634	1360
TiP_2	$Pnnm$	7580	204
CuP_2	$P2_1/c$	514	515
RuP_2	$Pnnm$	737	4680
CoP_2	$P2_1/c$	529	447
IrP_2	$P2_1/c$	639	4300
BeP_2	$C2/c$	628	371
RhP_2	$P2_1/c$	661	2730
PdP_2	$C2/c$	422	120
FeP_2	$Pnnm$	93.7	22.9
Zn_3P_2	$P4_2/nmc$	5560	20.9
Mg_3P_2	$Pn\bar{3}m$	216	391
Cd_3P_2	$P4_2/nmc$	485	122
NaZnP	$P4/nmm$	587	57.6
SrLiP	$P\bar{6}m2$	445	203
BaLiP	$P\bar{6}m2$	818	155
NaSnP	$P6_3mc$	599	39.7
MnP_4	$P\bar{1}$	149	186
MnP_4	$P\bar{1}$	189	182
FeP	$Pnma$	9640	44.4
Mg_3P_2	$Ia\bar{3}$	209	427
BP	$F\bar{4}3m$	813	661
GaP	$F\bar{4}3m$	661	237
PbTe	$Fm\bar{3}m$	1310	1520
Bi_2Te_3	$R\bar{3}m$	1070	1260

Table D.3: Computed n-type electrical conductivity using constant relaxation time, $\sigma_{el,const}$, and variable relaxation time, $\sigma_{el,variable}$, at 300 K. Electrical conductivity is shown in Figure 5.30 (a).

Compound	Space group	$n - \sigma_{el,const}$ / S cm^{-1}	$n - \sigma_{el,variable}$ / S cm^{-1}
NiP_2	$Pa\bar{3}$	3780	1260
NiP_2	$C2/c$	1250	345.1
ZnP_2	$P4_32_12$	238	136
ZnP_2	$P4_12_12$	237	135
AgP_2	$P2_1/c$	554	690
TiP_2	$Pnnm$	7630	213
CuP_2	$P2_1/c$	422	191
RuP_2	$Pnnm$	369	711
CoP_2	$P2_1/c$	238	55.5
IrP_2	$P2_1/c$	281	244
BeP_2	$C2/c$	569	498
RhP_2	$P2_1/c$	148	71.5
PdP_2	$C2/c$	1050	4580
FeP_2	$Pnnm$	214	299
Zn_3P_2	$P4_2/nmc$	867	426
Mg_3P_2	$Pn\bar{3}m$	720	501
Cd_3P_2	$P4_2/nmc$	1400	441
NaZnP	$P4/nmm$	942	264
SrLiP	$P\bar{6}m2$	297	106
BaLiP	$P\bar{6}m2$	952	420
NaSnP	$P6_3mc$	883	563
MnP_4	$P\bar{1}$	92.7	51.5
MnP_4	$P\bar{1}$	252	42.8
FeP	$Pnma$	9690	44.2
Mg_3P_2	$Ia\bar{3}$	755	542
BP	$F\bar{4}3m$	823	1480
GaP	$F\bar{4}3m$	1170	7990
PbTe	$Fm\bar{3}m$	1240	1530
Bi_2Te_3	$R\bar{3}m$	1170	1110

Table D.4: Computed p-type electrical conductivity using constant relaxation time, $\sigma_{el,const}$, and variable relaxation time, $\sigma_{el,variable}$, at 1300 K. Electrical conductivity is shown in Figure 5.30 (b).

Compound	Space group	$p-\sigma_{el,const}$ / S cm^{-1}	$p-\sigma_{el,variable}$ / S cm^{-1}
NiP_2	$Pa\bar{3}$	9030	245
NiP_2	$C2/c$	1320	122
ZnP_2	$P4_32_12$	126	23.3
ZnP_2	$P4_12_12$	126	23.3
AgP_2	$P2_1/c$	412	158
TiP_2	$Pnnm$	10127	27.7
CuP_2	$P2_1/c$	337	50.8
RuP_2	$Pnnm$	529	365
CoP_2	$P2_1/c$	802	88.0
IrP_2	$P2_1/c$	467	436
BeP_2	$C2/c$	470	41.6
RhP_2	$P2_1/c$	1080	558
PdP_2	$C2/c$	1151	347
FeP_2	$Pnnm$	795	98.6
Zn_3P_2	$P4_2/nmc$	604	11.3
Mg_3P_2	$Pn\bar{3}m$	148	31.5
Cd_3P_2	$P4_2/nmc$	683	36.4
NaZnP	$P4/nmm$	443	5.90
SrLiP	$P\bar{6}m2$	303	18.9
BaLiP	$P\bar{6}m2$	279	10.3
NaSnP	$P6_3mc$	568	9.89
MnP_4	$P\bar{1}$	245	34.0
MnP_4	$P\bar{1}$	564	46.8
FeP	$Pnma$	11400	5.36
Mg_3P_2	$Ia\bar{3}$	119	35.5
BP	$F\bar{4}3m$	718	82.8
GaP	$F\bar{4}3m$	600	28.8
PbTe	$Fm\bar{3}m$	900	158
Bi_2Te_3	$R\bar{3}m$	678	155

Table D.5: Computed n-type electrical conductivity using constant relaxation time, $\sigma_{el,const}$, and variable relaxation time, $\sigma_{el,variable}$, at 1300 K. Electrical conductivity is shown in Figure 5.30 (b).

Compound	Space group	$n - \sigma_{el,const}$ / S cm^{-1}	$n - \sigma_{el,variable}$ / S cm^{-1}
NiP_2	$Pa\bar{3}$	8680	238
NiP_2	$C2/c$	1675	108
ZnP_2	$P4_32_12$	180	13.3
ZnP_2	$P4_12_12$	180	13.3
AgP_2	$P2_1/c$	354	71.6
TiP_2	$Pnnm$	10200	28.3
CuP_2	$P2_1/c$	301	21.0
RuP_2	$Pnnm$	546	201
CoP_2	$P2_1/c$	763	59.1
IrP_2	$P2_1/c$	241	50.2
BeP_2	$C2/c$	406	49.8
RhP_2	$P2_1/c$	760	298
PdP_2	$C2/c$	1360	746
FeP_2	$Pnnm$	883	121
Zn_3P_2	$P4_2/nmc$	729	72.7
Mg_3P_2	$Pn\bar{3}m$	620	71.1
Cd_3P_2	$P4_2/nmc$	1300	89.5
NaZnP	$P4/nmm$	778	37.6
SrLiP	$P\bar{6}m2$	258	11.7
BaLiP	$P\bar{6}m2$	319	29.2
NaSnP	$P6_3mc$	837	73
MnP_4	$P\bar{1}$	219	26.0
MnP_4	$P\bar{1}$	577	32.7
FeP	$Pnma$	11500.86	5.35
Mg_3P_2	$Ia\bar{3}$	664	84.2
BP	$F\bar{4}3m$	686	172
GaP	$F\bar{4}3m$	877	865
PbTe	$Fm\bar{3}m$	1050	211
Bi_2Te_3	$R\bar{3}m$	941	186

Table D.6: Computed band gap energy of various metal phosphides using PBE-GGA and HSE06 exchange functionals.

Compound	Space group	HSE (PBE-GGA) / eV
NiP_2	$Pa\bar{3}$	0.13 (0.00)
NiP_2	$C2/c$	1.15 (0.53)
ZnP_2	$P4_32_12$	2.20 (1.46)
ZnP_2	$P4_12_12$	2.20 (1.46)
AgP_2	$P2_1/c$	1.30 (0.66)
TiP_2	$Pnnm$	0.00 (0.00)
CuP_2	$P2_1/c$	(0.86)
RuP_2	$Pnnm$	(0.48)
CoP_2	$P2_1/c$	(0.44)
IrP_2	$P2_1/c$	(0.78)
BeP_2	$C2/c$	(0.83)
RhP_2	$P2_1/c$	(0.37)
PdP_2	$C2/c$	(0.46)
FeP_2	$Pnnm$	(0.43)
Zn_3P_2	$P4_2/nmc$	1.17 (0.31)
Mg_3P_2	$Pn\bar{3}m$	(1.11)
Cd_3P_2	$P4_2/nmc$	(0.19)
NaZnP	$P4/nmm$	(0.91)
SrLiP	$P\bar{6}m2$	(0.80)
BaLiP	$P\bar{6}m2$	(0.70)
NaSnP	$P6_3mc$	(0.58)
MnP_4	$P\bar{1}$	(0.48)
MnP_4	$P\bar{1}$	1.58 (0.44)
FeP	$Pnma$	0.00 (0.00)
Mg_3P_2	$Ia\bar{3}$	2.20 (1.61)
BP	$F\bar{4}3m$	1.98 (1.24)
GaP	$F\bar{4}3m$	(1.59)
PbTe	$Fm\bar{3}m$	(0.81)
Bi_2Te_3	$R\bar{3}m$	(0.25)

Table D.7: Minimum thermal conductivity using different models. Using static disordering, $\kappa_{min,static}$, and an average phonon mean speed indicates the amorphous limit. The minimum thermal conductivities using the Cahill-Pohl model where the speed of sounds were calculated from bulk and shear moduli, $\kappa_{min,CP,E}$, predict the highest values.

Compound	Space group	$\kappa_{min,CP,HT}$ / W m^{-1} K^{-1}	$\kappa_{min,CP,E}$ / W m^{-1} K^{-1}	$\kappa_{min,static}$ / W m^{-1} K^{-1}	$\kappa_{min,dyn}$ / W m^{-1} K^{-1}
NiP_2	$Pa\bar{3}$	1.60	1.36	0.81	1.22
NiP_2	$C2/c$	1.32	1.06	0.53	0.80
ZnP_2	$P4_32_12$	1.14	0.86	0.39	0.58
ZnP_2	$P4_12_12$	0.97	0.86	0.47	0.71
AgP_2	$P2_1/c$	0.95	0.58	0.39	0.58
Zn_3P_2	$P4_2/nmc$	0.92	0.71	0.34	0.51
Mg_3P_2	$Pn\bar{3}m$	1.07	0.92	0.44	0.67
MnP_4	$P\bar{1}$	1.77	1.57	0.91	1.41
BP	$F\bar{4}3m$	2.81	2.43	0.89	1.34
GaP	$F\bar{4}3m$	0.97	0.68	0.27	0.40

Table D.8: Comparison of minimum thermal conductivity using the Cahill, Watson, and Pohl model [66, 67] with the thermal conductivity from the semi-empirical model [68]. Thermal conductivities are shown in Figure 5.36.

Compound	Space group	$\kappa_{min,CP,HT}$ / W m^{-1} K^{-1}	κ_{SE} / W m^{-1} K^{-1}
NiP_2	$Pa\bar{3}$	1.60	12.7
NiP_2	$C2/c$	1.32	14.3
ZnP_2	$P4_32_12$	0.97	6.36
ZnP_2	$P4_12_12$	1.14	6.36
AgP_2	$P2_1/c$	0.95	4.18
TiP_2	$Pnnm$	1.60	4.88
CuP_2	$P2_1/c$	1.12	6.90
RuP_2	$Pnnm$	1.66	13.2
CoP_2	$P2_1/c$	1.78	9.69
IrP_2	$P2_1/c$	1.24	10.2
BeP_2	$C2/c$	9.19	10.9
RhP_2	$P2_1/c$	1.51	9.65
PdP_2	$C2/c$	1.04	13.1
FeP_2	$Pnnm$	2.00	13.4
Zn_3P_2	$P4_2/nmc$	0.92	2.60
Mg_3P_2	$Pn\bar{3}m$	1.14	4.18
Cd_3P_2	$P4_2/nmc$	0.52	1.84
NaZnP	$P4/nmm$	0.80	1.84
SrLiP	$P\bar{6}m2$	0.79	2.12
BaLiP	$P\bar{6}m2$	0.60	1.55
NaSnP	$P6_3mc$	0.52	1.75
MnP_4	$P\bar{1}$	1.78	8.44
MnP_4	$P\bar{1}$	1.73	4.85
FeP	$Pnma$	1.73	4.85
Mg_3P_2	$Ia\bar{3}$	1.07	–
BP	$F\bar{4}3m$	2.81	240
GaP	$F\bar{4}3m$	0.97	48
PbTe	$Fm\bar{3}m$	0.34	2.26
Bi_2Te_3	$R\bar{3}m$	0.22	0.56

Table D.9: Rietveld refined PXRD data for c-NiP_2. The diffractogram of$c$-NiP_2 is shown in Figure 5.41.

Parameter	c-NiP_2
Space group	$Pa\bar{3}$ (No. 205)
a / Å	5.469
b / Å	5.469
c / Å	5.469
α / °	90.000
β / °	90.000
γ / °	90.000
Number of molecules per unit cell, Z	4
Volume / Å^3	164
Calculated density / g cm^{-3}	4.899
R_p	11.21
R_{wp}	16.96
χ^2	1.65

Atom	Site	x	y	z	Occupation
Ni	4a	0.000	0.000	0.000	1.000
P	8c	0.385	0.385	0.385	2.001

Table D.10: Heat capacity data of c-NiP_2: 27.820 mg with ^{4}He option; in order of data collection. The heat capacity is plotted as function of temperature in Figure 5.43.

T / K	C_p / J mol^{-1} K^{-1}	T / K	C_p / J mol^{-1} K^{-1}	T / K	C_p / J mol^{-1} K^{-1}
303.637	67.0±0.7	53.289	7.99±0.08	9.960	0.133±0.001
283.407	65.8±0.7	48.282	6.32±0.06	9.024	0.111±0.001
263.263	63.1±0.6	43.737	4.96±0.05	8.167	0.0940±0.0009
243.058	60.6±0.6	39.625	3.87±0.04	7.396	0.0806±0.0008
222.891	57.9±0.6	35.906	2.99±0.03	6.698	0.0718±0.0007
202.693	54.6±0.5	32.534	2.31±0.02	6.076	0.0623±0.0006
182.479	50.8±0.5	29.481	1.78±0.02	5.494	0.0565±0.0006
162.265	46.2±0.5	26.715	1.38±0.01	4.975	0.0520±0.0005
142.046	40.6±0.4	24.207	1.05±0.01	4.506	0.0478±0.0005
121.793	34.1±0.3	21.939	0.815±0.008	4.081	0.0445±0.0004
101.570	26.7±0.3	19.892	0.636±0.006	3.696	0.0417±0.0004
96.532	24.6±0.2	18.015	0.494±0.005	3.345	0.0391±0.0004
87.451	20.7±0.2	16.327	0.390±0.004	3.027	0.0371±0.0004
79.243	17.7±0.2	14.785	0.307±0.003	2.743	0.0358±0.0004
71.746	14.9±0.1	13.395	0.245±0.002	2.486	0.0333±0.0003
65.061	12.1±0.1	12.136	0.198±0.002	2.251	0.0321±0.0003
58.838	9.98±0.10	10.996	0.160±0.002	2.039	0.0301±0.0003

Table D.11: Heat capacity data of c-NiP_2: 21.010 mg with ^{3}He option; in order of data collection. The heat capacity is plotted as function of temperature in Figure 5.43.

T / K	C_p / mJ mol^{-1} K^{-1}	T / K	C_p / mJ mol^{-1} K^{-1}	T / K	C_p / mJ mol^{-1} K^{-1}
301.882	69900±700	3.446	32.3±1.6	1.100	15.9±0.8
10.054	125±1	3.175	31.0±1.6	1.016	14.9±0.8
9.260	106±1	2.925	29.4±1.5	0.938	13.7±0.7
8.524	90.8±0.9	2.694	27.9±1.4	0.867	12.8±0.6
7.848	78.6±0.8	2.482	26.7±1.3	0.799	11.8±0.6
7.223	68.8±0.7	2.288	26.1±1.3	0.739	10.7±0.5
6.652	60.4±0.6	2.107	24.8±1.2	0.685	10.2±0.5
6.125	54.4±0.5	1.942	23.6±1.2	0.629	9.32±0.47
5.648	49.3±0.5	1.790	22.7±1.1	0.585	9.26±0.46
5.201	45.0±0.5	1.650	21.6±1.1	0.541	8.36±0.42
4.790	41.5±2.1	1.521	20.3±1.0	0.499	7.99±0.40
4.413	38.5±1.9	1.403	19.1±1.0	0.465	7.88±0.39
4.066	36.0±1.8	1.293	18.0±0.9	0.435	6.92±0.35
3.740	34.2±1.7	1.193	17.0±0.9		

Table D.12: Electrical resistivity of c-NiP_2; in order of data collection. The electrical resistivity is plotted as function of temperature in Figure 5.45 (a).

T / K	ρ_{el} / mΩ cm (c-NiP_2)	T / K	ρ_{el} / mΩ cm (c-NiP_2)	T / K	ρ_{el} / mΩ cm (c-NiP_2)
295.25	9.05±0.45	444.75	7.92±0.40	587.85	6.75±0.34
298.45	9.01±0.45	449.55	7.89±0.39	592.75	6.70±0.34
299.65	8.99±0.45	454.25	7.86±0.39	597.55	6.66±0.33
304.75	8.93±0.45	459.15	7.83±0.39	602.25	6.61±0.33
314.05	8.86±0.44	463.75	7.80±0.39	607.15	6.56±0.33
321.85	8.82±0.44	468.65	7.76±0.39	611.65	6.51±0.33
326.15	8.80±0.44	473.65	7.72±0.39	616.75	6.47±0.32
329.75	8.77±0.44	478.05	7.69±0.38	621.35	6.42±0.32
334.15	8.73±0.44	482.85	7.65±0.38	626.15	6.37±0.32
339.45	8.70±0.44	487.65	7.61±0.38	630.95	6.33±0.32
344.65	8.66±0.43	492.35	7.58±0.38	635.65	6.28±0.31
349.55	8.62±0.43	497.15	7.54±0.38	640.45	6.24±0.31
354.25	8.59±0.43	501.85	7.50±0.38	645.45	6.19±0.31
358.85	8.55±0.43	506.75	7.46±0.37	649.95	6.15±0.31
363.65	8.52±0.43	511.45	7.42±0.37	654.55	6.11±0.31
368.65	8.48±0.42	516.15	7.39±0.37	659.45	6.06±0.30
373.05	8.45±0.42	521.05	7.34±0.37	664.25	6.01±0.30
377.95	8.42±0.42	525.85	7.31±0.37	669.05	5.96±0.30
382.75	8.38±0.42	530.45	7.27±0.36	673.75	5.92±0.30
387.45	8.35±0.42	535.35	7.23±0.36	678.45	5.87±0.29
392.25	8.32±0.42	540.35	7.18±0.36	683.35	5.82±0.29
397.15	8.28±0.41	544.85	7.14±0.36	687.95	5.77±0.29
401.75	8.25±0.41	549.85	7.10±0.36	692.85	5.71±0.29
406.55	8.21±0.41	554.35	7.06±0.35	697.65	5.66±0.28
411.45	8.17±0.41	559.15	7.02±0.35	702.35	5.60±0.28
415.95	8.14±0.41	563.95	6.97±0.35	707.05	5.55±0.28
420.75	8.1±0.41	568.55	6.93±0.35	712.05	5.49±0.27
425.85	8.06±0.40	573.65	6.88±0.34	716.75	5.43±0.27
430.35	8.03±0.40	578.35	6.84±0.34	721.55	5.37±0.27
435.25	7.99±0.40	583.15	6.79±0.34	726.15	5.31±0.27
439.85	7.96±0.40				

T / K	ρ_{el} / mΩ cm (c-NiP_2)	T / K	ρ_{el} / mΩ cm (c-NiP_2)	T / K	ρ_{el} / mΩ cm (c-NiP_2)
391.850	9.00±0.45	261.808	10.5±0.5	18.547	13.3±0.7
371.958	8.82±0.44	126.815	12.6±0.6	15.604	13.3±0.7
352.085	8.71±0.44	101.573	12.9±0.6	10.496	13.4±0.7
332.210	8.79±0.44	81.347	13.0±0.7	8.290	13.4±0.7
312.272	9.11±0.46	51.092	13.2±0.7	6.282	13.4±0.7
161.134	12.4±0.6	31.097	13.3±0.7	4.354	13.5±0.7
211.319	11.6±0.6	20.580	13.3±0.7	2.413	13.6±0.7

Table D.13: Hall mobility of c-NiP_2; in order of data collection. The Hall mobility is plotted as function of temperature in Figure 5.45 (b).

T / K	μ_H / cm^2 V s^{-1} (c-NiP_2)	T / K	μ_H / cm^2 V s^{-1} (c-NiP_2)	T / K	μ_H / cm^2 V s^{-1} (c-NiP_2)
295.25	-0.32±0.02	444.75	-0.33±0.02	587.85	-0.74±0.04
298.45	-0.25±0.01	449.55	-0.54±0.03	592.75	-0.56±0.03
299.65	-0.78±0.04	454.25	-0.49±0.02	597.55	-0.37±0.02
304.75	-1.1±0.1	459.15	-0.43±0.02	602.25	-0.73±0.04
314.05	-0.84±0.04	463.75	-0.58±0.03	607.15	-0.68±0.03
321.85	-0.52±0.03	468.65	-0.47±0.02	611.65	-0.65±0.03
326.15	-0.64±0.03	473.65	-0.58±0.03	616.75	-0.69±0.03
329.75	-0.73±0.04	478.05	-0.44±0.02	621.35	-0.51±0.03
334.15	-0.61±0.03	482.85	-0.48±0.02	626.15	-0.59±0.03
339.45	-0.82±0.04	487.65	-0.50±0.03	630.95	-0.47±0.02
344.65	-0.74±0.04	492.35	-0.63±0.03	635.65	-0.58±0.03
349.55	-0.70±0.04	497.15	-0.53±0.03	640.45	-0.57±0.03
354.25	-0.65±0.03	501.85	-0.45±0.02	645.45	-0.56±0.03
358.85	-0.65±0.03	506.75	-0.49±0.02	649.95	-0.57±0.03
363.65	-0.64±0.03	511.45	-0.49±0.02	654.55	-0.55±0.03
368.65	-0.59±0.03	516.15	-0.70±0.04	659.45	-0.76±0.04
373.05	-0.65±0.03	521.05	-0.43±0.02	664.25	-0.42±0.02
377.95	-0.65±0.03	525.85	-0.52±0.03	669.05	-0.60±0.03
382.75	-0.47±0.02	530.45	-0.51±0.03	673.75	-0.46±0.02
387.45	-0.40±0.02	535.35	-0.75±0.04	678.45	-0.56±0.03
392.25	-0.63±0.03	540.35	-0.47±0.02	683.35	-0.46±0.02
397.15	-0.53±0.03	544.85	-0.59±0.03	687.95	-0.52±0.03
401.75	-0.67±0.03	549.85	-0.52±0.03	692.85	-0.11±0.01
406.55	-0.66±0.03	554.35	-0.53±0.03	697.65	-0.22±0.01
411.45	-0.42±0.02	559.15	-0.88±0.04	702.35	-0.24±0.01
415.95	-0.76±0.04	563.95	-0.51±0.03	707.05	-0.33±0.02
420.75	-0.57±0.03	568.55	-0.72±0.04	712.05	-0.19±0.01
425.85	-0.53±0.03	573.65	-0.52±0.03	716.75	-0.31±0.02
430.35	-0.39±0.02	578.35	-0.66±0.03	721.55	-0.27±0.01
435.25	-0.55±0.03	583.15	-0.72±0.04	726.15	-0.31±0.02
439.85	-0.50±0.03				

Table D.14: Hall carrier concentration of c-NiP_2; in order of data collection. The Hall carrier concentration is plotted as function of temperature in Figure 5.45 (c).

T / K	n_H / 10^{21} e^-cm^{-3} (c-NiP_2)	T / K	n_H / 10^{21} e^-cm^{-3} (c-NiP_2)	T / K	μ_H / 10^{21} e^-cm^{-3} (c-NiP_2)
295.25	2.1±0.1	444.75	2.4±0.1	587.85	1.3±0.1
298.45	2.8±0.1	449.55	1.5±0.1	592.75	1.7±0.1
299.65	0.89±0.04	454.25	1.6±0.1	597.55	2.5±0.1
304.75	0.62±0.03	459.15	1.9±0.1	602.25	1.3±0.1
314.05	0.84±0.04	463.75	1.4±0.1	607.15	1.4±0.1
321.85	1.4±0.1	468.65	1.7±0.1	611.65	1.5±0.1
326.15	1.1±0.1	473.65	1.4±0.1	616.75	1.4±0.1
329.75	0.97±0.05	478.05	1.8±0.1	621.35	1.9±0.1
334.15	1.2±0.1	482.85	1.7±0.1	626.15	1.7±0.1
339.45	0.88±0.04	487.65	1.6±0.1	630.95	2.1±0.1
344.65	0.97±0.05	492.35	1.3±0.1	635.65	1.7±0.1
349.55	1.0±0.1	497.15	1.6±0.1	640.45	1.8±0.1
354.25	1.1±0.1	501.85	1.9±0.1	645.45	1.8±0.1
358.85	1.1±0.1	506.75	1.7±0.1	649.95	1.8±0.1
363.65	1.1±0.1	511.45	1.7±0.1	654.55	1.9±0.1
368.65	1.2±0.1	516.15	1.2±0.1	659.45	1.4±0.1
373.05	1.1±0.1	521.05	2.0±0.1	664.25	2.5±0.1
377.95	1.1±0.1	525.85	1.7±0.1	669.05	1.8±0.1
382.75	1.6±0.1	530.45	1.7±0.1	673.75	2.3±0.1
387.45	1.9±0.1	535.35	1.2±0.1	678.45	1.9±0.1
392.25	1.2±0.1	540.35	1.8±0.1	683.35	2.4±0.1
397.15	1.4±0.1	544.85	1.5±0.1	687.95	2.1±0.1
401.75	1.1±0.1	549.85	1.7±0.1	692.85	9.5±0.5
406.55	1.2±0.1	554.35	1.7±0.1	697.65	5.1±0.3
411.45	1.8±0.1	559.15	1.0±0.1	702.35	4.6±0.2
415.95	1.0±0.1	563.95	1.7±0.1	707.05	3.4±0.2
420.75	1.4±0.1	568.55	1.3±0.1	712.05	6.0±0.3
425.85	1.5±0.1	573.65	1.8±0.1	716.75	3.7±0.2
430.35	2.0±0.1	578.35	1.4±0.1	721.55	4.3±0.2
435.25	1.4±0.1	583.15	1.3±0.1	726.15	3.8±0.2
439.85	1.6±0.1				

Table D.15: Seebeck coefficient of c-NiP_2; in order of data collection. The Seebeck coefficient is plotted as function of temperature in Figure 5.46.

T / K	S / µV K^{-1} (c-NiP_2)	T / K	S / µV K^{-1} (c-NiP_2)	T / K	S / µV K^{-1} (c-NiP_2)
324.55	-37.6±1.9	391.863	-40.9±2.04	126.761	-23.5±1.2
369.63	-41.0±2.1	371.974	-40.7±2.04	101.573	-16.2±0.8
415.88	-44.3±2.2	352.103	-41.0±2.05	81.347	-15.3±0.8
462.83	-47.5±2.4	332.220	-39.7±1.98	51.092	-10.1±0.5
511.20	-50.8±2.5	312.281	-39.1±1.95	31.097	-4.79±0.24
559.07	-55.1±2.8	292.295	-39.5±1.97	20.580	-2.89±0.14
606.79	-57.7±2.9	272.334	-37.7±1.88	18.547	-3.97±0.20
654.87	-55.6±2.8	252.398	-36.6±1.83	15.604	-2.02±0.10
701.40	-51.5±2.6	226.915	-34.6±1.73	10.496	-0.86±0.04
748.50	-44.8±2.2	202.037	-32.2±1.61	8.290	-2.54±0.13
		176.810	-29.2±1.5	4.354	-1.73±0.09
		151.928	-26.5±1.3	2.413	-1.41±0.07

Table D.16: Thermal conductivity of c-NiP_2; in order of data collection. Thermal conductivity was not corrected to zero porosity. The thermal conductivity is plotted as function of temperature in Figure 5.47.

T / K	κ / W m^{-1} K^{-1} (c-NiP_2)	κ_{el} / W m^{-1} K^{-1} (c-NiP_2)	κ_{pho} / W m^{-1} K^{-1} (c-NiP_2)
323.45	0.918±0.138	0.085±0.013	0.83±0.13
375.15	0.966±0.145	0.10±0.02	0.87±0.13
425.45	1.00±0.15	0.13±0.02	0.88±0.13
475.15	1.04±0.16	0.14±0.02	0.90±0.13
524.95	1.07±0.16	0.16±0.02	0.91±0.14
574.55	1.11±0.17	0.19±0.03	0.92±0.14
624.35	1.16±0.17	0.22±0.03	0.93±0.14
674.25	1.20±0.18	0.29±0.04	0.91±0.14
724.15	1.24±0.19		

T / K	κ / W m^{-1} K^{-1} (c-NiP_2)	T / K	κ / W m^{-1} K^{-1} (c-NiP_2)
312.281	1.16±0.12	51.092	0.331±0.033
292.295	1.12±0.11	31.097	0.171±0.017
272.334	1.08±0.11	20.579	0.0909±0.0091
252.398	1.05±0.10	18.560	0.0771±0.0077
226.915	0.987±0.099	15.624	0.0599±0.0060
202.037	0.936±0.094	10.508	0.0324±0.0032
176.810	0.881±0.088	8.295	0.0220±0.0022
151.928	0.863±0.086	6.298	0.0147±0.0015
126.761	0.753±0.075	4.361	0.00877±0.00088
101.573	0.621±0.062	2.420	0.00400±0.00040
81.347	0.523±0.052		

Appendix E

Germanium Clathrates with Partial Filling by Sodium

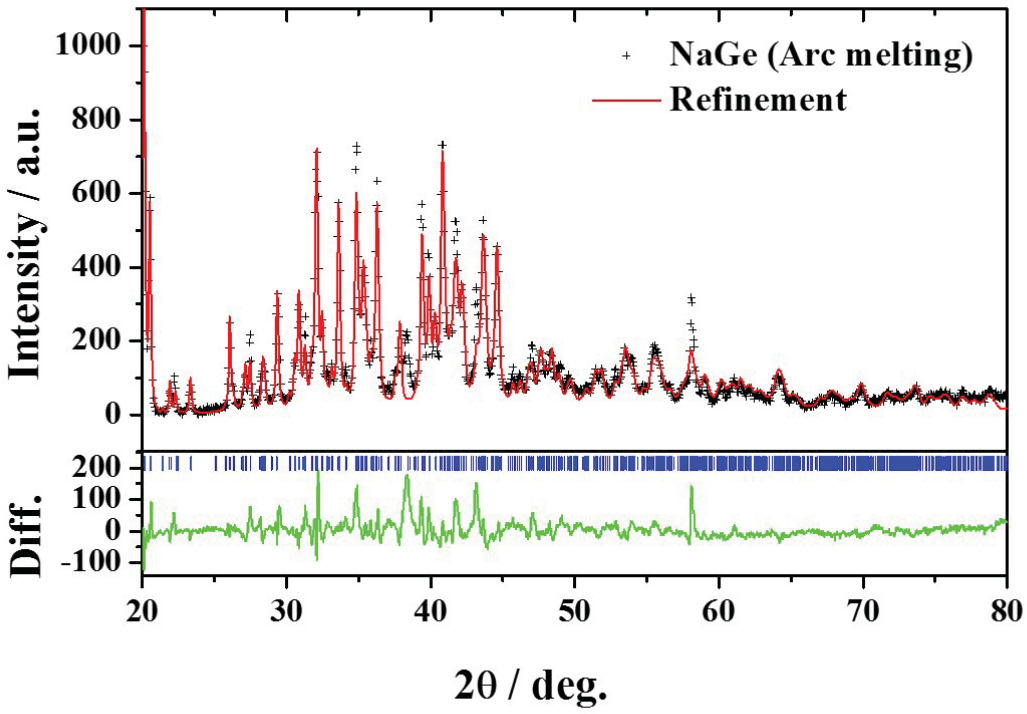

Figure E.1: Rietveld refined PXRD pattern of NaGe precursor (see Section 5.3). Blue ticks mark the calculated position of the reflections. Refined data are given in Table E.1.

Table E.1: Rietveld refined PXRD data for NaGe precursor. The diffractograms of NaGe precursor is shown in Figure E.1.

Parameter	NaGe Precursor
Space group	$P2_1/c$ (No. 14)
a / Å	12.365
b / Å	6.657
c / Å	11.475
α / °	90.000
β / °	120.187
γ / °	90.000
Number of molecules per unit cell, Z	4
Volume / Å^3	1529
Calculated density / g cm^{-3}	3.109
R_p	13.48
R_{wp}	17.24
χ^2	3.38

Atom	Site	x	y	z	Occupation
Ge	4e	0.19469	0.96721	0.34901	1.000
Ge	4e	0.32138	0.97469	0.22239	1.000
Ge	4e	0.32204	0.27880	0.35490	1.000
Ge	4e	0.12352	0.19570	0.12922	1.000
Na	4e	0.11933	0.40142	0.37248	1.000
Na	4e	0.40305	0.37526	0.11621	1.000
Na	4e	0.41601	0.71108	0.49633	1.000
Na	4e	0.14404	0.64833	0.08210	1.000

Table E.2: Rietveld refined PXRD data for $Na_{3.4}Ge_{136}$ clathrates. The diffractograms of $Na_{3.4}Ge_{136}$ clathrates is shown in Figure 5.49.

Parameter	NaGe Precursor
Space group	$Fd\bar{3}m$(No. 227)
a / Å	15.219
b / Å	15.219
c / Å	15.219
α / °	90.000
β / °	90.000
γ / °	90.000
Number of molecules per unit cell, Z	1
Volume / Å^3	3526
Calculated density / g cm^{-3}	4.609
R_p	16.67
R_{wp}	22.52
χ^2	2.73

Atom	Site	x	y	z	Occupation
Ge	8a	0.8750	0.8750	0.8750	1.000
Ge	32e	0.7815	0.7815	0.7815	1.000
Ge	96g	0.8167	0.8167	0.6296	1.000
Na	8b	0.3750	0.3750	0.3750	0.430

Table E.3: Heat capacity data of $Na_{3.1}Ge_{136}$: 4.190 mg with ^{4}He option; in order of data collection. The heat capacity is plotted as function of temperature in Figure 5.51.

T / K	C_p / J mol^{-1} K^{-1}	T / K	C_p / J mol^{-1} K^{-1}	T / K	C_p / J mol^{-1} K^{-1}
96.504	2440±20	25.564	423±4	6.789	17.9±0.2
84.479	2160±20	22.395	322±3	5.937	12.1±0.1
74.011	1890±20	19.602	242±2	5.186	8.44±0.08
64.806	1630±20	17.156	179±2	4.539	5.83±0.29
56.738	1400±10	15.025	131±1	3.971	3.95±0.20
49.676	1190±10	13.169	94.9±1.0	3.474	2.69±0.13
43.493	999±10	11.536	68.8±0.7	3.039	1.89±0.09
38.074	827±8	10.097	49.1±0.5	2.658	1.33±0.07
33.334	676±7	8.835	35.6±0.4	2.327	0.993±0.050
29.191	538±5	7.731	24.9±0.3	2.036	0.747±0.038

Table E.4: Thermal conductivity of $Na_{3.1}Ge_{136}$; in order of data collection. Thermal conductivity was corrected to zero porosity. The thermal conductivity is plotted as function of temperature in Figure 5.52.

T / K	κ / W m^{-1} K^{-1} ($Na_{3.1}Ge_{136}$.)	T / K	κ / W m^{-1} K^{-1} ($Na_{3.1}Ge_{136}$.)
302.427	2.38±0.12	61.849	1.49±0.07
327.555	2.20±0.11	41.119	1.06±0.05
352.804	1.98±0.10	30.762	0.694±0.035
377.875	1.9±0.10	20.586	0.435±0.022
252.325	2.45±0.12	10.748	0.184±0.009
202.407	2.35±0.12	8.867	0.142±0.007
152.331	2.20±0.11	6.989	0.102±0.005
102.554	1.94±0.1	5.067	0.0645±0.003
82.385	1.75±0.09	3.11	0.0330±0.002

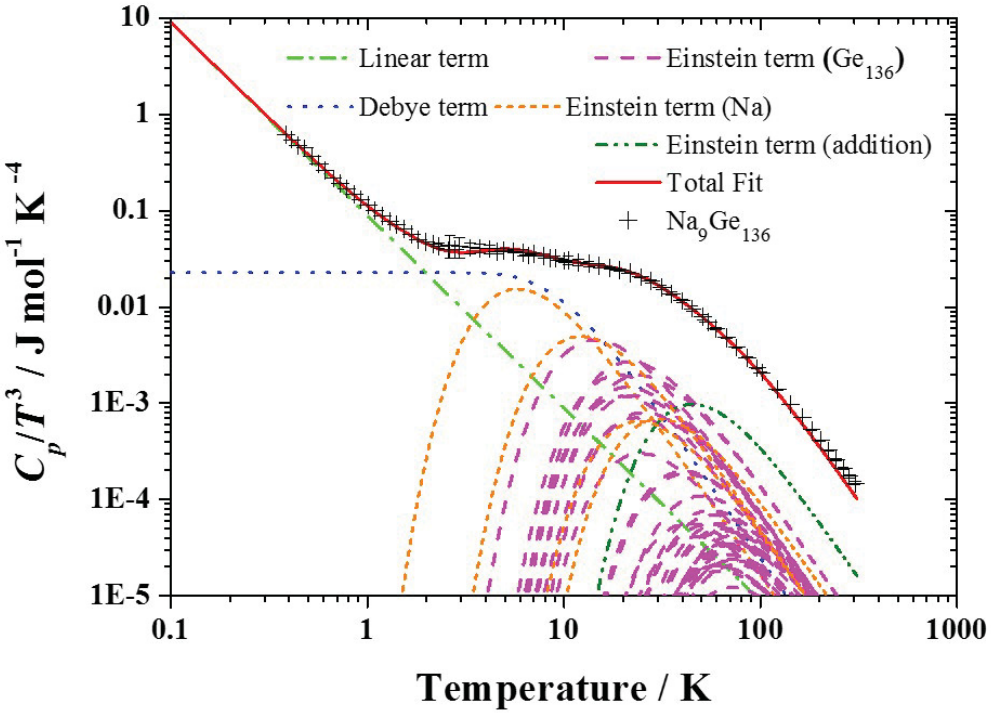

Figure E.2: C_pT^{-3} *vs* T fits of $Na_{3.1}Ge_{136}$ including three Debye modes, a linear electronic term, and Einstein modes for Ge_{136} and Na. Additional Einstein modes were applied to compensate for the softening of the optical Ge_{136} modes. Uncertainty in C_p was estimated to be 5% from 0.4 K to 5 K and 1% from 5 K to 300 K.

Appendix F

Permissions

printable details

License Number	4116010938045
License date	May 25, 2017
Licensed Content Publisher	Elsevier
Licensed Content Publication	Materials Today
Licensed Content Title	Lead telluride alloy thermoelectrics
Licensed Content Author	Aaron D. LaLonde,Yanzhong Pei,Heng Wang,G. Jeffrey Snyder
Licensed Content Date	Nov 1, 2011
Licensed Content Volume	14
Licensed Content Issue	11
Licensed Content Pages	7
Type of Use	reuse in a thesis/dissertation
Portion	figures/tables/illustrations
Number of figures/tables/illustrations	1
Format	both print and electronic
Are you the author of this Elsevier article?	No
Will you be translating?	No
Order reference number	
Original figure numbers	Figure 3
Title of your thesis/dissertation	Ultralow Thermal Conductivity and Novel Thermoelectric Materials
Expected completion date	Aug 2017
Estimated size (number of pages)	400
Elsevier VAT number	GB 494 6272 12
Requestor Location	Dalhousie Universitsy 6274 Coburg

printable details

License Number	4115120419003
License date	May 23, 2017
Licensed Content Publisher	Nature Publishing Group
Licensed Content Publication	Nature Materials
Licensed Content Title	Complex thermoelectric materials
Licensed Content Author	G. Jeffrey SnyderandEric S. Toberer
Licensed Content Date	Feb 1, 2008
Licensed Content Volume	7
Licensed Content Issue	2
Type of Use	reuse in a dissertation / thesis
Requestor type	academic/educational
Format	print and electronic
Portion	figures/tables/illustrations
Number of figures/tables/illustrations	1
High-res required	no
Figures	Figure 1
Author of this NPG article	no
Your reference number	
Title of your thesis / dissertation	Ultralow Thermal Conductivity and Novel Thermoelectric Materials
Expected completion date	Aug 2017
Estimated size (number of pages)	400
Requestor Location	Dalhousie Universitsy 6274 Coburg

References

[1] J. R. Sootsman, D. Y. Chung, and M. G. Kanatzidis, "New and Old Concepts in Thermoelectric Materials," *Angewandte Chemie International Edition*, vol. 48, pp. 8616–8639, 2009.

[2] Lawrence Livermore National Laboratory, "Estimated U.S. Energy Use in 2014: ∼98.3 Quads." `https://www.llnl.gov/sites/default/files/2014_us_energy.png`, 2015. [Online; accessed 2017-05-28].

[3] C. Yu and K. T. Chau, "Thermoelectric automotive waste heat energy recovery using maximum power point tracking," *Energy Conversion and Management*, vol. 50, pp. 1506–1512, 2009.

[4] P. Ball, "Harvesting Heat," *Chemistry World*, pp. 52–55, 2014.

[5] G. J. Snyder and E. S. Toberer, "Complex thermoelectric materials," *Nature Materials*, vol. 7, pp. 105–114, 2008.

[6] Y. P. Prilepo, A. A. Pustovalov, V. V. Sinyavskiy, N. M. Sudak, and O. B. Yatsenko, "Problems of Designing Radioisotope Thermoelectric Power Generators with a Service Life of Decades for Use in Outer Space Exploration Vehicles," *Thermal Engineering*, vol. 59, pp. 981–983, 2012.

[7] J. R. Salvador, J. Y. Cho, Z. Ye, J. E. Moczygemba, A. J. Thompson, J. W. Sharp, J. D. Koenig, R. Maloney, T. Thompson, J. Sakamoto, H. Wang, and A. A. Wereszczak, "Conversion efficiency of skutterudite-based thermoelectric modules," *Physical Chemistry Chemical Physics*, vol. 16, pp. 12510–12520, 2014.

[8] NASA, "Voyager Mission Operations Status Report." `https://voyager.jpl.nasa.gov/mission/weekly-reports/index.htm`, 2015. [Online; accessed 2017-05-23].

[9] S. Sharma, V. K. Dwivedi, and S. N. Pandit, "A Review of Thermoelectric Devices for Cooling Applications," *International Journal of Green Energy*, vol. 11, pp. 899–909, 2014.

[10] T. M. Tritt, H. Böttner, and L. Chen, "Thermoelectrics: Direct Solar Thermal Energy Conversion," *MRS Bulletin*, vol. 33, pp. 366–368, 2008.

[11] H. J. Goldsmid, *The Thermoelectric and Related Effects*, ch. 1, pp. 1–7. Berlin, Heidelberg: Springer Berlin Heidelberg, 2016.

[12] T. J. Seebeck, "Ueber die magnetische Polarisation der Metalle und Erze durch Temperatur-Differenz," *Annalen der Physik*, vol. 82, pp. 133–160, 1826.

[13] T. M. Tritt, "Thermoelectric Phenomena, Materials, and Applications," *Annual Review of Materials Research*, vol. 41, pp. 433–448, 2011.

[14] H. Ibach and H. Lüth, *Solid State Physics: An Introduction to Principles of Materials Science*. Berlin Heidelheim: Springer-Verlag, 4 ed., 2009.

[15] A. Shakouri, "Recent Developments in Semiconductor Thermoelectric Physics and Materials," *Annual Review of Materials Research*, vol. 41, pp. 399–431, 2011.

[16] G. S. Nolas, J. Sharp, and H. J. Goldschmid, *Thermoelectrics: Basic Principles and New Materials Developments*. Berlin Heidelberg: Springer Verlag, 1 ed., 2001.

[17] D. M. Rowe, *Thermoelectrics Handbook: Macro to Nano*. Boca Raton, FL: CRC Press - Taylor & Francis Group, 1 ed., 2006.

[18] K. Biswas, J. He, I. D. Blum, C.-I. Wu, T. P. Hogan, D. N. Seidman, V. P. Dravid, and M. G. Kanatzidis, "High-performance bulk thermoelectrics with all-scale hierarchical architectures," *Nature*, vol. 489, pp. 414–418, 2012.

[19] U. Aydemir, C. Candolfi, H. Borrmann, M. Baitinger, A. Ormeci, W. Carrillo-Cabrera, C. Chubilleau, B. Lenoir, A. Dauscher, N. Oeschler, F. Steglich, and Y. Grin, "Crystal structure and transport properties of $Ba_8Ge_{43}\square_3$," *Dalton Transactions*, vol. 39, pp. 1078–1088, 2010.

[20] S. Ohno, U. Aydemir, M. Amsler, J.-H. Pöhls, S. Chanakian, A. Zevalkink, M. A. White, S. K. Bux, C. Wolverton, and G. J. Snyder, "Achieving zT > 1 in Inexpensive Zintl Phase $Ca_9Zn_{4+x}Sb_9$ by Phase Boundary Mapping," *Advanced Functional Materials*, vol. 27, p. 1606361, 2017.

[21] J. S. Tse and M. A. White, "Origin of Glassy Crystalline Behavior in the Thermal Properties of Clathrate Hydrates: A Thermal Conductivity Study of Tetrahydrofuran Hydrate," *The Journal of Physical Chemistry*, vol. 92, pp. 5006–5011, 1988.

[22] D. Paul, *Thermoelectric Energy Harvesting*, ch. 4, pp. 49–78. Rijeka, Croatia: InTech, 2014.

[23] P. Atkins and J. de Paula, *Atkins' Physical Chemistry*. Oxford, UK: Oxford University Press, 8 ed., 2006.

[24] J. P. Heremans, "The ugly duckling," *Nature*, vol. 508, pp. 327–328, 2014.

[25] D. Nemir and J. Beck, "On the Significance of the Thermoelectric Figure of Merit Z," *Journal of Electronic Materials*, vol. 39, pp. 1897 – 1901, 2010.

[26] L.-D. Zhao, S.-H. Lo, Y. Zhang, H. Sun, G. Tan, C. Uher, C. Wolverton, V. P. Dravid, and M. G. Kanatzidis, "Ultralow thermal conductivity and high thermoelectric figure of merit in SnSe crystals," *Nature*, vol. 508, pp. 373–377, 2014.

[27] L.-D. Zhao, C. Chang, G. Tan, and M. G. Kanatzidis, "SnSe: a remarkable new thermoelectric material," *Energy & Environmental Science*, vol. 9, pp. 3044–3060, 2016.

[28] A. D. LaLonde, Y. Pei, H. Wang, and G. J. Snyder, "Lead telluride alloy thermoelectrics," *Materials Today*, vol. 14, pp. 526–532, 2011.

[29] Y. Pei, X. Shi, A. LaLonde, H. Wang, L. Chen, and G. J. Snyder, "Convergence of electronic bands for highperformance bulk thermoelectrics," *Nature*, vol. 473, pp. 66–69, 2011.

[30] W. Haken, "Beitrag zur Kenntnis der thermoelektrischen Eigenschaften der Metallegierungen," *Annalen der Physik*, vol. 832, pp. 291–336, 1910.

[31] Z. Chen, Z. Jian, W. Li, Y. Chang, B. Ge, R. Hanus, J. Yang, Y. Chen, M. Huang, G. J. Snyder, and Y. Pei, "Lattice Dislocations Enhancing Thermoelectric PbTe in Addition to Band Convergence," *Advanced Materials*, vol. 29, p. 1606768, 2017.

[32] M. Hong, T. C. Chasapis, Z.-G. Chen, L. Yang, M. G. Kanatzidis, G. J. Snyder, and J. Zou, "*n*-Type $Bi_2Te_{3x}Se_x$ Nanoplates with Enhanced Thermoelectric Efficiency Driven by Wide-Frequency Phonon Scatterings and Synergistic Carrier Scatterings," *ACS Nano*, vol. 10, pp. 4719–4727, 2016.

[33] Q. Zhang, J. Liao, Y. Tang, M. Gu, C. Ming, P. Qiu, S. Bai, X. Shi, C. Uher, and L. Chen, "Realizing a thermoelectric conversion efficiency of 12% in bismuth telluride/skutterudite segmented modules through full-parameter optimization andenergy-loss minimized integration," *Energy & Environmental Science*, vol. 10, pp. 956–963, 2017.

[34] F. J. DiSalvo, "Thermoelectric Cooling and Power Generation," *Science*, vol. 285, pp. 703–706, 1999.

[35] W. Chen, J.-H. Pöhls, G. Hautier, D. Broberg, S. Bajaj, U. Aydemir, Z. M. Gibbs, H. Zhu, M. Asta, G. J. Snyder, B. Meredig, M. A. White, K. Persson, and A. Jain, "Understanding thermoelectric properties from high-throughput calculations: trends, insights, and comparisons with experiment," *Journal of Materials Chemistry C*, vol. 4, pp. 4414–4426, 2016.

[36] G. Ceder, "Opportunities and challenges for first-principles materials design and applications to Li battery materials," *Materials Research Society Bulletin*, vol. 35, pp. 693–701, 2010.

[37] H. Chen, Q. Hao, O. Zivkovic, G. Hautier, L.-S. Du, Y. Tang, Y.-Y. Hu, X. Ma, C. P. Grey, and G. Ceder, "Sidorenkite ($Na_3MnPO_4CO_3$): A New Intercalation Cathode Material for Na-Ion Batteries," *Chemistry of Materials*, vol. 8, pp. 2777–2786, 2013.

[38] Q. Yan, G. Li, P. F. Newhouse, J. Yu, K. A. Persson, J. M. Gregoire, and J. B. Neaton, "$Mn_2V_2O_7$: An Earth Abundant Light Absorber for Solar Water Splitting," *Advanced Energy Materials*, vol. 5, p. 1401840, 2015.

[39] J. Carrete, N. Mingo, S. Wang, and S. Curtarolo, "Nanograined Half-Heusler Semiconductors as Advanced Thermoelectrics: An Ab Initio High-Throughput Statistical Study," *Advanced Functional Materials*, vol. 24, pp. 7427–7432, 2014.

[40] J. He, M. Amsler, Y. Xia, S. S. Naghavi, V. I. Hegde, S. Hao, S. Goedecker, V. Ozoliņš, and C. Wolverton, "Ultralow Thermal Conductivity in Full Heusler Semiconductors," *Physical Review Letters*, vol. 117, p. 046602, 2016.

[41] I. Opahle, A. Parma, E. J. McEniry, R. Drautz, and G. K. H. Madsen, "High-throughput study of the structural stability and thermoelectric properties of transition metal silicides," *New Journal of Physics*, vol. 15, p. 105010, 2013.

[42] G. K. H. Madsen, "Automated Search for New Thermoelectric Materials: The Case of LiZnSb," *Journal of American Chemical Society*, vol. 128, pp. 12140–12146, 2006.

[43] L. Bjerg, G. K. H. Madsen, and B. B. Iversen, "Enhanced Thermoelectric Properties in Zinc Antimonides," *Chemistry of Materials*, vol. 23, pp. 3907–3914, 2011.

[44] P. Gorai, E. S. Toberer, and V. Stevanović, "Thermoelectricity in transition metal compounds: the role of spin disorder," *Physical Chemistry Chemical Physics*, vol. 18, pp. 31777–31786, 2016.

[45] P. Gorai, D. Gao, B. Ortiz, S. Miller, S. A. Barnett, T. Mason, Q. Lv, V. Stevanović, and E. S. Toberer, "TE Design Lab: A virtual laboratory for thermoelectric material design," *Computational Materials Science*, vol. 112, pp. 368–376, 2016.

[46] J. Yan, P. Gorai, B. Ortiz, S. Miller, S. A. Barnett, T. Mason, V. Stevanović, and E. S. Toberer, "Material descriptors for predicting thermoelectric performance," *Energy & Environmental Science*, vol. 8, pp. 983–994, 2015.

[47] M. W. Gaultois, A. O. Oliynyk, A. Mar, T. D. Sparks, G. J. Mulholland, and B. Meredig, "A Recommendation engine for suggesting unexpected thermoelectric chemistries," *arXiv [1502.07635v3]*, 2016.

[48] A. Jain, S. P. Ong, G. Hautier, W. Chen, W. D. Richards, S. Dacek, S. Cholia, D. Gunter, D. Skinner, G. Ceder, and K. A. Persson, "The Materials Project: A materials genome approach to accelerating materials innovation," *APL Materials*, vol. 1, p. 011002, 2013.

[49] G. K. Madsen and D. J. Singh, "BoltzTraP. A code for calculating band-structure dependent quantities," *Computer Physics Communications*, vol. 175, pp. 67–71, 2006.

[50] H. Wang, Y. Pei, A. D. LaLonde, and G. J. Snyder, *Material Design Considerations Based on Thermoelectric Quality Factor*, pp. 3–32. Berlin, Heidelberg: Springer Berlin Heidelberg, 2013.

[51] J. P. Perdew, K. Burke, and M. Ernzerhof, "Generalized Gradient Approximation Made Simple," *Physical Review Letters*, vol. 77, pp. 3865–3868, 1996.

[52] G. Kresse and D. Joubert, "From ultrasoft pseudopotentials to the projector augmented-wave method," *Physical Review B*, vol. 59, pp. 1758–1775, 1999.

[53] M. K. Y. Chan and G. Ceder, "Efficient Band Gap Prediction for Solids," *Physical Review Letters*, vol. 105, p. 196403, 2010.

[54] W. Setyawan, R. M. Gaume, S. Lam, R. S. Feigelson, and S. Curtarolo, "High-Throughput Combinatorial Database of Electronic Band Structures for Inorganic Scintillator Materials," *ACS Combinatorial Science*, vol. 13, pp. 382–390, 2011.

[55] Y. Tang, R. Hanus, S. wen Chen, and G. J. Snyder, "Solubility design leading to high figure of merit in low-cost Ce-$CoSb_3$ skutterudites," *Nature Communications*, vol. 6, p. 7584, 2015.

[56] M. W. Gaultois, T. D. Sparks, C. K. H. Borg, R. Seshadri, W. D. Bonificio, and D. R. Clarke, "Data-Driven Review of Thermoelectric Materials: Performance and Resource Considerations," *Chemistry of Materials*, vol. 25, pp. 2911–2920, 2013.

[57] Z. Tian, S. Lee, and G. Chen, "Heat Transfer in Thermoelectric Materials and Devices," *Journal of Heat Transfer*, vol. 135, p. 061605, 2013.

[58] A. Zunger, "Practical doping principles," *Applied Physics Letters*, vol. 83, pp. 57–59, 2003.

[59] A. van Roekeghem, J. Carrete, C. Oses, S. Curtarolo, and N. Mingo, "High-Throughput Computation of Thermal Conductivity of High-Temperature Solid Phases: The Case of Oxide and Fluoride Perovskites," *Physical Review X*, vol. 6, p. 041061, 2016.

[60] A. Togo and I. Tanaka, "First principles phonon calculations in materials science," *Scripta Materialia*, vol. 108, pp. 1–5, 2015.

[61] J. M. Ziman, *Electrons and Phonons*. London, UK: Oxford University Press, 1 ed., 1960.

[62] D. A. Broido, M. Malorny, G. Birner, N. Mingo, and D. A. Stewart, "Intrinsic lattice thermal conductivity of semiconductors from first principles," *Applied Physics Letters*, vol. 91, p. 231922, 2007.

[63] X. Tang and J. Dong, "Lattice thermal conductivity of mgo at conditions of earths interior," *PNAS*, vol. 107, pp. 4539–4543, 2010.

[64] C. Carbogno, R. Ramprasad, and M. Scheffler, "*Ab Initio* green-kubo approach for the thermal conductivity of solidsr," *Physical Review Letters*, vol. 118, p. 175901, 2017.

[65] A. Einstein, "Elementare Betrachtungen über die thermische Molekularbewegung in festen Körpern," *Annalen der Physik*, vol. 9, pp. 679–694, 1911.

[66] D. G. Cahill and R. O. Pohl, "Lattice Vibrations and Heat Transport in Crystals and Glasses," *Annual Review of Physical Chemistry*, vol. 39, pp. 93–121, 1992.

[67] D. G. Cahill, S. K. Watson, and R. O. Pohl, "Lower limit to the thermal conductivity of disordered crystals," *Physical Review B*, vol. 46, pp. 6131–6140, 1992.

[68] S. A. Miller, P. Gorai, B. R. Ortiz, A. Goyal, D. Gao, S. A. Barnett, T. O. Mason, G. J. Snyder, Q. Lv, V. Stevanovič, and E. S. Toberer, "Capturing anharmonicity in a lattice thermal conductivity model for high-throughput predictions," *Chemistry of Materials*, vol. 29, pp. 2494–2501, 2017.

[69] J. C. Duda, P. E. Hopkins, Y. Shen, and M. C. Gupta, "Exceptionally Low Thermal Conductivities of Films of the Fullerene Derivative PCBM," *Physical Review Letters*, vol. 110, p. 015902, 2013.

[70] M. Schmoluchowski, "O przewodnictwie cieplnem cial sproszkowanych. Sur la conductibilité calorifique des corps pulvérisés," *Bull. Int. Acad. Sci. Cracovie. Classe des sciences math. et naturelles, sér. A*, pp. 129–153, 1910.

[71] Z. Klemensiewicz, "Thermal Conductivity of Powders," *Nature*, vol. 164, p. 589, 1949.

[72] G. A. Slack, "New Materials and Performance Limits for Thermoelectric Cooling," in *CRC Handbook of Thermoelectrics* (D. M. Rowe, ed.), ch. 34, pp. 407–440, Boca Raton, Florida: CRC Press, 1995.

[73] M. A. White, *Physical Properties of Materials*. Boca Raton, FL: CRC Press - Taylor & Francis group, 2 ed., 2012.

[74] C. S. Sunandana, *Introduction to Solid State Ionics*. Boca Raton, FL: CRC Press - Taylor & Francis group, 1 ed., 2016.

[75] C. Kittel, *Introduction to Solid State Physics*. New York, NY: John Wiley & Sons, 8 ed., 2006.

[76] R. Siegel and C. M. Spuckler, "Analysis of thermal radiation effects on temperatures in turbine engine thermal barrier coatings," *Materials Science and Engineering*, vol. A245, pp. 150–159, 1998.

[77] R. A. Serway, C. J. Moses, and C. A. Moyer, *Modern Physics*. Belmont, CA: Brooks/Cole-Thomson Learning, 3 ed., 2005.

[78] E. S. Toberer, L. L. Baranowski, and C. Dames, "Advances in Thermal Conductivity," *Annual Review of Materials Research*, vol. 42, pp. 179–209, 2012.

[79] T. R. Anthony, W. F. Banholzer, J. F. Fleischer, L. Wei, P. K. Kuo, R. L. Thomas, and R. W. Pryor, "Thermal diffusivity of isotopically enriched ^{12}C diamond," *Physical Review B*, vol. 42, pp. 1104–1111, 1990.

[80] B. Fultz, "Vibrational thermodynamics of materials," *Progress in Materials Science*, vol. 55, pp. 247–352, 2010.

[81] J. Callaway, "Model for Lattice Thermal Conductivity at Low Temperatures," *Physical Review*, vol. 113, pp. 1046–1051, 1959.

[82] E. S. Toberer, A. Zevalkink, and G. J. Snyder, "Phonon engineering through crystal chemistry," *Journal of Materials Chemistry*, vol. 21, pp. 15843–15852, 2011.

[83] P. Harris and L. Avrami, "Some physics about the grüneisen parameter," tech. rep., Picatinny Arsenal Dover, New Jersey, 1972.

[84] H.-S. Kim, Z. M. Gibbs, Y. Tang, H. Wang, and G. J. Snyder, "Characterization of Lorenz number with Seebeck coefficient measurement," *APL Materials*, vol. 3, p. 041506, 2015.

[85] M. Cutler, J. F. Leavy, and R. L. Fitzpatrick, "Electronic Transport in Semimetallic Cerium Sulfide," *Physical Review*, vol. 133, pp. A1143–A1152, 1964.

[86] Z. M. Gibbs, H.-S. Kim, H. Wang, and G. J. Snyder, "From ultrasoft pseudopotentials to the projector augmented-wave method," *Applied Physics Letters*, vol. 106, p. 022112, 2015.

[87] J. F. Shackelford, *Introduction to Materials Science for Engineers* . New York, NY: Macmillan Publishing Company, 3 ed., 1992.

[88] D. Wolpert and P. Ampadu, *Temperature Effects in Semiconductors*, ch. 2, pp. 15–33. New York, NY: Springer New York, 2012.

[89] D. R. Askeland, *The Science and Engineering of Materials*. Boston, MA: PWS Publishing Company, 3 ed., 1994.

[90] A. F. May, E. S. Toberer, A. Saramat, and G. J. Snyder, "Characterization and analysis of thermoelectric transport in n-type $Ba_8Ga_{16x}Ge_{30+x}$," *Physical Review B*, vol. 80, p. 125205, 2009.

[91] M. Lundstrom and C. Jeong, *Near-Equilibrium Transport*. Singapore: World Scientific, 1 ed., 2013.

[92] S. V. Tsybulya, S. V. Cherepanova, and G. N. Kryukova, "Full Profile Analysis of X-ray Diffraction Patterns for Investigations of Nanocrystalline Systems," in *Diffraction Analysis of the Microstructure of Materials* (E. J. Mittemeijer and P. Scardi, eds.), ch. 4, pp. 93–124, Berlin Heidelberg: Springer-Verlag, 2004.

[93] P. Scherrer, "Bestimmung der Größe und der inneren Struktur von Kolloidteilchen mittels Röntgenstrahlen (Determination of the size and internal structure of colloidal particles using X-rays)," *Nachrichten von der Gesellschaft der Wissenschaften zu Göttingen, Mathematisch-Physikalische Klasse*, vol. 1918, pp. 98–100, 1918.

[94] A. R. Stokes and A. J. C. Wilson, "The diffraction of X rays by distorted crystal aggregates," *Proceedings of the Physical Society*, vol. 56, pp. 174–181, 1944.

[95] G. K. Williamson and W. H. Hall, "X-ray line broadening from filed aluminium and wolfram," *Acta Metallurgica*, vol. 1, pp. 22–31, 1953.

[96] B. E. Warren and B. L. Averbach, "The Effect of Cold-Work Distortion on X-Ray Patterns," *Journal of Applied Physics*, vol. 21, pp. 595–599, 1950.

[97] D. Balzar, "BREADTH – a Program for Analyzing Diffraction Line Broadening," *Journal of Applied Crystallography*, vol. 28, pp. 244–245, 1995.

[98] D. Balzar, "Accurate Modeling of Size and Strain Broadening in the Rietveld Refinement: the "Double-Voigt" Approach," *Advances in X-ray Analysis*, vol. 38, pp. 397–404, 1995.

[99] Y. Waseda, E. Matsubara, and K. Shinoda, *X-Ray Diffraction Crystallography: Introduction, Examples and Solved Problems*. Berlin Heidelheim: Springer-Verlag, 1 ed., 2011.

[100] International Centre for Diffraction Data, Newton Square, PA, *PDF-2 Powder Diffraction Database*, 2012.

[101] Match! Computer Software, "Match!." http://www.crystalimpact.com/match/. [Online; accessed 2016-11-13].

[102] B. Hunter, "Rietica - A visual Rietveld program: International Union of Crystallography Commission on Powder Diffraction Newsletter No. 20." http://www.rietica.org, 1998. [Online; accessed 2016-11-13].

[103] A. L. Bail, "Whole powder pattern decomposition methods and applications: A retrospection," *Powder Diffraction*, vol. 20, pp. 316–326, 2005.

[104] H. M. Rietveld, "A profile refinement method for nuclear and magnetic structures," *Journal of Applied Crystallography*, vol. 2, pp. 65–71, 1969.

[105] T. J. Ympa, "Historical Development of the Newton-Raphson Method," *SIAM Review*, vol. 37, pp. 531–551, 1995.

[106] J.-H. Pöhls, "XRD Refinement using Rietica." http://mawhite.chem.dal.ca//Rietica.pdf, 2013. [Online; accessed 2016-11-13].

[107] D. B. Chase and J. F. Rabolt, *Fourier Transform Raman Spectroscopy: From Concept to Experiment*. Oxford, UK: Academic Press, 1 ed., 1993.

[108] S. J. B. Reed, "Electron microprobe microanalysis," in *Microprobe Techniques in the Earth Science* (P. J. Potts, J. F. W. Bowles, S. J. B. Reed, and M. R. Cave, eds.), ch. 2, pp. 49–90, London, UK: Chapman& Hall, 1995.

[109] R. W. C. Frs and E. Lifshin, *Concise Encyclopedia of Materials Characterization*. San Diego, CA: Pergamon Press, 1 ed., 1994.

[110] J. V. P. Long, "Micro analysis from 1950 to the 1990s," in *Microprobe Techniques in the Earth Science* (P. J. Potts, J. F. W. Bowles, S. J. B. Reed, and M. R. Cave, eds.), ch. 1, pp. 1–48, London, UK: Chapman& Hall, 1995.

[111] R. Reichelt, "Full profile analysis of x-ray diffraction patterns for investigations of nanocrystalline systems," in *Science of Microscopy* (P. W. Hawkes and J. C. H. Spence, eds.), ch. 3, pp. 133–272, New York, NY: Springer-Science+Business Media, 2007.

[112] H. Bubert, J. C. Rivière, and W. S. M. Werner, "X-Ray Photoelectron Spectroscopy (XPS)," in *Surface and Thin Films Analysis: A Compendium of Principles, Instrumentation, and Applications* (G. Friedbacher and H. Bubert, eds.), ch. 2, pp. 9–42, Weinheim, Germany: Wiley VCH Verlag, 2011.

[113] NIST, "NIST X-ray Photoelectron Spectroscopy (XPS) Database, Data Field Definition." https://srdata.nist.gov/xps/DataDefinition.aspx, 2007. [Online; accessed 2017-03-06].

[114] R. Schlaf, " Calibration of Photoemission Spectra and Work Function Determination." http://rsl.eng.usf.edu/Documents/Tutorials/PEScalibration.pdf. [Online; accessed 2016-11-22].

[115] C. McMahon, "Design of an inverse photoemission spectrometer for the study of strongly correlated materials," Master's thesis, Department of Physics, University of Waterloo, Waterloo, Ontario, Canada, 2012.

[116] T. Hatakeyama and L. Zhenhai, *Handbook of Thermal Analysis*. New York, NY: JohnWiley & Sons, 1 ed., 1998.

[117] M. B. Johnson and M. A. White, "Thermal methods," in *Inorganic Materials: Multi-Length Scale Characterisation* (D. W. Bruce, D. O'Hare, and R. I. Walton, eds.), ch. 2, pp. 63–119, West Sussex, UK: John Wiley & Sons, 2014.

[118] G. W. H. Höhne, W. F. Hemminger, and H.-J. Flammersheim, *Differential Scanning Calorimetry: An Introduction for Practitioners*. Berlin Heidelheim: Springer-Verlag, 2 ed., 2011.

[119] TA Instruments, "DSC brochure." http://nfec.ntis.go.kr/com/model/file/19413, 2016. [Online; accessed 2016-11-16].

[120] R. L. Danley, "New heat flux DSC measurement technique," *Thermochimica Acta*, vol. 395, pp. 201–208, 2002.

[121] TA Instruments, "Thermal analysis brochure." http://www.tainstruments.com/pdf/brochure/2012%20DSC%20Brochure%20r1.pdf, 2012. [Online; accessed 2016-11-16].

[122] S. C. Mraw and D. F. Naas, "The measurement of accurate heat capacities by differential scanning calorimetry: Comparison of d.s.c. results on pyrite (100 to 800 K) with literature values from precision adiabatic calorimetry," *The Journal of Chemical Thermodynamics*, vol. 11, pp. 567–584, 1979.

[123] D. R. Archer, "Thermodynamic Properties of Synthetic Sapphire (α-Al_2O_3), Standard Reference Material 720 and the Effect of Temperature-Scale Differences on Thermodynamic Properties," *Journal of Physical and Chemical Reference Data*, vol. 22, pp. 1441–1453, 1993.

[124] O. A. M. Al-Qatami, "Thermal study of a triglyceride mixture," Master's thesis, Department of Process Engineering and Applied Science, Dalhousie Universiy, Halifax, Nova Scotia, Canada, 2011.

[125] H. Wang, W. D. Porter, H. Böttner, J. König, L. Chen, S. Bai, T. M. Tritt, A. Mayolet, J. Senawiratne, C. Smith, F. Harris, P. Gilbert, J. W. Sharp, J. Lo, H. Kleinke, and L. Kiss, "Transport Properties of Bulk Thermoelectrics - An International Round-Robin Study, Part II: Thermal Diffusivity, Specific Heat, and Thermal Conductivity," *Journal of Electronic Materials*, vol. 42, pp. 1073–1084, 2013.

[126] J.-H. Pöhls, "Physical properties of a carbon nanotube tape," Master's thesis, Department of Chemistry, Dalhousie University, Halifax, Nova Scotia, Canada, 2012.

[127] C. A. Kennedy, M. Stancescu, R. A. Marriott, and M. A. White, "Recommendations for accurate heat capacity measurements using a Quantum Design physical property measurement system," *Cyrogenics*, vol. 47, pp. 107–112, 2007.

[128] Quantum Design, San Diego, CA, *Physical Property Measurement System: Heat Capacity Option Users Manual*, 2002.

[129] W. Schnelle, J. Engelhardt, and E. Gmelin, "Specific heat capacity of Apiezon N high vacuum grease and of Duran borosilicate glass," *Cyrogenics*, vol. 39, pp. 271–275, 1999.

[130] S. Kahwaji, M. B. Johnson, A. C. Kheirabadi, D. Groulx, and M. A. White, "Stable, low-cost phase change material for building applications: The eutectic mixture of decanoic acid and tetradecanoic acid," *Applied Energy*, vol. 168, pp. 457 – 464, 2016.

[131] Quantum Design, San Diego, CA, *Physical Property Measurement System: Thermal Transport Option Users Manual*, 2002.

[132] W. J. Parker, R. J. Jenkins, C. P. Butler, and G. L. Abbott, "Flash Method of Determining Thermal Diffusivity, Heat Capacity, and Thermal Conductivity," *Journal of Applied Physics*, vol. 32, pp. 1679–1684, 1961.

[133] R. D. Cowan, "Pulse Method of Measuring Thermal Diffusivity at High Temperatures," *Journal of Applied Physics*, vol. 34, pp. 926–927, 1963.

[134] J. A. Cape1 and G. W. Lehman, "Temperature and Finite PulseTime Effects in the Flash Method for Measuring Thermal Diffusivity," *Journal of Applied Physics*, vol. 34, pp. 1909–1913, 1963.

[135] K. A. Borup, J. de Boo, H. Wang, F. Drymiotis, F. Gascoin, X. Shi, L. Chen, M. I. Fedorov, E. Muller, B. B. Iversena, and G. J. Snyder, "Measuring thermoelectric transport properties of materials," *Energy and Environmental Science*, vol. 8, pp. 423–435, 2015.

[136] H. Wang, Y. Pei, A. D. LaLonde, and G. J. Snyder, "Weak electron-phonon coupling contributing to high thermoelectric performance in n-type PbSe," *Proceedings of the National Academy of Sciences*, vol. 109, pp. 9705–9709, 2012.

[137] W. Stryczniewicz and A. J. Panas, "Numerical data processing from a laser flash experiment on thin graphite layer," *Computer Assisted Methods in Engineering and Science*, vol. 22, pp. 279–287, 2015.

[138] S. Iwanaga, E. S. Toberer, A. LaLonde, and G. J. Snyder, "A high temperature apparatus for measurement of the Seebeck coefficient," *Review of Scientific Instruments*, vol. 82, p. 063905, 2011.

[139] J. Martin, "Protocols for the high temperature measurement of the Seebeck coefficient in thermoelectric materials," *Measurement Science and Technology*, vol. 24, p. 085601, 2013.

[140] H. Wang, W. D. Porter, H. Böttner, J. König, L. Chen, S. Bai, T. M. Tritt, A. Mayolet, J. Senawiratne, C. Smith, F. Harris, P. Gilbert, J. W. Sharp, J. Lo, H. Kleinke, and L. Kiss, "Transport Properties of Bulk Thermoelectrics - An International Round-Robin Study, Part I: Seebeck Coefficient and Electrical Resistivity," *Journal of Electronic Materials*, vol. 42, pp. 654–664, 2013.

[141] K. A. Borup, E. S. Toberer, L. D. Zoltan, G. Nakatsukasa, M. Errico, J.-P. Fleurial, B. B. Iversen, and G. J. Snyder, "Measurement of the electrical resistivity and Hall coefficient at high temperatures," *Review of Scientific Instruments*, vol. 83, p. 123902, 2012.

[142] Quantum Design, San Diego, CA, *Physical Property Measurement System: AC Measurement System (ACMS) Option Users Manual*, 2003.

[143] P. Laugier and G. Haïat, "Introduction to the physics of ultrasound," in *Bone Quantitative Ultrasound* (P. Laugier and G. Haïat, eds.), ch. 2, pp. 29–45, Heidelheim, Germany: Springer Science+Business Media, 2011.

[144] D. E. Newcomb and B. Birgisson, *Measuring In Situ Mechanical Properties of Pavement Subgrade Soils*. Washington, D.C.: National Academy Press, 1 ed., 1999.

[145] A. J. Davies, *The Finite Element Method: An Introduction with Partial Differential Equations*. Oxford, UK: Oxford University Press, 2 ed., 2005.

[146] COMSOL, *Heat Transfer Module Users Guide*, 2012.

[147] J.-H. Pöhls, M. B. Johnson, and M. A. White, "Origins of ultralow thermal conductivity in bulk [6,6]-phenyl-C_{61}-butyric acid methyl ester (PCBM)," *Physical Chemistry Chemical Physics*, vol. 18, pp. 1185–1190, 2016.

[148] R. M. Costescu, D. G. Cahill, F. H. Fabreguette, Z. A. Sechrist, and S. M. George, "Ultra-Low Thermal Conductivity in W/Al_2O_3 Nanolaminates," *Science*, vol. 303, pp. 989–990, 2004.

[149] C. Chiritescu, D. G. Cahill, N. Nguyen, D. Johnson, A. Bodapati, P. Keblinski, and P. Zschack, "Ultralow Thermal Conductivity in Disordered, Layered WSe_2 Crystals," *Science*, vol. 315, pp. 351–353, 2007.

[150] J. P. Feser, E. M. Chan, A. Majumdar, R. A. Segalman, and J. J. Urban, "Ultralow Thermal Conductivity in Polycrystalline CdSe Thin Films with Controlled Grain Size," *Nano Letters*, vol. 13, pp. 2122–2127, 2013.

[151] X. Wang, C. D. Liman, N. D. Treat, M. L. Chabinyc, and D. G. Cahill, "Ultralow thermal conductivity of fullerene derivatives," *Physical Review B*, vol. 88, p. 075310, 2013.

[152] Z. Guo, D. Lee, J. Strzalka, H. Gao, L. Huang, A. M. Khounsary, and T. Luo, "Thermal conductivity of organic bulk heterojunction solar cells: an unusual binary mixing effect," *Physical Chemistry Chemical Physics*, vol. 16, pp. 26359–26364, 2014.

[153] L. Chen, X. Wang, and S. Kumar, "Thermal Transport in Fullerene Derivatives Using Molecular Dynamics Simulations," *Scientific Reports*, vol. 5, p. 12763, 2015.

[154] F. Gascoin and A. Maignan, "Order-Disorder Transition in $AgCrSe_2$: a New Route to Efficient Thermoelectrics," *Chemistry of Materials*, vol. 23, pp. 2510–2513, 2011.

[155] E. Pop, D. Mann, Q. Wang, K. Goodson, and H. Dai, "Thermal Conductance of an Individual Single-Wall Carbon Nanotube above Room Temperature," *Nano Letters*, vol. 6, pp. 96–100, 2006.

[156] S. Tennant, "On the nature of the diamond," *Philosophical Transactions of the Royal Society of London*, vol. 87, pp. 123–127, 1796.

[157] H. W. Kroto, J. R. Heath, S. O'Brien, R. F. Curl, and R. E. Smalley, "C_{60}: Buckminsterfullerene," *Nature*, vol. 318, pp. 162–163, 1985.

[158] S. Iijima, "Helical microtubules of graphitic carbon," *Nature*, vol. 354, pp. 56–58, 1991.

[159] K. S. Novoselov, A. K. Geim, S. V. Morozov, D. Jiang, Y. Zhang, S. V. Dubonos, I. V. Grigorieva, and A. A. Firsov, "Electric Field Effect in Atomically Thin Carbon Films," *Science*, vol. 306, pp. 666–669, 2004.

[160] A. Krüger, *Carbon Materials and Nanotechnology*. Weinheim: Wiley-VCH Verlag, 1 ed., 2010.

[161] B. Sundqvist, "Polymeric Fullerene Phases Formed Under Pressure," *Structure and Bonding*, vol. 109, pp. 85–126, 2004.

[162] V. Blank, M. Popov, G. Pivovarov, N. Lvova, K. Gogolinsky, and V. Reshetov, "Ultrahard and superhard phases of fullerite C_{60}: comparison with diamond on hardness and wear," *Diamond and Related Materials*, vol. 7, pp. 427–431, 1998.

[163] C. B. Winkelmann, N. Roch, W. Wernsdorfer, V. Bouchiat, and F. Balestro, "Superconductivity in a single-C_{60} transistor," *Nature Physics*, vol. 5, pp. 876–879, 2009.

[164] M. C. Scharber, D. Mühlbacher, M. Koppe, P. Denk, C. Waldauf, A. J. Heeger, and C. J. Brabec, "Design Rules for Donors in Bulk-Heterojunction Solar Cells-Towards 10 % Energy-Conversion Efficiency," *Advanced Materials*, vol. 18, pp. 789–794, 2006.

[165] J.-S. Huang, C.-Y. Chou, and C.-F. Lin, "Enhancing performance of organicinorganic hybrid solar cells using a fullerene interlayer from all-solution processing," *Solar Energy Materials & Solar Cells*, vol. 94, pp. 182–186, 2010.

[166] T. Erb, U. Zhokhavets, G. Gobsch, S. Raleva, B. Stühn, P. Schilinsky, C. Waldauf, and C. J. Brabec, "Correlation Between Structural and Optical Properties of Composite Polymer/Fullerene Films for Organic Solar Cells," *Advanced Functional Materials*, vol. 15, pp. 1193–1196, 2005.

[167] R. Mens, P. Adriaensens, L. Lutsen, A. Swinnen, S. Bertho, B. Ruttens, J. D'Haen, J.Manca, T. Cleij, D. Vanderzande, and J. Gelan, "NMR Study of the Nanomorphology in Thin Films of Polymer Blends Used in Organic PV Devices: MDMO-PPV/PCBM," *Journal of Polymer Science: Part A: Polymer Chemistry*, vol. 46, pp. 138–145, 2008.

[168] J. C. Hummelen, B. W. Knight, F. LePeq, and F. Wudl, "Preparation and Characterization of Fulleroid and Methanofullerene Derivatives," *Journal of Organic Chemistry*, vol. 60, pp. 532–538, 1995.

[169] C. Hadad, Z. Syrgiannis, A. Bonasera, and M. Prato, "Efficient Microwave-Assisted Synthesis of PCBM Methanofullerenes (C_{60} and C_{70})," *European Journal of Organic Chemistry*, pp. 1423–1427, 2015.

[170] X. Yang, J. Loos, S. C. Veenstra, W. J. H. Verhees, M. M. Wienk, J. M. Kroon, M. A. J. Michels, and R. A. J. Janssen, "Nanoscale Morphology of High-Performance Polymer Solar Cells," *Nano Letters*, vol. 5, pp. 579–583, 2005.

[171] M. Casalegno, S. Zanardi, F. Frigerio, R. Po, C. Carbonera, G. Marra, T. Nicolini, G. Raos, and S. V. Meille, "Solvent-free phenyl-C61-butyric acid methyl ester (PCBM) from clathrates: insights for organic photovoltaics from crystal structures and molecular dynamics," *Chemical Communications*, vol. 49, pp. 4525–4527, 2013.

[172] P. A. Heiney, J. E. Fischer, A. R. McGhie, W. J. Romanow, A. M. Denenstein, J. John P. McCauley, and I. Amos B. Smith, "Orientational Ordering Transition in Solid C_{60}," *Physical Review Letters*, vol. 66, pp. 2911–2914, 1991.

[173] T. Ameri, J. Min, N. Li, F. Machui, D. Baran, M. Forster, K. J. Schottler, D. Dolfen, U. Scherf, and C. J. Brabec, "Performance Enhancement of the P3HT/PCBM Solar Cells through NIR Sensitization Using a Small-Bandgap Polymer," *Advanced Energy Materials*, vol. 2, pp. 1198–1202, 2012.

[174] S. H. Yoo, J. M. Kum, and S. O. Cho, "Tuning the electronic band structure of PCBM by electron irradiation," *Nanoscale Research Letters*, vol. 6, p. 545, 2011.

[175] R. Mens, S. Chambon, S. Bertho, G. Reggers, B. Ruttens, J. DHaen, J. Manca, R. Carleer, D. Vanderzande, and P. Adriaensens, "Description of the nanostructured morphology of [6,6]-phenyl-C_{61}-butyric acid methyl ester (PCBM) by XRD, DSC and solid-state NMR," *Magnetic Resonance in Chemistry*, vol. 49, pp. 242–247, 2011.

[176] N. R. Tummala, S. Mehraeen, Y.-T. Fu, C. Risko, and J.-L. Brédas, "Materials-Scale Implications of Solvent and Temperature on [6,6]-Phenyl-C61-butyric Acid Methyl Ester (PCBM): A Theoretical Perspective," *Advanced Functional Materials*, vol. 23, pp. 5800–5813, 2013.

[177] M. S. Dresselhaus, G. Dresselhaus, and P. C. Eklund, "Raman Scattering in Fullerenes," *Journal of Raman Spectoscopy*, vol. 27, pp. 351–371, 1996.

[178] C. Yang, S. Cho, A. J. Heeger, and F. Wudl, "Heteroanalogues of PCBM: N-Bridged Imino-PCBMs for Organic Field-Effect Transistors," *Angewandte Chemie International Edition*, vol. 48, pp. 1592–1595, 2009.

[179] S. Falke, P. Eravuchir, A. Materny, and C. Lienau, "Raman spectroscopic identification of fullerene inclusions in polymer/fullerene blends," *Journal of Raman Spectoscopy*, vol. 42, pp. 1897–1900, 2011.

[180] H.-H. Liu, S.-H. Lin, and N.-T. Yu, "Resonance Raman enhancement of phenyl ring vibrational modes in phenyl iron complex of myoglobin," *Biophysical Journal*, vol. 57, pp. 851–856, 1990.

[181] C. Zhang, H. Chen, Y. Chen, Z. Wei, and Z. Pu, "DFT Study on Methanofullerene Derivative [6,6]-Phenyl-C61 Butyric Acid Methyl Ester," *Acta Physico-Chimica Sinica*, vol. 24, pp. 1353–1358, 2008.

[182] T. T. Ngo, D. N. Nguyen, and V. T. Nguyen, "Glass transition of PCBM, P3HT and their blends in quenched state," *Advances in Natural Sciences: Nanoscience and Nanotechnology*, vol. 3, p. 045001, 2012.

[183] P. Nagel, V. Pasler, S. Lebedkin, A. Soldatov, C. Meingast, B. Sundqvist, P.-A. Persson, T. Tanaka, K. Komatsu, S. Buga, and A. Inaba, "C_{60} one- and two-dimensional polymers, dimers, and hard fullerite: Thermal expansion, anharmonicity, and kinetics of depolymerization," *Physical Review B*, vol. 60, pp. 16920 – 16927, 1999.

[184] J. R. Olson, K. A. Topp, and R. O. Pohl, "Specific Heat and Thermal Conductivity of Solid Fullerenes," *Science*, vol. 259, pp. 1145 – 1148, 1993.

[185] P. G. Klemens, "Thermal conductivity of inhomogeneous media," *High Temperatures-High Pressures*, vol. 23, pp. 241 – 248, 1991.

[186] T. Matsuo, H. Suga, W. I. F. David, R. M. Ibberson, P. Bernier, A. Zahab, C. Fabre, A. Rassat, and A. Dworkin, "The Heat Capacity of Solid C_{60}," *Solid State Communications*, vol. 83, pp. 711–715, 1992.

[187] C. A. Kennedy and M. A. White, "Unusual thermal conductivity of the negative thermal expansion material, ZrW_2O_8," *Solid State Communications*, vol. 134, pp. 271–276, 2005.

[188] Y. M. Galperin, V. G. Karpov, and V. I. Kozub, "Localized states in glasses," *Advances in Physics*, vol. 189, pp. 669–737, 1989.

[189] W. A. Phillips, "Two-level states in glasses," *Reports on Progress in Physics*, vol. 50, pp. 1657–1708, 1987.

[190] B. Rufflè, D. A. Parshin, E. Courtens, , and R. Vacher, "Boson Peak and its Relation to Acoustic Attenuation in Glasses," *Physical Review Letters*, vol. 100, p. 015501, 2008.

[191] W. P. Beyermann, M. F. Hundley, J. D. Thompson, F. N. Diederich, and G. Grüner, "Low-Temperature Specific Heat of C_{60}," *Physical Review Letters*, vol. 68, pp. 2046–2049, 1992.

[192] P. J. Horoyski, J. A. Wolk, and M. L. W. Thewalt, "The Pressure Dependence of Raman Active Libron Modes in Crystalline C_{60}," *Solid State Communications*, vol. 93, pp. 575–578, 1995.

[193] M. I. Bagatskii, V. V. Sumarokov, M. S. Barabashko, A. V. Dolbin, and B. Sundqvist, "The low-temperature heat capacity of fullerite C_{60}," *Low Temperature Physics*, vol. 41, pp. 630–636, 2015.

[194] W. Krätschmer, L. D. Lamb, K. Fostiropoulos, and D. R. Huffman, "Solid C_{60}: a new form of carbon," *Nature*, vol. 347, pp. 354–358, 1990.

[195] D. A. Neumann, J. R. D. Copley, W. A. Kamitakahara, J. J. Rush, R. L. Cappelletti, N. Coustel, J. E. Fischer, J. P. McCauley, Jr., A. B. Smith, III, K. M. Creegan, and D. M. Cox, "Rotational dynamics and orientational melting of C_{60}: A neutron scattering study," *Solid State Communications*, vol. 96, pp. 8631–8633, 1992.

[196] R. C. Zeller and R. O. Pohl, "Thermal Conductivity and Specific Heat of Noncrystalline Solids," *Physical Review B*, vol. 4, pp. 2029–2041, 1971.

[197] C. Lee and X. Gonze, "*Ab initio* calculation of the thermodynamic properties and atomic temperature factors of SiO_2 α-quartz and stishovite," *Physical Review B*, vol. 51, pp. 8610–2041, 1995.

[198] M. Born and T. von Kármán, "Über Schwingungen in Raumgittern," *Physikalische Zeitschriften*, vol. 13, pp. 297–309, 1912.

[199] C. Hua and A. J. Minnich, "Importance of frequency-dependent grain boundary scattering in nanocrystalline silicon and silicon-germanium thermoelectrics," *Semiconductor Science and Technology*, vol. 29, p. 124004, 2013.

[200] S. Huang, W. C. Qingquan He and, J. Zai, Q. Qiao, and X. Qian, "3D hierarchical $FeSe_2$ microspheres: Controlled synthesis and applications in dye-sensitized solar cells," *Nano Energy*, vol. 15, pp. 205–215, 2015.

[201] L. Qie, W. Chen, H. Xu, X. Xiong, Y. Jiang, F. Zou, X. Hu, Y. Xin, Z. Zhang, and Y. Huang, "Synthesis of functionalized 3D hierarchical porous carbon for high-performance supercapacitors," *Energy & Environmental Science*, vol. 6, pp. 2497–2504, 2013.

[202] J. Bai, X. Li, G. Liu, Y. Qian, and S. Xiong, "Unusual Formation of $ZnCo_2O_4$ 3D Hierarchical Twin Microspheres as a High-Rate and Ultralong-Life Lithium-Ion Battery Anode Material," *Advanced Functional Materials*, vol. 24, pp. 3012–3020, 2014.

[203] M. C. Newton and P. A. Warburton, "ZnO tetrapod nanocrystals," *Materials Today*, vol. 10, pp. 50–54, 2007.

[204] Y. K. Mishra, S. Kaps, A. Schuchardt, I. Paulowicz, X. Jin, D. Gedamu, S. Freitag, M. Claus, S. Wille, A. Kovalev, S. N. Gorb, and R. Adelung, "Fabrication of Macroscopically Flexible and Highly Porous 3D Semiconductor Networks from Interpenetrating Nanostructures by a Simple Flame Transport Approach," *Particle & Particle Systems Characterization*, vol. 30, pp. 775–783, 2013.

[205] J. Gröttrup, I. Paulowicz, A. Schuchardt, V. Kaidas, S. Kaps, O. Lupan, R. Adelung, and Y. K. Mishra, "Three-dimensional flexible ceramics based on interconnected network of highly porous pure and metal alloyed ZnO tetrapods," *Ceramics International*, vol. 42, pp. 8664–8676, 2016.

[206] S. Kahwaji, M. B. Johnson, A. C. Kheirabadi, D. Groulx, and M. A. White, "Stable, low-cost phase change material for building applications:the eutectic mixture of decanoic acid and tetradecanoic acid," *Applied Energy*, vol. 168, pp. 457–464, 2017.

[207] H. Wang, S. in Yi, X. Pu, and C. Yu, "Simultaneously Improving Electrical Conductivity and Thermopower of Polyaniline Composites by Utilizing Carbon Nanotubes as High Mobility Conduits," *ACS Applied Materials & Interfaces*, vol. 7, pp. 9589–9597, 2015.

[208] T. Tsubota, M. Ohtaki, K. Eguchi, and H. Arai, "Thermoelectric properties of Al-doped ZnO as a promising oxide material for high-temperature thermoelectric conversion," *Journal of Materials Chemistry*, vol. 7, pp. 85–90, 1997.

[209] A. B. Djurišíc, A. M. C. Ng, and X. Y. Chen, "ZnO nanostructures for optoelectronics: Material properties and device applications," *Progress in Quantum Electronics*, vol. 34, pp. 191–259, 2010.

[210] Y. Zhang, T. R. Nayak, H. Hong, and W. Cai, "Biomedical Applications of Zinc Oxide Nanomaterials," *Current Molecular Medicine*, vol. 13, pp. 1633–1645, 2013.

[211] S. Takeuchi, H. Iwanaga, and M. Fujii, "Octahedral multiple-twin model of tetrapod ZnO crystals," *Philosophical Magazine A*, vol. 69, pp. 1125–1129, 1994.

[212] C. Ronning, N. G. Shang, I. Gerhards, H. Hofsässi, and M. Seibt, "Nucleation mechanism of the seed of tetrapod ZnO nanostructures," *Journal of Applied Physics*, vol. 98, p. 034307, 2005.

[213] V. Postica, J. Gröttrup, R. Adelung, O. Lupan, A. K. Mishra, N. H. de Leeuw, N. Ababii, J. F. C. Carreira, J. Rodrigues, N. B. Sedrine, M. R. Correia, T. Monteiro, V. Sontea, and Y. K. Mishra, "Multifunctional Materials: A Case Study of the Effects of Metal Doping on ZnO Tetrapods with Bismuth and Tin Oxides," *Advanced Functional Materials*, vol. 27, p. 1604676, 2017.

[214] O. Lupan, V. Postica, J. Gröttrup, A. K. Mishra, N. H. de Leeuw, J. F. C. Carreira, J. Rodrigues, N. B. Sedrine, M. R. Correia, T. Monteiro, V. Cretu, I. Tiginyanu, D. Smazna, Y. K. Mishra, and R. Adelung, "Hybridization of Zinc Oxide Tetrapods for Selective Gas Sensing Applications," *ACS Applied Materials & Interfaces*, vol. 9, pp. 4084–4099, 2017.

[215] D. G. Cahill, "Thermal conductivity measurement from 30 to 750 K: the 3ω method," *Review of Scientific Instruments*, vol. 61, pp. 802–808, 1990.

[216] K. Kanga, Y. K. Koh, C. Chiritescu, X. Zheng, and D. G. Cahill, "Two-tint pump-probe measurements using a femtosecond laser oscillator and sharp-edged optical filters," *Review of Scientific Instruments*, vol. 79, p. 114901, 2008.

[217] D. G. Cahill, P. V. Braun, G. Chen, D. R. Clarke, S. Fan, K. E. Goodson, P. Keblinski, W. P. King, G. D. Mahan, A. Majumdar, H. J. Maris, S. R. Phillpot, E. Pop, and L. Shi, "Nanoscale thermal transport. II. 2003-2012," *Applied Physics Review*, vol. 1, p. 011305, 2014.

[218] M. Ruoho, K. Valset, T. Finstad, and I. Tittonen, "Measurement of thin film thermal conductivity using the laser flash method," *Nanotechnology*, vol. 26, p. 195706, 2015.

[219] M. Fujii, X. Zhang, H. Xie, H. Ago, K. Takahashi, T. Ikuta, H. Abe, and T. Shimizu, "Measuring the thermal conductivity of a single carbon nanotube," *Physical Review Letters*, vol. 95, p. 065502, 2005.

[220] M. Jakubinek, M. White, G. Li, C. Jayasinghe, W. Cho, M. J. Schulz, and V. Shanov, "Thermal and electrical conductivity of tall, vertically aligned carbon nanotube arrays," *Carbon*, vol. 48, pp. 3947–3952, 2010.

[221] M. B. Jakubinek, M. B. Johnson, M. A. White, C. Jayasinghe, G. Li, W. Choe, M. J. Schulz, and V. Shanov, "Thermal and electrical conductivity of array-spun multi-walled carbon nanotube yarns," *Carbon*, vol. 50, pp. 244–248, 2012.

[222] J. F. Niven, M. B. Johnson, S. M. Juckes, M. A. White, N. T. Alvarezd, and V. Shanov, "Influence of annealing on thermal and electrical properties of carbon nanotube yarns," *Carbon*, vol. 99, pp. 485–490, 2016.

[223] J.-H. Pöhls, M. B. Johnson, M. A. White, R. Malik, B. Ruff, C. Jayasinghe, M. J. Schulz, and V. Shanov, "Physical properties of carbon nanotube sheets drawn from nanotube arrays," *Carbon*, vol. 50, pp. 4175–4183, 2012.

[224] T. S. Gspann, S. M. Juckes, J. F. Niven, M. B. Johnson, J. A. Elliott, M. A. White, and A. H. Windle, "High thermal conductivities of carbon nanotube films and micro-fibres and their dependence on morphology," *Carbon*, vol. 114, pp. 160–168, 2017.

[225] K. R. Aaron, "Measurement of the in-plane thermal conductivity of single crystals by the modified parallel thermal conductance technique," Master's thesis, Department of Physics and Astronomy, Clemson University, Clemson, SC, USA, 2005.

[226] H. M. Roder, "A Transient Hot Wire Thermal Conductivity Apparatus for Fluids," *Journal of Research of the National Bureau of Standards*, vol. 86, pp. 457–493, 1981.

[227] D. Sánchez-Rodríguez, J. P. López-Olmedo, J. Farjas, and P. Roura, "Determination of thermal conductivity of powders in different atmospheres by differential scanning calorimetry," *Journal of Thermal Analysis and Calorimetry*, vol. 121, pp. 469–473, 2015.

[228] L. Jin, J. Park, C. Lee, and S. Jeong, "Prediction of the effective thermal conductivity of powder insulation," *Physics Procedia*, vol. 67, pp. 970 – 975, 2015.

[229] L. Huang and M. S. El-Genk, "Thermal conductivity measurements of alumina powders and molded Min-K in vacuum," *Energy Conversion and Management*, vol. 42, pp. 599–612, 2001.

[230] R. K. Kirby, "Thermal Expansion of Polytetrafluoroethylene (Teflon) From -190° to +300° C," *Journal of Research of the National Bureau of Standards*, vol. 57, pp. 91–94, 1956.

[231] A. C1113, "Standard test method for thermal conductivity of refractories by hot wire (platinum resistance thermometer technique)," tech. rep., ASTM, 2013.

[232] COMSOL Multiphysics, "Software COMSOL." `http://www.comsol.com`. [Online; accessed 2017-4-11].

[233] The Engineering ToolBox, "Emissivity Coefficients of some common Materials." `http://www.engineeringtoolbox.com/emissivity-coefficients-d_447.html`. [Online; accessed 2017-4-11].

[234] GoodFellow, "Brass (Cu63/Zn27) - Material Information." `http://www.goodfellow.com/E/Brass.html`. [Online; accessed 2017-4-11].

[235] A. Benisek, E. Dachs, M. Salihović, A. Paunovic, and M. E. Maier, "The vibrational and configurational entropy of α-brass," *The Journal of Chemical Thermodynamics*, vol. 71, pp. 126–132, 2013.

[236] J. W. Park, D. K. Shin, J. Ahn, and J. Y. Lee, "Thermal property of transparent silver nanowire films," *Semiconductor Science and Technology*, vol. 29, p. 015002, 2014.

[237] O. Madelung, U. Rössler, and M. Schulz, eds., *Zinc oxide (ZnO) Debye temperature, heat capacity, density, melting point, vapor pressure, hardness*, pp. 1–5. Berlin, Heidelberg: Springer Berlin Heidelberg, 1999.

[238] T. Engineer, "Emissivity." `http://www.engineering.com/Library/ArticlesPage/tabid/85/ArticleID/151/Emissivity.aspx`, 2006. [Online; accessed 2017-4-11].

[239] M. Takeda, T. Onishi, S. Nakakubo, and S. Fujimoto, "Physical Properties of Iron-Oxide Scales on Si-Containing Steels at High Temperature," *Materials Transactions*, vol. 50, pp. 2242–2246, 2009.

[240] N. J. van der Laag, M. D. Snel, P. C. M. M. Magusin, and G. de With, "Structural, elastic, thermophysical and dielectric properties of zinc aluminate ($ZnAl_2O_4$)," *Journal of the European Ceramic Society*, vol. 24, pp. 2417–2424, 2004.

[241] J.-L. Battaglia and A. Kusiak, "Thermophysical Characterization of a CuO Thin Deposit," *International Journal of Thermophysics*, vol. 28, pp. 1563–1577, 2007.

[242] N. I. Anisimova, G. A. Bordovsky, V. A. Bordovsby, and V. I. Seldayev, "Electrical and Thermal Properties of Bi_2O_3, PbO and Mixed Oxides of Bi_2O_3-PbO System," *International Conference on Solid Dielectrics, Toulouse, France*, 2004.

[243] S. Singh, A. Singh, M. Wan, R. R. Yadav, P. Tandon, S. S. A. Rasool, and B. C. Yadav, "Fabrication of self-assembled hierarchical flower like zinc stannate thin film and its application as liquefied petroleum gas sensor," *Sensors and Actuators B: Chemical*, vol. 205, pp. 102–110, 2014.

[244] C. A. Kennedy, M. A. White, A. P. Wilkinson, and T. Varga, "Low thermal conductivity of the negative thermal expansion material, $HfMo_2O_8$," *Applied Physics Letters*, vol. 90, p. 151906, 2007.

[245] T. Olorunyolemi, A. Birnboim, Y. Carmel, O. C. W. Jr., and I. K. Lloyd, "Thermal Conductivity of Zinc Oxide: From Green to Sintered State," *Journal of the American Ceramic Society*, vol. 85, pp. 1249–1253, 2002.

[246] O. Madelung, U. Rössler, and M. Schulz, eds., *Zinc oxide (ZnO) thermal conductivity*, pp. 1–5. Berlin, Heidelberg: Springer Berlin Heidelberg, 1999.

[247] A. Lekawa-Raus, L. Kurzepa, G. Kozlowski, S. C. Hopkins, M. Wozniak, D. Lukawski, B. A. Glowacki, and K. K. Koziol, "Influence of atmospheric water vapour on electrical performance of carbon nanotube fibres," *Carbon*, vol. 87, pp. 18–28, 2015.

[248] J. P. H. Miller, "The electrical conductivity of zinc oxide," *Physical Review*, vol. 60, pp. 890–895, 1941.

[249] M. S. Dresselhaus, A. Jorio, A. G. S. Filho, and R. Saito, "Defect characterization in graphene and carbon nanotubes using Raman spectroscopy," *Philosophical Transactions of the Royal Society A*, vol. 368, pp. 5355–5377, 2010.

[250] M. S. Dresselhaus, G. Dresselhaus, R. Saito, and A. Jorio, "Raman spectroscopy of carbon nanotubes," *Physics Reports*, vol. 409, pp. 47–99, 2005.

[251] M. A. Pimenta, G. Dresselhaus, M. S. Dresselhaus, L. G. Cançado, A. Jorio, and R. Saito, "Studying disorder in graphite-based systems by Raman spectroscopy," *Physical Chemistry Chemical Physics*, vol. 9, pp. 1276–1291, 2007.

[252] M. W. Wolf and J. J. Martin, "Low Temperature Thermal Conductivity of Zinc Oxide," *physica status solidi (a)*, vol. 17, pp. 215–220, 1973.

[253] Y. Pei, H. Wang, and G. J. Snyder, "Band Engineering of Thermoelectric Materials," *Advanced Materials*, vol. 24, pp. 6125–6135, 2012.

[254] J. M. Cole, K. S. Low, H. Ozoe, P. Stathi, C. Kitamura, H. Kurata, P. Rudolf, and T. Kawase, "Data mining with molecular design rules identifies new class of dyes for dye-sensitised solar cells," *Physical Chemistry Chemical Physics*, vol. 16, pp. 26684–26690, 2014.

[255] H. Lin, H. Chen, J.-N. Shen, L. Chen, and L.-M. Wu, "Chemical Modification and Energetically Favorable Atomic Disorder of a Layered Thermoelectric Material $TmCuTe_2$ Leading to High Performance," *Chemistry - A European Journal*, vol. 20, pp. 15401–15408, 2014.

[256] G. Kresse and J. Furthmüller, "Efficient iterative schemes for *ab initio* total-energy calculations using a plane-wave basis set," *Physical Review B*, vol. 54, pp. 11169–11186, 1996.

[257] P. E. Blöchl, O. Jepsen, and O. K. Andersen, "Improved tetrahedron method for Brillouin zone integration," *Physical Review B*, vol. 49, pp. 16223–16233, 2014.

[258] J. Heyd, G. E. Scuseria, and M. Ernzerhof, "Hybrid functionals based on a screened Coulomb potential," *The Journal of Chemical Physics*, vol. 118, pp. 8207–8215, 2003.

[259] J. Paier, M. Marsman, K. Hummer, and G. Kresse, "Screened hybrid density functionals applied to solids," *The Journal of Chemcial Physics*, vol. 124, p. 154709, 2006.

[260] M. de Jong, W. Chen, T. Angsten, A. Jain, R. Notestine, A. Gamst, M. Sluiter, C. K. Ande, S. van der Zwaag, J. J. Plata, C. Toher, S. Curtarolo, G. Ceder, K. A. Persson, and M. Asta, "Charting the complete elastic properties of inorganic crystalline compounds," *Scientific Data*, vol. 2, p. 150009, 2015.

[261] R. Hill, "The Elastic Behaviour of a Crystalline Aggregate," *Proceedings of the Physical Society. Section A*, vol. 65, pp. 349–354, 1952.

[262] S. P. Ong, W. D. Richards, A. Jain, G. Hautier, M. Kocher, S. Cholia, D. Gunter, V. L. Chevrier, K. A. Persson, and G. Ceder, "Python Materials Genomics (pymatgen): A robust, open-source python library for materials analysis," *Computational Materials Science*, vol. 68, pp. 314–319, 2013.

[263] A. Jain, S. P. Ong, W. Chen, B. Medasani, X. Qu, M. Kocher, M. Brafman, G. Petretto, G.-M. Rignanese, G. Hautier, D. Gunter, and K. A. Persson, "FireWorks: a dynamic workflow system designed for high throughput applications," *Concurrency and Computation: Practice and Experience*, vol. 27, pp. 5037–5059, 2015.

[264] A. van de Walle, M. Asta, and G. Ceder, "The Alloy Theoretic Automated Toolkit: A User Guide ," *Calphad*, vol. 26, pp. 539–553, 2002.

[265] S. B. Zhang and J. E. Northrup, "Chemical Potential Dependence of Defect Formation Energies in GaAs: Application to Ga Self-Diffusion," *Physical Review Letters*, vol. 67, pp. 2339–2343, 1991.

[266] C. Freysoldt, J. Neugebauer, and C. G. van de Walle, "Fully Ab Initio Finite-Size Corrections for Charged-Defect Supercell Calculations," *Physical Review Letters*, vol. 102, p. 016402, 2009.

[267] A. Kuwabara, "Theoretical investigation to thermal equilibrium concentration of point defect through first-principles calculation," *Science and Technology of Advanced Materials*, vol. 8, pp. 519–523, 2007.

[268] S. Grimme, J. Antony, S. Ehrlich, and H. Krieg, "A consistent and accurate ab initio parametrization of density functional dispersion correction (DFT-D) for the 94 elements H-Pu," *The Journal of Chemical Physics*, vol. 132, p. 154104, 2010.

[269] M. S. Christian, S. R. Whittleton, A. O. de-la Roza, and E. R. Johnson, "Chemical bonding and surface interactions in Bi_2Se_3 and Bi_4e_3," *Computational and Theoretical Chemistry*, vol. 1053, pp. 238–244, 2015.

[270] T. Bučko, J. Hafner, S. Lebègue, and J. G. Àngyán, "Improved Description of the Structure of Molecular and Layered Crystals: Ab Initio DFT Calculations with van der Waals Corrections," *The Journal of Physical Chemistry*, vol. 114, pp. 11814–11824, 2010.

[271] Y. Pei, N. A. Heinz, and G. J. Snyder, "Alloying to increase the band gap for improving thermoelectric properties of Ag_2Te," *Journal of Materials Chemistry*, vol. 21, pp. 18256–18260, 2011.

[272] B. Du, H. Li, J. Xu, X. Tang, and C. Uher, "Enhanced Figure-of-Merit in Se-Doped p-Type $AgSbTe_2$ Thermoelectric Compound," *Chemistry of Materials*, vol. 22, pp. 5521–5527, 2010.

[273] T. Plirdpring, K. Kurosaki, A. Kosuga, T. Day, S. Firdosy, V. Ravi, G. J. Snyder, A. Harnwunggmoung, T. Sugahara, Y. Ohishi, H. Muta, and S. Yamanaka, "Chalcopyrite $CuGaTe_2$: A High-Efficiency Bulk Thermoelectric Material," *Advanced Materials*, vol. 24, pp. 3622–3626, 2012.

[274] H. Liu, X. Shi, F. Xu, L. Zhang, W. Zhang, L. Chen, Q. Li, C. Uher, T. Day, and G. J. Snyder, "Copper ion liquid-like thermoelectrics," *Nature Materials*, vol. 11, pp. 422–425, 2012.

[275] L. Zhao, X. Wang, F. Y. Fei, J. Wang, Z. Cheng, S. Dou, J. Wang, and G. J. Snyder, "High thermoelectric and mechanical performance in highly dense $CuS_2 - x$ bulks prepared by a melt-solidification technique," *Journal of Materials Chemistry A*, vol. 3, pp. 9432–9437, 2015.

[276] R. Liu, L. Xi, H. Liu, X. Shi, W. Zhang, and L. Chen, "Ternary compound $CuInTe_2$: a promising thermoelectric material with diamond-like structure," *Chemical Communications*, vol. 48, pp. 3818–3820, 2012.

[277] H. Zhu, G. Hautier, U. Aydemir, Z. M. Gibbs, G. Li, S. Bajaj, J.-H. Pöhls, D. Broberg, W. Chen, A. Jain, M. A. White, M. Asta, G. J. Snyder, K. Persson, and G. Ceder, "Computational and experimental investigation of $TmAgTe_2$ and XYZ_2 compounds, a new group of thermoelectric materials identified by first-principles high-throughput screening," *Journal of Materials Chemistry C*, vol. 3, pp. 10554–10565, 2015.

[278] C. Herring and E. Vogt, "Transport and Deformation-Potential Theory for Many-Valley Semiconductors with Anisotropic Scattering," *Physical Review*, vol. 101, pp. 944–961, 1956.

[279] L. Pauling, "The principles determining the structure of complex ionic crystals," *Journal of American Chemical Society*, vol. 51, pp. 1010–1026, 1929.

[280] G. Sposito, *The Chemistry of Soils*. Berlin Heidelheim: Oxford University Press, 3 ed., 2016.

[281] R. D. Shannon, "Revised Effective Ionic Radii and Systematic Studies of Interatomic Distances in Halides and Chalcogenides," *Acta Crystallographica Section A*, vol. A32, pp. 751–767, 1976.

[282] J. Slater, "Atomic Radii in Crystals," *The Journal of Chemical Physics*, vol. 41, pp. 3199–3204, 1964.

[283] L. Gulay, I. Olekseyuk, and A. Pietraszko, "Crystal structure of the $RAgTe_2$ (R =Y, Tb, Dy, Ho and Er) compounds," *Journal of Alloys and Compounds*, vol. 424, pp. 159–163, 2006.

[284] L. Gulay, J. Stępién-Damm, M. Daszkiewicz, and A. Pietraszko, "Crystal structure of the $TmAgTe_2$ compound," *Journal of Alloys and Compounds*, vol. 431, pp. L1–L3, 2007.

[285] A. D. LaLonde, T. Ikeda, and G. J. Snyder, "Rapid consolidation of powdered materials by induction hot pressing," *Review of Scientific Instruments*, vol. 82, p. 025104, 2011.

[286] G. G. Amatucci, J. M. Tarascon, and L. C. Klein, "CoO_2, The End Member of the Li_xCoO_2 Solid Solution," *Journal of Electrochemical Society*, vol. 143, pp. 1114–1123, 1996.

[287] C. Delmas, C. Fouassie, and P. Hagenmuller, "Structural classification and properties of the layered oxides," *Physica B+C*, vol. 99, pp. 81–85, 1980.

[288] F. Ortmann, F. Bechstedt, and W. G. Schmidt, "Semiempirical van der Waals correction to the density functional description of solids and molecular structures," *Physical Review B*, vol. 72, p. 205101, 2006.

[289] A. O. de-la Roza and E. R. Johnson, "Van der Waals interactions in solids using the exchange-hole dipole moment model," *The Journal of Chemical Physics*, vol. 136, p. 174109, 2012.

[290] M.-P. Pardo, M. Julien-Pouzol, and M. J. Flahaut, "Les composés $AgLTe_2$ formés par les éléments des terres rares," *Chimie Minérale*, vol. 273, pp. 599–602, 1973.

[291] L. D. Gulay, M. Daszkiewicz, and V. Y. Shemet, "Crystal structure of $\sim RCu_3S_3$ and $\sim RCuTe_2$ (R=GdLu) compounds," *Journal of Solid State Chemistry*, vol. 186, pp. 142–148, 2012.

[292] U. Aydemir, J.-H. Pöhls, H. Zhu, G. Hautier, S. Bajaj, Z. M. Gibbs, W. Chen, G. Li, S. Ohno, D. Broberg, S. D. Kang, M. Asta, G. Ceder, M. A. White, K. Persson, A. Jain, and G. J. Snyder, "$YCuTe_2$: a member of a new class of thermoelectric materials with $CuTe_4$-based layered structure," *Journal of Materials Chemistry A*, vol. 4, pp. 2461–2472, 2016.

[293] L. Akselrud and Y. Grin, "WinCSD: software package for crystallographic calculations (Version 4)," *Journal of Applied Crystallography*, vol. 47, pp. 803–805, 2014.

[294] M.-P. Pardo and J. Flahaut, "High tellurides of the rare earth elements of the L_2-Te_5 and LTe_3 types," *Bulletin de la Societe Chimique de France*, vol. 10, pp. 3658–3664, 1967.

[295] J. Wang, H. Feng, K. Chen, W. Fana, and Q. Yang, "Solution-phase catalytic synthesis, characterization and growth kinetics of Ag_2SCdS matchstick-like heteronanostructures," *Dalton Transactions*, vol. 43, pp. 3990–3998, 2014.

[296] R. Harpeness, O. Palchik, A. Gedanken, V. Palchik, S. Amiel, M. A. Slifkin, and A. M. Weiss, "Preparation and Characterization of Ag_2E (E = Se, Te) Using the Sonochemically Assisted Polyol Method," *Chemistry of Materials*, vol. 14, pp. 2094–2102, 2002.

[297] S. A. Aliev, F. F. Aliev, and Z. S. Gasanov, "Thermodynamic parameters of diffuse phase transitions in Ag_2Te," *Physics of the Solid State*, vol. 40, pp. 1540–1543, 1998.

[298] S. D. Kang, S. A. Danilkin, U. Aydemir, M. Avdeev, A. Studer, and G. J. Snyder, "Apparent critical phenomena in the superionic phase transition of $Cu_{2-x}Se$," *New Journal of Physics*, vol. 18, p. 013024, 2016.

[299] Y. He, T. Day, T. Zhang, X. S. Huili Liu, L. Chen, and G. J. Snyder, "High Thermoelectric Performance in Non-Toxic Earth-Abundant Copper Sulfide," *Advanced Materials*, vol. 26, pp. 3974–3978, 2014.

[300] S. Ballikaya, H. Chi, J. R. Salvador, and C. Uher, "Thermoelectric properties of Ag-doped Cu_2Se and Cu_2Te," *Journal of Materials Chemistry A*, vol. 1, pp. 12478–12484, 2013.

[301] N. Vouroutzis and C. Manolikas, "Phase Transformations and Discommensurations in Hexagonal Cuprous Telluride," *physica status solidi (a)*, vol. 115, pp. 399–412, 1989.

[302] A. G. Khachaturyan, "Ordering in Substitutional and Interstitial Solid Solutions," *Progress in Materials Science*, vol. 22, pp. 1–150, 1978.

[303] L. D. Landau and E. M. Lifshitz, *Statistical Physics - Part 1*. Oxford, England: Pergamon Press Ltd., 3 ed., 1980.

[304] M. T. Dove, *Structure and Dynamics - An atomic view of materials*. Oxford, England: Oxford University Press, 1 ed., 2003.

[305] W. G. Zeier, A. Zevalkink, Z. M. Gibbs, G. Hautier, M. G. Kanatzidis, and G. J. Snyder, "Thinking Like a Chemist: Intuition in Thermoelectric Materials," *Angewandte Chemie International Edition*, vol. 55, pp. 6826–6841, 2016.

[306] K. Honma and K. Iida, "Specific Heat of Superionic Conductor Ag_2S, Ag_2Se and Ag_2Te in α-Phase," *Journal of the Physical Society of Japan*, vol. 56, pp. 1828–1836, 1987.

[307] B. Saparov, F. Hong, J.-P. Sun, H.-S. Duan, W. Meng, S. Cameron, I. G. Hill, Y. Yan, , and D. B. Mitzi, "Thin-Film Preparation and Characterization of $Cs_3Sb_2I_9$: A Lead-Free Layered Perovskite Semiconductor," *Chemistry of Materials*, vol. 27, pp. 5622–5632, 2015.

[308] J. P. C. Ruff, J. P. Clancy, A. Bourque, M. A. White, M. Ramazanoglu, J. S. Gardner, Y. Qiu, J. R. D. Copley, M. B. Johnson, H. A. Dabkowska, and B. D. Gaulin, "Spin Waves and Quantum Criticality in the Frustrated XY Pyrochlore Antiferromagnet $Er_2Ti_2O_7$," *Physical Review Letters*, vol. 101, p. 147205, 2008.

[309] J. F. Niven, M. B. Johnson, A. Bourque, P. J. Murray, D. D. James, H. A. Dąbkowska, B. D. Gaulin, and M. A. White, "Magnetic phase transitions and magnetic entropy in the XY antiferromagnetic pyrochlores $(Er_{1x}Y_x)_2Ti_2O_7$," *Proceedings of the Royal Society A*, vol. 470, 2014.

[310] V. V. Novikov, N. A. Zhemoedov, N. V. Mitroshenkov, and A. V. Matovnikov, "Anomalies in thermal expansion and heat capacity of TmB_{50} at low temperatures: magnetic phase transition and crystal electric field effect," *Dalton Transactions*, vol. 45, pp. 17447–17452, 2016.

[311] I. Kudman and E. F. Steigmeier, "Thermal Conductivity and Seebeck Coefficient of InP," *Physical Review*, vol. 133, pp. A1665–A1667, 1964.

[312] J. V. Zaikina, K. A. Kovnir, A. N. Sobolev, I. A. Presniakov, V. G. Kytin, V. A. Kulbachinskii, A. V. Olenev, O. I. Lebedev, G. V. Tendeloo, E. V. Dikarev, and A. V. Shevelkov, "Highly Disordered Crystal Structure and Thermoelectric Properties of Sn_3P_4," *Chemistry of Materials*, vol. 20, pp. 2476–2483, 2008.

[313] Y. Kumashiro, M. Hirabayashi, T. Koshiro, and Y. Okada, "Thermoelectric properties of boron phosphide," *Journal of the Less Common Metals*, vol. 143, pp. 159–165, 1988.

[314] A. Watcharapasorn, R. C. DeMattei, R. S. Feigelson, T. Caillat, A. Borshchevsky, G. J. Snyder, and J.-P. Fleurial, "Thermoelectric properties of boron phosphide," *Journal of Applied Physics*, vol. 86, pp. 6213–6217, 1999.

[315] H. J. L. J. Zhang, L. Cheng, J. Wei, J. H. Liang, D. D. Fan, P. H. Jiang, L. Sun, and J. Shi, "High thermoelectric performance can be achieved in black phosphorus," *Journal of Materials Chemistry C*, vol. 4, pp. 991–998, 2016.

[316] T. Yi, G. Zhang, N. Tsujii, J.-P. Fleurial, A. Zevalkink, G. J. Snyder, N. Grønbech-Jensen, and S. M. Kauzlarich, "Phase Characterization, Thermal Stability, High-Temperature Transport Properties, and Electronic Structure of Rare-Earth Zintl Phosphides $Eu_3M_2P_4$ (M = Ga, In)," *Inorganic Chemistry*, vol. 52, pp. 3787–3794, 2013.

[317] W. D. Thompson, R. Vaddi, and B. E. W. Jr., "Low thermal conductivity in nanocrystalline Zn_3P_2," *Journal of Alloys and Compounds*, vol. 687, pp. 813–820, 2016.

[318] V. S. Babu, P. R. Vaya, and J. Sobhanadri, "Electrical and thermoelectrical properties of Zn_3P_2 films grown by the hot wall epitaxy technique," *Journal of Applied Physics*, vol. 64, pp. 1922–1926, 1988.

[319] W. Tang, E. Sanville, and G. Henkelman, "A grid-based Bader analysis algorithm without lattice bias," *Journal of Physics: Condensed Matter*, vol. 21, p. 084204, 2009.

[320] X. Gonze, B. Amadon, P.-M. Anglade, J.-M. Beuken, F. Bottin, P. Boulanger, F. Bruneval, D.Caliste, R. Caracas, M. T. Deutsch, L. Genovese, P. Ghosez, M. Giantomassi, S. Goedecker, D. Hamann, P. Hermet, F. Jollet, G. Jomard, S. Leroux, M. Mancini, S. Mazevet, M. J. T. Oliveira, G. Onida, Y. Pouillon, T. Rangel, G.-M. Rignanese, D. Sangalli, R. Shaltaf, M. Torrent, M. J. Verstraete, G. Zerah, and J. W. Zwanziger, "ABINIT: First-principles approach to material and nanosystem properties," *Computer Physics Communications*, vol. 180, pp. 2582–2615, 2009.

[321] X. Gonze, "First-principles responses of solids to atomic displacements and homogeous electric fields: Implementation of a conjugate-gradient algorithm," *Physical Review B*, vol. 55, pp. 10337–10354, 1997.

[322] X. Gonze and C. Lee, "Dynamical matrices, Born effective charges, dielectric permittivity tensors, and interatomic force constants from density-functional perturbation theory," *Physical Review B*, vol. 55, pp. 10355–10368, 1997.

[323] X. Gonze, F. Jollet, F. A. Araujo, D. Adams, B. Amadon, T. Applencourt, C. Audouze, J.-M. Beuken, J. Bieder, A. Bokhanchuk, E. Bousquet, F. Bruneval, D. Caliste, M. Côté, F. Dahm, F. D. Pieve, M. Delaveau, M. D. Gennaro, B. Dorado, C. Espejo, G. Geneste, L. Genovese, A. Gerossier, M. Giantomassi, Y. Gillet, D. R. Hamann, L. He, G. Jomard, J. L. Janssen, S. L. Roux, A. Levitt, A. Lherbier, F. Liu, I. Lukačević, A. Martin, C. Martins, M. J. T. Oliveira, S. Poncé, Y. Pouillon, T. Rangel, G.-M. Rignanese, A. Romero, B. Rousseau, O. Rubel, A. A. Shukri, M. Stankovski, M. Torrent, M. J. V. Setten, B. V. Troeye, M. J. Verstraete, D. Waroquiers, J. Wiktor, B. Xu, A. Zhou, and J. W. Zwanziger, "Recent developments in the ABINIT software package," *Computer Physics Communications*, vol. 205, pp. 106–131, 2016.

[324] J. P. Perdew and M. Levy, "Physical Content of the Exact Kohn-Sham Orbital Energies: Band Gaps and Derivative Discontinuities," *Physical Review Letters*, vol. 51, pp. 1884–1887, 1983.

[325] L. J. Sham and M. Schlüter, "Density-Functional Theory of the Energy Gap," *Physical Review Letters*, vol. 51, pp. 1888–1891, 1983.

[326] W. Weber, "Adiabatic bond charge model for the phonons in diamond, Si, Ge, and α-Sn," *Physical Review B*, vol. 15, pp. 4789 – 4803, 1977.

[327] D. Strauch and B. Dorner, "Phonon dispersion in GaAs," *Journal of Physics: Condensed Matter*, vol. 2, pp. 1457 – 1474, 1990.

[328] O. Madelung, U. Rössler, and M. Schulz, eds., *Gallium phosphide (GaP), transport mechanisms, electrical and thermal conductivity*, pp. 1–8. Berlin, Heidelberg: Springer Berlin Heidelberg, 2002.

[329] Y. Kumashiro, T. Mitsuhashi, S. Okaya, F. Muta, T. Koshiro, Y. Takahashi, and M. Mirabayashi, "Thermal conductivity of a boron phosphide single-crystal wafer up to high temperature," *Journal of Applied Physics*, vol. 65, pp. 2417 – 2418, 1988.

[330] Y. Pei, Z. M. Gibbs, A. Gloskovskii, B. Balke, W. G. Zeier, and G. J. Snyder, "Optimum Carrier Concentration in n-Type PbTe Thermoelectrics," *Advanced Energy Materials*, vol. 4, p. 1400486, 2014.

[331] F. Gillot, S. Boyanov, L. Dupont, M.-L. Doublet, M. Morcrette, L. Monconduit, and J.-M. Tarascon, "Electrochemical Reactivity and Design of NiP_2 Negative Electrodes for Secondary Li-Ion Batteries," *Chemistry of Materials*, vol. 17, pp. 6327–6337, 2005.

[332] P. C. Donohue, T. A. Bither, and H. S. Young, "High-Pressure Synthesis of Pyrite-Type Nickel Diphosphide and Nickel Diarsenide," *Inorganic Chemistry*, vol. 7, pp. 998–1001, 1968.

[333] Y. W. Gao, Y. Z. He, and L. L. Zhu, "Impact of grain size on the Seebeck coefficient of bulk polycrystalline thermoelectric materials," *Chinese Science Bulletin*, vol. 55, pp. 16–21, 2010.

[334] K. Kishimoto and T. Koyanagi, "Preparation of sintered degenerate n-type PbTe with a small grain size and its thermoelectric properties," *Journal of Applied Physics*, vol. 92, pp. 2544–2549, 2002.

[335] A. F. May, E. S. Toberer, and G. J. Snyder, "Transport properties of the layered Zintl compound $SrZnSb_2$," *Journal of Applied Physics*, vol. 106, p. 013706, 2009.

[336] A. J. Garza and G. E. Scuseria, "Predicting Band Gaps with Hybrid Density Functionals," *arXiv [1608.04796v3]*, 2016.

[337] G. S. Nolas, J. L. Cohn, G. A. Slack, and S. B. Schujman, "Semiconducting Ge clathrates: Promising candidates for thermoelectric applications," *Applied Physics Letters*, vol. 73, pp. 178–180, 1998.

[338] C. Uher, "Skutterudites: Prospective novel thermoelectrics," in *Semiconductors and Semimetals* (T. M. Tritt, ed.), ch. 5, pp. 139–153, San Diego: Academic, 2000.

[339] A. Ammar, C. Cros, M. Pouchard, N. Jaussaud, J.-M. Bassat, G. Villeneuve, M. Duttine, M. Ménétriera, and E. Reny, "On the clathrate form of elemental silicon, $Si_1 36$: preparation and characterisation of $Na_xSi_1 36$ ($x \rightarrow 0$)," *Solid State Sciences*, vol. 8, pp. 393–400, 2004.

[340] J. Gryko, R. F. Marzke, J. G. A. Lamberton, T. M. Tritt, M. Beekman, and G. S. Nolas, "Electron structure and temperature-dependent shifts in ^{133}Cs NMR spectra of the Cs_8Ge_{136} clathrate," *Physical Review B*, vol. 71, p. 115208, 2005.

[341] A. D. Ritchie, M. B. Johnson, J. F. Niven, M. Beekman, G. S. Nolas, J. Gryko, and M. A. White, "Influence of guest loading on thermal properties of Na_xSi_{136} clathrates," *Journal of Physics: Condensed Matter*, vol. 25, p. 435401, 2013.

[342] S. Stefanoski, C. D. Malliakas, M. G. Kanatzidis, and G. S. Nolas, "Synthesis and Structural Characterization of Na_xSi_{136} ($0 < x \leq 24$) Single Crystals and Low-Temperature Transport of Polycrystalline Specimens," *Inorganic Chemistry*, vol. 51, pp. 8686–8692, 2012.

[343] G. S. Nolas, C. A. Kendziora, J. Gryko, J. Dong, C. W. Myles, A. Poddar, and O. F. Sankey, "Raman scattering study of stoichiometric Si and Ge type II clathrates," *Jorunal of Applied Physics*, vol. 92, pp. 7225–7230, 2002.

[344] A. M. Guloy, R. Ramlau, Z. Tang, W. Schnelle, M. Baitinger, and Y. Grin, "A guest-free germanium clathrate," *Nature*, vol. 443, pp. 320–323, 2006.

[345] B. Böhme, S. Hoffmann, M. Baitinger, and Y. Grin, "Application of *n*-Dodecyltrimethylammonium Chloride for the Oxidation of Intermetallic Phases," *Zeitschrift für Naturforschung*, vol. 66b, pp. 230–238, 2011.

[346] A. M. Guloy, Z. Tang, R. Ramlau, B. Böhme, M. Baitinger, and Y. Grin, "Synthesis of the Clathrate-II $K_{8.6(4)}Ge_{136}$ by Oxidation of K_4Ge_9 in an Ionic Liquid," *European Journal of Inorganic Chemistry*, vol. 17, pp. 2455–2458, 2009.

[347] B. Böhme, *Neue Präparationswege für intermetallische Verbindungen*. Berlin: Logos Verlag, 1 ed., 2010.

[348] B. Böhme, M. Reibold, G. Auffermann, H. Lichte, M. Baitinger, and Y. Grin, "Preparation of anionic clathrate-II $K_{24-x}Ge_{136}$ by filling of Ge(cF136)," *Zeitschrift für Kristallograhie*, vol. 229, pp. 677–686, 2014.

[349] A. D. Ritchie, *Characterization of Na-Loaded Type II Si and Ge Clathrates: A Systematic Structure-Property Evaluation of Thermoelectric Materials*. PhD thesis, Department of Chemistry, Dalhousie University, 2011.

[350] Y. Wang, P. Wang, D. Zhao, B. Hu, Y. Du, H. Xu, and K. Chang, "Thermodynamic description of the GeNa and GeK systems using the CALPHAD approach supported by first-principles calculations," *CALPHAD: Computer Coupling of Phase Diagrams and Thermochemistry*, vol. 37, pp. 72–76, 2012.

[351] J. Erling Grovenstein and R. W. Stevens, "Carbanions. 111. Cleavage of Tetraalkylammonium Halides by Sodium in Liquid Ammonia," *Journal of the American Chemical Society*, vol. 81, pp. 4850–4857, 1959.

[352] CrystalMaker Software, "CrystalDiffract for Windows," 2011.

[353] A. Karttunen and T. F. Fässler, "Structural Principles and Thermoelectric Properties of Polytypic Group 14 Clathrate-II Frameworks," *ChemPhysChem*, vol. 14, pp. 1807–1817, 2013.

[354] U. Schwarz, A. Wosylus, B. Böhme, M. Baitinger, M. Hanfland, and Y. Grin, "A 3D Network of Four-Bonded Germanium: A Link between Open and Dense," *Angewandte Chemie International Edition*, vol. 47, pp. 6790 –6793, 2008.

[355] H. Zhang, W. Li, X. Xu, G. Mu, X. Xie, and F. Huang, "Structure and properties of type-II clathrate $Cs_8Na_{16x}Tl_xGe_{136}$," *Dalton Transactions*, vol. 44, pp. 16937 –16945, 2015.

[356] J. Dong and O. F. Sankey, "Theoretical study of two expanded phases of crystalline germanium: clathrate-I and clathrate-II," *Journal of Physics: Condensed Matter*, vol. 11, pp. 6129–6145, 1999.

[357] C. W. Myles, J. Dong, and O. F. Sankey, "Rattling guest atoms in Si, Ge, and Sn-based type-II clathrate materials," *physica status solidi*, vol. 239, pp. 26–34, 2003.

[358] D. R. Brown, T. Day, T. Caillat, and G. J. Snyder, "Chemical Stability of $(Ag,Cu)_2Se$: a Historical Overview," *Journal of Electronic Materials*, vol. 42, pp. 2014–2019, 2013.